

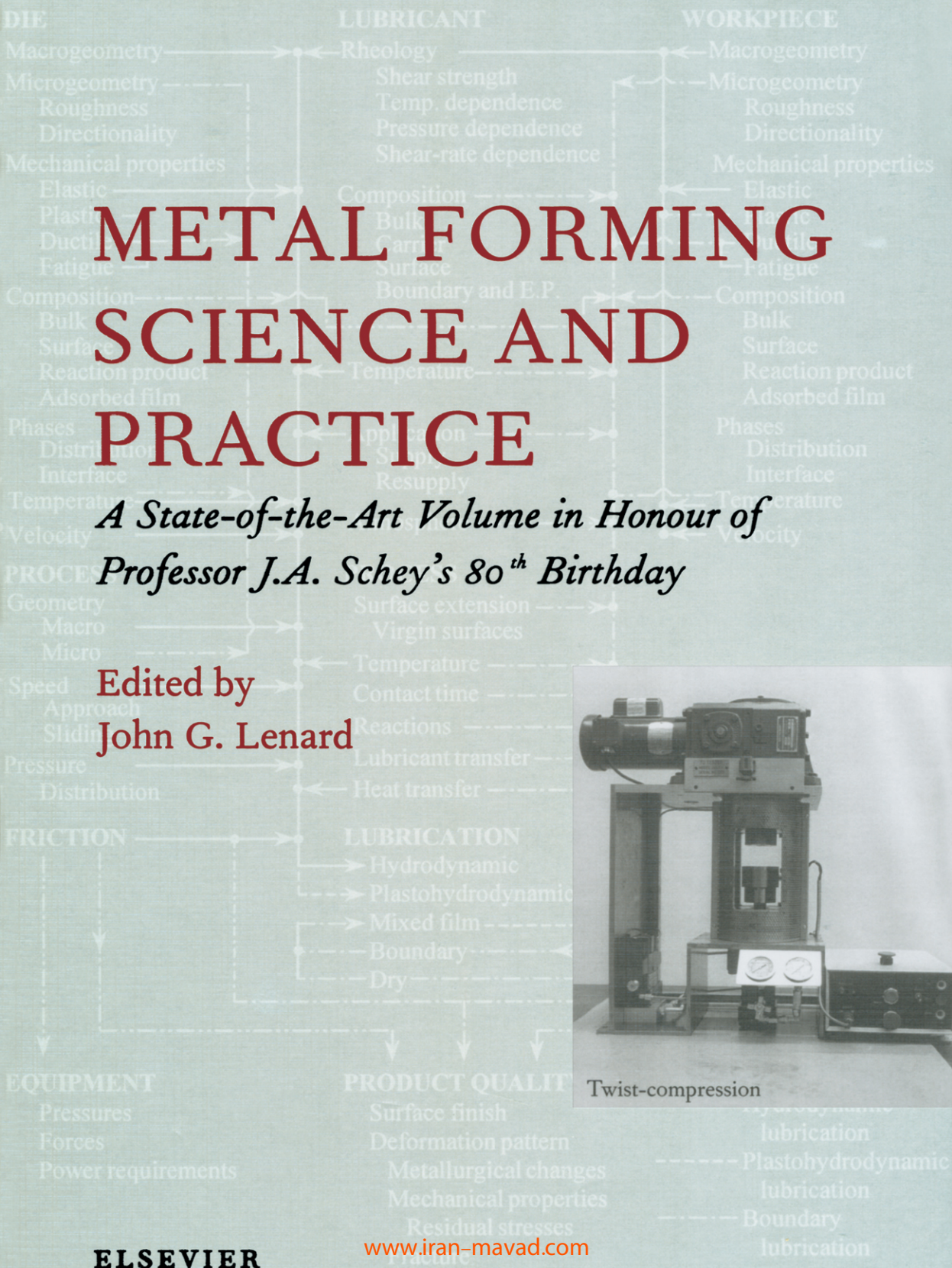
به نام خدا



# مرکز دانلود رایگان مهندسی متالورژی و مواد

[www.Iran-mavad.com](http://www.Iran-mavad.com)





**ELSEVIER**

[www.iran-mavad.com](http://www.iran-mavad.com)

مرجع دانشجویان و مهندسين مواد



# **METAL FORMING SCIENCE AND PRACTICE**

**A State-of-the-Art Volume in Honour of  
Professor J.A. Schey's 80<sup>th</sup> Birthday**

## **Elsevier Science Internet Homepage:**

<http://www.elsevier.com>

## **ScienceDirect Homepage:**

<http://www.sciencedirect.com>

## **Related Journals**

*Journal of Tribology*

*Journal of Materials Processing Technology*

## **To Contact the Publisher**

Elsevier Science welcomes enquiries concerning publishing proposals: books, journal special issues, conference proceedings, etc. All formats and media can be considered. Should you have a publishing proposal you wish to discuss, please contact, without obligation, the publisher responsible for Elsevier's material science publishing programme:

David Sleeman  
Publishing Editor  
Elsevier Science Ltd  
The Boulevard,  
Langford Lane,  
Kidlington, Oxford  
OX5 1GB

Phone: +44 1865 843265  
Fax: +44 1865 843920  
Email: [d.sleeman@elsevier.com](mailto:d.sleeman@elsevier.com)

General enquiries including placing orders, should be directed to Elsevier's Regional Sales Offices – please access the Elsevier homepage for full contact details (homepage at the top of this page).



# METAL FORMING SCIENCE AND PRACTICE

A State-of-the-Art Volume in Honour of  
Professor J.A. Schey's 80<sup>th</sup> Birthday

*This volume is a tribute to Professor Schey - pioneer in the field of  
metal forming - from his students, colleagues and friends for his years  
of dedication, mentoring and inspiration*

Edited by

**J.G. Lenard**

*Department of Mechanical Engineering,  
University of Waterloo, Ontario, Canada*



2002

ELSEVIER

AMSTERDAM – BOSTON – LONDON – NEW YORK – OXFORD – PARIS  
SAN DIEGO – SAN FRANCISCO – SINGAPORE – SYDNEY – TOKYO

[www.iran-mavad.com](http://www.iran-mavad.com)

مرجع دانشجویان و مهندسين مواد

ELSEVIER SCIENCE Ltd  
The Boulevard, Langford Lane  
Kidlington, Oxford OX5 1GB, UK

© 2002 Elsevier Science Ltd. All rights reserved.

This work is protected under copyright by Elsevier Science, and the following terms and conditions apply to its use:

#### Photocopying

Single photocopies of single chapters may be made for personal use as allowed by national copyright laws. Permission of the Publisher and payment of a fee is required for all other photocopying, including multiple or systematic copying, copying for advertising or promotional purposes, resale, and all forms of document delivery. Special rates are available for educational institutions that wish to make photocopies for non-profit educational classroom use.

Permissions may be sought directly from Elsevier Science via their homepage (<http://www.elsevier.com>) by selecting 'Customer support' and then 'Permissions'. Alternatively you can send an e-mail to: [permissions@elsevier.com](mailto:permissions@elsevier.com), or fax to: (+44) 1865 853333.

In the USA, users may clear permissions and make payments through the Copyright Clearance Center, Inc., 222 Rosewood Drive, Danvers, MA 01923, USA; phone: (+1) (978) 7508400, fax: (+1) (978) 7504744, and in the UK through the Copyright Licensing Agency Rapid Clearance Service (CLARCS), 90 Tottenham Court Road, London W1P 0LP, UK; phone: (+44) 207 631 5555; fax: (+44) 207 631 5500. Other countries may have a local reprographic rights agency for payments.

#### Derivative Works

Tables of contents may be reproduced for internal circulation, but permission of Elsevier Science is required for external resale or distribution of such material.

Permission of the Publisher is required for all other derivative works, including compilations and translations.

#### Electronic Storage or Usage

Permission of the Publisher is required to store or use electronically any material contained in this work, including any chapter or part of a chapter.

Except as outlined above, no part of this work may be reproduced, stored in a retrieval system or transmitted in any form or by any means, electronic, mechanical, photocopying, recording or otherwise, without prior written permission of the Publisher.

Address permissions requests to: Elsevier Science Global Rights Department, at the fax and e-mail addresses noted above.

#### Notice

No responsibility is assumed by the Publisher for any injury and/or damage to persons or property as a matter of products liability, negligence or otherwise, or from any use or operation of any methods, products, instructions or ideas contained in the material herein. Because of rapid advances in the medical sciences, in particular, independent verification of diagnoses and drug dosages should be made.

First edition 2002

Library of Congress Cataloging in Publication Data

Metal forming science and practice : a state-of-the-art volume in honour of Professor J.A.

Schey's 80<sup>th</sup> birthday / edited by J.G. Lenard.

p. cm.

Includes bibliographical references and index.

ISBN 0-08-044024-X (alk. paper)

1. Metal-work. I. Lenard, John G., 1937- II. Schey, John A.

TS205 .M4663 2002

671--dc21

2002029419

British Library Cataloguing in Publication Data

A catalogue record from the British Library has been applied for.

ISBN: 0-08-044024-X

© The paper used in this publication meets the requirements of ANSI/NISO Z39.48-1992 (Permanence of Paper).

Printed in The Netherlands.

[www.iran-mavad.com](http://www.iran-mavad.com)

مرجع دانشجویان و مهندسين مواد



## Preface

This publication is to honour the contribution to science and education of one of the outstanding academics of our day, Distinguished Professor Emeritus John A. Schey, on the occasion of his 80<sup>th</sup> birthday. The contributors to this book are among the countless researchers who have read, studied and learned from Professor Schey's work, which includes a most impressive list of publications: books, research monographs, invited papers, keynote papers, papers in scientific journals and in conferences, too many to list in this monograph. The topics in these publications cover an equally impressive range; they deal with manufacturing, sheet and bulk metal forming and tribology, among others. In each, the insight of Professor Schey is evident. New ideas abound and the inspiration they give has been acknowledged in countless instances.

Professor Schey's background, educational history, and academic and industrial experience are well known to his friends and colleagues. Attention is drawn to the appreciation expressed by his former students, in Chapter 2, entitled "Recollections". These personal comments indicate clearly and better than anything else, his contribution to the lives of many engineers. It is also enlightening to read the acknowledgements from the many MASc and PhD theses Professor Schey supervised. Without exception, his students recount a highly enjoyable learning experience. When contacted, all of them were pleased and eager to write about their academic experience.

I also wish to express my personal feelings in organizing and compiling this book: it was pure pleasure. The co-operation offered by all contributors and the quality of the content of their chapters made the production process easy. I am grateful to them all.

I am pleased to be able to offer this volume to Professor Schey and I am certain that his students, the present contributors, his colleagues and many friends join me in wishing him a very happy 80<sup>th</sup> birthday.

John G. Lenard  
May 6, 2002

This Page Intentionally Left Blank



# Table of Contents

## *Chapter 1*

<b>Recollections (graduate students)</b>	<b>1</b>
--	----------

## *Chapter 2*

<b>John Schey and Value-Added Manufacturing (Brzustowski)</b>	<b>9</b>
---	----------

<b>2.1 STRIKING CLARITY</b>	<b>9</b>
<b>2.2 AN ECONOMIC FACT</b>	<b>9</b>
<b>2.3 RICH IN IDEAS</b>	<b>10</b>
<b>2.4 JUST ONE OF MANY CONTRIBUTIONS</b>	<b>11</b>
<b>REFERENCES</b>	<b>11</b>

## *Chapter 3*

<b>Introduction – The Scheme of the Book (Lenard)</b>	<b>13</b>
---	-----------

<b>3.1 INTRODUCTION</b>	<b>13</b>
<b>3.2 THE TECHNICAL PRESENTATIONS</b>	<b>13</b>
<b>REFERENCES</b>	<b>18</b>

## *Chapter 4*

<b>Surface Finish and Friction in Cold Metal Rolling (Sutcliffe)</b>	<b>19</b>
--	-----------

<b>4.1 INTRODUCTION</b>	<b>19</b>
<b>4.2 UNLUBRICATED ROLLING</b>	<b>21</b>
4.2.1 Without bulk deformation	21
4.2.2 With bulk deformation	22
4.2.3 Random rough surfaces	28
<b>4.3 MIXED LUBRICATION</b>	<b>29</b>
4.3.1 Modelling	29
4.3.1.1 Asperity deformation	29
4.3.1.2 Hydrodynamic equations	29
4.3.1.3 Method of solution	30
4.3.1.4 Friction modelling	31
4.3.1.5 Summary of models	32
4.3.2 Experimental methods	33
4.3.3 Theoretical results and comparison with experiments	35
4.3.4 Other experimental results	41

4.3.5	Foil and temper rolling	42
4.3.6	Thermal effects	43
<b>4.4</b>	<b>MICRO-PLASTO-HYDRODYNAMIC LUBRICATION (MPHL)</b>	<b>43</b>
4.4.1	Micro-plasto-hydrodynamic lubrication in the mixed lubrication regime	44
4.4.2	Micro-plasto-hydrodynamic lubrication of pits	45
4.4.2.1	Measurement of pit geometry	45
4.4.2.2	Modelling and comparison with experiments	47
<b>4.5</b>	<b>BOUNDARY LUBRICATION</b>	<b>50</b>
<b>4.6</b>	<b>TRANSFER LAYERS</b>	<b>51</b>
<b>4.7</b>	<b>CONCLUSIONS</b>	<b>54</b>
	<b>REFERENCES</b>	<b>55</b>

### Chapter 5

<b>Direct Observation of Interface for Tribology in Metal Forming (Azushima)</b>	<b>61</b>
<b>5.1 DIRECT OBSERVATION OF INTERFACE IN SHEET DRAWING</b>	<b>62</b>
5.1.1 Apparatus for direct observation	63
5.1.2 Direct observation of micro-PHL	64
5.1.3 Mechanism of micro-PHL	67
5.1.4 Speed dependence of coefficient of friction under micro-PHL	69
<b>5.2 DIRECT OBSERVATION OF INTERFACE IN FLAT TOOL DRAWING</b>	<b>71</b>
5.2.1 Direct observation of the interface	72
5.2.2 Pressure dependence of the coefficient of friction	73
5.2.3 Effect of surface topography of the workpiece	78
<b>REFERENCES</b>	<b>83</b>

### Chapter 6

<b>An Examination of the Coefficient of Friction (Lenard)</b>	<b>85</b>
<b>6.1 INTRODUCTION</b>	<b>85</b>
<b>6.2 FUNDAMENTAL IDEAS</b>	<b>86</b>
6.2.1 Mechanisms of friction	86
6.2.2 The adhesion hypothesis	87
6.2.3 The parameters affecting surface interactions	87
6.2.4 Determining the coefficient of friction	88
6.2.4.1 Experimental approach	88
6.2.4.2 Semi-empirical formulae - cold rolling	90
6.2.4.3 Inverse calculations	93
6.2.5 Application of a lubricant	94
6.2.5.1 The lubrication regimes	94

## TABLE OF CONTENTS

6.2.5.2	The sensitivity of the lubricant's viscosity to the pressure and the temperature	95
6.2.5.3	Entrainment of the lubricants	97
<b>6.3</b>	<b>EXPERIMENTAL STUDIES</b>	97
6.3.1	Equipment and procedure	98
<b>6.4</b>	<b>THE COEFFICIENT OF FRICTION IN FLAT ROLLING</b>	99
6.4.1	Dry rolling of aluminium alloy strips	99
6.4.2	Cold rolling of an aluminium alloy, using lubricants with boundary additives	100
6.4.3	Cold rolling steel strips, using lubricants and emulsions	101
6.4.3.1	Neat oils	102
6.4.3.2	Neat oils and emulsions	104
6.4.4	Hot rolling aluminium alloys using emulsions	106
6.4.5	Hot rolling steel strips	107
<b>6.5</b>	<b>THE DEPENDENCE OF THE COEFFICIENT OF FRICTION ON PROCESS AND MATERIAL PARAMETERS</b>	108
	<b>REFERENCES</b>	111
 <i>Chapter 7</i>		
	<b>Studies on Micro Plasto Hydrodynamic Lubrication in Metal Forming (Bay, Bech, Andreasen and Shimizu)</b>	115
<b>7.1</b>	<b>INTRODCUTION</b>	115
<b>7.2</b>	<b>EXPERIMENTAL INVESTIGATION</b>	116
7.2.1	Equipment and basic procedures	116
7.2.2	Lubricant imprints on deformed strips	118
7.2.3	Influence of materials and process parameters on lubricant escape	118
7.2.4	Influence of pocket geometry on lubricant escape	120
7.2.4.1	Hydrostatic pressure increase	120
7.2.4.2	Influence of pocket volume	121
7.2.4.3	Influence of angle to the edge	123
7.2.4.4	Influence of radius of curvature on the edge	125
<b>7.3</b>	<b>MATHEMATICAL MODEL OF MICRO PLASTO HYDROSTATIC AND HYDRODYNAMIC LUBRICATION</b>	128
<b>7.4</b>	<b>CONCLUSIONS</b>	133
	<b>REFERENCES</b>	134
 <i>Chapter 8</i>		
	<b>Numerical Simulation of Sheet Metal Forming (Worswick)</b>	135
<b>8.1</b>	<b>INTRODUCTION TO STAMPING SIMULATION - A DEEP DRAWN CUP</b>	136
8.1.1	Finite element mesh	137
8.1.2	Boundary conditions and contact treatment	138

8.1.3	Forming predictions	139
<b>8.2</b>	<b>EXPLICIT DYNAMIC VERSUS IMPLICIT FORMULATIONS</b>	140
8.2.1	Explicit dynamic method	141
8.2.2	Static implicit method	142
8.2.3	Choosing between implicit and explicit methods	142
<b>8.3</b>	<b>MODELLING THE CONSTITUTIVE RESPONSE OF SHEET METALS</b>	143
8.3.1	Phenomenological yield loci	144
8.3.2	Formability predictions	151
8.3.2.1	Forming limit diagram approach	151
8.3.2.2	Damage-based constitutive models	151
<b>8.4</b>	<b>SIMULATION OF STRETCH FLANGE FORMING</b>	153
<b>8.5</b>	<b>SIMULATION OF ALUMINUM ALLOY TAILOR WELDED BLANKS</b>	156
8.5.1	Simulation of small-scale TWBs	158
8.5.2	Simulation of large-scale TWBs	160
8.5.3	Damage prediction in the weld region	162
<b>8.6</b>	<b>SIMULATION OF ELECTROMAGNETIC FORMING</b>	165
8.6.1	EMF equations	166
8.6.2	Electromagnetic forming finite element model	167
8.6.3	EM field modelling	167
8.6.4	Structural modelling	168
<b>8.7</b>	<b>MODELLING PRODUCT PERFORMANCE – DENT RESISTANCE</b>	170
8.7.1	Numerical simulation of panel forming and denting	171
8.7.2	Closure sheet-inner panel interactions	174
<b>8.8</b>	<b>SUMMARY AND FUTURE ACKNOWLEDGEMENTS REFERENCES</b>	175 176 176
<i>Chapter 9</i>		
<b>Geometric and Mechanics Model of Sheet Forming (Duncan)</b>		183
<b>9.1</b>	<b>INTRODUCTION</b>	183
<b>9.2</b>	<b>PLANE STRESS DEFORMATION</b>	184
<b>9.3</b>	<b>FORCE PER UNIT WIDTH, OR “TENSION”</b>	186
9.3.1	“Constant tension” assumption	187
<b>9.4</b>	<b>BENDING AND UNBENDING MODELS</b>	188
<b>9.5</b>	<b>SUPPORTING SOFTWARE</b>	190
<b>9.6</b>	<b>CONCLUSIONS</b>	191
	<b>ACKNOWLEDGEMENTS</b>	191
<i>Chapter 10</i>		
<b>Modelling and Optimization of Metal Forming Processes (Manninen, Larkiola, Cser, Revuelta and Korhonen)</b>		193
<b>10.1</b>	<b>INTRODUCTION</b>	193



## TABLE OF CONTENTS

<b>10.2</b>	<b>ON MODELLING AND OPTIMIZATION</b>	194
<b>10.3</b>	<b>ROLLING OF METALS</b>	195
10.3.1	Prediction of the rolling force	195
10.3.2	Analysis of factors influencing the product quality	196
<b>10.4</b>	<b>DEEP DRAWING OF STAINLESS STEEL</b>	199
<b>10.5</b>	<b>CONTINUOUS EXTRUSION</b>	203
<b>10.6</b>	<b>DRY TURNING OF Ca-TREATED STEEL</b>	204
<b>10.7</b>	<b>OPTIMIZING THE TUBE HYDROFORMING PROCESS</b>	205
10.7.1	Principles of the hydroforming process	205
10.7.2	Hydroforming process simulation	206
10.7.3	Optimization of the parameters	206
10.7.3.1	Qualitative definition	206
10.7.3.2	Quantitative definition	206
10.7.3.3	Optimization setup	209
10.7.3.4	Optimizing and results	210
<b>10.8</b>	<b>SUMMARY AND CONCLUSIONS</b>	210
	<b>REFERENCES</b>	211
 <i>Chapter 11</i>		
	<b>The Mathematical Modelling of Hot Rolling of Steel (Yue)</b>	213
<b>11.1</b>	<b>OVERVIEW</b>	213
<b>11.2</b>	<b>THE CANMET – MCGILL MATHEMATICAL MODEL FOR MICROSTRUCTURAL EVOLUTION OF STEELS DURING HOT ROLLING</b>	214
11.2.1	Stages of hot rolling	214
11.2.2	Model inputs	215
11.2.3	Model outputs	216
11.2.4	Calculation steps	216
11.2.5	Transformation during cooling to coiling (on the runout table)	222
11.2.6	Effective austenite surface area per unit volume	222
11.2.7	Ferrite grain size	223
11.2.8	Austenite transformation to ferrite, pearlite and bainite	223
11.2.9	Precipitation in transformed austenite	224
11.2.10	Mechanical properties	224
<b>11.3</b>	<b>DISCUSSION</b>	224
	<b>REFERENCES</b>	225
 <i>Chapter 12</i>		
	<b>Identification of Rheological and Tribological Parameters (Szeliga and Pietrzyk)</b>	227
<b>12.1</b>	<b>THE INVERSE METHOD</b>	228
12.1.1	Definition of the inverse problem	228
12.1.2	Experiment	230
12.1.3	Direct problem	231

12.1.4	Goal function and optimization procedure	232
12.1.5	Two-step inverse algorithm	234
<b>12.2</b>	<b>RESULTS</b>	237
12.2.1	Identification of rheological and friction properties	237
12.2.2	Identification of internal variable model parameters and friction properties	242
12.2.3	Identification of material properties from axisymmetrical test performed using various plastometric simulators	247
12.2.4	Identification of material properties from axisymmetrical and plane strain compression test	250
<b>12.3</b>	<b>DISCUSSION</b>	254
<b>12.4</b>	<b>CONCLUSIONS</b>	255
	<b>ACKNOWLEDGEMENTS</b>	255
	<b>REFERENCES</b>	255
 <i>Chapter 13</i>		
	<b>Oxide Behaviour in Hot Rolling (Krzyzanowski and Beynon)</b>	259
<b>13.1</b>	<b>FACTORS INFLUENCING FRICTION, HEAT TRANSFER AND QUALITY OF THE PRODUCT IN HOT ROLLING</b>	259
<b>13.2</b>	<b>OXIDE FAILURE DURING HOT TENSILE TESTING</b>	261
13.2.1	Experimental	261
13.2.2	Modes of oxide scale failure in tension and measurement of separation loads	263
<b>13.3</b>	<b>MATHEMATICAL MODEL</b>	266
13.3.1	Model of oxide scale failure	266
<b>13.4</b>	<b>EFFECT OF CHANGING STEEL COMPOSITION</b>	271
13.4.1	Comparison of oxide scale growth and morphology	271
13.4.2	Comparison of failure modes	274
<b>13.5</b>	<b>ANALYSIS OF OXIDE SCALE FAILURE AT ENTRY INTO THE ROLL GAP</b>	279
13.5.1	Effect of initial stock temperature	280
13.5.2	Effect of oxide scale thickness	282
13.5.3	Verification of the model prediction using stalled hot rolling tests	284
<b>13.6</b>	<b>OXIDE SCALE FAILURE IN THE ROLL GAP</b>	286
<b>13.7</b>	<b>ANALYSIS OF DESCALING EVENTS</b>	289
13.7.1	Hydraulic descaling	289
13.7.2	Mechanical descaling	289
	<b>ACKNOWLEDGEMENTS</b>	294
	<b>REFERENCES</b>	294

## TABLE OF CONTENTS

### Chapter 14

#### **Friction, Lubrication and Surface Response in Wire Drawing (Wright)**

297

#### **14.1 BASIC CONCEPTS**

297

14.1.1 Frictional stress characterization

297

14.1.2 Determining friction mode by wire surface analysis

300

#### **14.2 THE EFFECT OF TEMPERATURE**

303

#### **14.3 VELOCITY – TEMPERATURE INTERACTIONS**

305

#### **14.4 PROCESS DESIGN EFFECTS**

305

14.4.1 Lubricant selection

305

14.4.2 Die material and die angle

307

14.4.3 Sequential drawing effects

307

#### **14.5 THE DRAWING OF SHAPES**

307

#### **14.6 THE GENERATION OF FINES**

309

#### **REFERENCES**

311

### Chapter 15

#### **Modelling and Control of Temper Rolling and Skin Pass Rolling (Wiklund and Sandberg)**

313

#### **15.1 INTRODUCTION**

313

15.1.1 What do we mean by temper rolling and skin pass rolling?

313

15.1.2 Why

313

15.1.3 How

314

15.1.3.1 Mechanical properties

314

15.1.3.2 Coining and smoothing of the surface

316

15.1.3.3 Improving the flatness

317

#### **15.2 MODELLING OF THE ROLL GAP**

319

15.2.1 Failure of conventional cold rolling models

319

15.2.2 Fleck and Johnson

319

15.2.3 A hybrid model

320

15.2.4 FEM

321

15.2.4.1 The FEM tool

321

15.2.4.2 Simulations with a simple constitutive model

321

15.2.4.3 Simulations with an advanced constitutive model

322

15.2.5 Making fast predicting models from FEM simulations

326

#### **15.3 MODELLING OF THE ROLL FORCE**

328

15.3.1 FEM

328

15.3.2 Hybrid modelling

328

15.3.2.1 The neural network tool

329

15.3.2.2 Process data set 1

329

15.3.2.3 Modelling with process data set 1

330

15.3.2.4	Process data set 2	332
15.3.2.5	The old set-up model and a neural network model	332
15.3.2.6	A physically based model, a neural network model and a hybrid model	333
15.3.2.7	Classic cold rolling theory	334
15.3.2.8	Detection of flat zones within the roll gap	336
15.3.2.9	Process data set 3 and a neural model	338
15.3.2.10	Hybrid model combining a classic model and a neural network model	338
<b>15.4</b>	<b>CONCLUSIONS FROM THE MODELLING EXERCISES</b>	<b>340</b>
<b>15.5</b>	<b>PROCESS CONTROL</b>	<b>341</b>
15.5.1	Set-up before the rolling pass	341
15.5.2	Feed-back control during the rolling pass using the mass flow method	341
15.5.3	Forward and backward tension	341
<b>15.6</b>	<b>DEVELOPMENT TRENDS</b>	<b>341</b>
15.6.1	Modelling and control	341
15.6.2	Temper rolling and tension levelling	342
	<b>ACKNOWLEDGEMENTS</b>	<b>342</b>
	<b>REFERENCES</b>	<b>342</b>
	<b>AUTHOR INDEX</b>	<b>345</b>
	<b>SUBJECT INDEX</b>	<b>353</b>

## Chapter 1

# Recollections

**John Schey: A man who is truly outstanding in his field!**

**Jean V. Reid**  
**IRDI**  
**Midland, Ontario**

We affectionately called him Poppa John or Poppa Schey as he patiently taught us the ABC's of Tribology. However, there was no question of our respect for him. To the outside world, he was still "Professor Schey", a mentor we strived to be worthy of.

I first met John when I chose him as my project supervisor in the fourth year of my ME program at the University of Waterloo. I had chosen the study of hydrodynamic lubrication in aluminum strip rolling. Little did I know as I met with him that the direction for my career in engineering had been set. From that point on, my course was set to study and work in the Tribology of Manufacturing. I learned high quality experimental techniques for designing experiments, collecting and analyzing data, as well as the art of writing publications and making short technical presentations. I returned to the U of W to study lubrication mechanisms of solid lubricants under John's guidance for my MASc program. Following my graduation, I worked at General Motors, and at Ontario Hydro Research in the field of tribology. Then, I decided it was once again time to return to the university and study with John; I went back and did my Ph.D investigating adhesion in the unlubricated sliding of stainless steel and copper alloys. It was through his contacts that I moved to Virginia and accepted a job in Reynolds Metals Research. Many years later, it was through John that I once again returned to Canada and am now working at the Industrial Research & Development Institute in Midland, Ontario.

Through the years John has always "been there" to give some friendly advice on Tribology problems or career moves or just say "hello". Faithfully, by his side, also has been his wife Gitta; she is a pleasure to know as I have seen her as a hard-worker and a serene loving presence supporting his many works while accomplishing much on her own. Their love of music and travel was well known; packing to travel lightly and effortlessly was an art that they had developed.

John set high standards for himself and inspired his students to do the same. He considered an 80-hour work-week to be a standard for his students. He totally believed in

learning-by-doing and patiently corrected us when we made mistakes. He did not support paying technicians to do work that we should be able to do for our graduate programs. Thus, I had the challenge of preparing the surface of many of the specimens required for my experimental work. This included many hours of surface grinding with some milling and turning thrown in for variety. Some students chose not to work with John because of his high expectations; for those of us who did, I don't think we ever regretted our decision. For me personally, it was a joy and an honour to have the tutelage of such a great man.

He pushed and prodded us into areas even when we lacked the confidence. I recall the time shortly after I'd started my graduate program that he asked me to teach the class on surface roughness. At that time, this was a subject that I knew virtually nothing about. I did some background work and taught the class with shaking knees and amazingly enough made it through the lecture period. This is an area that I ended up working in years later, and it all started with a request from John to do something I didn't think I could do.

I also vividly recall taking my thesis to him for 'editing'. He told me that "I could write" so I should go ahead and do it. The message (although so gently given) was that I should not be giving him less than my best and expect him to "fix it" for me. He never spoon-fed his students but patiently pushed us to develop our abilities and think about what we were doing. He quickly taught us the error in mindlessly generating data without considering its relevance.

John was a welcome speaker at many technical meetings...his lectures were never boring. He could temper the theory with colourful stories from industry to bring the whole picture to life; instead of just words, we were given the animation to go with it.

It is hard to express the honour of having had the opportunity and blessing of being mentored by John Schey. I was struck by his humility; he always gave us credit for work that he had guided us through. He encouraged us to write and present papers, and accept all challenges that we met in life. Any contribution that students made to work he was involved in was gratefully acknowledged. He was never too busy to appreciate any small thing that we did as students. He was always there with an encouraging word if we were dealing with any problems, whether of a technical or personal nature.

All in all, my life as a student, researcher and engineer has been shaped and motivated by John.

### **John Schey - A Passion for Tribology in Manufacturing**

**Gopal Nadkarni**  
**Ispat Inland Inc.**  
**East Chicago, USA**

In 1982, I came to the University of Waterloo as a Rotary International Scholar to pursue a short program in Manufacturing Engineering. I had completed my engineering apprenticeship with a cutting tool manufacturing company in India and knew I wanted to study "machinability". John put me to work on a project determining the effect of lubricant viscosity on machinability; he even funded me when my scholarship ran out. Now, nearly twenty years later, my primary recollections of John are tinged with feelings of affection for John the humanist rather than the awe I felt at his towering intellectual accomplishments.

John worked 16-hour days at his passion - Tribology & Manufacturing. He was exacting, demanding and impatient with sloppy work and gifted with an unusual sense of "practicality in research". He patiently guided his students with compassion and firmness, and used unique methods to educate and inspire them.

I remember well the day he asked me "to help him" proofread several chapters of his "Tribology in Metalworking" book. I was proud and eager to help him; I worked hard for several months reading and re-reading the chapters and giving him my suggestions and ideas. Little did I know that I was being educated in John's inimitable style; I gained an understanding of the system complexities of tribology and an appreciation of his crisp, concise writing style that was always his hallmark. To this day, I have, on my desk, a well-thumbed copy of this book, with John's scripted note of gratitude for "helping" him!

No mention of John can pass without mentioning Gitta, his dear wife who always has been a bedrock of support for him and who took care of all his graduate students with affection. All in all, a unique and gifted couple who have given to society more than they have taken from it!

### Thoughts on John Schey

**Greg Dalton**  
**President**  
**TrybSys Inc.**  
**Sudbury, Ontario**

I first met Professor John Schey while I was working in the Graphics Lab as a teaching assistant. I was impressed by John's attention to detail and obvious interest in helping the first year students. The next year I had the privilege of being in his final class of Manufacturing Processes where, with the rest of the class, I came to marvel at his breadth of knowledge in manufacturing. Of all my professors through 7 years of engineering John was best at giving the students a sense of intimacy with the topic...you were there with John seeing the process through his eyes.

When the opportunity came to spend my last work term in John's tribology lab I jumped at the chance. John seemed to recognize that I was not as interested in the mundane task of data collection but was more interested in finding ways in collecting better data, easier. He encouraged my digressions, and in a matter of weeks he found a skill in me that would become the foundation for my career.

I continued to work with John through my 4<sup>th</sup> year project and managed to just qualify for Master's degree funding from NSERC. As one of John's last graduate students I profited from his guidance for many hours each week. If pressed I could summarize what I learned in three concepts:

1. all data are meaningful...but it takes careful analysis to make them useful
2. don't rely just on the numerical data, observe and compare specimens using a "rogues' gallery"



3. trust in the power of your brain to make sense of data and observations when it has had time to incubate.

Great engineering careers can be measured in many ways: published papers, books, designs and patents. I have colleagues who refer to “Tribology in Metalworking” as the “bible” of metal stamping lubricant development and I know a company president who keeps “Introduction to Manufacturing Processes” on his desk so he can become an instant expert on just about any manufacturing process.

However, I believe that John’s legacy to the metalworking research community is his enthusiasm and integrity in the empirical process. Personally, John has been and continues to be a tremendous teacher, mentor, and friend. I wish John and Gitta all the best on the 80<sup>th</sup> birthday of a true renaissance man.

**John A. Schey**

**Matthias Wandel**

**RIM**

**Waterloo, Ontario**

I first met Dr. Schey when he interviewed me for a summer co-op job in 1990. He was searching around his office saying ‘Now, where did I put my glasses’. I was pretty sure he didn’t mean the pair he had atop his head, but after a bit of looking, I timidly asked if maybe he was looking for the ones on his head. Sure enough, those were the ones! The interview beyond that point went all right, and I got the summer job.

The job was working with the ‘draw bead simulator’ in the Manufacturing Research Lab at the University of Waterloo. There were four students working in the lab that summer. There was one drawbead simulator machine, plus one of a new, more fancy and more automated design that was just being completed. My work revolved around writing software to operate the new machine, as well as some of the debugging of the new machine.

Those machines took a lot of work to operate, with lots of precision measurements and adjustments that had to be made for each new specimen under test. One of us nicknamed Dr. Schey as ‘Dr. Shim’ for his insistence that adjustments be made by adding varying amounts of brass shims, as opposed to having any sort of adjustment screws on the apparatus.

What I came to appreciate about Dr. Schey is that he is very hands-on. He is certainly not afraid of getting his hands dirty. I learned a lot about problems in machinery that was supposed to apply high forces, with high precision. High forces can make even the sturdiest of machines bend visibly, I found. Problems were also found with the load cells, rubber washers, electronics, wiring and everything imaginable. Being just a student, that suited me just fine – debugging the machine was much more fun than operating it. Fortunately, Dr. Schey had much patience both with the machine and with my attitude towards it. When it came to understanding the subtleties of machinery, Dr. Schey could not be beat.

There were various gems of philosophy I picked up from Dr. Schey. One of the best pieces of wisdom I took away from that summer is about adjustments. On one of the

many discussions of the topic, Dr. Schey mentioned that industrial dies used to have many many adjustment screws, and it would take skilled people days to set one up. So I asked, how this was different now. He said 'Nowadays, they just make them accurate'. It's a piece of wisdom I have often used in software design. Don't make your software overly adjustable and configurable. Just make it right, so it won't need adjustment.

Eventually, towards the end of the summer, the new machine did get to a point where its data could be trusted. For subsequent terms, there were other students working with the machines, still using the software I had written for it. Over the course of subsequent years, Dr. Schey produced more machines of similar design, which were sold to various manufacturers for doing drawbead simulations. With the machines went the computer, running the software I had written. Each machine was in some way different from the previous one, requiring some sort of software customisation and more often than not, some debugging of the electronics. Dr. Schey paid me generously for this work, more than I would have dared to ask.

On occasion, changes needed to be made to the software while I was not around. I was quite surprised to find Dr. Schey going into the software and making some changes to it himself. That really impressed me, that a man this 'old' should be that at ease with making changes to programs – more at ease with it than most university students. It made me realize that being able to use computers doesn't have anything to do with age.

### **A Tribute to Dr. John Schey**

**Claudio Girolami**  
**Engineering Manager**  
**Oshawa Truck Assembly Centre**  
**GM of Canada**

I first 'met' Dr. Schey in a telephone call as I was finishing my undergraduate studies at Concordia University in Montreal in the spring of 1977. Although we had all been assured employment upon graduation by the media a year earlier, reality set in and there were very few jobs available. By then I had decided to pursue graduate studies, and the University of Waterloo was one of my finalists.

It was one of those phone calls where I remember exactly where I was standing, the exact time of day and what else was going on around me. In hindsight, it was a decision of a lifetime, which I look back on quite fondly.

In that telephone conversation, the nature of work I would pursue under Dr. Schey's guidance sounded very attractive and I accepted on the spot. I then visited him and the University later that summer while I was working for Esso Chemical in Sarnia.

Dr. Schey came across very European, which made me feel at ease as most of my ancestry were natives of Europe. His rich German/Hungarian/English accent made for a very imposing presence as well.

He also sounded extremely knowledgeable. By the time of my arrival at the University, he of course had been there for several years and was already an institution among the faculty and the students in Mechanical Engineering. He told me he came to The

University of Waterloo from The Illinois Institute of Technology in Chicago. Before that, he had worked for British Aluminium in England for several years.

I had the privilege of working with Dr. Schey for two years. My office was at the back of one of the Mechanical Engineering labs in E3 (specifically Room 2106). During our weekly meetings to review my progress, I found out quickly that Dr. Schey was one for having things correct and accurate. After all, if not that way, why bother? It also fit his reputation as a 'slave driver' which I had heard from his undergraduate students. As always, when you're in the middle of whatever you're working on, it's hard to see the long-term benefit.

Those learnings have served me very well over my 23 years at General Motors. I find myself editing employees business cases for capital expenditures the same way Dr. Schey reviewed my thesis at the end of my stay at Waterloo. It feels like he set a standard that perhaps doesn't exist any more. Most of people's work now seems watered down in comparison.

After leaving Waterloo, I had several job offers but selected GM having come from a family of engineers and a life-long admiration and fascination for motor vehicles. It was as natural a fit as I could possibly expect between work and personal interest.

Looking back, my stay at The University of Waterloo were my best developmental years ever. I have kept in contact with Dr. Schey every year through a Christmas card, and I always receive one in return from him. I chuckled when he told me he had officially retired several years back. When I visited the campus a few months later while recruiting for students, I was told he was still hanging around E3 a lot of time. I knew Dr. Schey wasn't the type to stay home.

Dr. Schey, thanks for the solid professional training experience and your guidance. Anyone who hasn't had the experience to work with you doesn't know what he or she missed.

**Dr. J.A. Schey**

**Rolf Fisher**  
**Tooling Manager**  
**Plastmo Ltd.**

I have nothing but praise for Dr. John Schey. Whoever came in contact with him were impressed with his intelligence, professionalism, and uncompromising work ethic. He made study and research an exciting pleasure. Because of his efforts, hundreds of students became better engineers. He is a credit to the profession and sets a high standard for others to strive towards.

I would like to extend my best wishes to you and your family on your 80<sup>th</sup> birthday. You are a first class person and it has been an honour and privilege to work with you.

**John A. Schey**

**Phil Abramowitz**

**Ford Motor Company (ret.)**

I first met Professor Schey in 1966 while I was working for Babcock & Wilcox and he was consulting for the company. I was impressed with the "common sense" approach he employed to solve problems, which earlier had seemed somewhat insurmountable. I stayed in touch with Professor Schey while I went back to school and obtained a Master's degree.

Then, in 1969, I went to the University of Illinois at Circle Campus to work on my doctoral degree. The campus was new and Professor Schey was setting up an undergraduate metalworking laboratory with all new equipment. I helped with the start up of the lab. It was an exciting time highlighted by Professor Schey's enthusiasm for teaching and metalworking research. It also was at this time that Professor Schey was editing the first edition of Metal Deformation Processes and I had the opportunity to do a bit of proofreading for him.

Of course, I have many fond memoirs of my work under Professor Schey. Perhaps the least fond was my struggle to meet the language requirement. Professor Schey felt that if between us we could read 5 languages, we would be able to cover most of the important literature in our field. English was no problem, and Professor Schey could handle French and German. That left Russian or Japanese. I selected Russian and suffered for two years trying to master it before the school dropped the language requirement. Fortunately, I never had the need to translate a Russian article.

My thesis work involved incremental forging and we presented a paper at the first North American Research Conference, which is sponsored by NAMRI of which Professor Schey was a founding member. This is particularly noteworthy to me in that in January 2002 I will assume the presidency of NAMRI. In 1986, Professor Schey alerted me of a position at Ford Motor Company and this led to 12 enjoyable years there. Professor Schey did some consulting for Ford during this period.

I have profited greatly from my association with John, and my wife, Marian, and I wish him all the best.

**Prof. John A. Schey**

**Stephen M. Woodall**

**SMW Engineering Inc.**

**Waterloo**

I was John Schey's first graduate student at the University of Waterloo, starting my M.A.Sc studies in the fall of 1974. As a graduate student I was always impressed with John's knowledge, not only in his field of lubrication in metalworking processes but also in the areas of metallurgy, heat transfer, chemistry, hydraulics, mathematics, fluid mechanics and electrical engineering as it applied to instrumentation and control.

John is a tireless worker. I can remember that he used to rise very early in the morning to work on the book that he always seemed to be writing. He would work for a couple of hours each morning before he went into the university. We were always quite different in our working habits: John liked to start things early in the morning whereas I always preferred to work very late into the evening, often beyond midnight, and start work later in the morning. By the time that I got to the university, usually about 10:00 am, John had already done a half day's work! This was not usually a great problem but I remember when I took a graduate course from him he insisted on holding it at 8:30 in the morning. Because it was a small class (I believe there were four of us) he held it in his office. If one was late it was always very apparent!

As a student I was always aware of John's practical nature. He had a wealth of industrial experience which he was always able to draw upon when he taught. As an example of this I can remember him recounting an instance when he was working in industry. He had been asked to solve a particularly troublesome sheet metal working operation. He demonstrated that an increase, rather than a decrease, in friction in the particular forming operation was required to accomplish a successful result. To achieve the higher friction he placed a piece of emery cloth between the forming tool and the work piece!

When John first arrived at the University of Waterloo he had limited funding, consequently I had to do work that would normally be carried out by support services. An example of this was the machining of test specimens. I had to learn how to use the equipment in the student machine shop to make test samples for my research. I spent many hours in that shop and eventually became quite adept in the operation of the various machines. The experience gained there has proven to be extremely valuable as I now operate my own commercial machine shop!

Since leaving university I have collaborated with John on several occasions, the last time being to manufacture lubricant test equipment of his design. I believe that the Twist Compression test and the Drawbead Simulator test, the results of a lifetime of work, will find increasing application in the metalworking industries.

Throughout the time that I have known John he has demonstrated an incredible amount of knowledge, drive and enthusiasm for his field; he is a man of great integrity and honesty and I feel that this book is a fitting tribute to these qualities.

## Chapter 2

# John Schey and Value-Added Manufacturing

THOMAS A. BRZUSTOWSKI

*Natural Sciences and Engineering Research Council of Canada*

*350 Albert Street*

*Ottawa, Canada K1A 1H5*

### 2.1 STRIKING CLARITY

The following paragraph, striking in its clarity, is found in the introductory chapter of the third edition of John Schey's magnificent text on manufacturing (Schey, 2000):

"If one analyzes the components of the GNP, it is evident that material wealth comes from only two substantial, basic sources: material resources and the knowledge and energy that people apply in utilizing these resources. Agriculture and mining are of prime importance, yet they represent only 3-8% of the GNP of industrially developed nations. Manufacturing claimed the largest single share until the 1950s. Since then, much of the growth has taken place in the service sector, and recent data ..... would suggest that -- at least in highly developed economies -- material wealth is independent of the contribution of manufacturing to the GNP. This is, however, an illusion. What the numbers fail to show is that increasing wealth is based on an increasingly sophisticated manufacturing sector; this in turn creates the need for many similarly sophisticated supporting activities such as research, design, and financial services, distribution, maintenance, and field service of products, and even the hospitality and travel industry connected with manufacturing. For statistical purposes, all these supporting activities are classified as services. Yet, unless a nation is exceptionally well endowed with natural resources, a strong service sector can exist only if there is a similarly strong manufacturing sector. Only the interactions of the two can secure competitive advantages in a global economy where the simpler tasks migrate to low-wage environments. It is often said that, in the information age, knowledge is the most valuable commodity. this is quite true, but it is also true that knowledge itself can be bought relatively cheaply. Wealth is generated most abundantly by *producing tradable articles in which knowledge is embodied.*" [emphasis in the original]

### 2.2 AN ECONOMIC FACT

This remarkable paragraph says a great deal in a few words. It offers a concise and unmistakable statement of an economic fact that needs to be understood not just by manufacturing engineers but by all the principal actors in the economy. However, the recent

pronouncements and actions of many people whose activities in the economy receive widespread attention through the media suggest that it is not understood nearly as widely as one might expect.

A clear statement of an economic fact is always timely, because one can always see something happening in the economy that will be explained by it. Consider the last two sentences in the paragraph quoted above. They link wealth creation to adding value by embodying knowledge in traded goods. This connection is the key to prosperity in an open global economy. It is why there can be rich countries, such as Japan and Switzerland, that have no natural resources. The causal link between adding value and creating wealth points the way to some very important indicators of economic performance. Thus the value added per employee is a good measure of the wealth-creation performance of an enterprise, and the value added per employee net of the cost of capital per employee is a good measure of labour productivity in wealth creation.

John Schey's ideas on knowledge and wealth creation are very timely as this is being written, several months after the bursting of the "dot-com bubble". Quite apart from the effects of the downturn in the business cycle, some huge losses have been reported by big companies that had splurged on buying start-ups that had no profits, no sales, and no product on the market - but had knowledge that might otherwise have been acquired by the competition. These losses are sometimes euphemistically described as "good will" - implying that they're something other than real money, but falling share prices, with all the consequences that they produce, say the contrary. Far too much money was spent by far too many companies on knowledge that had the potential to be used to create wealth but was not creating any yet, and the value of that knowledge collapsed when the prospects of actually using it to create wealth disappeared because of a fall in demand.

### 2.3 RICH IN IDEAS

The concise paragraph on the economic role of manufacturing is rich in ideas. Consider the statement that sophisticated manufacturing creates a corresponding demand for sophisticated services. This is the mechanism by which sophisticated manufacturing creates a multiplier effect in the economy that greatly exceeds the multiplier resulting just from the consumer demand of the skilled manufacturing workers earning good wages. It is also an important reason why countries seek to attract foreign direct investment (FDI) by multinational manufacturers. Communities that already have the infrastructure of sophisticated support services meeting the needs of the local value-added manufacturers find it easier to attract more such manufacturers - that's the economist's virtuous cycle at work (or the engineer's positive feedback). Conversely, it also explains the plight of one-industry towns that lose their most advanced manufacturing plant. The demand for the supporting services then drops, and eventually a broad economic decline sets in.

In the sentence that follows, John Schey notes that the activities that support sophisticated manufacturing are counted as services. Early in the paragraph, he points out that the share of services in the GNP has grown, even as the share of manufacturing has declined. Paradoxically, some part of that growth in the share of services relative to the share of manufacturing is, in fact, driven by manufacturing. It is the result of a need for increasingly sophisticated -- and thus expensive -- services, as manufacturing enterprises produce increasingly sophisticated products that depend on more and better global connections with sources of knowledge, with suppliers, and with customers. Still another part



of the relative growth of services may be related to what the economists call "a measurement issue" reflecting recent trends in business organization. When a firm's internal design department is spun off as a "design boutique" from which the manufacturer now buys the design services previously produced in house, or when the internal IT department is closed down and the same service bought from an external computer service organization, activities previously counted under manufacturing now appear as purchased services.

These two examples illustrate that hard and fast mutually exclusive categories of economic activity may no longer provide a complete, or even useful, picture of an economy that is becoming increasingly connected. They just reinforce John Schey's point that it is wrong to think that a country's prosperity is independent of the contribution of manufacturing to the GNP. In fact, the prosperity depends not just on the share of manufacturing in the GNP, but also very strongly on the degree of sophistication of that manufacturing.

## 2.4 JUST ONE OF MANY CONTRIBUTIONS

I have dealt very narrowly with just one of the very many important contributions that John Schey has made to his field - the ideas in one paragraph of the magnificent textbook that, in its three editions so far, has been shaping the thinking of many thousands of young engineers. This wonderfully written didactic treatise is the work of a great intellect. It reveals encyclopedic knowledge of the subject combined with the ability to provide clear and concise explanations, with just the right balance between practical details and underlying principles. The discussion of the management and the economics of manufacturing processes alerts students to the fact that there are always choices to be made, and points them toward making good choices. And the single paragraph on which I have focussed these remarks shows that John Schey has a very clear view of the big picture, of the pervasive impact of value-added manufacturing on the prosperity of a nation that makes his own professional work so very important.

Such broad and, at the same time, deep understanding of the technical questions and the surrounding issues is the fruit of a long career of creative intellectual work that includes very important contributions in research, in design, and in solving industrial problems.

I feel very fortunate to be one of the many who have learned - even if only informally - from this remarkable man. It is a privilege for me to participate in this tribute to John Schey, one of the great engineers of our time and, I am proud to say, a close friend.

## REFERENCES

Schey, J.A. (2000) *Introduction to Manufacturing Processes*, 3<sup>rd</sup> Ed. (McGraw-Hill, Boston).

This Page Intentionally Left Blank

## Chapter 3

# Introduction – The Scheme of The Book

JOHN G. LENARD  
*Department of Mechanical Engineering*  
*University of Waterloo*  
*Waterloo, Ontario N2L 3G1*  
*Canada*

### 3.1 INTRODUCTION

As the reader would have noticed by now, there are two chapters that precede the introduction to the technical content of this book. The first one, Chapter 1, contains the recollections of several former graduate students of Professor Schey. There is a general trend in each of these comments, reflecting the appreciation of the education received, in addition to an acknowledgement of the firm, demanding but respectful treatment by their professor. Unfortunately, some of the students could not be located for their comments. All that were reached were more than pleased to be given the opportunity to say thanks in public to the man who shaped their careers.

The second chapter is a tribute by Dr. Brzustowski, the president of the Natural Sciences and Engineering Research Council of Canada. He specifically comments on the third edition of Prof. Schey's text *Introduction to Manufacturing Processes*, and quotes from the book, describing Prof. Schey's thoughts on value-added manufacturing.

### 3.2 THE TECHNICAL PRESENTATIONS

The technical content begins with Chapter 4. In what follows, the scheme of the book is discussed, in terms of a metal forming system and how each of the contributors' chapters fits in the concept of *Metal Forming Science and Practice*.

A metal forming system is best defined in terms of its components: the machine, the work piece and the interface in between the two, where the transfer of mechanical and thermal energies takes place. The forge, the extrusion press and the draw bench are a few of the simple examples of the forming machine. In the rolling process the machine refers to the rolling mill, including the driving motor, the work rolls, the back-up rolls, the screw-down system, the mill frame, the bearings, the drive spindles, the scale breakers, the coilers, loopers and the mill's control system. The work piece, the material that is to be subjected to a permanent change of shape, is the second component and its importance is not less than that

of the forming machine. Its attributes affect the forming process in very significant ways. These attributes include its resistance to deformation, its surfaces and its chemical composition. The surface of contact in between the machine and the work piece and the tribological mechanisms there determine the efficiency of the process.

The interaction of the components is perhaps best indicated by Schey (1980) in describing the tribological system in terms of the die, the lubricant and the work piece. His figure is reproduced here as Figure 3.1, below.

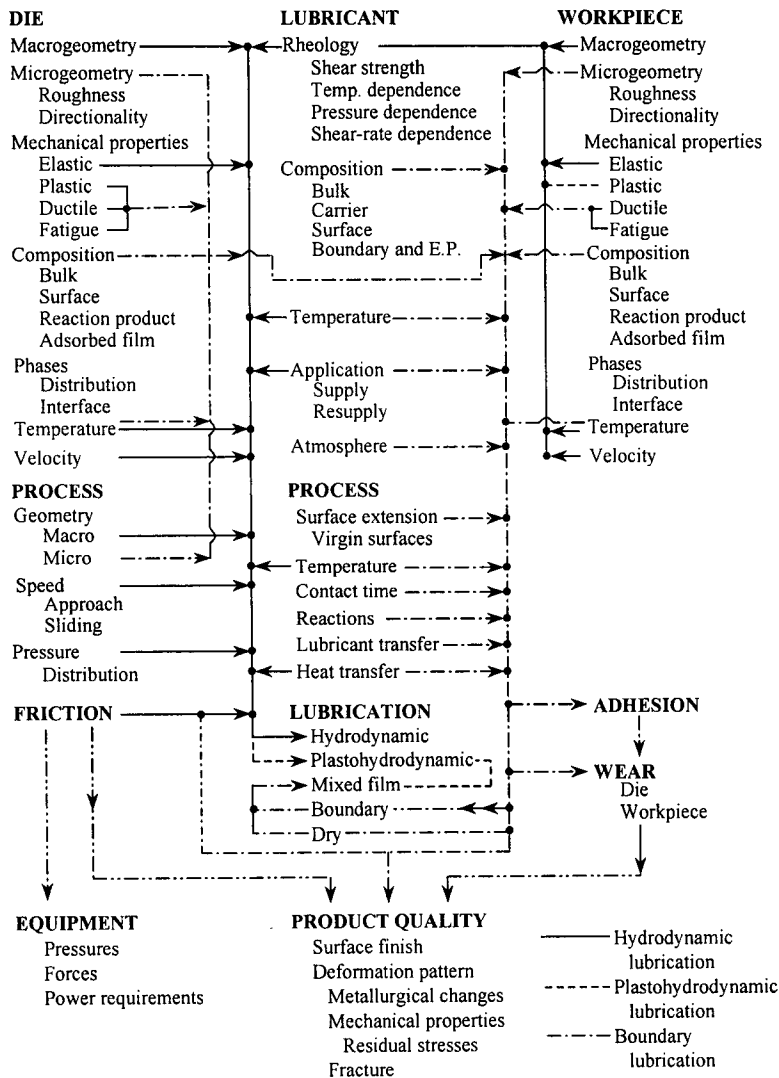


Figure 3.1 Elements of a metal forming lubrication system (Schey, 1980)

In the figure the die represents the forming machine, at least that component of the machine that is in direct contact with the work piece. The interface is identified as the lubricant. The third component, the work piece is also indicated on the right side of the figure. Arrows and lines indicate the interconnections. As many of these items as possible are discussed in this book. There are essentially six parts in the monograph. In the first portion, containing Chapters 4, 5, 6 and 7, fundamental ideas are described. This is followed by a consideration of sheet metal forming, involving Chapters 8 and 9. The application of various modelling techniques is given in Chapter 10. The effect of high temperatures on metal forming is demonstrated in the next three chapters, 11, 12 and 13. Another bulk forming method, drawing, is the topic of Chapter 14. The technical content is closed by Chapter 15, which examines the difficult process of temper rolling.

In Chapter 4, Sutcliffe considers “Surface finish and friction in cold metal rolling”. He writes about the real and the apparent area of contact and how their ratio changes as the metal forming process - and specifically the flat rolling process - continues. He discusses dry rolling and the use of lubricants, with and without bulk deformation. He examines the manner of asperity crushing. Each of these phenomena is presented in terms of mathematical models in addition to experimental data. In modelling frictional effects, he considers friction for the areas in contact in addition to friction in the valley regions. Experimental techniques are also presented in Chapter 4 and their results are compared to the predictions of the models. Further, the phenomenon of micro-plasto-hydrodynamic lubrication is given in addition to a discussion of pits and their geometry. Boundary lubrication, critical in cold rolling, and the importance of transfer films follow, leading to the conclusions of the chapter.

The next chapter, Chapter 5, written by Professor Azushima, is entitled “Direct observation of interface for tribology in metal forming”. He writes that in order to interpret the dependence of the coefficient of friction on the pressure and the relative velocity, a new lubrication regime needs to be considered. In order to achieve his purpose, he describes a new experimental device, which enables the researchers to observe the microcontact behaviour in metal forming, in-situ. The first experiment is concerned with the coefficient of friction in sheet drawing. A schematic diagram then introduces the concept of micro-plasto-hydrodynamic lubrication by giving a schematic diagram of the surfaces in contact. Also given is the schematic diagram of the apparatus, which employs a quartz die, a microscope and a CCD camera. Photographs of the permeation behaviour of the lubricant trapped in a pyramidal pocket indicate how the lubricant is squeezed when subjected to normal pressures and relative velocities. Professor Azushima then discusses the mechanisms of micro-plasto-hydrodynamic lubrication and presents experimental results on the dependence of the coefficient of friction on the velocity and on the interfacial pressure. In general, the results indicate that the coefficient of friction falls as the relative velocity and the pressure increase.

In Chapter 6, written by Prof. Lenard, the effect of the process parameters on the coefficient of friction in flat rolling is considered. The concentration is still on the introduction of fundamental ideas and in the first portion of the chapter, the mechanisms of friction, the adhesion hypothesis and the parameters of surface interactions are discussed. The available methods to determine the coefficient of friction are introduced next; these include experimental techniques and inverse modelling. The lubrication regimes, the Stribeck curve and the dependence of the lubricant's viscosity on the pressure and on the temperature is given. An examination of experimental results follows the fundamentals. These include dry and lubricated rolling of aluminium strips; cold rolling of steel strips; the use of emulsions; hot rolling of aluminium and hot rolling of steel. The effect of the process

parameters is presented in the form of two charts, showing the important phenomena and their effects on the coefficient of friction.

The influence of work piece surface topography on friction, lubrication and the final surface quality is examined in "Studies of micro-plasto-hydrodynamic lubrication in metal forming" by Bay, Bech, Andreasen and Shimizu, in Chapter 7. The chapter begins with the description of the experimental equipment, used to visualize lubricant entrainment in the process of sheet drawing. This is followed by the list of the independent variables, which are the lubricant viscosity, drawing speed, reduction, die angle, back tension, strain hardening exponent and the coefficient of friction. Attention is paid to the effect of process and material parameters on the escape of the lubricant. A mathematical model, based on the solution of Reynolds' equation, of micro-plastic hydrostatic and hydrodynamic lubrication mechanisms is given next. The predictions of the models and the measured data are compared and the predictive abilities of the models are emphasized.

Application of the fundamental ideas forms the next part of the book. The first concern is the forming of sheet metals. Chapter 8, written by Prof. Worswick, deals with the numerical simulation, by the finite - element method, of the sheet metal forming processes. The first discussion concerns a typical operation: that of the drawing of a cylindrical cup. Formulation of the finite-element mesh, the boundary conditions and the treatment of contacting surfaces are given next. A comparative and critical description of explicit and implicit formulations follows with some advice on how a choice between the two should be made. The constitutive response of sheet metals is presented next, including a discussion of yield loci. The finite element models are used then to predict limits of formability in sheet metal forming operations, considering both the forming limit diagram and the damage based models. Simulations of stretch flange forming, and small-scale and large-scale tailor welded blanks are treated in addition to an analysis of the prediction of damage in the weld region. These studies are followed by the analyses of electromagnetic forming, dent resistance and sheet-inner panel interactions. The chapter closes with a presentation of future needs in the modelling of the processes.

The next chapter, Chapter 9, has been written by Professor Duncan. The approach is rather different than in the preceding study. As Prof. Duncan writes, the developments in computing ability have greatly enhanced the level of sheet metal engineering, but there are several areas where improvements have been less marked. One is in the tools available to the engineer at the conceptual design stage. Engineering models are needed that can be applied locally to determine quantitatively the changes the designer should make in the die. To put it another way, there should be something better than using an expensive and sophisticated numerical analysis as a tool for a 'trial and error' approach.

Another problem associated with emphasis on numerical modelling at the expense of the basic mechanics of sheet metal forming is that it has been hard to develop good education programs in this field. Anecdotal evidence shows that the ability to 'operate' large finite element systems does not, of itself, provide an understanding of the forming process being analysed. Not only is training in numerical modelling an insufficient education for sheet metal engineers, but the mechanics that would be the basis of a course of study exist only in a piecemeal fashion and have not been established as a valid, albeit specialized field of engineering science.

This 'strength of materials' approach to sheet metal forming consists of identifying the elemental sheet forming processes such as drawing or bending and unbending over a radius. A complex process would be considered as an assembly of such elements that are identified by the designer and analysed using simplified models. In any tool the number of

such elements is few and the designer will examine the output of each calculation and gain a feel for the way the elements are interconnected. This aids the understanding the whole process in a way that is not possible in numerical analyses where many thousand elements are involved and much information is hidden in the plethora of data.

This chapter outlines a few of the simple models that exist for elements of sheet forming and discusses some systems and tools that help a student or a designer use this elemental approach in the study and design of sheet metal forming processes.

“Modelling and optimization of metal forming processes” is dealt with in Chapter 10, prepared by Manninen, Larkiola, Cser, Revuelta and Korhonen. The modelling tools discussed include numerical modelling, artificial intelligence techniques and data mining. These methods are applied to flat rolling, deep drawing of stainless steel kitchen sinks, hydroforming, continuous extrusion and metal cutting. The authors define “optimization” as a branch of mathematics that aims to find the best solution to a given problem, having a certain number of variables and subject to certain constraints. In the first example, the finite element code ABAQUS is combined with a model of the development of the microstructure during hot rolling. The results indicate that the roll force was calculated very accurately. This section is followed by a presentation of factors that influence the quality of the rolled product. Self-Organizing Maps and data mining are then introduced and discussed in some detail and are applied to the analysis of hot flat rolling of metals. Further, the LS-Dyna3D finite element program is used to analyse the deep drawing process and forming limit diagrams for the forming of stainless steel sinks are calculated. Metal cutting, continuous extrusion and hydroforming are also discussed in terms of mathematical modelling. A general chart, giving the details of the optimization process, is also presented.

In Chapter 11, Prof. Yue describes the CANMET - McGill model of hot rolling of steels, with special attention to the development of the microstructure during the various stages of the hot rolling process: reheating, roughing, finishing, cooling and coiling. The required input variables are defined: these are the chemical composition of the steel and the steel type. Prof. Yue then lists and describes the mechanical parameters needed for the computations and the steps in the computations. The chapter gives the specific metallurgical equations used in the model in addition to a discussion of the capabilities of the approach.

The combination of mathematical modelling and the determination of material parameters is the topic of the next chapter, Chapter 12, entitled “Identification of rheological and tribological parameters in metal forming” by Szeliga and Pietrzyk. The authors emphasize the importance of the rheological parameters in describing the resistance of the material to deformation in addition to the importance of the boundary conditions, which are the tribological parameters, both needed in the precise formulations of models. While there are experimental techniques that enable the researchers to determine these parameters, the large number of tests required for the accurate mathematical descriptions of both often cause delays and difficulties. The inverse method for the evaluation of the parameters, given in Chapter 12, is aimed at reducing the number of tests. The problem is formulated in terms of a vector of measured output parameters, a vector of model parameters and a vector of process variables. The objective is the evaluation of the optimum values of the model parameters, accomplished by minimizing the distance between the vectors of the calculated and measured values. A flow chart of the algorithm is given and the process is then applied to axially symmetric and plane strain compression and ring compression.

The authors conclude that the application of the inverse analysis to the interpretation of plastometric tests presents numerous advantages. Less effort is spent on experimental analysis. Various types of parameters, including rheological and friction ones, can be



evaluated simultaneously from one type of tests. The method is designed for the identification of various types of metal forming process parameters. Results are presented in terms of examples of typical applications.

In Chapter 13, Krzyzanowski and Beynon deal with the effects of the layer of scale on the surface of hot-formed steel products. The chapter is entitled "Oxide behaviour in hot rolling: heat transfer, friction and surface finish aspects". As they write, the layer of scale on the surface of the steel plays a pivotal role in thermomechanical processing and in the resulting surface quality. They concentrate on hot rolling of steels, stating that this involves probably the most complicated oxide layer. The chapter includes a description of laboratory tests, rolling tests, microstructural investigation and detailed finite element analyses. A physically based model for the behaviour of the layer of scale has been developed. The first topic discusses the factors that influence interfacial phenomena: heat transfer, friction and the resulting surface quality. This is followed by the description of the experiments and the attendant mathematical modelling. Oxide failure during hot tensile testing indicates the mode of failure: cracking or separation from the parent metal. The model developed is shown to be successful in correctly predicting the observations and the measurements. The effect of the chemical composition of the steel is considered next, followed by a presentation of failure modes. The scale failure at the entry to the roll bite is analysed. The effect of the initial temperature is considered. The thickness of the scale is examined. Descaling is discussed.

The next two chapters consider two further processes: that of drawing of metals and temper rolling. Chapter 14, written by Professor Wright, deals with drawing while Chapter 15 discusses temper rolling.

In Chapter 14, "Friction, lubrication and surface response in wire drawing" by Prof. Wright, frictional stresses are characterized, followed by specific attention to the surfaces created under various process conditions. The effect of the temperature on the tribological phenomena is considered, in addition to the velocity - temperature interactions. The selection of the appropriate lubricant, the die material and the die angle is presented. This is followed by an examination of the drawing of shapes.

Wiklund and Sandberg present the topic of temper rolling in Chapter 15, entitled "Modelling and control of temper rolling and skin pass rolling". The definitions of both temper rolling and skin pass rolling are given first and the reasons for the processes and the procedure usually followed in industry are presented. The failure of conventional mathematical models in analyzing the temper rolling process is discussed: the reasons are the very small reductions, high friction and the significant flattening of the work roll, not described well by the traditional models of the flat rolling process. The models recently presented in the technical literature are then shown, including the model of Fleck and Johnson and Dixon. This is followed by the application of the finite element method, modelling the deformation of the strip and the roll. Roll pressure distributions, including the "double peak" distribution, are demonstrated along with the corresponding deformations of the rolled strips. The authors also consider the use of artificial intelligence in predicting the roll separating forces. The chapter closes with a clear description of process control.

## REFERENCES

Schey, J.A., (1980) in *Proc. 4<sup>th</sup> Int. Conf. Production Engineering*, Japanese Society of Precision Engineering, Tokyo, 102-115.

## Chapter 4

# Surface Finish and Friction in Cold Metal Rolling

MICHAEL P.F. SUTCLIFFE  
*Department of Engineering*  
*University of Cambridge*  
*Trumpington Street*  
*Cambridge, CB2 1PZ*  
*U.K.*

### 4.1 INTRODUCTION

The cold metal rolling industry needs reliable and accurate models to improve predictions of surface finish and friction and thus increase productivity and improve quality. These models are used in setup programs for schedule optimisation, for on-line control algorithms and to help determine process improvements.

In most cold rolling operations, lubricant is used to reduce frictional forces, to protect the roll and strip surfaces, and to act as a coolant. The amount of oil drawn into the roll bite and the initial surface roughness are the critical factors determining friction in the contact and surface finish of the product (Schey, 1983a and 1983b). Figure 4.1(a) illustrates schematically the inlet to the bite during a strip rolling operation. Neglecting for the moment the surface roughness on the roll and strip, a 'smooth' film thickness  $h_s$  at the end of the inlet can be determined by integrating Reynold's equation. Wilson and Walowit (1972) derive an expression for  $h_s$  as

$$h_s = \frac{6\eta_0\alpha\bar{u}}{\theta_0(1 - \exp(-\alpha Y))} \quad (4.1)$$

where  $\bar{u}$  is the average entraining velocity,  $\theta_0$  is the inlet angle between the strip and roll,  $Y$  is the plain strain yield strength of the strip and  $\eta_0$  is the viscosity of the lubricant at ambient pressure. The pressure viscosity coefficient  $\alpha$  in the Barus equation  $\eta = \eta_0 \exp(\alpha p)$  is used to describe the variation of viscosity  $\eta$  with pressure  $p$ .

In practice both the roll and the strip surfaces are rough. In many rolling processes, the roll grinding process leads to a roll roughness with a pronounced lay, with asperities running along the rolling direction. This longitudinal roughness is in turn transferred to the strip. Isotropic roughness is also common, for example where the surface has been produced by shot blasting, while transverse roughness, with asperities

running perpendicular to the rolling direction, seems to be less common. In the presence of roughness, the ratio  $A_s = h_s/\sigma_0$  of the smooth film thickness  $h_s$  to the combined roll and strip roughness  $\sigma_0$  ( $\sigma_0^2 = \sigma_r^2 + \sigma_s^2$ ) is used to characterise the lubrication regime. For large  $A_s$  the surfaces are kept apart by a continuous film of oil. However the surface tends to roughen in these circumstances, probably due to differential deformation of grains in a manner akin to the surface roughening observed in a tensile test (Schey, 1983a). Various authors have derived models of friction under these full film conditions (e.g. Sa and Wilson, 1994). However, to generate a good surface finish, most cold rolling operates in the 'mixed lubrication' regime, where there is some hydrodynamic action drawing lubricant into the bite, but also some contact between the asperities on the roll and strip. First asperity contact occurs with  $A_s$  below about 3, so that to give substantial asperity contact and a good imprint of the smooth rolls onto the strip,  $A_s$  needs to be below about 1. Figure 4.1(b) shows schematically the contact in these circumstances, with areas of 'contact' between the roll and strip and areas separated by an oil film. The ratio of the areas of close contact to the nominal contact area is termed the contact area ratio  $A$ .

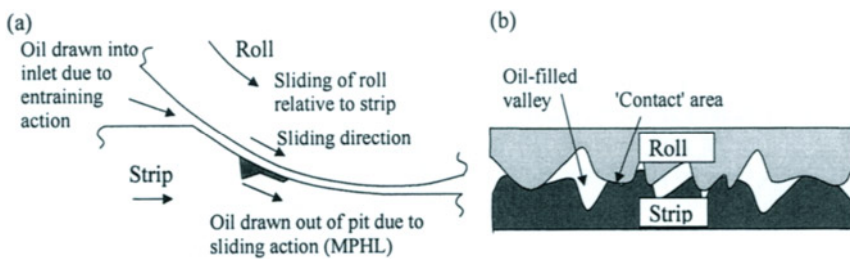


**Figure 4.1** (a) Schematic of lubrication mechanisms in rolling, (b) details of contact

Prediction of the area of contact ratio  $A$  requires detailed models of how the asperity contacts deform (reviewed in section 4.2) and the role of the pressurised oil separating the roll and strip. The average friction stress through the bite can then be determined using appropriate expressions for the frictional stress on the contact areas and in the valleys. Section 4.3 describes such models, and corresponding experimental findings.

Figures 4.2(a) and (b) illustrate the way in which the roll imprints its roughness onto aluminium foil in the mixed lubrication regime. It seems probable that the pits observed on the foil surface are associated with surface roughening in regions where there is a significant oil film separating the roll and foil.

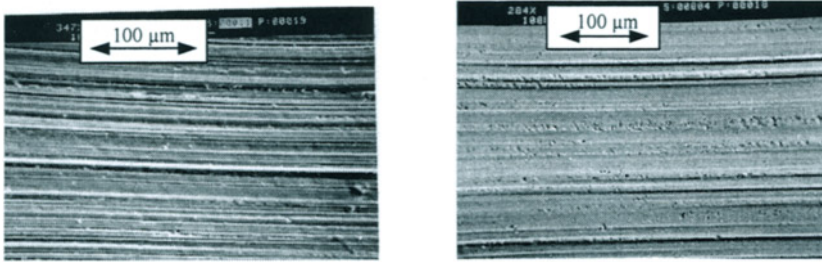


**Figure 4.2** SEM micrographs of: (a) roll surface, (b) aluminium foil surface.  
The rolling direction runs horizontal, and the roll roughness is derived from a replica.

Although it is frequently assumed that the interface between the roll and strip can be separated into 'contact' and valley areas, in fact it is an open question as to the nature of the contact, which may be dry, or separated by a boundary or thin hydrodynamic film. The answer probably depends on rolling and local conditions. The mechanism of lubrication under these asperity contacts has been termed micro-plasto-hydrodynamic lubrication (MPHL). A similar mechanism can occur in stainless steel rolling, where the shot-blast finish on the hot band prior to rolling tends to generate pits on the surface during subsequent deformation. Oil trapped in the pits can be drawn out due to the sliding between the roll and strip, as illustrated in Figure 4.1. Further details of the MPHL mechanism are given in section 4.4, while section 4.5 describes work on boundary lubrication. Finally the significant effect of transfer films formed on roll surfaces is reviewed in section 4.6.

## **4.2 UNLUBRICATED ROLLING**

Although it is sometimes possible to roll without lubrication, in general lubricant is applied during cold rolling to act as a coolant, to prevent surface damage and to reduce friction. Nevertheless the deformation of surfaces under unlubricated conditions provides a useful starting point for lubricated rolling, and points up the key features in the mechanics of asperity deformation.

### **4.2.1 Without bulk deformation**

Bowden and Tabor (1950) introduced the idea of asperity junctions as a mechanism for friction between rough surfaces. In the simplest case each asperity contact acts as a small indentation, so that the area of each contact equals the ratio of the

force at the contact to the material hardness  $H$ . Summing up all the contacts, the ratio  $A$  of the true to the nominal area of contact is related to the average contact pressure  $\bar{p}$  by

$$A = \frac{\bar{p}}{H} \quad (4.2)$$

This expression would indicate an area of contact ratio close to one third at a typical mean contact pressure equal to the yield stress of the strip. Modifications to this theory at higher pressure, for example by Childs (1977) and Bay and Wanheim (1976), allow for interaction between adjacent contacts, which tends to limit the amount of asperity flattening. Wave models have also been proposed to account for sliding between the tool and surface (Challen and Oxley, 1979). Although these models have been widely used in metal working, they do not allow for deformation of the bulk material, so that only the surface of the workpiece undergoes large strains. As we shall see in the following section, this seriously limits the applicability of these models to metal forming problems.

#### 4.2.2 With bulk deformation

The effect of bulk plasticity was highlighted by the results of Greenwood and Rowe (1965) and Fogg (1968), who showed that the presence of sub-surface deformation allows the asperities to be crushed considerably more than in the absence of bulk deformation. The deformation throughout the substrate means that it is at the point of yield and acts as a soft 'swamp'; differences in normal velocity at the surface associated with differences in contact pressure can easily be accommodated by a perturbation to the uniform plastic strain field. Sheu and Wilson (1983), Wilson and Sheu (1988) and Sutcliffe (1988) show how the evolution of the workpiece roughness topography depends on the bulk strain of the material. Depending on the orientation of the roughness relative to the bulk strain direction, either upper-bound or slip line field solutions are used to derive the velocity field at the surface and the corresponding relationship between contact pressure and asperity flattening rate. Figure 4.3 shows Sutcliffe's idealisation of the contact geometry for transverse roughness with a periodic array of flat indenters of width  $A\lambda$  spaced a distance  $\lambda$  apart, loading the surface of the workpiece with a mean contact pressure  $\bar{p}$ . Figure 4.4 shows the corresponding slip line field. The local field under the indenter is that due to Hill (1950) for indentation of a strip of limited height. This can be matched up with a uniform deformation pattern in the centre of the strip, given by a series of square rigid blocks separated by velocity discontinuities. The region at the surface between the asperities is rigid and undeforming. The flattening rate is expressed in terms of a dimensionless flattening rate  $W$

$$W = \frac{2\Delta v}{\lambda \dot{\epsilon}} \quad (4.3)$$

where  $\Delta v = v_c - v_v$  is the relative flattening velocity between the plateau and valley of each asperity and  $\dot{\epsilon}$  is the bulk strain rate.

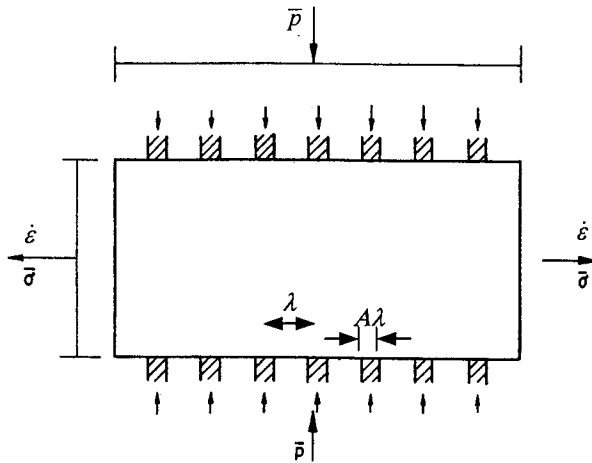


**Figure 4.3** Schematic of asperity contact model (Sutcliffe, 1988)

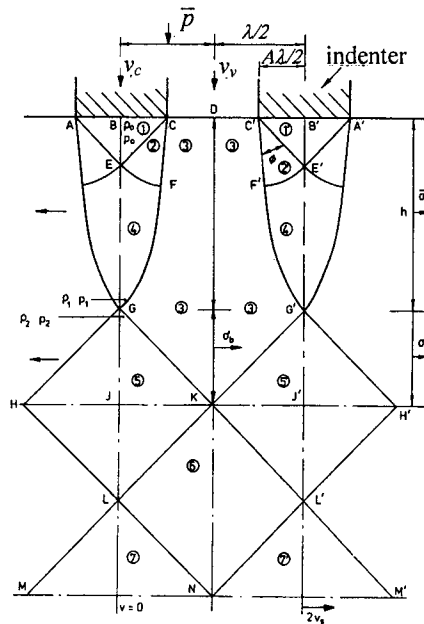


**Figure 4.4** Slip line field solution for transverse roughness (Sutcliffe, 1988)

The flattening rate  $W$  is a function of the real area of contact area ratio  $A$  and the ratio  $\bar{p}/Y$  of the mean contact pressure to the plane strain yield stress of the strip, i.e.

$$W = W\left(\frac{\bar{p}}{Y}, A\right) \quad (4.4)$$

The theoretical flattening rate  $W$  is in the range 1–8, increasing with increasing mean pressure and falling with increasing area of contact ratio.

Sheu and Wilson (1983) and Sutcliffe (1988) used upper-bound theory to address the closely related and industrially more relevant problem of roughness running along the rolling direction. Wilson and co workers adopt an alternative formulation<sup>1</sup>, expressing the problem in terms of an equivalent asperity hardness  $H$ , given by the mean asperity pressure  $\bar{p}/A$  divided by the workpiece shear yield stress  $k$  ( $k = Y/2$  for plane strain conditions),

$$H = \frac{\bar{p}}{Ak} \quad (4.5)$$

The hardness  $H$  is expressed as a function of a dimensionless strain rate  $E$ , where

$$E = \frac{\lambda \dot{\epsilon}}{2\Delta v} \quad (4.6)$$

Note that  $E$  is equal to  $1/W$ . Hence the problem has the functional form

$$H = H(E, A) \quad (4.7)$$

Where there is bulk deformation, so that  $E$  is not zero, the hardness  $H$  is much less than the normal material hardness  $H$  without bulk deformation. The hardness  $H$  falls with increasing  $E$  and rises with increasing area of contact ratio  $A$ .

To use these asperity flattening models to predict the change in asperity geometry and contact area during rolling, consider the schematic geometry of Figure 4.5, with an array of triangular asperities of slope  $\theta$ , which it is assumed does not change during the subsequent deformation (experiments and finite element calculations suggest that this is a reasonable assumption). For longitudinal roughness (where the asperities run along the rolling direction), the rate of change of contact area with bulk strain is given by

---

<sup>1</sup> Note that Wilson uses the semi-wavelength  $\lambda/2$  in his work.

$$\frac{dA}{d\varepsilon} = \frac{W}{\tan \theta} \quad (4.8)$$

while for transverse roughness the equation is modified to take into account the increase in indenter spacing:

$$\frac{dA}{d\varepsilon} = \frac{1}{1 + \varepsilon} \left( \frac{W}{\tan \theta} - A \right) \quad (4.9)$$

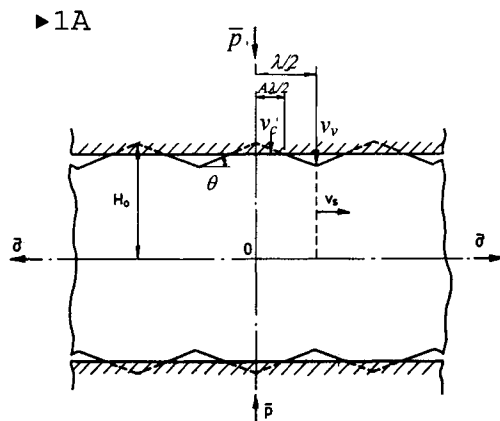


**Figure 4.5** Schematic of asperity crushing model (Sutcliffe, 1988)

Equations (4.8) and (4.9) show how the increase in contact area, and hence the reduction in surface roughness, depends on the bulk strain. Increasing the normal pressure corresponds to a larger value of the crushing rate  $W$ , and so an increase in the rate at which the contacts grow. Increasing asperity slope reduces the crushing rate. Although the crushing rate  $W$  has been expressed in terms of the bulk strain rate and a flattening velocity, the time dependence of these terms is only included as a convenient way of modelling the rate of asperity flattening. The evolution of the contact area does not depend on bulk strain rate, per se.

Sutcliffe (1988) describes a series of experiments in which he deformed copper blocks containing machined triangular asperities using flat rigid platens. Figure 4.6 shows the side of one such specimen, for the case where the roughness lay is transverse to the bulk straining direction. The bright areas show regions where a film of dark die applied to the surface has been disrupted due to straining. The pattern of deformation, with non-deforming regions between indenters and a square pattern of intense shear lines in the middle of the block, is remarkably similar to the corresponding theory shown in Figure 4.4.



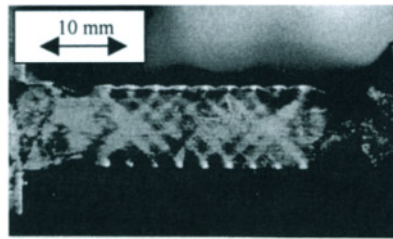


**Figure 4.6** Flattening of triangular asperities (at the top and bottom of the central region) on a copper block deformed by smooth indenters top and bottom and tension at the ends of the specimen (Sutcliffe, 1988)

A comparison of experimental measurements with theoretical predictions of the evolution with bulk strain of the contact area is shown in Figure 4.7(a). Good agreement is seen for high normal pressures. Note that the area of contact ratio rapidly rises above the value of about 1/3 associated with zero bulk strain. The excellent conformance achievable between the surfaces explains the remarkable efficiency of rolling as a process to produce good surface finish by imprinting a bright roll finish. At lower normal pressures, the applied end tension (equivalent to coiling tensions in rolling) must be correspondingly higher to cause the bulk material to yield. In these circumstances the agreement is not so good, perhaps related to work hardening in the experiments or to changes in the geometry of the asperities during the deformation (see also the calculations of Korzekwa et al, 1992). Wilson and Sheu (1988) show excellent agreement between the predictions of their model and measurements of the change in contact area after rolling aluminium strips with model asperities, see Figure 4.7(b). The change in contact area is the same for either single or multiple pass rolling, depending only on the total bulk strain.

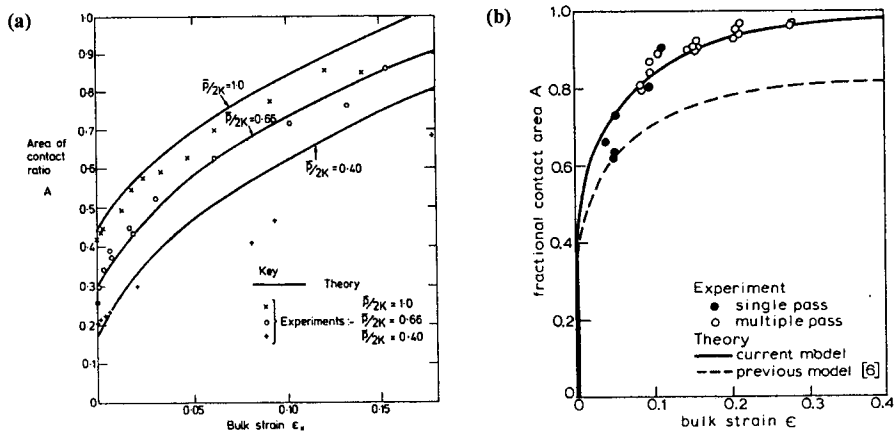


**Figure 4.7** Change of area of contact ratio with bulk strain for (a) transverse roughness (Sutcliffe, 1988), (b) longitudinal roughness (Wilson and Sheu, 1988)

Various researchers have addressed the asperity crushing problem using finite elements. Makinouchi et al (1987) and Ike and Makinouchi (1990) considered transverse roughness, finding a similar pattern of non-deforming and deforming regions to that predicted by Sutcliffe. Korzekwa et al (1992) have undertaken a comprehensive series of numerical simulations to investigate the effect of strain direction on the asperity flattening rate. Their numerical results for transverse roughness show good agreement with the slip line field solutions of Sutcliffe for relatively high flattening rates. At the lowest flattening rates the slip line field solution predicts higher flattening rates. Probably the rigid-perfectly plastic assumption used in the slip line field leads to an overestimate of the flattening rate in these cases. For longitudinal roughness Korzekwa's results show similar quantitative results to the upper-bound calculations of Wilson and Sheu (1988), although they differ quantitatively. Korzekwa's results for this case have been fitted using appropriate polynomial functions by Sutcliffe (1999).

In the above analyses the contact geometry is idealised by assuming that the tool is smooth and all the roughness resides on the strip. In practice the roll tends to have a very similar roughness to the strip, not least because the strip surface conforms to the tool roughness after the first pass of a multi-pass schedule. Where the roughness is entirely longitudinal, the smooth tool and equivalent strip approximation is appropriate. However for transverse roughness there is an additional ploughing effect, as the relative motion between the surfaces induces continual deformation (see Figure 4.8). Wilson and Sheu (1988) and Wilson (1991) consider this case for a rough tool and smooth strip. Now the flattening rate only depends on the local tool slope at the contact, rather than the history of pressure and strain.

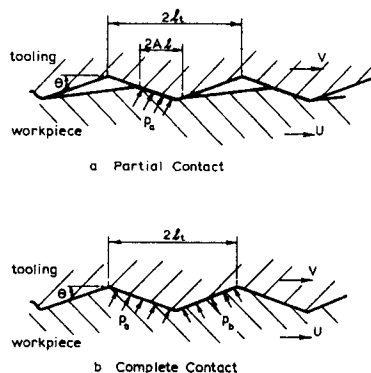


**Figure 4.8** Schematic of boundary friction model of transverse roughness with sliding;  
(a) partial contact, (b) complete contact (Wilson, 1991)

#### 4.2.3 Random rough surfaces

The above studies relate to asperity geometries consisting of a series of identical triangular asperities. Real rough surfaces generally contain a random profile. By choosing the initial shape of the asperity with the same height distribution as the real surface, the distribution in asperity heights can be modelled, for example using the pseudo-Gaussian distribution of Christensen (1970). The variation in asperity spacing is also important, since the crushing rate is inversely proportional to the asperity slope.

Steffensen and Wanheim (1977) show how the inclusion of short wavelength asperities, superimposed on long wave length asperities, can reduce significantly the predicted area of contact ratio between tool and workpiece in the case where there is no bulk deformation. Although this may make relatively little difference to the roughness amplitude, section 4.3.3 shows that it can impact significantly on predictions of friction. Wilson (1991) describes a model including bulk deformation, with long and short wavelength asperities on the strip tool, respectively.

Sutcliffe (1999) treated a two-wavelength longitudinal surface profile, applying the asperity flattening model to each wavelength in turn. The long wavelength components are predicted to be eliminated more quickly than the short wavelength, high slope components, c.f. Eq. (4.8). Figure 4.9 shows the excellent agreement obtained between predictions and measurements of the change with bulk strain of the amplitude of the two components of roughness. Measurements were taken from as-received aluminium strips which were cold rolled to various reductions. The amplitudes of the roughness components were extracted by Fourier analysis. One important conclusion from this work was that the short wavelength components (typically with wavelengths less than  $30\text{ }\mu\text{m}$ ) can be expected to have a significant impact on friction, while the longer wavelength components, although making a greater contribution to the initial amplitude of roughness, are nevertheless crushed rather quickly so are less important. It is also important to note that, for these typical roughness slopes, the asperities have almost entirely conformed to the roll roughness after a bulk strain of only 10%.

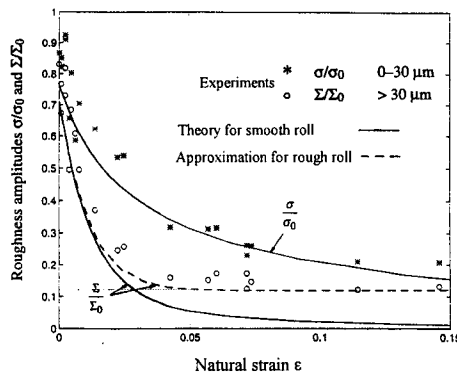


**Figure 4.9** Change with bulk strain in strip roughness amplitudes  $\sigma$  and  $\Sigma$  for short and long wavelength components respectively, normalised by their initial amplitudes  $\sigma_0$  and  $\Sigma_0$  (Sutcliffe, 1999)

### 4.3 MIXED LUBRICATION

The previous section has revealed the importance of bulk deformation in allowing a close conformance of the strip surface to that of the roll. In practice lubricant is applied to act as a coolant and to reduce friction. In this section we show how the presence of lubricant reduces the extent to which the strip and tool surfaces can come into contact. This section considers with 'mixed lubrication', where the amount of oil drawn into the contact is determined by oil entrainment at the inlet to the bite. Montmitonnet (2001) provides a useful summary of recent modelling approaches in this regime. Section 4.4 deals with an alternative mechanism, whereby oil is trapped in pits at the inlet, and then drawn out from the pits due to sliding action in the bite.

This chapter considers lubrication with neat lubricants. In practice the lubricant is frequently applied as an emulsion of water and oil. A review of how this affects the tribological conditions is given by Schmid and Wilson (1995).

#### 4.3.1 Modelling

This section reviews the key elements in a tribological rolling model. The various approaches adopted by different authors are summarised in section 4.3.1.5, experimental methods are described in section 4.3.2 and the predictions are compared with experiments in 4.3.3. Further experimental findings are reviewed in section 4.3.4.

**4.3.1.1 Asperity deformation.** Section 4.2 describes appropriate models of asperity deformation. As indicated there, it is essential to include the effect of bulk deformation, modelling the evolution of contact area with bulk strain. The hydrodynamic oil pressure  $p_v$  generated in the valleys tends to reduce the crushing rate, since it is the difference between the plateau and valley pressures  $p_p$  and  $p_v$  that drives asperity crushing. This oil pressure can simply be accounted by subtracting  $p_v$  off the mean pressure  $\bar{p}$ , to be used in Eqs. (4.4) or (4.5) for the crushing rate. Longitudinal, transverse and isotropic roughness orientations have been considered in the various models of mixed lubrication.

Several models of rolling consider the contact area as a function only of the local pressure, ignoring the effect of bulk strain on the evolution of the geometry (as indicated in Tables 4.1 and 4.2). Although simpler, this approach is not appropriate where there is bulk strain.

**4.3.1.2 Hydrodynamic equations.** A hydrodynamic model is needed to predict the change through the contact in the oil pressure  $p_v$  generated in the valleys. The basis for all the models is Reynolds' equation, which for steady flow with smooth surfaces separated by a film of thickness  $h$  takes the form

$$\frac{dp_v}{dx} = 12\eta\bar{u} \frac{h-h^*}{h^3} \quad (4.10)$$

where  $h^*$  is a constant. In many cases  $h^*$  is equal to the film thickness at the start of the bite, where the pressure gradient approaches zero. Used in this form, Wilson and Walowit's equation would be recovered for a straight inlet wedge. A 'correction' to include roughness has been used by making some assumption about the height of the asperities in the work zone, and hence the oil trapped there. In fact adherents to this method do not allow for the critical effects of hydrodynamic pressure and bulk deformation on the mechanics of asperity crushing, limiting its accuracy.

Two approaches have been widely used to include roughness in the Reynolds' equation. For an assumed deterministic roughness geometry, an 'averaged Reynolds' equation' can be derived (Christensen, 1970) to give the variation in the rolling direction, along the  $x$  axis, of the reduced hydrodynamic pressure  $q_v$  of the lubricant as

$$\frac{d(\alpha q_v)}{dx} = 12\eta_0 \alpha \bar{u} \frac{h_v - h^*}{h_v^3 (1 + 3\sigma^2 / h_v^2)} \quad (4.11)$$

where  $h_v$  is the mean film thickness, averaged across the valley, and  $\sigma^2$  is the local combined variance of the roll and strip roughnesses. As the asperities are crushed through the bite the geometry parameters  $h_v$  and  $\sigma^2$  fall. The reduced and actual lubricant pressures  $q_v$  and  $p_v$  are related by  $\alpha q_v = 1 - \exp(\alpha p_v)$ .

An alternative 'flow factor' model is based on the numerical simulations of Patir and Cheng (1978, 1979). Following improvements by Lo and Wilson (1999), Chang et al (1998) derive a modified Reynolds' equation for Gaussian roughness as

$$\frac{d}{dx} \left( \phi_x \frac{h_t^3}{12\eta} \frac{dp_v}{dx} \right) = \bar{u} \frac{dh_t}{dx} + \frac{\Delta u}{2} \sigma \frac{d\phi_s}{dx} \quad (4.12)$$

where  $h_t$  is the mean film thickness,  $\Delta u$  is the sliding speed and  $\phi_x$  and  $\phi_s$  are pressure and shear flow factors. These flow factors depend on the Peklenik surface orientation parameter  $\gamma$ , which is the ratio of correlation lengths in the rolling and transverse directions. Values of Peklenik parameter of infinity, 0 and 1 correspond to longitudinal, transverse and isotropic roughness, respectively. The flow factors are fitted with semi-empirical equations by Wilson and Marsault (1998) and given by Lin et al (1998) as explicit functions of the depth of the pits and the orientation parameter  $\gamma$ .

**4.3.1.3 Method of solution.** Models of rolling need to couple the asperity mechanics and hydrodynamic equations. As the asperities are crushed in the bite, the film thickness falls, thus leading to an increase in valley oil pressure. Conversely this increase in valley pressure limits the crushing process. For 'high speed' conditions, the crushing process takes up only a short part of the entry region. Sheu and Wilson (1994) introduce short entry and transition regions at the inlet, prior to and after the onset of bulk

plasticity, respectively. At the end of the transition region, the oil and plateau pressures are effectively the same. In the work zone there is some subsequent reduction in asperity height, as elongation of the strip leads to stretching of the oil film and a corresponding reduction in film thickness. Solution of the coupled ordinary differential equations for the asperity crushing and oil pressure mechanisms gives the oil flow rate through the bite and hence the film thickness in the bite. This approach has been widely used (e.g. Lin et. al., 1998, Marsault, 1998). Sutcliffe and Johnson (1990b) adopt a similar approach, but only consider an inlet analysis, in which the bite region is not modelled explicitly.

Le and Sutcliffe (2000a, 2001a) extend this approach to include more than one wavelength of roughness. A first iteration considered the oil pressure to be the same in each valley. This was subsequently enhanced to model variations in pressure across the strip width, depending on the local asperity height.

For 'low speed' conditions, it is no longer appropriate to make the assumption that there is a short region in the inlet during which the oil pressure approaches the mean pressure. Instead the oil pressure is significantly below the mean pressure throughout the bite, and the whole bite needs to be modelling using the coupled equations (Chang et al, 1996). Qui et al (1999) describe an alternative approach, using a finite difference method, which allows them to generate a more stable solution method which can be applied to both the 'high' and 'low' speed cases. Examples of these solutions are given in section 4.2.3 below.

**4.3.1.4 Friction modelling.** The tribological models described above allow the contact geometry, area of contact ratio, contact pressure and oil hydrodynamic pressure to be found through the bite. Noting that the valley and asperity pressures equal the mean pressure in the work zone for high speed conditions, the effective friction coefficient  $\mu$  is given

$$\mu = A\mu_c + (1 - A)\mu_v \quad (4.13)$$

where  $\mu_c$  and  $\mu_v$  are friction coefficients for the areas of contact and valley regions respectively. An alternative approach uses a friction factor  $m$ , where the local shear stress  $\tau$  equals  $mk$ , with  $k$  the shear yield stress of the workpiece ( $Y = 2k$  for plane strain conditions). Then the effective friction factor  $m$  is given by

$$m = Am_c + (1 - A)m_v \quad (4.14)$$

where  $m_c$  and  $m_v$  are friction factors for the contact and valley regions.

The contribution from the contact areas tends to dominate, since the contact area is normally greater than the valley area and the frictional stresses are higher on the contact areas. Hence it is important to use an accurate value for  $\mu_c$  or  $m_c$ . Unfortunately it is not clear what an appropriate value should be, or how to model it. Clearly this will depend on the mechanism of friction on the contact regions, but this still remains an

open question, with boundary lubrication or some form of thin hydrodynamic film perhaps governing friction. Guidance on this has to come from experimental measurements, and to a certain extent it remains a fitting parameter. Further details of this point are discussed in sections 4.4, 4.5 and 4.6 below. A typical value used in current models seems to be of the order  $\mu_c = 0.1$  or  $m_c = 0.2$ . One refinement to the model allows the friction coefficient or factor to depend on the smooth film thickness or rolling speed. The rationale behind this approach is that there is some hydrodynamic component to friction under these contact areas. Montmitonnet et al (2001) infer an appropriate variation in friction coefficient from rolling mill trials, while Le and Sutcliffe propose a 'semi-empirical' friction law (2001b), using the simpler strip-drawing test to derive a variation of contact friction coefficient with smooth film thickness.

The frictional stress  $\tau$  in the valley regions, and hence the valley friction coefficient  $\mu_v$  or friction factor or  $m_v$ , can be estimated using the Newtonian viscosity;

$$\tau = \eta \dot{\gamma} \quad (4.15)$$

where the strain rate  $\dot{\gamma}$  is estimated from the sliding speed and valley film thickness in the bite and the viscosity is taken at the pressure in the bite.

An improved estimate of the frictional stress considers non-Newtonian behaviour. Measurements of lubricant behaviour, for example in a pressured cell (Bair and Winer, 1982), or inferred from twin-disc experiments (Evans and Johnson, 1986), show that the effective viscosity falls at high shear rate, and may reach a plastic limit in some cases. Evans and Johnson follow the Eyring model,

$$\tau = \tau_0 \sinh^{-1} \left( \frac{\eta \dot{\gamma}}{\tau_0} \right) \quad (4.16)$$

where  $\tau_0$  is the Eyring stress at which significant non-linearity sets in. A limit on the shear stress is imposed, associated with plastic behaviour. Bair and Winer propose a relationship which gives a smooth transition from Newtonian to perfectly-plastic behaviour. Even without such a non-Newtonian model, it seems sensible to set an upper limit on shear stress, for example equal to the corresponding boundary friction coefficient. In general the hydrodynamic component will be a small contribution compared with the contact friction. An exception to this occurs when the pressure or strain rate is very high, as for example occurs in foil rolling or under asperity contacts.

#### 4.3.1.5 Summary of models

The above sections have described the key factors included in modelling of mixed lubrication. Tables 4.1 and 4.2 summarise the actual methods adopted by various authors, for strip and foil rolling respectively. The foil models include significant roll

elasticity, as described in section 4.3.5. Examples of the results are given in section 4.3.3 below. The second column of each table indicates whether the effects of bulk deformation and hydrodynamic pressure generated in the valleys are included in the model of asperity flattening.

**Table 4.1** Summary of mixed lubrication models for strip rolling

	Bulk deformation and valley pressure?	Reynolds' equation	Rolling 'speed'	Notes
Tsao and Sargent, 1977	No	Smooth	–	
Keife and Sjögren, 1994	No	Smooth	–	
Li, 1995	–	Smooth	–	Empirical correction for roughness
Rasp and Häfele, 1998	No	'Corrected'	–	
Le and Sutcliffe, 2001b	Yes	Averaged	High	Semi-empirical boundary friction
Le and Sutcliffe, 2000a, 2001a	Yes	Averaged	High	Two wavelength roughness
Sutcliffe and Johnson, 1990b	Yes	Averaged	High	Inlet analysis
Sheu and Wilson, 1994	Yes	Flow factor	High	
Wilson and Chang, 1996	Yes	Flow factor	Low	
Chang et al, 1996	Yes	Flow factor	Low	
Lin et al, 1998	Yes	Flow factor	High or low	
Marsault, 1998	Yes	Flow factor	High or low	Includes roll elastic deformation
Qui et al, 1999	Yes	Flow factor	High or low	Finite difference

**Table 4.2** Summary of mixed lubrication models for foil rolling

	Bulk deformation and valley pressure?	Reynolds' equation
Domanti and Edwards, 1997	Yes	Dry
Keife and Jonsäter, 1997	No	'Corrected'
Luo and Keife, 1997	No	'Corrected'
Pawelski et al, 1998	No	Hydrostatic
Sutcliffe and Montmitonnet, 2001	Yes	Flow factor
Le and Sutcliffe, 2002a	Yes	Averaged

### 4.3.2 Experimental methods

Although there is an abundance of measurements of surface finish and friction in rolling, it can be difficult to apply the findings with confidence without information about the tribological mechanisms involved. Since experimental mills are invariably unable to replicate the industrial conditions, laboratory measurements must always be treated with caution. One way to overcome the slower speeds generally found in experimental mills is to use more viscous oils, although the boundary lubrication



conditions may not then be matched. Alternative metal deformation processes, notably strip drawing and plane strain compression, have been widely used to investigate the tribology of metal rolling. Again these experiments can give valuable insight, but care needs to be taken in applying them to rolling.

Measurements of surface finish in rolling are relatively easy to obtain, by taking samples either from lab experiments or industrially rolled coils. In the later case it is important to take the samples from a portion of the coil which has been rolled at normal speed, to ensure that the hydrodynamic conditions are appropriate. The surface finish can then be measured on a profilometer. Replica techniques are valuable to measure roughness of the roll. A recent development by Testex corporation, in which a crushable foam film replicates the roll profile, seems to be preferable to other replica techniques. Stout and Blunt (2000) give a comprehensive review of profilometry methods. Traditional line-trace profilometers are adequate to extract values of  $R_q$  roughness. Some judgement needs to be made about appropriate filtering, to eliminate long wavelength components associated with roll form error or lack of flatness in the samples. Although a filter cut-off of 800  $\mu\text{m}$  is often used, the results of Sutcliffe (1999) for dry rolling (see section 4.2.3 above) suggest that this may over-emphasise the long wavelengths of roughness. A shorter wavelength cut-off, of say 300  $\mu\text{m}$ , may be more appropriate. Modern three-dimensional profilometers give valuable additional information about the shape of the surface topographic features. They have the additional advantage of scanning more of the surface for a given reading, so that the surface roughness tends to be averaged more effectively. To attain the required resolution, three dimensional measurements typically cover an area with side length of a few hundreds of microns, so that there is an inherent filtering effect in these measurements. An example of more sophisticated analysis of the surface is given in section 4.4.2, to characterise pits formed on stainless steel strip. Images using a scanning electron microscope (SEM) are also essential to confirm that the mechanisms of friction are similar to those found in the corresponding industrial application.

Azushima (1978) pioneered the use of the 'oil drop' experiment to estimate the amount of oil drawn into the bite. A small measured drop of oil of known weight is placed onto the cleaned strip which is rolled using cleaned rolls. As it passes through the bite the drop spreads over the surface of the strip. The cigar-shaped area of the drop can easily be identified because of differences in surface roughness between lubricated and unlubricated regions. Knowing this area and the lubricant density, the mean film thickness can be found. Sutcliffe and Johnson (1990a) show that this measurement corresponds well to the film thickness found from surface roughness measurements, and that starvation effects due to the limited oil drop size can be easily avoided. Li (1995) describes an alternative method using ellipsometry, while recent work has used laser fluorescence to measure film thickness directly (Azushima et al, 2000 - see also Chapter 5).

A direct measurement of friction in the roll bite can be found by using a pin embedded in the roll (e.g. Al-Salehi, 1973 and Jeswiet, 1998). Although the inferred

measurements seem reasonable, some concern arises in the mixed regime that the presence of the pins may disturb the oil film found at the measurement point.

A widely used method is to infer friction from measurements of rolling parameters. In principle a measurement of the rolling load can be used to deduce the friction coefficient in the bite. However results will be sensitive to errors in the assumed yield stress. A more accurate inverse method is to use the additional information of the measured forward slip (i.e. the relative slip between the strip and roll at the exit, divided by the roll speed). This can be inferred from the distance between imprints transferred from the roll onto the strip or from direct measurements of the roll and strip speed. The strip speed can be measured using optical methods or from a bridge roll speed. Direct measurements of strip speed are more relevant to industrial rolling, where the roll and strip speeds are relatively stable, while it is not appropriate to mark the rolls. Inversion of an appropriate rolling model can then give the mean friction coefficient through the bite. Differences in inferred friction arise from different models of rolling. The method can be made more accurate by adjusting the coiling tensions so that the neutral point moves to the exit plane (zero forward slip). In this case the inferred frictional stress is less sensitive to the assumed distribution of friction stress through the bite.

#### 4.3.3 Theoretical results and comparison with experiments

Figure 4.10 shows a typical result from Sheu and Wilson (1994) for the variation in pressure and contact area at the inlet to the bite. The mean pressure rises in the inlet region, for large  $X$ , due to hydrodynamic effects. At a dimensionless position  $X \approx 2$ , there is contact between the roll and strip asperities, leading to a non-zero area of contact ratio  $A$  and a mean pressure  $p$  above the valley pressure  $p_b$ . At the end of the inlet region the mean pressure reaches the yield stress so that bulk deformation begins. Further asperity flattening occurs in the transition zone, driven by the difference between the asperity and valley pressures. For the case shown, the increase in contact area is small; a more significant increase will occur at slower speeds.

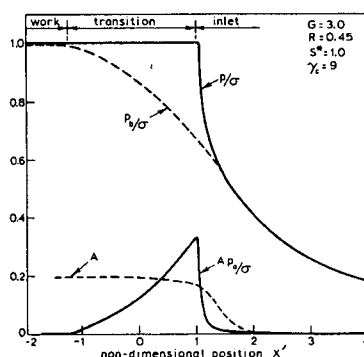


**Figure 4.10** Variation at the inlet to the bite of the mean pressure  $p$ , valley pressure  $p_b$  and contribution from asperity contacts  $A p_b$ , with corresponding increase in area of contact ratio  $A$  (Sheu and Wilson, 1994)

Figure 4.11, from the predictions of Montmitonnet et al (2001), shows how the pressure variation through the bite varies with roll speed for typical rolling conditions. At high speed,  $v_r = 10$  m/s, the results are similar to those of Sheu and Wilson, with the hydrodynamic pressure  $p_b$  reaching the mean pressure  $p$  in a very short inlet zone. The variation of pressure through the rest of the bite then shows the familiar friction hill. For a speed of 0.1 m/s, conditions are in the 'low speed' regime, where the hydrodynamic pressure lies below the mean pressure throughout the work zone. At very low speed,  $v_r = 0.001$  m/s, the hydrodynamic effects are very small. Instead the asperities crush very quickly in the inlet, and oil is trapped in isolated pockets, reaching the mean pressure due to hydrostatic action. The subsequent asperity deformation would be governed in these circumstances by the MPHL mechanism (section 4.4.2).

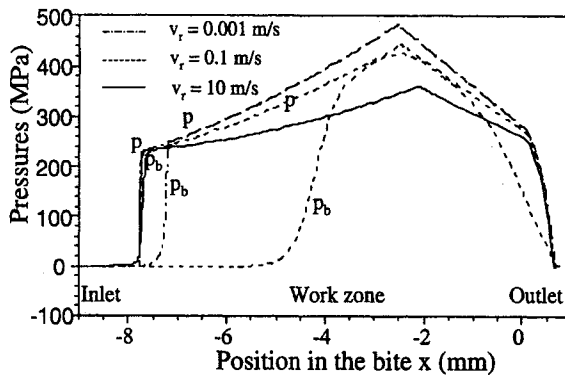
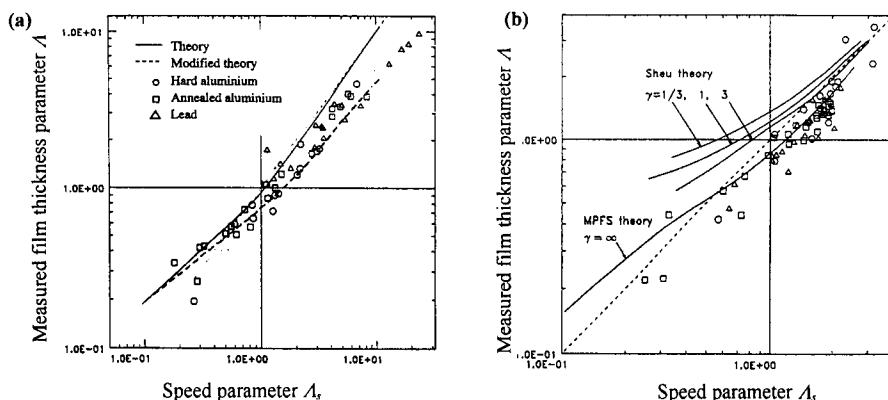


Figure 4.11 Variation through the bite of the mean pressure  $p$  and valley pressure  $p_b$  for three different rolling speeds (Montmitonnet et al, 2001)

Predictions of film thickness from the various models are in broad agreement, showing that the film thickness depends primarily on the rolling speed, oil properties and inlet geometry (Sutcliffe and Johnson, 1990a, Sheu and Wilson, 1994, Lin et al, 1998, Montmitonnet et al, 2001). The effects of yield stress, strip thickness, asperity geometry and entry tension are of secondary importance. Figure 4.12(a) shows reasonable agreement between experimental measurements of film thickness (Sutcliffe and Johnson, 1990b), measured using an oil drop experiment and theoretical predictions (Sutcliffe and Johnson, 1990a). The independent variable  $A_s$  is the ratio of the smooth film thickness, Eq. (4.1), to the initial combined surface roughness, so that values of this speed parameter below one correspond to significant asperity contact. The dependent variable  $A$  is the corresponding ratio of measured or predicted mean film thickness to the initial surface roughness. The modification to theory given in Figure 4.12(a) is associated with the asymmetrical lubrication conditions in these experiments.



**Figure 4.12** Comparison of predicted and measured film thickness parameter  $\lambda$  as a function of the speed parameter  $\lambda_s$ , (a) Sutcliffe and Johnson, 1990a, (b) Sheu's experiments (Sutcliffe and Johnson, 1990a)

Note the small dependence of results on the yield stress  $Y$  of the strip. Corresponding results from Sheu and Wilson (1994) are given in Figure 4.12(b) for cold rolling of aluminium strip<sup>2</sup>. Again agreement is good. Both the results shown in Figure 4.12 are for longitudinal roughness, i.e. the roughness lay runs in the rolling direction. Marsault (1998) shows reasonable agreement between experiments of Lin (1998) and theory, where the roughness is transverse, isotropic or longitudinal.

Rasp and Häfele (1998) provide a comprehensive series of measurements of film thickness under mixed lubrication conditions, using the oil drop technique on cold rolled aluminium, as illustrated in the results of Figure 4.13.

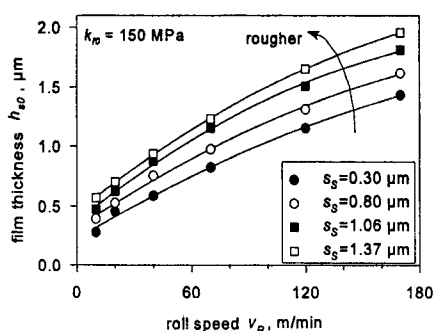
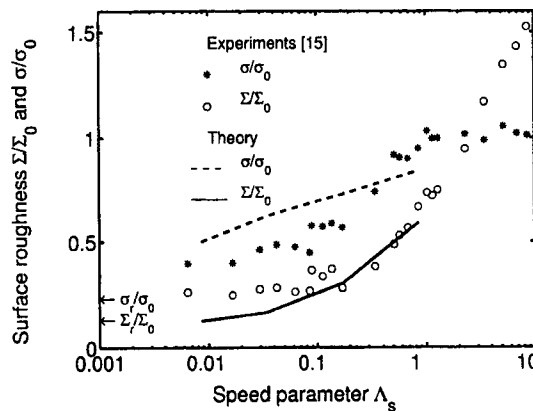


**Figure 4.13** Variation of measured film thickness with roll speed during rolling of aluminium with various roll roughnesses  $s_r$  (Rasp and Häfele, 1998)

<sup>2</sup> Experimental points differ from those given by Wilson and Sheu because inaccurate pressure and temperature viscosity coefficients used by them have been corrected.

Figure 4.13 shows how the entrained film thickness increases with increasing rolling speed and roll roughness. The effect of roughness orientation is also explored. By considering modifications to the smooth film thickness formula, Eq. (4.1), associated with roughness and thermal effects, Rasp and Häfele are able to show a good correlation between predicted and measured film thicknesses. However their model does not include the details of asperity flattening described in section 4.2.2 above, limiting its predictive capability.

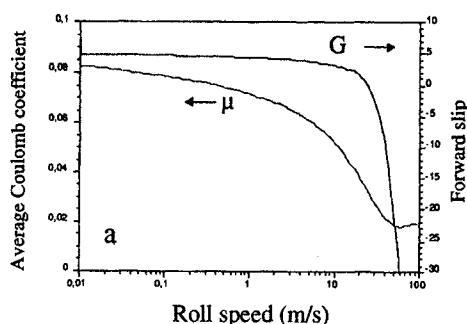
As shown in section 4.2.3, roughness wavelength has a significant effect on asperity flattening. To investigate this effect, Sutcliffe and Le (2000) performed a series of cold rolling experiments on as-received aluminium strip, which initially had a typical industrial longitudinal roughness. The changes in lubrication parameter  $A_s$  were achieved by varying the rolling speed and by using three mineral oils spanning a wide range of viscosities. Figure 4.14 compares theoretical predictions using a two-wavelength model with measurements of the effect of lubrication parameter  $A_s$  on the change in surface roughness amplitudes  $\sigma$  and  $\Sigma$  for the short and long wavelength components. Predictions are in good agreement with measurements in this case, for a strip thickness reduction of 25%. Note that, for  $A_s > 1$ , the surfaces roughen on the scale of the grain size during rolling, because the roll and strip are no longer in sufficiently close contact. For a higher reduction of 50%, agreement is still good for the long wavelength components, but less good for the shorter wavelengths. This difference is ascribed to difficulties in modelling what happens to the newly created surface and to the effect of sliding between the roll and strip. As with unlubricated rolling, inclusion of a short wavelength component reduces significantly the predicted true contact area between the roll and strip. This confirms the supposition that short wavelengths must be included to develop an accurate friction model for cold rolling.



**Figure 4.14** Change in amplitude of short and long wavelength strip roughness components  $\sigma$  and  $\Sigma$ , normalised by their initial amplitudes  $\sigma_0$  and  $\Sigma_0$  as a function of speed parameter  $A_s$  (Le and Sutcliffe, 2001a)

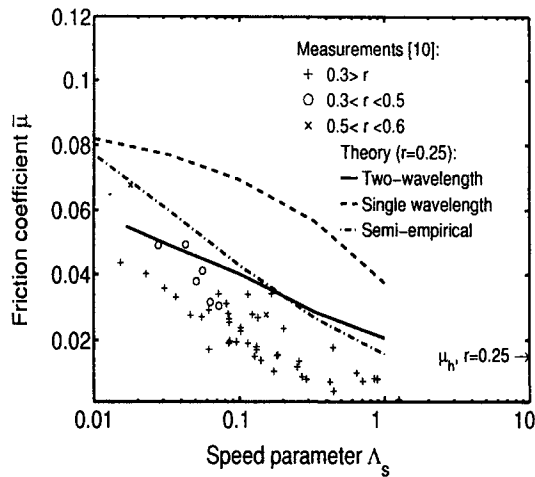
Trials performed at an industrial aluminium foil rolling plant illustrate the practical importance of this conclusion, showing how the change in roughness spectrum due to roll wear is reflected in the change in foil roughness (Le and Sutcliffe, 2000b). The observed reduction in short wavelength components on the roll would significantly reduce the friction coefficient and hence strip reduction. To maintain the same friction level as the roll wears, the mill speed needs to fall to draw less oil into the bite.

Figure 4.15 shows the predictions of Montmitonnet et al (2001) for the change in mean friction coefficient  $\mu$  and forward slip  $G$  with roll speed. The friction curve takes on the typical Stiebeck form. At very low speed the contact area ratio approaches the limiting value of 1, and the mean friction coefficient is governed by the assumed boundary friction law on the contacts. As speed increases the amount of oil entrained into the bite rises and the area of contact ratio falls. This leads to a drop in friction coefficient. At very high speeds friction is dominated by shearing of the oil, explaining the small rise in friction at the end of the plot. At the highest speeds the value of forward slip become negative, indicating skidding which would lead to poor mill control.



**Figure 4.15** Predicted variation of average Coulomb friction coefficient  $\mu$  and forward slip  $G$  with roll speed (Montmitonnet et al, 2001)

Tabary et al (1996) describe a series of experimental measurements of strip roughness and corresponding friction coefficient when cold rolling aluminium using smooth or rough rolls in the mixed lubrication regime. A comparison between the inferred friction coefficient from these trials and the predictions of the two-wavelength model of Le and Sutcliffe (2001a) is given in Figure 4.16. Three approaches are used to model friction. In the simplified 'semi-empirical' approach, the surface roughness is modelled using only a single wavelength of roughness, but the boundary friction coefficient is allowed to vary with smooth film thickness according to measurements on a strip drawing rig. The two-wavelength model tracks the change in roughness amplitude for two wavelengths of roughness, using a simple Coulomb friction



**Figure 4.16** Comparison of predictions with measurements for the variation of mean friction coefficient with speed parameter;  $r$  is the strip reduction (Le and Sutcliffe, 2001a)

coefficient of  $\mu_b = 0.09$  on the contact areas. Both theories give reasonable agreement with experiments, showing the transition from high to low friction coefficient as the speed and hence lubrication parameter  $\Lambda_s$  increases. The semi-empirical model benefits from being simple to use, but requires some input from strip-drawing or similar experimental data. It is expected that this would be the most suitable model for commercial exploitation. The two-wavelength model, while being more difficult to implement, does not require input from empirical data, so that it serves as a valuable research tool to justify and calibrate the semi-empirical model. By comparison, the theoretical predictions shown on Figure 4.16 for a constant friction coefficient and a single wavelength are not able to predict the measured friction values satisfactorily. Montmitonnet et al (2001) compared predictions of their model with these trial data, and found that good agreement could be obtained by assuming that the boundary friction factor fell with increasing rolling speed. It was suggested that this fall was due to increasingly effective micro-hydrodynamic lubrication of the plateaux (see section 4.4.1).

Tabary et al (1996) found that the variation of friction with rolling speed was not significantly different when using rough rolls and smooth strip, or vice versa, Figure 4.17. This implies that the use of a composite roughness for the roll and strip roughnesses is appropriate, and that ploughing of the strip by asperities on the roll does not make a significant contribution to friction, for the conditions of these experiments with longitudinal roughness.

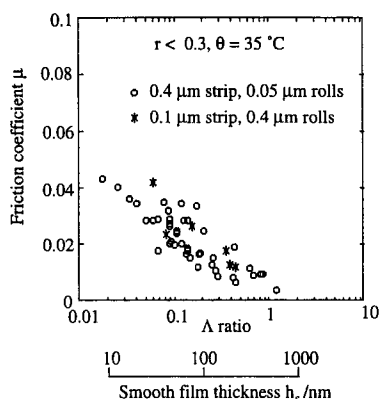


**Figure 4.17** Measured variation of mean friction coefficient  $\mu$  with speed parameter  $\Lambda$  and smooth film thickness  $h_s$  for rough strip and smooth rolls, or vice versa (Tabary et al, 1996)

Li (1995) describes a series of rolling experiments on aluminium and low carbon steel in the mixed lubrication regime. They find that the inferred friction coefficient increases with increasing reduction for both materials and decreases with rolling speed. Friction correlates well with the lubrication parameter  $\Lambda_s$ , allowing them to derive a simple empirical friction model. As with the film thickness model of Rasp and Häfele (1998), this model does not include the details of hydrodynamic lubrication and asperity flattening described in section 4.3.1 above.

#### 4.3.4 Other experimental results

An abundance of early measurements of strip surface roughness and friction in cold rolling is reviewed by Schey (1970, 1983b) and Roberts (1978), although it can be hard to interpret these measurements without corresponding observations and measurement of surface finish. As expected, where conditions are in the mixed lubrication regime, frictional conditions fall with increasing rolling speed. The dependence of friction on strip reduction is not clear. Lenard (2000) presents typical results for a low carbon steel, showing a fall in friction coefficient with increasing rolling speed and reduction. By contrast, in common with the findings of Tabary et al (1996), he shows an increase in friction coefficient with increasing reduction for various aluminium alloys. It is not clear why these two metals should show such differing behaviour. Perhaps boundary friction and the role of transfer films are significantly different in these cases (see sections 4.5 and 4.6 below).



#### 4.3.5 Foil and temper rolling

For thin foil or temper rolling, elastic deformation of the rolls needs to be included to predict the shape of the bite region (Fleck et al, 1992). Because the bite is very long compared with the thickness of the strip, the rolling load or reduction is particularly sensitive to friction. Table 4.2, section 4.3.1.5, summarises a number of tribological foil models. Coupled solutions including roll deformation are described by Sutcliffe and Montmitonnet (2001) and Le and Sutcliffe (2002a). Luo and Keife (1997), Keife and Jonsäter (1997) and Pawelski et al (1998) present foil models coupled with simplified tribological models, in which the change in contact ratio does not take into account the hydrodynamic pressure in the valleys or the effect of bulk straining. Domanti and Edwards (1996) perform dry calculations for temper and foil rolling to predict frictional and rolling parameters in the bite.

The predictions of Sutcliffe and Montmitonnet (2001) highlight the critical importance of friction in foil rolling. Figure 4.18 illustrates typical results for the variation of rolling load with rolling speed, at constant reduction. Note that the variation in load is plotted on logarithmic axes. As the speed falls, the area of contact ratio rises leading to a rise in friction and a very large increase in rolling load. Le and Sutcliffe compare model predictions with measurements from mill trials, in which aluminium foil was reduced in thickness from about 30 to 15  $\mu\text{m}$  under typical industrial conditions, see Figure 4.19. Because of the considerable roll flattening in this pass, the predicted load is very sensitive to the details of both the friction and elastic roll deformation models, so that the reasonable agreement found confirms the accuracy of these models. The differences between predictions and measurement of forward slip are explained by variations in friction coefficient through the bite, perhaps arising from thermal or tribo-chemical effects. Good agreement between measured and predicted loads is achieved at the less demanding earlier passes where there is less roll deformation.

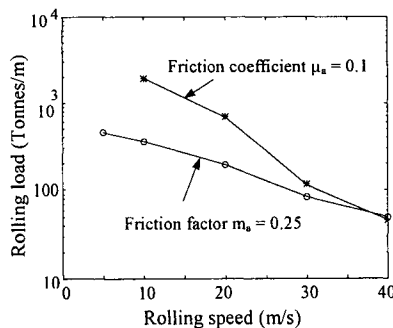
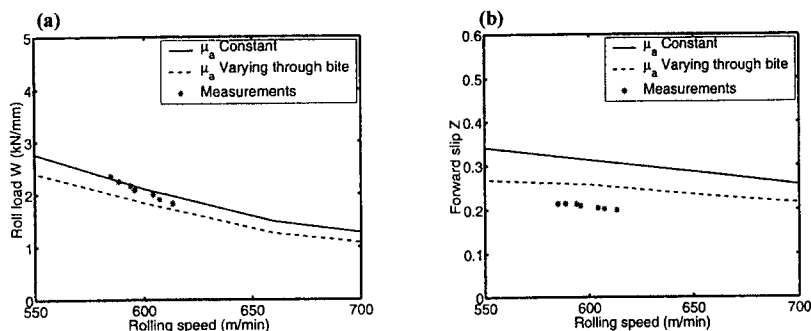


Figure 4.18 Predicted variation of rolling load with speed for thin foil (Sutcliffe and Montmitonnet, 2001)



**Figure 4.19** Comparison of measured and predicted variation of (a) rolling load and (b) forward slip with rolling speed for an aluminium foil pass from 30 to 15  $\mu\text{m}$  (Le and Sutcliffe, 2002a)

### 4.3.6 Thermal effects

Although thermal effects are much less significant in cold than in hot metal rolling, nevertheless there are significant temperature gradients in the bite, with both deformation work and friction generating heat. From a tribological point of view, temperature rises are important because they can give a substantial reduction in viscosity and because they can affect the tribo-chemistry in the bite, particularly in the presence of additives. In the inlet the oil temperature will be close to that of the roll and strip at that location. However these surfaces, in turn, will tend to be close in temperature to that of the lubricant as it is applied in abundance as a coolant. Some viscous heating of the oil will occur in the inlet region. The magnitude of this effect can be estimated from the results of Wilson and Murch (1976). Significant rises in oil temperature experienced in the bite will not affect the amount of oil entrained, but will affect friction, via changes in viscosity, or possibly via changes in additive performance. Sa and Wilson (1994) present an appropriate model for full film lubrication. In the mixed lubrication regime changes in heat transfer coefficient at the interface will significantly affect the apportioning of heat between the strip and roll.

## 4.4 MICRO-PLASTO-HYDRODYNAMIC LUBRICATION (MPHL)

For concentrated contact of elastic solids, so-called micro-elasto-hydrodynamic lubrication (micro-EHL) theory has been developed to investigate the tribological conditions under asperity contacts. By analogy, micro-plasto-hydrodynamic lubrication (MPHL) addresses this issue for the case where the workpiece is deforming plastically.

The importance of the MPHL mechanism can be judged from the work of Mizuno and Okamoto (1982), who measured sliding friction between a steel tool and a copper workpiece. The material was first deformed using the plane strain compression test (see Figure 4.27) and then the top platen was slid relative to the workpiece.

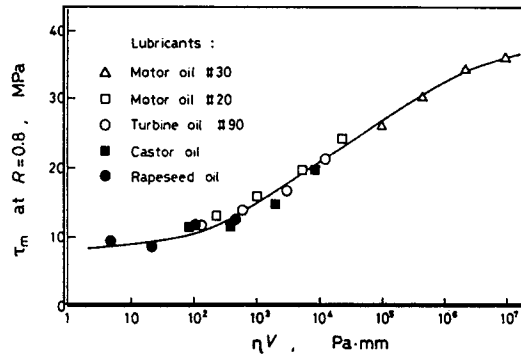


**Figure 4.20** Variation of friction stress  $\tau_m$  with product of viscosity  $\eta$  and sliding speed  $V$  for a copper workpiece slid relative to a flat platen, after being compressed (Mizuno and Okamoto, 1982)

Although the material was not deforming during sliding, nevertheless the deformation prior to sliding ensured that it conformed closely to the tool and was at the point of yield. They observed that the measured friction stress could be correlated with the product  $\eta V$  of the viscosity and the sliding speed, as shown in Figure 4.20. Below a value of  $\eta V$  of about 100 Pa mm the friction stress is independent of sliding speed, suggesting that lubrication is due to shearing of adsorbed boundary molecules (see section 4.5). Above this value, the increase of friction with  $\eta V$  indicates that hydrodynamic effects control friction. It was suggested that the hydrodynamic film was created by outflow of oil from the pits during the sliding process. By assuming that friction is all due to bulk shearing of the fluid under the contacts, a film thickness can be inferred (Sutcliffe 1989). For values of  $\eta V$  equal to 100 and 1000 Pa mm the corresponding film thicknesses are 8 and 53 nm. Note that these inferred film thicknesses are larger than the length of a typical additive (Schey, 1970, gives a value of 3nm for calcium stearate), so that it seems reasonable to suppose that friction could be due to shearing of such a MPHL film.

Although micro-EHL modelling has become a relatively well-filled field of research, the same is not true of MPHL. Montmitonnet (2001) notes that the range of finite element techniques used for micro-EHL could usefully be brought to bear on MPHL, although complications arising from the need to model the effect of bulk plasticity make this task appear formidable.

#### 4.4.1 Micro-plasto-hydrodynamic lubrication in the mixed lubrication regime

In section 4.3 on mixed lubrication, it was supposed that the interface between roll and strip could be divided into 'contact' areas and valleys. In practice, it may be possible to generate a very thin film even in the contact areas. Sutcliffe and Johnson

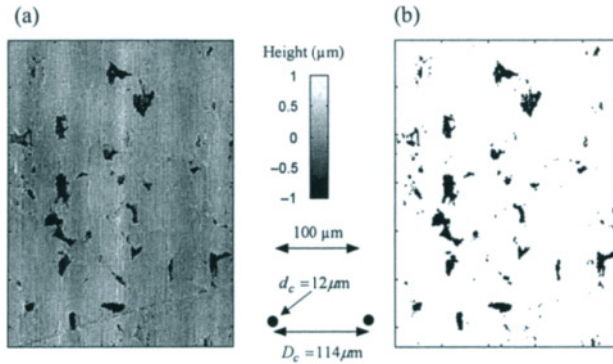
(1990b) present a simple analysis for MPHL at the entry to the bite. They adopt a simple geometric model for an asperity which is at the point of making contact with the roll. Using a finite difference method they calculate the 2-dimensional pressure distribution and film thickness under the asperity contact.

A more sophisticated model, tracking the evolution of valley pressure and asperity geometry around the point where the asperities first make nominal contact, would be needed to provide more confidence in the above approach. It is also likely that non-Newtonian viscous behaviour of the lubricant (see section 4.3.1.4) will play a significant role, because of the high strain rates associated with the thin films (Sheu and Wilson, 1982).

#### ***4.4.2 Micro-plasto-hydrodynamic lubrication of pits***

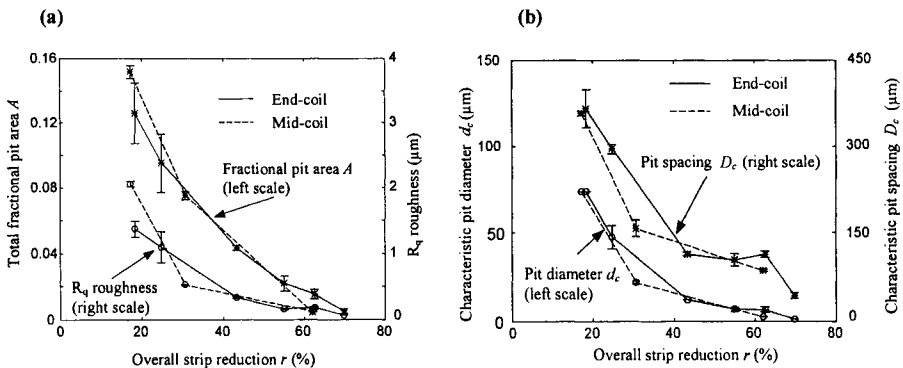
Micro-PHL theory has been much more successfully applied to lubrication from isolated pits, probably because of the simpler geometry in this case than in the mixed lubrication problem. Such pits are typically found for isotropic surfaces, such as generated from the shot-blast finish on stainless steel strip. Build-up of hydrostatic pressure in the pits as they are reduced in volume tends to prevent the pits being eliminated (Kudo, 1965). However, in the presence of sliding between the tool and strip, this oil can be drawn out of the pits due to hydrodynamic action. Lo (1994) identifies a 'percolation threshold', below which isolated pits will form. Various experimental studies have considered MPHL, frequently using artificial indents to help observe the phenomenon (Fudanoki, 1997, Kudo and Azushima, 1987, Kihara et al, 1992, Wang et al, 1997). An extension to this idea is provided by Sheu et al (1998, 1999), who propose a two-scale topography. The coarse scale (e.g. deep pits) allows transport of lubricant into the work zone, while the finer scale roughness delivers lubricant throughout the surface

***4.4.2.1 Measurement of pit geometry.*** Pitting on a cold-rolled strip surface tends to be irregular, with a range of pits of different sizes and shapes. Here 3-D profilometry is invaluable in gathering the data, but it is not obvious how to synthesise it. Ahmed and Sutcliffe (2000) and Sutcliffe and Georgiades (2001) show how the raw data can be used to extract statistics of the pit geometry and hence a 'characteristic' pit diameter, spacing, depth and slope. The method is illustrated for samples of industrially-rolled bright annealed stainless steel, which had a rough shot-blast finish prior to cold rolling. The pit identification method is illustrated in Figure 4.21, for a strip reduction of 43% relative to the initial shot-blast hot band. Figure 4.21(a) shows the raw data from the profilometer, while Figure 4.21(b) shows the individual pits which have been identified, along with the 'characteristic' pit diameter and spacing. The method is effective at identifying pits seen visually, while the characteristic values of pit diameter and spacing seem reasonable.



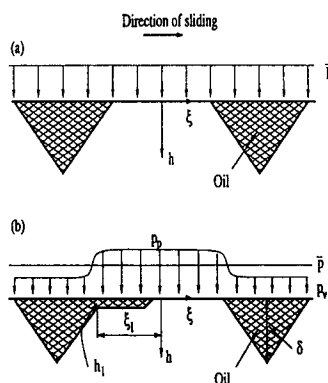
**Figure 4.21** Example of pit identification on stainless steel strip; (a) Profilometry data. The greyscale gives the surface height, with darker colours being pits, (b) Pits identified in black. Values of a characteristic pit diameter  $d_c$  and spacing  $D_c$  for this sample are indicated on the figure (Sutcliffe and Georgiades, 2001)

Figure 4.22(a) shows the change through the pass schedule in total pit area and roughness amplitude with overall strip thickness reduction. As the strip is reduced in thickness, both the percentage pit area and the strip roughness fall, with a good correlation between the area and roughness. The change in characteristic pit diameter and spacing through the pass schedule is shown on Figure 4.22(b). The characteristic pit diameter falls from about 75  $\mu\text{m}$  after the first pass to only a few microns at the end of the schedule, as the large features coming from the shot-blasting process are progressively flattened.



**Figure 4.22** Variation of surface parameters with overall strip reduction during rolling of stainless steel (a) fractional pit area and  $R_q$  roughness, (b) pit diameter and spacing (Sutcliffe and Georgiades, 2001)

**4.4.2.2 Modelling and comparison with experiments.** The starting point for the analysis is the work of Kudo (1965), who shows how hydrostatic pressure can build up during bulk deformation. Azushima (2000) uses the finite element method (FEM) to analyse the generation of hydrostatic pressure in the pits. He takes into account oil compressibility but ignores oil leakage via the interface. Lo and Wilson (1999) and Lo and Horng (1999) derive a theoretical model using hydrodynamic theory, showing how pit crushing depends on pit geometry and hydrodynamic conditions. A schematic model of the problem is shown in Figure 4.23. The rise in oil pressure at the trailing edge of the pit can be found by hydrodynamics. The oil flow rate out of the pit is also determined by the asperity crushing rate, which in turn is governed by the difference between the valley and plateau pressures. The solution for the change in asperity geometry and corresponding oil film thickness at the trailing edge is given by coupling the hydrodynamic and mass flow equations for the oil with the mechanics model for deformation of asperities. This model was further developed and applied to the rolling and drawing processes by Sutcliffe et al (2001) and Le and Sutcliffe (2002b). Sheu et al (1999) developed a FEM model to investigate work-piece material extrusion into artificial cavities on a tool surface with trapped oil. The fluid cavity is modelled as a porous foam filled with oil that can permeate via a porous media in the interface between the tool and work-piece. This allows for the coupling of hydrostatic permeation and surface deformation.



**Figure 4.23** Schematic of MPHL mechanism drawing oil out of pits due to relative sliding between tool and workpiece (after Lo and Wilson, 1999)

Figure 4.24 shows Le and Sutcliffe's (2002b) comparison of theoretical predictions of pit area with measurements from industrial samples of cold rolled strip with an initial shot-blast surface. In general agreement is good; the difference between results would probably be closed up by considering the statistical variation in pit geometries.

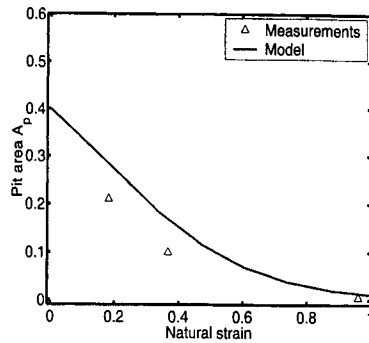


**Figure 4.24** Comparison of predicted and measured variation in pit area with bulk strain for rolling of stainless steel strip (Le and Sutcliffe, 2002b)

The effect of oil entrainment at the inlet can be estimated by the lubrication parameter  $A_s$ , here denoted as  $A_i$ . Ahmed and Sutcliffe (2001) suggest a corresponding parameter  $A_m$  to characterise the MPHL lubrication mechanism, as the ratio of the initial pit volume to an estimate of the volume drawn out during sliding. Regime maps have been constructed both from theoretical simulations and from experimental measurements of surface roughness, by plotting the change through the pass schedule in the lubrication parameters  $A_i$  and  $A_m$ . Figure 4.25 illustrates such a map for a theoretical simulation of a multi-pass schedule, with each pass having a strip reduction of 15% (Le and Sutcliffe, 2002b). Initially the inlet parameter  $A_i$  is very much less than one, indicating that there is negligible oil film entrained at the inlet. The value of  $A_m$  is also less than one, showing that it is relatively difficult to draw oil out of the pit in the initial pass. Further down the schedule the inlet and MPHL parameters rise, as the pit depth reduces. The increase in  $A_m$  above one indicates that the oil is very rapidly drawn out by the MPHL mechanism, so that this is not a limiting factor. Instead conditions can be expected to be similar to that for dry rolling. Towards the final pass, particularly for the shallowest pits and at the higher rolling speed, the inlet parameter  $A_i$  approaches one, indicating that there is now a significant oil film entrained at the inlet, which tends to inhibit the elimination of the pits. Corresponding regime maps derived from experiments are shown in Figure 4.26 (Sutcliffe and Georgiades, 2001). For each pit on a given sample, values of the lubrication parameters  $A_m$  and  $A_i$  are calculated and

plotted on the figure. Deeper pits are towards the bottom left of each line. These results are in good qualitative agreement with the theoretical predictions.

An alternative mechanism for oil flow from pits has been described by Bech et al (1999) and Shimizu et al (2001), in which the gradients of hydrostatic pressure can lead to oil flow. This micro-hydrostatic lubrication mechanism is more relevant to low speed rolling; at high speeds hydrodynamic lubrication dominates. See also Chapter 7.

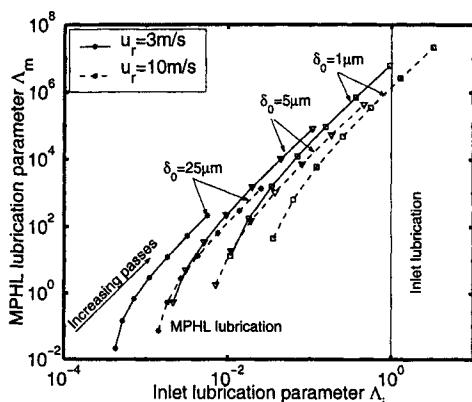


**Figure 4.25** Theoretical regime map showing the predicted change in the lubrication parameters  $\Lambda_m$  and  $\Lambda_i$  for MPHL and inlet lubricant entrainment of pits. The trajectories show the change in lubrication regime during a typical pass schedule associated with the progressive reduction in pit depth (Le and Sutcliffe, 2002b)

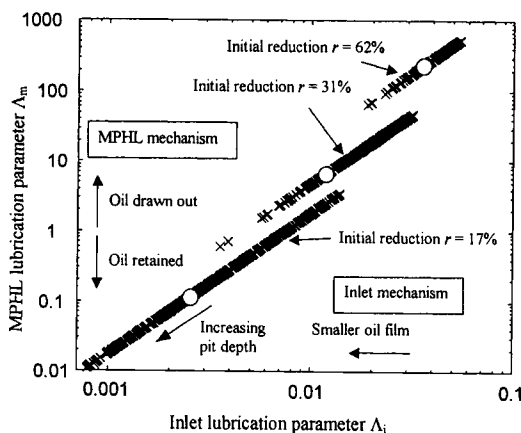


**Figure 4.26** Experimental regime map showing the change in lubrication parameters  $\Lambda_m$  and  $\Lambda_i$  for MPHL and inlet lubricant entrainment of pits on strip samples (Sutcliffe and Georgiades, 2001)



#### 4.5 BOUNDARY LUBRICATION

The original definition of boundary lubrication was for 'lubrication in which friction depends not only on the properties of the lubricant but also on the chemical nature of the solid boundaries' (Hardy and Doubleday, 1922). However, as Ike (1999) notes, the distinction between hydrodynamic and boundary lubrication has become increasingly blurred as both measurement and modelling have reached down to molecular dimensions. Interferometry measurements on oil films which are only a few molecules thick show quasi-hydrodynamic behaviour; atomic force microscopy (AFM) measurements show solidification of liquid near a crystalline solid and models of lubricant flow are increasingly concerned with simulation at a molecular level (see reviews by Spikes, 2000 and Bushan, 1995). On a practical level, it is in any case very difficult to distinguish between MPHL and boundary lubrication. For elastic contacts, this problem can be avoided by using atomically smooth surfaces (e.g. surface force apparatus or AFM, see Bushan, 1995), but during metal-forming processes new surface is continually being created, so that this approach is not feasible. Probably, as suggested by Montmitonnet et al (2001), the situation in the contact areas in much metal forming is a mixture of MPHL and boundary lubrication, with perhaps some unlubricated regions as well. Some authors refer to this as the thin film regime. In this section we follow the original definition of boundary lubrication as depending on the physico-chemical interactions at the interface, although it is unlikely that the experimental results discussed below are free from MPHL influences.

An estimate of the film thickness under these 'thin film' conditions is made by Ike (1999), based on the roughness, measured using AFM, of surfaces deformed by a very smooth gauge block. He postulated that the measured roughness of the strip after deformation was equal to the film thickness separating the surfaces. Results suggest that the film thickness is of the order of 1 nm, comparable to several molecular widths.

Although boundary friction is critical in cold rolling, there is rather scant information on how to model it. The great bulk of published research on boundary lubrication, both experimental and theoretical, considers the more common case where there is little if any deformation of the surfaces in contact and cannot be applied directly to modelling of boundary lubrication in metal working. Early work on boundary lubrication concentrated on the role of adsorbed molecules (Rowe, 1966). However it is clear that reactive molecules will absorb chemically on the surface, particularly where, as in metal rolling, there is considerable fresh metal surface formed in the bite. Wakabayashi et al (1995) illustrated this for gas-phase lubrication of orthogonal machining, where they showed that frictional behaviour can only be understood in terms of a chemisorption of the lubricant at the tool-workpiece interface. Mori et al (1982) present a study of chemisorption by organic compounds on a clean aluminium surface prepared by cutting. They find that the rate of absorption was proportional to the cutting speed, with absorption taking place both during and after cutting. It was suggested that the absorption rate was related to the formation rate of new aluminium surface. Equally

it might be expected that the oxide film behaviour will be important (Milner and Rowe, 1962, Li et al, 1999).

Other work on boundary lubrication in metal forming highlights the role of additives. Chambat et al (1987) showed that organo-metallic compounds were produced during industrial foil rolling of aluminium. Increasing the concentration of an additive package from 0.1 to 4% was found to bring about a significant reduction in friction factor during plane strain compression tests on steel (Kubié, 1980). Oleic acid at a concentration greater than 1% was effective for aluminium and stearyl amine was effective at much lower concentrations (Kubié, 1980, Johnston and Atkinson, 1976). Stearic acid at 1% in mineral oil was effective at preventing metal transfer in twist compression tests using aluminium while the shorter chain lauric acid was ineffective, as was the unsaturated oleic acid (Nautiyal and Schey, 1990). In these tests a dark non-metallic appearance to the tool developed with the stearic acid, through which details of the anvil could be observed in the SEM. It was suggested that this film was due to reaction products (see section 4.6 below). Increasing the chain length of saturated acids at a 1% concentration in hexadecane increased the effectiveness of boundary lubrication for ball-on-cylinder tests (both components being steel), with a loss of effectiveness for the stearic acid at about 130°C (Jahanmir, 1985). A transition temperature was observed in these tests at low speed, while none was observed at higher speeds for the 16 and 18 carbon atom additives. From this evidence it was suggested that adsorbed monolayers controlled friction at low speeds, while at higher speeds partial hydrodynamic lubrication occurred, with the influence of the additives arising from the presence of ordered monolayers. Matching of the additive and base oil chain lengths was not found to influence the friction coefficient. In the twist-compression and ball-on-cylinder tests there was no bulk plastic deformation. However the high local pressures at the asperity tops will lead to deformation there, particular for the twist-compression tests with aluminium. It is not clear how results without bulk deformation can be used for metal forming processes. This will depend on the mechanisms controlling boundary friction, and hence the importance of the bare metal surface created during metal forming.

Finally, leaving aside for a moment the question of the frictional stress at the interface, Wilson (1991) presents a series of models for boundary lubrication where roughness interactions between the roll and strip play a role (for example generating a ploughing term). The contact ratio depends on a balance between the flattening mechanism discussed in section 4.2 and opening up of gaps between the roll and strip as asperities slide past one another, as illustrated in Figure 4.9.

#### **4.6 TRANSFER LAYERS**

Montmitonnet et al (2000) have recently highlighted the role of transfer films in metal rolling. Transfer films have been observed in the laboratory both in rolling and plane strain compression testing of a variety of metals. The formation of these films provides the key to understanding the evolution of friction during both types of tests.

Moreover similar films are seen in industrial practice; rolls used for aluminium develop a blueish sheen, while a brown film adheres to rolls used for stainless steel. The most extensive series of tests have been undertaken by Kubié (1980) (see Delamare et al, 1982), using the plane strain compression test shown schematically in Figure 4.27. Flat strip is compressed between flat parallel platens. For appropriate strip and platen geometries, the deformation mode is similar to that in cold metal rolling, justifying the use of such a test to model rolling, although tribological conditions may differ.

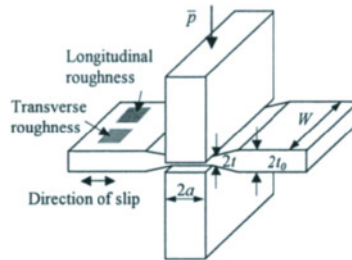


Figure 4.27 Schematic of plane strain compression test

In Kubié's studies, a series of indentations was made on the strip (using a fresh part of the strip for each indentation). Figure 4.28 shows a typical variation in friction stress with indentation number on stainless steel. As a 'low friction slurry' transfer layer builds up on the initially clean tool, the friction stress drops significantly. After 12 indentations the tool was cleaned with an absorbent paper, removing the transfer layer and restoring the frictional stress to its original value. AES studies showed this film to be composed of strip metal (plus additives and lubricant, as deduced from its slurry-like behaviour). The slurry tended to reduce the roughness of the tool by filling in the valleys. For Zircaloy alloys a much more solid transfer layer was formed on the tool, giving rise to a significant rise in friction factor with indentation number.

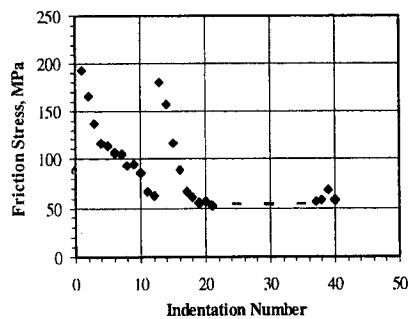
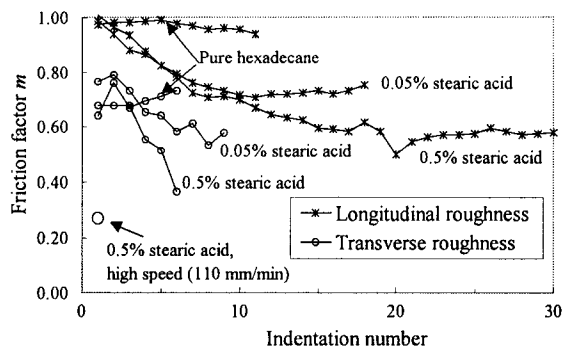


Figure 4.28 Variation of friction stress with indentation number for plane strain compression of stainless steel. The tool is cleaned after indentation number 12 (Montmitonnet et al, 2000)

Recent work by Dauchot et al (1997, 1999, 2001) compared rolling and plane strain compression of both aluminium and steel, and related results to ToF-SIMS analysis (Time-of-Flight Secondary Ion Mass Spectroscopy). Rolls used to deform aluminium alloy show an accumulation of a relatively thick transfer film, with thicker films formed at the edges of the strip where lubrication is poor, suggesting that the formation of the transfer film is a function both of the lubrication conditions and the chemistry at the interface.

Sutcliffe et al (2002) describe a detailed series of plane strain compression tests on aluminium strip to investigate the tribology in the thin film regime. Both a formulated lubricant containing ester as additive and a lubricant comprised of hexadecane plus stearic acid additive in concentrations of 0, 0.05 and 0.5% were used. The friction factor  $m$  was estimated for a variety of process conditions, and correlated with surface analysis techniques, including SEM, profilometry and ToF-SIMS. The strip surface conformed very closely to the tool except at the middle of the indent, suggesting that only a very thin oil film, if any, could separate the tool and strip surfaces. Figure 4.29 shows typical results for the variation in friction factor with indentation number, using hexadecane plus stearic acid as lubricant. For the first few indents the friction factor is close to one, implying shearing of the strip metal surface. Results are independent of additive concentration. After a few indents a transfer layer built up on the tool, leading to a significant fall in friction factor. This transfer layer was of the 'low friction slurry' type, and could be easily removed with an absorbent paper. The reduction in friction associated with this transfer layer increased with increasing additive concentration and more effective hydrodynamic or hydrostatic lubrication (as evidenced by effects of speed, roughness orientation and oil starvation). It seems that, in this case, the role of the additive lies not in protecting the surfaces in the first instance, but in generating a better transfer layer.



**Figure 4.29** Variation of friction factor with indentation number for plane strain compression of aluminium strip using hexadecane and stearic acid as lubricant (Sutcliffe et al, 2002)

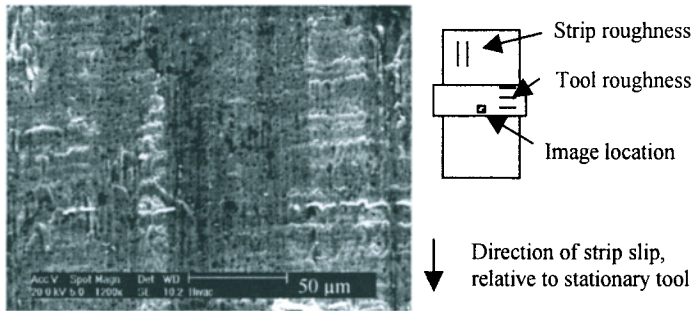


**Figure 4.30** SEM image near the edge of an aluminium strip after 9 indents by plane strain compression using hexadecane and 0.5% stearic acid as lubricant (Sutcliffe et al, 2002)

Figure 4.30 shows an SEM image of a strip after 9 indents. An imprint of the tool surface roughness is clearly seen running horizontally on the strip, indicating thin film conditions. It appears that dark areas seen on the strip correlate with regions where the tool roughness is not imprinted on the strip. Presumably both the dark areas and the change in strip topography are due to a transfer layer forming on the tool. ToF-SIMS analysis revealed the presence of stearate and aluminium stearate ions on both the tool and strip, spreading from the edge of the indent towards the middle with increasing indentation number. The presence of aluminium stearate gave evidence of adsorption and reaction of the stearic acid with the bare aluminium surface. Aluminium stearate was not found due to mere contact of the aluminium with stearic acid, in the absence of bulk deformation.

#### 4.7 CONCLUSIONS

The results described in this chapter show how the mechanics of lubrication in cold rolling in the industrially-relevant mixed lubrication regime is now reasonably well understood. Section 4.2 identifies the importance of bulk deformation of the strip in facilitating asperity crushing. Hydrodynamic pressure is induced in the lubricant due to the entraining action of the roll and strip. Modifications to Reynolds' equation to include the effect of roughness are described. The interaction between the deformation of asperities and the hydrodynamic pressure has been effectively modelled and predictions of film thickness and surface roughness are in good agreements with measurements. Details of the roughness topography are seen to be important; in particular the importance of short wavelengths of roughness is highlighted.

Frictional models have also been successfully developed for the mixed lubrication regime, both for strip and foil rolling. However the mechanisms of friction on the contact areas are still not clear. Although traditionally this has been supposed to be due to boundary lubrication, empirical models suggest some hydrodynamic action,

probably due to a micro-plasto-hydrodynamic lubrication (MPHL) oil film. Models for such an MPHL film generated in the inlet are not well established.

However useful models of MPHL have been developed for the alternative scenario, where oil trapped in isolated pits in the inlet is drawn out in the bite due to sliding between the roll and strip. Measurements and analysis of the pit geometry using 3D profilometry are described, to show how the pits change during a roll schedule.

The chapter finishes with two sections on boundary lubrication and transfer films. Our knowledge of this area is largely empirical, with details expected to depend on the metal and lubricant chemistry. However the application of modern surface analysis techniques, in conjunction with further modelling, shows promise in developing our understanding of these phenomena. It is likely that appropriate models will need to include the asperity mechanics and MPHL models described above, along with the tribo-chemistry of the contact.

## REFERENCES

- Ahmed, R and Sutcliffe, M.P.F. (2000) *Wear*, **244**, 60-70.
- Ahmed, R and Sutcliffe, M.P.F. (2001) *ASME J. Tribology*, **123**, 1-7
- Al-Salehi, F.A.K., Firbank, T.C. and Lancaster, P.G. (1973) *Int. J. Mech Sci*, **15**, 693-710
- Azushima, A. (1978) in *Proc. 1st Int Conf. On Lubrication Challenges in Metalworking and Processing*, (IITRI, Chicago).
- Azushima, A. (2000) *ASME J. Trib.*, **122**, 822-827.
- Azushima, A., Natsui, M., Inagaki, S., and Sugai, T. (2000) *J. Iron and Steel Inst. Japan*, 47-52.
- Bair, S. and Winer, W. (1982) *J. Lubr. Tech.* **101**, 251-257
- Bay, N. and Wanheim, T. (1976) *Wear*, **38**, 201-209.
- Bech, J., Bay, N., Eriksen, M. (1999) *Wear*, **232**, 134-139.
- Bhusan B., Israelachvili J.N. and Landman U. (1995) *Nature*, **374**, 607-616.
- Bowden F.P. and Tabor, D. (1950) *The friction and lubrication of solids Vol 1*, Clarendon Press, Oxford, p. 98-100.
- Challen J.M. and Oxley, P.L.B. (1979) *Wear*, **53**, 229-243
- Chambat, F., Lashermes, M and Hendricks, H. (1987) *Lubrication Engineering.*, **43** 522-527
- Chang, D.F., Marsault, N., and Wilson, W.R.D. (1996) *Trib. Trans.*, **39**, 407-415.
- Childs, T.H.C. (1977) *Proc. Roy. Soc. London*, **A353**, 35-53.
- Christensen, H. (1970) *Proc. Instn Mech Engrs*, **104**, Pt 1, 1013-1022.
- Dauchot G. (1999) *Tribochimie du laminage à froid des aciers bas carbone et des alliages d'aluminium. Étude par ToF-SIMS de la chimisorption des additifs de lubrification*, PhD Thesis, École des Mines de Paris. (in French)

- Dauchot G., Combarieu R., Montmitonnet P., Repoux M., Dessalces G., and Delamare F. (2001) *Revue de Métallurgie- CIT/Science et Génie des Matériaux*, 159-169. (in French)
- Dauchot G., De Puydt Y., Combarieu R., Repoux M., and Delamare F. (1997) in *Proc. of the SIMS XI Conf*, ed. Gillen G., Lareau R., Bennett J., Stevie F., John Wiley & Sons, 513-516.
- Delamare, F, de Vathaire, M. and Kubié, J. (1982) *J. Lub. Tech.* **104**, 545-551.
- Domanti S. and Edwards, J. (1996) in *Proc. World Congress, Manufacturing Technology towards 2000, Sept 1997, Cairns Australia*
- Evans, C.R. and Johnson, K.L. (1986) *Proc. Instn. Mech. Engrs.*, **200C**, 313-324
- Fleck, N.A., Johnson, K.L., Mear, M.E. and Zhang, L.C. (1992) *Proc. Instn. Mech. Engrs*, **206**, 119-131
- Fogg, B. (1968) *Proc. Conf. On Properties and metrology of surfaces* (Inst. Mech. Engrs.)
- Fudanoki, F. (1997) in *Proc. 1st Int. Conf. on tribology in manufacturing Processes*, Gifu, Japan, p. 378-383.
- Greenwood, J.A. and Rowe, G.W. (1965) *Wear*, **38**, 201-209.
- Hardy, W.B. and Doubleday, I. (1922) *Proc. Roy. Soc. London*, **A100**, 550-574.
- Hill, R. *The mathematical theory of plasticity* (Oxford Clarendon Press)
- Ike, H. (1999) *Wear*, **224**, 73-88.
- Ike, H. and Makinouchi, A. (1990) *Wear*. **140**, 17-38
- Jahanmir S, (1985) *Wear*, **102**, 331-349
- Jeswiet, J. (1998) in *Proc 7th Int. Conf. Metal Forming 98, Birmingham*, p239-244
- Johnston W.G. and Atkinson R.E. (1976) *Lubr. Engng*, **32**, 242
- Keife, H. and Jonsäter, T. (1997) *ASME J. Trib.*, **119**, 349-357.
- Keife, H. and Sjögren. (1997) *Wear*, **179**, 137-142.
- Kihara, J., Kataoka, S., and Aizawat, T. (1992) *Journal of Japan Society for Technology of Plasticity*, **33-376**, 556-561.
- Korzekwa, D.A., Dawson, P.R. and Wilson, W.R.D. (1992) *Int. J. Mech. Sci.* **34**, 521-539.
- Kubié, J. (1980) *Le test de bipoinçonnement: étude théorique – application à l'étude du transfert de matière dans un contact frottant*, PhD Thesis, École des Mines de Paris (in French)
- Kudo, H. (1965) *Int. J. Mech. Sci.* **7**, 383-388
- Kudo, H. and Azushima, A. (1987) in *Proc. 2<sup>nd</sup>. Int. Conf. On Adv. Technol. of Plasticity*, Stuttgart, p. 373 .
- Le, H.R. and Sutcliffe, M.P.F. (2000a) *STLE Trib. Trans.*, **43(4)**, 595-602.
- Le, H.R. and Sutcliffe, M.P.F. (2000b) *Wear*, **244**, 71-78.
- Le, H.R. and Sutcliffe, M.P.F. (2001a) *Submitted to ASME J Trib*,
- Le, H.R. and Sutcliffe, M.P.F. (2001b) *STLE Trib. Trans.*, **44**, 284-290.

- Le, H.R. and Sutcliffe, M.P.F. (2002a) *ASME J Trib*, **124**, 129-136
- Le, H.R. and Sutcliffe, M.P.F. (2002b) *Submitted to ASME J Trib*
- Lenard, J.G. (2000) *Tribology International*, **35**(2), 123-128
- Li, G.Y. (1995) *Friction in cold rolling force prediction*, PhD Thesis, The Royal Inst. of Tech, Stockholm
- Li, Y.H., Krzyzanowski, M., Beynon, J.H. and Sellars, C.M. (1999) *Proc 3rd Int. Conf. on Physical and numerical simulation of materials and hot working (ICPNS '99)*, Beijing, China
- Lin, H.S. (1998) *A mixed lubrication model for cold strip rolling*. Ph.D. Thesis, Mechanical Engineering, Northwestern University.
- Lin, H.S., Marsault, N., and Wilson, W.R.D. (1998) *STLE Trib. Trans.*, **41**, 3, 317-326.
- Lo, S.W. (1994) *ASME J. Tribology*, **116**, 640-647
- Lo, S.W. and Horng, T.C. (1999) *ASME J. Trib.*, **121**, 633-638.
- Lo, S.W. and Wilson, W.R.D. (1999) *ASME J. Trib.*, **121**, 731-738.
- Luo, C. and Keife, H. (1997) *Proc. 1st Int. Conf. Tribology in Manufacturing Processes*, Gifu, Japan, p364-371
- Makinouchi, A., Ike, H., Murakawa, M. Koga, N. and Ciupik, L.F. (1987) *Proc. 2nd Int. Conf. Technol. Plasticity, Stuttgart*, 56-66
- Marsault, N, Montmitonnet, P, Deneuille, P and Gratacos, P. (1998) *Proc. NUMIFORM 98*, Twente University, Netherlands, A.A. Balkema (Rotterdam) 715-720.
- Marsault, N. (1998) *Modélisation du régime de lubrification mixte en laminage à froid*. PhD Thesis, École des Mines de Paris, France (in French)
- Milner, D.R. and Rowe, G.W. (1962) *Metallurgical Reviews*, **7**, 433-480
- Mizuno, T., and Okamoto, M. (1982) *ASME J. Lub. Tech.* **104**, 53-59.
- Montmitonnet P, Delamare F, and Rizoulières B. (2000) *Wear*, **245**(1-2), 125-135.
- Montmitonnet, P. (2001), *C.R. Acad. Sci. Paris, Série IV*, **12**, 729-737.
- Montmitonnet, P., Marsault, N., Deneuille, P. and Gratacos, P. (2001), *Revue de Metallurgie - Cahiers d'informations techniques*, **98**(5), 423-433 (in French)
- Mori, S., Suginoia, M., and Tamai, Y. (1982) *ASLE Trans.* **25**, 261-266.
- Nautiyal P.C. and Schey, J.A. (1990) *ASME J Trib.* **112**, 282-287
- Patir, N. and Cheng, H.S. (1978) *ASME J. Lub. Tech*, **100**, 12-17.
- Patir, N. and Cheng, H.S. (1979) *ASME J. Lub. Tech*, **101**, 220-230.
- Pawelski, O., Rasp, W., Häfele, P. and Wengenroth, W. (1998) In *Proc. 1st Esaform Conf. on Material Forming*, Sophia-Antipolis (France), March 1998
- Qui, Z.L., Yuen, W.Y.D and Tieu, A.K. (1999) *ASME J. Trib.*, **121**, 908-915.
- Rasp W and Häfele, P. (1998) *Steel Researchs*, **69**, 154-160



- Roberts, W.L. (1978) *Cold rolling of steel* (Marcel Dekker, New York)
- Rowe, C.N. (1966) *ASLE Trans*, **9**, 101-11
- Sa C-Y. and Wilson, W.R.D. (1994) *ASME J. Trib.*, **116**, 569-576
- Schey, J.A. (1970) *Metal deformation processes: friction and lubrication* (Marcel Dekker Inc, New York).
- Schey, J.A. (1983a) *Lub. Engng*, **39**, 376-382.
- Schey, J.A. (1983b) *Tribology in metal working* (ASM, Metals Park, Ohio).
- Schmid, S.R. and Wilson, W.R.D. (1995) *Trib. Trans*. **38**, 452-458
- Sheu, S. (1985) *Mixed lubrication in bulk metal forming*. PhD Thesis, Northwestern Univ., Illinois, USA.
- Sheu, S. and Wilson, W.R.D. (1982) *ASME J. Lub. Tech.*, **104**, 568-574.
- Sheu, S. and Wilson, W.R.D. (1983) *Proc. NAMRC XI*, 172-178.
- Sheu, S. and Wilson, W.R.D. (1994) *STLE Tribology Trans*, **37**, 483-493.
- Sheu, S., Hector, L.G., and Karabin, M.E. (1999) *The integration of material, process and product design*, Zabarar, et al (eds), AA Balkema, Rotterdam, p157-166.
- Sheu, S., Hector, L.G., and Richmond, O. (1998) *ASME J. Trib.*, **120**, 517-527.
- Shimizu, I., Anreasen, J.L., Bech, J.I. and Bay, N. (2001) *ASME J. Trib.*, **123**, 290-294
- Spikes, H. (2000) *Proc. Instn Mech Engrs*, **214C** 23-37.
- Steffensen, H. and Wanheim, T. (1977) *Wear*, **43**, 89-98.
- Stout, K.J. and Blunt, L. (2000) *Three-dimensional surface topography* (Penton Press)
- Sutcliffe, M.P.F. (1988) *Int. J. of Mech. Sciences*, **30**, 847-868.
- Sutcliffe, M.P.F. (1989) *Friction and Lubrication in Metal Rolling*, PhD thesis, University of Cambridge.
- Sutcliffe, M.P.F. (1999) *ASME J. Trib.* **12**, pp433-440
- Sutcliffe, M.P.F. (1999) *ASME J. Trib.* **121**, 433-440
- Sutcliffe, M.P.F. and Georgiades F. (2001) *Submitted to Wear*,
- Sutcliffe, M.P.F. and Johnson, K.L. (1990a) *Proc. Instn Mech Engrs*, **204**, 263-273.
- Sutcliffe, M.P.F. and Johnson, K.L. (1990b) *Proc. Instn Mech Engrs*, **204**, 249-261.
- Sutcliffe, M.P.F. and Le, H.R. (2000) *STLE Tribology Transactions*, **43**, 39-44.
- Sutcliffe, M.P.F. and Montmitonnet, P. (2001) *Revue de Metallurgie - Cahiers d'informations techniques*, **98**(5), 435-442.
- Sutcliffe, M.P.F., Combarieu, R, Repoux, M and Montmitonnet, P. (2002) *Submitted to Wear*.
- Sutcliffe, M.P.F., Le, H.R. and Ahmed, R. (2001) *ASME J Tribology*, **123**, 1-7.

- Tabary, P.T., Sutcliffe, M.P.F., Porral, F. and Deneuille, P. (1996) *ASME J. Tribology*, **118**, 629-636.
- Tsao, P. and Sargent, L.E. (1977) *ASLE Trans*, **20**, 55-63.
- Wakabayashi, T, Williams, JA. and Hutchings, IM. (1995) *Proc. Instn Mech Engrs*, **209**, 131-136.
- Wang, Z., Dohda, K., Yokoi, N. and Haruyama, Y. (1997) *First International Conference on Tribology in Manufacturing Processes*, Gifu, Japan, 77-82.
- Wilson, W.R.D. (1991) *J. Engng Materials and Tech.*, **113**, 60-68
- Wilson, W.R.D. and Chang D.F. (1994) *ASME J Trib*, **118**, 83-89.
- Wilson, W.R.D. and Murch, L.E. (1976) *J. Lubrication Tech.*, **98**, 426-432
- Wilson, W.R.D. and Sheu, S. (1988) *Int. J. Mech. Sci.*, **30**, 475-489.
- Wilson, W.R.D. and Walowit, J.A. (1972) *Proc. of Tribology Convention*, I. Mech. E., London, 1971, 164-172.
- Wilson, W.R.D., and Marsault, N., 1998, *ASME, J. Tribology*, **120**, pp 1-5.

This Page Intentionally Left Blank

## Chapter 5

# Direct Observation of Interface for Tribology in Metal Forming

AKIRA AZUSHIMA

*Department of Mechanical Engineering  
Yokohama National University  
79-5 Tokiwadai Hodogaya-ku, Yokohama 240-8501  
Japan*

*Knowledge of the interaction between surface asperities and lubricant in the micro-contact mechanism at the interface between a tool and a workpiece is of great importance in clarifying tribological effects and the improvement of tribological techniques in cold metal-forming processes (Schey, 1983; Kudo and Azushima, 1986). The microcontact mechanism in the presence of lubricant has generally been classified into the regimes of boundary, mixed and hydrodynamic lubrication, depending on the average lubricant film thickness. In the mixed lubrication regime of metal-forming processes, the lubricant fills small pockets on the workpiece surface and a hydrostatic pressure by which part of the normal contact load is supported is generated in these surface pockets. In such a regime of mixed lubrication in metal forming, Kudo et al (1976) have observed an increase in the coefficient of friction with increasing speed of sheet drawing, and Azushima et al (1993) have observed an increase in the coefficient of friction with increasing contact pressure during flat tool drawing.*

*In order to interpret the speed and contact pressure dependences of the coefficient of friction, a new lubrication regime must be considered. Moreover, in order to develop a new model of the microcontact behavior in metal forming, direct in situ observation of the lubricant behavior at the interface between the tool and the workpiece is the most effective, if it is possible. In this chapter, for the purpose of interpreting the above speed and contact pressure dependences of the coefficient of friction and of establishing a model of microcontact behavior at the interface between the tool and the workpiece, the microcontact behavior at the interface is observed in situ using a direct observation apparatus.*

## 5.1 DIRECT OBSERVATION OF INTERFACE IN SHEET DRAWING

Kudo et al (1976) have observed an increase in the coefficient of friction  $\mu_N$  with increasing speed in sheet drawing experiments of aluminum with an etched surface roughness  $R_{max}$  of 2 to 3  $\mu m$  in a drawing speed range of  $10^{-3}$  to 1 m/s, as shown in Figure 5.1. At speeds ranging from approximately 0.01 to 1 m/s, the coefficient of friction increases with increasing speed. In order to interpret this phenomenon, they introduced the micro-PHL (plasto-hydrodynamic lubrication) mechanism proposed by Mizuno et al (1978) in which lubricant trapped in surface pockets permeates into the area of actual contact and a thin hydrodynamic film with a thickness of the order of 0.1  $\mu m$  is formed, as shown in Figure 5.2.

In order to establish this dynamic model of the microcontact behavior in sheet drawing, Azushima et al (1990) attempted direct in-situ observation of the lubricant behavior at the interface between the tool and the workpiece by using a newly developed sheet drawing apparatus.

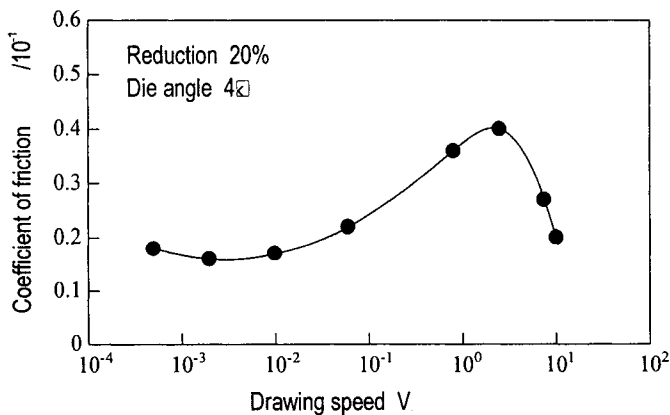


**Figure 5.1** Effect of drawing speed upon coefficient of friction in sheet drawing experiments of aluminum with an etched rough surface, using an oil having a viscosity of 1800 cSt.

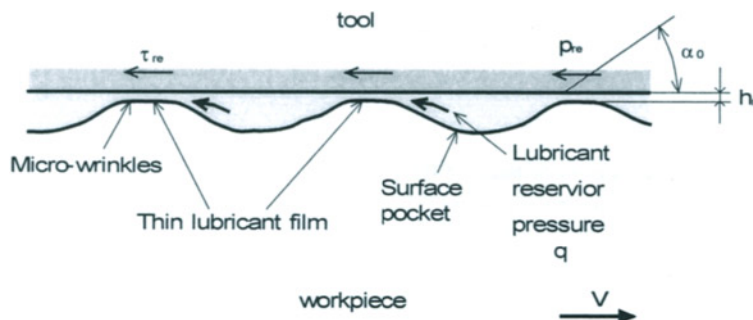


**Figure 5.2** Model of micro-plasto-hydrodynamic lubrication mechanism.

### 5.1.1 Apparatus for direct observation

The schematic representation of the apparatus used for direct observation of the interface between the tool and the workpiece is shown in Figure 5.3 (Azushima et al, 1989). The experimental apparatus consists of a pair of die halves, one made of tool steel and the other made of transparent quartz, a microscope with a CCD camera and a video system. A specimen sheet chucked at the end of the horizontal actuator ram head is pressed between the quartz die half and the tool steel die half by the vertical hydraulic actuator. The vertical actuator generates normal loads of up to 5000 N and the horizontal actuator lateral loads of up to 1000 N at the maximum drawing speed of 100 mm/s over a stroke range of up to 1000 mm. The drawing load is measured by means of a strain gauge load cell installed between the ram head and the chuck for the assessment of the coefficient of friction. The die angle is 3 ° and the thickness of the quartz die is 20 mm.

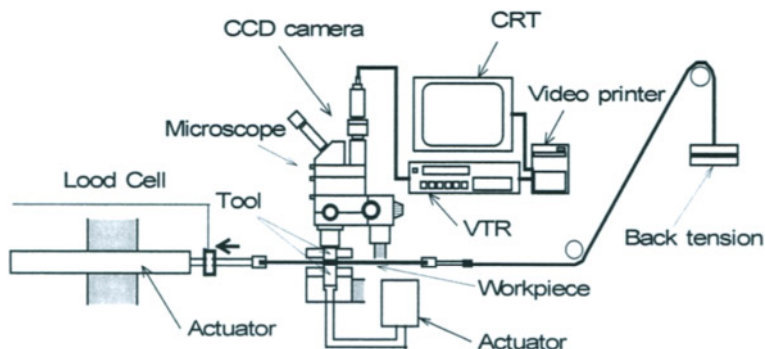


**Figure 5.3** Schematic representation of apparatus for in-situ observation of interface between tool and workpiece during sheet drawing.

In order to magnify the image of the interface, video images are taken through the microscope. The fiber optic light and lamp are used for illumination. The overall magnification of CRT images is about  $\times 60$ .

### 5.1.2 Direct observation of micro-PHL (Azushima et al, 1990)

The workpiece used is A1100 aluminum, 2 mm thick, 10 mm wide and 500 mm long with a Vickers hardness of 24.4. The workpiece sheets are provided with uniformly distributed pyramidal indentation, as shown in Figure 5.4. The distance between pyramidal indentations is 2 mm and the angle is  $160^\circ$ . The length of one side of the square of the indentation is 0.63 mm and the depth is about 0.056 mm. The specimen sheets are drawn at a speed of 0.8 mm/s with lubricants of various viscosities.

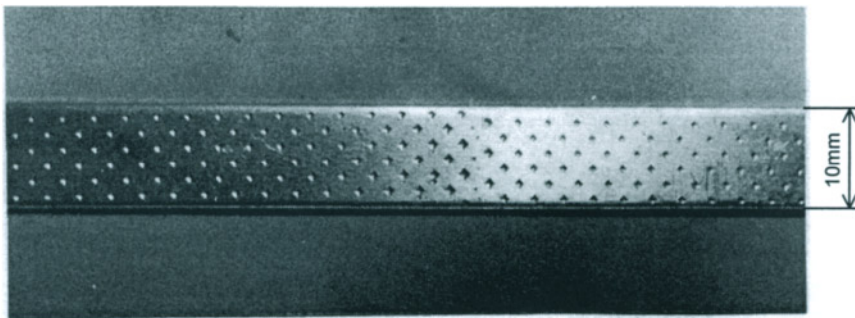


**Figure 5.4** Surface of aluminum sheet provided with uniformly distributed pyramidal indentation.

Figure 5.5 shows the sequential images of the working area taken during drawing at a reduction of 9.7% with a lubricant having a viscosity of 100 cSt. Figure 5.6 shows the sequential images taken during drawing at a reduction of 9.2% with a lubricant having a viscosity of 1000 cSt. They clearly show lubricant being squeezed out from the oil pockets, and the permeation of the lubricant that was trapped in the surface pockets into the actual contact area is evident.

In Figure 5.5, the lubricant in the surface pockets permeates forward and backward at the same time into the actual contact area and the permeation area around the actual contact area extends, accompanied by a reduction in thickness. It is seen that the amount of lubricant permeating forward from the pocket is greater than that of lubricant permeating backward. In Figure 5.6, for a lubricant having higher viscosity, more lubricant in the pocket seems to be squeezed backward into the real contact area than forward.

In some experiments conducted at higher drawing speeds, the backward permeation is observed to prevail against the forward permeation. From these direct observations, it is seen that the permeation behavior of lubricant in the pocket considerably depends on the viscosity of the lubricant and the drawing speed.

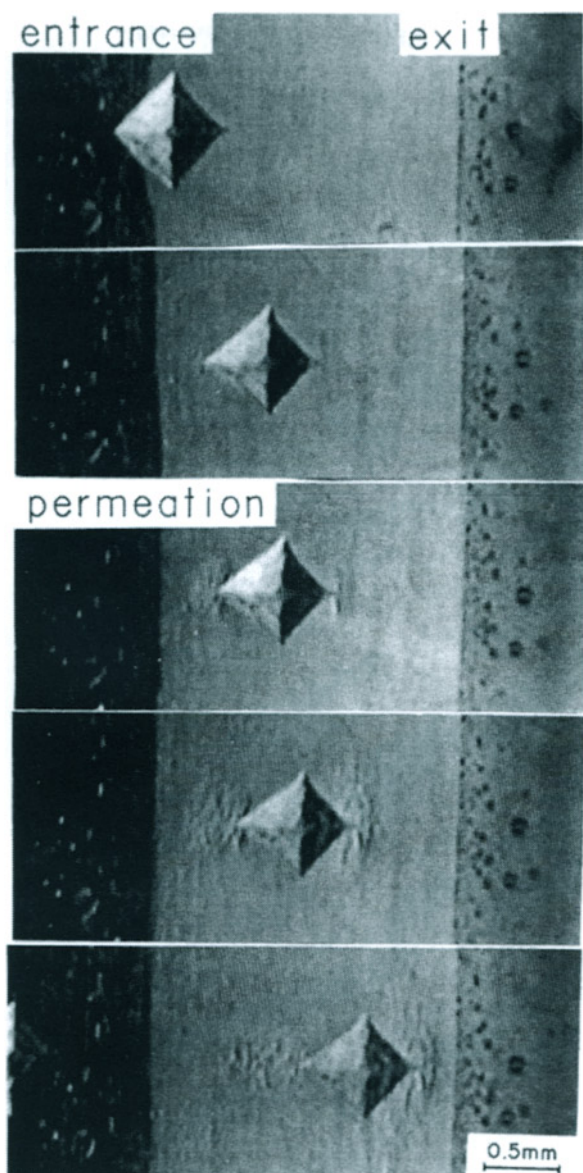


**Figure 5.5** Sequence images of the permeation behavior of lubricant trapped in the pyramidal pocket during sheet drawing at a drawing speed of 0.8 mm/s and reduction of 9.7% with a lubricant having a viscosity of 100 cSt.



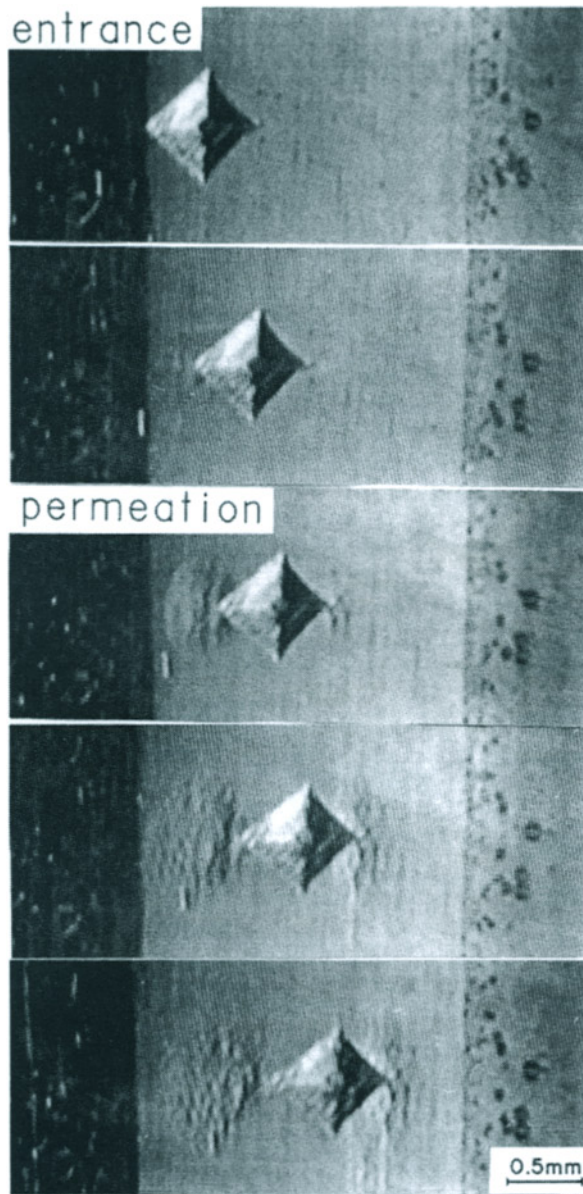


**Figure 5.6** Sequence photographs of the permeation behavior of lubricant trapped in the pyramidal pocket during sheet drawing at a drawing speed of 0.8 mm/s and reduction of 9.2% with a lubricant having a viscosity of 1000 cSt.

### 5.1.3 Mechanism of micro-PHL

From these direct observations, it can be confirmed that the trapped lubricant permeates forward and backward into the real contact area during sheet drawing. In this section, the behavior of the permeating lubricant will be considered qualitatively.

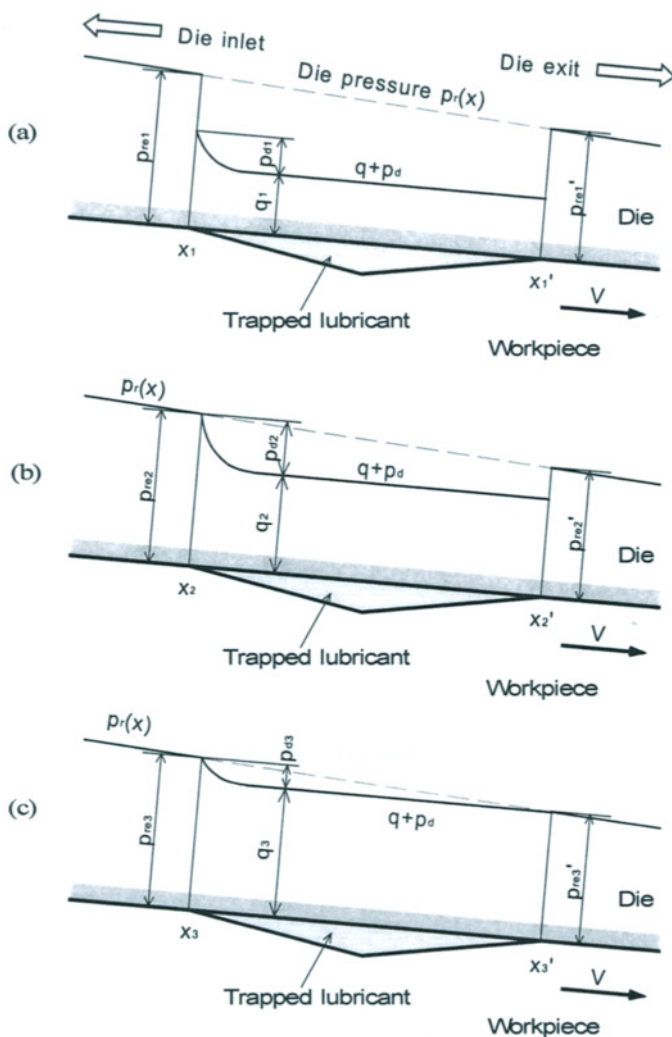


**Figure 5.7** Models of lubricant permeation from surface pocket into real contact area.  
(a) No permeation, (b) Backward permeation, (c) Backward and forward permeations

Figure 5.7 shows the schematic representation of the two-dimensional models of the lubricant permeation shown in Figures 5.5 and 5.6. It is anticipated, based on the assessment of the lubricant pressure  $q$  in the surface pocket and the observation of the marked volume reduction of the pocket of pyramidal indentation, that  $q$  becomes close to pressure  $p_{re}(x)$  on the real contact area when the workpiece undergoes bulk deformation. Moreover, it is expected that  $p_d$  will rise at the back edge of the pocket due to the hydrodynamic effect, depending on the product of the lubricant viscosity and drawing speed  $\eta V$ .

Figure 5.7(a) shows the general relationship among  $p_{re}(x)$ ,  $q$  and  $p_d$  when the pocket exists near the entrance point of the working area. The hydrodynamic pressure  $p_d$  can be derived using the Reynolds equation.  $p_{re}(x)$  generally decreases toward the die exit in the sheet drawing process, but  $q$  increases with the movement of the pocket from the die entrance toward the die exit. It is expected that  $q_2 + p_{d2}$  will reach  $p_{r2}$  first at the back edge of the pocket (Figure 5.7(b)). High  $\eta V$  results in backward permeation of the trapped lubricant. This model is in good agreement with the experimental results shown in Figure 5.6. Moreover, when the pocket moves toward the die exit, it is expected that  $q_3$  will reach  $p_{re3}$  at the front edge of the pocket (Figure 5.7(c)), resulting in backward and forward permeation.

On the other hand, when the lubricant viscosity or the drawing speed is low, it is expected that  $q$  will reach  $p'_{re}$  first at the front edge of the pocket, before  $q+p_d$  reaches  $p_{re}$  at the back edge (see Figure 5.8), resulting in forward permeation. When the pocket moves toward the die exit,  $q$  reaches  $p_{re}+p_d$  at the back edge of the pocket, resulting in forward and backward permeation as shown in Figure 5.5.

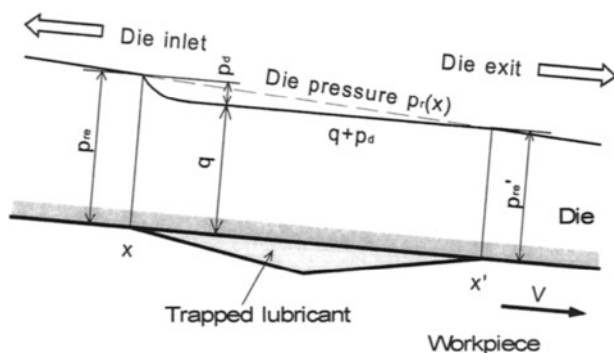


**Figure 5.8** Model of forward permeation of lubricant trapped in pocket.

#### 5.1.4 Speed dependence of coefficient of friction under micro-PHL (Azushima and Uda, 1991)

In order to investigate the possibility of the micro-PHL mechanism in the reconciliation of low friction and a smooth surface finish in metal forming processes, the dependence of the coefficient of friction on speed is examined under the same experimental conditions as described above. The increase in the coefficient of friction with increasing drawing speed is interpreted in terms of the in situ measured volume of the lubricant that permeated from the surface pocket into the surrounding real contact area.

In order to measure the current volume of the lubricant that permeated from the surface pocket during sheet drawing, the sheet-drawing apparatus for direct observation shown in Figure 5.3 and an image processor are used. This is because a significant change in the volume of the pyramidal indentation was observed in the previous work as the pocket left the die exit. The dimensions and area of a pyramidal indentation on the sequential CRT photographs are measured using the image processor. The geometrical changes of the pyramidal indentation within the working area extending from the entrance point to the exit point are used for the assessment of the volume of the lubricant that permeated from the surface pocket. The drawing experiments are carried out at drawing speeds of 0.13, 0.65 and 1.48 mm/s with thickness reductions of up to 25%. The same lubricant, as in the previous work, is used.

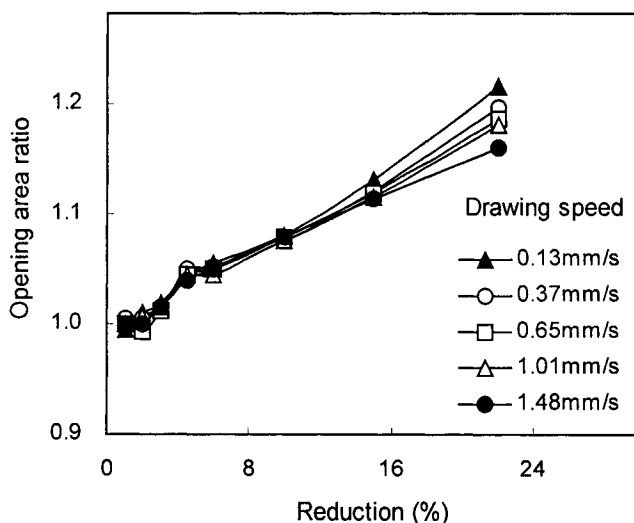


**Figure 5.9** Relationships between opening area ratio of pyramidal indentation and thickness reduction percentage for three drawing speeds of 0.16, 0.65 and 1.48 mm/s.

In order to measure the volume of that lubricant permeated from the pyramidal indentation, the changes in the area of the pyramidal indentation on the sequence CRT photographs are measured. Figure 5.9 shows the relationship between the open area ratio of indentation and the percentage of thickness reduction. In the beginning stage of thickness reduction in sheet drawing, the open area ratio of indentation decreases with increasing the percentage of thickness reduction. As the percentage of thickness reduction exceeds 4%, the ratio increases with increasing percentage of thickness reduction for all drawing speeds tested. As the drawing speed increases, the open area ratio of indentation tends to decrease slightly.

In order to estimate the coefficient of friction between the tool and the workpiece under the micro-PHL condition, an attempt is made to calculate the mean oil film thickness over the real contact area, using the estimated volume of lubricant that permeated from the pyramidal indentation. In order to estimate this volume, the following three factors which cause the change in the open area of indentation, as shown in Figure 5.10, are taken into consideration:

- (1) the volume shrinkage of the indentation associated with the volume contraction of the trapped lubricant under hydrostatic pressure and the bulk yield of the workpiece material,
- (2) the volume shrinkage of the indentation caused by lubricant permeation, and
- (3) the elongation of the longitudinal dimension of the open area corresponding to the percentage of thickness reduction, which takes place without change of the pyramidal geometry.

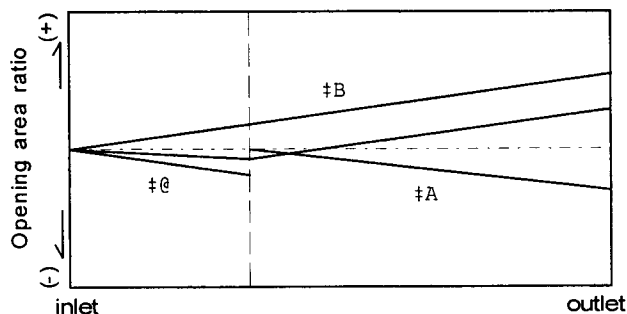


**Figure 5.10** Schematic representation of the change of opening area ratio of pyramidal indentation in the working area.

The mean film thickness is then calculated by dividing the estimated volume of permeated lubricant by the real contact area. From the measured open area ratio of indentation shown in Figure 5.9, the volume of permeated lubricant that corresponds to the reduction of 15% is  $0.0006 \text{ mm}^3$  at a drawing speed of  $0.13 \text{ mm/s}$  and  $0.0012 \text{ mm}^3$  at  $1.4 \text{ mm/s}$ , resulting in the mean oil film thicknesses of  $0.14 \text{ }\mu\text{m}$  and  $0.29 \text{ }\mu\text{m}$ ,

respectively. Thus, even if the drawing speed is increased tenfold, the mean oil film thickness increases only twofold. The values of mean oil film thickness obtained are roughly the same as those obtained by the surface roughness measurement in previous work.

By applying the conventional Navier-Stokes theory for two-dimensional isothermal hydrodynamic lubrication, the mean coefficient of friction  $\mu_m$  for a lubricant with viscosity of  $\eta$  at a mean sliding speed of  $V_m$  is given by

$$\mu_m = \eta \frac{V_m}{h_m p_m} \cdot \frac{A_r}{A_a} \quad , \quad (5.1)$$

where  $p_m$  stands for the mean pressure on the apparent contact area,  $A_r$  the real contact area and  $A_a$  the apparent contact area.  $h_m$  does not increase as much as  $V_m$ , as indicated above. Equation 5.1 indicates a positive dependence of the coefficient of friction on the drawing speed. However, the  $\mu$  values calculated using Equation 5.1 on the basis of the estimated  $h_m$  values obtained experimentally are poor in comparison with those obtained by Ruan, Kudo et al, (1987). This suggests that we must consider the thermal effect, the non-Newtonian property of the lubricant and the sub-microcontact behavior in the real contact area; this requires modification of the present micro-PHL mechanism.

## 5.2 DIRECT OBSERVATION OF INTERFACE IN FLAT TOOL DRAWING

In sheet-metal-forming simulation, the normal contact pressure generated in the conventional simulators is low to cover the practical pressure range, i.e., the ratio of the average pressure to the yield stress or proof stress ( $\sigma_f$  or  $\sigma_{0.2}$ ) of the workpiece material is generally less than 0.2. In a normal sheet-metal-forming operation, the pressure can reach a high value of  $0.4\sigma_f$ . Under such pressure conditions, some of the relationships obtained in the previous research (Fogg, 1967; Balbach, 1987; Emmens, 1988; MOnfort and Defourny, 1990) may lose their validity.

In order to first examine the pressure dependence of the coefficient of friction, Azushima et al, (1993) developed a new tribosimulator of the sheet-draw test between flat tools for flat workpiece which operates under a wide load range from 1 to 16 kN corresponding to  $p_m$  of 8 to 130 MPa. Figure 5.11 illustrates the relationships between the nominal coefficient of friction  $\mu_N$  and average contact pressure  $p_m$  obtained with 1-mm-thick, 20-mm-wide and 500-mm-long workpiece sheets of Al-Si alloy having a proof stress of 130MPa and a dull surface roughness  $R_{max}$  of around 3  $\mu m$ . The sheets are drawn at a drawing speed of 15mm/min through a pair of flat die halves of high-speed steel having a surface roughness  $R_{max}$  of 0.1 $\mu m$ , using a mineral oil with 5% oleic acid as a lubricant. Figure 5.11 indicates that  $\mu_N$  remains constant in the low contact pressure range, while beyond 40 MPa, i.e.,  $0.3\sigma_f$ , it decreases with increasing average contact pressure  $p_m$ , contrary to what is generally expected.

In order to interpret the above results and establish a model of microcontact behavior at the interface between the tool and the workpiece, Azushima (1995)

attempted a direct in-situ observation of the lubricant behavior at the interface using a newly developed flat tool sheet-drawing apparatus.

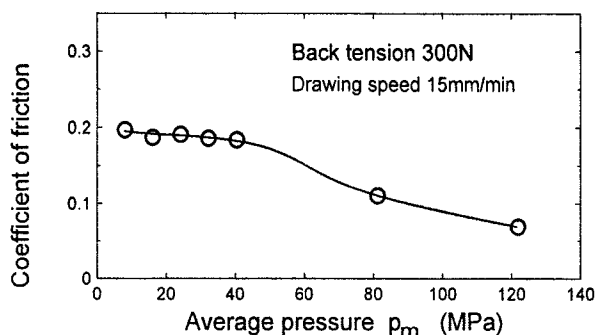


**Figure 5.11** Relationship between coefficient of friction and average pressure when Al-Si alloy sheets are drawn at a drawing speed of 15 mm/min through a pair of flat die halves.

### 5.2.1 Direct observation of the interface (Azushima, 1995)

The apparatus used in this experiment for the direct in situ observation of the interface between the tool and the workpiece in flat tool sheet drawing is similar in principle to that developed by Azushima et al.<sup>4)</sup> and is shown in Figure 5.3. The thickness of the quartz die is 20 mm, the flat width is 5 mm and the inlet angle is 3°.

The model workpiece material is commercially available pure annealed A1100 aluminum sheets 1 mm thick, 10 mm wide and 500 mm long. The aluminum sheets are rolled at a constant reduction of 5% with a light mineral oil, using shot blast dull rolls in order to provide an intentionally high surface roughness  $R_{max}$  of 20  $\mu\text{m}$  on the specimen sheet. The proof stress is 64 MPa.

The flat tool sheet-drawing experiments are carried out at a constant speed of 8.4 mm/min at 6 average contact pressures within the range from 19 to 56 MPa. Paraffinic base oil having a viscosity of 1480 cSt with 5% oleic acid is used as a lubricant. In each experiment, the normal force and the drawing force are measured to determine the nominal coefficient of friction  $\mu_N$ . At the same time, video photographs of the microcontact at the interface between the quartz die and the workpiece are taken through the microscope with a CCD camera. The real contact area between the quartz die and the asperities of the workpiece surface, as defined by the bright patterns on sequential CRT photographs, is assessed using an image processor.

Figure 5.12 illustrates the relationship between the nominal coefficient of friction  $\mu_N$  and the average contact pressure  $p_m$ . The values of  $p_m$  are calculated by

dividing the measured normal force  $F_N$  by the nominal contact area  $A_N$  which is measured from the CRT image of the interface obtained using the in situ observation apparatus.  $\mu_N$  remains constant at 0.23 up to  $p_m$  of 42 MPa and decreases from 0.23 to 0.12 below 51 MPa.

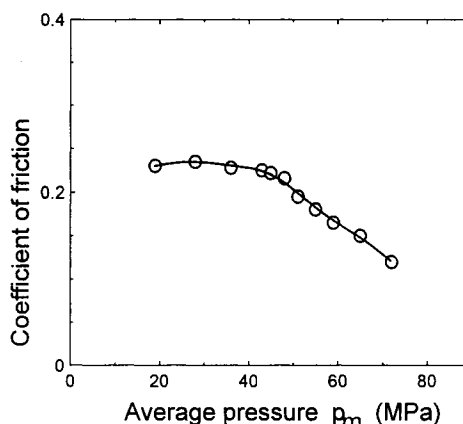


**Figure 5.12** Relationships between nominal coefficient of friction and average contact pressure.

In Figure 5.13, the interfaces at six different average contact pressures between 19 to 56 MPa are compared. At the low average contact pressures of 19 and 34 MPa, the real contact zones are isolated. The average area of the individual zones and the sum of the real contact area become larger as the pressure increases. The video photographs clearly show the free lateral flow of the lubricant under such low average contact pressures. As the normal contact pressure increases to 41 MPa, the real contact zones grow and some of them start to connect so as to form closed lubricant pools in which no lateral flow is observable. Beyond 41 MPa, the number of isolated lubricant pockets increases gradually with increasing average contact pressure. As  $p_m$  increases to 50 MPa, the bright area of real contact suddenly becomes dull, suggesting that a kind of microroughening takes place. The contact area ratio at this stage is about 70%.

### 5.2.2 Pressure dependence of the coefficient of friction

The experimental results show that the nominal coefficient of friction  $\mu_N$  remains constant in the low-pressure range, while in the high-pressure range, it decreases significantly with increasing pressure. This is in qualitative accordance with the results obtained by Shaw et al (1960) and Wanheim & Bay (1978) who predicted that boundary friction is associated with a constant real shear stress  $\tau_{re}$ . Kasuga et al (1968) and Kudo (1965) suggested qualitative models to account for the similar



dependence of  $\mu_N$  in some deformation processes with a thick liquid film lubricant. Although they considered the role of lubricant trapped within the surface pockets, their models lacked sound physical evidence.

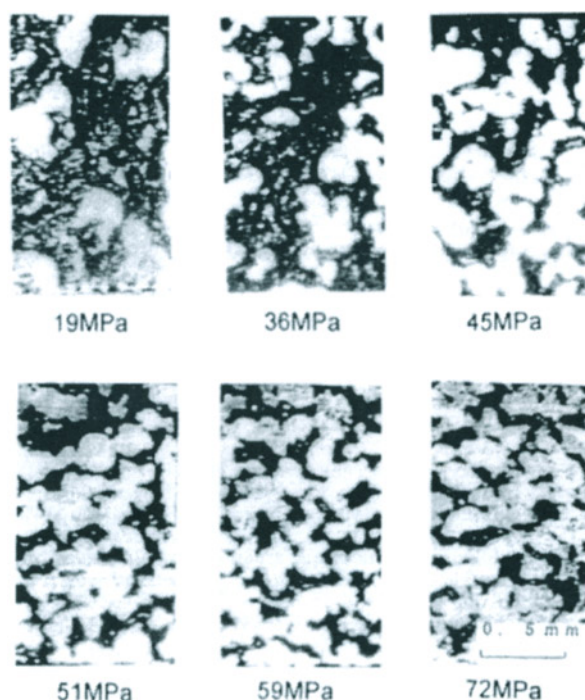


**Figure 5.13** Video images of test aluminum workpiece surface for six different average contact pressures.

The constant nominal coefficient of friction in the low-pressure range from 19 to 41 MPa, where the lubricant flows freely out through the interface gap and accordingly the hydrostatic pressure within the lubricant is not generated, can be accounted for by using the Bowden & Tabor (1954) model for the boundary lubrication mechanism, as shown in Figure 5.14. The normal force  $F_N$  and the tangential force  $F_T$  are given by

$$F_N = p_{re}A_{re} \quad , \quad F_T = \tau_{re}A_{re} \quad , \quad (5.2)$$

where  $p_{re}$  is the real contact pressure and  $\tau_{re}$  the real shear stress.

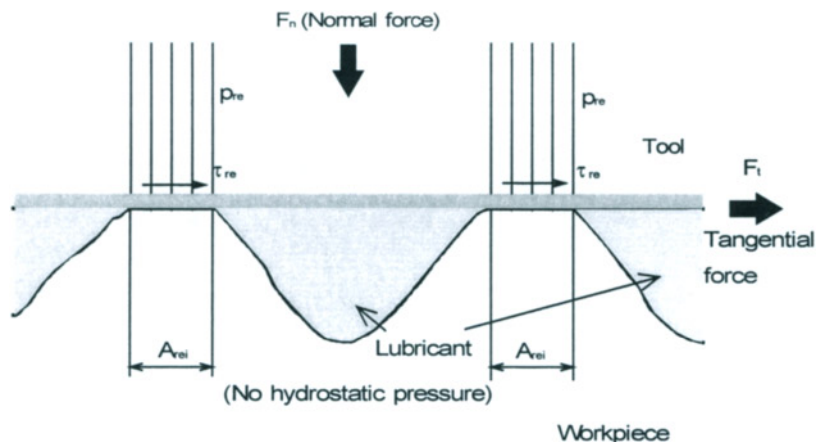


**Figure 5.14** Schematic representation of contact model between tool and workpiece in boundary lubrication.

From the measured values of  $F_N$  and  $F_T$ , the nominal coefficient of friction  $\mu_N$  on the nominal contact area  $A_N$  can be given by

$$\mu_N = \frac{F_T}{F_N} = \frac{\tau_{re} A_{re}}{p_{re} A_{re}} = \frac{\tau_{re}}{p_{re}} = \mu_{re} \quad , \quad (5.3)$$

where  $\mu_N$  corresponds to the value of the coefficient of friction measured in the experiments and  $\mu_{re}$  is the apparent boundary coefficient of friction on the real contact zone.

Beyond the average contact pressure of 41 MPa,  $\mu_N$  decreases with increasing average contact pressure  $p_m$ . In the pressure ranges from 41 to 50 MPa, it is confirmed from the CRT image of the interface that some of the real contact zones start to connect so as to form closed lubricant pools in which no lubricant flow is observable. Butler (1960) first suggested that if liquid lubricant is introduced at the interface, the lubricant is trapped within the pocket on the workpiece surface. Also, Kudo (1965) and Wanheim et al (1978) theoretically assessed the hydrostatic pressure  $q$  generated within the lubricant trapped in the surface pocket. We will attempt to explain the pressure dependence of the nominal coefficient of friction in terms of the hydrostatic-boundary lubrication mechanism.

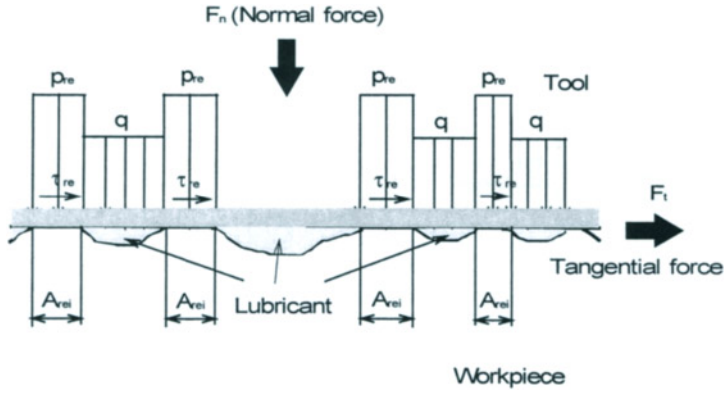


**Figure 5.15** Schematic representation of contact model between tool and workpiece in hydrostatic-boundary lubrication.

The schematic representation of this hydrostatic-boundary lubrication is shown in Figure 5.15. In the hydrostatic-boundary lubrication regime, some of the normal load  $F_N$  is supported by the hydrostatic pressure  $q$  generated within the oil pocket on the workpiece surface and the remainder is supported by the asperities, while the shear stress within the lubricant pool is negligible. Thus, the normal load  $F_N$  is given by

$$F_N = p_{re}A_{re} + qA_{hp} , \quad (5.4)$$

where  $A_{hp}$  denotes the total area of the closed lubricant pool. The tangential force  $F_T$  is

$$F_T = \tau_{re}A_{re} , \quad (5.5)$$

and we then have

$$\eta_N = \frac{F_T}{F_N} = \frac{\tau_{re}A_{re}}{p_{re}A_{re} + qA_{hp}} = \frac{\mu_{re}}{1 + \frac{qA_{hp}}{p_{re}A_{re}}} , \quad (5.6)$$

which coincides with Equation 5.3 when  $q=0$ .

In this pressure range, the values of  $A_{hp}$  and  $q$  must be determined in order to assess the value of  $\mu_N$ . In order to determine the value of  $A_{hp}$  in relation to  $p_m$ , the total area of closed lubricant pools in which no lubricant flow is observable must be measured from the video photographs of the interface. However, this is impossible in the present experiment. When the lubricant is trapped in the pocket on the workpiece surface, it is evident also from the experimental observation that the value of  $A_{re}/A_N$  does not approach unity. Moreover, Riu et al (1993) suggested that the hydrostatic pressure  $q$  generated within the lubricant pool rapidly approaches the real contact

pressure  $p_{re}$  acting on the real contact at a light reduction of the asperity height.

$A_{hp}$  increases with increasing average contact pressure  $p_m$  and approaches ( $A_r$ - $A_{re}$ ) when hydrostatic pressure is generated within all of the closed lubricant pools. Therefore, we then have

$$\mu_N = \frac{\mu_{re}}{1 + \frac{q}{p_{re}} \left( \frac{A_N}{A_{re}} - 1 \right)} . \quad (5.7)$$

The hydrostatic pressure  $q$  generated within the lubricant trapped in the surface pocket is assessed without considering the bulk deformation of the workpiece (Wanheim and Bay, 1978; Kudo, 1965). However, Kasuga and Yamaguchi (1968) and Riu et al (1993) suggested that  $q$  approaches  $p_{re}$  with the progress of bulk deformation. Consequently, as  $q=p_{re}$ , instead of Equation 5.7,  $\mu_N$  is given by

$$\mu_N = \frac{A_{re}}{A_N} \mu_{re} . \quad (5.8)$$

Since  $A_{re}/A_N=0.7$  from the obtained results, the decrease of the nominal coefficient of friction from 0.23 to 0.12 cannot be explained.

Lastly, above the average contact pressure of 50 MPa, it is observed in the CRT image that the bright zone of real contact suddenly becomes dull, suggesting that a kind of microroughening takes place and that the lubricant trapped in the pocket permeates into the real contact area. In order to describe this phenomenon, Mizuno et al (1982) proposed the concept of micro-plasto-hydrodynamic lubrication. Later, Azushima et al (1990) confirmed this hypothesis by observing the surface during sheet drawing through a transparent die. The mechanism also supports the hypothesis that  $q$  approaches  $p_{re}$ . The schematic representation of the lubrication mechanism is shown in Figure 5.16. Detailed modeling of this mechanism has not yet been achieved. When the lubricant trapped within the pocket permeates into the real contact area, it is presumed that the coefficient of friction  $\mu'_{re}$  on the contact area is lower than the boundary coefficient of friction  $\mu_{re}$ . We thus have

$$\mu'_{re} = \beta \mu_{re} , \quad (5.9)$$

where  $\beta$  ( $\leq 1$ ) represents the effect of the permeated lubricant. In this case,  $\mu_N$  is given by

$$\mu_N = \frac{A_{re}}{A_N} \beta \mu_{re} . \quad (5.10)$$

From the present experimental data,  $\beta$  is found to be 0.74 at the average pressure of 72 MPa.

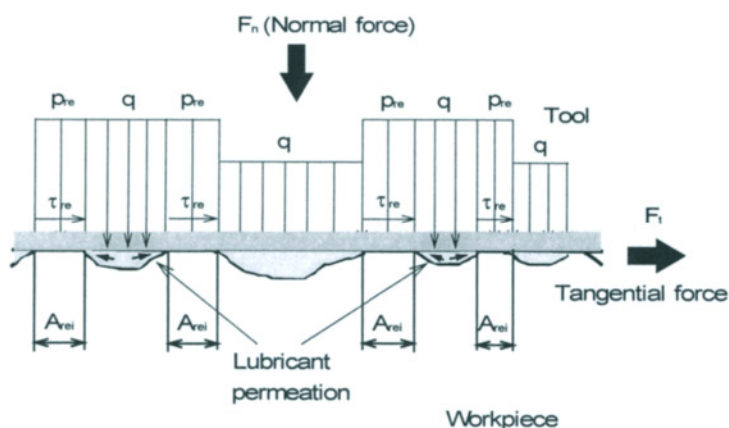


**Figure 5.16** Schematic representation of contact model between tool and workpiece in boundary-hydrostatic-micro-PHL lubrication.

### 5.2.3 Effect of surface topography of the workpiece (Azushima et al, 1997)

The examination of the surface topography of the sheet metal is very useful for characterizing the frictional mechanism in sheet metal forming. It is desired that the effect of the surface topography on the tribological behavior be investigated. Azushima (1995) measured the pressure dependence of the coefficient of friction and have directly observed the microcontact behavior of asperity and the lubricant behavior at the interface between the tool and the workpiece in situ, changing the surface topography workpiece using the flat tool sheet drawing apparatus.

The model workpiece material is commercially available pure annealed A1100 aluminum sheets 1 mm thick, 10 mm wide and 500 mm long. The sheets are rolled at a constant reduction of 7% with a light mineral oil using shot flat blast rolls having a surface roughness  $R_a$  of  $3.6 \mu\text{m}$  in order to intentionally roughen the surface of the specimen sheets. They are then rolled to five levels of reduction ranging from 1 to 5%, with a light mineral oil using a ground roll having a smooth surface of  $R_a$   $0.02 \mu\text{m}$  roughness in order to flatten the asperities on the sheet surface. In Figure 5.17, the 3D surface profiles of specimens A, B, C, D and E are shown and in Figure 5.18, the surface micrographs are shown. The flattening area ratio and the surface roughness  $R_a$  obtained from the surface micrographs are summarized in Table 1. The proof stresses of the specimens are around 64 MPa.

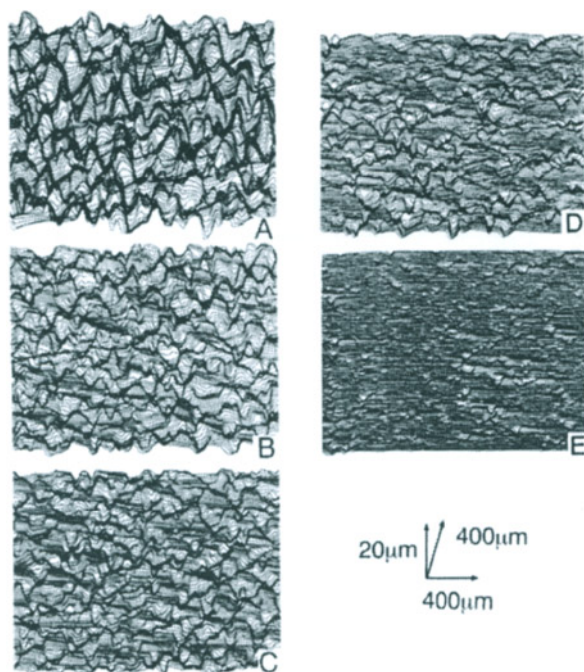


**Figure 5.17** 3D surface profiles of specimens A, B, C, D and E

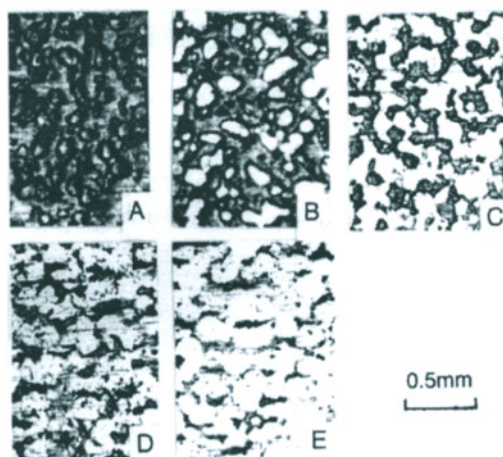


**Figure 5.18** Micrographs of surface of specimens A, B, C, D and E

The flat tool sheet-drawing experiments are carried out at a constant speed of 0.14 mm/s for six levels of average contact pressure within a range from 23 to 56 MPa. Paraffinic oil having a viscosity of 1460 cSt with 5% oleic acid is used as a lubricant. In each experiment, the normal force  $F_N$  and the drawing force  $F_D$  are recorded to determine the nominal coefficient of friction  $\mu_N$ .

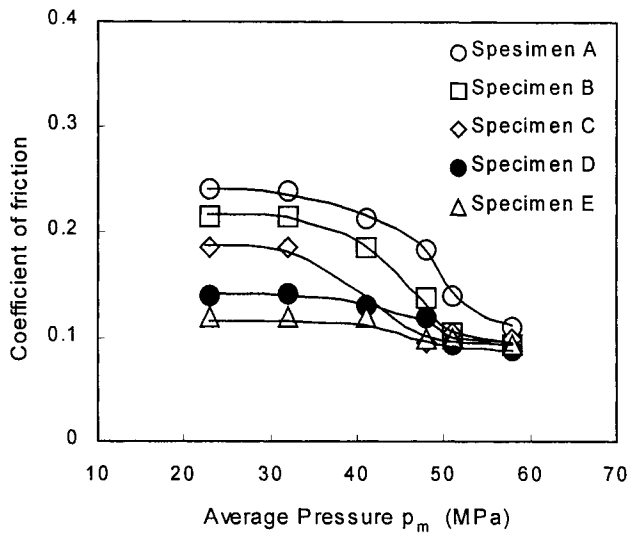


**Figure 5.19** Relationships between nominal coefficient of friction and average contact pressure for specimens A, B, C, D and E

Figure 5.19 illustrates the relationships between the nominal coefficient of friction and average contact pressure. For specimen A having a randomly rough surface, the value of  $\mu_N$  remains constant at 0.23 in the range of low average constant pressure up to 40 MPa and then decreases from 0.23 to 0.11 up to 56 MPa. For specimen B having a flattening area ratio of 0.31,  $\mu_N$  remains constant at the same value of 0.23 up to 31 MPa and then decreases to 0.10. For specimen C having a flattening area ratio of 0.45,  $\mu_N$  remains constant at a lower value of 0.18 up to 31 MPa and then decreases to 0.1. For specimens D and E having higher flattening area ratios of 0.58 and 0.70, the values of  $\mu_N$  decrease gradually with increasing average contact pressure. The higher the flattening area ratio becomes, the lower the values of  $\mu_N$  become in the range of low average contact pressure. In Figure 5.20, the interfaces of specimen A for six different average contact pressures from 23 to 56 MPa are shown. At the average contact pressures of 23 and 31 MPa, the real contact zones are isolated. The average area of the individual zone and the sum of the real contact area become larger as the pressure increases. At the average pressure of 40 MPa, the real contact zones grow and some of them start to connect so as to form isolated lubricant pools. Beyond 40 MPa, the number of the isolated lubricant pools increases gradually with increasing average contact



pressure. As  $p_m$  increases to 50 MPa, the bright areas of real contact suddenly become dull suggesting that the permeation of trapped lubricant into the real contact area takes place.

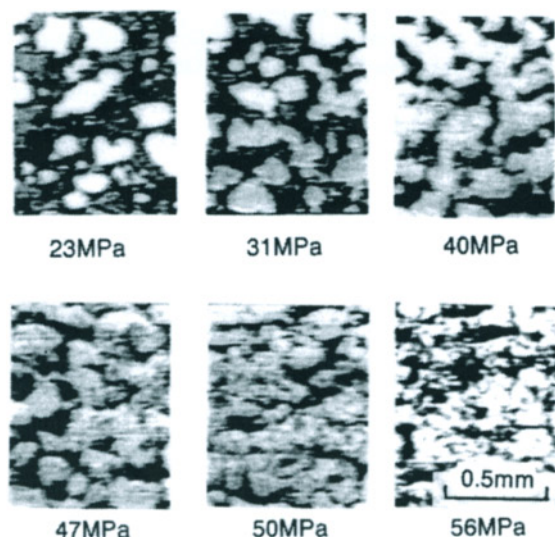


**Figure 5.20** Video images of surface of test specimen A for six different average contact pressures.

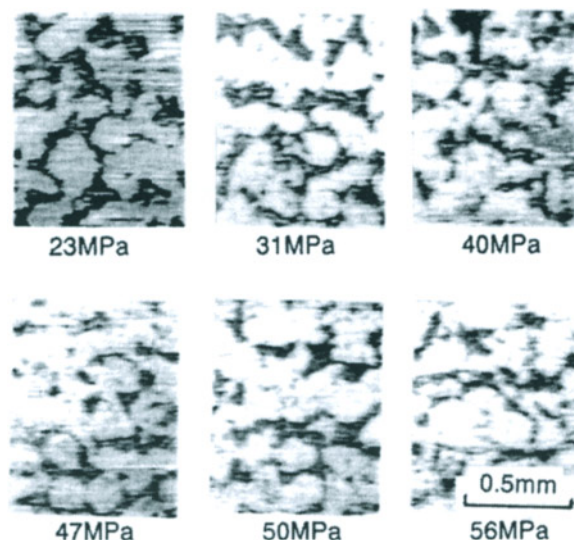


**Figure 5.21** Video images of surface of test specimen D for six different average contact pressures.



In Figure 5.21, the surfaces of specimen D under six different average contact pressures are shown. For each average pressure, the real contact area defined by the bright pattern is large and the lubricant pools are isolated. As  $p_m$  increases from 23 to 40 MPa, the real contact area increases gradually and above 40 MPa, it remains constant. Under a high average contact pressure, the permeation of the trapped lubricant into the real contact area cannot be observed, unlike specimen A. As mentioned above, the microcontact mechanism for specimen A is boundary lubrication at low average contact pressures, boundary-hydrostatic lubrication at the intermediate average contact pressures and the boundary, hydrostatic and micro-photo-hydrodynamic lubrication at high average contact pressures.

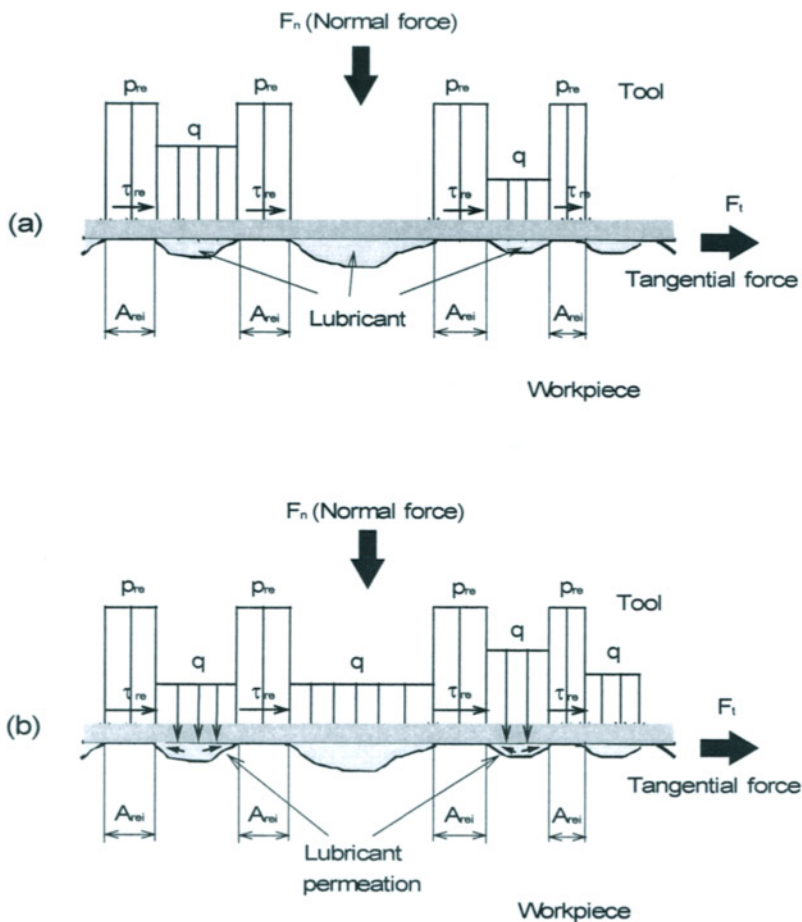


**Figure 5.22** Schematic representation of contact model between tool and workpiece for specimen D having a smooth surface.

The schematic representation of the microcontact model for specimen D having a smooth surface is shown in Figures 5.22 (a) and (b). In the average contact pressure range from 23 to 40 MPa, the coefficient of friction remains constant and the value is lower than those measured for specimen A having a rough surface. The real contact area also remains constant and the lubricant pools are isolated. It is anticipated that hydrostatic pressure is not generated within most lubricant pools. The real contact pressure  $p_{re}$  of specimen D is lower than that of specimen A, indicating that the lubricant film thickness introduced at the interface between the tool and the real contact zone for specimen A is larger.

Consequently, the coefficient of friction for a specimen having a smoother surface is lower. Above 40 MPa, the coefficient of friction decreases gradually with increasing average contact pressure. It is anticipated that hydrostatic pressure is generated within the lubricant pool. However, the permeation of the trapped lubricant into the real contact area does not occur, unlike specimen A.

## REFERENCES

- Azushima, A. et al., 1989, Experimental Confirmation of the Micro-Plasto-Hydrodynamic Lubrication Mechanism at the Interface between Workpiece and Forming Die, J. Japan Soc. Technol. of Plasticity, 30:1631-1638.
- Azushima, A., Tsubouchi, M. and Kudo, H., 1990, Direct Observation of Lubricant Behaviors under the Micro-PHL at the Interface between Workpiece and Die, Proc. 3rd Int. Conf. Technol. Plasticity, 1:551-556.
- Azushima, A., M. Uda, 1991, An Interpretation of the Speed Dependence of the Coefficient of Friction under the Micro-PHL Condition in Sheet Drawing, Annals of the CIRP, 40-1:227-230.
- Azushima, A. and Igarashi, K., 1993, Development of a New Sheet Metal Forming Simulator Controlled by Computer, Proc. Japanese Spring Conf. Technol. of Plasticity, 79-82
- Azushima, A., 1995, Direct Observation of Contact Behavior to Interpret the Pressure Dependence of the Coefficient of Friction in Sheet Metal Forming, Ann. CIRP, 44:209-212.
- Azushima, A., Miyamoto, J. and Kudo, H., 1997, Effect of Surface of Workpiece on Pressure Dependence of Coefficient of Friction in Sheet Metal Forming, Annals of the CIRP 47/1, 479-482.
- Balbach, R., 1987, The Relationship Between the Blank and Product Surface Microstructures on the Tribology in Aluminum Sheet Metal Forming, Ann. CIRP, 36:181-184.
- Bowden, F. B. and Tabor, D., 1954, The Friction and Lubrication of Solids, Oxford, Clarendon Press.
- Butler, L. H., 1960, Surface Conformation of Metals under High Normal Contact Pressure, Metallurgia, 58:167-174.

- Fogg, B, 1967, The Relationship Between the Blank and Product Surface Finish and Lubrication in Deep-Drawing and Stretching Operations, *Sheet Metal Industries*, 44:95-112.
- Emmens, W. C., The Influence of Surface Roughness on Friction, 1988, *Proc. 15th IDDRG Congress*, 63-70.
- Kasuga, Y. and Yamaguchi, K., 1968, Friction and Lubrication in the Deformation Processing of Metals, 1st-3rd Reports, *Bull. J.S.M.E.*, 11:344-365.
- Kudo, H., 1965, A note on the Role of Microscopically Trapped Lubricant at the Tool-Work Interface, *Int. J. Mech. Sci.*, 7:383-388.
- Kudo, H., Tanaka, S., Imamura, K. and Suzuki, K., 1976, Investigation of Cold Forming Friction and Lubrication with a Sheet Drawing Test, *Annals of the CIRP*, 25-1:179-184.
- Kudo, H. and Azushima, A., 1986, A Proposal toward Systematization of Tribology in forming Processes, *J. Japan Soc. Technol. of Plasticity*, 27:72-80.
- Mizuno, T., Kamiya, S. and Okamoto, M., 1978, Lubricant Behaviors in the Compression-Friction Test of Strip Metals, *Bull. J.S.M.E.*, 21, 1424.
- Mizuno, T. and Okamoto, M., 1982, Effects of Lubricant Vissosity at Pressure and Sliding Velocity on Lubricating Conditions in the Compression-Friction Test on Sheet Metals, *J. Lubr. Technol.*, ASME, 104:53-59.
- Monfort, G. and Defourny, J., 1990, Tribological Factors in the Stamping of Coated and Uncoated Steel Sheets, *Proc. 17th IDDRG Congress*, 197-205.
- Riu, D., Azushima, A. and Shima, T., 1993, Behavior of Hydrostatic Pressure of Lubiricant Trapped in Surface Pocket on Workpiece at Upsetting Process, *J. Japan Soc. Technol. of Plasticity*, 34:1240-1245.
- Ruan, F., Kudo, H., 1987, Experimental Evidence of Micro-Hydrodynamic Lubrication Mechanism, *J. Japan Soc. Technol. of Plasticity*, 28:41-48.
- Shaw, M. C., Ber, A. and Mamin, P. A., 1960, Friction Characteristics of Sliding Surfaces Undergoing Subsurface Plastic Flow, *J. Basic Eng.*, 82:342-346.
- Schey, J. A., 1983, *Tribology in Metalworking-Friction, Lubirication and Wear*, Metal Park, Amer. Soc. Metals.
- Wanheim, T. and Bay, N. , 1978, A Model for Friction in Metal Forming Processes, *Ann. CIRP*, 27:189-194.

## Chapter 6

# An Examination of the Coefficient of Friction

JOHN G. LENARD  
*Department of Mechanical Engineering*  
*University of Waterloo*  
*Waterloo, Ontario N2L 3G1*  
*Canada*

### 6.1 INTRODUCTION

Product and process design, needed for the development of draft schedules in the flat rolling industry, make use of off-line mathematical models of the process. These models vary broadly in their complexities and sophistication. They include simple, one-dimensional descriptions, which may be based on the original Orowan – von Karman approach. Alternatively, they may be especially written, dedicated finite-element or finite-difference descriptions of the process. All of them may be used to gain insight into the behaviour of the three components of the metal rolling system - the mill, the rolled metal and their interface - or they may be employed to predict the significant rolling parameters - the roll force, torque, forward slip and the resulting attributes - the yield strength and the hardness - of the product; the mill stretch and vibrations of the rolling mill, roll flattening, bending and the thermal camber of the rolls. When hot rolling is modeled, the resulting grain distribution, the retained strain, the amount of recrystallization and precipitation may also be calculated. To a large extent, the success of either endeavour depends on the appropriate formulation of the boundary conditions, which should be as sophisticated as the model itself. The boundary conditions are often expressed in terms of the coefficient of friction and the coefficient of heat transfer. In the cold rolling process with adequate application of lubrication the coefficient of friction is, arguably, the more important of the two, while in hot rolling both coefficients are of significant importance.

Yuen et al (1996) write that since the trend in modern strip rolling is to produce thinner gauges of higher strength metals, the control of friction in the roll bite is most important. It is also useful to recall the comments of Roberts (1997)

*"Of all the variables associated with rolling, none is more important than friction in the roll bite. Friction in rolling, as in many other mechanical processes can be a best*

friend or a mortal enemy, and its control within an optimum range for each process is essential."

In what follows the dependence of the coefficient of friction on process and material parameters is examined. It is understood that the coefficient of friction may not be the best description of interfacial activity in between the roll and the rolled metal. Several arguments have been made, criticizing the use of the coefficient. The first one arises from the fundamental definition of the Coulomb-Amonton coefficient, as the ratio of the interfacial shear stress to the interfacial pressure,  $\mu = \tau/p$ . In the flat rolling process the normal pressure,  $p$ , controlled by the forming machine, may increase significantly beyond the material's flow strength. The interfacial shear stress,  $\tau$ , may also increase but it cannot rise above the rolled metal's yield strength in pure shear,  $k$ , since if it did, shearing of the surface layer of the softer metal and not relative motion of the roll and rolled material would result. At that limit the original definition of the coefficient of friction becomes meaningless.

This problem may be overcome by the use of the friction factor instead, defined as the ratio of the interfacial shear stress to the metal's flow strength in pure shear,  $m = \tau/k$ , as done when the extremum principles are utilized to analyze the process. A discussion of these issues is well presented by Mróz and Stupkiewicz (1998) who write that the Amonton-Coulomb friction law is not applicable in most metal forming processes. Bay (1987) presents a general friction model, which includes both constant coefficient of friction and constant friction factors. It is necessary to realize, however, that the coefficient of friction is the term used and understood by the engineers in the metal forming and in the flat rolling industry. As will be shown below, experimental data confirm the comments of Azarkhin and Richmond (1992), who report that the limiting case of the interfacial shear stress equaling the yield strength is usually not reached. Further, the Coulomb-Amonton coefficient is also used in most of the available mathematical models.

## 6.2 FUNDAMENTAL IDEAS

### 6.2.1 Mechanisms of friction

Surfaces are always rough and contaminated (Batchelor and Stachowiak, 1995). When the surfaces of the work roll and the strip approach one-another at the entry to the roll bite, contact occurs only at the asperities, the tips of which deform plastically as the pressures increase. The authors discuss the three most important mechanisms of surface interactions; their figure is reproduced below as Figure 6.1.

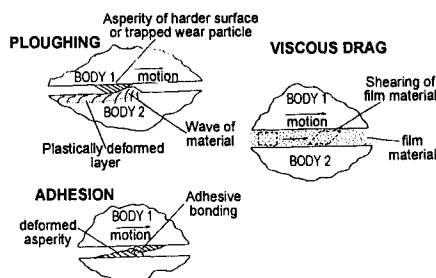


Figure 6.1 Mechanisms of friction: ploughing, viscous drag and adhesion (Batchelor & Stachowiak, 1995).

According to the authors, the most common cause of friction is elastic and plastic deformation of the asperities, identified as ploughing in Figure 6.1. Solid state adhesion is ranked as the second most common cause, resulting in very high coefficients. Viscous drag is identified as the third, causing low frictional resistance, that is, hydrodynamic lubrication.

In the third mode of friction the surfaces are separated completely and the resistance to relative motion is caused by the need to overcome frictional resistance in the third body, usually but not always, the oil film material, separating the surfaces. Heshmat et al (1995) reviewed modeling of friction, interface tribology and wear for powder-lubricated systems and for solid contacts. He stated that anything in between the contacting surfaces is a lubricant, be it a powder, a contaminant, layer of scale or in fact, oil. In a typical metal forming process, such as flat rolling, the most likely mechanism may comprise metal-to-metal contact at the asperity tips in addition to metal-to-lubricant contact at the valleys (Sutcliffe, 1999).

One of the important parameters is therefore the area over which actual metal-to-metal contact occurs. This is taken to be the sum of all flattened areas of all asperity tips, and is defined as the true area of contact,  $A_r$ . The rate at which the true area of contact approaches the apparent area has an important effect on surface interactions and on the magnitude of the coefficient of friction. Liu et al (1999) reviewed the mathematical models that are available for the analysis of contact between rough surfaces. They considered the description of rough surface profiles, the relations between the contact pressure and the deformation of the surface and the techniques of solution of the contact equations. They included a very useful table in which formulae for asperity contact simulations were given. The parameters included in these relations are numerous, indicating the complexity of the phenomena. Sutcliffe (1999) writes that frictional conditions are dictated by the way in which asperities on the work piece and the tool conform to each other and the frictional conditions on those areas of contact and in the intervening valleys. Bulk deformation enhances the ability of asperity tips to sink into the underlying material; analyses that ignore the deformation of the substrate are of little use.

### 6.2.2 *The adhesion hypothesis*

The phenomenon at the contacting asperity tips is best explained in terms of the adhesion hypothesis (Bowden and Tabor, 1950). The hypothesis states that the resistance to relative motion is caused by adhesive bonds formed between the contacting asperity tips, which are an interatomic distance apart. Rabinowicz (1995) examined the often-stated critique of the adhesion hypothesis and also discussed the counter-arguments. It is safe to state that the hypothesis is almost universally accepted and in the present study, it will be used to explain experimental observations.

### 6.2.3 *The parameters affecting surface interactions*

The parameters affecting surface interactions are many. The most comprehensive discussion of the parameters and variables of a tribological system, including their interactions and interdependence, is given by Schey (1983). The following list, extracted from that of Schey, is most certainly incomplete but it includes those deemed of significance. Process parameters include the temperature, speed, and the reduction. The stiffness and dynamic response of the rolling mill also affect tribology. The work roll and the back up roll dimensions, their hardness, surface roughness magnitude and direction, cooling systems, lubricant delivery

systems, including the locations of nozzles, all contribute here. Mechanical properties of the rolls and the work piece, including their resistance to deformation, surface and bulk hardness, Young's and shear modulus, density and stored elastic energy as well as the thermo-physical properties influence the interactions. The contributions of surface parameters, such as the chemical reactivity, the tendency to adsorb molecules from the environment, the adsorption of water vapor and oxygen and surface energy need to be understood. The nature of scale formation, the chemical composition of the scale and the strength of the adhesion between the scale and the parent metal must be accounted for. Lubricants affect surface interactions and their properties must be precisely described. The chemical composition, the additives and their concentration in the base oil, the chain length, density, viscosity, viscosity - temperature, viscosity - pressure coefficients are also needed. If emulsions are used, the composition, the emulsifier and the droplet dimensions are of importance.

Including all of the above in a mathematical model of the dependence of the coefficient of friction is, of course, highly impractical. Choices are necessary and in what follows, the relative velocity of the roll and the rolled metal, the surface temperature at the entry and the reduction/pass are taken as the most important process parameters. The attributes of the rolled metal to be included are limited to the model that describes its resistance to deformation. In cold rolling a true stress – true strain relation is used, while in hot rolling, the true stresses are to be related to the strain, the rate of strain, the temperature and a metallurgical parameter. This parameter may be the activation energy for plastic deformation, as in the Arrhenius type, hyperbolic sine equations, or the carbon equivalent, as used by Shida (Lenard et al, 1999; Shida, 1974). The parameters of the contact surfaces include the strip and the roll roughness and the thickness of the layer of scale. When lubricants are used, the viscosity and its dependence on the temperature and the pressure are also to be considered. When emulsions are employed, as in the cold rolling of steel strips, the concentration of the oil in the water and the droplet dimensions should be known.

#### **6.2.4 Determining the coefficient of friction**

Since the coefficient of friction is defined as a ratio of forces, it cannot be measured directly. It can be determined, however, by experiments in which the shearing and normal forces are monitored and their ratio is averaged and calculated. Care should be exercised in the choice of these experiments. Tests, in which the metal flow is similar to that found in the process being simulated, are preferred to pin-on-disk type experimentation.

Several semi-empirical formulae have been published, giving the coefficient in terms of some of the significant parameters, usually the roll separating force, the radius of the deformed work roll, the resistance to deformation in addition to the entry and exit thickness of the rolled strip.

The coefficient can also be computed using an inverse approach, coupled with mathematical models of the process of more or less sophistication. These approaches are discussed below.

##### **6.2.4.1 Experimental approach**

**The embedded pin - transducer technique.** The original idea has been suggested by Siebel and Lueg (1933) in the rolling process and adapted by van Rooyen and Backofen (1960) and Al-Salehi et al (1973). The method has been applied to measure interfacial stresses in several bulk forming processes. Warm and cold rolling of aluminium strips were studied (Karagiozis and Lenard, 1985; Lenard and Malinowski, 1993; Lim and Lenard, 1984);



variations have been presented by Lenard (1990, 1991) and Yoneyama and Hatamura (1987, 1989). A strain-gauged cantilever with its tip in the contact zone, and its refinements were presented by Banerji and Rice (1972) and Jeswiet (1991, 2000). Detailed information on the distributions of interfacial frictional shear stresses, roll pressures and their ratio, the coefficient of friction, may be obtained by these methods, but the set-up and the data acquisition are elaborate and costly.

The major criticism of the use of the embedded pin – transducer approach concerns the possibility of some contamination intruding into the clearance between the pins and their housing (Stephenson, 1983). This contamination may consist of wear debris, aluminium oxide particles or pieces of scaling, for example. While the mathematical model of the pin-transducer combination includes an account of the possible contamination, it is still necessary to substantiate the results by independent means.

The substantiation has been performed successfully while hot rolling aluminium alloy strips using emulsions (Hum et al, 1996). The authors compared the integrals of the roll pressure distributions to the independently measured roll separating forces by transducers placed under the bottom roll and the integrals of the interfacial shear forces, multiplied by the roll radius to the roll torque; the companions were successful. Further, they used the experimentally obtained coefficients of friction in a one-dimensional mathematical model of the flat rolling process, again successfully predicting the measured roll separating forces and the roll torques. The accuracy of these comparisons indicated that the embedded pins and the transducers, if handled carefully, cleaned and adjusted appropriately, yield acceptable values for the coefficient of friction. Photographs of the embedded transducers and the pins are shown in Figure 6.2.

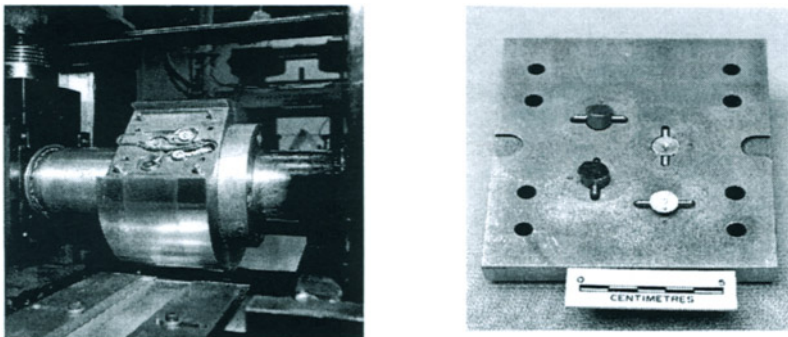


**Figure 6.2** The embedded transducers and the pins (Lenard et al 1999)

The photograph on the left shows the four transducers, two of which are oriented in the radial direction and two are positioned at  $25^\circ$  from that direction. The pins, made of drill rod material, are shown in the right. Their bottom surfaces are in contact with the transducers; small springs, not shown, ensure that contact is maintained. The diameter of the pins is 1.8 mm; their top surfaces are ground so that they are flush with the roll surface under load and that their surface roughness is of the same order of magnitude as that of the surface of the work roll.



**Determining the average friction factor.** The most applicable test to determine the friction factor for use in metal forming processes has proven to be the ring compression test (Male and Cockroft, 1964; Male and DePierre, 1970). In the test a ring of specific dimensions is compressed and the changes of its dimensions are related directly to the friction factor. The schematic diagram of the ring test and a typical calibration chart are shown in Figure 6.3.

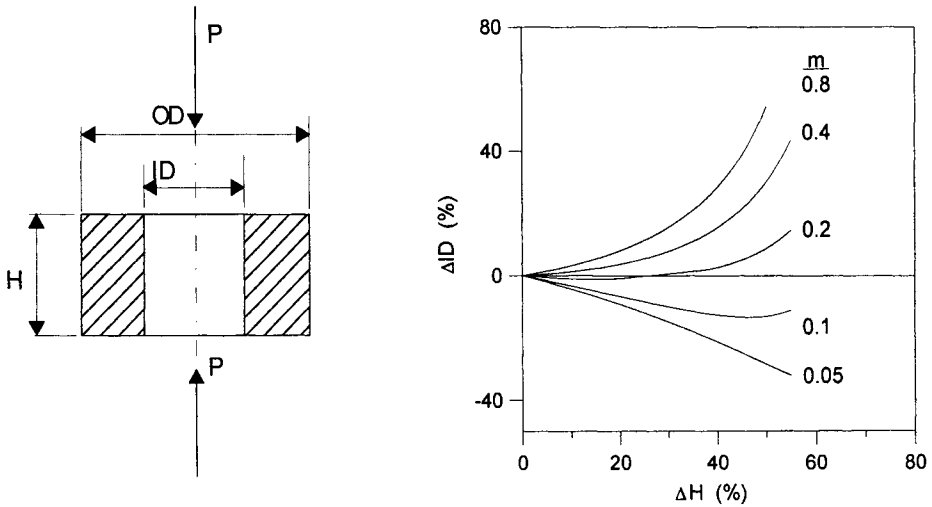


Figure 6.3 The ring compression test and a typical calibration chart

**6.2.4.2 Semi-empirical formulae - cold rolling.** Most of these rely on matching the measured and calculated roll separating force and choosing the coefficient of friction to allow that match. One of the often-used formulae, given by Hill is quoted by Hoffman and Sachs (1953) in the form:

$$\mu = \frac{\frac{P_r}{\bar{\sigma} \sqrt{R' \Delta h}} - 1.08 + 1.02 \left( 1 - \frac{h_{exit}}{h_{entry}} \right)}{1.79 \left( 1 - \frac{h_{exit}}{h_{entry}} \right) \sqrt{\frac{R'}{h_{entry}}}} \quad (6.1)$$

where  $P_r$  is the roll separating force per unit width,  $\bar{\sigma}$  is the average plane-strain flow strength in the pass and  $R'$  is the radius of the flattened roll.

Roberts (1967) derived a relationship for the coefficient of friction in terms of the roll separating force  $P_r$ , the radius of the flattened roll  $R'$ , the reduction  $r$ , the average of the

tensile stresses at the entry and exit  $\sigma_1$ , the average flow strength of the metal in the pass,  $\bar{\sigma}$ , and the entry thickness of the strip,  $h_{entry}$ :

$$\mu = 2 \sqrt{\frac{h_{entry}}{R'r}} \left[ \frac{P_r(1-r)}{\bar{\sigma} - \sigma_1} \sqrt{\frac{1}{R'h_{entry}r}} - 1 + \frac{5r}{4} \right] \quad (6.2)$$

Ekelund's equation, given by Rowe (1977) in the form of the roll separating force in terms of material and geometrical parameters and the coefficient of friction may be inverted to yield the coefficient of friction:

$$\mu = \frac{\left[ \left( \frac{P_r}{\bar{\sigma} \sqrt{R'\Delta h}} - 1 \right) (h_{entry} + h_{exit}) + 1.2\Delta h \right]}{1.6 \sqrt{R'\Delta h}} \quad (6.3)$$

A comparison of the predicted magnitudes of the coefficient by these formulae is shown in Figure 6.4, using data obtained while cold rolling steel strips, lubricated with a light mineral seal oil. Two nominal reductions are considered. The first is for 15% and the second is for 50%, of originally 0.96 mm thick, 25 mm wide, AISI 1005 carbon steel strips. The metal's uniaxial flow strength, in MPa, is  $\sigma = 150(1 + 234\varepsilon)^{0.251}$ .

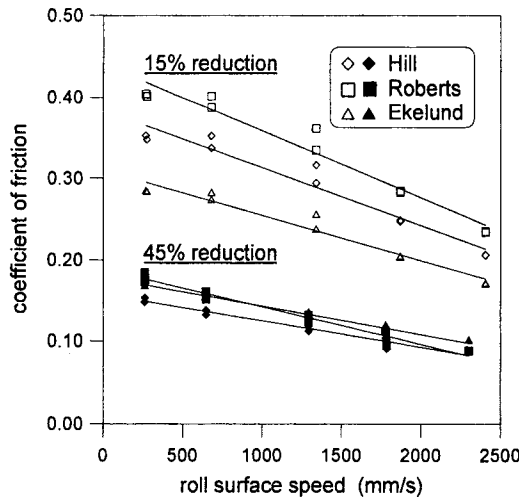


**Figure 6.4** The coefficient of friction, as predicted by Hill's, Roberts' and Ekelund's formulae, for cold rolling of a low carbon steel (Lenard et al, 1999)

The tests were repeated at progressively increasing roll surface velocities, from a low of 0.2 m/s to 2.4 m/s. Care was taken to apply the same amount of lubricant in each test; ten drops of the oil on each side of the strip, spread evenly.

In the figure, the coefficient of friction is plotted versus the roll surface velocity, which does not appear in any of the above formulae in an explicit manner. However, the effect of increasing speed is felt by the roll force, which, as expected, is reduced as the relative velocity at the contact surface increases. Increasing velocity brings more lubricant to the entry to the contact zone. The dropping frictional resistance indicates the efficient entrainment of the lubricant and its distribution in between the roll and the strip surfaces. No starvation of the contacting surfaces is observed.

All three formulae give realistic, albeit somewhat high numbers for the coefficient of friction and all predict the expected trend of lower frictional resistance with increasing velocity. As well, the coefficient of friction is indicated to decrease as the reductions increase, demonstrating the combined effects of the increasing number of contact points, the increasing temperature and the increasing normal pressures.

The first two phenomena result in increasing frictional resistance with reduction. The third causes increasing viscosity and hence, decreasing friction and, as shown by the data, it has the dominant effect on the coefficient of friction. The magnitudes vary over a wide range, however, indicating that the mathematical model influences the results in a significant manner.

**Hot rolling.** Formulae, specifically obtained for flat, hot rolling of steel have also been published. Those given by Roberts (1983) and by Geleji, quoted by Wusatowski (1969), are presented below. Roberts' formula indicates that the coefficient of friction increases with the temperature. Geleji's relations indicate the opposite trend. Roberts combined the data obtained from an experimental 2-high mill, an 84 inch hot strip mill and a 132 inch hot strip mill, all rolling well descaled strips, and used a simple mathematical model to calculate the frictional coefficient. Linear regression analysis then led to the relation:

$$\mu = 2.7 \times 10^{-4} T - 0.08 \quad (6.4)$$

where  $T$  is the temperature of the workpiece in °F. Geleji's formulae, given below, have also been obtained by the inverse method, matching the measured and calculated roll forces. For steel rolls the coefficient of friction is given by:

$$\mu = 1.05 - 0.0005T - 0.056v \quad (6.5)$$

where the temperature is  $T$ , given here in °C and  $v$  is the rolling velocity in m/s. For double poured and cast rolls the relevant formula is:

$$\mu = 0.94 - 0.0005T - 0.056v \quad (6.6)$$

and for ground steel rolls:

$$\mu = 0.82 - 0.0005T - 0.056v \quad (6.7)$$

It is observed that Geleji's relations, indicating decreasing frictional resistance with increasing temperature and rolling speed, confirm experimental trends.

Rowe (1977) also gives Ekelund's formula for the coefficient of friction in hot rolling of steel:

$$\mu = 0.84 - 0.0004T \quad (6.8)$$

where the temperature is to be in excess of 700°C, again indicating that increasing temperatures lead to lower values of the coefficient of friction.

Underwood (1950) attributes another equation to Ekelund, similar to those above, giving the coefficient of friction as:

$$\mu = 1.05 - 0.0005T \quad (6.9)$$

A comparison of the predictions indicates that the relations may not be completely reliable in all instances. For example, for a steel roll and a strip temperature of 1000°C, rolled at a velocity of 3 m/s, Roberts predicts a coefficient of friction of 0.415 while Geleji's relation gives 0.382, indicating that the numbers are close. When 900°C is considered, Roberts' coefficient becomes 0.366 and Geleji's increases to 0.432, creating a large difference. Ekelund's predictions are 0.44 and 0.48, at 900°C and 1000°C, respectively.

**6.2.4.3 Inverse calculations.** Inverse calculations are used often to determine the coefficient of friction, realizing that the result is an "effective value" only, not the actual one. As is well known, the technique requires some of the parameters of the process to be measured experimentally; in the flat rolling process this parameter is usually the roll separating force. A model, which calculates these parameters, is then used, the coefficient of friction in the model is treated as a free parameter and is adjusted until the measurements and predictions match to within an acceptable tolerance. The result may mask some phenomena which affect the parameter but are accounted for in the model. It is understood that the more rigorous the model, the closer the inferred coefficient of friction may be to the actual value. As well, increasing the number of measured and calculated parameters to be matched also increases the predicted accuracy.

Two versions of a one-dimensional model of the flat rolling process have been used successfully to infer the coefficient of friction. The first (Roychoudhry and Lenard, 1984) uses the original Orowan equation of equilibrium, combined with an exact one-dimensional analysis of the elastic entry and exit regions and a two-dimensional analysis of the flattening of the work roll. The other (Lenard and Zhang, 2000) improves on the 1984 model by introducing two values of the coefficient of friction, on either side of the neutral point, eliminating the friction hill and allows the matching of the roll force, roll torque and the forward slip. Since three parameters are matched by the choice of two values of the coefficient, the model's predictions are expected to be closer to reality than other, less sophisticated methods.

An improvement of the inverse method by Gelin and Ghouati (1994, 1995) combines the FE simulation of a process with the measurements of overall parameters, (Kusiak et al 1995; Malinowski et al 1995; Khoddam et al 1996; Gavrus et al 1996) which are compared then with the predictions of the FE method. An error norm is defined as the vector of distances between the measured and calculated values. Minimization of the norm

leads to the unknown parameters. This approach was followed by Szyndler et al (2000) in estimating the friction factor in the hot ring compression test. A detailed description of the approach is given by Szeliga and Pietrzyk in Chapter 12 of this book.

### 6.2.5 Application of a lubricant

**6.2.5.1 The lubrication regimes.** Boundary lubrication is characterized by significant amounts of metal-to-metal contact and some lubricating pockets. The thickness of the film is low and the asperities pierce through the lubricant. As the viscosity or the relative velocity are increased, a mixed mode of lubrication is observed, in which more lubricant pockets and less asperity contact are found. In these regimes the surface roughness of the resulting product decreases as a consequence of the contact and approaches that of the die. The hydrodynamic regime follows with complete separation of the surfaces. The lubricant film is thicker than the combined surface roughness of the die and plastically deformed work piece. Free plastic deformation of the surface causes roughening. Further subdivision of the hydrodynamic regime is possible by identifying elasto-hydrodynamic or plasto-hydrodynamic lubrication, depending on the deformation of the asperities, their resistance to deformation.

It is possible to determine the nature of the lubricating regime by comparing the thickness of the oil film and the combined asperity heights of the rolls and the rolled metal. Their ratio is defined (Hutchings, 1992) as

$$\lambda = \frac{h_{\min}}{\sigma^*} \quad (6.10)$$

where  $h_{\min}$  is the oil film thickness by eq. 6.19 and  $\sigma^*$  is the r.m.s. roughness of the two surfaces, given by

$$\sigma = \sqrt{R_{q1}^2 + R_{q2}^2} \quad (6.11)$$

and  $R_{q1}$  and  $R_{q2}$  are the r.m.s. surface roughness values of the two surfaces. When the oil film thickness to surface roughness ratio is less than unity, boundary lubrication is present. When  $1 \leq \lambda \leq 3$  mixed lubrication prevails while for a ratio over three, hydrodynamic conditions and full separation of the contacting surfaces are present.

**The Stribeck curve.** The lubrication regimes may be illustrated by making reference to the Stribeck curve, first plotted to study friction in the bearings of rail car wheels. In the Stribeck curve (Hutchings, 1992), the coefficient of friction is plotted against the modified Sommerfeld number (Mortier and Orszulik, 1992, identify the dimensionless group as the Hersey number) defined as:

$$S = \frac{\eta \Delta v}{p} \quad (6.12)$$

where the dynamic viscosity is  $\eta$ , the relative velocity is  $\Delta v$  and  $p$  is the pressure. A schematic diagram of the Stribeck curve is shown in Figure 6.5, with the boundary, mixed and hydrodynamic mode of lubrication identified.

As indicated, the coefficient of friction's dependence on the Sommerfeld number varies according to the nature of the lubrication regime. The coefficient is large in the dry regime in which full metal-to-metal contact occurs at the asperity tips. Plastic deformation of the asperities creates new material, satisfying the requirement of the adhesion hypothesis: clean surfaces close together. As the viscosity and/or the relative velocity increase, the coefficient drops, a phenomenon which has often been observed in several metal forming processes in general and in flat rolling, in particular. Increasing interfacial pressures also result in lower resistance to relative motion. As the speed and the viscosity increase further, the coefficient reaches a minimum and the hydrodynamic regime of complete separation of the surfaces begins. In this regime frictional resistance is caused by the need to overcome the shear strength of the lubricant film, separating the surfaces. Free plastic deformation leads to surface roughening.

It is, however, somewhat misleading to examine the behavior of the coefficient of friction as a function of one of the parameters only. There is a very strong interdependence of all significant parameters and in realistic experiments it is very difficult, if not impossible, to change only one while keeping all else constant.

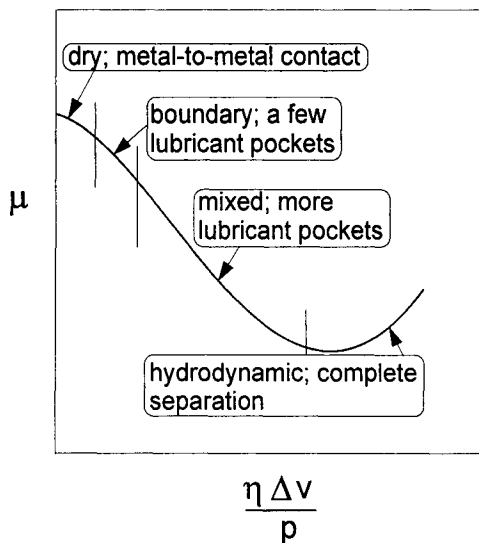


Figure 6.5 The Stribeck curve

**6.2.5.2 The sensitivity of the lubricant's viscosity to the pressure and the temperature.** In the calculations for the thickness of the lubricant film, or establishing the lubrication regimes using the Stribeck curve, it is necessary to account for the changes of the viscosity as the temperature and the pressure change. Several relations have been published in the technical literature, giving the dependence of the viscosity on both parameters. In the flat rolling

process both increase significantly at the contact surface, in between the roll and the rolled strip. The relationship often used is:

$$\eta = \eta_0 \exp(\gamma p - \delta T) \quad (6.13)$$

where  $\gamma$  is the pressure - viscosity coefficient and the temperature - viscosity coefficient is  $\delta$ . The uncorrected viscosity is  $\eta_0$ . Sa and Wilson (1994) introduced a cross-coefficient,  $\mathcal{G}$ , to account for the interaction of  $\gamma$  and  $\delta$

$$\eta = \eta_0 \exp(\gamma p - \mathcal{G} p T - \delta T) \quad (6.14)$$

The interaction of the temperature and pressure effects on the viscosity may well be very significant. However, no easy way of determining the cross-coefficient appears to be available at the present time. While values for the coefficients are difficult to find for special lubricants, a good collection of data is presented by Booser (1984, 1997).

Increasing pressures increase the viscosity of oils. This dependence can be described in terms of an exponential relationship. The viscosity needs to be corrected to account for the effects of the temperature and pressure. Values for the coefficients are difficult to find and using the incorrect magnitudes leads to large errors. For example, Yamamoto and Uehori (1989) give  $0.07 \text{ MPa}^{-1}$  for the pressure - viscosity coefficient and  $0.06 \text{ }^{\circ}\text{C}^{-1}$  for the temperature - viscosity coefficient. At a normal pressure of 300 MPa and an oil temperature of  $100^{\circ}\text{C}$ , the viscosity is indicated to increase by  $3.3 \times 10^6$ , clearly not realistic. The magnitudes given by Booser (1997) are much lower. The correct magnitudes of the two coefficients are necessary to plot the Stribeck curve.

For mineral oils, the viscosity - pressure coefficient is given by Hutchings (1992) as:

$$\gamma \approx (0.6 + 0.965 \log_{10} \eta_0) \times 10^{-8} \quad (6.15)$$

where the viscosity at zero pressure,  $\eta_0$ , is in centipoise and the viscosity - pressure coefficient is in  $\text{Pa}^{-1}$ .

The pressure - viscosity coefficients can also be calculated following the study of Wu, Klaus and Duda (1989) who quote the formula of So and Klaus (1980), giving the coefficient as

$$\gamma = 1.030 + 3.509 (\log \mu_0)^{3.0627} + 2.412 \times 10^{-4} m_0^{5.1903} (\log \mu_0)^{1.5976} - 3.387 (\log \mu_0)^{3.0975} \rho^{0.1162} \quad (6.16)$$

in units of  $\text{kPa}^{-1} \times 10^5$ ; the predictions are shown by the authors to be very accurate. The constant  $m_0$  is defined as the viscosity - temperature property, given by the ASTM slope divided by 0.2. The slope is given by Briant, Denis and Parc (1989) and the coefficient  $m_0$  is then obtained from:

$$m_0 = \left( \frac{1}{0.2} \right) \frac{[\log \log(\mu_0 + 0.7) - \log \log(\mu + 0.7)]}{\log T_0 - \log T} \quad (6.17)$$

Information regarding the viscosity - temperature coefficient may also be extracted from the table by assuming a linear variation between 40 and 100°C. The Walther equation may also be used, provided the constants are available (Booser, 1984):

$$\log \log(\mu + c) = a - b \log T \quad (6.18)$$

where  $a$  and  $b$  are constants,  $c$  varies with the viscosity and  $\mu$  is the kinematic viscosity in centistokes. Details concerning these constants and their magnitudes are given by the D341 ASTM standards.

**The oil film thickness:** The oil film thickness at the inlet may be calculated by the formula of Wilson and Walowit (1971)

$$h = \frac{3\eta_0\gamma(v_{entry} + v_{roll})R'}{l[1 - \exp(-\gamma\sigma_y)]} \quad (6.19)$$

where  $\eta_0$  is the dynamic viscosity at 38°C, in Pa s, and  $\gamma$  is the pressure - viscosity coefficient in Pa<sup>-1</sup>. The radius of the flattened roll, calculated by the Hitchcock formula, is designated by  $R'$  in m, the roll surface velocity is  $v_{roll}$ , the entry velocity of the strip is  $v_{entry}$ , both in m/s and  $l$  stands for the projected contact length, also in m. The average flow strength is given by  $\sigma_y$ , in units that match those of  $\gamma$ .

**6.2.5.3 Entrainment of the lubricants.** Entrainment of the lubricant, critical in establishing the tribological conditions in the rolling process is examined in detail in Chapter 7 of this study, entitled "Studies on micro plasto hydrodynamic lubrication in metal forming" by Niels Bay, Jakob I. Bech, Jan L. Andreasen and Ichiro Shimizu.

### 6.3 EXPERIMENTAL STUDIES

Flat rolling tests have been carried out in the Manufacturing Processes Laboratory of the Department of Mechanical Engineering, University of Waterloo during the last decade, with several objectives, among them the determination of the dependence of the coefficient of friction on process and material parameters. As mentioned above, the process parameters are limited to the speed of rolling, the reduction per pass, the temperature, the lubricants or emulsions used and their attributes. The materials are various aluminium alloys and low carbon steels of various carbon contents. In each experiment, one pass is used, with neither front nor back tensions. The roll forces, the roll torques, the forward slip, the rolling speed, the temperature and reduction per pass are measured and/or monitored in each test.

In what follows, the coefficients of friction as functions of process and material parameters and determined in various ways in several tests are given. The tests include dry rolling of aluminium alloy strips at slow speeds; use of several neat oils with various



boundary additives while cold rolling aluminium alloys; hot rolling of commercially pure aluminium alloys using an emulsion; cold rolling of low carbon steel strips, using neat oils and emulsions and finally, hot rolling of low carbon steel strips.

### 6.3.1 Equipment and procedure

Two, two-high rolling mills have been used in the tests. In the larger, the rolls of 250 mm diameter and 150 mm length are made of D2 tool steel, hardened to  $R_c = 64$ . The mill is driven by a 30 kW, constant torque DC motor, whose speed is controlled by a TYRAK controller. The speed is continuously variable, up to a maximum of 3 m/s. The maximum allowable roll separating force is 500 kN.

The other mill is made by STANAT. Two sets of rolls, both of 150 mm diameter, are available. For hot rolling the rolls are made of D2 tool steel, hardened to  $R_c = 55$ . The rolls for cold rolling are of L3 tool steel, containing 1% C, 1.5% Cr and 0.2% V, hardened to Shore 90. The motor power is 12 kW, with the highest speed of 1.2 m/s. The maximum allowable roll separating force is 800 kN. Both mills are instrumented to measure the roll separating force, the roll torque, the exit velocity of the strip and hence, the forward slip, the rolling speed, the temperature at entry and exit and the reduction. All data collection is done automatically, using personal computers and LABVIEW.

When neat oils are used, several drops of the lubricant are applied to the surface and spread evenly. VEEJET nozzles and pump are used to spray the emulsions during cold rolling of steels and during hot rolling of aluminium and steels. A schematic diagram of the experimental set-up, for hot rolling of aluminium strips, is shown in Figure 6.6.

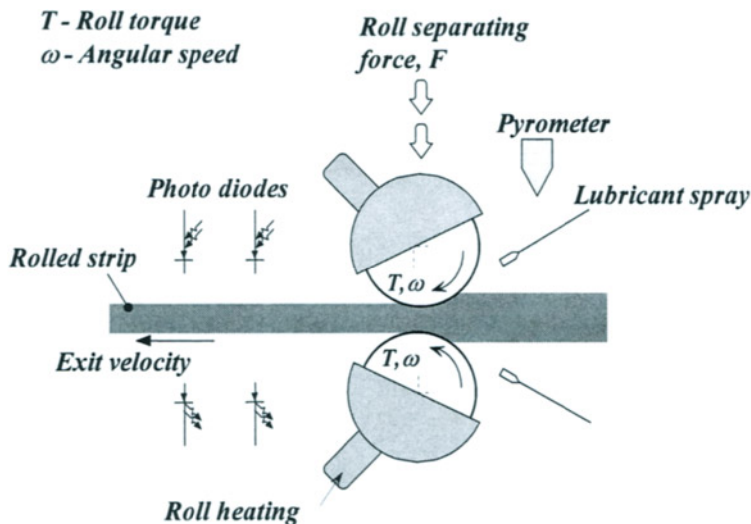


Figure 6.6 Schematic diagram of the rolling mill, set up for hot rolling of aluminium strips, using emulsions

## 6.4 THE COEFFICIENT OF FRICTION IN FLAT ROLLING

**6.4.1 Dry rolling of aluminium alloy strips (Lim and Lenard, 1984; Karagiozis and Lenard, 1985)**

Three aluminium alloy strips were cold rolled, at a slow speed of 78 mm/s, with no lubricant. Commercially pure aluminium, 1100 – H0, half hard 1100 – H14 and a 5052 – H34 alloys were selected. Before each pass the strips' and the rolls' surfaces were cleaned using a neutral cleaner. The independent variable was the reduction per pass. Using the embedded transducer - pin combinations of Figure 6.2, the roll pressures, the interfacial shear stresses, and their ratio, the coefficient of friction were monitored in addition to the roll separating forces and the roll torques.

Typical distributions of interfacial stresses are shown in Figures 6.7 and 6.8, for the 1100-T0 and the 2024-T3 alloys, respectively, giving the angular variable on the abscissa and the roll pressure and interfacial shear stress on the ordinate. The dependence of the coefficients of friction on the reduction for these alloys in addition to the 5052-H34 is demonstrated in Figure 6.9.

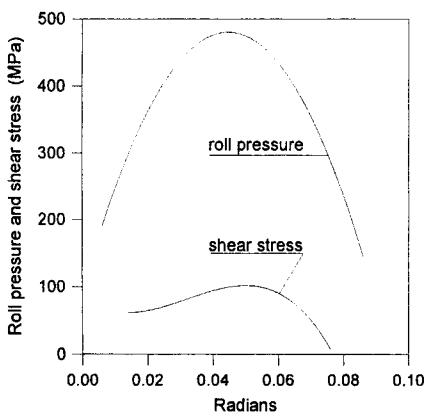


**Figure 6.7** The roll pressure and the interfacial shear stress distribution; 2024 – T3 aluminium alloy, rolled at 78 mm/s, to a reduction of 8.9% (Lim and Lenard, 1984)

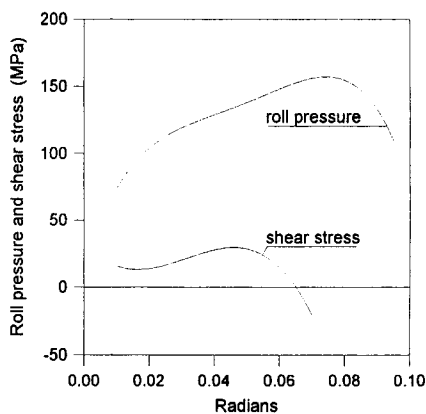


**Figure 6.8** The roll pressure and the interfacial shear stress distribution; 1100 – H0 aluminium alloy, rolled at 78 mm/s, to a reduction of 14.3% (Lim and Lenard, 1984)

As expected, the roll pressures rise at a steep slope at the entry and drop sharply as the strip nears the exit. The distributions are smooth, agreeing with the results of Siebel and Lueg (1933), van Rooyen and Backofen (1960) and Al Salehi et al (1973), indicating the inapplicability of the traditional friction hill in depicting the pressures on the work roll. The ratio of the shear stress to the roll pressure varies from entry to exit, demonstrating the variation of the coefficient in the contact zone as the pressure and the temperature change.

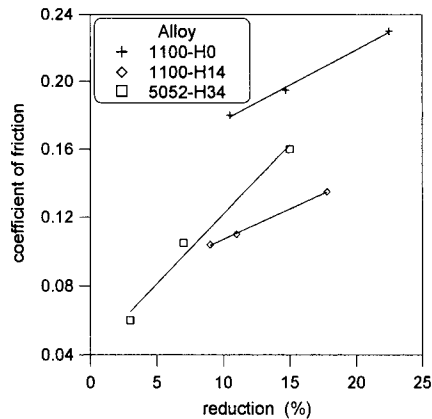


**Figure 6.9** The dependence of the coefficient of friction on the reduction during cold rolling of aluminium alloys, with no lubrication. The roll surface velocity was 78 mm/s (Karagiozis and Lenard, 1985)

The coefficient of friction, obtained by taking the average of the ratio of the interfacial shear stress to the normal pressure, is shown to depend on the reduction in Figure 6.9. As well, the effect of the alloys is observed, indicating that the metals' resistance to deformation and the chemical composition of the alloys influence surface interaction in a significant manner.

The information shown in Figure 6.9 leads to two observations. The first is the rising magnitude of the coefficient of friction with the reduction and the second is the drop of the coefficient with the increasing strain hardening of the rolled alloys. Both phenomena may be well explained by the adhesion hypothesis. As mentioned above, the plastic deformation of the rolled surface creates new material on which the requirements for adhesion are satisfied. Increasing reductions create progressively increasing number of adhesive bonds, leading to higher resistance to relative motion. The asperities of a material with strong strain hardening characteristics will, however, deform less than a metal with lower strain hardening and subjected to the same load, thus creating a smaller real area of contact, fewer bonds and lower frictional resistance.

#### 6.4.2 Cold rolling of an aluminium alloy, using lubricants with boundary additives (Lenard, 1998)

The effect of four boundary additives - lauryl alcohol, stearyl alcohol, lauric acid and stearic acid - in mineral seal oil, on the coefficient of friction, obtained by the use of Hill's empirical relation, was investigated. The independent variables were the rolling speed, reduction and the concentration of the additives. The density of the mineral seal oil is measured to be 850 kg/m<sup>3</sup>; its kinematic viscosity is 4.5 mm<sup>2</sup>/s, at 40°C. The additive concentration is 1 to 5%, (v/v). Commercially pure aluminium alloy strips of 1 mm thickness, 25 mm width, 1100-H14, were rolled. The plane strain true stress – strain curve of the metal is  $\sigma = 111(1 + 100\varepsilon)^{0.11}$  MPa. The coefficients of friction, as functions of the reduction, the rolling speed and the additives, are shown in Figures 6.10 and 6.11. It is observed that both

drop and increase of frictional resistance are present and that the use of the boundary additive has a significant effect on the reaction of the coefficient of friction to loads.

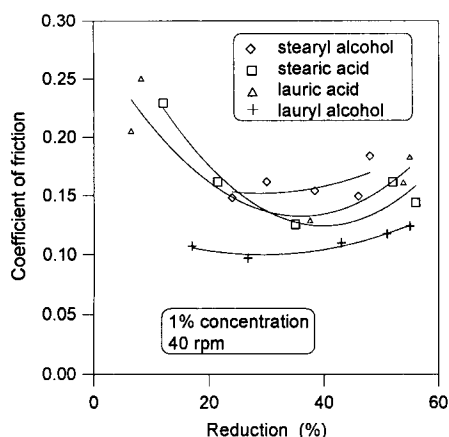


**Figure 6.10** The coefficient of friction vs the reduction; cold rolling of 1100-H14 aluminium alloy, using four boundary additives; at 0.52 m/s roll surface velocity

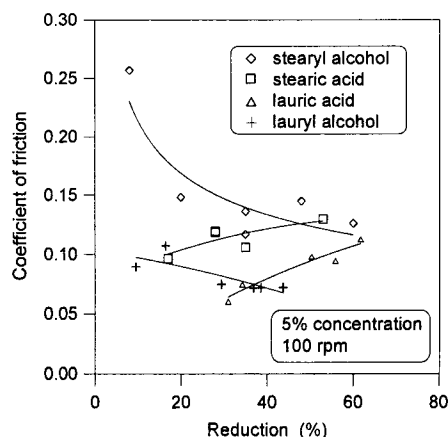


**Figure 6.11** The coefficient of friction vs the reduction; cold rolling of 1100-H14 aluminium alloy, using four boundary additives; at 1.3 m/s roll surface velocity

Chemical adsorption (chemisorption) is the mechanism that leads to the creation of the boundary films. The strength of these films and their adhesion to the base metal during the rolling process will have a strong effect on the coefficient of friction. The molecular weights affect the separation of the surfaces and therefore the coefficient of friction. There is evidence that as they increase, the frictional resistance decreases. The molecular weights of the additives are given in the Table 6.1 (West, 1976-77).

**Table 6.1** The molecular weights of the additives

Lauryl alcohol	186.33
Lauric acid	200.32
Stearyl alcohol	270.48
Stearic acid	284.49

Lauryl alcohol was the most effective in reducing the roll separating force while stearyl alcohol caused the largest reduction of the roll torque. The coefficient of friction was the lowest when lauryl alcohol was used.

#### 6.4.3 Cold rolling steel strips, using lubricants and emulsions (McConnell and Lenard, 2000; Shirizly and Lenard, 2000)

In these projects low carbon steel strips were rolled, using the mill with the 250 mm diameter work rolls. In the first, neat oils were used; in the second, the effects of neat oils on the rolling process were compared to those while using emulsions. In both projects the coefficients of friction were determined by inverse calculations.

**6.4.3.1 Neat oils (McConnell and Lenard, 2000).** Six commercial lubricants of Imperial Oil are tested for their ability to lower the loads on the mill during cold rolling of low carbon steel strips. The roll separating forces, roll torques and the forward slip are monitored during the rolling process in which the reduction and the speed of rolling are taken to be the independent variables.

The coefficient of friction is determined by three mathematical models: Hills' formula (see above, Equation 6.1), a one-dimensional model of the rolling process, based on a refinement of the Orowan approach (Roychoudhury and Lenard, 1984) and another one-dimensional model in which the friction hill is not used (Lenard and Zhang, 1987) and different values of the coefficient of friction on either side of the neutral region are permitted.

While the viscosities of the oils vary over a fairly large range, their effects on the roll forces and torques are not very pronounced. The coefficients of friction decrease with increasing speeds and reductions. Their magnitudes are strongly dependent on the quality of the model used in their computations.

Details of the six oils are, as follows. Oil A is a forming and cutting oil, called Exxcut 225, prepared with petroleum base oils, sulfurized hydrocarbons, fats and esters as the additives with a viscosity of 25.15 mm<sup>2</sup>/s at 40 °C. Oil B is identical to oil A, containing no additives, and of somewhat lower viscosity. Oil C is again the same as A, containing only one additive, a lubricity contributing ester. Oil D is a commercial cutting oil, 1033A. This is a highly sulfurized petroleum based oil of low viscosity. Oil E is a commercial rolling oil, known as Roll Oil 981. This is a petroleum based oil of the lowest viscosity of all six, containing small amounts of esters as additives. Oil F is a hydrocarbon synthetic lubricant with no additives. Its viscosity is somewhat less than that of oil A. The kinematic viscosity at 40°C and at 100°C and the density of the six lubricants are given in Table 6.2.

**Table 6.2** The properties of the lubricants

Lubricant	Kinematic viscosity (mm <sup>2</sup> /s)		Density (kg/m <sup>3</sup> )
	40°C	100°C	40°C
A	25.15	4.97	869.3
B	19.85	3.96	861.6
C	20.05	4.03	863.0
D	14.30	3.28	886.6
E	5.95	1.88	853.1
F	17.32	3.89	819.4

The effect of the model on the inferred, effective coefficient of friction is demonstrated in Figure 6.12, where the predictions of Hill's formula and the two one-dimensional mathematical models, mentioned above, are compared. The computations considered the results obtained using Lubricant A.

In Figure 6.12 "Hill" refers to the use of Hill's formula for the calculation of the coefficient of friction, Eq. 6.1; "Coldraj" refers to the model given in Roychoudhury and Lenard (1984) while "varying friction" indicates results, obtained by the model of Lenard

and Zhang (1997). All three models indicate the expected trend of falling coefficients of friction with increasing rolling speeds. Hill's predictions are approximately 40-50% higher than the ones by the model that considers the dependence of the coefficient on the roll pressure.

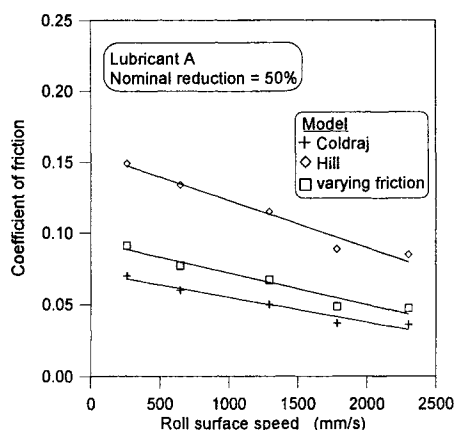


**Figure 6.12** The coefficient of friction, as predicted by three models; lubricant A; 50% nominal reduction

The variation of the coefficient of friction, as calculated by the model of Lenard and Zhang, (2000), as a function of the rolling speed for all six lubricants is demonstrated in Figure 6.13, for nominal reductions of 15 and 50%. The differences are not very large.

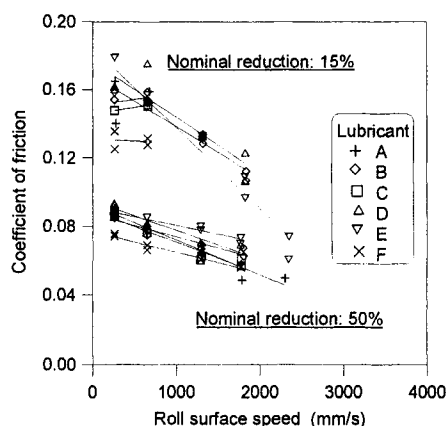


**Figure 6.13** The variation of the coefficient of friction with the roll surface speed. All six lubricants are included. The 1D model of Lenard and Zhang (1997) has been used to infer the magnitude of the coefficient of friction.

The dependence of the coefficient of friction on the Sommerfeld number is indicated in Figure 6.14. At low speeds the coefficient of friction is high and the boundary lubrication regime is predominant. As the speed is increased, the mixed regime is reached and the coefficient falls. The hydrodynamic regime is approached but it is not reached; for if it were, the rolling process with no front or back tension would likely become unstable. In determining the values of the viscosity for use in the abscissa, the appropriate values of the viscosity-temperature and the viscosity-pressure coefficients were employed.

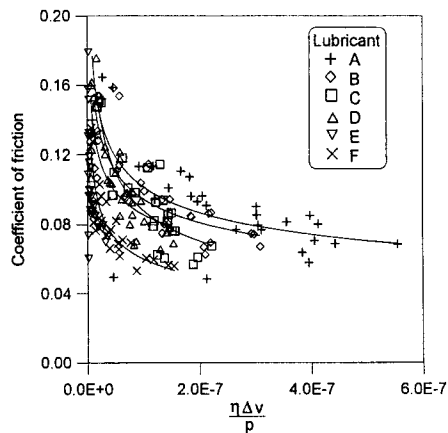


Figure 6.14 The Stribeck curve, for all six lubricants

Table 6.3 Temperature – viscosity and pressure – viscosity coefficients

Lubricant	Temperature – viscosity coefficient ( $K^{-1}$ )	Pressure – viscosity coefficient ( $MPa^{-1}$ )
A	0.0270	0.01458
B	0.0269	0.01388
C	0.0267	0.01390
D	0.0245	0.01276
E	0.0192	0.01128
F	0.0249	0.01381

**6.4.3.2 Neat oils and emulsions (Shirizly and Lenard, 2000).** The objectives here are formulated to answer the following question. As demonstrated above, the use of neat oils results in significant reduction of the loads on the mill. The traditional industry practice is to use oil-in-water emulsions and not neat oils while cold rolling steel strips. Hence the question: How do emulsions affect the coefficient of friction as compared to neat oils? In order to be able to compare the emulsion's effects, dry rolling and rolling with water only are also performed.

Four lubricants were compared in the study, in addition to dry rolling and using water only, for their abilities to affect the loads on the mill, the frictional conditions and the resulting roughness. The lubricants included the SAE 10 and SAE 60 automotive oils, the SAE 10 base oil with 5% oleic acid added and the SAE 10 base oil, emulsified, using water and polyoxyethylene lauryl alcohol as the emulsifier, 4% by volume. Oleic acid was chosen as the boundary additive since it was shown to react to pressure and temperature less than several other fatty oils (Schey, 1987). The properties of the two base oils are given in Table 4. While the automotive lubricants were not formulated for use in the flat rolling process, their properties are well known, and that is the reason for their choice in this comparative study. Reid and Schey (1977) also used automotive oils in their study of full film lubrication during rolling of aluminium alloys.

**Table 6.4** Properties of the base oils

Description		Viscosity, mm <sup>2</sup> /s		Density
		40°C	100°C	gm/cm <sup>3</sup> , 15°C
SAE 10	Paraffinic, refined, dewaxed	29.6	4.9	0.871
SAE 60	Paraffinic, refined, dewaxed	283.7	22.6	0.875

In the tests the roll separating forces, roll torques and the forward slip were determined. The reduction, the speed and the lubricant were the independent variables. The coefficient of friction was determined by Hill's formula; since comparative values were wanted, this approach was deemed adequate. The coefficients of friction, obtained at 20 and 160 rpm rolling speeds (corresponding to 0.26 and 2 m/s surface velocity), are shown in Figures 6.15 and 6.16, below.

In general and as expected, the highest frictional resistance is observed at low speeds and dry conditions. At 20 rpm, the lowest magnitudes for the coefficient of friction are produced by water only as the lubricant, confirming the trend noted above with the loads on the mill. No significant differences in frictional resistance are noted when any of the oils, neat or emulsified, are used. In all cases the coefficient of friction is reduced as the reduction is increased. Rolling in the dry condition resulted in frictional values that are among the highest, but surprisingly not *the* highest.

There is an unmistakable, albeit not very pronounced, dependence of the frictional resistance on the lubricant viscosity at the 160 rpm rolling speed. Of the four lubricants, the most viscous, SAE 60, appears to yield the lowest coefficient of friction and the highest values are obtained under no lubricating conditions. The magnitude of frictional resistance with the SAE 10, containing the oleic acid additive, is significantly lower than those rolled dry, as expected. The SAE 10, neat or emulsified, leads to friction values that are practically identical and not very much different from SAE 10 and the boundary additive. When using the four lubricants, the coefficient of friction reduces with increasing reduction. As well, the coefficient of friction is observed to decrease as the speed of rolling increases, under both dry and lubricated conditions.

The adhesion hypothesis provides a reasonable explanation for the lower magnitudes of the frictional resistance with increasing relative velocity. It was mentioned above that the friction forces arise when the adhesive bonds are broken, and as such, they are dependent on either the materials' or the bonds' strengths. Since bond formation is a time



dependent phenomenon, higher speeds leave less time for them to form and fewer of the bonds are to be separated, leading to less friction. Under lubricated conditions the additional operating mechanism is the increasing volume of the lubricant drawn into the roll gap, adding to lower friction. The lack of any major viscosity effect when cold rolling steels is somewhat surprising. The data of Lin et al (1991), also obtained by Hill's formula for the coefficient of friction, supports the present observations.

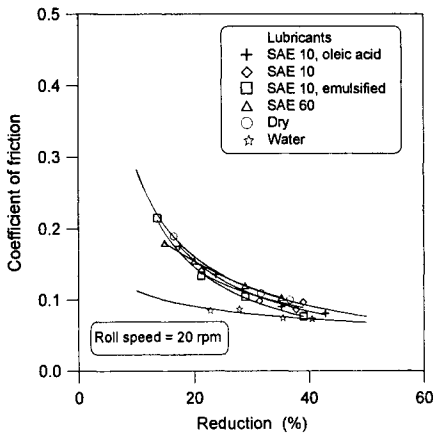


**Figure 6.15** The coefficient of friction as a function of the reduction; 0.26 m/s surface velocity

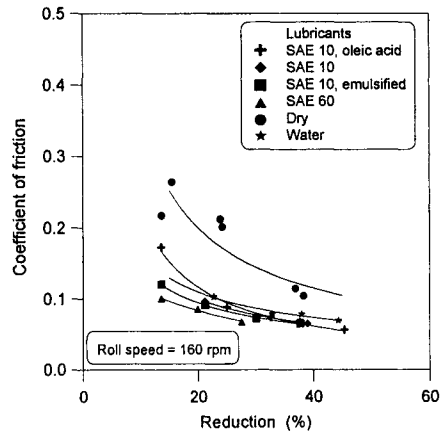


**Figure 6.16** The coefficient of friction as a function of the reduction; 2 m/s surface velocity

#### 6.4.4 Hot rolling aluminium alloys using emulsions (Hum et al 1996)

In order to establish the dependence of the coefficient of friction on rolling speed and the reduction, commercially pure aluminium strips were rolled at 500°C, using a 2% oil/water emulsion as the lubricant. The roll separating forces, roll torques, the forward slip, the roll pressure and the interfacial shear stress were measured as a function of the reduction and the rolling speed. The coefficient of friction was determined from the shear stress and the roll pressure distributions and its magnitude was validated independently. The coefficient of friction was found to increase with reduction and, in general, decrease with rolling speed.

The roll pressure and interfacial shear stress distributions, obtained at reductions of 39.4 and 30.4%, respectively are shown in Figures 6.17 and 6.18.

The coefficients of friction, determined by taking the averages of the ratios of the shear and the normal stresses, are shown in Figure 6.19, as functions of the speed and the reduction. As the figure demonstrates, the coefficient of friction increases as the reduction increases during hot rolling of commercially pure aluminium alloy strips. This phenomenon has been discussed above in terms of the adhesion hypothesis and the development of the adhesive bonds at the contacting asperities. This development is dependent on the load and the response of the rolled metal to that load. With the relatively soft alloy, the asperities flatten in a pronounced manner, leading to the growth of the real area of contact and hence to the growth of frictional resistance with increasing loads.

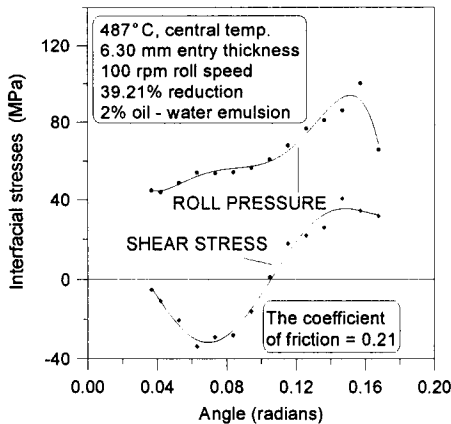


**Figure 6.17** The roll pressure and the interfacial shear stress; hot rolling of aluminium with an emulsion, at 487° C, 39.21 % reduction, 1.3 m/s velocity

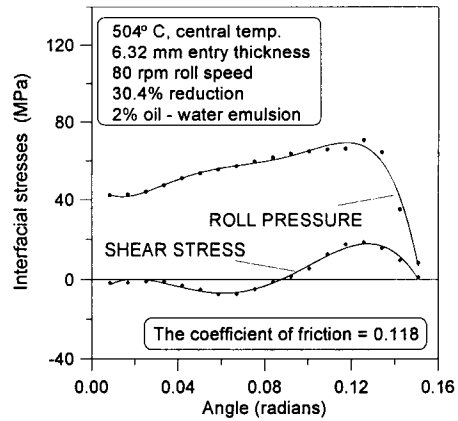


**Figure 6.18** The roll pressure and the interfacial shear stress; hot rolling of aluminium with an emulsion, at 504° C, 30.4 % reduction, 1 m/s velocity

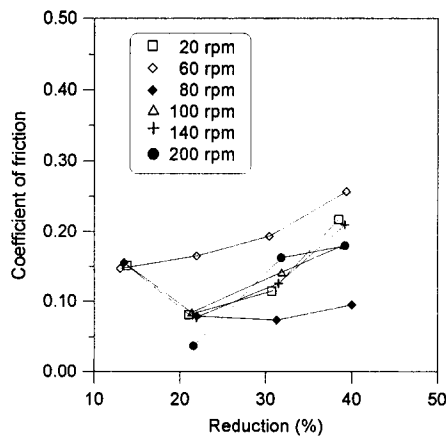


**Figure 6.19** The coefficient of friction, obtained by the embedded transducer – pin apparatus, during hot rolling of an aluminium alloy (Hum et al 1996)

#### 6.4.5 Hot rolling steel strips (Munther and Lenard, 1995)

AISI 1018 (0.19% C, 0.7% Mn) carbon steel slabs were used in all experiments. The steel was delivered in the form of cold rolled bars. The samples were machined to 12.7 mm thickness, 50.8 mm width and 305 mm length. Three reductions were investigated: 10, 20, and 30% at temperatures from 825°C to 1125°C. The roll speed was 25 rpm in all experiments, giving a roll surface velocity of 196 mm/s. The specimens were rolled with the scale which acted both as an insulator and as a lubricant during the rolling operation, even

though it was eventually broken off. Each experiment was repeated three to five times and average values of the roll separating forces, roll torques and the forward slip were reported.

A rigid-plastic finite element model, presented in (Pietrzyk and Lenard, 1991), was used to correlate the measured values of the forward slip and the coefficient of friction. Shida's equations (1971), which give the steel's resistance to deformation in terms of the strain, rate of strain, the temperature and the carbon content, are used for estimation of the mean plane-strain flow stress. In the calculations, the magnitude of the coefficient of friction was inferred by matching the measured and calculated values of the forward slip, roll force and torque. The results are given in Figure 6.20.

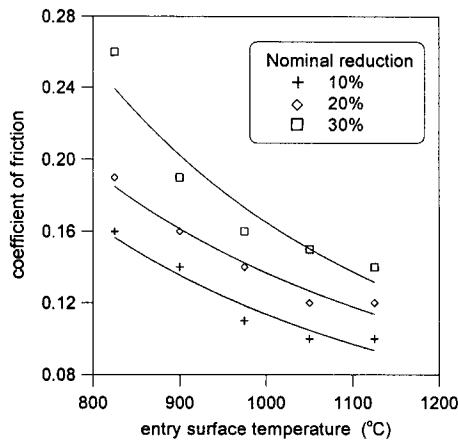


**Figure 6.20** The coefficient of friction in hot rolling of an AISI 1018 steel. The coefficient was inferred by matching roll forces and temperature changes, using Elroll, a commercially available FE program.

#### 6.5 THE DEPENDENCE OF THE COEFFICIENT OF FRICTION ON PROCESS AND MATERIAL PARAMETERS (Lenard, 2001)

The interactions of the phenomena determining the nature of the mechanisms in the contact zone are illustrated in Figures 6.21 and 6.22. The effects of the reduction on the process are shown in Figure 6.21 while that of the relative velocity are given in Figure 6.22. During a particular rolling pass the following competing mechanisms are active:

- the rate at which the pressure on the lubricant increases;
- the rate at which the viscosity of the oil increases, leading to lower friction;
- the rate at which the number of contacting asperities grows, leading to higher friction;
- the pressure at which the lubricant layer breaks up, leading to higher friction;
- the relative velocity and the amount of lubricant drawn into the contact region;

## AN EXAMINATION OF THE COEFFICIENT OF FRICTION

- the orientation of the grooves formed by the asperities, aiding or impeding the spread of the lubricant within the contact zone;
- the growth of the bite angle, leading to more oil in the roll gap and the increasing surface temperature with increasing loads, leading to lower viscosity and thus, higher friction and
- the adhesion of the lubricants to the roll and the work piece surfaces.

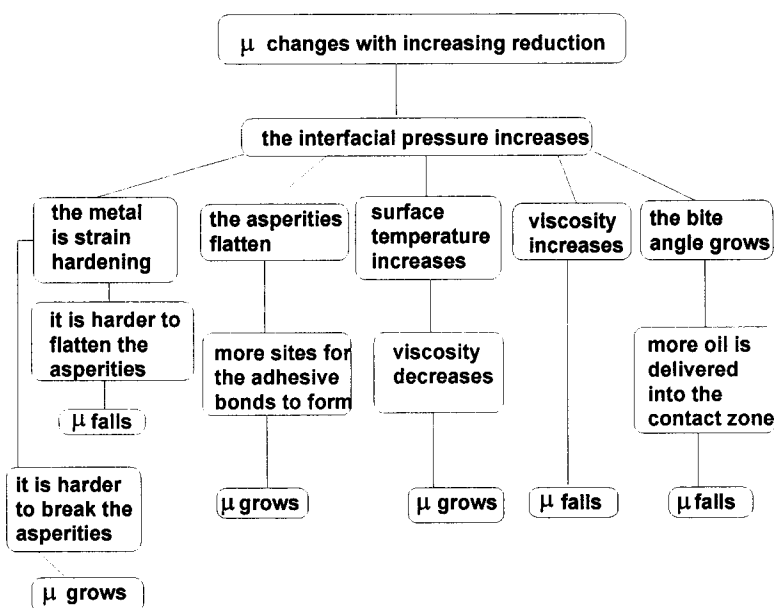


**Figure 6.21** The effect of the reduction on the mechanisms that affect the coefficient of friction

The figure indicates the effects of six mechanisms on the coefficient of friction, as a result of increasing the reduction per pass. The first phenomenon concerns the effect of straining as the rolling pass proceeds and the attendant strain hardening of the metal. The increasing resistance to deformation will require more expenditure of energy to flatten the asperities and thus, will cause the true area of contact to approach the apparent area at a slower rate. Fewer sites for the formation of adhesive bonds will be available. A material, which is more strain hardening, will therefore experience a lower magnitude coefficient of friction than one with a lower strain-hardening exponent.

It is also to be realized that the metal, which has hardened will possess asperities that are harder to break. If this metal is contacting another to which it has a high chemical affinity, the resistance to relative motion will probably increase since it is likely that it is the bond that will have to be broken to overcome frictional resistance.

The asperities of a softer metal will flatten with relative ease when compared to a harder metal. More sites for bonds may then be available and the coefficient of friction will likely be higher than for the hard metal, subjected to the same load.

When lubricants are introduced into the conjunction, their response to the increased pressure and increased temperature will affect the tribological system in a very significant manner. In general, increasing pressures increase the lubricant's viscosity, which will result in lower resistance to relative motion. Higher temperatures will lower the viscosity, causing higher frictional resistance.

The last contributor, resulting from larger reduction, is the increased angle of bite. This would make more oil available for entry to the contact zone. After successful entrainment, further reduction of the coefficient of friction may result.

The actual coefficient of friction will, of course, be the result of the contributing, competing mechanisms. A mathematical model to account for these and to predict the coefficient of friction is not available as yet.

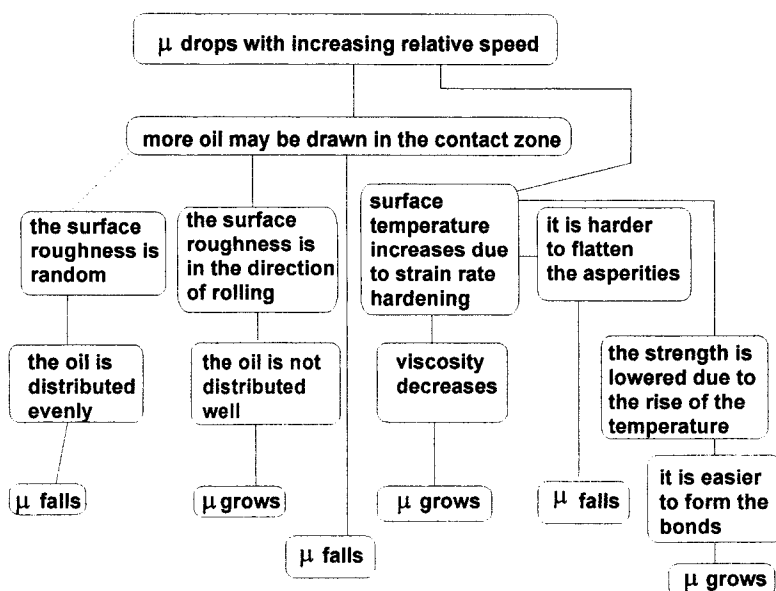


**Figure 6.22** The effect of the relative velocity on the mechanisms that affect the coefficient of friction

The effect of the velocity on the coefficient of friction is indicated in Figure 22 as a function of potentially another six mechanisms that bear some similarities to those mentioned above. The first two concern the direction of the roughness on the work roll and how that may affect the distribution of the lubricant in the contact. The traditional technique to prepare the work roll surfaces is by grinding. The grinding wheel rotates and translates along the roll axis and the likely roughness direction thus obtained will contain grooves around the roll. These grooves will prove not highly efficient in distributing the lubricant.

Random roughness directions are expected to be much more efficient in the distribution and when roll surfaces are prepared that way, frictional resistance and the coefficient of friction will be lower than those obtained in the traditional manner.

Increasing relative velocity will increase the surface temperature and in materials whose resistance to deformation is rate sensitive, the flow strength will also rise. The arguments made above while considering the effect of increasing reduction are applicable here, as well, and Figure 6.22 indicates these effects. All of these mechanisms act together to determine the actual resistance to relative motion during the rolling process.

## REFERENCES

- Azarkhin, A. and Richmond, O., (1992) Limits to Adhesive Friction, in *Num. Meth. Ind. Form. Proc.*, ed. Chenot, J-L., Wood & Zienkiewicz, Balkema, 143-148
- Al-Salehi, F.A.K., Firkbank, T.C. and Lancaster, P.G., (1973) An Experimental Determination of the Roll Pressure Distribution in Cold Rolling, *Int. Journal Mech. Sci.*, **15**, 693-710.
- Banerji, A. and Rice, W.B., (1972) Experimental Determination of Normal Pressure and Friction Stress in the Rolling Gap During Cold Rolling, *Annals of the CIRP*, **21**, 53-54.
- Batchelor, A.W. and Stachowiak, G.W., (1995) Tribology in Materials Processing, *J. Mat. Proc. Techn.*, **48**, 503-515.
- Bay, N. and Wanheim, T., (1976) Real Area of Contact and Friction Stress at High Pressure Sliding Contact, *Wear*, **38**, 201-209.
- Bay, N., (1987) Friction Stress and Normal Stress in Bulk Metal-Forming Processes, *J. Mech. Working Techn.*, **14**, 203-223.
- Booser, E. R., (1997) *Tribology Data Handbook*, (CRC Press, Boca Raton, Florida).
- Bowden, F.P. and Tabor, D., (1950) *The Friction and Lubrication of Solids*, (Clarendon Press, Oxford).
- Bowden, F.P. and Tabor, D., (1973) *Friction - An Introduction to Tribology*, (Heinemann Educational Books Ltd., London).
- Briant, J., Denis, J. and Parc, G., (1989) *Rheological Properties of Lubricants*, (Éditions Technip, Paris).
- Gavrus, A., Massoni, E. and Chenot, J.L., (1996) An Inverse Analysis Using a Finite Element Model for Identification of Rheological Parameters, *Proc. Metal Forming '96*, ed. Pietrzyk, M., Kusiak, J., Hartley, P. and Pillinger, I., *J. Mat. Proc. Techn.*, **60**, 447-454.
- Gelin, J.C. and Ghouati, O., (1994) The Inverse Method for Determining Viscoplastic Properties of Aluminium Alloys, ed. Hartley, P., Pillinger, I., Sturgess, C.E.N., Hall, R., Pietrzyk, M. and Kusiak, J., *Proc. Metal Forming '94*, Birmingham, *J. Mat. Proc. Techn.*, **34**, 435-440.
- Gelin, J.C. and Ghouati, O., (1995) Inverse Identification Methods for Material Parameters Estimation in Large Plastic Deformations, *Proc. COMPLAS 4*, ed. Owen, D.R.J., Onate, E. and Hinton, E., (Pineridge Press, Barcelona), 767-778.
- Heshmat, H., Godet M. and Berthier, Y., (1995) On the Role and Mechanism of Dry Triboparticulate Lubrication, *Lubrication Engineering*, **51**, 557-564.
- Hoffman, O. and Sach, G., (1953) *Introduction to the Theory of Plasticity for Engineers*, (McGraw-Hill. Inc.), New York.
- Hum, B, Colquhoun, H.W. and Lenard, J.G. (1996) Measurements of friction during hot rolling of

- aluminum strips, *J. Mat. Proc. Techn.*, **60**, 331-338.
- Hutchings, I.M., (1992) *Tribology: friction and wear of engineering materials*, (CRC Press, Boca Raton).
- Jeswiet, J., (1991), A Friction Sensor for Sheet Metal Rolling, *Annals of the CIRP*, **40**, 231-234.
- Karagiozis, A.N. and Lenard, J.G., (1985) The Effect of Material Properties on the Coefficient of Friction in Cold Rolling, *Proc. Eurotrib'95*, Lyon, 1-7.
- Khoddam, S., Lam, Y.C. and Thomson, P.F., (1996) Numerical Results Achieved with an Inverse Computational Method for Determining the Constitutive Parameters using the Hot Torsion Test Results, *steel research*, **67**, 39-43.
- Kusiak, J., Pietrzyk, M. and Lenard, J.G., (1995), Application of FE Simulation of the Compression Test to the Evaluation of Constitutive Equations for Steels at Elevated Temperatures, *Proc. NUMIFORM'95*, ed. Shen, S.F. and Dawson, P.R., Ithaca, 277-282.
- Lenard, J.G., (1990) An Experimental Study of Boundary Conditions in Hot and Cold Flat Rolling, *Annals of the CIRP*, **39**, 279-282.
- Lenard, J.G., (1991), Measurements of Friction in Cold Flat Rolling, *J. Mater. Shaping Technol.*, **9**, 171-180.
- Lenard, J.G. and Zhang, S., (1997) A Study of Friction During Lubricated Cold Rolling of an Aluminum Alloy, *J. Mat. Proc. Techn.*, **72**, 293-301.
- Lenard, J.G., (1998) The effect of lubricant additives on the coefficient of friction in cold rolling, *J. Mat. Proc. Techn.*, **80-81**, 232-238.
- Lenard, J.G., (2001) Friction During Flat Rolling of Metals", *Int. J. Forming Processes*, **4**, 23-42.
- Lenard J.G. and Z. Malinowski, (1993), Measurements of Friction During Warm Rolling of Aluminium, *J. Mat. Proc. Techn.*, **39**, 357-371.
- Lenard, J.G., Pietrzyk, M. and Cser, L., (1999), *Mathematical and Physical Simulation of the Properties of Hot Rolled Products*, (Elsevier, Oxford).
- Lim, Lai-Seng and Lenard, J.G., (1984) Study of Friction in Cold Strip Rolling, *ASME, J. Eng. Mat. Techn.*, **106**, 139-146.
- Lin, J.F., Huang, T.K. and Hsu, T.C., (1991), Evaluation of Lubricants for Cold Strip Rolling, *Wear*, **147**, 79-91.
- Liu, G., Wang, Q. and Lin, C., (1999) A Survey of Current Models for Simulating the Contact between Rough Surfaces, *Trib. Trans.*, **42**, 581-591.
- Male, A.T. and Cockroft, M.G., (1964) A Method for Determination of the Coefficient of Friction of Metals Under Conditions of Bulk Plastic Deformation, *Journal of the Institute of Metals*, **93**, 38-46.
- Male, A.T. and DePierre, V., (1970) The Validity of Mathematical Solutions for Determining Friction from the Ring Compression Test, *ASME, J. Lub. Techn.*, **92**, 389-397.
- Malinowski, Z., Kusiak, J. and Pietrzyk, M., (1995) Application of the Inverse Techniques to the Experimental Tests, *Proc. Conf. Application of Mathematical Methods in Science and Technique*, Krakow, Vol. 2, 43-52.
- McConnell, C. and Lenard, J.G., (2000) Friction in cold rolling of a low carbon steel with lubricants, *J. Mat. Proc. Techn.*, **99**, 86-93.
- Mortier, R.M., and Orszulik, S.T., (1992) *Chemistry and Technology of Lubricants*, (Blackie and Sons, Glasgow).

- Mróz, Z. and Stupkiewicz, S., (1998) Constitutive Model of Adhesive and Ploughing Friction in Metal-Forming Processes, *Int. J. Mech. Sci.*, **40**, 281-303.
- Munther, P. and Lenard, J.G. (1995), Tribology During Hot Flat Rolling of Steels, *Annals of the CIRP*, **44**, 213-216.
- Pietrzyk, M. and Lenard, J.G., (1991) *Thermal-Mechanical Modelling of the Flat Rolling Process*, (Springer-Verlag, Heidelberg)
- Rabinowicz, E., (1995) *Friction and Wear of Materials*, 2<sup>nd</sup> ed., (John Wiley and Sons, Inc., New York).
- Reid, J. V. and Schey, J.A., (1977) Full Fluid Film Lubrication in Aluminum Strip Rolling<sup>6</sup>, *ASLE Trans.*, **21**, 191-200.
- Roberts, W.L., (1967) Computing the Coefficient of Friction in the Roll Bite from Mill Data, *Blast Furnace and Steel Plant*, 499-508.
- Roberts, W.L., (1983) *Hot Rolling of Steel*, (Marcel Dekker, Inc., New York).
- Roberts, C.D., (1997) Mechanical Principles of Rolling, *Iron and Steelmaker*, **24**, 113-114.
- Rowe, G.W., (1977) *Principles of Industrial Metalworking Processes*, (Edward Arnold, London).
- Roychoudhury, R. and Lenard, J.G., (1984) A Mathematical Model for Cold Rolling – Experimental Substantiation, *Proc. 1<sup>st</sup> Int. Conf. Techn. Plast.*, Tokyo, 1138-1145.
- Sa, C-Y. and Wilson, W.R.D., (1994) Full Film Lubrication of Strip Rolling, *ASME, J. Trib.*, **116**, 569-576.
- Schey, J.A., (1983) *Tribology in Metalworking*, (ASM, Metals Park, Ohio).
- Schey, J.A., (1987), *Introduction to Manufacturing Processes*, (McGraw Hill Inc., New York).
- Shida, S., (1974) Effect of Carbon Content, Temperature and Strain Rate on Compressive Flow Stress of Carbon Steel, *Hitachi Res. Lab. Report*, 1-9.
- Shirizly, A. and Lenard, J.G., (2000) Emulsions versus neat oils in the cold rolling of carbon steel strips, *ASME J. Trib.*, **122**, 550-556.
- Siebel, E., and Lueg, W., (1933) Investigations Into The Distribution Of Pressure At The Surface Of The Material In Contact With The Rolls, *Mitt. K.W. Inst. Eisenf.*, **15**, 1-14.
- So, B.Y.C. and Klaus, E.E., (1980) Viscosity-Pressure Correlation of Liquids, *ASLE Transactions*, **23**, 409-421.
- Stephenson, D.A., (1983) Friction in Cold Strip Rolling, *Wear*, **92**, 293-311
- Sutcliffe, M.P.F., (1999) Flattening of Random Rough Surfaces in Metal-Forming Processes, *ASME, J. Trib.*, **121**, 433-440.
- Szyndler, D., Pietrzyk, M., Lenard, J.G. and Fyke, S.H., (2000) Inverse Analysis applied to the Evaluation of Friction and Rheological Parameters in Hot Forming of Steels, *Metal Forming 2000*, ed. Pietrzyk, M., Kusiak, J., Majta, J., Hartley, P. and Pillinger, I., (Balkema), 101-106.
- Underwood, L.R., (1950) *The Rolling of Metals*, (John Wiley & Sons, Inc., New York).
- van Rooyen, G.T. and Backofen, W.A., (1960) A Study of Interface Friction in Plastic Compression, *Int. J. Mech. Sci.*, 1-27.
- Wanheim, T., (1973) Friction at High Normal Pressures, *Wear*, **25**, 225-244.



- Wanheim, T., Bay, N. and Petersen, A.S., (1974) A Theoretically Determined Model for Friction in Metal Working Processes, *Wear*, **28**, 251-258.
- Wanheim, T. and Bay, N., (1978) A Model for Friction in Metal Forming Processes, *Annals of the CIRP*, **27**, 189-194.
- West, R.C. (ed), (1976-77) *Handbook of Chemistry and Physics*, 57<sup>th</sup> edition, (CRC Press, Cleveland).
- Wilson, W.R.D. and Walowit, J.A., (1971) An Isothermal Hydrodynamic Lubrication Theory for Strip Rolling with Front and Back Tension, *Proc. Tribology Convention*, (I.Mech.E., London), 169-172.
- Wu, C.S., Klaus E.E. and Duda, J.L., (1989) Development of a Method for the Prediction of Pressure-Viscosity Coefficients of Lubricating Oils Based on free-Volume Theory, *ASME, J. Trib.*, **111**, 121-128.
- Wusatowski, Z., (1969) *Fundamentals of Rolling*, (Pergamon Press, Oxford).
- Yamamoto, H. and Uehori, Y., (1989) Analyses of Friction Coefficients and Lubrication Control in Cold Rolling of Metal Strip, *Proc. Eurotrib 85*, 464-469.
- Yoneyama, T. and Hatamura, Y., (1987) The Development of a Die Sensor, *JSME International*, **30**, 670-677.
- Yoneyama, T. and Hatamura, Y., (1989) Measurement of Actual Stress and Temperature on the Roll Surface During Rolling, *JSME International*, **32**, 113-117.
- Yuen, W.Y.D., Popelianski, Y. and Prouten, M., (1996) Variations of friction in the Roll Bite and Their Effects on Cold Strip Rolling, *Iron and Steelmaker*, **23**, 33-39.

## Chapter 7

# Studies on Micro Plasto Hydrodynamic Lubrication in Metal Forming

NIELS BAY, JAKOB I. BECH, JAN L. ANDREASEN  
*Department of Manufacturing Engineering and Management*  
*Technical University of Denmark*  
*Building 425*  
*Dk-2800 Lyngby*  
*Denmark*  
ICHIRO SHIMIZU  
*The Graduate School of Natural Science and Technology*  
*Okayama University*  
*3-1-1 Tsushima-naka*  
*700-8530 Okayama*  
*Japan*

### 7.1 INTRODUCTION

The influence of work piece surface topography on friction and lubrication and final surface quality in metal forming operations is well known and has been pointed out by many researchers, see Schey (1983) and Bay and Wanheim (1990). This is especially the case when liquid lubrication is applied, where increased surface roughness facilitates the lubricant intake and mechanical entrapment. The potential of these mechanisms is, however, not fully utilized due to lack of understanding of the influence of individual parameters on the tribological system. In recently developed surface characterization models the potential entrapment of a lubricant in closed reservoirs is used as a parameter to predetermine the formability of a sheet metal, Steinhoff et al. (1996), Geiger et al. (1997) and Schmoeckel et al. (1997).

In experimental studies on friction in metal forming applying the strip drawing test, Kudo et al. (1976 and 1982) discovered that the friction stress increased with the product of lubricant viscosity and drawing speed in the mixed lubrication regime. Mizuno and Okamoto (1982) noticed the same phenomenon in compression-sliding experiments, and proposed the explanation to be trapping of lubricant in closed pockets in the surface and subsequent permeation of the viscous lubricant into areas of contact between the flattened work piece asperities and the tool surface. They named this

lubrication mechanism MicroPlasto HydroDynamic Lubrication (MPHDL). In studies of plane strip drawing of aluminum strips provided with artificial lubricant pockets by local indentation Azushima and Kudo et al. (1990, 1991, 1995) verified this mechanism applying a transparent die. They showed that lubricant escape from the pockets was influenced by the degree of reduction, drawing speed and lubricant viscosity.

The pioneering work on MPHDL by Kudo and Azushima and Mizuno and Okamoto has inspired the present authors to further research in this field carrying out experimental studies continuing and elaborating the work by Azushima and Kudo by showing the influence of work piece material, friction and pocket geometry and establishing a mathematical model predicting the onset of lubricant escape. The present paper presents an overview of these studies on MPHDL in metal forming carried out at the Technical University of Denmark.

## 7.2 EXPERIMENTAL INVESTIGATION

### 7.2.1 Equipment and basic procedures

In an initial work by Bech et al. (1998, 1999) the experimental equipment was established and a first parametric study was carried out investigating the influence of materials and process parameters in sheet drawing on MPHDL. Figure 7.1 shows the equipment developed for plane strip drawing through a wedge shaped die where the tool/work piece interface may be observed and video-filmed with a CCD-camera through a transparent die. The lower, wedge shaped die was made of hardened cold work steel. As work piece material different types of 140×20×2 mm aluminium strips were applied, all provided with lubricant pockets of pyramidal shape. The side angle of the pyramids was app. 10°; the base was 1×1 mm. The pockets were placed in rows of four across the strip with a distance between the rows large enough to ensure that only one row at a time were present in the deformation zone.

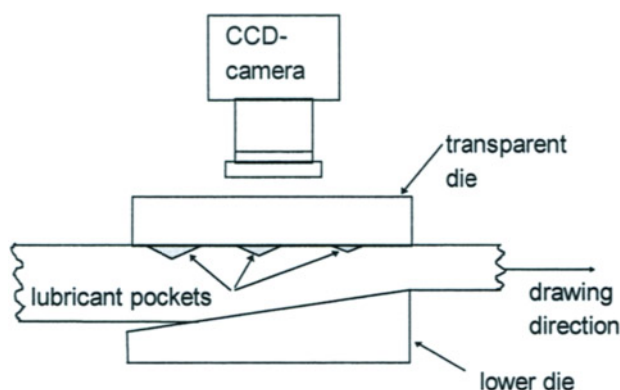























Figure 7.1 Schematic outline of experimental equipment

Figure 7.2 shows an overview of the experimental investigation. Seven different parameters are analyzed. For each parameter a reference value, marked with a **REF**, as well as two other values are investigated keeping the six other parameters as the

*STUDIES ON MICRO PLASTO HYDRODYNAMIC LUBRICATION IN METAL FORMING*

lubricant viscosity	 $\eta = \text{cSt}$ <b>A1</b>	 $\eta = 126 \text{ cSt}$ <b>B1</b> <b>REF</b>	 $\eta = 700 \text{ cSt}$ <b>C1</b>
drawing speed	 $u = 0.2 \text{ mm/sec}$ <b>A2</b>	 $u = 0.5 \text{ mm/sec}$ <b>B2</b> <b>REF</b>	 $u = 5 \text{ mm/sec}$ <b>C2</b>
reduction	 $r = 0.10$ <b>A3</b>	 $r = 0.15$ <b>B3</b>	 $r = 0.20$ <b>C3</b> <b>REF</b>
die angle	 $\alpha = 2^\circ$ <b>A4</b>	 $\alpha = 3^\circ$ <b>B4</b> <b>REF</b>	 $\alpha = 5^\circ$ <b>C4</b>
back tension	 $\sigma_b = 0 \text{ MPa}$ <b>A5</b> <b>REF</b>	 $\sigma_b = 62 \text{ Mpa}$ <b>B5</b>	 $\sigma_b = 105 \text{ MPa}$ <b>C5</b>
work piece material strain hardening exponent	 $n = 0.08$ <b>A6</b> <b>REF</b>	 $n = 0.16$ <b>B6</b>	 $n = 0.21$ <b>C6</b>
friction	 $\mu = 0.025$ <b>A7</b> <b>REF</b>	 $\mu = 0.05$ <b>B7</b>	 $\mu = 0.28$ <b>C7</b>

**Figure 7.2** Overview of experimental investigation of lubricant escape

reference value. Each parameter combination has a specific code combining a letter, A, B or C, indicating the column and a number, 1, 2, ...7, indicating the row.

### 7.2.2 Lubricant imprints on deformed strips

The video recordings showed that the lubricant escapes from the pockets to the surrounding plateaux during deformation. After deformation, imprints of significantly increased roughness are visible in areas where a lubricant film has caused separation between the tool and work piece surface compared to areas where the two surfaces are in direct contact. The imprints were observed in stereomicroscope after deformation. They are shown in Figure 7.2. The strip drawing direction is from the left to the right. The lubricant may escape either backward, i.e. opposite to the direction of strip drawing, or forward, or both. The backward escape is identified as MicroPlasto HydroDynamic Lubrication (MPHDL) caused by viscous forces due to the relative sliding speed between strip and tool surface. Distinguished from this the forward escape is here interpreted as MicroPlasto HydroStatic Lubrication (MPHSL) occurring when the hydrostatic pressure in the trapped lubricant exceeds the tool/work piece interface pressure on the surrounding plateau.

Measurements of roughness profiles around pockets after drawing confirm the visual observations. Figure 7.3 shows increased roughness (a): behind the lubricant pocket, when hydrodynamic lubricant escape has occurred, and (b): in front of the pocket when hydrostatic lubricant escape has taken place.

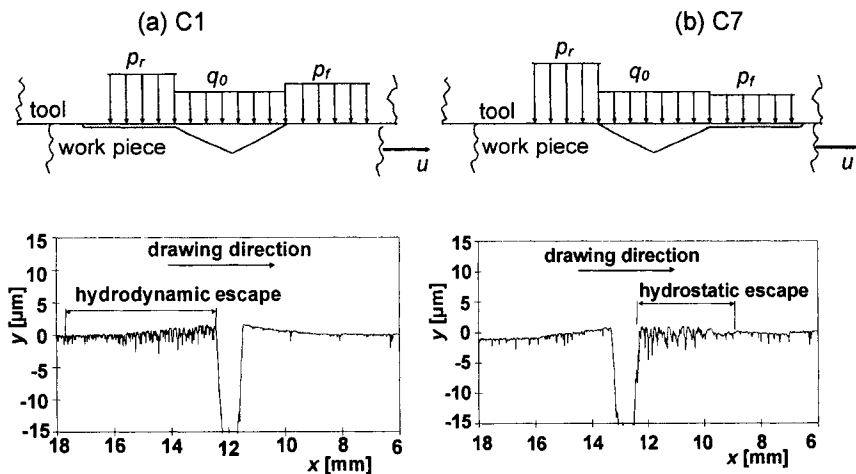


Figure 7.3 Principles of lubricant escape and roughness profiles around pockets, (a) C1-MPHDL, (b) C7-MPHSL. The codes C1 and C7 refer to the parameter combinations shown in Figure 7.2.

### 7.2.3 Influence of materials and process parameters on lubricant escape

The influence of each parameter on the lubricant escape is shown in Figure 7.2 and discussed below.

**Viscosity of lubricant:** Figure 7.2 shows a significant influence of viscosity on the mechanisms of lubrication. Low viscosity results in pure MPHSL (A1); the high

viscosity oil results in pure MPHDL (C1), whereas both lubrication mechanisms are active in case of medium viscosity (B1).

**Drawing speed:** As to be expected an increased tendency to MPHDL film formation is noticed with increasing speed in the same way as by increasing viscosity.

**Degree of reduction:** In the three cases,  $r = 10\%$ ,  $15\%$  and  $20\%$ , pressure gradient, lubricant, material, and drawing speed are the same, the only difference being the termination of reduction. Since the escape of lubricant has occurred before the reduction reaches  $10\%$ , only minor quantitative differences are observed.

**Die angle:** Increasing die angle results in steeper decrease of pressure  $dp/dx$  towards the exit and thus increasing tendency to MPHSL as seen in Figure 7.2 (experiments A4, B4 and C4).

**Back tension:** Increasing back tension is noticed to cause less MPHDL film formation and larger MPHS film. Larger back tension implies a lower die pressure level and less liquid pressure in the trapped lubricant. As viscosity increases exponentially with pressure, lower normal pressure implies lower viscosity and thus less hydrodynamic film formation.

**Work piece material:** Al 57S aluminum alloy was used as the reference work piece material. The two other materials were annealed and semi hard Al 99.5. The stress-strain curves of the three materials were:

$$\sigma_{\text{alloy}} = 321 \times \varepsilon^{0.08}, \quad \sigma_{\text{Al, 99.5, Semi hard}} = 128 \times \varepsilon^{0.16} \quad \sigma_{\text{Al, 99.5, annealed}} = 120 \times \varepsilon^{0.21} \quad [\text{MPa}]$$

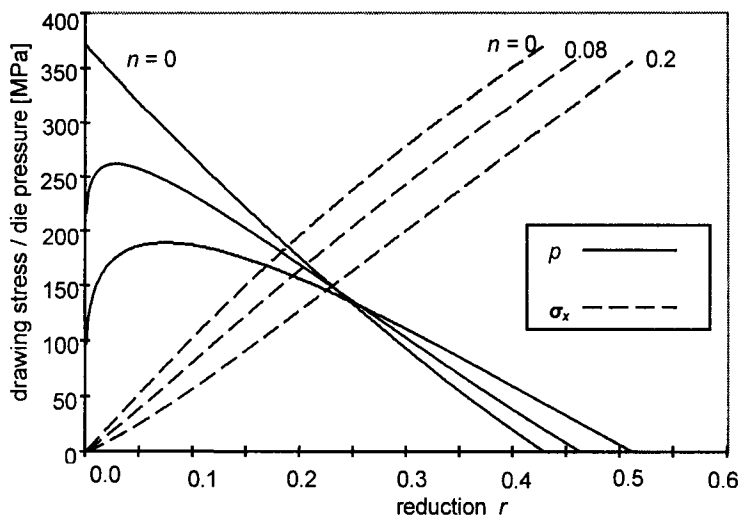


**Figure 7.4** Pressure distribution and drawing stress as a function of reduction with strain hardening as a parameter

Comparing the two experiments with Al 99.5 (B6 and C6) it is noticed that increasing strain hardening exponent results in increased tendency to MPHDL and decreased MPHS film formation. This is due to a more flat pressure distribution with a smaller pressure gradient limiting forward lubricant escape thus increasing the possibility of backward lubricant escape (MPHDL) instead. Figure 7.4 illustrates this showing the influence of the strain hardening exponent on the pressure distribution determined by a slab method of analysis (Bech et al. 1998). In case of annealed material (C6) micro channels are formed by grain reorientation during deformation facilitating lubricant escape.

**Friction:** Friction is varied on the lower steel tool side of the strip. Larger friction results in a larger pressure gradient increasing the tendency to MPHSL. The experiment with high friction, C7, confirms this showing only forward escape of lubricant. Medium friction, B7, results in a balanced ratio between MPHSL and MPHDL, whereas the experiment with low friction, REF, has a less pronounced MPHS film formation.

Summarising the above observations it may be concluded that the influence of the different parameters on the mechanisms of lubricant escape can be qualitatively explained.

#### 7.2.4 Influence of pocket geometry on lubricant escape

The influence of pocket geometry on MPHDL and MPHSL were studied by Soerensen et al. (1999) and Shimizu et al. (2001) investigating the volume, shape, slope of the side to the edge and radius of curvature on the edge of the lubricant pockets.

The lower die angle was 3°, the reduction 20% and the drawing speed 2 mm/s. As lubricants two base oils were selected with the same pressure-viscosity index but with different viscosity (125 cSt and 475 cSt at 40°C respectively) in order to promote either the MPHS or MPHD lubrication mechanism.

As work piece material AlMg2.5 (DIN 1725) aluminum strips (500×20×2 mm) were applied. They were provided with macroscopic lubricant pockets, which had a base area of approximately 1×1 mm. The pockets were made by coining in a pattern similar to the one adopted in the earlier experiments.

Pockets of pyramidal and flat-bottomed pyramidal shape were applied to the work piece strips by coining. Besides these pocket geometries a flat-bottomed circular pocket shape was examined. These pockets were made by excimer laser ablation in a collaborative work at the University of Erlangen, Soerensen et al. (1999). The experimental plan involved nine different lubricant pockets, three different geometries, each of three different volumes (small =  $V_1$ , medium =  $V_2$  and large =  $V_3$ ). The actual volume of each pocket was measured using a 3-dimensional optical measuring device (UBM Microfocus 1080) and the software SAM (Surface Analysis Module (Geiger et al. 1997)). Also the actual angle to the edge of each pocket is determined prior to drawing using a 2-dimensional stylus instrument (RTH 5-120).

**7.2.4.1 Hydrostatic pressure increase.** When the rear edge of the lubricant pocket enters the deformation zone, the pocket is sealed, and the lubricant is trapped. By compression of the lubricant the volume of the pocket is reduced, and the hydrostatic pressure is increasing due to the plastic deformation of the surrounding material. This is the first, and perhaps the most important state of the lubrication mechanism leading to the later

escape as the final state. Experimental data on the lubricant properties gives the relation between relative density and pressure (Anon. 1953).

In order to examine the decrease in volume of one pocket during deformation and thus the hydrostatic pressure increase, three strips with pyramidal lubricant pockets were drawn and the process was stopped at three different steps of reduction. Three-dimensional surface measurements were conducted and the volumes were evaluated using SAM. Volumes of a pocket before deformation and a pocket in the fully reduced strip at 20% reduction were measured too. Assuming that the pyramidal indentations maintain their geometrical shape, while the size is reduced, the ratio between the initial volume at zero pressure,  $V_0$ , and the actual volume,  $V$ , can be calculated as a function of the initial and actual base-areas of the pockets;  $V_0/V = (A_0/A)^{3/2}$ . The base-area of the pockets were measured at the given reductions using the image processing technique. The result is illustrated in Figure 7.5 where the obtained volume and area are plotted as functions of the reduction.

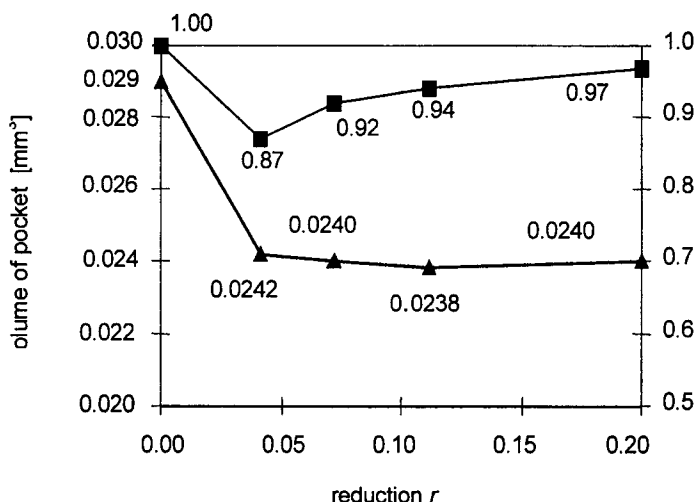


Figure 7.5 Pocket volume and area change versus the reduction during a strip drawing test.

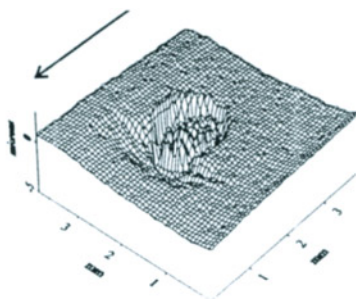
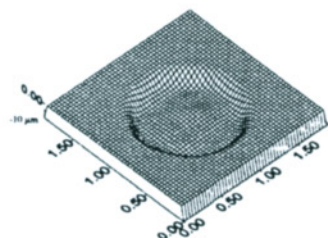
It is seen that the volume/area decrease occurs in the very beginning of the process. The volume measurements show a decrease ( $V_0/V = 1.20$ ) after a reduction of approximately 4% and only a slight decrease occurring hereafter. The corresponding area decrease is measured as  $A_0/A = 1.15$ , implying a calculated volume decrease  $(A_0/A)^{3/2} = 1.23$ . Based on these results it is found that the assumed relation between area and volume is valid in the beginning of the process. Hereafter, the obtained hydrostatic pressure suppresses further reduction of the pocket volume. The area, on the other hand, increases again after a reduction of approximately 4%. This is due to the deformation in the strip drawing where the surface is stretched and consequently the pocket becomes less deep.

**7.2.4.2 Influence of pocket volume.** For the flat-bottomed circular pockets, made by excimer laser ablation, the volumes were measured as:  $V_1 = 0.012 \text{ mm}^3$ ,  $V_2 = 0.025 \text{ mm}^3$  and  $V_3 = 0.036 \text{ mm}^3$ , and the angle to the edges are found to be:  $\nu_1 = 15^\circ$ ,  $\nu_2 = 27^\circ$  and  $\nu_3 = 27^\circ$ . These angles were too steep to promote the MPHDL mechanism and therefore

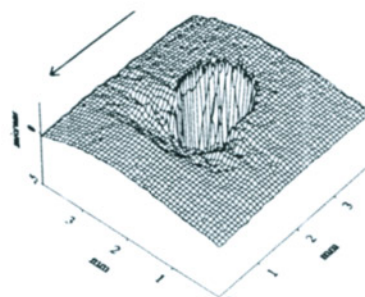
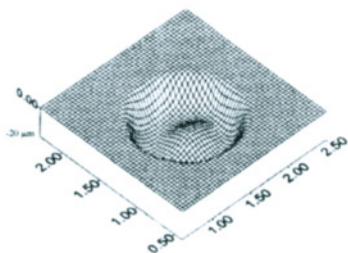


these pockets were used to evaluate the MPHSL mechanism. Nelleman et al. (1977) showed that the angle is of minor importance to the hydrostatic pressure increase. To

$$V_1 = 0.012 \text{ mm}^3$$



$$V_2 = 0.025 \text{ mm}^3$$



$$V_3 = 0.035 \text{ mm}^3$$

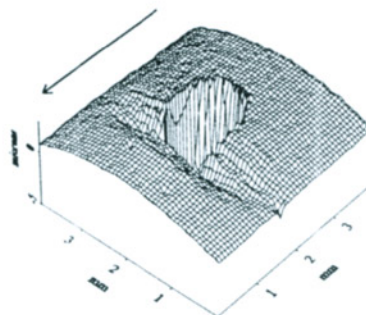
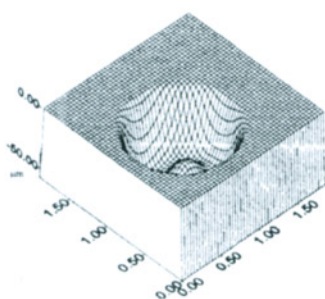


**Figure 7.6** Circular pockets from where the MPHS lubrication mechanism was active. The difference in emerged lubricant can be detected at the front edge of the pocket. Displayed area: 4x4 mm.

promote the MPHSL mechanism high friction was ensured by establishing pick-up on the lower die ( $\mu \approx 0.17$ ). On the transparent upper die a low viscosity lubricant (125 cSt)

were applied ( $\mu \approx 0.05$ ). The larger friction on the lower die results in a larger pressure gradient increasing the tendency to MPHSL.

In Figure 7.6 three surface topography maps of the lubricant pockets before and after deformation are displayed. A correspondence between the area of emerged lubricant and the initial pocket volume can be detected. It was observed that the onset of the mechanism occurred at a reduction of approximately 16% for all the volumes. This indicates that the generated hydrostatic pressure in the individual pockets were at the same level regardless of the volume.

It is noticed that larger pocket volume results in larger volume of the MPHSL-emerged lubricant pool. This is due to the fact that the pressure decrease in the pocket caused by lubricant escape is a function of the ratio between escape volume and pocket volume. Consequently, a larger pocket volume will result in a larger lubricant escape in case of the same pressure drop, Figure 7.7.

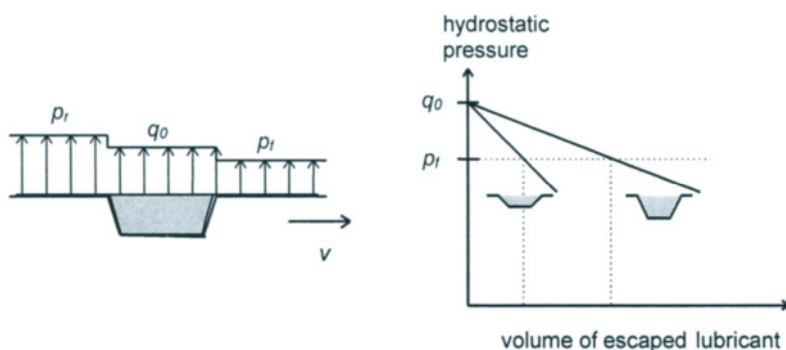


**Figure 7.7** Influence of pocket volume on pressure drop vs. escaped volume

**7.2.4.3 Influence of angle to the edge.** The pyramidal and the flat-bottomed pyramidal lubricant pockets have angles to the edges between  $3.6^\circ$  and  $15.0^\circ$ . These pockets are therefore suitable for examining the MPHDL mechanism. Table 7.1 presents the actual geometries for the coined pockets. A high viscosity lubricant were applied (475 cSt) to promote the MPHDL mechanism.

**Table 7.1** Initial volume and angle to the edge of the pyramidal and flat-bottomed pyramidal lubricant pockets

Shape →	Pyramidal		Flat-bottomed pyramidal	
Volume	Volume	Angle	Volume	Angle
Angle ↓	$[10^{-3} \text{ mm}^3]$	$[^\circ]$	$[10^{-3} \text{ mm}^3]$	$[^\circ]$
$V_1/v_1$	3.7	3.6	6.2	6.4
$V_2/v_2$	5.8	7.5	9.0	11.0
$V_3/v_3$	7.6	11.0	14.0	15.0

In order to evaluate the performance of the lubricant pockets, the area of the emerging lubricant pool as well as the onset of the escape were measured using an image processing technique. In Figure 7.8 the emerged area of lubricant per unit length

of the emerging edge is displayed. An approximately linear relation between the area and the angle to the edge is observed.

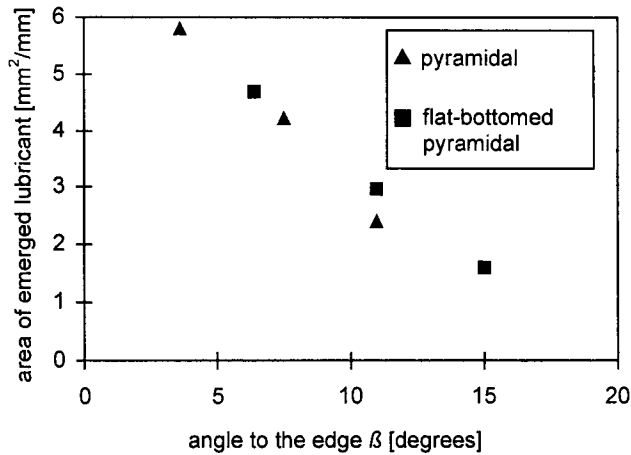


Figure 7.8 Area of emerged lubricant versus angle to the edge

Observing the onset of the MPHDL mechanism as a function of the angle to the edge, Figure 7.9, it is obvious that a connection between these parameters exists. When the angle to the edge is smaller onset of the mechanism is initiated at a lower reduction. The shape of the lubricant pocket (pyramidal or flat-bottomed pyramidal) is seen not to influence the MPHDL mechanism in terms of escaped lubricant pool or the onset of the mechanism.

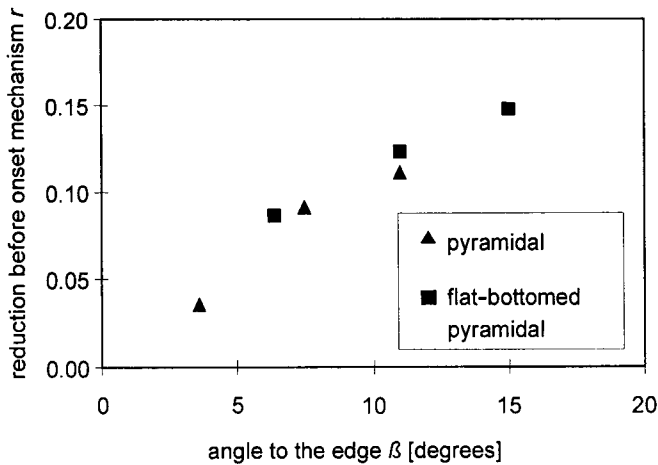
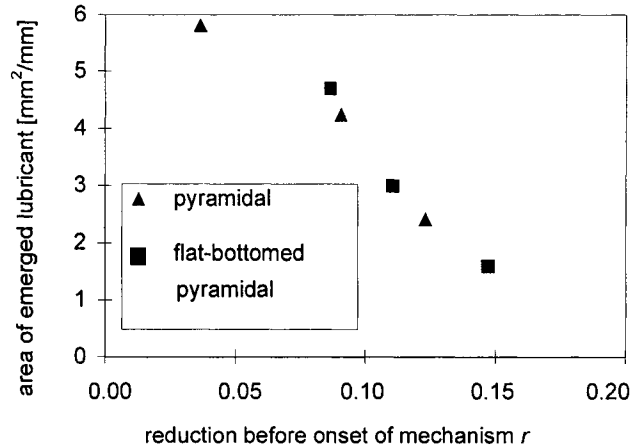


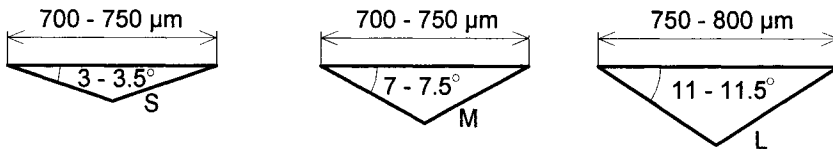
Figure 7.9 Required reduction before onset of the MPHDL mechanism versus the angle to the edge

Figure 7.10 shows a direct comparison between the area of emerged lubricant and the onset of the MPHDL mechanism. This relation indicates, that the onset-reduction, which is a function of the angle to the edge, is decisive for the area of emerged lubricant. Once the outflow is initiated the area of emerged lubricant is thought to be constant. This could be due to the fact that the geometrical conditions at the emerging edge are decisive for the actual initiation of the mechanism, but once the escaping lubricant has deformed the edge and caused micro-roughening, the angle to the edge/radius of curvature is no longer the same. It is thought that the conditions at the edge now are having the same characteristics for all pockets, and thus the outflow is constant regardless of the original shape.



**Figure 7.10** Area of emerged lubricant as a function of the onset-reduction of the MPHDL mechanism

**7.2.4.4 Influence of radius of curvature on the edge.** A dedicated series of experiments were conducted by Shimizu et al. (2001) to investigate the combined influence of angle to the edge and the radius of curvature on the edge of pyramidal lubricant pockets. Work piece material and test conditions were similar to the ones described above in section 7.2.4 but the base area of the pyramidal indentations was somewhat less, app.  $0.75 \times 0.75$  mm. Three types of pyramidal pockets with different angles to the edge as shown in Fig. 7.11 were made by coining. The pockets with angles to the edge  $\beta \approx 3-$



**Figure 7.11** Cross section of small, medium and large size lubricant pockets

$3.5^\circ$ ,  $7-7.5^\circ$  and  $11-11.5^\circ$  are hereafter referred to as S, M and L pockets corresponding to Small, Medium and Large respectively. After coining the pockets, the strip surface was polished with abrasive paper grade #2000 in order to remove the banks surrounding the pocket and obtaining a roughness  $R_a < 0.15 \mu\text{m}$ . The radius of curvature on the edge was controlled by electro polishing with varying polishing time thus obtaining a radius

of curvature in the range of 30-270  $\mu\text{m}$ . The profile of the finished pocket edge was measured by a stylus instrument.

Examples on patterns of lubricant permeation in strip drawing are shown in Figure 7.12. In all examples backward escape of lubricant was observed, while forward escape was only noticed for the pockets without electro polishing. By the direct observation during strip drawing it was noticed that the escape occurred almost simultaneously in

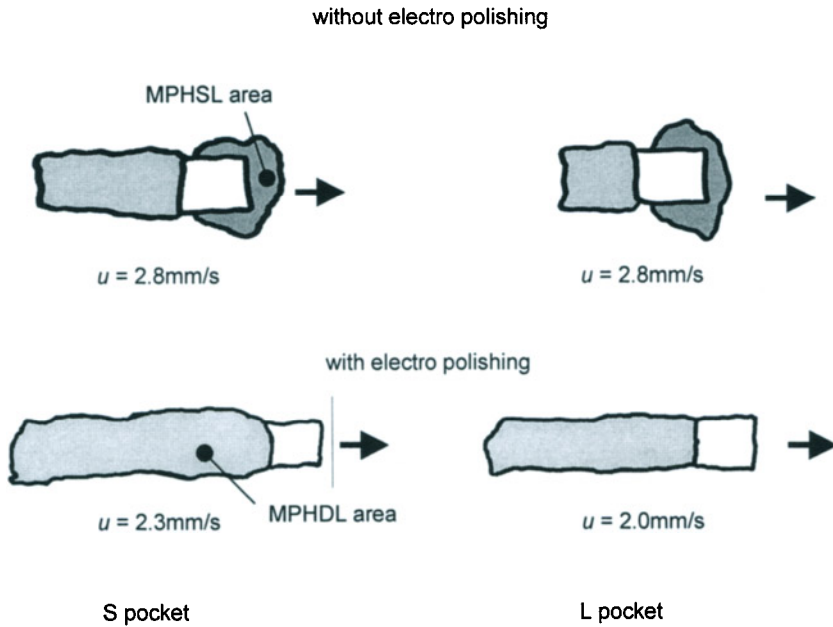


**Figure 7.12** Examples on lubricant permeation for small and large pockets without and with electro polishing

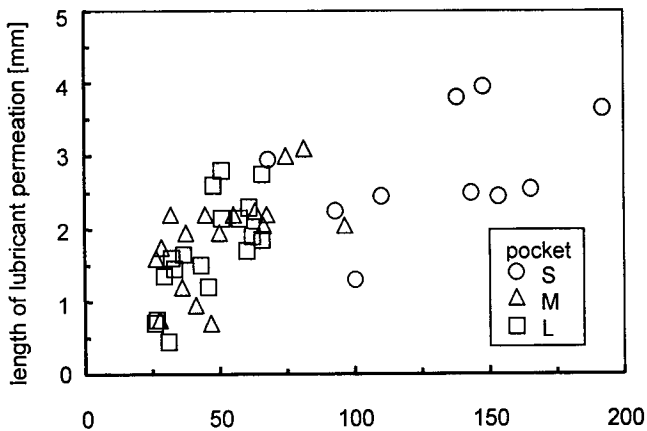


**Figure 7.13** Relationship between length of backward permeation and radius of curvature on pocket edge

backward and forward direction. The backward escape of lubricant, which is caused by MPHDL mechanism, is more conspicuous in case of electro polished pockets. A plot of the relationship between the extent of backward permeation of lubricant (plotted as its length) and the radius of curvature on the rear edge is shown in Figure 7.13. For the same type of pockets the length of backward lubricant permeation increases with the radius of curvature. It is also seen that the length of permeation of S pockets is larger than those of M and L pockets. These results indicate that larger radius of curvature and smaller angle to edge facilitate the MPHDL mechanism.

The change in the onset-reduction of backward escape of lubricant with the radius of curvature on the rear edge is shown in Fig. 7.14. The onset-reduction is determined by the images recorded on the videotape during strip drawing. It is clearly seen that the onset of lubricant escape for L pockets occurs earlier with larger radius of curvature. The onset-reduction in case of S pockets is smaller than that of L pockets and seems to have reached a minimum value almost independent of the radius of curvature. A qualitative understanding of these differences in the onset reduction of lubricant escape between S and L pockets is given in the following.

The shape of the converging gap is very important to the hydrodynamic pressure build-up, which occurs due to the wedge effect when the lubricant is drawn out of the pocket by the relative motion of the surfaces. A long converging gap with "slowly" approaching surfaces creates a higher hydrodynamic pressure build-up. Such a geometry can be obtained either by a small angle to the edge or by a large radius of curvature. At very small angles the pressure is mainly build up along the linear slope of the pocket side, and the size of the radius of curvature is not important. For larger angles to the edge and large radius of curvature the pressure builds up between the radius of curvature and the tool, and the angle to the edge is not important whereas the radius of curvature is. This is in good correspondance with the experimental results shown in Fig. 7.14.

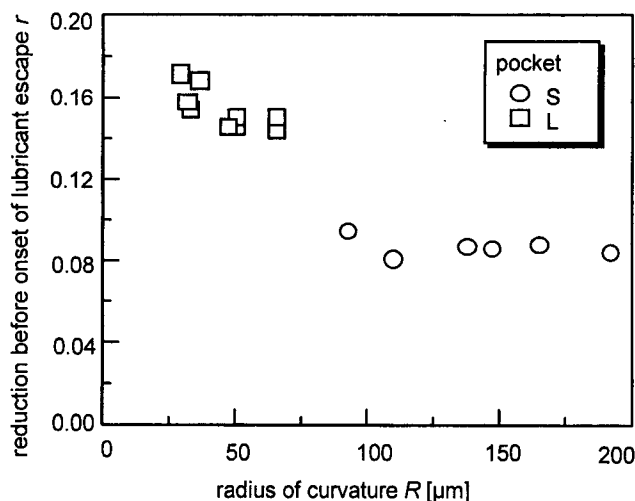


**Figure 7.14** Relationship between onset-reduction for MPHDL and radius of curvature on pocket edge

### 7.3 MATHEMATICAL MODEL OF MICROPLASTO HYDROSTATIC AND HYDRODYNAMIC LUBRICATION

Figure 7.15a and 7.15b (after Azushima et al. 1990) illustrates the pressure distribution in the lubricant pocket causing MPHSL or MPHDL respectively. Figure 7.15a shows the condition for forward escape by MPHSL, which is when the hydrostatic pressure in the pocket exceeds the local die pressure, i.e.  $q_0 > p$ . Figure 7.15b shows the condition for backward escape by MPHDL established, when the sum of the hydrostatic pressure in the pocket and the pressure increase at the rear pocket edge exceeds the local die pressure, i.e.  $q_0 + \Delta q > p$ .

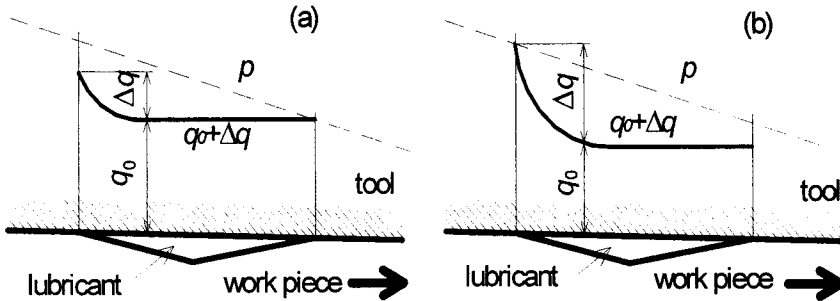


**Figure 7.15** Pressure conditions for lubricant escape. a. Forward escape by MPHSL, b. Backward escape by MPHDL (Azushima et al. 1990)

Bech et al. established a mathematical model of the escape mechanisms by combining an analysis of the die pressure distribution applying the slab method of analysis (see Figure 7.4) and an analysis of the liquid pressure rise  $\Delta q$  due to MPHDL using Reynolds' equation:

$$\frac{dq}{dx} = \frac{d(q_0 + \Delta q)}{dx} = 6\eta u \frac{h - h_m}{h^3} \quad (7.1)$$

where  $q_0$  is the liquid pressure in the pocket remote from the edge,  $\Delta q = \Delta q(x)$  is the local pressure increase at the rear edge due to hydrodynamic effects,  $x$  is the position in the drawing direction,  $h = h(x)$  is the local film thickness and  $h_m$  is the minimum film thickness equal to the average film thickness on the plateau of flattened asperities.  $\eta$  is the absolute viscosity of lubricant, which is expressed as:

$$\eta = \eta_0 \exp\{\lambda(q_0 + \Delta q)\} \quad [\text{Pa s}] \quad (7.2)$$

where  $\eta_0$  is the absolute viscosity at atmospheric pressure and  $\lambda$  is the pressure-viscosity coefficient. When calculating the hydrodynamic pressure the reference values of respective parameters were chosen as follows:

- Angle to edge of pocket:  $\beta = 8.0^\circ$
- Radius of curvature on rear edge:  $R = 80 \mu\text{m}$
- Absolute viscosity at atmospheric pressure:  $\eta_0 = 0.28 \text{ Pa s}$
- Pressure-viscosity coefficient of lubricant:  $\lambda = 2.2 \times 10^{-8} \text{ Pa}^{-1}$
- Drawing speed:  $u = 2.0 \text{ mm/s}$
- Minimum film thickness:  $h_m = 0.2 \mu\text{m}$

To give an estimate of the value of the minimum film thickness  $h_m$  a contact condition is considered where a perfectly smooth tool surface is resting on the highest asperities of the rough work piece surface. Under such conditions  $h_m$  can be correlated to the roughness of the work piece surface in the outflow region. In the present work the arithmetic average roughness  $R_a$  is chosen as a qualified estimate for  $h_m$ .

The variation of the maximum pressure,  $q_0 + \Delta q$ , in the lubricant with the angle to the edge  $\beta$  of the pocket, the radius of curvature  $R$  on the rear edge, the drawing speed  $u$  and the minimum film thickness  $h_m$  is shown in Figure 7.16. For each of the four figures the investigated parameter is varied, while the other parameters are fixed as the reference values. The maximum pressure always appears at the rear pocket edge. It is noticed that smaller angle to the edge and larger drawing speed create higher hydrodynamic pressure thus facilitating MPHDL. When the size of the liquid pressure has reached that of the sealing pressure at the pocket edge, as indicated in Figure 7.15, MPHDL occur.  $\Delta q = p - q_0$  is thus determined as the difference between the local normal pressure  $p$  in the tool/work piece interface caused by plastic deformation of the strip and the liquid pressure  $q_0$  in the pocket. The size of  $\Delta q$  is typically in the range of 5-20 MPa. The high liquid pressure values shown in Figure 7.16, for example in case of very small

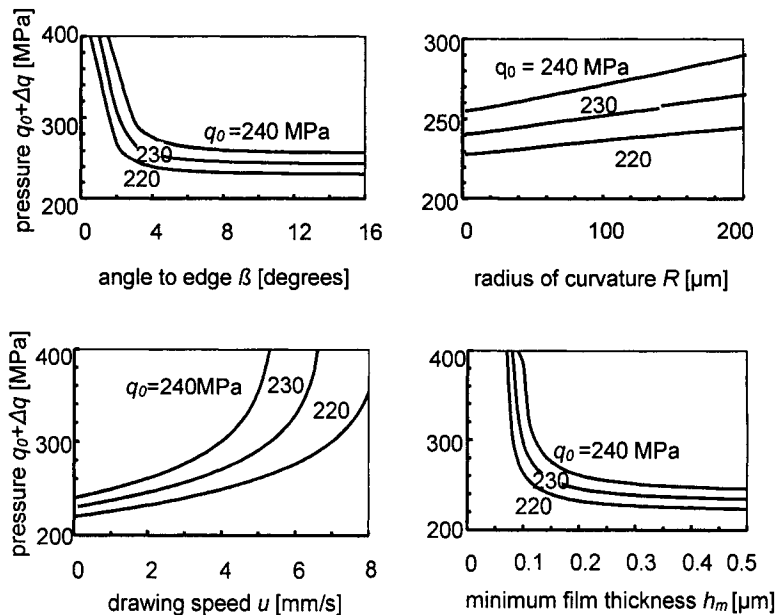


**Figure 7.16** Variation in max. pressure of lubricant,  $q_0 + \Delta q$  with varying angle to the pocket edge  $\beta$ , radius of curvature on edge  $R$ , drawing speed  $u$  and minimum film thickness  $h_m$  for  $q_0 = 220, 230$  and  $240 \text{ MPa}$ .



angles to the edge, are thus not realistic since small angles in practice would not lead to a very high hydrodynamic pressure increase,  $q$ , but instead result in a film thickness larger than the assumed  $0.2 \mu\text{m}$ . In other words, the obtained film thickness is dictated by the applied load (or pressure). The purpose of the illustrations in Figure 7.16 is thus merely to indicate the importance of different parameters. It is seen that increasing radius of curvature to the edge implies increasing pressure. Comparing the four graphs it is, however, noticed that the influence of the radius of curvature on the variation in pressure is moderate compared to the influence of the angle to the edge and the drawing speed.

Using the above-mentioned approach combining an analysis of the die pressure distribution applying the slab method of analysis and an analysis of the liquid pressure rise due to MPHDL using Reynolds' equation the possible onset of lubricant escape has been predicted for varying angles to the edge of the pyramidal and flat-bottomed pyramidal pocket shapes (Soerensen et al. 1999) taking strain hardening of the work piece material and friction in the tool/work piece interface into account. In Figure 7.17 the calculated drawing stress,  $\sigma_x$ , and the die pressure,  $p$ , are shown. The dotted, vertical lines indicate the calculated onset of the MPHDL mechanism. These onset-reductions are determined as described below. The hydrostatic pressure,  $q_0$ , in a pocket is estimated to increase to 218 MPa before the first 4% of reduction. Applying the experiment with  $3.6^\circ$  pocket slope as a reference, the onset of MPHDL in this case is observed to occur at a reduction of 4% in which case the required pressure increase to initiate MPHDL is noticed from Figure 7.17 to be 50 MPa. Assuming a film thickness equal to the  $R_a$ -value  $h_m = 0.32 \mu\text{m}$ , the radius of curvature of the edge required to cause a pressure increase of 50 MPa is calculated by Reynolds' equation to  $R = 20 \mu\text{m}$ . Determination of the onset reductions for MPHDL in case of the other experimentally investigated pocket slopes of  $6.4^\circ$ ,  $7.5^\circ$ ,  $11^\circ$  and  $15^\circ$  are now done by calculating the resulting pressure increase adopting the same parameter values as for the  $3.6^\circ$  pocket slope, i.e.:

- $q_0 = 218 \text{ N/mm}^2$
- $h_m = 0.32 \mu\text{m}$
- $R = 20 \mu\text{m}$

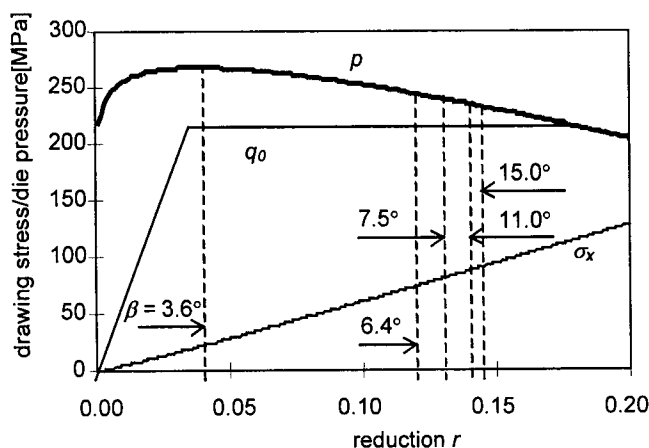
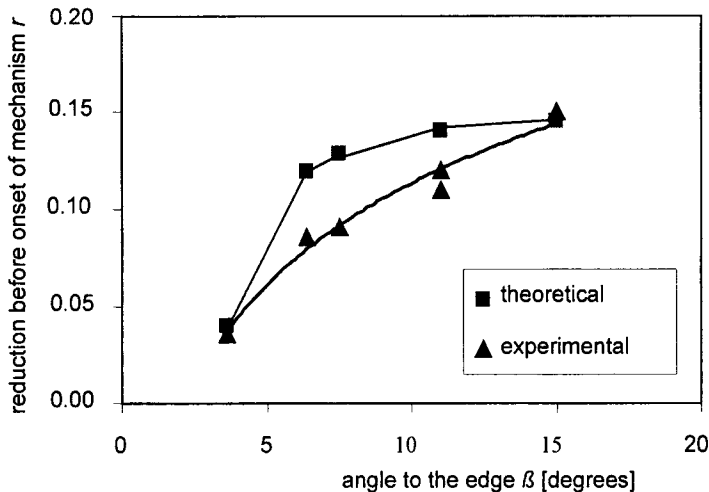


Figure 7.17 Progress in die pressure and drawing stress as the reduction increases. Theoretically determined onset of MPHDL for different angles to the edges.

Using the die pressure distribution curve, the theoretical reductions at which MPHDL is initiated can be derived, see Figure 7.17.

A comparison between the theoretically and experimentally determined onset-reduction for MPHDL is shown in Figure 7.18 indicating remarkably good agreement.



**Figure 7.18** Theoretically and experimentally determined onset-reduction for MPHDL versus the angle to the edge.

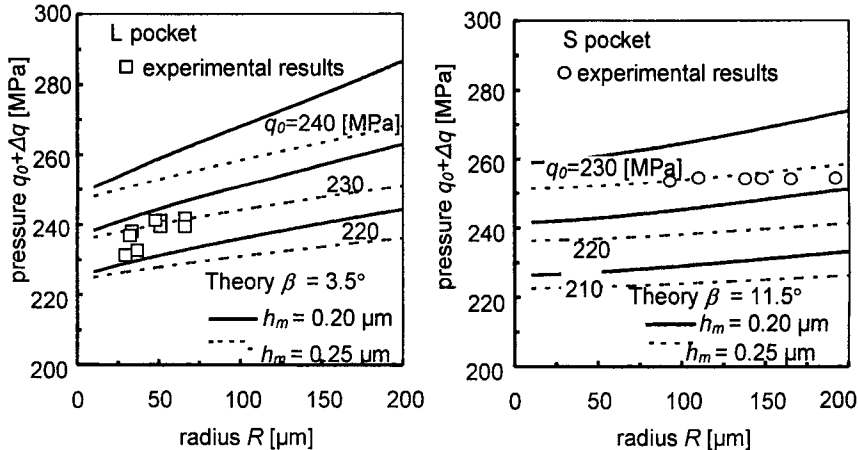


**Figure 7.19** Required liquid pressure for MPHDL versus radius of curvature on pocket edge with hydrostatic pressure, minimum film thickness and pocket size as parameters. Curves correspond to theoretical calculations, marker points to experimental results.

Comparing the experimental results in Figure 7.14 with the calculated die pressure distribution an experimental estimate of the die pressure at the onset of lubricant escape is determined for varying radius of curvature and pocket size (Shimizu et al. 2001). The results are plotted as marker points in Figure 7.19 together with theoretical curves on the liquid pressure causing MPHDL as calculated by Reynolds' equation. The

evaluated pressures based on the experimental results show rather good agreement with the theoretical ones assuming a hydrostatic pressure in the lubricant pocket  $q_0 = 230$  MPa and a minimum film thickness  $h_m = 0.25 \mu\text{m}$ . In previous work, by Bech et al. (1998) and Soerensen et al. (1999), using the same material and lubricant, the hydrostatic pressure  $q_0 = 230$  MPa of the trapped lubricant was determined by measuring the decreasing area of the pockets and calculating the volume reduction. During the first few percent of reduction the volume is reduced to about 90% corresponding to a pressure increase to about 230-250 MPa. In Bech et al. (1998) this pressure increase was confirmed by estimation of  $q_0$  from observations of the onset point for hydrostatic escape and correlating it to  $p$  calculated by the slab method of analysis.

In order to improve the model a theoretical calculation of the hydrostatic pressure in the pocket should be developed. Lo and Wilson (1999) have developed a theoretical model calculating the hydrostatic pressure in the trapped lubricant by an upper bound analysis. Another approach based on a plastic FEM analysis of the strip drawing process is under development by the principal author, Shimizu (1999). Furthermore, a direct experimental determination of the film thickness would improve the mathematical model of micro lubrication mechanisms.

Measurements of the drawing force during strip drawing shows that the drawing force oscillates with a frequency corresponding to the distance between the rows of lubricant pockets and a maximum variation (peak to peak) of up to 12% of the total drawing force. In order to study this phenomenon it was decided directly to combine the observations of pocket position and lubricant escape on video with the size of the force. For this purpose a tone generator was developed transforming the force transducer signal to an audible tone with a frequency proportional to the size of the force. Observing the video-film with this technique it was obvious to see the connection between the size of the force and the observed lubricant escape from the pockets. The force was largest when no pockets were present in the die contact and it did not drop significantly when a row of pockets entered the die contact. Only when lubricant escape occurred by MPHSL or MPHDL or both, a significant drop in drawing force was observed, the force reaching a minimum value when the oil film had reached its maximum distribution which appeared to be just before the pockets were leaving the die.

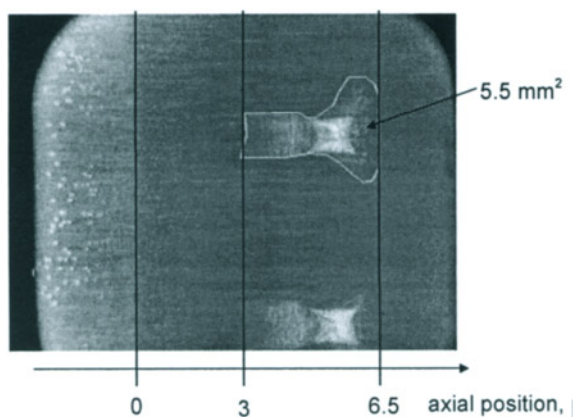
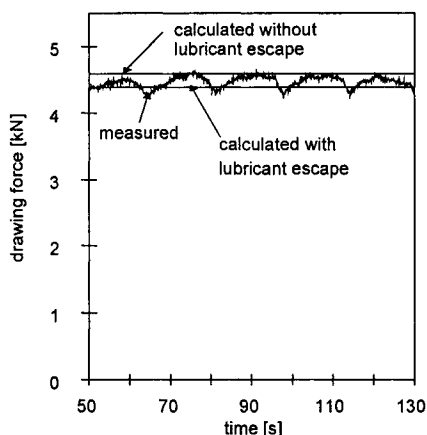


Figure 7.20 Micrograph from video showing the situation where minimum force appears.

Figure 7.20 shows a micrograph taken from the video-film of experiment B7 when the force had reached its minimum value. Figure 7.21 shows the recorded force oscillations in the same experiment. Applying the developed slab analysis for calculation of the drawing force taking into account the differential friction conditions in this case assuming zero friction in the die area provided with escaped lubricant (marked in Figure 7.20) the minimum drawing force was determined as indicated in Figure 7.21. The maximum force was calculated assuming no lubricant escape. It is seen that the calculated force variation corresponds well with the measured thus supporting the assumption that the escaping lubricant film ensures complete separation between the strip and the die surface. Similar calculations for other of the experimental conditions confirm the assumptions, Bech (1997).



**Figure 7.21** Experimentally measured force oscillations during strip drawing with lubricant pockets and corresponding calculation of maximum and minimum force.

#### 7.4 CONCLUSIONS

The microscopic lubrication mechanisms induced by trapped lubricant in pockets of the work piece surface have been studied in strip drawing applying a transparent die and providing the work piece with model pockets in the surface. The mechanisms of backward lubricant escape in MPHDL and forward escape by MPHSL have been identified and shown to be greatly influenced by materials and process parameters. The hydrostatic pressure increase is occurring within the beginning of the process after which the obtained liquid pressure suppresses further pocket deformation. The level at which the hydrostatic pressure is stabilised is independent of the volume of a pocket.

The MPHS lubrication mechanism shows proportionality between the volume of emerged lubricant and the volume of the pocket. This is explained by the rate of pressure decrease in the pocket once the MPHS lubrication mechanism is initiated. The smaller pocket reaches the die pressure faster and consequently a smaller volume of lubricant has emerged.

The MPHD lubrication mechanism has proven, both experimentally and theoretically, to be dependent on the angle to the edge and the radius of curvature on the

edge. The lower the angle to the edge and the larger the radius of curvature is, the earlier the onset of MPHDL and the larger the area of emerged lubricant. The pocket volume has been observed not to influence the MPHD lubrication mechanism during the experiments. The onset of the MPHD mechanism and the area of emerged lubricant are proportional to each other and therefore only one of the parameters needs to be obtained in future experiments evaluating the MPHD lubrication mechanism.

A mathematical model for the lubricant escape has been established determining the onset-reduction for MPHD lubrication as a function of pocket geometry and material parameters such as strain hardening exponent and lubricant viscosity and process parameters such as die angle and drawing speed. The calculations show good agreement with experiments.

## REFERENCES

- Anon. (1953) Pressure-Viscosity Report. American Society of Mechanical Engineers, ASME Research Publication, PB-244 827.
- Azushima, A., Tsubouchi, T. and Kudo, H. (1990) in *Proceedings of 3<sup>rd</sup> International Conference on Technology of Plasticity*, Vol. I (Kyoto), pp. 551-556.
- Azushima, A., Uda, M. and Kudo, H. (1991) *Ann. CIRP*, **40/1**, 227-230.
- Azushima, A. (1995) *Ann. CIRP*, **44/1**, 209-212.
- Bay, N. and Wanheim, T. (1990) in *Proceedings of 3<sup>rd</sup> International Conference on Technology of Plasticity*, Vol. IV (Kyoto) pp. 1677-1691.
- Bech, J.I. (1997) Lubrication Mechanisms in Metal Forming, MM-report No. 97.79, M.Sc.-thesis (in Danish), Techn. Univ. of Denmark.
- Bech, J.I., Bay, N. and Eriksen, M. (1998) *Ann. CIRP* **47/1**, 221-226.
- Bech, J.I., Bay, N. and Eriksen, M. (1999) *Wear* **232**, 134-139.
- Geiger, M., Engel, U. and Pfestorf, M. (1997) *Ann. CIRP* **46/1**, 171-174.
- Kudo, H., Tanaka, S., Imamura, K. and Suzuki, K. (1976) *Ann. CIRP*, **25**, 179-184.
- Kudo, H., Tsubouchi, M., Takada, H. and Okamura, K. (1982) *Ann. CIRP*, **31/1**, 175-180.
- Lo, S.W. and Wilson, W.R.D. (1999) *Trans. ASME J. Tribology*, **121**, 731-738.
- Mizuno, T. and Okamoto, M. (1982) *Trans. ASME, J. of Lubr. Technol.* **104**, 53-59.
- Nellemann, T., Bay, N. and Wanheim, T. (1977) *Wear*, **43**, 45-53.
- Schey, J.A. (1983) *Tribology in Metalworking. Friction, Lubrication and Wear*. (The American Society for Metals, Metals Park, Ohio).
- Schmoedel, D., Prier, M. and Staeves, J. (1997) *Ann. CIRP*, **46/1**, 175-178.
- Shimizu, I. (1999) Lubrication Mechanisms during Strip Drawing. MM-report No. 97.79, Techn. Univ. of Denmark.
- Shimizu, I., Andreasen, J.L., Bech, J.I. and Bay, N. (2001) *ASME, J. Tribology* **123**, 290-294.
- Steinhoff, K., Rasp, W. and Pawelski, O. (1996) *J. Mater. Process. Technol.* **60**, 355-361.
- Soerensen, C.G., Bech, J.I., Andreasen, J.L., Bay, N., Engel, U. and Neudecker, T. (1999) *Ann. CIRP* **48/1**, 203-208.

## Chapter 8

# Numerical Simulation of Sheet Metal Forming

M.J. Worswick  
*Department of Mechanical Engineering*  
*University of Waterloo*  
*Waterloo, Ontario, N2L 3G1*  
*Canada*

Considerable progress has been made in the past few decades in the development of mathematical models of sheet metal forming operations. The explosion of computing capability has provided the necessary computational speed to support ever-increasing levels of realism in mathematical representation of material behavior, lubrication and tooling geometry, along with increased levels of resolution. While in the past, mathematical models often lagged actual fabrication and try-out of tooling for stamping operations, it is now common for computational models to lead the way in development and optimization of tooling and stamping processes.

This chapter presents recent developments in the numerical simulation of sheet metal forming processes, both at the University of Waterloo and elsewhere. The studies presented herein focus primarily on the simulation of aluminum alloy sheet forming operations, in particular for automotive applications; however, the methods described are equally applicable for other sheet materials. The recent emphasis on aluminum is motivated by the lack of industrial experience in forming aluminum in volume automotive production; hence, an analytical approach is desirable to compensate for the lack of prior experience in optimization of aluminum forming operations.

This chapter opens with a presentation of a typical sheet forming simulation, a relatively simple cup draw. This model serves to illustrate the nature of sheet forming modeling after which more in-depth discussion of numerical modeling formulations and applications are presented. Here, we debate the merits of implicit versus dynamic explicit numerical formulations for sheet forming simulation. Available mathematical descriptions of material response are presented, in particular, appropriate, cost effective approaches to capture material crystallographic and anisotropic behavior. Approaches to predicting material formability are also discussed, including damage-based models at both the continuum and micro-scale. Several novel forming operations are presented, including simulation of aluminum alloy stretch flanges, multi-gage tailor welded blanks (TWBs), and electromagnetic forming. Product performance modeling is introduced, in particular the numerical prediction of closure panel dent resistance. Many of these operations are multi-

stage, involving multiple forming operations, and numerical techniques to handle intervening springback and trimming steps are presented. In all of the discussion to follow, we emphasize that many aspects of numerical simulation, as applied to forming operations, still rely upon a degree of artisanship on the part of the practitioner. A balance is required, accurately capturing the physics of the deformation process to be modeled while maintaining an acceptable level of computational cost. Techniques to ensure such a balance are presented throughout this chapter.

## 8.1 INTRODUCTION TO STAMPING SIMULATION – A DEEP DRAWN CUP

As an example of a typical sheet forming operation, we consider a cylindrical cup draw operation (Chung and Swift, 1951; Budiansky and Wang, 1966; Chiang and Kobayashi, 1966; Woo, 1968; Chu et al, 1988). Figure 8.1 depicts the tooling and sheet metal blank used in this simple deep draw operation, modeled by Harpell et al (2000) using the LS-DYNA finite element code (Hallquist, 1998). A circular sheet metal blank is forced into the die opening by a punch, thereby taking on the desired cylindrical part shape. Compressive stresses are induced in the sheet metal as it is drawn into the die cavity, often leading to wrinkling in the flange and sidewall of the part. To prevent or control wrinkling, the flange region of the blank is often clamped between the die and binder tools, such that the flange slides between the two surfaces, suppressing normal deflection and inducing higher levels of tension in the work piece. These basic tooling elements, punch, die and binder, are common to most stamping operations; thus, the techniques used to simulate this simple cup draw case can easily be extended to more complex commercial stampings.

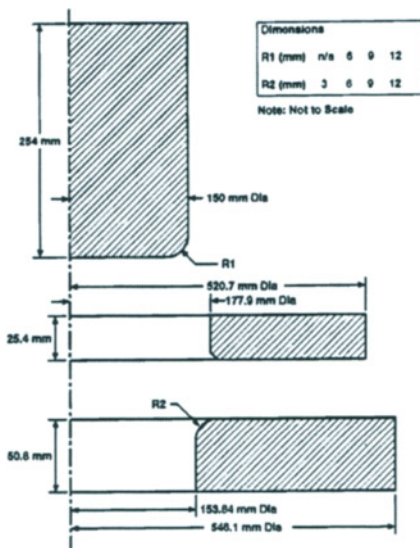


**Figure 8.1** Tooling geometry used in model of cylindrical cup draw experiment. (Harpell, 1997)



**Figure 8.2** Exploded view of mesh used to simulate cylindrical cup draw (Harpell, 1997)

The following presents a description of a numerical model of this cup draw operation using an explicit finite element formulation. The details of this type of formulation and alternative formulations are presented in Section 8.2, below. For now, we focus on the nature of the simulation and the results that can be obtained. An exploded view of a typical finite element mesh used by Harpell et al (2000) to model this operation is shown in Figure 8.2. In this case, the model considers a 150 mm (5.9") diameter punch, with 6 mm die and punch profile radii tooling, acting on a 317.5 mm (12.5") diameter blank. The blank is an automotive grade aluminum alloy sheet, AA5754-O, with a uniaxial stress-strain response given in Figure 8.3.

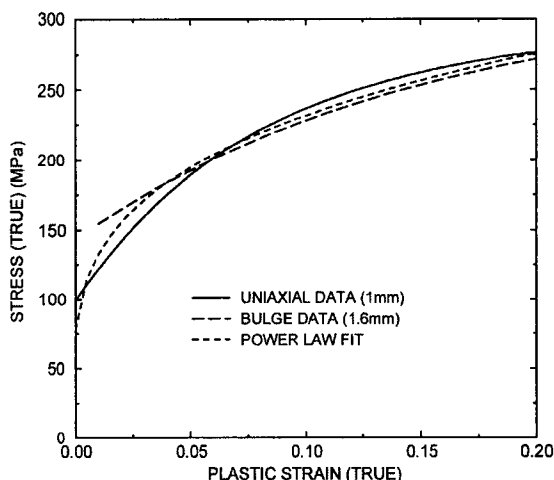


**Figure 8.3** Measured stress versus plastic strain curves with a regression fit considering power law hardening. The 1.6 mm thick bulge test data compares reasonably well to the tensile test data on 1.0 mm material (Harpell, 1997).

### 8.1.1 Finite element mesh

In most sheet forming simulations, the tooling is treated as rigid and only the tooling surfaces are discretized, in this case using rigid, four-node quadrilateral shell elements. Thin shell elements are normally used to describe the deformable blank; in this model, four-node quadrilateral, Belytschko-Lin-Tsay (Belytschko et al, 1984) shell elements were adopted with a thickness update option due to Hughes and Carnoy (1981). One-quarter of the geometry was modeled, taking advantage of symmetry to reduce computational expense. The elements in the outer region have been biased to carefully control their aspect ratio, ensuring they are nearly square when transiting the die profile radius. Through-thickness variations due to bending are captured using five or more through-thickness integration points. A single in-plane integration point is utilized to improve solution time; this choice of in-plane integration scheme allows so-called zero energy modes, known as hourglassing, to occur. The hourglass control technique of Flanagan and Belytschko (1981) was adopted to suppress these zero-energy kinematic deformation modes.



The description of the actual material behaviour is complex and the topic of much research. This topic is described in detail in Section 8.3, below.

### 8.1.2 Boundary conditions and contact treatment

Penalty function-based contact interfaces (Hallquist, 1998) are used to enforce the intermittent contact and sliding boundary condition between the sheet metal and the tooling elements. Other techniques, such as Lagrangian contact descriptions or simple kinematic descriptions, are also possible. Thickness-based contact is normally adopted in which separate reference surfaces, corresponding to the top and bottom surfaces of the sheet, are used to enforce contact with the tooling. This contact option is more expensive computationally, compared to a membrane contact formulation, but is necessary for most deep drawing operations to simulate local variations in clamping pressure due to sheet thickening and ironing. Standard Coulomb friction is normally imposed between the contact interfaces of the sheet and the tooling surfaces with prescribed coefficients of static and kinematic friction. In the current cup draw example, a constant friction coefficient of 0.06 was adopted that would correspond to a solid sheet Teflon lubricant.

The die is held fixed using imposed translational and rotational constraints about all three coordinate axes. Both the punch and binder are constrained so as to allow movement only in the z-direction, corresponding to the direction of the punch axis. A load corresponding to the binder force in the experiments is applied to the binder in the negative z-direction.

As noted above, the finite element equations are solved using an explicit dynamic formulation. This technique is described in detail below, but essentially entails treating the stamping operation as a dynamic event with greatly elevated tooling velocities. The motivation for this approach is the extremely simple nature of the explicit dynamic formulation over conventional static implicit formulations, allowing very inexpensive time steps and greatly simplified contact treatment. Unfortunately, the allowable time step size is quite small, thus increased tooling velocities are employed to reduce computational run times. Care must be taken to avoid introduction of inertial effects due to accelerated punch speeds. By comparison, conventional stamping operations are often performed with punch speeds less than 1 m/s, whereas simulated punch speeds may reach 50 m/s. To reduce inertial effects, the punch motion was specified using a sinusoidal velocity profile, as illustrated in Figure 8.4. This figure shows a typical loading curve used to describe the motion of the punch, to a depth of 150 mm. Also shown is the binder force time-history, the force held at 60 kN after an initial ramp-up. The motion of the punch was delayed by 0.1 ms to allow the binder force to be engaged and stabilize. As can be seen, the punch velocity profile has a peak sinusoidal velocity of 40 m/s and a punch stroke duration of roughly 5 to 7 ms, corresponding to a total draw depth of 150 mm. Comparison of numerical results using the accelerated profiles with those using much slower loading revealed only minor differences up to the velocities shown in Figure 8.4.

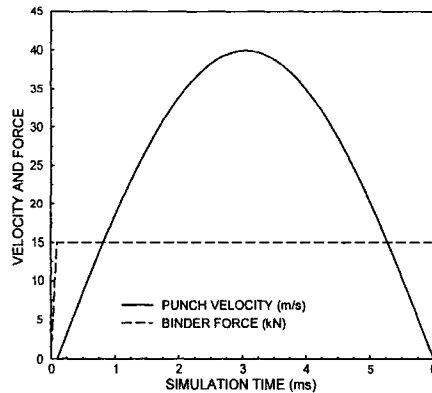


**Figure 8.4** Typical load curves specifying the binder force and punch velocity used in the cup draw model. The 15 kN binder force is applied to the quarter geometry, representing a total force of 60 kN (Harpell, 1997).

The motion of the binder is additionally controlled using a so-called “rigid body stopper” constraint implemented in LS-DYNA (Hallquist, 1998). This constraint limits the velocity of the binder to 0.01 m/s during the ramped loading of the binder to the clamping force and then imposes a maximum velocity of 0.001 m/s between the binder and the die for the duration of the drawing process. Use of this constraint suppresses oscillation or “chatter” of the binder which can result in premature localization of the sheet as the flange region of the blank is suddenly pinned between the surfaces due to “bounce” of the binder. The level of chatter can also be controlled using so-called contact damping techniques in which the penalty function stiffness is supplemented with a damping coefficient, specified as a fraction of critical damping, to suppress oscillatory contact forces.

### 8.1.3 Forming Predictions

Figure 8.5 depicts a typical predicted thickness distribution in a deep drawn cup (Harpell, 1997). Post-processing of forming models often utilizes predicted in-plane principal strains which are directly comparable to strain measurements using conventional circle grid techniques for formability assessment (Hecker, 1974; Ghosh, 1975). To examine the evolution of strain during the punch stroke, interrupted experiments were modeled considering a 305 mm blank. Measured and predicted strains for three interrupted states at 30, 50, and 90 mm punch stroke, as well as those for a fully drawn cup are shown in Figure 8.6. The numerical model shows good correlation with the measured values. The predictions in the mid-wall appear to fall below the experimentally determined values, again by approximately 4 to 5 percent strain, and over predict the principal strains in the cup bottom. The results show good qualitative prediction of strain distribution development with increasing punch depth. Predicted strain distributions were shown to compare well with measured values for a number of other tooling geometries and blank sizes, as described further by Harpell (1997).

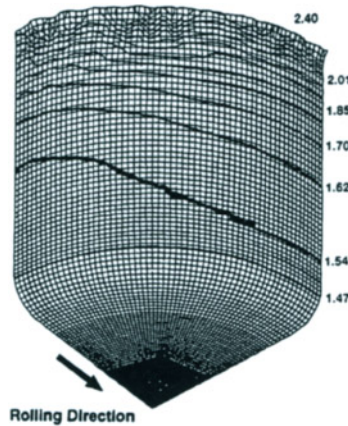


**Figure 8.5** Contours of predicted thickness for a deep drawn cup (Harpell, 1997).

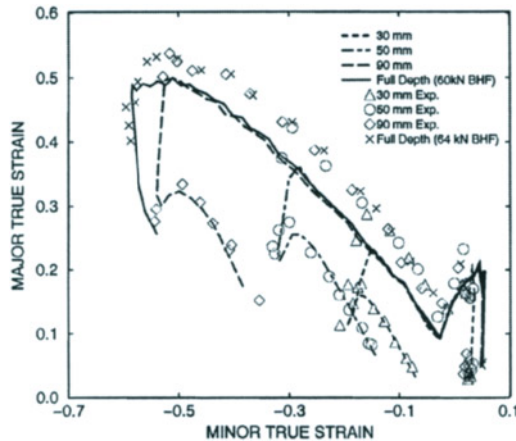


**Figure 8.6** Comparison of measured and predicted strain distributions for interrupted tests using a 305 mm blank. The blank holder force was 52 kN, except for the fully drawn cases, as indicated. (Harpell, 1997).

## 8.2 EXPLICIT DYNAMIC VERSUS IMPLICIT FORMULATIONS

Sheet metal forming simulations almost always involve non-linear geometric and material response, as well as intermittent contact between the tooling and work piece, all of which necessitate a non-linear solution method. There are two main finite element methods commonly used in sheet metal forming simulations. Depending on the nature of the problem one solution method is often more suitable than the other. A simulation may be classified as either quasi-static or dynamic depending on the level of dynamic excitation involved in the

process. For dynamic problems, and using conventional finite element approximations, the fundamental differential equation that must be solved is

$$\{\ddot{r}^{ext}\} = \{\ddot{r}^{int}\} + [M]\{\ddot{d}\} + [C]\{\dot{d}\} \quad (8.1)$$

$\{\ddot{r}^{ext}\}$  is the vector of externally applied nodal forces,  $[M]$  is the mass matrix,  $[C]$  is a damping matrix, and  $\{\ddot{d}\}$  is the nodal displacement vector, with it's associated time derivatives for velocity and acceleration.  $\{\ddot{r}^{int}\}$  is the vector of internal nodal forces, summed over all elements,

$$\{\ddot{r}^{int}\} = \int_{V^e} [B]\{\sigma\} dV^e \quad (8.2)$$

$\{\ddot{r}^{int}\}$  is statically equivalent to the internal stresses,  $\{\sigma\}$ , with  $[B]$  the strain-displacement matrix and  $V^e$  denoting the element volume. The internal force vector incorporates material non-linearity and stiffness response. The damping term in the equation is often not included, as quantifying damping is difficult. When this term is included an arbitrary value is often selected.

### 8.2.1 Explicit dynamic method

Two different time integration algorithms are available for solving equations (8.1) and (8.2). The explicit dynamic solution will solve for acceleration for the current time step by inverting the mass matrix and multiplying it by the difference in internal and external forces.

$$\{\ddot{d}\}_{n+1} = [M]^{-1}(\{\ddot{r}^{ext}\} - \{\ddot{r}^{int}\}) \quad (8.3)$$

The mass matrix is often taken as a lumped mass, diagonal matrix, making inversion trivial and numerically inexpensive. Thus while the number of time steps, or iterations, will be large, the numerical cost is relatively low.

The dynamic explicit solution method is only conditionally stable, with a maximum time step size governed by the Courant criterion, estimated as

$$\Delta t_{max} = \frac{L_{min}}{\sqrt{E/\rho}}, \quad (8.4)$$

The maximum time step,  $\Delta t_{max}$ , is controlled by the smallest element size,  $L_{min}$ , and the speed of sound in the material,  $c = \sqrt{E/\rho}$ , a function of Young's Modulus,  $E$ , and density,  $\rho$ . For most metals used in sheet forming, equation (8.4) implies time steps on the order of 10ns-2μs. This extremely small time step motivates the acceleration of tooling velocities described in the previous section by one or two orders of magnitude above that used in conventional forming processes to achieve acceptable run times. The effect of increased velocity must be monitored as it may introduce artificial dynamic effects. An alternative to increased tooling velocity is to use so-called mass-scaling techniques in which the density of

all or selected elements governing the time step is artificially increased. As can be seen in equation (8.4) an increase in density will result in a larger minimum time step; however, this also increases inertia and dynamic effects must still be monitored.

### 8.2.2 Static implicit method

The implicit solution method is the alternative numerical option. This method is unconditionally stable and thus time step size is not a function of the material properties or minimum element size. However, this method is numerically very expensive as the solution method determines the displacement at the end of a time step,  $\{d_{n+1}\}$ , by solving for the displacement increment leading to equilibrium between the out-of-balance forces. The stiffness matrix,  $[K]$ , is inverted and multiplied by an effective force vector,  $\{r^{eff}\}$ ,

$$\{d_{n+1}\} = [K]^{-1} \{r_{n+1}^{eff}\} \quad (8.5)$$

For dynamic problems,  $\{r^{eff}\}$  is a function of the external force and dynamic terms at the current time step. The formation, storage and inversion of the stiffness matrix are numerically expensive. Also, the size of the time step must be chosen with care for highly non-linear problems, where large steps may achieve equilibrium while missing details of the non-linear deformation. The implicit solution is also well suited to quasi-static problems where the acceleration and velocity terms are both dropped from the governing equation. For these problems a simpler equation results, but the expensive stiffness matrix inversion remains.

$$\{d_{n+1}\} = [K]^{-1} \{r_{n+1}^{eff}\} \quad (8.6)$$

Implicit methods must iterate over a given time step to achieve static or dynamic equilibrium and can be effective, but add increased numerical costs as repeated formation and inversion of the stiffness matrix becomes necessary. Iterative stiffness updating when searching for equilibrium can lead to difficulties in achieving numerical convergence, particularly for metal forming problems for two primary reasons. First of all, the stiffness matrix resulting from a sheet metal blank is often ill-conditioned. This can be expressed numerically in terms of the ratio of the highest and lowest natural frequencies associated with the stiffness equations. Physically this reflects the fact that sheet metal is generally very stiff in-plane (high natural frequency terms), but exhibits low stiffness out-of-plane (low natural frequency). The second aspect of metal forming problems leading to poor convergence is the intermittent nature of contact between tooling and work piece that can introduce numerical "chatter", greatly degrading the convergence characteristics of implicit methods.

### 8.2.3 Choosing between implicit and explicit methods

For many problems that are not truly dynamic, it is often advisable to use an explicit dynamic solution. The inherent non-linearity of many forming problems, coupled with the convergence issues that can arise with implicit solutions, often dictate that an explicit solver be used. This is particularly so for large commercial stamping operations requiring many hundreds of thousands of elements, for which implicit solvers often breakdown due to convergence or contact algorithm failure. The decision to use an explicit dynamic formulation for a quasi-static process again raises issues with the introduction of artificial

dynamic effects, particularly when velocity or mass scaling is required. Interestingly, the poor numerical conditioning exhibited by sheet forming problems can also lead to significant round-off error when explicit dynamic solutions are run in “real time” without utilizing accelerated tooling velocities or mass scaling. Thus, solution accuracy is another important motivating factor for compressing solution time in explicit analysis.

One principle drawback of explicit solutions is the stage of the simulation after the forming process is complete. In an implicit solution the final step will represent an equilibrium state, but in an explicit solution the part will be oscillating dynamically after removal of the tooling elements and contact. This vibration after forming will not affect the part’s plastic strains, so the part formability can still be assessed based on predicted strains. However, in order to solve for the springback after the tooling is removed an explicit solution would require a large time period for the oscillation to damp out. An implicit solution is more suited for springback prediction as only a few implicit steps will find final equilibrium. Thus, the preferred numerical approach is often an explicit forming solution coupled with an implicit springback analysis. Naturally, the transition from the forming simulation to the springback simulation requires accurate transfer of the forming strains, stresses and thicknesses between solvers as well as compatible element formulations between solution types.

Considerable effort has gone into improving the efficiency and reliability of implicit algorithms for sheet metal forming problems. In particular, sparse matrix techniques have seen considerable success in improving solver efficiency and artificial stabilization techniques have improved convergence of static springback analyses (Maker et al, 2001). Implicit contact algorithms have improved considerably and hybrid formulations decoupling the shell element membrane and bending response have seen success in codes such as Otris and Autoform, used in simulating commercial stampings. Other hybrid approaches utilize a mixed explicit-implicit scheme, in which implicit time integration is used for most of the analysis, but invoking explicit integration if the implicit integration process “stalls” though non-convergence, for example.

### 8.3 MODELLING THE CONSTITUTIVE RESPONSE OF SHEET METALS

A complete mathematical description of the constitutive response of a sheet material can be very complex, depending upon the required level of realism in the simulation. Of course as complexity increases, so does computational cost; thus, as always, a balance between realism and cost must be attained.

The majority of material descriptions are formulated within a continuum-level framework, although descriptions of crystallographic plasticity response (Asaro and Needleman, 1985; Wu et al, 1996; Inal et al, 2002; Beaudoin et al, 1995; Sarma and Dawson, 1996) and discrete particle-level damage mechanics models (Chen et al, 2002; Worswick et al, 2001a; Thomson et al, 1999) are possible, for example. A continuum-level material model typically starts with a description of basic material parameters, such as density and elastic moduli. The plastic response generally requires input consisting of yield and work hardening response, as shown, for example, in Figure 8.3 for AA5754-O. Work hardening behaviour can be provided as a list of discrete stress versus plastic strain points or in terms of an algebraic fit to the material response, often using a power law-type fit, for example,

$$\bar{\sigma} = k(\varepsilon_o + \varepsilon_p)^n \quad (8.7)$$

in which  $\bar{\sigma}$  is the flow stress,  $\varepsilon_0$  is the strain to cause first yield, and  $\varepsilon_p$  is the plastic strain. Hardening parameters,  $k$  and  $n$ , are normally obtained from regression analysis of uniaxial stress-strain data. Numerous alternate forms of work hardening description exist.

### 8.3.1 Phenomenological yield loci

While an accurate description of hardening response is critical to capture material localization behaviour, it is merely a necessary first step in an accurate constitutive description. Of equal importance is the appropriate selection of a yield locus to accurately capture the crystallographic yielding response of sheet materials under multi-axial stress states. The description of the shape of the yield locus for sheet materials is generally complex and a consequence of the naturally evolving crystallographic texture during fabrication of the sheet. Detailed crystallographic plasticity models have been incorporated into finite element models of sheet forming processes that account, for example, for the frequency distribution of grains at a point (Asaro and Needleman, 1985; Wu et al, 1996; Inal et al, 2002) or even the spatial variation of texture within a work piece (Beaudoin et al, 1995; Sarma and Dawson, 1996). More commonly, mechanical measurements of material response from uniaxial or biaxial testing are used to characterize material multi-axial response within the context of phenomenological yield loci. Typical measurements may include uniaxial yield stresses measured from tensile tests performed at various orientations, commonly  $\sigma_0$ ,  $\sigma_{45}$ , and  $\sigma_{90}$ , corresponding to the yield stresses at 0, 45 and 90° relative to the sheet rolling direction, respectively. Also important are the Lankford coefficients or  $r$ -values,

$$r_\theta = \varepsilon_t / \varepsilon_e \quad (8.8)$$

where  $\varepsilon_t$  and  $\varepsilon_e$  are the thickness and width strains measured in a tensile test performed at some angle  $\theta$  relative to the rolling direction. In general, body centred cubic materials, such as sheet steels, will display high  $r$ -values, often in excess of 2.0, while face centred cubic materials, like aluminum alloy sheet, will exhibit low  $r$ -values in, typically 0.6-0.8.  $r$ -values are important since they characterize a resistance to thinning and reflect the local slope of the yield surface as determined by the flow rule.

Ideally, a phenomenological yield locus must accurately predict the behaviour of a material under plastic flow conditions as characterized by (i) the stresses required to initiate and sustain plastic flow and (ii) the slope of the locus as represented in stress-space. The former will determine the forming stresses and will influence localization while the latter will control the direction of plastic flow since the plastic strain tensor must always lie orthogonal to the yield locus under the assumption of associated flow. Under uniaxial conditions, the slope of the yield locus will determine the predicted  $r$ -values and, under biaxial conditions, the slope will determine the propensity to transition to plane strain deformation with accompanying reduction in formability.

Classical yield theories were first proposed by Tresca and von Mises. Tresca suggested that yielding initiated once a critical shear stress was reached within a metal:

$$\tau_{\max} = \tau \quad (8.9)$$

where

$$\tau_{\max} = \frac{1}{2} \max(|\sigma_1 - \sigma_2|, |\sigma_2 - \sigma_3|, |\sigma_3 - \sigma_1|) \quad (8.10)$$

in which  $\sigma_i$  are the principal stresses and  $\tau = \sigma_0 / 2$  becomes the yield stress under pure shear conditions (as predicted by Tresca) which becomes one-half of the uniaxial yield strength,  $\sigma_0$ .

von Mises introduced the concept that yielding occurs under multiaxial stress conditions when the distortion energy reaches the level required to cause yielding under uniaxial conditions. For convenience, let us assume that the  $x$ - $y$  axis system lies within the plane of the sheet; thus, for thin sheet materials under plane stress conditions  $\sigma_z = 0$  and the von Mises or distortion energy criterion becomes

$$\Phi_{Mises} = \left( \frac{\sigma_x + \sigma_y}{2} \right)^2 + 3 \left[ \left( \frac{\sigma_x - \sigma_y}{2} \right)^2 + \tau_{xy}^2 \right] - \sigma_0^2 = 0 \quad (8.11)$$

A draw-back of the von Mises yield function when applied to sheet forming is the assumption of isotropic material behaviour resulting in an inability to account for the effect of texture and anisotropy on plastic flow. In addition, due to the nature of slip within polycrystalline materials, the quadratic dependence on stress predicted by von Mises is not observed experimentally. Hill (1948) introduced an anisotropic yield theory which attempts to account for differences in yield strengths observed along various directions in a rolled sheet material,

$$\Phi_{Hill-48} = (G + H)\sigma_x^2 - 2H\sigma_x\sigma_y + (F + H)\sigma_y^2 + 2N\tau_{xy}^2 - 1 = 0 \quad (8.12)$$

Material constants  $F$ ,  $G$ ,  $H$  and  $N$  can be fit to either measured yield stresses or  $r$ -values. Using yield stress data, one obtains

$$(G + H)^{-1/2} = \sigma_0 \quad (8.13a)$$

$$(F + H)^{-1/2} = \sigma_{45} \quad (8.13b)$$

$$(F + G)^{-1/2} = \sigma_{90} \quad (8.13c)$$

and

$$(2N)^{-1/2} = \tau \quad (8.13d)$$

Alternatively, the yield locus can be fit using measured  $r$ -values:

$$r_0 = \frac{H}{G} \quad (8.14a)$$



$$r_{90} = \frac{H}{F} \quad (8.14b)$$

$$r_{45} = \frac{N}{F+G} - \frac{1}{2} \quad (8.14c)$$

One draw-back of the Hill-48 yield function is an inability to properly capture both accurate biaxial yield stress and uniaxial  $r$ -values for low  $r$ -value ( $r < 1$ ) materials such as aluminum (Logan et al, 1986). In order to better capture polycrystalline yield behaviour, particularly for low  $r$ -value materials, a number of so-called non-quadratic yield criteria have been proposed (Hosford, 1972; Hill, 1979; Barlat and Lian, 1989; Barlat, et al, 1991; Karafillis and Boyce, 1993; Hill, 1990; Barlat et al, 1997; Barlat et al, 2000). Strain rate potentials have also been proposed (Barlat et al, 1993; Barlat and Chung, 1993). Of these, the most commonly utilized yield criteria for sheet metal forming are the Hill-90 and the Barlat-89 models. Hill (1990) proposed a homogeneous function of arbitrary degree  $m$  based on his earlier quadratic criterion (equation 8.12),

$$\begin{aligned} \Phi_{Hill-90} = & \left| \sigma_x + \sigma_y \right|^m + (\sigma / \tau)^m \left| (\sigma_x - \sigma_y)^2 + 4\tau_{xy}^2 \right|^{m/2} \\ & + \left| \sigma_x^2 + \sigma_y^2 + 2\sigma_{xy}^2 \right|^{(m/2)-1} \left[ -2a(\sigma_x^2 - \sigma_y^2) + b(\sigma_x - \sigma_y)^2 \right] - (2\sigma)^m = 0 \end{aligned} \quad (8.15)$$

where  $a$  and  $b$  are material constants in addition to  $\sigma$ ,  $\tau$ , and  $m$ . Typically,  $m$  ranges between 1 and 2 for low- $r$  materials, such as aluminum, and is greater than 2 for high  $r$ -values, as in steel.

Barlat (1979) proposed an alternate non-quadratic yield function based on earlier work by Hosford (1972)

$$\Phi_{Barlat-89} = a|K_1 + K_2|^M + a|K_1 - K_2|^M + c|2K_2|^M - 2\sigma_0^M = 0 \quad (8.16)$$

where

$$\begin{aligned} K_1 = \frac{\sigma_x + h\sigma_y}{2} \quad \text{and} \\ K_2 = \left[ \left( \frac{\sigma_x + h\sigma_y}{2} \right)^2 + p^2 \tau_{xy}^2 \right]^{\frac{1}{2}} \end{aligned} \quad (8.17)$$

Barlat demonstrated from crystallographic plasticity considerations that  $M=8$  is an appropriate choice for FCC materials, whereas  $M=6$  works well for BCC materials. The anisotropic material parameters  $a$ ,  $c$ ,  $h$ , and  $p$  can be determined from the Lankford coefficients,  $r_0$ ,  $r_{45}$ , and  $r_{90}$ , and the uniaxial yield strength measured along the rolling

direction,  $\sigma_0$ . Note that constant  $a$  and yield exponents  $M$  and  $m$  in equations (8.15) and (8.16) are not equivalent.

If one assumes in-plane isotropy ( $r_0 = r_{45} = r_{90} = \bar{r}$ ) then equations (8.16) and (8.17) simplify to

$$\frac{2\bar{r}}{1+\bar{r}}|\sigma_1 - \sigma_2|^M + \frac{2}{1+\bar{r}}|\sigma_2 - \sigma_3|^M + \frac{2}{1+\bar{r}}|\sigma_3 - \sigma_1|^M - 2\sigma_0^M = 0 \quad (8.18)$$

which corresponds to the case of transverse anisotropy. If the yield function exponent  $M$  is set to 2, then equation (8.18) reverts to the Hill-48 quadratic yield function (equation 8.12) for the case of transverse anisotropy,

$$\frac{2\bar{r}}{1+\bar{r}}(\sigma_1 - \sigma_2)^2 + \frac{2}{1+\bar{r}}(\sigma_2 - \sigma_3)^2 + \frac{2}{1+\bar{r}}(\sigma_3 - \sigma_1)^2 - 2\sigma_0^2 = 0 \quad (8.19)$$

Finally, for isotropic behaviour ( $\bar{r} = 1$ ), equation (8.19) simplifies to a von Mises response,

$$(\sigma_1 - \sigma_2)^2 + (\sigma_2 - \sigma_3)^2 + (\sigma_3 - \sigma_1)^2 - 2\sigma_0^2 = 0 \quad (8.20)$$

The choice of constitutive formulation was shown by Logan et al (1986) to be one of the most significant factors in the assumptions made in modeling sheet metal forming. They further indicated that the use of the Hill-48 criterion (Hill, 1948) overestimated the effect of  $r$ -value on the predictions of limiting draw ratio (LDR). This criterion, while often used in the past for steels, is questionable in its applicability towards low- $r$  materials such as aluminum. A comparison of the predicted yield loci using several of the proposed yield functions presented herein is provided in Figure 8.7. The loci are plotted using  $\bar{r} = 0.7$  and  $M = 8$ , corresponding to a low  $r$ -value material, such as aluminum. It can be seen that the Hill-48 criterion exhibits a significant reduction in biaxial yield stress compared to the von Mises and Tresca criteria. In contrast, the Hill-90 and Barlat-89 non-quadratic criteria retain high biaxial yield strengths. It can also be observed that the Barlat-89 locus lies intermediate to the Tresca and von Mises loci; furthermore, the Barlat-89 locus exhibits a flattening of the yield surface in the plane strain region, in accord with expected crystallographic response (Barlat, 1989) and in contrast with the Hill-90 predictions.

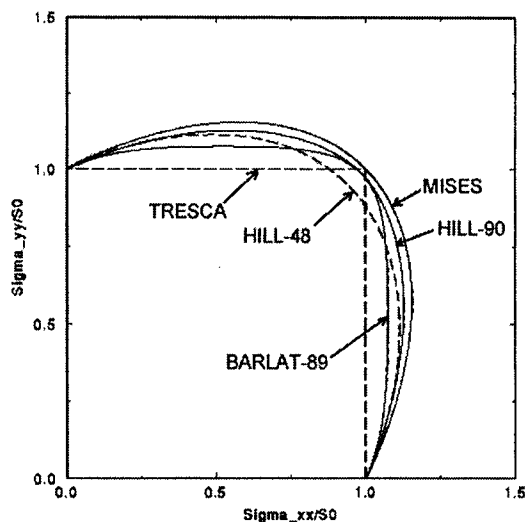
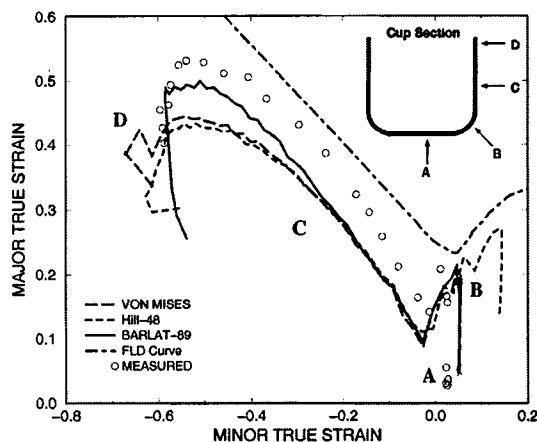
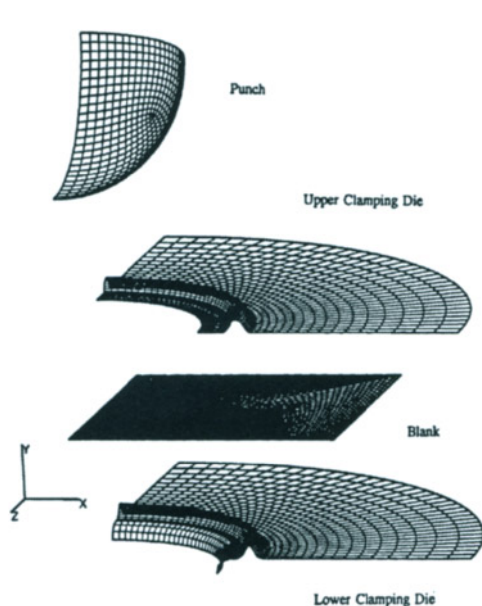


Figure 8.7 Yield loci comparison

It has only been recently (Chung and Shah, 1992; Shah and Dick; 1995; Harpell et al, 1996a,b, 2000) where advanced constitutive formulations have been applied in efforts to capture the forming behavior of low- $r$  materials such as aluminum. Hayashida et al (1995) performed a study to evaluate the six component anisotropic yield criterion developed by Barlat et al (1991). In this work Hayashida et al discussed the effect of yield surface shape on formability. A cup drawing investigation was also performed which demonstrated that this criterion provided a reasonable description of the plastic behaviour of an aluminum alloy. Additional investigations, involving cup drawing and utilizing this criterion, have been performed by Chung and Shah (1992) and Shah and Dick (1995). The results of both studies indicated that the new criterion provided better agreement with experiment than either the Hill-48 or von Mises criteria. Predicted strain loci from Harpell et al (1996a,b) for the cup draw model of Section 8.1 are shown in Figure 8.8. In general, the three-parameter Barlat-89 criterion (Barlat and Lian, 1989) provides predictions of strain in the deformed cups in better accord with the measured strains than those obtained using either the Hill-48 or the von Mises criteria. Similar results were obtained for simulations of hemi-spherical dome tests (Figure 8.9) by Lamontagne et al (1995) and Harpell et al (1996b) as shown in Figure 8.10.



**Figure 8.8** Loci of major versus minor true strain along a radial line originally parallel to the rolling direction. The blank diameter was 305 mm. The symbols indicate measured data. The predictions (lines) are from calculations using the Barlat-89, Hill-48 and von Mises yield criteria, assuming transverse anisotropy only. (Harpell, 1997).



**Figure 8.9** Mesh used by Lamontagne et al (1995) to simulate the hemispherical dome test.

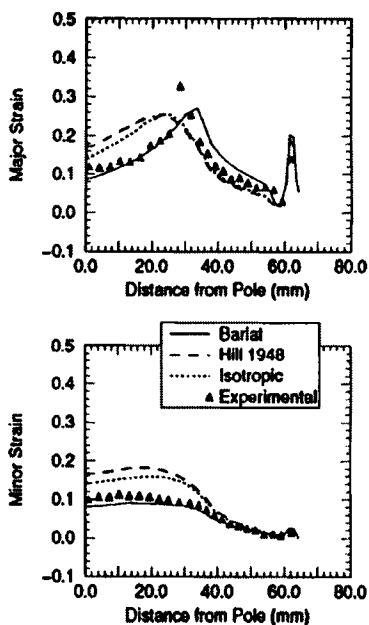


**Figure 8.10** Comparison between predicted and measured strains using various yield assumptions (Lamontagne et al, 1995)

In-plane anisotropy is often characterized in terms of the magnitude of  $\delta r$ , commonly determined using

$$\delta r = \frac{r_0 - 2r_{45} + r_{90}}{4} \quad (8.21)$$

Figure 8.11 shows strain loci for the cup draw model using measured  $r$ -values,  $r_0=0.74$ ,  $r_{45}=0.72$ , and  $r_{90}=0.8$ , and serves to demonstrate the influence of in-plane anisotropy. The predicted strain loci are indicated as lines while the measured strains are plotted as series of individual points. The three measured and three predicted distributions are taken along radial lines oriented in the rolling, transverse, and compound (CD, 45° from the RD) directions. The experimental data indicates only small differences between the strain distributions along each material direction. The predicted distributions show slightly larger variations at the cup rim, largely due to wrinkling that develops as the edge of the blank exits the binder. Away from the cup rim, the predicted distributions show little variation with material direction, further demonstrating that in-plane anisotropy exerts only a minor influence on the overall strain distribution within the cups. A relatively strong effect of in-plane  $r$ -value variation on predicted thickness within the cup can be seen from observation of Figure 8.5. Clearly, larger in-plane variations in  $r$ -value could exert a larger influence in predicted strains than that seen in Figure 8.11.

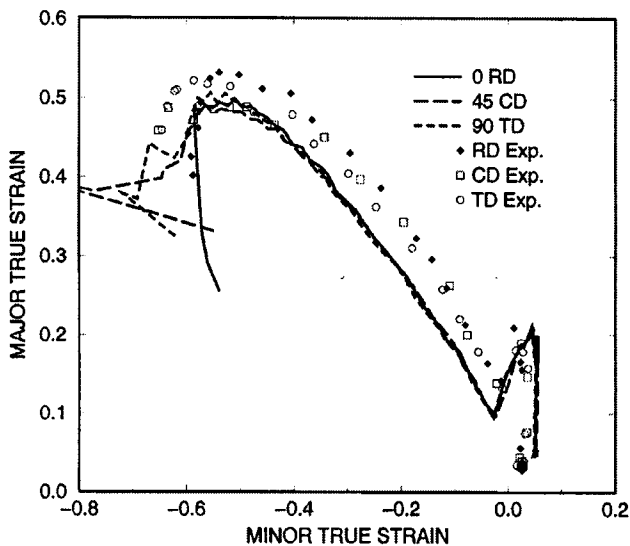


**Figure 8.11** Comparison of measured and predicted strain distributions with respect to material direction. Fully drawn 305 mm blank. (Harpell, 1997).

Other more complex yield criteria exist with greater ability to reproduce measured material behaviour (Barlat et al, 1997; Barlat et al, 2000; Cazacu and Barlat, 2001). As algebraic complexity increases, however, often so do computational costs. In experience to-date, we have experienced reasonable success utilizing the Barlat-89 yield criterion for commercial sheet materials, with an increase in computational cost (computing time) of about 70% over a conventional von Mises yield function, as implemented in the LS-DYNA

finite element code (Hallquist, 1998). As more complex yield criteria become available in commercial codes, they will undoubtedly see increased utilization.

### 8.3.2 Formability prediction

**8.3.2.1 Forming limit diagram approach** Sheet formability is often predicted utilizing the so-called forming limit diagram (FLD) approach (Hecker, 1974; Ghosh, 1975) in a manner mimicking press floor methods to assess measured strains from circle grid measurements. Predicted in-plane principal strains are compared to measured forming limit curves as shown, for example, in Figure 8.8 for the deep drawn cup model. If the predicted strains lie below the forming limit curve, the part is predicted to be “safe”. The approach is confounded by numerous influences, such as local bending strains which tend to elevate predicted strains, but often do not affect actual part formability to the extent reflected by the FLD approach. Other factors, such as strain path variation, often affect formability or limit strain (Ghosh and Laukonis, 1976; Graf and Hosford, 1993, 1994), but are not accounted for in the FLD approach which generally considers monotonic strain paths. Thus considerable judgement is required in interpreting FLD results, from both numerical and experimental studies. Further examples of the application of the FLD approach are given in Section 8.5.

Alternative FLD approaches are possible, such as the stress-based FLD approach advocated by Stoughton (2000). So-called M-K analyses (Marciniak and Kuczynski, 1967) can also be performed using predicted strain paths from the finite element model of the sheet forming process as input to an M-K model.

**8.3.2.2 Damage-based constitutive models** Another approach gaining increasing attention is the use of continuum damage-based material descriptions to predict failure during sheet metal forming processes. The most commonly adopted damage model for this application is the so-called Gurson-Tvergaard-Needleman (GTN) damage model, based upon the Gurson yield function (Gurson, 1975, 1977), as modified by Tvergaard (1981) and Tvergaard and Needleman (1984).

$$\Phi_{GTN} = \left( \frac{\Sigma_{eq}}{\bar{\sigma}} \right)^2 + 2f^* q_1 \cosh \left( q_2 \frac{3\Sigma_m}{2\bar{\sigma}} \right) - 1 - q_1^2 f^{*2} = 0 \quad (8.22)$$

where  $f^*$  is the effective void volume fraction,  $\Sigma_{eq}$  and  $\Sigma_m$  are the von Mises effective stress and hydrostatic stress, respectively, and  $\bar{\sigma}$  is the matrix flow stress. The “ $q$ ” coefficients are “calibration coefficients” introduced by Tvergaard (1981) to better represent void interaction effects in plastically deforming materials. The function  $f^*$  was introduced by Tvergaard and Needleman (1984) to account for the onset of void coalescence,

$$f^* = \begin{cases} f & \text{if } f \leq f_c \\ f_c + \frac{f_u - f_c}{f_f - f_c} (f - f_c) & \text{if } f > f_c \end{cases} \quad (8.23)$$

It is seen from equation (8.24) that fracture through void coalescence is assumed to initiate once the porosity reaches a critical value,  $f_c$ .

The rate of increase of void volume fraction is due to the growth of existing voids and the nucleation of new voids:

$$\dot{f} = \dot{f}_{growth} + \dot{f}_{nucleation} \quad (8.24)$$

Assuming the material is plastically incompressible, the growth of existing voids is related to the hydrostatic component of plastic strain by:

$$\dot{f}_{growth} = (1 - f) \dot{\epsilon}_{kk} \quad (8.25)$$

The contribution of void nucleation will be material dependent. Void nucleation is often assumed to be plastic strain-controlled nucleation rule, with nucleation at second phase particles following a normal distribution of nucleation strain for the total population of particles (Gurson, 1975),

$$\dot{f}_{nucleation} = A \dot{\epsilon}^P \quad (8.26)$$

in which

$$A = \frac{f_N}{s_N \sqrt{2\pi}} \exp \left[ -\frac{1}{2} \left( \frac{\epsilon^P - \epsilon_N}{s_N} \right)^2 \right] \quad (8.27)$$

The term  $f_N$  represents the volume fraction of void-nucleating particles while  $\epsilon_N$  and  $s_N$  are the average and standard deviation of the strains at which particles nucleate voids. A description of the implementation of the GTN model within an explicit dynamic formulation is given by Worswick and Pelletier (1998).

In general, the GTN model predictions the evolution of damage with tensile plastic deformation and the influence of stress state (triaxiality or biaxiality) in elevating damage rate. With increased levels of damage, equation (8.22) also predicts the onset of constitutive softening, seen as a reduction in the ratio of effective stress to flow stress. Examples of the application of damage-based models to sheet formability include work by Lievers et al (2000, 2001, 2002) examining the role of damage in promoting shear bands in tight radius bending (hemming) of aluminum alloy sheet (Figure 8.12) and by Cinotti et al (2001) who considered damage in stretch flange forming operations involving draw beads. Further elaboration of the work by Cinotti et al will be presented in Section 8.4.

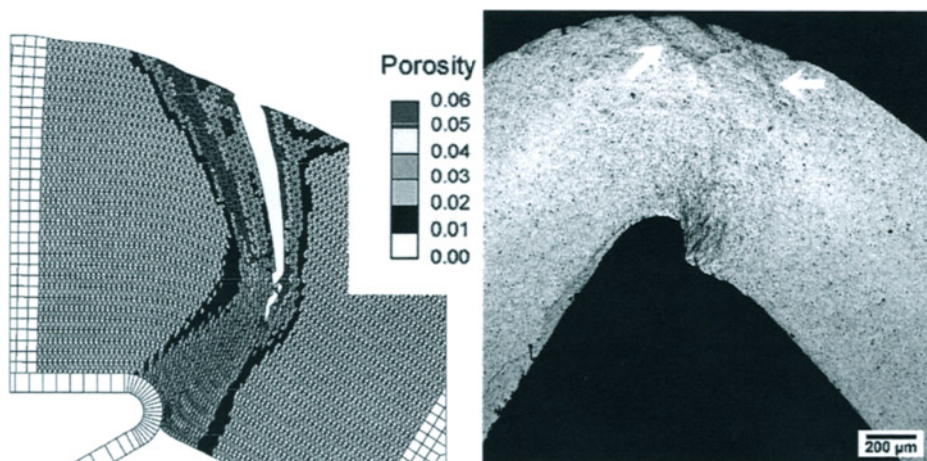


**Figure 8.12** Predicted contours of porosity for the wrap-bend model (left) and typical observed shear band localization (right) (Lievers, 2001).

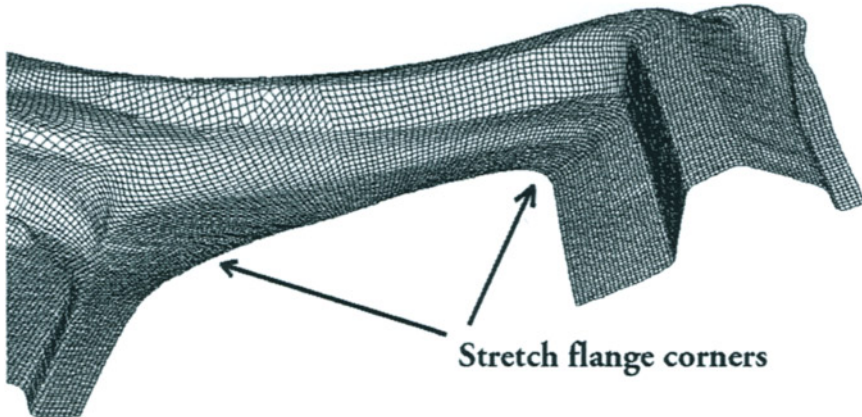
Numerous extensions of the GTN model have been proposed, some of which are pertinent to sheet forming. These include merging of the GTN yield function with various anisotropic and/or non-quadratic yield criteria (Chen et al, 2000; Huang et al, 2000). Other extensions of the Gurson yield criterion include incorporation of kinematic and/or mixed kinematic-isotropic hardening by Mear and Hutchinson (1985) and Tvergaard (1987a,b), as applied to sheet bending by Lievers et al (2002). Kinematic hardening results in yield surface translation in stress space rather than yield surface expansion during plastic deformation. A sharper yield surface curvature is maintained, approximating a yield surface vertex and facilitating easier localization through shear band formation coupled with void damage (Lievers et al, 2002), an important failure mode for low-rate hardening aluminum alloys.

#### 8.4 SIMULATION OF STRETCH FLANGE FORMING

Stretch flanges are features within sheet metal blanks consisting of circular or square cut-outs with corner radii that expand over a punch during stamping. These geometric features are of particular interest since formability acceptance of deep-drawn automotive inner components is often controlled by the predicted strains in these regions. Figure 8.13, from Worswick and Finn (2000), shows a close-up of a window cutout region in a model of typical automotive inner panel (half-symmetry model). The strains in the corners of the cutout are often extremely high and can exceed the material formability limit. The situation is exacerbated by the presence of draw-beads that are included in the tooling (not shown in the figure), running around the periphery of the cutout to control the rate of expansion of the cutout. Drawbeads introduce redundant work through repeated bending and unbending of the sheet which, for aluminum alloy sheet, can often introduce damage. Most finite element models of stamping operations do not explicitly include the drawbead geometry in the

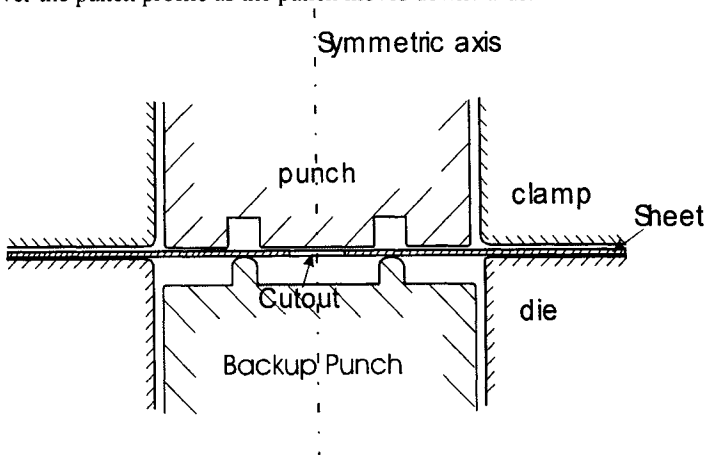


tooling because of the high level of required detail and resulting computational expense, instead utilizing so-called analytical drawbeads (Maker, 2000) that impose representative restraining tractions along the drawbead length. The damage associated with the flow of the sheet metal through the drawbead is not captured when utilizing analytical drawbeads.



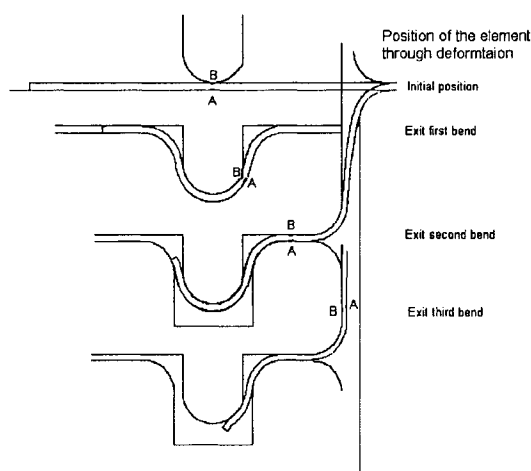
**Figure 8.13** Deformed finite element mesh (half-symmetry model) showing commercial inner panel with stretch flange corner features (Worswick and Finn, 2000).

To simulate the forming characteristics of the stretch flange corners depicted in Figure 8.13, an axisymmetric tooling set is under development by Cinotti et al (2001), as illustrated in Figure 8.14. The tooling includes a main punch and back-up punch to form a so-called z-flange geometry that incorporates a drawbead profile to control the cutout expansion rate. The punch diameters are 290 mm and typical cutout sizes range from 170 to 200mm in diameter. The outer flange region of the blank is fully clamped, forcing the cutout to expand over the punch profile as the punch moves downwards.



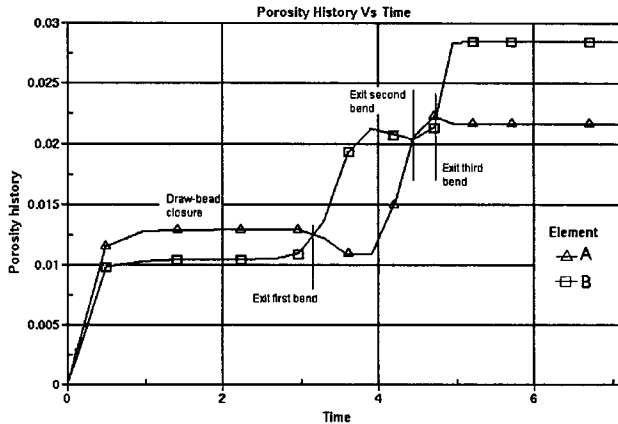
**Figure 8.14** Axisymmetric stretch flange tooling incorporating back-up punch with mating drawbeads (not to scale) (Chen et al, 2002).

Figure 8.15 shows a predicted deformation sequence for a 1.2 mm thick, AA5182 stretch flange with a 186 mm cutout (Cinotti et al, 2001). The model utilizes two-dimensional axi-symmetric solid continuum elements in order to capture the tight radius bends (6mm radius) in the drawbead region. Damage development is predicted using the GTN constitutive model described in Section 8.3.2.2, with  $\varepsilon_N = 0.20$ ,  $s_N = 0.01$ , and  $f_N = 0.0167$ , based on metallurgical studies by Worswick et al (2001a). Further description of the model is provided by Cinotti et al (2001).



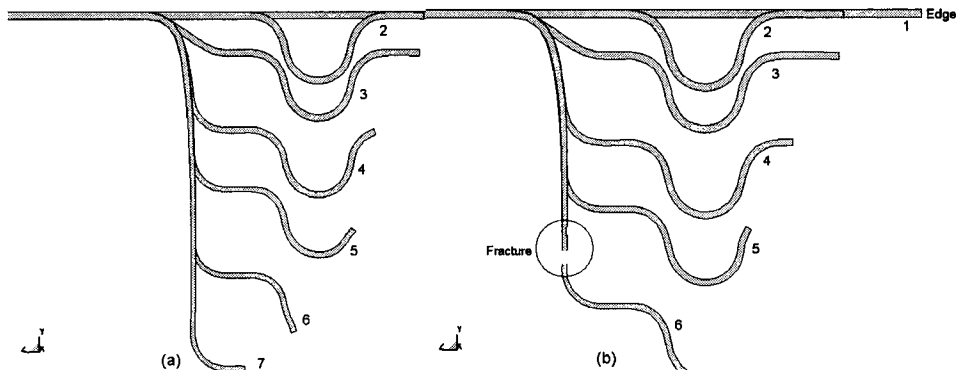
**Figure 8.15** Predicted deformation sequence for an AA5182 stretch flange with a 186 mm cutout (Cinotti et al, 2001).

Figure 8.16 shows predicted porosity versus time histories for two elements initially located immediately below the male drawbead, at the upper surface (B) and lower surface (A), for an inner cutout diameter of 186.0 mm. The first section of the curve shows growth in porosity to 1.0%-1.25% as the draw-bead is fully closed. The porosity value reaches a plateau until exiting the first bend. At this point, the bending strain reverses in sign, becoming compressive and closing the porosity on the bottom surface. The top surface, originally under compression (B), changes to a tensile state (see the intersection of the curves at the exit of the first bend). After the second bend, there is an increase in porosity to approximately 2.0% and the bending strains change sign again. At this stage, voids start to interact and coalesce. After the elements exit the third bend, they are subjected to higher tensile stress in the wall of the flange, reaching a porosity level between 2.2% to 2.8%, depending on the sheet surface.



**Figure 8.16** Porosity history of the bend/unbend effect for 186.0 mm inner hole (Cinotti et al, 2001)

The simulation also predicts necking localization and fracture if the cutout diameter is too small. Reducing the cutout diameter from 186 mm to 180 mm increases the axial strain in the wall region. This further stretching promotes void interaction until a critical porosity value is reached and a macro-crack or fracture appears as is shown in Figure 8.17(b).



**Figure 8.17** Z-flange deformation sequence for two different cutout diameters: (a) 186 mm; (b) 180 mm (Cinotti et al, 2001).

### 8.5 SIMULATION OF ALUMINUM ALLOY TAILOR WELDED BLANKS

Optimization of automotive parts has reached a point where traditional design methods are no longer sufficient or satisfactory for all applications. New applications of high strength steels, aluminum and magnesium alloys, hydroforming, tailored blanking, and various novel design and manufacturing techniques are currently being put into practice by the automotive industry. Tailored blanking is one of these technologies and techniques to simulate and predict the formability of multi-gauge, aluminum alloy tailor welded blanks (TWBs) are presented in this section.

Multi-gauge TWBs consist of two sheets of differing thickness, butt-welded together to form a blank with a step in thickness (Figure 8.18.) For aluminum alloy sheet, the currently favoured welding techniques are generally CO<sub>2</sub> or Nd:YAG laser, although other methods are certainly possible. The use of multi-gauge TWBs is desirable for aluminum sheet since, in addition to greater weight and material tailoring potential within the blank, the formability of multi-gauge aluminum blanks is generally superior to that of equal gauge blanks. In general, the weld metal strength in welded aluminum alloy blanks is less than that of the parent metal (Shi et al, 1993; Stasik et al, 1996; Buste et al, 1999), which contrasts the behaviour of steel welds that tend to be overmatched. Thus higher gauge ratios tend to push failure away from the weld into the more ductile thinner gauge material.

Figure 8.18 shows a typical weld cross-section. It can be observed that the weld is not ideal and exhibits undercut at the top surface (the surface through which the heat was input) and some weld metal porosity. More detailed analysis of typical aluminum TWB weld metallurgy is given by Shakeri et al (2001).

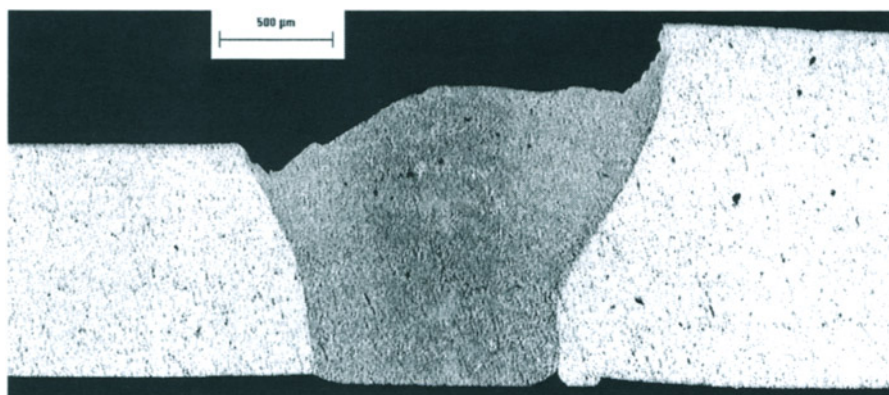


**Figure 8.18** Typical weld cross-section. AA5754 TWB, 1.6 mm sheet joined to 1 mm sheet using Nd:YAG process (Lee, 2002).

Traditional sheet formability tests are more difficult to apply to aluminum alloy TWBs. Buste et al (1999, 2000), report difficulty in promoting large minor strains, on both the draw and stretch sides of the FLD, using the traditional method of varying blank geometry in limiting dome height experiments. Buste et al found that the constraint of the thicker welded sheet prevented large minor strains in the thinner sheet. More recently, large drawing strains were successfully produced using a deep drawn cup test by Lee et al (2000) for the same sheet combinations considered by Buste et al. By combining the two sets of limit strain data from LDH and cup draw experiments, Lee (2002) has successfully extended the FLD for several multi-gauge aluminum alloy TWBs, an example of which is shown in Figure 8.19. Note that the measured limit strain data is taken from circle grid measurements in the thinner sheet adjacent to the weld line as application of grids and actual strain measurement from the irregular weld surface itself was too difficult. The data clustered around the major strain axis (solid symbols) is from the LDH testing (Buste et al, 1999, 2000) from a variety of sample widths, all of which yield nearly plane strain conditions. The

open symbols are from the cup draw tests by Lee et al (2000) and are all “safe” data points, but with large minor strain levels on the draw side of the FLD. The TWB forming limit is drawn as a lower-upper bound region. The upper bound is based upon the LDH data while the lower bound is based upon the cup draw data, as well as known FLD data for the thinner 1 mm sheet material (the solid curve.) In general, Lee et al (2000) and Buste et al (2000) found that the plane strain limit for a multi-gauge aluminum alloy TWB would lie about 20-30% lower than the corresponding value for the thinner parent metal sheet, assuming a good quality weld.

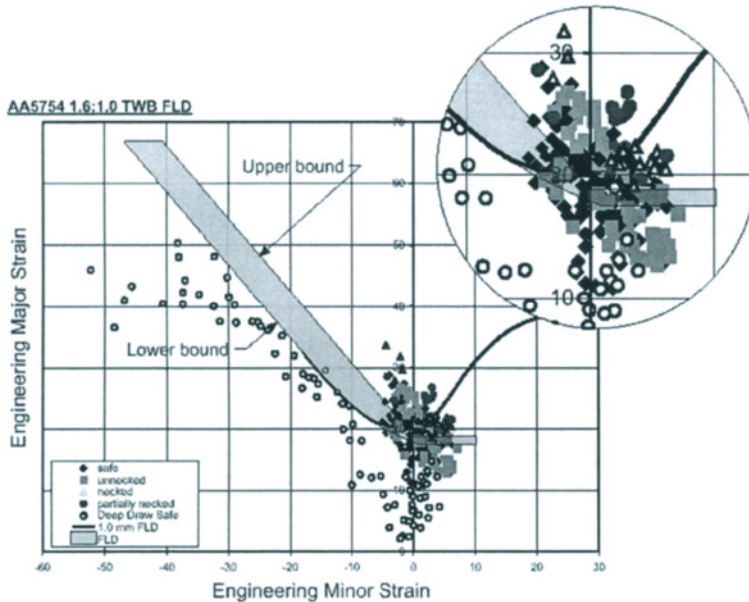


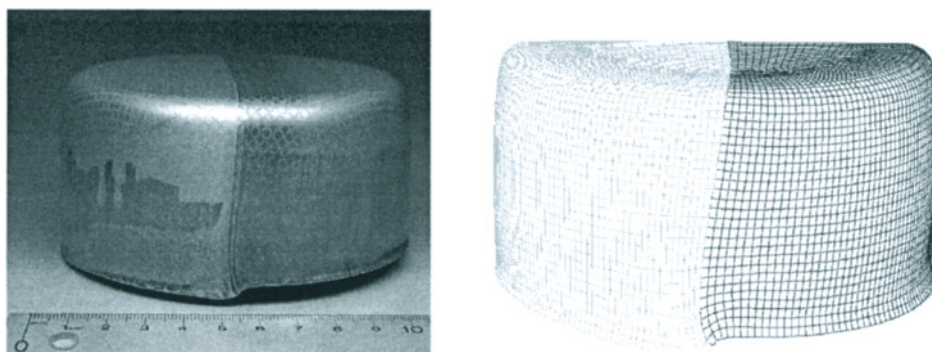
**Figure 8.19** FLD constructed from LDH tests (data shown in inset figure) and cup draw experiments (circles) for AA5754 1.6:1.0 (mm:mm) TWB (Lee, 2002).

### 8.5.1 Simulation of small-scale TWBs

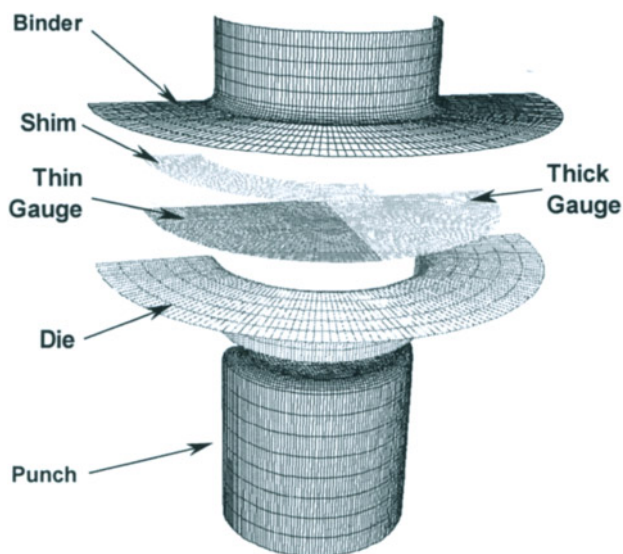
Numerical simulation of the cup draw experiment was performed by Lee et al (2000), using the methods described in Sections 8.1-8.3. The tooling in this case considered a 100 mm diameter punch and incorporated a shim between the thinner side of the blank and the die in order to ensure uniform clamping. Due to the difference in thickness, there was an unequal rate of draw-in between the thick and thin sides of the blank; thus, the weld line was initially offset relative to the punch center to obtain a good final cup profile (Figure 8.20).

Figure 8.21 shows the numerical model used to simulate the cup draw process. The model includes the shim between the blank top surface tooling. The weld line is treated in a simplified fashion as an abrupt change in shell thickness across the weld line. The element reference surfaces are offset an amount equal to the sheet centerline offset in the actual blanks. The abutting elements along the weld line are tied together using a kinematic constraint that enforces translational and rotational continuity across the weld line, thus ensuring the internal moment generated by the sheet offset is captured in the model.

Unfortunately, the use of shell elements does not allow enforcement of through-thickness continuity across the weld line. Thus the through-thickness constraint of the thick sheet on the thinner sheet (and weld region) is not modeled. In addition, the weld itself is not modeled; thus, predicted strains in the thinner sheet are compared to the FLD data (eg. Figure 8.19) in assessment of formability. Buste et al (1999) have shown that the sudden step in shell element size can lead to premature localization in the models, particularly when the loading is principally transverse to the weld line. Examples are presented below.



**Figure 8.20** Photograph (left) of AA5754 cup formed from 178mm, 1.6:1.0 (mm:mm) AA5754 TWB. Predicted shape shown on right. (Lee et al, 2000).



**Figure 8.21** Exploded view of mesh used for TWB cup draw simulation (Lee et al, 2000)



The predicted shape of the blank (also shown in Figure 8.20) agrees well with the observed profiles. Lee et al (2000) also demonstrate that predictions of process variables, such as punch load-displacement history, as well as predicted strain distributions agree relatively well with experimental data.

### 8.5.2 Simulation of large scale TWBs

Numerical simulation of a large scale stamping operation utilizing aluminum alloy TWBs has been undertaken by Lee et al (2001a, b). The part formed is a deep drawn pan, with a punch size of roughly 600 x 400 mm, incorporating a number of features including a double curvature crown and an undulating front sidewall (Figure 8.22.) The tooling for this part also contains drawbeads to control material flow. Unfortunately the tooling was originally created for use with conventional blanks; therefore, it is not designed to accommodate blanks of varying thickness. As in the cup draw model, shims are used to make up the difference in material thickness, preventing wrinkling in the thinner gauge material while providing clamping. The shims are steel and were trimmed to butt up against the outside edge of the drawbeads in the experiment. The model utilized analytical drawbeads; the drawbead locations are also indicated in Figure 8.22.

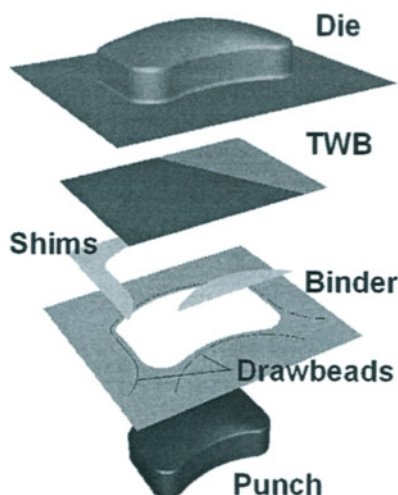


**Figure 8.22** Geometry used by Lee et al, (2001a, b) in their model of a large-scale TWB stamping operation.

The weld line in Figure 8.22 can be discerned as the transition in shading of the blank in the figure and was placed so that the weld line ran across the corner of the final part. Thus the weld experiences stretching across the punch corner as well as a deep draw strain state in the part sidewall. Note that such a placement represents a rather extreme loading case, but was considered by Lee et al (2001a,b) who were primarily concerned with formability prediction and simulation accuracy.

Prior to testing the large scale TWBs, small-scale LDH experiments were performed to check the formability of the welded blanks. It was determined that the large-scale blanks exhibited poor transverse formability as seen in Figure 8.23 which plots plane strain limit strain, as a function of gauge ratio and major strain orientation, for both AA5754

and AA5182 (Lee, 2002.) The third generation blanks referred to in the figure caption are the large-scale blanks, whereas the second generation blanks were earlier, smaller sized TWBs used to generate the FLD data in Figure 8.19. From this data, it can be seen that the 1.6:1.0 (mm:mm) AA5754 TWB has a very low transverse formability of roughly 8% versus a longitudinal limit strain of about 18%.

Figure 8.24 shows the predicted and measured major versus minor strain loci along the weld line for a large scale AA5182 TWB with a 1.5:0.9 (mm:mm) gauge ratio (Lee et al, 2002). The measured strains are plotted as solid symbols while the open symbols are predicted values. It can be seen that there is generally good agreement between the predicted and measured strain distributions. Also plotted are the measured transverse and longitudinal limit strains from the LDH data in Figure 8.23. In the large-scale blank, the major strains in the punch nose region of the weld lie along the longitudinal direction, or along the weld, whereas the minor strains are transverse. Hence, the longitudinal and transverse limits have been plotted as a bounding box on the stretch side of the FLD plot. It was determined that depths of draw in excess of 110mm lead to splitting of the weld at the punch nose. Thus the fact that the measured (and predicted) strains lie just inside the limit strain values for this "safe" blank supports the use of small-scale limit strain data for prediction of formability for large-scale TWBs (Lee, 2002). Additional formability assessment and model validation results for a range of TWBs and blank configurations are given by Lee (2002).

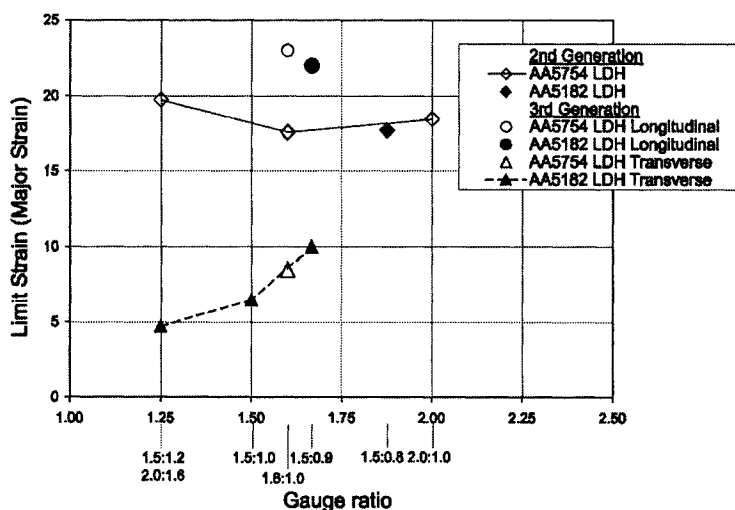
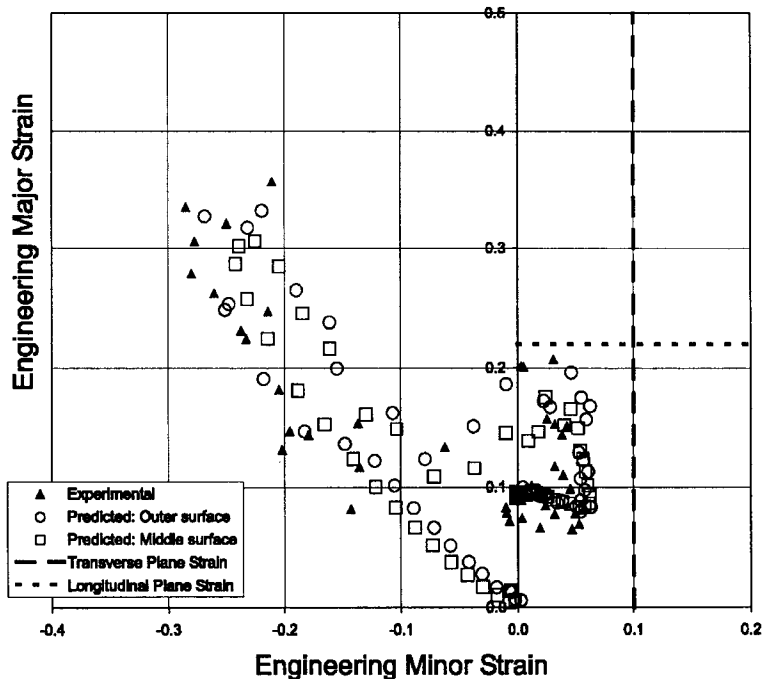


Figure 8.23 Plane strain limit as a function of gauge ratios for AA5754 and AA5182 TWBs (Lee, 2002).





**Figure 8.24** Predicted and measured strain loci for an AA5182 1.5:0.9 (mm:mm) TWB. Depth of draw was 110 mm. (Lee, 2002).

### 8.5.3 Damage prediction in the weld region

Of particular interest in the optimization of TWB welding processes is the role of defects, such as weld metal porosity, in controlling weld fracture (Shakeri et al, 2001). Studies of the influence of porosity in promoting ductile fracture of the weld have been performed by Worswick et al (2001b), utilizing the GTN constitutive model described in Section 8.3.2.2. A simple “strip model” was considered (Figure 8.25) that included the weld region as well as a length of the parent metal sheets on either side of the weld. The weld region was simplified with a concave radius of curvature of 5mm. The mesh shown in Figure 8.25 corresponds to a 2 mm sheet welded to a 1 mm sheet; other gauge combinations, 2:1.6 and 1.6:1 (mm:mm), were also considered, corresponding to experimental configurations tested by Buste et al (1999, 2000). The weld cross-section was meshed fully using brick elements. A plane strain boundary condition was prescribed on the two parallel faces of the model perpendicular to the weld line, with transverse loading applied perpendicular to the weld line along the length of the strip. This corresponds to the transverse plane strain case that should represent the lowest formability condition, as reflected by the data in Figure 8.23.

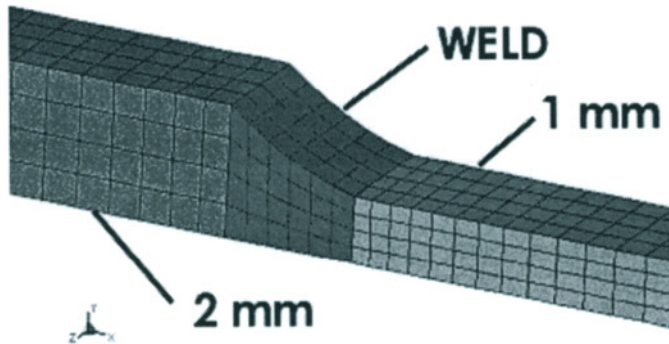


**Figure 8.25** Strip model used to model initial defects and damage in weld region (Worswick et al, 2001b)

The weld metal hardening response was taken to be the same as that of the parent metal. To consider the influence of weld metal porosity, initial porosity values in the weld were assigned ranging from 0% to 2%. Figure 8.26 shows a sequence of a typical predicted necking behavior and final failure for the 2:1 gauge ratio for the case of zero initial porosity. This figure serves to demonstrate the rotation of the weld due to the offset introduced by the alignment of the sheets along a common side. In the absence of weld failure, necking is pushed away from the weld region and weld toe into the thinner parent metal sheet, as observed by Buste et al (1999, 2000), due to the through-thickness constraint of the thicker sheet and weld. Ductile fracture through void nucleation, growth and coalescence, ensues within the thinner parent sheet, with a nominal failure strain of about 17%.

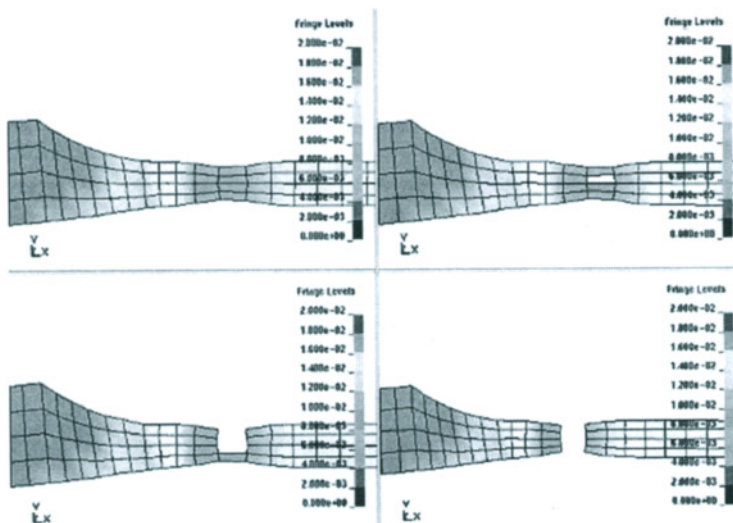


**Figure 8.26** Sequence of neck development for a 2:1 TWB with zero weld porosity. Fringes are of predicted porosity and range from 0 to 2%. (Worswick et al, 2001b).

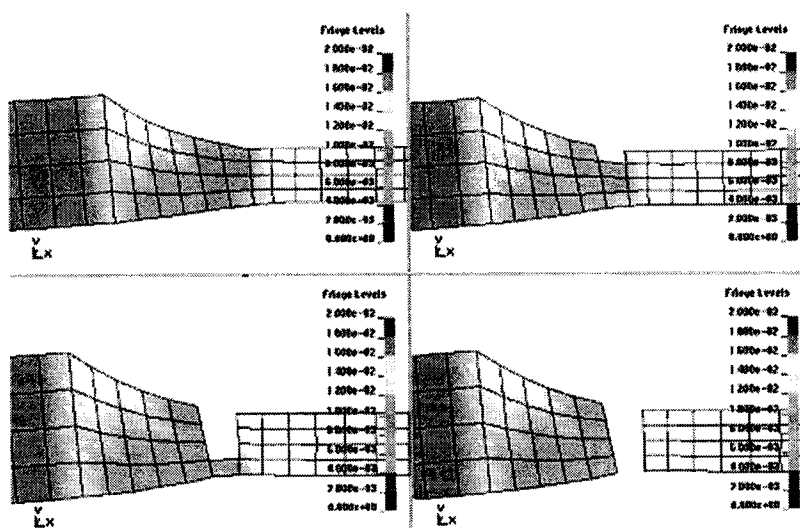


**Figure 8.27** Sequence of weld failure for a 2:1 TWB with 1.6% initial weld porosity. Fringes are of predicted porosity and range from 0 to 2%. (Worswick et al, 2001b).

Figure 8.27 shows the predicted failure sequence for an initial weld porosity of 1.6%. In this case, failure is predicted in the weld metal near the weld toe at a major strain of about 16%. The growth and coalescence of pre-existing cavities or porosity in the weld was high enough to cause fracture in the weld, despite the thicker cross-section. In general, there will be a transition from parent metal failure to weld failure as weld porosity increases. This transition will also be a function of gauge ratio, as shown in Figure 8.28 from Worswick et al (2001b), with lower gauge ratio TWBs being more sensitive to weld defects.

Although it is recognized that the numerical results are quite mesh sensitive, the trends of these curves are considered a good estimate of the impact of initial weld porosity in TWB specimens under plane strain tension. The trends seen in the predictions by Worswick et al (2001b) agree with observed failure behaviour in NVEB and Nd:YAG TWBs reported by Shakeri et al (2001). In that work, the NVEB welds exhibited solidification shrinkage porosity in excess of 1.0%. For these NVEB cases, weld failure occurs in all 2:1.6 gauge ratios and some 1.6:1 samples, while only parent failures are observed in 2:1 gauge ratio blanks. In contrast, the Nd:YAG welds exhibit very low porosity and do not experience weld failures under transverse loading for all gauge ratios tested.

### Major Failure Strain Vs Initial Weld Porosity

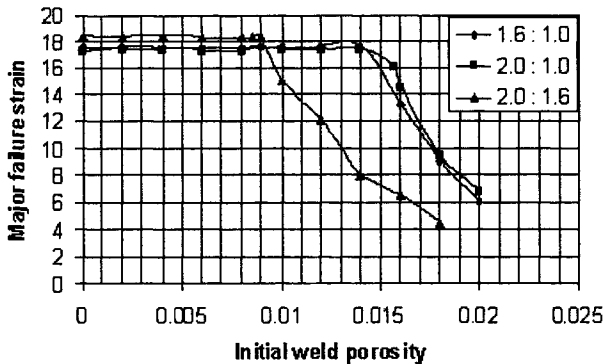


Figure 8.28 Predicted TWB failure strain as a function of initial weld porosity and gauge ratio. (Worswick et al, 2001b).

## 8.6 SIMULATION OF ELECTROMAGNETIC FORMING

The phenomenon of hyperplasticity, which allows significant increases in strain due to the inertial and strain rate stabilisation of material failure modes, is utilised in high velocity forming processes. Experimental work in high velocity forming such as electromagnetic forming has been shown by Padmanabhan (1997) to promote increased formability, suppress wrinkling, reduce springback and improve surface finish. Typical strain rates observed by Padmanabhan (1997) are  $10^3$ - $10^4$ /s corresponding to velocities ranging from 50-250m/s. Electromagnetic (EM) forming typically requires only a few hundred microseconds to form a part.

To better understand the physics and behaviour of EM forming, a numerical model of the process is highly desired. Finite element modelling of EM forming is challenging due to its complex nature, which requires tight coupling of EM phenomena with changing work piece geometry. Numerical simulation of EM fields during sheet forming was undertaken by Oliveira et al (2001a,b) using the transient EM field simulation module within ANSYS/Multiphysics. Simulation of the work piece and air deformation was performed using LS-DYNA (Hallquist, 1998). EM calculations differ from conventional sheet forming in the requirement to mesh the free space surrounding the coil/workpiece system. Due to the drastically different air and sheet metal properties, preserving the quality of the air elements is challenging. Poor element quality in the air elements can reduce the time step severely, which substantially increases the run times of the simulation to unacceptable levels. These elements not only cause problems in the explicit code but also lead to inaccuracies in the EM field simulation.

An analysis of an EM forming operation by Oliveira et al (2001a,b) is presented in which the interaction between the EM and structural codes is treated as a "loosely" coupled problem. The EM analysis is performed while continuously updating the geometry over several steps during deformation. The EM forming of a hemispherical dome with a single "bar" coil is considered.

### 8.6.1 EMF equations

Maxwell's equations are the basis of all electrical and magnetic phenomena. The EM forming components can be lumped together and simplified into a circuit containing a capacitor (C), resistor ( $R_a$ ) and inductor ( $L_a$ ). Note that  $L_a$  and  $R_a$  are lumped parameters of the system. This circuit is inductively coupled to a short circuit comprised of an inductor ( $L_b$ ) and a resistor ( $R_b$ ) representing the sheet metal.

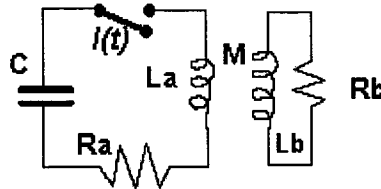


Figure 8.29 Lumped Parameter EM Circuit

The behavior of such a system is described by the following differential equation, which is derived from Maxwell's equations.

$$\frac{d^2 I(t)}{dt^2} + 2\xi\omega \frac{dI(t)}{dt} + \omega^2 I(t) = 0 \quad (8.28)$$

where  $I(t)$  is the current caused by discharging capacitor,  $\xi$  is the damping term, given by

$$\xi = 0.5 * R_a \sqrt{C / L_a} \text{ and } \omega \text{ is the natural frequency, given by } \omega = \sqrt{1 / L_a C}.$$

In electromagnetic forming  $\xi$  is less than unity, which represents an underdamped system. In arriving at the above differential equation two assumptions are required. The workpiece is assumed to remain stationary and static pressures are assumed to be uniform as presented by Panshikar (2000). Solving the above differential equation provides the current as a function of time in the circuit.

$$I(t) = \frac{V_o \sqrt{C / L_a}}{\sqrt{1 - \xi^2}} e^{-\xi\omega t} \sin(\omega t) \quad (8.29)$$

where  $V_o$  is the original voltage across the capacitor. The voltage behavior can be approximated by the following equation from Beley et al (1996).

$$V(t) = V_o e^{-Ra/2La} \sin(\omega t) \quad (8.30)$$

The time varying currents in the coil produce a transient magnetic flux. It is the interaction between the two circuits that gives rise to an induced electromotive force through a process known as mutual induction. Mutual inductance ( $M$ ) depends on the geometry of both circuits and their orientation with respect to one another. As the separation distance increases,  $M$  decreases due to the decreased flux linkage between the two circuits. It is significant to note that, due to the strong dependence on geometry, the inductance of the

blank changes through time. The frequency of the current ( $\omega$ ) determines how long the peak current is going to last. With higher frequencies the duration of the peak current is reduced, which decreases forming efficiency.

### 8.6.2 Electromagnetic forming finite element model

A straight bar copper coil (50mm x 10mm x 200mm) is located 1mm away from an aluminum AA5754 sheet (200mm x 1.6mm x 200mm), as depicted in Figure 8.30 which shows a half-model of the system. The blank is fastened to the die by a clamp around the perimeter. The die has the shape of a hemispherical dome of radius 30mm and height of 20mm. The resistivities of copper and aluminum were taken as  $1.7\text{e-}8$  and  $2.77\text{e-}8$  ohm/m respectively.

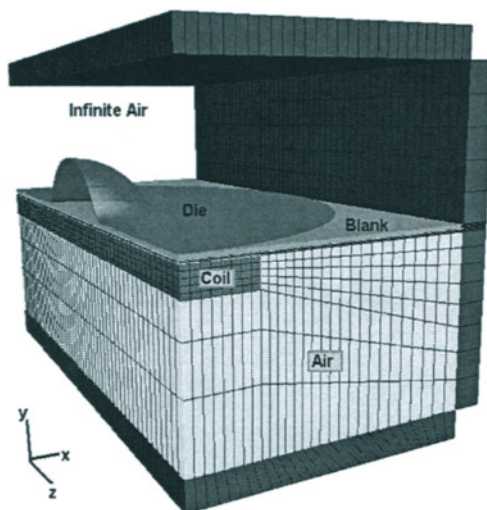


Figure 8.30 Finite Element Components (Oliveira et al, 2001b).

In simulating the electromagnetic phenomena, the air surrounding the system is required to model the magnetic field generated by the coil and blank. So-called infinite air elements are also used to simulate the field at “large” distances from the system. Note that the air elements above the blank were not modelled for numerical efficiency. The omission of these air elements reduces the EM force acting on the blank by a small percentage. A scale factor on the force is introduced in order to compensate for this reduction.

In-house software (Oliveira et al, 2001a,b) was developed to allow the two finite element codes to interact with one another. The process of performing the electromagnetic analysis while updating the geometry is performed over a series of  $4\mu\text{s}$  steps during the entire deformation time. Details of the finite element field equations are omitted here, but are described by Olivera (2001a)

### 8.6.3 EM field modelling

The capacitance, inductance and resistance of the system are  $2.5\text{e-}4$  F,  $2.02\text{e-}7$  H and  $5.66\text{e-}3$  ohms, respectively, and the charging voltage is 10kV. The current in the coil (from equation 8.29) is specified over the period of each time step. In order to capture the transient magnetic field a sufficient number of air elements are required between the coil and the workpiece.

The current density distribution in the coil is highest in the regions that are nearest to the workpiece due to the interaction of the magnetic fields generated by the two conductors (coil and workpiece). The current density distribution in the workpiece follows the geometrical profile of the coil. As the workpiece begins to deform the current density distribution becomes most intense at areas near the rim of the hemispherical dome. Hence, the current density distribution throughout the coil and sheet will change with time due to changes in geometry. Other parameters such as self-inductance, mutual inductance and flux are also affected.

The intensity of the force in regions of the workpiece is proportional to the current density in that region. Figure 8.31 illustrates the current density in the z-direction along the surface of the blank facing the coil at a time of  $100\mu\text{s}$ . Current flow in the blank is opposite to the direction in the coil and in the early stages follows the same geometrical path as the current in the coil. As the blank deforms, the current density distribution is greatest near the rim of the dome. Consequently the EM forces are lower near the centre of the dome, from which it can be concluded that the straight bar coil is not well suited for deformation of a blank into a hemispherical dome. To overcome this limitation, Oliveira et al (2001a,b) scaled the forces acting on the blank in order to have the desired deformation occur. The emphasis of the use of this model is placed on understanding the effect of changing workpiece geometry on the physics of the problem at hand. A more appropriate coil would be the spiral or “pancake” coil that would promote the current density to concentrate in the deforming regions of the blank. As a simplifying assumption the effect of the steel die on the system is neglected.

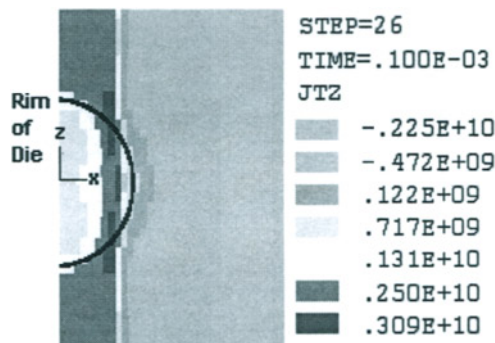


Figure 8.31 Current density distribution in z-direction at  $t=100\mu\text{s}$  (Oliveira et al, 2001b).

#### 8.6.4 Structural Modelling

As a simplifying assumption, a non-rate dependant material model was adopted by Oliveira et al (2001a,b). A high strain rate material model incorporating rate and temperature effects is currently under development. The blank has five solid elements through thickness in order to capture bending. The total time for forming is approximately  $300\mu\text{s}$ , with most of the momentum being transferred to the blank in the first pulse ( $22.3\mu\text{s}$  or half period) of force as observed by Oliveira et al (2001a).

The deformation of the blank at intermediate stages is shown in Figure 8.32. A cross section of the blank illustrates the behaviour of the workpiece during deformation. In the first state the blank is initially at rest, while at  $57\mu\text{s}$  the edges of the blank are actually at



a higher position than the centre. At  $77\mu\text{s}$  the blank is forming into the dome with the centre still lagging behind the edges. The final profile is obtained after  $300\mu\text{s}$ , see Figure 8.33.

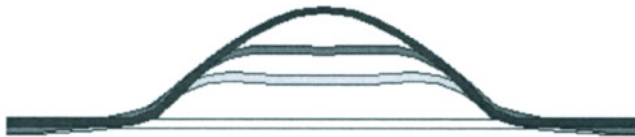


**Figure 8.32** Intermediate Stages of a Cross Section of the Blank During Deformation (Oliveira et al, 2001b).

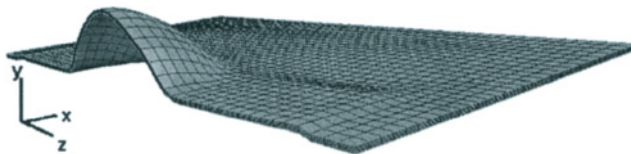


**Figure 8.33** EM Formed Dome (Oliveira et al, 2001b).

The evolution in time of the maximum principal strain along the mid-surface of the blank is presented in Figure 8.34. In the first  $90\mu\text{s}$ , the strain is the largest in the region in contact with the rim of the die. It is of interest to note that in the first  $60\mu\text{s}$ , regions just inside of the rim undergo much more strain than at the center which experiences only a very small amount of strain during this period. Between  $80\text{--}100\mu\text{s}$  the strain rate in the centre becomes quite large, reaching rates in the range  $10^3 - 10^4 \text{ s}^{-1}$ , since the material in the centre is allowed a greater free flight distance to accelerate prior to contacting the die. The final strain profile is as expected, with the largest strains of 0.22 at the centre and 0.13 at the rim.

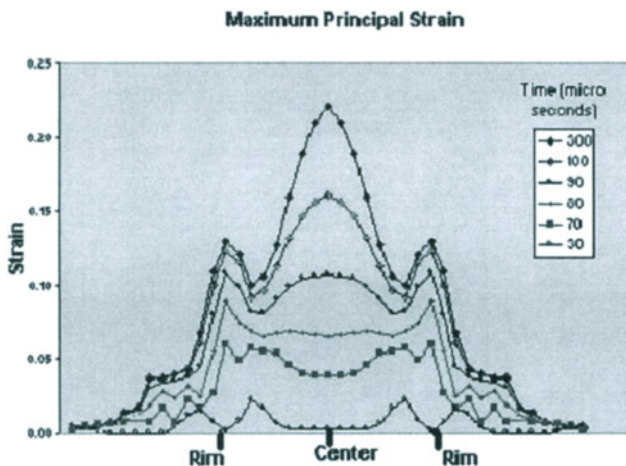


**Figure 8.34** Time Evolution of Maximum Principal Strain (Oliveira et al, 2001b).



## 8.7 MODELLING PRODUCT PERFORMANCE – DENT RESISTANCE

A natural extension of simulation of the forming of a sheet metal panel is the simulation of the performance of the product in-service. One example of product performance modeling, as applied to stamped panels, is the numerical simulation of panel dent resistance. Dent resistance is an important issue in the automotive sector since panel dent resistance often governs how thin a panel can be made, which impacts vehicle cost and weight. When considering dent resistance, there are two different mechanisms by which the panel can be dented. These mechanisms are generally termed static or dynamic denting, the difference being the rate of load application. Here, both of these denting mechanisms are examined and the finite element modelling practices that best capture the denting processes.

Automotive panel stiffness is known to influence the dent resistance characteristics of the panel. When considering static dent resistance, there have been conflicting statements regarding the role of stiffness. Whereas DiCello *et al* (1974) concluded that decreased panel stiffness aided static dent resistance, Yutori *et al* (1980) concluded that increased panel stiffness aided static dent resistance. Their conflicting statements were due to their differing definitions of static dent resistance. DiCello *et al* defined a panel as having good static dent resistance if it could absorb more energy before a permanent indentation occurred. Conversely, Yutori *et al* defined a panel as having good static dent resistance if it could support a large load prior to permanent indentation.

The role stiffness plays in the dynamic dent resistance of a panel has also been debated. There is one certainty, however, that dent resistance, both static and dynamic, is a function of many coupled influences, such as panel thickness, yield strength, curvature and support conditions. The presence of these many coupled influences make the use of finite element analysis an attractive method for prediction of the dent resistance characteristics of automotive panels.

One of the earliest examples of a FEM simulation of static denting was in 1980 by Yutori *et al* (1980) who used FEA to look at strain levels underneath the indenter as the panel was displaced. Their model used only 30 axis-symmetric elements and the indenter was described as a point load. Following this study, the work of Sakai *et al* (1983) compared finite element stiffness values to those obtained from laboratory panels. They were able to show good correlation between panel stiffnesses in both the primary and secondary stiffness regions; however, convergence issues prevented them from obtaining a residual dent depth after unloading. As more computing power became available, the size of the models used in static dent resistance computations became larger and more complex. Alaniz *et al* (1990) showed the applicability of the finite element method to predict panel stiffness in the secondary and final stiffness regions, but did not incorporate panel forming data in their analysis. Predictions of dynamic dent resistance are given by Nomura *et al* (1984).

Finite element codes have progressed as well. Werner (1993) compared the results of static dent tests obtained using three different finite element codes, MARC, ABAQUS, and LS-DYNA. Interestingly, this was the first time a meshed indenter was used instead of a point load at the dent site. It was also the first time a residual dent depth was obtained after unloading of the indenter. Unfortunately, poor correlation with the experimental results was obtained.

Montgomery *et al* (1994) performed several finite element analyses on laboratory type panels of varying curvature. They were able to show that for stiffer panels, significant dents can occur at loads slightly greater than the oil-canning load; however, for less stiff panels, the dent initiation load was farther along the secondary stiffness curve. Sabbagh *et al* (1995) predicted static dent depths in actual automotive panels. Two doors were modelled,

both considering several dent locations. One of the doors was a complete assembly, including the inner and outer panel, with the mastic modelled as a linear spring. Their work was also the first to include local refinement of the finite element mesh in the denting region in order to gain sufficient resolution. Material stress-strain data for the finite element simulations was obtained from tensile sections cut from existing doors. They were able to establish that FEA was a viable technique to predict the denting characteristics of automotive panels. Chavali *et al* (1996) continued the work of Sabbagh *et al* (1995) but used a forming simulation instead of tensile data to account for the initial forming of the door panel. This was the first example of incorporating forming strains from a finite element analysis directly into a subsequent denting analysis.

The work of Raghavan *et al* (1997) again used forming strains from a forming analysis performed using LS-DYNA. The results of this analysis were subsequently used in a static denting analysis using the implicit LS-NIKE software code. No local mesh refinement was used between the forming and denting steps, as the samples tested were small and could be refined prior to the forming simulation. Interestingly, they concluded that there was a need for better interfaces between implicit and explicit finite element codes to solve complex multi-stage forming problems such as denting.

#### **8.7.1 Numerical simulation of panel forming and denting**

Recent work at the University of Waterloo (Hodgins *et al*, 2000, 2001; Thomas *et al*, 2002) has examined the numerical prediction of automotive panel dent resistance under both static and dynamic loading. This research has included consideration of the entire panel forming process prior to dent loading. In this manner, the degree of work hardening and panel thinning can be properly accounted for in the denting analysis. In addition, the strengthening effect associated with heat treatment during the paint bake cycle has also been considered for heat treatable closure sheet alloys, such as AA6111 (Lloyd, 1998).

Thomas *et al* (2001, 2002) developed a finite element model considering the stamping of a medium-scale panel followed by dynamic and static dent loading. The tooling is essentially that considered by Lee *et al* (2001a,b) in their study of TWB formability, described in Section 8.5 of this chapter. Figure 8.35 shows the explicit dynamic finite element model used by Thomas *et al* (2001, 2002) to simulate the forming process. AA6111-T4 sheet of three different thickness values, 0.81, 0.93 and 1.00mm, was simulated. Initially, 5785 deformable elements were used in the blank, however this number increased to more than 12000 elements during the forming simulation, as adaptive refinement was used to refine the mesh in the blank during forming. The material was modeled using the Barlat-89 yield criterion (Barlat *et al*, 1989) to capture anisotropy, particularly during forming.

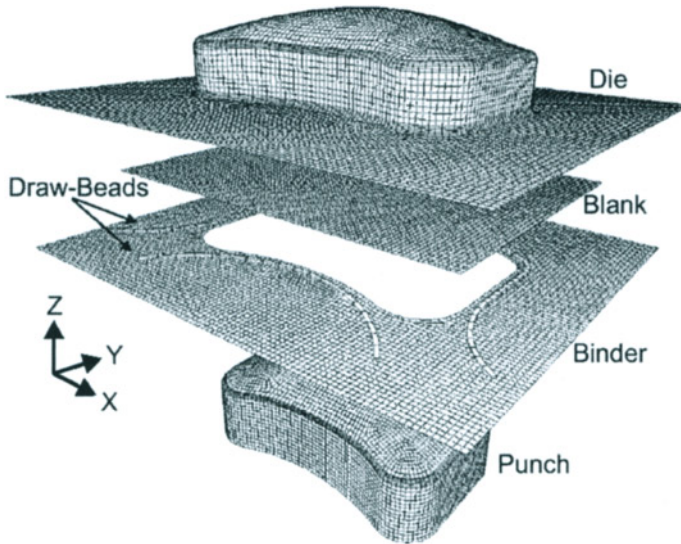


**Figure 8.35** Finite element model of panel forming process used prior to dent analysis (Thomas, 2001).

After forming, the tooling was deleted and an implicit springback analysis was performed to obtain a final part shape. Tensile properties were adjusted to account for the paint bake heat treatment. This amounted to an increase in flow stress on the order of 70-80 MPa (Thomas et al, 2001, 2002). Support conditions were added to the flange region of the formed blank and local mesh refinement (Figure 8.36) was performed in the region of the indenter using an in-house code developed by Thomas (2001). This code first generates a bi-cubic Hermite F-patch representation of the meshed surface to be refined. New nodes created during refinement are positioned on this surface, ensuring a smooth representation of the curvature of the refined surface. The refined mesh features 1mm sized elements under the indenter.

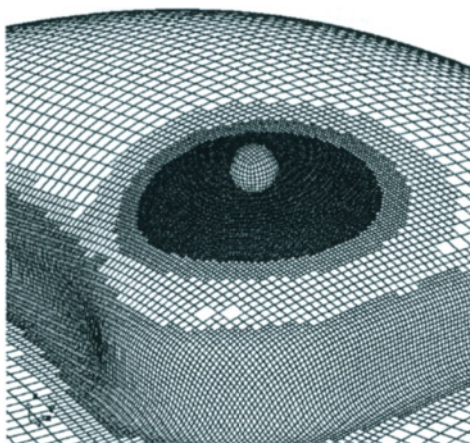


**Figure 8.36** Refined mesh and indenter positioned prior to dent analysis (Thomas, 2001).

Both static and dynamic analyses were performed on the formed panels using static implicit and explicit dynamic calculations, respectively. Figure 8.37 shows the predicted and measured static load-displacement behaviour of one dent site on a 0.93mm panel. The response is highly non-linear, exhibiting a knee in the curve indicative of “oil canning” or “snap through” behavior. The residual dent depth as a function of applied static load is shown in Figure 8.38 for the same panel and location.

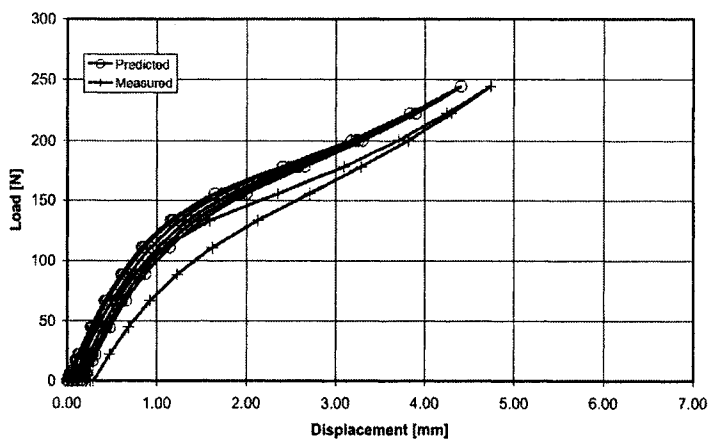


**Figure 8.37** Predicted and measured load versus displacement response for a formed and paint baked 0.93mm AA6111 panel (Thomas, 2001).

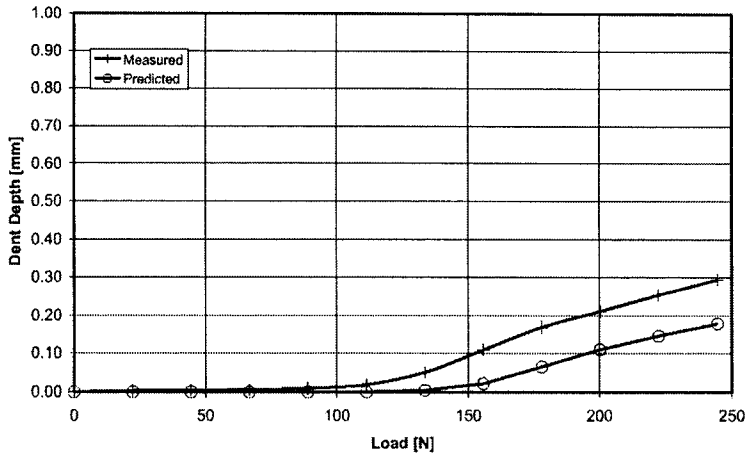


**Figure 8.38** Predicted and measured residual static dent depth for a formed and paint baked 0.93mm AA6111 panel (Thomas, 2001).

Predicted dynamic denting behavior for the 0.93mm AA6111 panel is plotted in Figure 8.39. In general, Thomas et al (2001, 2002) concluded that static and dynamic dent analysis could capture observed dent behavior, but suffered quantitative errors due to the extremely small levels of indentation associated with a “barely visible dent”.

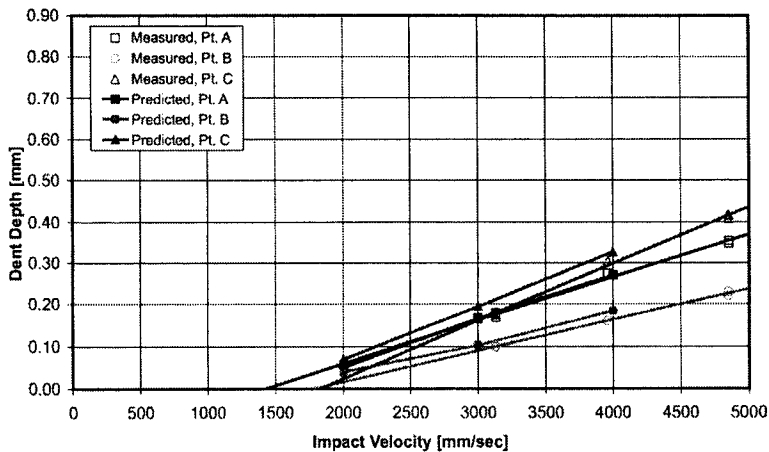


**Figure 8.39** Predicted and measured residual dent depth for several sites on a formed and paint baked 0.93mm AA6111 panel impacted by a 25mm steel ball bearing (Thomas, 2001).

### 8.7.2 Closure sheet-inner panel interactions

Automotive panels are often assemblies comprising an outer closure sheet supported by an inner panel or inner panel assembly. The two are typically joined using spot welds along a hem flange on the outside edge of the panel assembly and soft adhesive mastic beads are

used inside the span of the panel to support the outer closure panel. Incorporation of inner support panels within automotive dent simulations has been undertaken by Hodgins et al (2001). Figure 8.40 shows the type of panel assembly simulated by Hodgins et al which features both the mastic and spot weld support between the closure and inner panels. In general, Hodgins (2001) found that the dent predictions accounted for the effect of the inner support panel relatively well; however, there exists a requirement to improve the numerical description of the mastic material between the closure and inner panels.

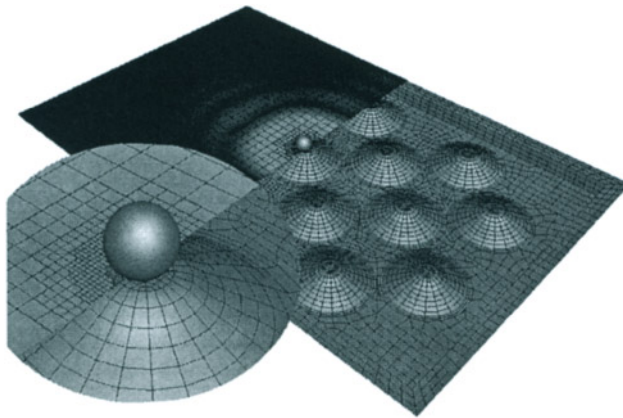


**Figure 8.40** Structural panel assembly modelled by Hodgins (2001).

## 8.8 SUMMARY AND FUTURE

Progress in mathematical representation of sheet metal forming processes over the last decades has indeed been impressive and has lead to an extremely realistic predictive capability. Modeling now often leads the way in tooling development and can greatly reduce die try-out time. There still exists a requirement for improvements in material constitutive and tribological models, for example, to reduce the uncertainty remaining in our predictions. The algorithmic cost of these models will be supported by future increases in computing capacity, in particular in terms of massively parallel computing architectures which offer extreme scalability. Visualization and immersive virtual reality environments will offer revolutionary opportunities for tooling and process designers to experience true virtual prototyping prior to cutting of tooling. The fidelity of the calculations and algorithms that drive virtual reality predictions is critical to ensure the success of virtual reality forming environments. Our ability to simulate forming processes will be further taxed through the introduction of new higher strength or lighter materials, which in turn will promote the use of simulation to reduce risk associated with their introduction into a manufacturing process.

## ACKNOWLEDGEMENTS

I wish to thank and acknowledge the contributions made to this research by Professor Keith Pilkey of Queens University, as well as my own students, Z.T. Chen, N. Cinotti, N. Dwyer, E. Harpell, B. Hodgins, C. Lamontagne, Y. Lee, D. Oliviera, D. Thomas, C. Thomson, and K. Williams, and research associates, A. Buste, D.W. Jung, X. Lalbin, H. Shakeri and S. Truttmann. I also thank M.J. Finn, D.J. Lloyd, K. Gong, F. Feng and Jo Ann Clarke of ALCAN International, B. Lievers of Queens University, Professor M. Jain of McMaster University and P. Martin of CANMET. Financial support for this research was provided by the Natural Sciences and Engineering Research Council of Canada, Materials and Manufacturing Ontario, and ALCAN International Limited.

## REFERENCES

- Alaniz, C.L., Brookes, L.E., and Seel, T.N. (1990), Investigation of body panel stiffness as predicted by finite element analysis, SAE Paper 900716.
- Asaro, R.J., and Needleman, A. (1985), Texture development and strain hardening in rate dependent polycrystals, *Acta Metallurgica*, **33**, 923-953.
- Barlat, F., and Lian, J.I. (1989), Plastic Behavior and Stretchability of Sheet Metals Part I: A Yield Function for Orthotropic Sheets Under Plane Stress Conditions, *Int. J. Plast.*, **5**, 51-56.
- Barlat, F., Lege, D.J., and Brem, J.C. (1991), A Six-Component Yield Function for Anisotropic Materials, *Int. J. Plast.*, **7**, 693-712.
- Barlat, F., and Chung, K. (1993), Anisotropic potentials for plastically deforming metals, *Modelling and Simulation in Materials Science and Engineering* **1**, 403-416.
- Barlat, F., Chung, K., and Richmond, O. (1993), Strain rate potential for metals and its application to minimum work path calculations, *Int. J. Plast.*, **9**, 51-63.
- Barlat, F., Maeda, Y., Chung, K., Yanagawa, M., Brem, J.C., Hayashida, Y., Lege, D.J., Matsui, K., Murtha, S.J., Hattori, S., Becker, R.C., and Makosey, S., (1997), Yield function development for aluminum alloy sheets, *J. Mech. Phys. Solids*, **45**, 1727-1763.
- Barlat, F., Yoon, J.W., Dick, R.E., Pourboghrat, F., Choi, S.H., Brem, J.C., Chung, K., Lege, D.J., and Chu, E., (2000), Plane stress yield function for aluminum sheets, submitted to *Int. J. Mech. Sci.*
- Beaudoin, A.J., Dawson, P.R., Mathur, K.K. and Kocks, U.F. (1995), A hybrid finite element formulation for polycrystal plasticity with consideration of macrostructural and microstructural linking, *Int. J. Plast.*, **11**, 501-521.
- Beley, I.V., Ferrtik, S.M., and Khimenko L.T. (1996), *Electromagnetic Metal Forming Handbook*, English Version of Russian book translated by M.M. Altynova, Ohio State University.
- Belytschko, T., Lin, J. I., and Tsay, C. (1984), Explicit Algorithms for the Nonlinear Dynamics of Shells, *Comp. Meth. Appl. Mech. Engng.*, **42**, 225-251.
- Budiansky, B. and Wang, N.M. (1966), On the Swift Cup Test, *J. Mech. Phys. Solids*, **14**, 357-374.
- Buste, A., Lalbin, X., Worswick, M.J., Clarke, J.A., Finn, M.J., Altshuller, B., and Jain, M. (1999), Prediction of Strain Distribution in Aluminum Tailor Welded Blanks, *Proc. Numsheet'99*, France, September.
- Buste, A., Lalbin, X., Worswick, M.J., Clarke, J.A., Altshuller, B. Finn, M.J., and Jain, M. (2000), Prediction of Strain Distribution in Aluminum Tailor Welded Blanks for Different Welding Techniques, *Canadian Metallurgical Quarterly*, **39**, (3), 493-502.



- Cazacu, O. and Barlat, F. (2001), Generalization of Drucker's Yield Criterion to Orthotropy, *Math. Mech. Solids*, **6**, 613-630.
- Chavali, R.N. and Song, W. (1996), Coupling forming and denting simulation for automotive closure panels, ISATA 1996, Paper Number 96NM098.
- Chen, B., Wu P.D., Xia, Z.C., MacEwen, S.R., Tang, S.C., and Huang, Y. (2000), A dilatational plasticity theory for aluminum sheets, in *Multiscale Deformation and Fracture in Materials and Structures, the James R. Rice 60th Anniversary Volume* (eds. Chuang T-J and Rudnicki JW), Kluwer Academic Publishers, Dordrecht, The Netherlands, 17-30.
- Chen, Z.T., Worswick, M.J., Cinotti, N., Pilkey, A.K., and Lloyd, D.J. (2002), A Linked FEM-Percolation Damage Model of Aluminum Alloy Sheet Forming, submitted to *Int. J. Plast.*, March 6.
- Chiang, D. C. and Kobayashi, S. (1966), The Effect of Anisotropy and Work-Hardening Characteristics on the Stress and Strain Distribution in Deep Drawing, *J. Engng. Industry*, Transactions of the ASME, November, 443-448.
- Chu, E., Shi, M. F., and Gerdeen, J. C. (1988), Certain Aspects of the Limiting Drawing Ratio in Sheet Metal Forming Processes, *Controlling Sheet Metal Forming Processes*, Proceedings of the 15th Biennial Congress of the IDDRG, May 15-18, Dearborn, Michigan, 171-183.
- Chung, K. and Shah, K. (1992), Finite Element Simulations of Sheet Metal Forming For Planar Anisotropic Metals, *Int. J. Plast.*, **8**, 453-476.
- Chung, S. Y. and Swift, H. W. (1951), Cup-drawing from a Flat Blank: Part 1. Experimental Investigation, *Proc. Inst. Mech. Eng.*, **165**, 199-211.
- Cinotti, N., Worswick, M.J., Shakeri, H.R., Truttmann, S., Finn, M., Jain, M., and Lloyd, D.J. (2001), Stretch Flange Formability of Aluminum Alloy Sheet: Numerical Investigation, *Proc. of The 4th International ESAFORM Conference on Material Forming*, Liege, Belgium, 237-240.
- DiCello, J.A. and George, R.A. (1974), Design criteria for the dent resistance of auto body panels. SAE Paper 740081.
- Flanagan, D. P., and Belytschko, T. (1981), A Uniform Strain Hexahedron and Quadrilateral with Orthogonal Hourglass Control, *Int. J. Num. Meth. Engng.*, **17**, 679-706.
- Ghosh, A.K. (1975), The Effect of Lateral Draw-In on Stretch Formability, *Metals Engineering Quarterly*, **15** (3), 53-64.
- Ghosh, A.K., and Laukonis, J.V. (1976), The Influence of Strain-Path Changes on the Formability of Steel Sheet, *9<sup>th</sup> Biennial Congress of the IDDRG, Sheet Metal Forming and Energy Conservation*, ASM Publication.
- Graf, A., and Hosford, W. (1993), Calculations of Forming Limit Diagrams for Changing Strain Paths, *Metall. Trans.*, **A**, **24**, 2497-2501.
- Graf, A., and Hosford, W. (1994), The Influence of Strain Path Changes on Forming Limit Diagrams of Al6111-T4, *Int. J. Mech. Sci.*, **36** (10), 897-910.
- Gurson, A.L. (1975), *Plastic flow and fracture behaviour of ductile materials incorporating void nucleation, growth and interaction*, Ph. D. Thesis, Brown University, Providence, R.I.
- Gurson, A.L. (1977), Continuum theory of ductile rupture by void nucleation and growth-Part I. Yield criteria and flow rules for porous ductile media, *J. Engng. Mater. Tech.*, **99**, 2-15.
- Hallquist, J.O. (1998), *LS-DYNA Theoretical Manual*, Livermore Software Technology Corporation, Livermore, California, USA.



- Harpell, E.T. (1997), *Numerical Predictions of Limiting Draw Ratio in Aluminum Cylindrical Cup Drawing*, M.Eng. Thesis, Carleton University, Ottawa, Ontario, Canada.
- Harpell, E., Worswick, M.J., Finn, M., Jain, M., and Martin, P. (2000), Numerical Prediction of Limiting Draw Ratio of Aluminum Alloy Sheet, *J. Mat. Proc. Tech.*, **100** (1-3), 131-141.
- Harpell, E., Worswick, M. J., Finn, M., Galbraith, C., and Martin, P. (1996a), Limiting Draw Ratio Prediction and Anisotropy in 5754 Aluminum Alloy Sheet, *13th Symposium on Engineering Applications of Mechanics: Manufacturing Science and Engineering*, CSME Annual Forum, McMaster University, Hamilton, Ontario, Canada, May 7-9, 108-114.
- Harpell, E., Lamontagne, C., Worswick, M. J., Martin, P., Finn, M., and Galbraith, C. (1996b), Deep Drawing and Stretching of Al 5754 Sheet: LS-DYNA3D Simulation and Validation, *Numisheet 96': 3rd International Conference: Numerical Simulation of 3-D Sheet Metal Forming Processes - Verification of Simulations with Experiments*, Dearborn, Michigan, September 29 - October 3, 386-393.
- Hayashida, Y., Chung, K., Maeda, Y., Barlat, F., Matsui, K., Hashimoto, H., Brem, J.C., Hattori, S., Lege, D.J., Tanagawa, M., and Murtha, S.J. (1995), FEM Analysis of Punch Stretching and Cup Drawing Tests for Aluminum Alloys Using a Planar Anisotropic Yield Function, *Simulation of Materials Processing: Theory and Applications*, Numiform 95, Ithaca, New York, June 18-21, 717-722.
- Hecker, S.S. (1974), A Cup Test for Assessing Stretchability, *Metals Engineering Quarterly*, **14** (4), 30-36.
- Hill, R. (1948), A Theory of Yielding and Plastic Flow of Anisotropic Metals, *Proc. Royal Soc. A*, **193**, 281-297.
- Hill, R. (Hill, 1979), Theoretical Plasticity of Textured Aggregates, *Math. Proc. Cambridge Phil. Soc.*, **85**, 179-191.
- Hill R. (1990), Constitutive Modelling of Orthotropic Plasticity in Sheet Metals, *J. Mech. Phys. Sol.*, **38** (3), 405-417.
- Hodgins, B. (2001), *The Numerical Prediction of the Dent Resistance of Medium Scale Aluminum Structural Panel Assemblies*, M.A.Sc. Thesis, University of Waterloo, Waterloo, Ontario, Canada.
- Hodgins, B., Thomas, D., Jung, D.W., Worswick, M.J, Finn, M.J. and Gong, K. (2000), *Finite Element Modelling of Denting of Aluminum Autobody Panels*, Proceedings COM '2000, The Metallurgical Society of CIM, Ottawa, August 20-23.
- Hodgins, B., Worswick, M.J., Thomas, D., Finn, M., and Gong, K. (2001), Dent Resistance of Medium-Scale Aluminum Structural Assemblies, SAE Paper 01B-119.
- Hosford, W.F. (1972), A General Isotropic Yield Criterion, *J. Appl. Mech.*, **39**, 607.
- Huang, H.M., Pan, J., and Tang, S.C. (2000), Failure Prediction in Anisotropic Sheet Metals under Forming Operations with Consideration of Rotating Principal Stretching Directions *Int. J. Plast.*, **16**, 611-633.
- Hughes, T. J. R., and Carnoy, E. (1981), Nonlinear Finite Element Shell Formulation Accounting for Large Membrane Strains, *Trans. ASME*, **48**, 193-208.
- Inal, K., Wu, P. D., and Neale, K. W. (2002), Instability and localized deformation in polycrystalline solids under plane strain tension, *Int. J. Sol. Struct.*, **39**, 983-1002.
- Karafilis, A.P., and Boyce, M.C. (1993), A general anisotropic yield criterion using bounds and a transformation weighting tensor, *J. Mech. Phys. Sol.* **41**, 1859-1886.

- Lamontagne, C., Worswick, M.J. and Martin, P. (1995), Strain Prediction and Anisotropy in 6111 and 5754 Aluminum Sheet, *Proc. Aluminum and Magnesium for Automotive Applications*, TMS/ASM Materials Week '95, October 31-November 2, 105-121.
- Lee, Y. (2002), *Formability of Aluminum Alloy Tailor Welded Blanks*, M.A.Sc. Thesis, University of Waterloo, Waterloo, Ontario, Canada.
- Lee, Y., Worswick, M.J. Finn, M.J., Christy, W. and Jain, M. (2000), Simulated and Experimental Deep Drawing of Tailor Welded Blanks, *Proc. IDDRG 2000*, Ann Arbor, Mi, June 5-7.
- Lee, Y., Worswick, M.J., Truttmann, S., Shakeri, H., Finn, M., Feng, F., Christy, B., and Green, D. (2001a), Evaluation of Small Scale Formability Results on Large Scale Parts: Aluminum Alloy Tailor Welded Blanks, SAE Paper 2001-01-0823.
- Lee, Y., Worswick, M.J., Shakeri, H., Truttmann, S., Finn, M.J., Jain, M., Feng, F., and Christy, W. (2001b), Formability of Large-Scale AA5182 Tailor Welded Blanks, *Proc. The 4th International ESAFORM Conference on Material Forming*, Liege, Belgium, May.
- Lievers, W.B. (2001), *Effect of Void Damage and Shear Band Development on the Bendability of AA6111 Automotive Aluminum Alloy Sheet*, M.Eng. Thesis, Carleton University, Ottawa, Ontario.
- Lievers, B., Bissoon, S., Pilkey, A.K., Worswick, M.J., Jain, M. and Lloyd, D.J., Effect of Damage on the Bendability of AA6111 Aluminum Automotive Sheet, *Proc. Plasticity 2000*, ed. A. Kahn, Whistler, BC, July 17-21, 2000.
- Lievers, W.B., Pilkey, A.K. and Worswick, M.J. (2002), paper submitted to *Mech. Mat.*
- Lloyd, D.J (1998), Aluminum alloys used in automotive skin sheet, in *Advances in Industrial Materials*, Wilkinson, D.S., Poole, W.J., and Alpas, A. (eds.), pp. 3-17, The Metallurgical Society of CIM, ISBN:0919086-79-9.
- Logan, R. W., Meuleman, D. J., and Hosford, W. F. (1986), The Effects of Anisotropy on the Limiting Drawing Ratio, *Formability and Metallurgical Structure*, Proceedings of TMS-AIME, Orlando, Florida, Oct. 5-9, pp.159-173.
- Maker, B. (2000), On drawbeads in sheet metal forming, SAE Paper 2000-01-0776.
- Marciniak, Z., and Kuczynski, K. (1967), Limit strains in processes of stretch-forming sheet metal, *Int. J. Mech. Sci.*, **9**, 609-620.
- Mear, M., and Hutchinson, J. (1985), Influence of Yield Surface Curvature on Flow Localization in Dilatant Plasticity, *Mech. Mat.*, **4** (3-4), pp. 395-407.
- Montgomery, J., and Brooks, A. (1994), Influence of geometry on outer panel dent resistance as demonstrated through FEA, in IBEC'94, *International Body Engineering Conference, Automotive Body Materials*, 85-89, SAE.
- Nomura, S., Yutori, Y., Iwaya, J., Miyahara, M., and Kikub, I. (1984), A study of the dynamic dent resistance, *proc. IDDRG '84, International Deep Drawing Research Group*, 394-402.
- Oliveira, D., Worswick, M.J., and Finn, M. (2001a), Simulation of Electromagnetic Forming of Aluminum Alloy Sheet, SAE Paper 2001-01-0824.
- Oliveira, D.A. , Worswick M.J. and Finn, M.J. (2001b), Finite Element Modelling of the Electromagnetic Forming of Aluminum Alloy Sheet, *Proc. The 4<sup>th</sup> International ESAFORM Conference on Material Forming*, Liege, Belgium, 773-776, Volume II.
- Padmanabhan. M. (1997), *Wrinkling and Springback in Electromagnetic Sheet Metal Forming and Electromagnetic Ring Compression*, PH.D. Thesis, Ohio State University.

- Panshikar, H.M. (2000), *Electromagnetic Forming and Impact Welding*, PH.D. Thesis, Ohio State University.
- Raghavan, K.S. and Arwashaan, N. (1997), Analysis of quasi-static denting behavior of automotive sheet steels, SAE Paper 970984.
- Sabbagh, M.A., Chavali, R.N., and Montgomery, J.S. (1995), Quasi-static dent depth simulation using non-linear FEA, in *IBEC '95, International Body Engineering Conference, Materials and Body Testing*, 87-90, SAE.
- Sakai, H., Saito, K., and Tsukada, H. (1983), Stiffness and dent characteristics of body outer surface panel – finite element analysis and experiment, *Int. J. Vehicle Des.*, **4** (1), 13-22.
- Sarma G. B., and Dawson, P. (1996), Effects of interactions among crystals on the inhomogeneous deformation of polycrystals, *Acta Metall. Mater.*, **44**, 1937-1953.
- Shah, K., and Dick, R. E. (1995), Evaluation of Various Yield Criteria in LS-DYNA3D for Sheet Metal Forming Application for Aluminum, *Automotive Stamping Technology Symposium*, SAE Paper No. 950925.
- Shakeri, H., Buste, A., Worswick, M.J., Clarke, J.A., Feng, F., Jain, M., and Finn, M. (2001), Microstructural Study of Damage Initiation and Fracture in Aluminum Tailor Welded Blanks Made via Different Welding Techniques, Submitted to *Aluminum Transactions*.
- Shi, M., Pickett, K., and Bhatt, K. (1993), Formability Issues in the Application of Tailor Welded Blank Sheets, *SAE Paper* 930278.
- Stasik, M.C. and Wagoner, R.H. (1996), Forming of Tailor Welded Aluminum Blanks, *proc. Aluminum and Magnesium for Automotive Applications*, TMS, 69-83.
- Stoughton, T.B. (2000), A General Forming Limit Criterion for Sheet Metal Forming, *Int. J. Mech. Sci.*, **42**, 1-27.
- Thomas, D. (2001), *The Numerical Prediction of Panel Dent Resistance Incorporating Forming Strains*, M.A.Sc. Thesis, University of Waterloo, Waterloo, Ontario, Canada.
- Thomas, D., Hodgins, B., Worswick, M.J., Finn, M.J. and Gong, K. (2002), Static and Dynamic Denting of Paint Baked AA6111 Panels: Comparison of Finite Element Predictions and Experiments, for IBEC-2002, SAE paper number 01BECH-1.
- Thomson, C.I.A., Worswick, M.J., Pilkey, A.K., Lloyd, D.J. and Burger, G. (1999), Void Nucleation and Growth within Periodic Clusters of Voids, *J. Mech. Phys. Sol.*, **47**, 1-26.
- Tvergaard V. (1981), Influence of voids on shear band instabilities under plane strain conditions, *Int. J. Frac.*, **17**, 389-407
- Tvergaard, V. (1987a), Ductile Shear Fracture at the Surface of a Bent Specimen, *Mech. Mat.*, **6** (1), 53-69.
- Tvergaard, V. (1987b), Effect of Yield Surface Curvature and Void Nucleation on Plastic Flow, *J. Mech., Phys. Sol.*, **35** (1), 43-60.
- Tvergaard V. and Needleman A. (1984), Analysis of the cup-cone fracture in a round tensile test bar, *Acta Metall.*, **32**, 157-169.
- Werner, M.F. (1993), Finite element simulation of steel body panel performance for quasi-static dent resistance, in *IBEC '93, International Body Engineering Conference, Automotive Body Materials*, 87-90, SAE.

- Woo, D. M. (1968), On the Complete Solution of the Deep-drawing Problem, *Int. J. Mech. Sci.*, **10**, 83-94.
- Worswick, M.J. and Pelletier, P. (1998), Numerical Simulation of Ductile Fracture During High Strain Rate Deformation, *European Physical Journal, Applied Physics* **4**, 257-267.
- Worswick M.J. and Finn, M.J. (2000), The Numerical Simulation of Stretch Flange Forming, *Int. J. Plast.*, **16** (6), 701-720.
- Worswick M.J., Chen Z.T., Pilkey A.K., Lloyd D. and Court S. (2001a), Damage Characterization and Damage Percolation Modelling in Aluminum Alloy Sheet. *Acta. Mater.*, **49**, 2791-2803.
- Worswick, M.J., Lee, Y., Shakeri, H.R., Cinotti, N., Buste, A., Lalbin, X. ,and Zhou, X. (2001b), *Strain and Formability Prediction in Tailor Welded Blanks*, Final Report, Materials and Manufacturing Ontario, Project MP301, University of Waterloo, Waterloo, Ontario, Canada, February 15.
- Wu, P. D., Neale, K. W., Van der Giessen, E., (1996), Simulation of the behaviour of FCC polycrystals during reversed torsion, *Int. J. Plast.*, **12**, 1199-1219.
- Yutori, Y., Nomura, S., Kokubo, I., and Ishigaki, H. (1980), Studies on the static dent resistance, *Memoires Scientifiques Revue Metallurgie*, **77** (4), 561-569.

This Page Intentionally Left Blank

## Chapter 9

# Geometric and Mechanics Models of Sheet Forming Processes

JOHN L. DUNCAN  
*Professor Emeritus*  
*Department of Mechanical Engineering,*  
*The University of Auckland,*  
*Private Bag 92019, Auckland,*  
*New Zealand.*

### 9.1 INTRODUCTION

During the last two decades a large amount of sheet metal forming research has been directed at numerical techniques to predict the stress, strain and sheet surface during deformation in dies of complex shape. It is now possible, often using supercomputers, to obtain detailed information about the industrial stamping of intricate parts long before dies have been constructed. Depending on the software used, areas in which the sheet might split or wrinkle can be anticipated quite well, although it must be said that quantitative verification of results has not been widespread.

These developments have greatly enhanced the level of sheet metal engineering, but there are several areas where improvements have been less marked. One is in the tools available to the engineer at the conceptual design stage. Die design has been an empirical and rule-based procedure for a long time and designers in the past were craftsmen of long experience. To some extent this still survives and the advanced computer-aided systems have been overlaid on this base without many fundamental changes in the initial design approach. The result is that while detailed numerical modelling can identify problem areas, these models are essentially tools for analysis rather than for design; techniques used to determine the appropriate changes to be made to problem areas remain intuitive, or, at best, empirical. Engineering models are needed that can be applied locally to determine quantitatively the changes the designer should make in the die. In this way, an indication of the outcome of a design change can be made before submitting the whole tool to further costly numerical analysis. To put it another way, there should be something better than using an expensive and sophisticated numerical analysis as a tool for a 'trial and error' approach. The problem is compounded by the fact that usually the initial design of the tooling is based on previous experience that may not be adequate when new materials such as high strength steel or aluminium are to be formed. It is a misconception to believe that the initial design can be performed automatically using an elaborate computer-aided design system. This is never true in engineering. Conceptual design

requires a basic understanding of the mechanics of the process coupled with the ability to perform simple calculations to establish the main features of the design. If this is done well, CAD systems are effective in refining the design and adding detail.

Another problem associated with emphasis on numerical modelling at the expense of the basic mechanics of sheet metal forming is that it has been hard to develop good education programs in this field. Anecdotal evidence shows that the ability to 'operate' large finite element systems does not, of itself, provide an understanding of the forming process being analysed. Not only is training in numerical modelling an insufficient education for sheet metal engineers, but the mechanics that would be the basis of a course of study exist only in a piecemeal fashion and have not been established as a valid, albeit specialised field of engineering science. The problem can be illustrated by considering an analogous, but closely related field, namely machine design. Every engineer knows that at the initial stages of the design of some device, almost all of the structural analysis is performed using the well-developed subject of 'strength, or mechanics of materials'. In this subject, complicated parts are simplified to an assembly of tensile members, beams, shafts or shells and analysed by simple models that usually include a number of arbitrary but well-tested assumptions. What is needed is to develop a similar subject for sheet metal forming. The objective of this chapter is to demonstrate that this is not only possible, but highly necessary if the greatest use is to be made of the advanced numerical modelling tools that have become available.

This 'strength of materials' approach to sheet metal forming consists of identifying the elemental sheet forming processes such as drawing or bending and unbending over a radius. A complex process would be considered as an assembly of such elements that are identified by the designer and analysed using simplified models. In any tool the number of such elements is few and the designer will examine the output of each calculation and gain a feel for the way the elements are interconnected. This aids the understanding the whole process in a way that is not possible in numerical analyses where many thousand elements are involved and much information is hidden in the plethora of data.

This chapter will outline a few of the simple models that exist for elements of sheet forming and discuss some systems and tools that help a student or a designer use this elemental approach in the study and design of sheet metal forming processes.

## 9.2 PLANE STRESS DEFORMATION

Grid strain analysis and the use of the forming limit diagram has been a major advance in sheet metal engineering. It depends on the simplifying assumption that the deformation path is a plane stress, proportional one. The success of this approach suggests that a theory of plasticity using the same assumptions will apply to the majority of elements in sheet forming processes. There are, of course, exceptions, but these are easily recognised.

The current state of deformation of most elements can be described therefore by,

$$\begin{aligned} \varepsilon_1; \quad \varepsilon_2 = \beta \varepsilon_1; \quad \varepsilon_3 = -(1 + \beta) \varepsilon_1 \\ \sigma_1; \quad \sigma_2 = \alpha \sigma_1; \quad \sigma_3 = 0. \end{aligned} \quad (9.1)$$

where  $\alpha$  and  $\beta$  are the stress and strain ratios, respectively and are constant throughout the process; plane stress and constant volume deformation are also specified. The usual flow rule links the stress and strain ratios so that,

$$\alpha = \frac{2\beta+1}{2+\beta} \quad \text{and} \quad \beta = \frac{2\alpha-1}{2-\alpha} \quad (9.2)$$

Effective stress and strain can be expressed as,

$$\bar{\sigma} = \sqrt{\sigma_1^2 - \sigma_1\sigma_2 + \sigma_2^2} = \sqrt{1 - \alpha + \alpha^2} \cdot \sigma_1 \quad (9.3a)$$

$$\text{and, } \bar{\varepsilon} = \sqrt{\frac{4}{3} \{1 + \beta + \beta^2\}} \varepsilon_1 \quad (9.3b)$$

With these relations, it is easy to illustrate a deformation state as a point in the stress space in a similar fashion to showing strain in the forming limit diagram. In sheet metal forming, one of the principal stresses will be zero or greater, because it is exceptional to push on the edge of the sheet and create a state in which both membrane stresses are negative or compressive. Common deformation paths in the stress space will therefore lie along the yield locus between points *A* and *E* in Figure 9.1.

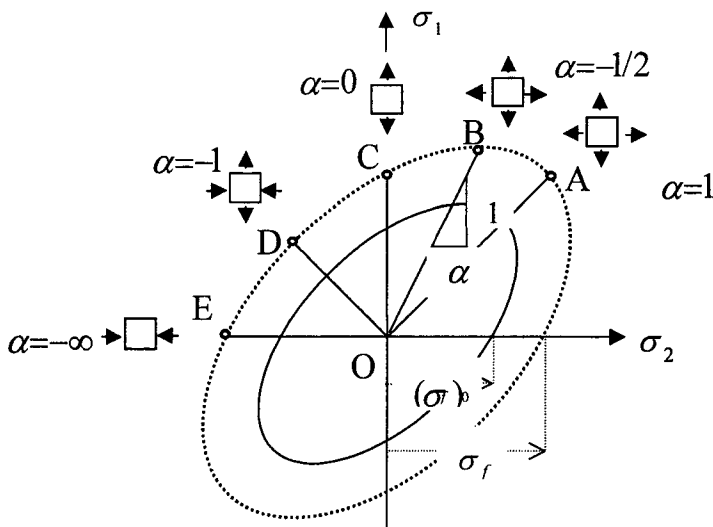


**Figure 9.1** Deformation paths illustrated in the stress space.



## 9.3 FORCE PER UNIT WIDTH, OR 'TENSION'

Shell theory is usually expressed in terms of 'stress resultants' which are the forces transmitted per unit width of shell or the product of membrane stress and thickness. The same variable, often called 'tension' or 'traction', is used by tool designers; for example, the effect of a draw bead will be given as a tension of so many lb/in or kg/mm developed in the sheet. Even though tension is an important quantity in understanding how a process works, it is unusual to see it emphasised in research papers. This is unfortunate. The importance of following the 'tension' distribution in a process is related to a fundamental aspect of sheet forming, namely that yielding of the sheet is achieved by forces transmitted *through* the sheet, rather than directly by contact stresses as in forging and rolling. A further consideration is that the process is likely to change dramatically when these forces reach a maximum. A quick estimate of the press tonnage required for an operation can also be obtained from the tensions in the side-wall. For these and other reasons, the designer or student should automatically approach a problem on the basis of *tension* rather than *stress*; for the purpose of discussion, an example of sheet tension is examined here. The effective stress strain law,

$$\bar{\sigma} = K(\epsilon_0 + \bar{\epsilon})^n = 650(0.003 + \bar{\epsilon})^{0.22} \text{ MPa} \quad (9.4a)$$

is typical of those that fit drawing quality sheet steel used in autobody stamping. If the original sheet thickness is,  $t_0$ , the principal tensions at a point where the strain ratio is,  $\beta$ , are given by,

$$T_1 = \sigma_1 t = \frac{K(\epsilon_0 + \bar{\epsilon})^n t_0 \cdot \exp[-(1 + \beta)\epsilon_1]}{\sqrt{1 - \alpha + \alpha^2}} \quad \text{and} \quad T_2 = \alpha T_1 \quad (9.4b)$$

From the above relations, the principal tensions can be determined as a function of the major strain and in Figure 9.2, the tensions for an element stretched in a process in which,  $\beta = 0.40$ , and,  $\alpha = 0.75$ , are shown.

In a region of uniform thickness deforming in a proportional process, the principal tensions will obey a yield criterion similar to the any of the criteria adopted for stress. It is possible to define an *effective tension*,  $\bar{T} = \bar{\sigma} t$ , where,  $t$ , is the current thickness.

For the reasons mentioned here, it is suggested that models of sheet metal forming should, wherever possible, be expressed in terms of tensions, rather than stresses as is done in general shell theory.

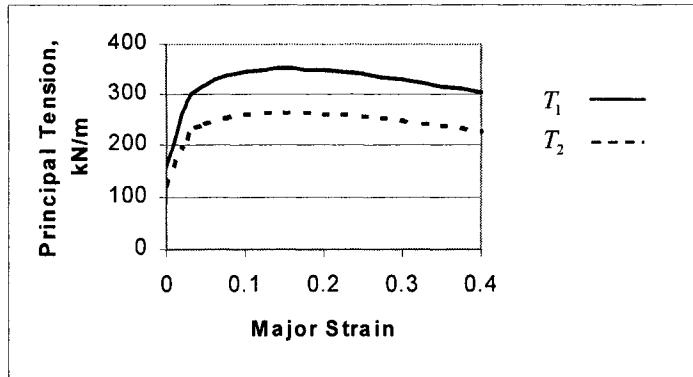


Figure 9.2 Principal tensions in stretchforming drawing quality steel along a given strain path

### 9.3.1 'Constant tension' assumption

In approximate analyses, particularly of axisymmetric processes such as deep drawing or tube forming, it is often sufficient to assume that the effective tension,  $\bar{T}$ , in the sheet remains constant at some predetermined level. This may seem a gross simplification, but it is usually more accurate than assuming a constant flow stress. The reason this is so has to do with the type of materials chosen for different processes. Figure 9.3 shows diagrammatically the typical forming limit curve for sheet and, to a first approximation, the level of the forming limit curve depends on the strain hardening index,  $n$ .

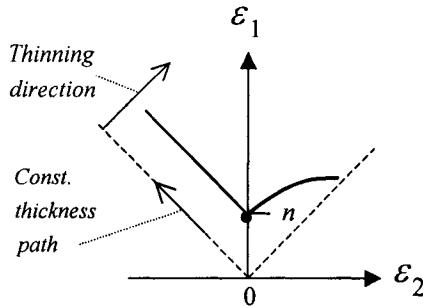


Figure 9.3 Typical forming limit diagram for a material with a strain hardening index,  $n$ .

The left-hand diagonal is a constant thickness forming path that is the dominant path in deep drawing; failure by tearing will not occur in such a process and for this reason sheet having a low strain hardening index is preferred. Thus, if there is little thinning, a low strain hardening material will be preferred. On the other hand, for a forming path in the first quadrant – the stretching region – thinning is rapid and failure by tearing will limit

the process. A high strain hardening material is therefore chosen and it may be seen from Figure 9.2 that strain hardening will roughly balance thinning to give an approximately constant tension during forming. In this example, the major principal tension in the strain range,  $0.05 < \varepsilon_1 < 0.4$ , only varies by about 50 kN/m or 15% and with a judicious choice of value, an analysis in which  $\bar{T}$  is constant will be satisfactory.

For an axisymmetric shell deforming under the action of a meridional tension,  $T_\phi$ , and hoop tension,  $T_\theta$ , the equilibrium equation for an element at a radius,  $r$ , is,

$$\frac{dT_\phi}{dr} - \frac{T_\theta - T_\phi}{r} = 0 \quad (9.5)$$

If the tensions obey a Tresca yield criterion and the above assumption is used, the locus shown in Figure 9.4 will remain of constant size and the above equation can be readily integrated to obtain simple, but instructive models for a number of common processes.

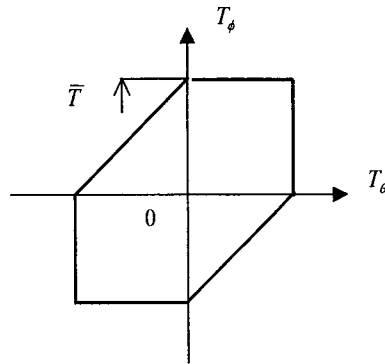


Figure 9.4 Tresca yield locus for tension in a deforming shell

#### 9.4 BENDING AND UNBENDING MODELS

A common elemental operation in sheet forming is sliding over a radius under tension. A two-dimensional plane strain case is shown in Figure 9.5.

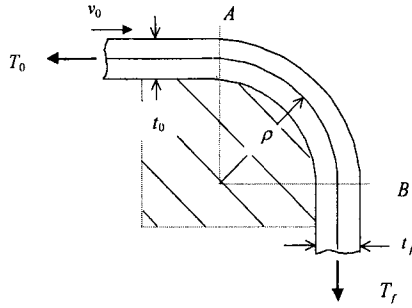


Figure 9.5 Sliding over a tool radius under tension

At A the sheet suddenly acquires a curvature of,  $1/\rho$ , and if the neutral surface lies within the sheet, a simple model of the behaviour at this point is obtained by assuming that the material is rigid, perfectly plastic with a yield tension of,  $T_y$ . At this point, plastic work is done both in stretching the element and in bending and to obtain an energy balance, there is some increase in the tension in the sheet which is given by,

$$\Delta T_0 = \frac{1}{4\eta} \cdot \frac{T_y}{(\rho/t_0)} \left[ 1 + \left( \frac{T_0}{T_y} \right)^2 \right] \quad (9.6)$$

where,  $\eta$ , is an efficiency factor and the other symbols are shown in the diagram.

There will also be a reduction in thickness given by,

$$\frac{\Delta t}{t} \approx \frac{1}{2(\rho/t_0)} \left( \frac{T_0}{T_y} \right) \quad (9.7)$$

As the sheet element passes A and slides over the radius, there is a further increase in tension due to friction at the tool interface. The increment in tension is given by,

$$\frac{dT}{T} = \mu.d\theta \quad (9.8)$$

These equations describe approximately the behaviour of sheet in many area of a die, such as bending and unbending over the die profile radius and can also be assembled into a model for drawbeads. They can be derived readily and presented to students in a familiar way and as an extension of the strength of materials they have already studied. Many readers of this chapter will be familiar with these or similar relations and it may be said that they are too simple and basic to be included in this book. The justification for doing so is that engineers who have spent a major part of their career in die design and technical management of stamping plants often are unaware that there is this engineering basis to many of the things they are familiar with. The experience is that they are keen to

study this material and while the accuracy of calculations based on these models is not high, practitioners prefer simple models they understand, rather than opaque calculations that may have greater accuracy.

## 9.6 SUPPORTING SOFTWARE

It suggested here that sheet metal forming should be introduced to students in a similar way to strength of materials, although it is accepted that there will be some fundamental differences. Strength of materials deals mainly with the linear elastic regime, whereas plastic deformation in sheet forming is essentially non-linear. Tutorial exercises in sheet forming may therefore require more extensive calculations, but this difficulty can be surmounted by providing appropriate software. The crucial point is not to provide another ‘black box’ that just gives results but rather a system that helps students acquire an understanding of sheet processes as efficiently as possible. The software should be based on the simple mechanics equations studied and relieve the student only of the need to write the code to obtain numerical results from these equations.

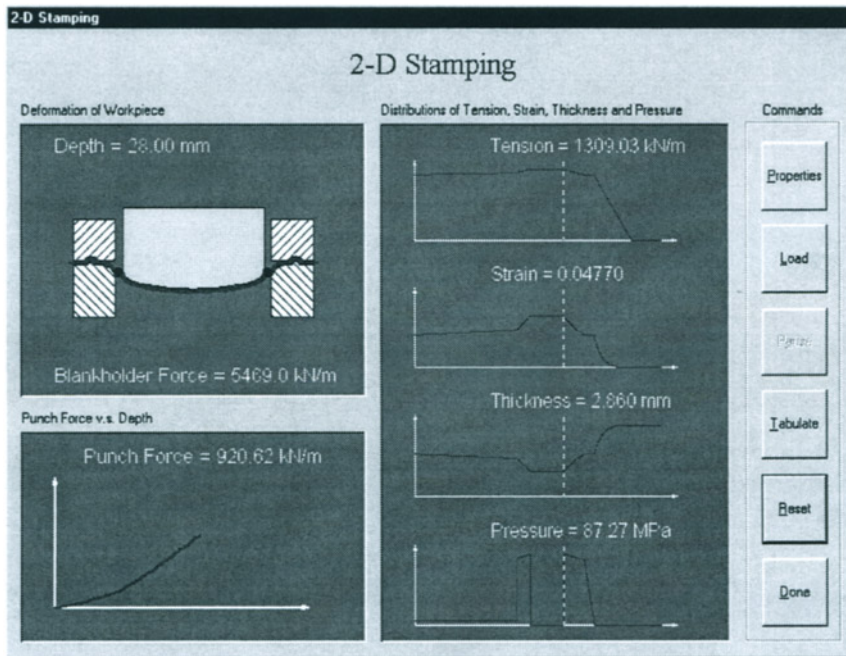


**Figure 9.6** Screen output from a module of software based on simple mechanics models. The case illustrated is for a section in a stamping or draw die.

Experience has been gained already with one software system designed on this basis. Typical modules include one that uses Equations 9.2 to 9.4 to show diagrams of tension versus strain for a given material and to transform a point identified in the forming limit diagram into a point in the stress space. The system is animated and interactive and

one can see, for example, the growth of the yield locus as the element progresses along the strain path. Other modules deal with bending and springback, cylindrical deep drawing and tube expansion. Figure 9.6 is an example of the screen output of this system for a section through a stamping or 'draw die'. This is modelled as a two-dimensional operation. The values of variables shown are for a point selected by the user and indicated by a black dot on the physical diagram and by the vertical white line on the different diagrams.

This software is designed primarily for tutorials and to aid visualisation and understanding. Experienced designers have also used it to perform calculations on local regions of tools during design or to diagnose problems in the stamping plant. Most of the calculations are done on a spreadsheet and information can be obtained from the tabulation.

## 9.7 CONCLUSIONS

The object here has been to show that by reducing sheet metal forming to plane stress proportional deformation, the theory of plasticity and many models of behaviour of elements in forming can be presented in a way that naturally follows the approach that students are familiar with in basic engineering sciences such as 'strength of materials'. Although the material presented is not comprehensive, sufficient examples are given to illustrate the concept. The importance of basing calculations on tension (force transmitted per unit width of sheet) rather than on stress has been emphasised and the use of interactive and animated software based on simple models has been demonstrated.

At the present time, many engineers in the sheet metal field are experiencing some difficulty. On the one hand, very powerful numerical modelling tools are being used to analyse the behaviour of complicated tool sets. These provide detailed results but very little indication of the interconnection between different regions of the sheet during forming and it is often difficult for users to understand what is happening. At the other end of the spectrum, die designers are required to accommodate new materials and practices that are outside the realm of previous rule-based experience. It is suggested therefore that attention be given to simple tools for the engineer to use during initial and conceptual design and that these will, at the same time, provide an understanding of the basic mechanics of sheet metal forming.

## ACKNOWLEDGEMENTS

*The simulation software discussed was developed at the University of Michigan by Frank Wang and his excellent work is acknowledged with much pleasure. The software is demonstrated on the website [www.mssinternational.com](http://www.mssinternational.com) and it has been used in industrial short courses for design engineers. It has been popular also with students in several universities at both the undergraduate and postgraduate level.*

*As this chapter is primarily one of discussion and deals with elementary and familiar models, no references are given. It is a pleasure to acknowledge that many concepts discussed were presented some time ago by Professor Z Marciniak of the Technical University of Warsaw and are embodied in his writings both in Polish and in the book entitled 'The Mechanics of Sheet Metal Forming' by Z Marciniak and J L*

*Duncan, published by Edward Arnold in 1992. More recently Professor S J Hu of the University of Michigan has assisted the authors in completely rewriting and expanding this work. A second edition will be published early in 2002 by Butterworth-Heinemann.*

## Chapter 10

# Modelling and Optimization of Metal Forming Processes

T. MANNINEN<sup>a</sup>, J. LARKIOLA<sup>b</sup>, L. CSER<sup>c</sup>, A. REVUELTA<sup>b</sup> and A.S. KORHONEN<sup>a</sup>

<sup>a</sup>*Helsinki University of Technology, Espoo, Finland*

<sup>b</sup>*VTT Manufacturing, Espoo, Finland*

<sup>c</sup>*Bay Zoltan Institute, Budapest, Hungary*

*This chapter discusses the application of advanced modelling tools in the plastic forming and processing of metals. The tools include numerical modelling techniques, such as the finite element method (FEM), and more recently, artificial intelligence techniques, such as various types of artificial neural networks as well as data mining. Examples of real production processes, such as the production of sheet by rolling, deep drawing of stainless steel kitchen sinks, continuous extrusion of electrical conductors as well cutting of metal and tube hydroforming, will be presented. It is shown that defects can be avoided and tool life increased through optimization of plastic forming processes.*

### 10.1 INTRODUCTION

With the advent of more and more powerful computers and better software, interest in computer modelling and optimization of metal forming processes has continued to grow. The production processes are often complicated. In some cases, such as in rolling, a lot of measurement data is readily available, and neural networks, based on the results of data mining (e.g. Cser et al. 2000), are therefore well suited for studying the interdependencies of the processing parameters. Good results have also been obtained in numerical modelling and optimization of both forming and fluid flow types of processes. Three-dimensional modelling of e.g. deep drawing of sheet metals has been commonly applied in automobile production since mid-1990s (Makinouchi et al., 1998). So far, however, relatively simple laws are mostly used to describe plastic deformation. Better constitutive models are required to improve the accuracy of modelling. Boundary conditions such as heat transfer and friction are often not well known. Detailed data and better models are also needed for them. The cutting of metals represents an example of intense plastic deformation. Productivity can be raised significantly by improving tool life. As an example we discuss the dry turning of Ca-treated steels with both uncoated and TiN-coated tools, and we show that the formation of a



protective layer on the rake face may improve the wear life of tools nearly 30-fold. As a final case, optimization of a tube hydroforming process is examined.

## 10.2 ON MODELLING AND OPTIMIZATION

In numerical simulation of metal forming processes the commonly applied hardening models are relatively simple. The hardening models in cold and hot forming are, of course, different, but the same type of yield conditions are usually applied in both cases. However, the models are more complicated than in elasticity. While, for example, elastic deformation can often be described with sufficient accuracy by a simple Hooke's law and even without taking anisotropy into account, three kinds of constitutive equations are needed to describe plastic deformation. They are:

- the yield condition
- the relations between stresses and strain increments (the so-called flow rule)
- the stress-strain curve (also called the flow curve)

Usually, the yield condition and its associated flow rule are of the same traditional type. In most cases it is assumed that hardening is isotropic and the yield condition is the Huber-von Mises yield condition (Korhonen and Eriksson, 1994) or, especially for sheets, a planar anisotropic version of the anisotropic modification proposed by Hill, where the ratio of yield stresses in the through thickness and plane directions remains constant and does not vary during deformation. The associated flow rule is derived from the yield condition. Depending on whether or not the elastic strains are taken into account, the flow rule is called the Levy-Mises or Prandtl-Reuss equation. In hot forming the elastic strains are usually neglected. Usually, an isotropic hardening rule is assumed. Hardening rules in hot and cold forming are different. Also the stress-strain curves are different in hot and cold forming. Strain or work hardening is often so pronounced in cold forming that in practical forming intermediate recrystallization annealing stages may be needed before forming can be continued. The effects of strain rate and temperature on the work hardening in cold forming are rather small. In hot forming, on the other hand, the effects of both strain rate and temperature become pronounced, while there is usually not much strain hardening – even strain softening may take place. Recently, microstructural recrystallization models have been included in the hot forming work hardening models. They may take into account static or dynamic recrystallization or both. Recently, cellular automata have also been applied to describe the recrystallization process itself.

Optimization, on the other hand, is a branch of mathematics. It aims at finding an optimal solution to a given problem containing a given set of variables with or without constraints. The aim is to find the values of the variables that minimize or maximize the objective function while satisfying the constraints. In practice the situation is much more complicated. The ultimate aim of metal forming, as in any other industrial activity, is to make a profit. In practice there are usually a lot of constraints, which include e.g. the society and its laws, environmental concerns and often limited resources such as energy or labor. In metal forming one usually has to deal with ill-defined, “fuzzy” problems. The physical laws are often complicated or even unknown and there are usually many variables. At best one may reach a so-called local or “false” minimum instead of a final optimum. In the following chapters we consider some examples of real forming processes and a tube hydroforming optimization case.

### 10.3 ROLLING OF METALS

#### 10.3.1 Prediction of the rolling force

High productivity and the ability to produce high-quality products both rapidly and cost effectively are central factors in determining the competitiveness of the rolling process. Although a lot of measured data is often collected from the rolling environment, it may not be fully utilized because the relationships between the process and quality variables are unknown. It has been possible to describe many relationships sufficiently well using physical models.

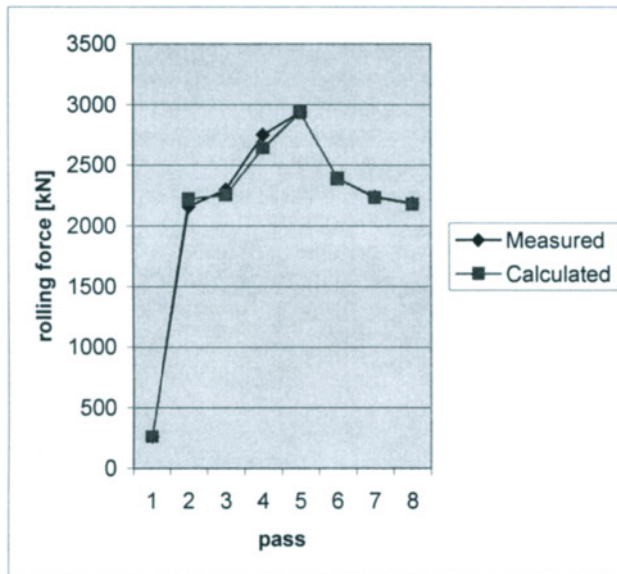


**Figure 10.1** Comparison of measured and calculated rolling force values (Rantanen et al, 1990).

By combining physical modelling with neural networks it has been possible to develop a new tool, the hybrid method, with which process scatter can be further reduced (Myllykoski et al., 1999; Larkiola et al., 1996).

Process models may be classified in various ways. Various numerical techniques can be used to solve e.g. the basic equations governing plastic flow and heat transfer provided that the boundary conditions are known. Physical models can be developed, for example, to describe the development of microstructure during hot working (Rantanen et al., 1990). Figure 1 shows an example of the modelling of steel plate rolling. In this case the Abaqus FEM code was combined with a recrystallization model called Micropla. The agreement between the measured and calculated rolling force was good, as was the agreement between the final calculated and measured ferrite grain sizes and the corresponding yield strength values.

The calculated ferrite grain size was 23  $\mu\text{m}$  on the surface and 26  $\mu\text{m}$  in the center. The yield strengths were 270 MPa and 260 MPa, while the measured average grain size was

26  $\mu\text{m}$  and the measured yield strength was 270 MPa. However, the processes are often so complicated that the models include great simplifications and are, at best, semi-empirical by nature. With the increasing amount of available data on the process, the basic physical laws become less important and various computational techniques can be used for modelling. These include fuzzy systems, neural computation, and traditional statistical methods.

### 10.3.2. Analysis of factors influencing the product quality

The quality of the flat rolled product depends in a complex manner on the geometric accuracy, surface quality and material properties. The quality of hot rolled strips is influenced by the entire forming system (Lenard et al. 1999). It is also affected by other factors, such as the chemical composition of the material to be rolled, and the history of each slab before and during casting, re-heating, and rolling. Factors influencing the quality are not independent of each other. They can have very complex *confluence*. The same is valid for the geometric quality parameters such as thickness, profile, flatness, width, wedge and surface roughness. Their interdependencies are obvious during the whole process.

The main control tasks in hot rolling mills are: optimal roll set-up, process monitoring, material flow control, data recording and report generation. In the control unit, mill settings for the incoming strip, before the strip actually enters the mill, are based on analytical models, but neural networks, based on both measured and simulated data, correct the roughly estimated values. An efficient process model should be able to predict rolling forces, torque, material properties, etc. By using artificial neural networks these goals can be reached, provided that sufficient process data is available. In addition, taking post-calculation into account, which means compensating the pre-calculation error by continuously adapting the models to the real-time process, neural networks are able to do both modelling and adaptation and to perform them equally well. For the control task a reasonable task sharing between the mathematical model and neural network based correction is necessary: the on-line computations should be performed by the networks, but the possibilities of mechanically correct mathematical modelling should be utilized. In order to set up the models for fine-tuning of the rolling mill control, it is necessary to analyze all factors that can cause scatter in quality parameters among the strips, as well as within the strip. Laboratory experiments are one way of analyzing the influencing factors and their effects. These experiments are rather expensive and carry all the dangers of physical modelling (scale factors, differences in boundary conditions, etc.). Another approach is to use and analyze the industrial data measured on-line during the actual rolling process using the methods of *data mining*, especially the visualizing possibilities of the *Self-Organizing Maps (SOM)*. In this case, the main objective of data mining is to detect complex relationships between the measured process parameters and product quality. The system behavior has been analyzed in a complex study in order to discover the hidden interdependencies between the technological parameters. The analysis consists firstly of macro modelling and analysis, which is based on the data collected from the higher hierarchy level of the computer system and contains average values and standard deviations.

Secondly, the analysis consists of micro modelling and analysis, which is based on the strip data collected on-line and aims at discovering the reasons for the scatter in quality parameters within the strip.

The Self-Organizing Map (SOM) (Kohonen, 1995) is a neural network algorithm based on unsupervised learning. Unlike supervised learning methods, the SOM can be used for clustering data without knowing the class memberships of the input data. It can, thus, be used to detect features inherent to the problem. The projection on the component planes can be interpreted as slicing the  $n$ -dimensional model vectors of the map into component planes.

Each component plane consists of values of a single vector component in all map units. In the case of hot rolling, the measured data characterizing the rolling of the strip represent a data vector. Components of these vectors change from strip to strip. Component planes can also be used for correlation hunting: discovering hidden *co-incidences*. The correlation between components can be seen as similar patterns in identical positions of component planes. Pattern matching is something that the human eye is very good at, and it is further enhanced by the regular shape of the map grid. Using component planes in correlation hunting is simple and it easy to select the "suspicious" component combinations for further investigations. An advantage of SOM is that it is not necessary to know the character of the correlation. It can also be non-linear. Similar patterns do not mean a causal connection. They can be caused by a third factor as well. However, only a human expert can give the final answer.

The first step of SOM-based data mining is data warehousing; the collection of data from different computers on different hierarchical levels of computer control in the rolling mill, and transforming the data into the same format. The problem to be solved in preparing data for the micro modelling of the rolling mill, as well as discovering new, hidden dependencies between the technological parameters and the local properties within the strip, is a typical data-warehousing problem. It means that data coming from different sources, collected at different times, and having different structures (mostly binary code), should be brought into correspondence with each other, cleaned, and transformed into the unified co-ordinate system.

Data collected by the measurement devices differ in terms of sampling frequency, precision and timing. The timing differences are connected with the different clocks of the control computers, as well as with the different reference points of beginning and finishing the measurement. Fig.10.2. shows an example of some temperature measurements during the rolling in different places. Each sensor has its own sampling frequency and clock signal. The measured temperatures at the same time co-ordinates can be seen in Fig. 10.3. When the temperatures corresponding to the same material point can be found, they describe the cooling history of the material in the chosen elementary volume (dotted line in Fig. 10.3). The same is valid for the deformations too. Grain size and mechanical properties depend on the simultaneous history of these factors (see e.g. Lenard et al. 1999).

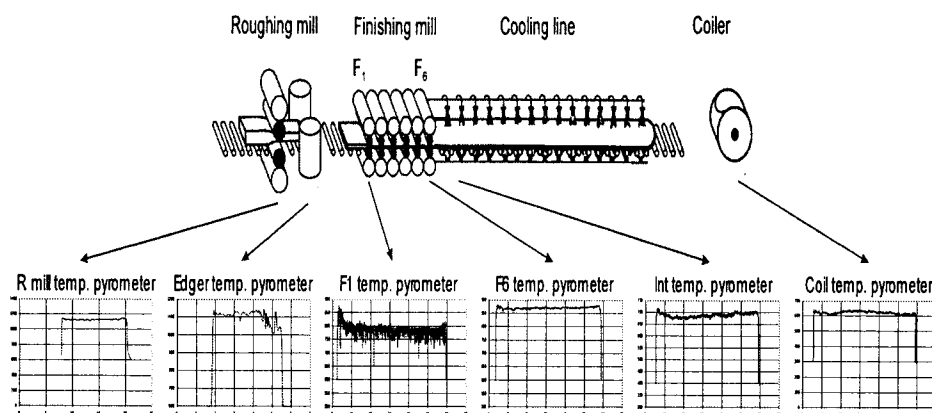
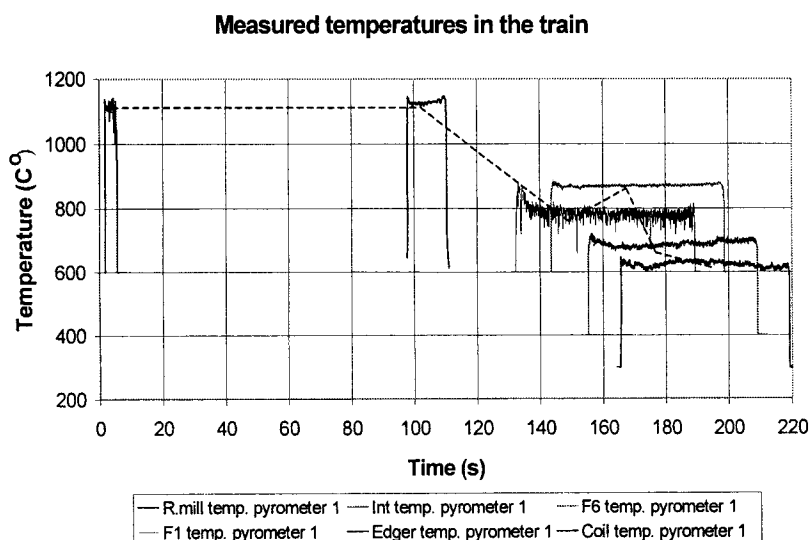


Figure 10.2 Strip temperatures measured at different places of the hot rolling mill

In order to find the hidden dependencies in the huge amount of measured data, collected from different sensors by different computers with different clock signals, and different frequencies, stored in different data structures, it is necessary to make some preliminary data preparation that should not change the tendencies in domains of the data set. This includes transforming the data into a unified format, as well as finding the reference points of beginning and finishing the process, transforming the data into a normalized length co-ordinate system, which is connected to the strip material (Euler-Lagrange transformation) and cleaning noise from the data.

An Euler-Lagrange transformation enables one to follow the “history” of the deformation in each elementary material volume of the hot rolled strip. In a recent study, which covered 70 measured variables at 300 to 12,000 points for each strip, comprehensive information about the process and the mill could be obtained. Fig. 10.4 shows the same temperatures, transformed into the normalized length co-ordinates of the strip.



**Figure 10.3** Strip temperatures, measured at different places of the hot rolling mill, transformed into the same time co-ordinates (dotted line indicates the cooling “history” of the same material point of the strip).

A Self Organizing Map based on the measurement data, which is cleaned and transformed as described above, reveals the hidden dependencies. In this case they included the measured temperatures, roll separating forces and the strip geometric accuracy (see Fig. 10.5). Similar patterns in similar places of two maps indicate simultaneous changes in the values.

The similar patterns on the left-hand sides of the first 4 maps indicate a connection of the different geometric parameters with the temperatures, measured before the 6<sup>th</sup> finishing mill stand. The similar patterns in the maps of the second row (**tf1**, **ff1**) show the well-known connection between the rolling temperatures and the roll separating forces.

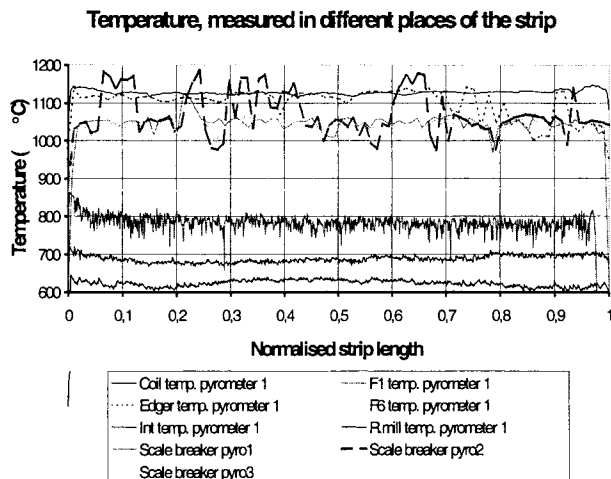
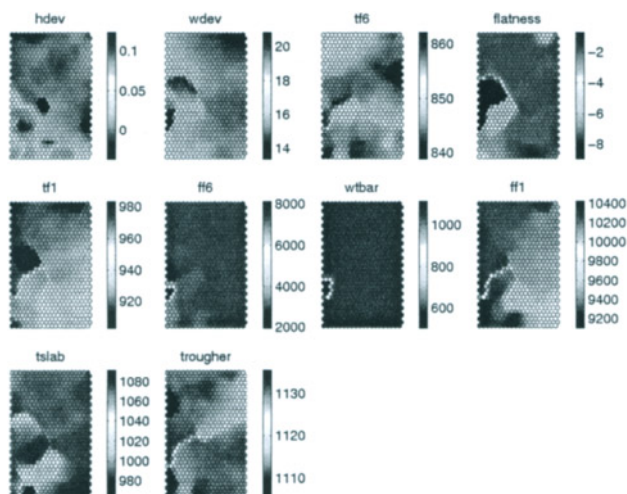


**Figure 10.4** Measured temperatures, transformed into the normalized length co-ordinates of the strip



Map: SOM 16-Dec-1998, Data: 14\_12\_98.txt, Size: 35 20

**Figure 10.5** Visualizing the connections among the parameters, measured during rolling and transformed into the length co-ordinates of the strip (**hdev** - thickness deviation, **wdev** - widths deviation, **tf6** - temperatures, measured before the 6<sup>th</sup> finishing stand, **flatness**).

#### 10.4 DEEP DRAWING OF STAINLESS STEEL

The consumption of stainless steel has been steadily increasing. Both austenitic and ferritic grades of steel sheet are commonly used in various applications. The formability of

austenitic grades is usually good due to their good work hardening capacity. For the same reason forming loads may sometimes become high, and even springback may sometimes become a problem. In a recent work (Manninen et al., 2000) we studied the simulation of deep drawing of austenitic double-bowl kitchen sinks using the LS-Dyna3D FEM program. Figure 10.5 shows an example of the tools used in this study.

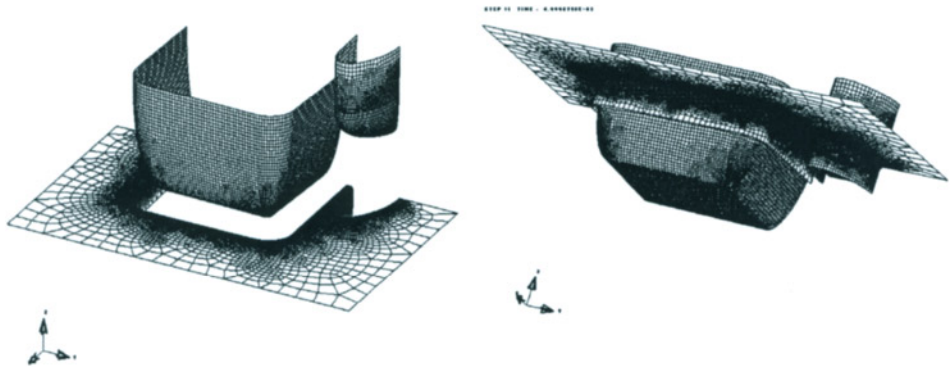


**Figure 10.6** Geometry of the tools for deep drawing of a double-bowl kitchen sink.

The effect of the temperature of the tools was studied experimentally and it was found that in the case of AISI 304 steel even a small change in the tool temperature could affect the drawing greatly.

The material model used for the blank was the transversely anisotropic elastic-plastic material model. The relationship between stress and strain was defined using a piecewise linear curve. The curve was taken from the tensile test results. Coulomb's law was used to describe the friction between the blank and the tools. The friction coefficient between the tools and the blank was measured using frictometer tests.

Simulations with the LS-Dyna3D program could predict the actual strain distributions in deep drawing of the kitchen sink. The results can be considered sufficiently accurate as compared with the deep drawing experiments. Two critical areas were observed in the simulations. They were the middle portion of the bottom of the smaller bowl of the kitchen sink and the wall of the smaller bowl. Also the connection of the two bowls showed strain near the critical values. Figure 10.7 shows an example of the calculated strain distribution in the forming limit diagram.

It is expected that the accuracy of the prediction of the strains could be improved further by improving the constitutive model. In the present case the difference between the calculated and measured thickness strains was about 10 %.

Using stress-strain data measured from biaxial tests instead of uniaxial test could help in predicting larger strains. Taking account of the phase transformation from austenite to martensite during deformation would also improve the accuracy of the simulation. Using a more advanced yield function instead of the simple Huber - von Mises type would make it possible to predict the residual stresses after forming.



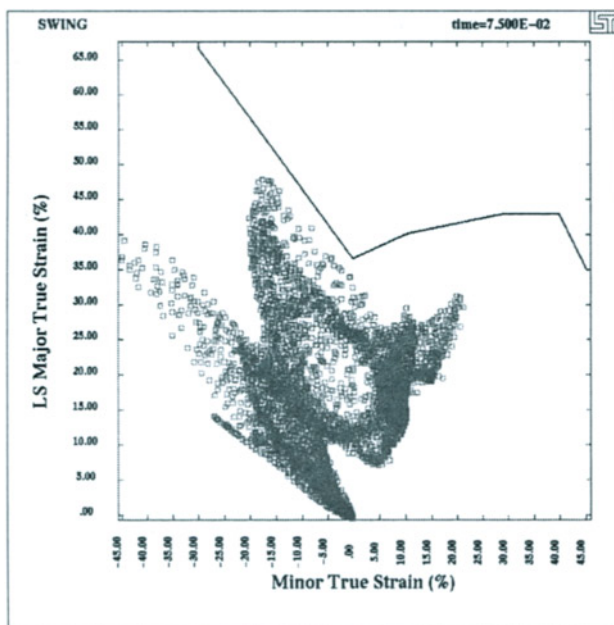


**Figure 10.7** The forming limit diagram and the calculated strains at 298 K (Manninen et al., 2000).

After verification simulations the goal was to decrease the corner radius of the draw-die utilizing FEM-simulations. The present radius was 20 mm and the tested ones were 15, 10, 5 mm and the elliptical shape where  $a$  was 10 mm and  $b$  was 12 mm. The effect of the elliptical shape has been studied by several authors (e.g. Danckert, 1994, 1995, Jensen et al 1998). In these papers it has been shown how the elliptical (or tractrix, three curvature) shape decreases the wear of the draw-die and the residual stresses of the sheet and, furthermore, it has a positive effect to the springback. During the simulations, the proportional movement of the two punches and the blank holding force were also studied. The results of the FEM-simulations are shown in Table 10.1. The corresponding measurement places can be seen in Figure 10.8.

Calculated results show the good effect of the elliptical corner shape on the thickness values (see Table 10.1 and Figure 10.9). The thickness values corresponding to the elliptical die rounding (D1) remain about the same as the ones corresponding to the two times larger corner radius of 20 mm (Test 1). Thus, it appears that decreasing of the radius of the curvature of the drawing die during the first draw becomes possible when the elliptical die shape is used.



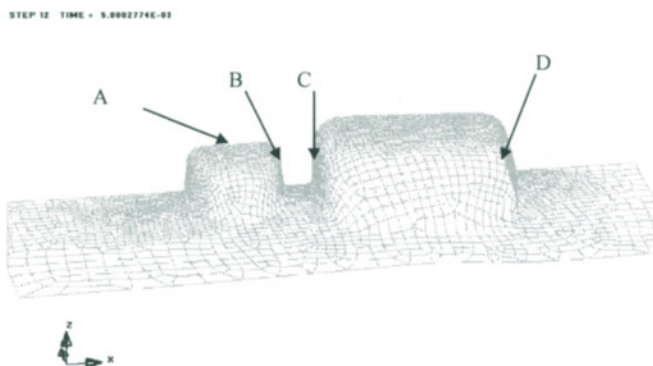
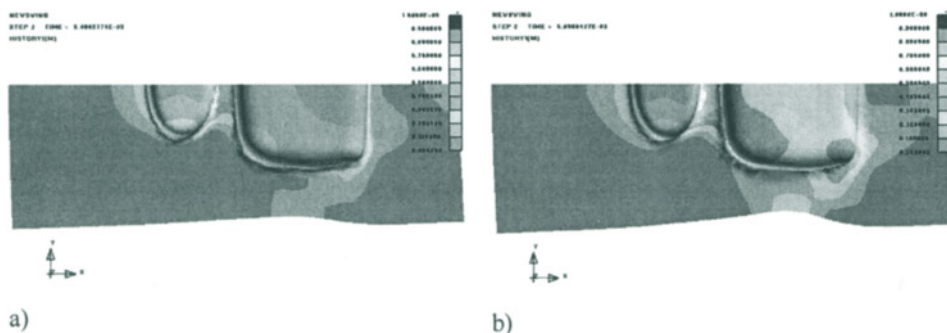
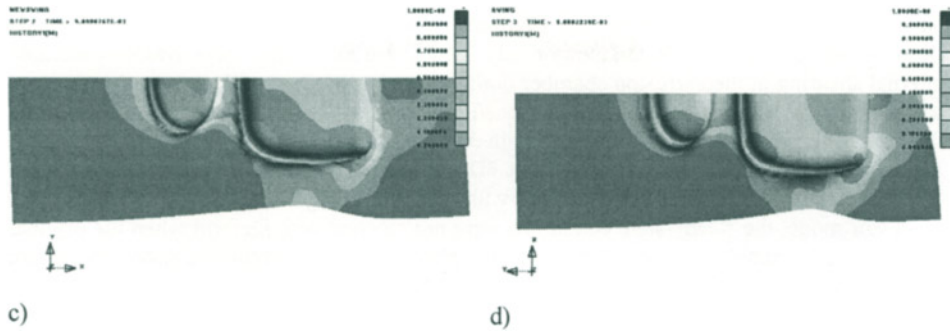


Figure 10.8 The measurement points in simulations.

**Table 10.1** Calculated thickness and FLD-values for different corner radii and blank holding forces (FLD-value compares calculated strain-values to the forming-limit-diagram of the material used).

Draw-die, $r = 20$ mm					
Test no	Pid F (kN)	Thickness (minimum), mm			
		A	B	C	D
1	500	0.54	0.63	0.64	0.61
Draw-die, $r = 15$ mm					
B1	500	0.45	0.56	0.57	0.55
B3	400	0.44	0.54	0.56	0.56
B4	700	0.42	0.52	0.51	0.51
Draw-die, $r = 10$ mm					
C1	500	0.41	0.43	0.54	0.45
C10	400	0.41	0.43	0.52	0.47
C2	700	0.4	0.4	0.53	0.44
C4	500	0.4	0.47	0.57	0.42
C5	500	0.38	0.5	0.57	0.43
C6	500	0.34	0.46	0.6	0.42
C7	500	0.405	0.46	0.58	0.44
C8	500-200	0.41	0.46	0.55	0.45
C9	500-200	0.4	0.44	0.54	0.45
Draw-die, $r = 10$ -12mm (elliptical shape)					
D1	500	0.55	0.64	0.65	0.65





**Figure 10.9.** Calculated FLD-values for different radii of curvature:  
a)  $r = 10$  mm, b)  $r = 15$  mm, c)  $r: a=10$  mm,  $b=12$  mm and d)  $r = 20$ mm (original).

### 10.5 CONTINUOUS EXTRUSION

Many different continuous extrusion processes have been proposed and studied. Of these the Conform process, originally developed by Green (1972) at the UKAEA, has been used most widely in industry. There have been many attempts to study the details of the process experimentally and more recently also by carrying out computer simulations.

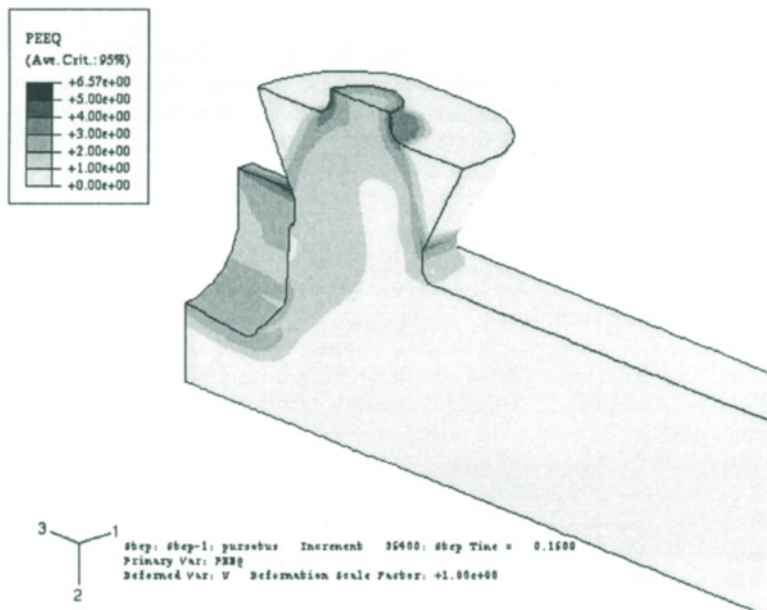


**Figure 10.10** Effective strain distribution during Conform extrusion of copper.

Two- and three-dimensional FEM simulation using Forge2 and Forge3 codes has been studied recently by Velay and Sheppard (2000). In the early 1990s we published results

on two-dimensional simulation of Conform extrusion using the Deform 2D code (Reinikainen et al., 1992; Reinikainen et al., 1993). We found that there was considerable internal shearing in the extrusion chamber during sidewise extrusion. More recently, we have carried out 3D simulation using the Abaqus/Explicit and Deform 3D codes. Figure 10.10 shows an example of the results obtained with Abaqus.

It should, however, be noted that 3D simulation is very time-consuming. Despite 100 hours of computational time spent with the SGI Origin 2000 computer in single processor mode, the steady-state conditions were not reached with Deform when the original curved wheel geometry was used. In simulations with Abaqus a simplified geometry, where the wheel was assumed to be straight, was used as shown in Fig. 10.10.

#### 10.6 DRY TURNING OF Ca-TREATED STEEL

Cutting represents an example of intense localized plastic deformation. Cutting fluids are usually used for cooling due to the high strain rates and concomitant deformation heating.

Over the past decade there has been a marked increase of interest in switching to dry machining to eliminate possibly polluting cutting fluids from industrial cutting operations. Car manufacturers are leading the way and setting an example for other machine shops to follow. In a modern car factory dry machining may today already account for 15% of the operations (Zielasko, 1996). New cutting methods that do not require cutting fluids are also being developed. For example, in gear hobbing it has been possible to increase the cutting speed from about 100 m/min to 600 m/min by switching from uncoated high-speed steel (HSS) hobs to PVD TiN-coated cemented carbide hobs. After doing this, the cutting fluid is no longer needed and clean chips can be obtained for recycling (Sulzer, 1996).

There has also been considerable interest in improving the machinability of workpiece materials. Ca-treatment of steels was first studied by König and Opitz et al. (Opitz et al., 1962a; Opitz et al., 1962b). Some steel companies are now applying it on a commercial scale, although not all steel producers use it. In some cases it has been difficult to obtain consistent results (Finn et al., 2000; Roelofs, 2000). There also appear to be considerable differences in the machinability of steels containing calcium. In an earlier paper (Kankaanpää et al., 1987) we showed that by using TiN-coated tools, the wear life of the tools could be increased considerably, provided that the workpiece material was calcium-treated steel. In a more recent paper (Harju et al., 1996) we compared three commercially available steels in dry turning with both uncoated and TiN-coated HSS tools. We found that the Ca-treated steel which was second best in turning with uncoated tools was best in turning with TiN-coated tools, giving a tool life 26 times longer than the worst steel and a wear life eight times longer than the steel which was best with uncoated tools.

The results are shown in Figures 10.11(a) and 10.11(b). With uncoated inserts steel B seemed to be slightly better than the two others. When the cutting speed was increased from 0.5 ms<sup>-1</sup> to 0.9 ms<sup>-1</sup> and TiN-coated inserts were used, the situation changed completely, as shown in Figure 10.11(b).

Steel C gave clearly the best life time values. Chemical analysis of the rake faces of the tools showed enrichment of alloying elements and the formation of a non-metallic protective layer in the case of steel C, which explains the results.

Secondary ion mass spectroscopy (SIMS) and energy dispersive spectroscopy (EDS) techniques were used to study the enrichment of alloying elements. Although the detailed composition of the protective layer could not be determined quantitatively, some previous results lead us to believe that the composition is near CaTiO<sub>3</sub>.

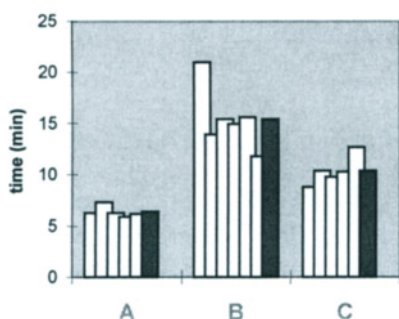


**Figure 10.11 (a)** Wear lives of the uncoated HSS inserts in dry turning of steels A, B and C.

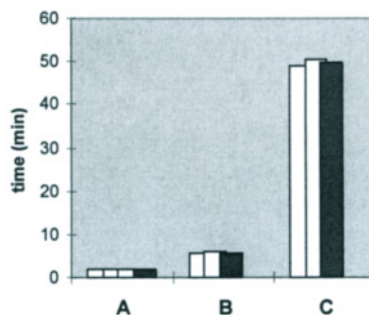


**Figure 10.11 (b)** Wear lives of the TiN-coated HSS inserts in dry turning of steels A, B and C.

## 10.7 OPTIMIZING THE TUBE HYDROFORMING PROCESS

### 10.7.1 Principles of the hydroforming process

Hydroforming is a metal forming process in which internal pressure is used as the main load for producing the deformation of the material being manufactured. This internal pressure is usually produced by hydraulic fluid, such as an emulsion of oil in water, but more recently, some foams have also been found to be suitable for producing this pressure.

Even though the internal pressure is the main load used for this process, it is not the only one, and often, if the geometry of the formed part allows, a secondary load is used in order to improve the formability. This secondary load is usually a force applied on the ends of the blank that forms the final part. This helps to feed material into the forming area, making it possible to avoid excessive thinning of some areas of the part and the possible subsequent bursting of the part due to thinning. However, when this additional feeding of material into the forming area is desired to avoid bursting, it must be done correctly, since an excessive force will lead to local buckling of the material and the produced part will be useless. If the pressure, on the other hand, is too high compared to the feeding force, then the risk of bursting increases. Somewhere in between these two extreme situations is the optimal pressure-feeding curve that will produce a part with the optimal properties. An example of the displacement-pressure curve is seen in Figure 10.12.

In this work we show how to find the optimal curve for a particular hydroformed part that uses a tube as the starting blank for the process. For this optimization procedure, we have studied a part in which the initial thickness of the blank will be rather small and which therefore will be very prone to buckling when a feeding force is applied during the forming process. Buckling phenomena will be the major restriction to the problem of finding an optimum, and due to its catastrophic behavior it will introduce high non-linearities to the problem. When designing the dies, also the springback effect after the forming must be taken into account.

The process starts from a cylindrical tube of stainless steel with an 85 mm nominal diameter and a thickness of 0.5 mm. This initial diameter is taken from the geometry of the die. The perimeter of the initial ellipse is used as a reference and the closest diameter tube (rounding to lower values) according to DIN 2393 that has the same perimeter is chosen.

When the dies close, pre-stamping is done in order to fit the tube better to the shape of the die, before actual hydroforming starts.

The product resulting from this stamping stage does not have a perfectly regular ellipsoidal section, since the shape of the dies is not regular and the tube will be unevenly deformed along the longitudinal axis of the die, but this irregular deformation is not relevant for the subsequent hydroforming process.

Once the dies are closed, the rams are placed at the ends of the tube and the system is then ready to start the hydroforming process itself. In the optimization the variables consists of the forces applied at the ends of the tube and the internal pressure.

Once the hydroforming stage is finished, the formed tube has to be cut to get the desired parts. Using this method two parts are produced at the same time.

### **10.7.2 Hydroforming process simulation**

To be able to optimize the parameters of hydroforming, simulation was carried out using an explicit FEM code, LS-DYNA. The simulation allows one to calculate the estimated thinning of the part due to the deformation process as well as the principal local strains.

Taking advantage of the symmetry of the model not only saved computational time but also helped to avoid errors due to the asymmetry of the finite element mesh used for the calculation. In this simulation, only an eighth of the model was used, which reduced the computational time considerably.

Belytschko-Tsay shell elements were used for the simulation. The friction between the tube and the die was assumed to obey the Coulomb friction criterion and the friction coefficients were taken to be 0.05 for both the static and the dynamic case. Proper boundary conditions must be used in the outer nodes of the model in order to accurately simulate the symmetry effects. A transversely anisotropic material model was used for the calculations.

Since the material model was assumed not to depend on strain rate, the velocity of the simulation could be artificially increased to decrease the simulation time, taking care not to introduce any undesired dynamic effects, however.

### **10.7.3 Optimization of the parameters**

The simulation process consisted of different steps that will be explained in the following in more detail. It was necessary to transform the problem into an equivalent mathematical formulation that describes the process as accurately as possible and enables one to determine the optimal set of parameters for the forming process. A schematic diagram of the optimization is shown in Figure 10.12.

#### **10.7.3.1 Qualitative definition**

Before starting any optimization process it is crucial to have a clear definition of both the real problem and the objective of the optimization. In this case, the objective was to manufacture a part with a minimal variation of thickness on its walls using hydroforming. It was also important to take into account other constraints that must be fulfilled to have a useful product. The final shape of the part must follow the shape of the dies. A correct fit to the dies must exist. The part should not burst or develop buckles.

#### **10.7.3.2 Quantitative definition**

The previously stated conditions must be transformed into a mathematical form in order to make optimization possible. The variation in the thickness of the final part was defined using the following expression:

$$OBJ = f(\mathbf{x}) = \sqrt{\sum_i^N \left| \frac{h_i(\mathbf{x}) - h_{0,i}}{h_{0,i}} \right|^2} \quad (10.1)$$

where  $N$  is the number of total nodes in the FE mesh used for the simulation,  $h_{0,i}$  is the initial thickness and  $h_i$  is the final thickness of each node.  $\mathbf{x}$  is the input set of parameters to be optimized. Once the objective is quantified, it is necessary to describe in the same way the constraints for the process.

The part was considered to fit the die properly when the distance of every node to the die was smaller than a certain value  $K_1$ . It can be assumed that no bursting takes place when all the major strain-minor strain pairs of the nodes in the mesh are under the forming limit curve. However, in the present optimization process, this constraint was not used. The part was checked only at the end of the process. For buckling an index (BI) was proposed. It predicts geometrically the presence of the defect. The part was considered to be correct when the maximum value of the BI in any node was under a limiting value  $K_2$ . The expression for the BI is:

$$BI = \frac{1}{\left\| \sum_i \hat{n}_i \right\|} - 0.25 \quad (10.2)$$

where  $\hat{n}_i$  is a normal vector to the shells surrounding the node. A high distortion of the mesh increases the value of this index.



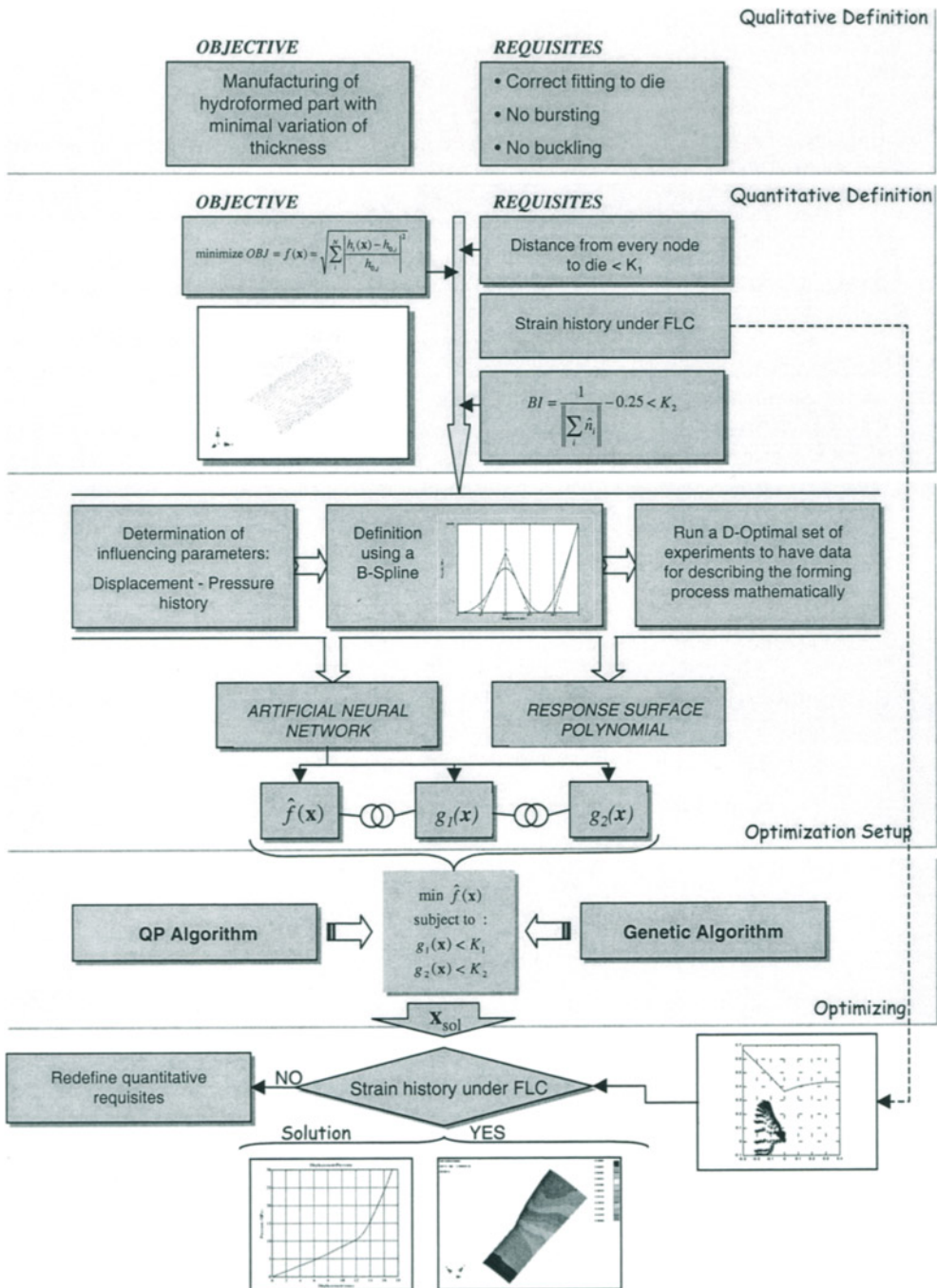


Figure 10.12 Schematic diagram of the optimization procedure.

### 10.7.3.3 Optimization setup

In order to optimize the loads acting on the part so as to get a good quality product, it is necessary to define the loads using a minimum number of parameters to reduce the complexity and computational effort in the optimization process. At the same time, however, the relationship between the feeding and the pressure, to be optimized here, must be complex enough in order to allow one to explore a wide range of possible combinations and not just simple ones. This trade-off between the number of parameters and the complexity of the definition has been nicely solved by Ghouati et al. (1999) using a Bezier curve and by Yang et al. (2001) using a B-spline. In the present work we decided to use a B-spline for the definition of the feeding-pressure curve. This curve can be created based on a few parameters and its ratio of complexity vs. achievable/parameters is very high, thus making it very suitable for the purpose of the present work.

Figure 10.13 gives the definition of a displacement-pressure curve using the B-spline. A total of five variable parameters were used. They consisted of the pressure components of the four control points in the middle of the curve and the total displacement  $d$ . The initial and final control points are fixed to  $(0,0)$  and  $(d, \text{MAXP})$ , respectively, and the displacement components of the four middle control points are each one fifth of the total displacement, as shown in Figure 10.14. MAXP is the value of the maximum pressure at the end of the hydroforming. It was fixed at the beginning of the optimization process and was the same for all the simulations. The velocity of feeding during the hydroforming process is considered constant. The pressure and the displacement ranges are from previous experience.

In this work, the optimization was not based directly on the FEM simulation. Instead, a mathematical model, so-called a metamodel, based on the results obtained from the finite element simulation, was created. To use this model it was necessary to run a set of simulations varying the parameters in order to study the whole hyperspace,  $\mathcal{R}^5$  of input variables. Two models were fitted to the data obtained from simulations. They were a second order polynomial model applying the response surface methodology (RSM) and the feedforward artificial neural network (ANN). The results of both systems were then compared and the model that fit better to the values was used for the calculations. The number of simulations run to fit the data was about five times the number of unknowns in the second order full quadratic polynomial. The number of simulations was chosen to be enough to fit the data correctly with both methods, but not too many to make the process impractical.

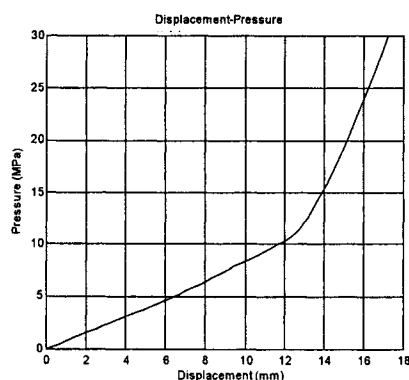


Figure 10.13 Displacement-pressure curve in tube hydroforming.

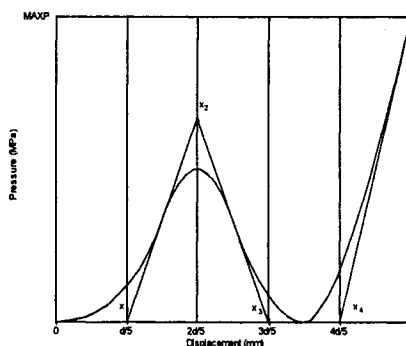


Figure 10.14 Five control points describing the displacement-pressure curve.



This trade-off between the accuracy of the fitted model and the computational time that the simulations need is important and should be carefully chosen. The set of experiments done were based in a D-optimal design for the full quadratic polynomial model. As a result of the previous process an objective function  $f(\mathbf{x})$  and two constraint functions  $g_1(\mathbf{x})$  and  $g_2(\mathbf{x})$  were obtained. In this case, all the resulting models correspond to neural networks.

#### 10.7.3.4 Optimizing and results

The optimization process can now be formulated as:

$$\min \hat{f}(\mathbf{x}) \quad (10.3)$$

subject to the constraints:

$$\begin{aligned} g_1(\mathbf{x}) &\leq k_1 \\ g_2(\mathbf{x}) &\leq k_2 \end{aligned} \quad (10.4)$$

where  $g_1$  and  $g_2$  are the distance and the buckling index fitted functions respectively,  $k_1$  and  $k_2$  are their limit values and  $\hat{f}(\mathbf{x})$  is the fitted objective value model.

To solve the constrained minimization problem, an algorithm based on quadratic programming (QP) was used. However, due to the nature of the fitted functions, those algorithms may lead to problems in reaching the global optimum, and they are likely to get stuck at local minima. Therefore, genetic algorithms (GA) were also used to help finding the global minimum. When using the GA, the problem becomes unconstrained and can be solved using Lagrange multipliers. After solving the problem, an optimal input parameter set is obtained.

The FEM simulation was then run again for that input set and the results were checked, using the forming limit diagram. Since all the qualitative constraints were fulfilled, the solution can be considered as reasonably correct. Had this not been the case, it would have been necessary to redefine the quantitative constraints and repeat the optimization process from that point.

### 10.8. SUMMARY AND CONCLUSIONS

There has been continuous development in numerical modelling and simulation techniques over the past thirty years. They have become more common in the optimization of metal forming processes.

In numerical simulation of metal forming processes the commonly applied hardening models are relatively simple. The hardening models in cold and hot forming are, of course, different, but the same type of yield conditions are usually applied in both cases. However, the models are more complicated than in elasticity. Here we studied four different cases of plastic deformation. They included hot rolling, deep drawing, continuous extrusion, dry turning and hydroforming of tubes. Optimization of each type of process was considered.

It was shown that in hot rolling, combining a recrystallization model with FEM enables one to calculate the rolling load, the final grain size and the resulting mechanical properties with good accuracy. In deep drawing of stainless steels the accuracy of the strain prediction was satisfactory, the difference between the calculated and measured strains being about 10 %.

In continuous extrusion the shape of the deformation zone could be predicted, although 3D simulation appeared to require a large amount of computing time. Dry turning was considered as a case of intense plastic deformation. It was shown that in cutting Ca-treated steel with TiN-coated tools, the wear life may increase nearly 30-fold, making it possible to achieve a significant increase in productivity by adjusting the cutting parameters.

It was shown how the finite element method could be used in combination with metamodels and how they could be used to search for an optimal set of input parameters and produce better quality parts in hydroforming. ANNs showed their ability to act as metamodels when they were correctly fitted to appropriate data. The use of classical optimization algorithms complemented with generic algorithms is a good choice when searching for an accurate global optimum. The combination of the aforementioned techniques appears to be an efficient way to optimize the forming parameters of a hydroforming process.

## REFERENCES

- Cser L., Simula O., Mäntylä P., Ruha P., and Larkiola J. (2000) Self Organising Maps (SOM) in Hot Rolling Intelligent Computation in Manufacturing Engineering (Ed. Roberto Teti), *Proc. of the ICME 2000*, 21/23 June 2000, Capri, Italy, pp.291-297
- Danckert, J. (1994), The residual stress distribution in the wall of a deep-drawn and ironed cup determined experimentally and by FEM, *Annals of the CIRP* **43**, 1, 249-252.
- Danckert, J. (1995) Reduction of the residual stresses in a deep-drawn cup by modifying the draw die profile, *Annals of the CIRP* **44**, 1, 259-262.
- Finn M.E. and Srivastava A.K. (2000) , Environmentally Friendly Free-Machining Steel, Presented at the *AMS International Materials Solutions 2000 Conference*, Oct. 9 –12, 2000, St. Louis, Missouri.
- Ghouati O., Baida M., Lenoir H., and Gelin, J.C. (1999) 3D numerical formulation of tube hydroforming in *Advanced Technology of Plasticity*, Vol. II, *Proc. of the 6<sup>th</sup> ICTP*, Nuremberg, Sept. 19-24, 1999, pp. 1211 – 1216.
- Green D. (1972), Continuous extrusion-forming of wire sections, *J. Inst. Met.* **100**, 295 – 300.
- Harju E., Korhonen A.S., Jiang Laizhu, and Ristolainen E. (1996), Effect of work material composition on the wear life of TiN-coated tools. *Surface and Coatings Technology* **85**, 3, 189-203.
- Jensen, M.R., Damborg, F., Nielsen, K., and Danckert, J. (1998) Optimisation of the draw-die design in conventional deep-drawing in order to minimise tool wear, *Journal of Materials Processing Technology*, **83**, 106-114.
- Kankaanpää H., Pöntinen H., and Korhonen A.S. (1987) *Mater. Sci. and Tech.*, **3**, 155 - 158
- Kohonen, T. (1995) *Self-Organizing Maps* (Springer, Berlin, Heidelberg).
- Larkiola, J., Nylander, J., Myllykoski, P., Korhonen, A.S. (1996) Determining tandem cold rolling efficiency using physical models and neural computing, in *Proc. of 2nd International Conference on Modelling of Metal Rolling Processes*, London, pp. 389-399.

- Lenard, J.G., Pietrzyk, M., and Cser, L. (1999) *Mathematical and Physical Modelling of Hot Rolling*, (Elsevier Science Ltd, Oxford, UK).
- Makinouchi A., Teodosiu C., and Nakagawa T. (1998) *Annals of the CIRP*, **47**, 2, 641 – 649.
- Manninen T., Toivanen T., Tarkiainen T., Myllykoski P., and Korhonen A.S., (2000) Deep drawing of double bowl kitchen sinks of stainless steel, in *Metal Forming 2000*, ed. Pietrzyk M., Kusiak J., Majta J., Hartley P. and Pillinger I. (Balkema), pp. 379 - 384.
- Myllykoski P., Larkiola J., Ahokainen T., Korhonen A., and Cser L. (1999) Modelling and Optimisation of Thermomechanical Processing of Metals, in *Advanced Technology of Plasticity*, Vol. III, Proc. of the 6<sup>th</sup> ICTP, Nuremberg, Sept. 19-24, 1999, pp. 1997 - 2006.
- Opitz H. and König W. (1962a), *Arch. Eisenhüttenw.* **33**, 831-839.
- Opitz H., Gappisch, M., König W., Pape R., and Wicher A. (1962b), *Arch. Eisenhüttenw.* **33**, 841-851.
- Rantanen, A., Malinen, M., and Korhonen, A.S. (1990) Prediction of the microstructure of steel during hot rolling., in *Advanced Technology of Plasticity*, Vol. II (The Japan Society for Technology of Plasticity), pp. 659-664.
- Roelofs H., von Moos Stahl AG, Private Communication, March 6, 2000.
- Sulzer G. (1996), Trockenwälzfräsen, a report presented at the VDI meeting Auf dem Weg zur Trockenbearbeitung, Feb. 13, 1996, Düsseldorf, 17p.
- Velay X. and Sheppard T. (2000), Plane strain and three-dimensional coupled thermomechanical simulation of the Conform process, in *ET 2000 Proceedings*, Volume I, (Aluminum Extruders Council, Chicago), pp. 505 – 517.
- Yang J-B., Jeon B-H., and Oh S-I. (2001) Design sensitivity analysis and optimization of the hydroforming process, *Journal of Materials Processing Technology* **113**, 666 – 672.
- Zielasko W. (1996), Trockenspannung in der Grossserienfertigung, in *Auf dem Weg zur Trockenbearbeitung. VDI Berichte 1240* (VDI Verlag GmbH, Düsseldorf, 1996, pp. 93-110.

## Chapter 11

# The Mathematical Modelling of Hot Rolling of Steel

S. Yue  
*Department of Mining, Metals and Materials Engineering*  
*McGill University*  
*Montreal, Quebec*  
*Canada*

### 11.1 OVERVIEW

In many ways, the best steel is one which has no alloying elements, and that includes the elimination of carbon. Apart from the obvious saving of alloying costs, other properties, in particular weldability, can be improved. Such a concept was made tangible by the discovery of the strong effect of Nb as a steel strengthener at only microalloying additions (0.03 to 0.06 wt%). This was followed by reductions in all alloying levels, with carbon contents routinely decreasing to 0.1 wt% or less. It was then realized that further increases in strength in these lean chemistries (or further reductions in alloying levels) could be obtained by controlling the hot rolling process, which had, hitherto, been merely a means to obtain the final gauge in the hot rolled product. This ushered in the era of thermomechanical processing, or controlled rolling.

By now, in 2002, models have been developed for all aspects of the hot rolling of steel. The most important of these are microstructural evolution (including the transformation after hot rolling), thermal evolution (including cooling after hot rolling) and rolling load prediction. Many of these models have been generated as stand-alone modules and, as such, have been very useful in helping understand what may be happening during hot rolling. Without some type of mathematical model, it is difficult to even qualitatively predict what will happen from pass to pass, let alone what will happen due to a complete rolling schedule.

To be able to comprehensively design a rolling schedule, however, all these stand-alone models should be coupled because all these individual events are coupled. For example, microstructure affects rolling load, which, in turn, affects temperature, which, in turn affects both the rolling load and the microstructural evolution, etc. Therefore, developing a complete and thorough model is a daunting task, and requires considerable resources to achieve. One of the consequences of this complexity is that there are very few 'complete' models, but there have been many attempts at generating each of the individual models.

The 'ideal' model should be generic, in the sense that the inputs are independent of the specific process or product. Unfortunately, truly generic models tend to be limited in 'numerical' accuracy. Much more accuracy can be gained by developing a model for a specific product (e.g. plate, strip, etc.) or steel type, or preferably both. This problem of generating a truly generic model serves to emphasise the complexity of the metallurgical events that are taking place during

hot rolling, and how sensitive these are to rolling process parameters and composition (which are, by and large, dictated by the product).

Thus, a model that can actually generate predictions of, for example, as-hot rolled strengths that are within a few MPa of the actual results, is usually restricted to a very narrow range of chemistries, processing routes and products. One of the possible applications of such a model in the future would be to use it to eliminate the necessity for performing mechanical tests on the as-hot rolled product to verify the properties. However, this is not a goal that can currently be realistically attained. On the other hand, any good generic model should be able to predict the direction of the trends, if not the magnitude of the trends. This is the strength of the current crop of mathematical models. Knowledge of trends is extremely useful with regard to troubleshooting, schedule and alloy design, as well as considerations of the possible effect on properties of changes in steel processing technique or technology.

In this chapter, the components of the CANMET-McGill model will be described. This is quite a simple, but effective model, and illustrates the main requirements of a mathematical model that can predict microstructural evolution during hot rolling. The strengths and weaknesses of this model will be described, and the future direction of models in general will be briefly discussed.

## 11.2 THE CANMET-MCGILL MATHEMATICAL MODEL FOR MICROSTRUCTURAL EVOLUTION OF STEELS DURING HOT ROLLING

### 11.2.1 Stages of hot rolling

Hot rolling is generally divided into the following stages:

- (i) **Reheating:** the first step, since most steel mills cool the steel to room temperature after casting. However, there are more contemporary processing routes that do not involve cooling of the cast strand to room temperature, i.e. direct rolling, or hot or warm charging. These have not been considered in most models. However, there is much published work to indicate that there are significant differences that are revealed during hot rolling when the steel is not allowed to cool to room temperature. In this chapter, only processes incorporating reheating will be considered.
- (ii) **Roughing:** a high temperature rolling stage that is responsible for the initial breakdown of the cast structure.
- (iii) **Finishing:** this stage of hot rolling is usually regarded as being one of the two stages at which the main characteristics of the final as-hot rolled microstructure are generated.
- (iv) **Cooling on the run-out table:** here, the transformation from austenite to, basically, the final structure, takes place, and it is therefore the other stage of thermomechanical processing that dictates the final structure.
- (v) **Coiling:** a stage at which further transformation can take place. This increment of microstructural evolution may lead to a strength change that could amount to some tens of MPa. For many high strength steel compositions that are being used at the highest strength possible, this degree of strength change could be critical.

In the following sections, the changes that occur at each stage, and the integration of each of these changes into the whole model, will be described. It should be noted that much research has been conducted in all the areas that will be described. In this chapter, most of the equations used in the CANMET-McGill model will be given. Many other equations and approaches can be

used within the framework of this and other models. The main justification for using any of these equations is that they combine to give reasonable predictions of published data.

### 11.2.2 Model Inputs

- (i) **Chemical composition:** In this particular model, the chemical composition is used to determine the type and amounts of the transformation products, and the mechanical properties.
- (ii) **Steel type:** In some models, the specific steel grade is an input, rather than the steel chemical composition. In this way, the corresponding TMP characteristics, such as recrystallization kinetics and CCT curves can be placed in the model in the form of databases specific to the steel in question, thus ensuring that numerically accurate predictions can be made. A truly generic model, in which the steel is only characterized by the chemical composition, must rely on interpolations or extrapolations of experimental data. A typical example is recrystallization kinetics equations, which are invariably generated from a few chemical compositions.

The CANMET-McGill model uses a hybrid approach to characterize the steel. As mentioned above, the generic chemical composition is used to characterize the austenite transformation. The steel 'type' is used to characterize the type of hot deformation behaviour. For example, if the 'Nb-Ti' steel type is selected by the 'user', the model performs calculations to determine whether or not rolling is taking place below the no recrystallization temperature. If the 'C-Mn' type is selected, the model does not perform these calculations.

- (iii) **Reheated (austenite) grain size:** There have been many investigations concerning the effect of reheating temperature on grain size. However, it is well known that, in a multi-stage hot rolling schedule, the influence of the reheated grain size on the final microstructure is insignificant. However, in processes in which the level of hot rolling is limited, for example thin slab or strip casting, the grain size just prior to hot rolling may significantly affect the as-hot rolled microstructure. In these cases, the input would be either the as cast grain size, the grain size after hot charging or the grain size after reheating, depending on the processing route.
- (iv) **Reheat temperature:** As noted above, the reheat temperature is not used to determine the reheated grain size, but it is needed to determine what elements are in solid solution.
- (v) **Number of passes:** The *roll speed* and the *roll diameter* are used to calculate the average strain rate through the roll gap, using the following simple approach illustrated in Fig. 11.1. The average strain rate is then simply the strain at the pass divided by the time taken for the roll to move the angular distance  $\alpha$  shown in Fig. 11.1. In reality, the strain rate is changing as the steel moves through the roll gap, but the use of the average strain rate has led to good predictions. The *strain at the pass*, or the relevant dimensional information is required to calculate the strain (e.g. if the product is strip, the thickness can be input and strain is calculated assuming plane strain deformation). *Interpass time* is used to determine the extent of any transformations taking place in between passes. *Cooling rate* during the runout and the *cooling stop* (i.e. coiling) temperature are needed. As mentioned in the previous section, the last two parameters control the type and amount of transformation of the hot rolled austenite.

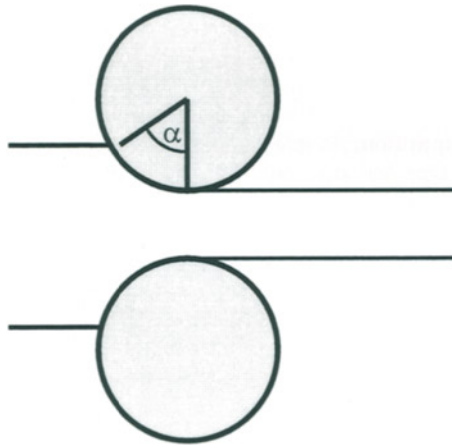


**Figure 11.1** Time taken to generate the strain during flat rolling equals the time taken for the roll to rotate the angular distance,  $\alpha$ .

### 11.2.3 Model Outputs

There are two types of data that are generated by the model:

- (i) **Characteristics of the final microstructure** and properties, i.e. average ferrite GS, phases present and volume fractions, pearlite interlamellar spacing, yield Strength, UTS and impact transition temperature.
- (ii) **The microstructural evolution** during hot rolling, i.e. temperature of no-recrystallization ( $T_{nr}$ ), average recrystallized grain size before the  $T_{nr}$ , average retained strain in grains recrystallized before the  $T_{nr}$ , average non-recrystallized grain size before the  $T_{nr}$ , average retained strain in grains non- recrystallized before the  $T_{nr}$ , Nb in solution and fraction precipitated, N and C in solution. These parameters can be used to help design and optimize rolling schedules.

### 11.2.4 Calculation Steps

#### (i) Reheating Stage

**Calculation:** to determine concentration of alloying elements in solution;

**Purpose:** used to predict precipitation rates and amounts during the rest of the schedule;

**Sub-model:** The simplest approach is to first determine what precipitate species may exist by a simple evaluation of the alloying elements present in the steel. Broadly speaking, in a microalloyed steel containing Nb, V and Ti, it is important to completely dissolve any Nb precipitates

(generically described as niobium carbonitrides, Nb(C,N)), since the effectiveness of these is maximized when precipitation takes place during hot rolling. Any precipitates of Nb that are not dissolved on reheating therefore represent a waste of this relatively expensive alloying element.

If the reheat temperature is high enough to dissolve all the Nb in a typically microalloyed steel, then all the V will go into solution, since the solubility of VN is much higher than that of Nb(C,N). (VN is the least soluble of the V precipitating species).

Unlike Nb and V, additions of Ti are designed to form TiN, which does not dissolve on reheating. These precipitates greatly retard austenite grain growth at all stages of hot rolling, including the reheat stage.

Thus, the optimum approach, for a given alloy, is to use a reheat temperature to completely dissolve Nb(C,N) (or, alternatively, for a given reheat temperature, to use an alloy which will lead to complete Nb precipitate dissolution). The simplest calculation is then based on the solubility of Nb(C,N), which is readily available in the literature. Solubility equations have the following form:

$$\log[M]^m[I]^n = A + \frac{B}{T} \quad (11.1)$$

where [M] and [I] are, respectively, the concentrations of the alloying element under consideration and interstitial (C or N) in the steel. In the case of Nb, since the exact chemical composition of Nb(C,N) varies with steel composition, a good approximation is to use the solubility equation of NbN to calculate the appropriate temperature or Nb level that will lead to complete NbN dissolution. Since the nitride has a lower solubility than the carbide, this calculation will generate, for example, a temperature that is the upper extreme, assuming that the actual precipitate is a carbonitride with a solubility in between that of the nitride and the carbide. A good rule of thumb, to ensure that the Nb is entirely dissolved, is to use a reheat temperature that is about 50 °C higher than the calculated temperature.

On the other hand, there are many practices in which the reheat temperature is not high enough to fully dissolved all the Nb precipitates present. In these circumstances, more precise approaches are recommended. In this regard, one issue that has been addressed by several workers is the effect of other all alloying elements on the solubility of the the carbides and nitrides. The effect of Mn, for example, is well documented, and is shown in the solubility equation below (Koyama et al, 1971a, 1971b):

$$\log[Nb][N] = -\frac{8500}{T} + 2.89 + \left(\frac{1085}{T} - 0.68\right)[Mn] - \left(\frac{48}{T} - 0.032\right)[Mn]^2 \quad (11.2)$$

This basically indicates that Mn increases the solubility of the nitride in austenite (i.e. full solubility of the nitride takes place at a lower temperature when Mn is present).

Another issue is the effect of the presence of several types of precipitates in one steel. This has been considered by Speer et al (1987) in which they determine the solubilities of all the alloying elements in a steel containing Nb and V by calculating the solubility of a  $(Nb_xV_{1-x}C_yN_{1-y})$  precipitate in which 1 mol of this precipitate is made up of: xy mol fraction NbC, x(1-y) mol fraction NbN, y(1-x) mol fraction VC and (1-x)(1-y) mol fraction VN. This is the sub-model that is used in the CANMET-McGill model.



Ideally, a model should embody the effects of all alloying elements and consider the simultaneous dissolution of all possible precipitate species. This is a task of some complexity, given the wide variety of alloying approaches that currently exist. This, once again underscores the difficulty of generating a model capable of numerical accuracy in prediction.

**(ii) Hot deformation stage (every pass during roughing and finishing)**

An overview of the hot deformation stage is shown in the flow diagram of Figure 11.2. The sub-models associated with this subroutine will be described following this overview.

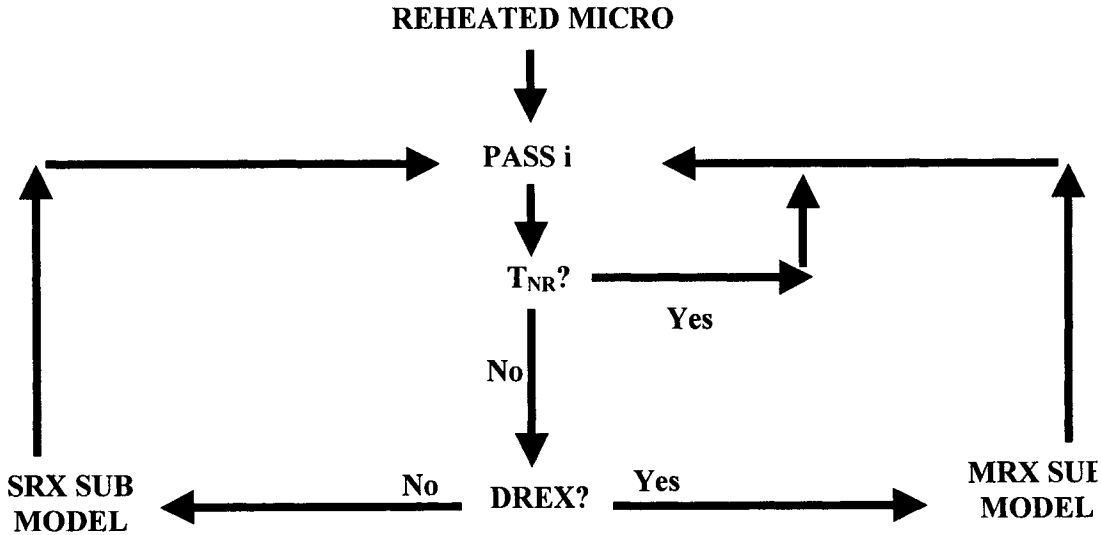


**Figure 11.2** Subroutine for all hot deformation passes.  $T_{nr}$  is the temperature of no recrystallization, DREX is dynamic recrystallization, SRX is static recrystallization and MRX is metadynamic recrystallization.

The first step of this subroutine is to feed the characteristics of the reheated microstructure, i.e. the input grain size and the calculated levels of alloying element in solid solution, into the first pass. The first calculation determines if the rolling temperature is below the temperature of no recrystallization. If it is (i.e., “YES”), then there is no restoration of any sort (including recovery) due to this pass, i.e. the microstructure does not change and no further calculations are required for this pass. The as-hot worked microstructure is then fed into the next pass ( $i = 2$ ), and strain is simply accumulated from pass to pass, eventually leading to pancaked austenite. It has been observed that the effect of accumulated strain in pancaked austenite reaches a saturation at between 1.5 to 2 strain. Therefore, in order to simplify this particular model, there is a maximum amount of strain that can be accumulated, and any strain above this level is not ignored.

If the temperature is above the  $T_{nr}$ , (i.e. “NO”), a calculation is performed to determine if the applied strain exceeds the critical strain to initiate dynamic recrystallization. If the critical strain is exceeded (“YES”), then, metadynamic recrystallization, in the interpass period, follows. If

not, then static recrystallization is assumed. In either case, the subsequent calculations generate values for the amount of recrystallization that takes place in the interpass time prior to the next pass and the recrystallized grain size.

The relevant microstructure at the end of this stage, i.e. the volume fraction recrystallized, the recrystallized grain size, the amount of strain in the unrecrystallized fraction (less recovery) and the amount of alloying element in solid solution, is fed into the next pass, where these calculations are repeated.

In the case of full recrystallization in a time that is less than the interpass time, and where there is no Ti in the steel, then grain coarsening is calculated (not indicated in Figure 11.2) before the microstructure is input into the next pass. Then the subsequent calculations are the same as for the first pass, as noted above. However, if partial recrystallization has occurred, then the model divides the microstructure into two separate fractions, one in which the microstructure has fully recrystallized and one in which the structure has been worked according to the strain delivered in the pass. These fractions are then treated separately in the next pass. The most complex scenario is that the strain in the pass is not enough to give complete recrystallization in either the fully recrystallized fraction or the non recrystallized fraction. Thus, the microstructure is then divided into 4 fractions. Clearly, in a multipass schedule, there is a possibility that the microstructure could be divided into a very large number of fractions as the hot deformation progresses. Because of the nature of the kinetics of recrystallization, there can be many occasions where the microstructure is within a few percent of being completely recrystallized or completely unrecrystallized. Therefore, many models have strategies to limit the number of fractions into which the microstructure will be divided. In this particular model, if the kinetics predict that the microstructure is within a few percent of being fully recrystallized (or unrecrystallized), then the model allows the microstructure to be fully recrystallized (or unrecrystallized), instead of dividing the microstructure into two parts. This is usually enough to limit the total number of fractions to a 'reasonable' number, from the point of view of data manipulations.

The submodels associated with the subroutine of Figure 11.2 are outlined below.

#### (ii-a) Recrystallization Kinetics

**Calculation:** time required for 5% recrystallization after a deformation pass.

**Purpose:** used to determine whether static recrystallization will occur before the next pass.

**Submodel:** The most common approach is based on the work of Dutta and Sellars (1987).

The 'basic' recrystallization equation is semi-empirical with the following form:

$$t_{0.05} = B \varepsilon^{-4} d_0^p Z^q \exp \frac{Q_{rex}}{RT} \quad (11.3)$$

$t_{0.05}$  = time for 5% recrystallization

$\varepsilon$  = strain

$d_0$  = grain size

$Z$  = Zener Hollomon parameter =  $\dot{\varepsilon} \cdot \exp(Q_{def} / RT)$ , where  $\dot{\varepsilon}$  is strain rate,  $T$  is temperature, and  $Q_{def}$  is the activation energy associated with plastic deformation.

Niobium in solid solution slows down the recrystallization rate, and there is a form of this basic equation that includes this effect in the form of the concentration of Nb (in austenite solid solution), the latter having already been calculated.

#### (ii-b) Precipitation Kinetics

**Calculation:** time required for 5% precipitation after a deformation pass.

**Purpose:** to determine whether static recrystallization will occur before the next pass.

**Submodel:** This is the second part of the Dutta and Sellars (1987) approach, and is essentially based on the classical precipitation nucleation and growth theory.

The form of the resulting equation that relates the time for 5% precipitation to the relevant parameters is:

$$t_{0.05} = A[Nb]^{-1} \varepsilon^{-1} Z^{-0.5} \exp\left(\frac{270\,000}{RT}\right) \exp\frac{B}{T^3 (\ln k_s)^2} \quad (11.4)$$

where  $k_s$  is 'chemical' driving force, which is the ratio of solubility products of the reheat temperature and the pass temperature. The constants A and B are chosen essentially to give the best fit to observed precipitation data.

#### (ii-c) Interaction of Precipitation and Recrystallization

**Calculation:** the 5% recrystallization and precipitation times are compared

**Purpose:** used to determine whether static recrystallization will occur before the next pass

**Submodel:** The third part of the Dutta and Sellars approach is to compare the calculated times for 5% recrystallization and precipitation:

if  $t_{0.05}(\text{recrystallization}) > t_{0.05}(\text{precipitation})$

then recrystallization will progress. It should be noted that, for a given rolling schedule, this calculation does not predict the  $T_{nr}$ , since this temperature is, for a given steel, the highest temperature at which recrystallization will not take place. If this submodel is applied for a given rolling schedule, it only indicates the first pass at which recrystallization is stopped. For a given steel, the  $T_{nr}$  will occur at a higher temperature than the temperature of this pass. To determine the  $T_{nr}$  using the model, one approach is to run the model, with the desired steel composition, using an idealized rolling schedule that has rolling passes at, say, 10 °C intervals. The temperature at which recrystallization is stopped will then be close to the  $T_{nr}$ .

#### (ii-d) Critical Strain for Dynamic Recrystallization

It is well known that the critical strain can be related in a simple empirical fashion to the austenite grain size and the Zener Hollomon parameter in the following way:

$$\varepsilon_c = A.d_0 Z^P \quad (11.5)$$

where A and p are empirical constants.

#### (ii-e) Kinetics of Metadynamic Recrystallization

Metadynamic recrystallization is recrystallization that takes place following dynamic recrystallization (which itself takes place whilst the steel is under load in the roll gap). The factors that influence the kinetics are revealed in the following equation for the time,  $t_x$ , required for a given fraction,  $x$ , of metadynamic recrystallization to occur:

$$t_x = K \cdot Z^q \cdot \exp(Q_{\text{mrx}} / RT) \quad (11.6)$$

where  $q$  and  $K$  are empirical constants, and  $Q_{\text{mrx}}$  is an activation energy associated with metadynamic recrystallization. As can be seen by comparing this expression with equation 3, which is the corresponding equation for classical static recrystallization, the only common processing parameter is the Zener Hollomon parameter. In the case of metadynamic recrystallization, the kinetics are *only* dependent on this parameter. For classical static recrystallization, the kinetics are additionally dependent on the grain size and the applied strain. It is therefore very important to determine whether or not dynamic recrystallization has been triggered.

#### (ii-f) Fraction Recrystallized

Regardless of whether static or metadynamic recrystallization is taking place, Johnson-Mehl-Avrami kinetics are assumed, i.e. :

$$\text{fraction recrystallised, } \zeta = 1 - \exp(-kt^n) \quad (11.7)$$

where  $t$  is the interpass time and  $n$  is a constant.

The constant,  $k$  can now be expressed in terms of  $t_{0.05}$ , which can be calculated from the equations given previously, i.e.

$$0.05 = 1 - \exp(-kt_{0.05}^n) \quad (11.8)$$

$$k = C / t_{0.05}^n \quad \text{where } C = -\ln(1 - 0.05)$$

Substitution back into original Avrami equation gives

$$\zeta = 1 - \exp(-0.05(t / t_{0.05})^n) \quad (11.9)$$

**(ii-g) Recrystallized Grain Size and Subsequent Grain Coarsening**

For static recrystallization, there are many different equations that can be found in the literature. These are mainly empirical equations. The CANMET-McGill model uses the relationship determined by Sellars (1980):

$$d_{rex} = 0.9d_0^{0.67} \epsilon^{-0.67} \quad (11.10)$$

As may be anticipated, the grain size after full metadynamic recrystallization depends only on the Zener-Hollomon parameter.

After full recrystallization, grain coarsening takes place. The equations used are variations of the theoretically derived form:

$$d^m = d_0^m + k_s t \exp\left(\frac{Q_g}{RT}\right) \quad (11.11)$$

where  $k_s$  and  $m$  are materials and processing dependent constants, and  $Q_g$  is the apparent activation energy for grain growth. Values for these constants can be found from the work of Hodgson and Gibbs (1992).

**(ii-h) Precipitation During Pancaking**

It has been shown that recrystallization is stopped during hot deformation by the formation of precipitates, dynamically, at each pass. In the interpass time, growth of these precipitates takes place. The number of nuclei formed dynamically has been estimated by Valdes and Sellars (1991). Growth of these precipitates can be calculated according to the classic Zener-Wert (1949) soft impingement model, eventually leading to an expression for the fraction precipitated, in the form of a Johnson-Mehl-Avrami kinetic equation (i.e. Equation 11.7). It is also assumed that only 'freshly' nucleated precipitates grow. Precipitates nucleated in previous passes stop growing once new precipitates are formed.

**11.2.5 Transformation during cooling to coiling (on the runout table)**

At this point, the austenite grain size, the amount of pancaking/retained strain and the alloying elements in solution have been calculated. The following calculations are performed to generate the final, as-hot rolled microstructure.

**11.2.6 Effective austenite surface area per unit volume**

The effect of pancaking is to increase the number of ferrite nucleation sites, which leads to ferrite grain refinement. Since austenite grain boundaries are the usual ferrite nucleation sites, the result of pancaking can be regarded as an effective increase in the austenite grain boundary area per unit volume. The origin of this effective austenite grain boundary increase is partly geometric, in that pancaked grains have more grain boundary area/per unit volume compared to an equiaxed structure, and partly due to the creation of nucleation sites within austenite grain boundaries at deformation bands. Cuddy (1986) has generated appropriate expressions in terms of grain morphology and size parameters, as well as retained strain.

### 11.2.7 Ferrite grain size

There are many expressions in the literature that can be used to predict the ferrite grain size resulting from the transformation of austenite. The CANMET-McGill model uses the empirical model generated by Hodgson and Gibbs (1992).

For the case in which there is no retained strain in the austenite prior to the transformation, the ferrite grain size is given by the following equation:

$$d\alpha_0 = (\beta_0 + \beta_1 C_{eq}) + (\beta_2 + \beta_3 C_{eq}) \dot{T}^{-0.5} + \beta_4 (1 - \exp(\beta_5 d\gamma)) \quad (11.12)$$

where

Carbon equivalent,  $C_{eq} = C + Mn/6$

$\dot{T}$  = cooling rate ( $^{\circ}C/s$ )

$d\gamma$  = austenite grain size ( $\mu m$ )

and all other values are constants, which depend on the carbon equivalent.

Any retained strain ( $\epsilon_r$ ) modifies the ferrite GS ( $d\alpha_0$ ) in the following manner:

$$d\alpha = d\alpha_0 (1 - 0.45 \sqrt{\epsilon_r}) \quad (11.13)$$

### 11.2.8 Austenite transformation to ferrite pearlite and bainite

Ideally, equations would be used that predict continuous cooling transformation behaviour in terms of alloying elements and austenite condition (grain size and retained strain). Such models are extremely complex and, in any case, have often been developed to model 'conventional' steel heat treatments, such as quenching and tempering. Therefore, these models have been developed for relatively highly alloyed, higher C steels, whereas the steels of interest in thermomechanical processing are microalloyed. Nevertheless, such models incorporate considerable experimental data concerning austenite transformations, and are therefore highly appropriate for generic microstructural models.

One approach that is particularly practical in terms of ease of integration into the whole model is that of Maynier et al (1970). They have generated empirical equations in terms of C, Mn, Ni, Cr, Mn, Mo and Nb to calculate critical cooling rates to obtain specified fractions of bainite and ferrite + pearlite. These have been further adjusted to include grain size and retained strain via the effective grain size. For example, to obtain 100% bainite, the minimum cooling rate,  $V_2$  ( $^{\circ}C/hr$ ) is expressed as:

$$V_{100B} = 10(10.17 - (3.8C + 1.07Mn + 0.7Ni + 0.57Cr + 1.58Mo + 2Nb + (\text{effective grain size})^2)) \quad (11.14)$$

with the effective grain size =  $1/S_v$ . Similar equations have been generated for a several microstructures. In order to use these equations, the result of the desired cooling rate is interpolated between two cooling rates with which give known microstructures. For example, if the cooling rate on the runout table is C, and it falls between  $V_{100B}$  and the corresponding cooling rate to obtain 90% bainite and 10% ferrite + pearlite,  $V_{90B}$ .

$$\text{Bainite fraction} = 1 - \left( \frac{V_{100B} - C}{V_{100B} - V_{90B}} \right) 0.1 \quad (11.15)$$

The fraction of pearlite is basically calculated on the basis of the steel equilibrium phase diagram, and an empirical equation is used to determine the pearlite interlamellar spacing.

One of the main drawbacks of this approach is that evolution of the transformation cannot be tracked. This means that certain processing techniques, such as rolling in the austenite + ferrite two phase region (intercritical rolling) or interrupted cooling, in which the steel is subjected to more than one cooling rate on the run-out table, cannot be modeled.

### 11.2.9 Precipitation in transformed austenite

This depends on the microalloying levels and interstitials left in solid solution, as well as the coiling temperature. A model such as the one derived by Dutta and Sellars for the precipitation kinetics of Nb in austenite would be ideal. One of the few efforts at generating such a submodel is by Lee et al (1997), who use a classical nucleation and growth approach.

### 11.2.10 Mechanical Properties

The largely empirical equations used in this model, are the ones derived by Pickering (1978). The concept is essentially based on considering that each component of the microstructure contributes to the properties according to a simple weighted average formula, for example, for yield strength (YS):

$$YS = f_{\alpha}\sigma_{\alpha} + f_p\sigma_p + f_b\sigma_b \quad (11.16)$$

with  $\sigma_i = f$  (size, morphology, chemical composition). Equations of this type have been generated for yield and ultimate tensile strengths, as well as impact transition temperature.

## 11.3 DISCUSSION

Most models of this type give a reasonable prediction of the yield and ultimate tensile strengths. The impact transition temperatures are not as reliable, probably because impact fracture is much more sensitive to inhomogeneities in the microstructure. In fact, even though much effort has been put into the event that partial recrystallization takes place, the final properties are generated on the basis of one microstructure. Perhaps a more rigorous model that takes into account partial recrystallization, and generates the relevant final inhomogenous microstructure and properties will lead to a better prediction of impact properties and fracture properties in general.

As noted before, although the general agreement between model and actual values is quite good, there is invariably some 'scatter'. One way to improve the agreement is to generate equations that are specific to the steel being processed. For example, all of the equations concerning the microstructural changes that occur during hot rolling have been generated by studies of relatively small number of steel chemistries. Thus, the constants in such equations will be different for specific steel chemistries. One user-friendly feature of the CANMET-McGill model is

the ability to change many of the constants of the equations without having to access the code. Thus, the model can be tailored to a specific steel grade.

Another approach that was used in the development of this model was to statistically analyze the influence of all parameters, calculated and measured, on the various properties. As may be expected, the agreement was much improved, but it is suggested that this approach be limited to one grade and one product.

Potentially, the most useful application of thermomechanical processing models is in assessing the impact of process changes. A natural progression of such a study is then schedule design. In other words, if a change in the process leads to an adverse effect on the properties, how can the rolling schedule be changed to compensate for this problem? Unfortunately, the set-up of such models is not very conducive to ease of schedule design. Ideally, the input should be, for example, the desired mechanical properties and the chemical composition, and the output should be the rolling schedule. As can be seen from the above description, the reverse is true for existing models. Moreover, the issue of coupled models is again raised, since a change in the rolling schedule must lead to a change in the rolling temperatures.

Nevertheless, even with such restrictions, generic mathematical models that predict as-hot rolled properties incorporate considerable information. The key to unlocking this information lies in imaginative use of the model capabilities. Whilst much work has gone into developing these models, very little effort has been made to develop strategies for effective use of these models. Once such strategies have been identified, then thermomechanical microstructural models may gain more industrial acceptance.

## REFERENCES

- Cuddy J., (1986) "The Effect of Accelerated Cooling on the Transformation Products That Develop in Deformed and in Recrystallized Austenites", in 'Accelerated Cooling of Steel', ed. P.D. Southwick, TMS-AIME Warrendale, Pa, p. 235.
- Dutta B. and Sellars C.M., (1987) "Effect of composition and process variables on Nb(C,N) precipitation in a Nb microalloyed austenite", *Mats. Sci and Technol.*, 3, p. 197.
- Hodgson P.D. and Gibbs R.K., (1992) "A Mathematical Model to Predict the Mechanical Properties of Hot Rolled C-Mn and Microalloyed Steels", *ISIJ International*, 32, p.1329.
- Koyama S., Ishii T. and Narita K., (1971) *Jap. Inst. of Metal J.*, 35, , p.698.
- Koyama S., Ishii T. and Narita K., (1971) *Jap. Inst. of Metal J.*, 35, , p.1089
- Lee J.K., Kwon , O. and Lee K.J., (1997) "Modelling of Precipitation During Coiling in Nb Bearing HSLA Steels", *Proceedings on Accelerated Cooling/Direct Quenching Steels, Materials Solutions, ASM*, p. 175
- Maynier Ph., Dollet J. and Bastien P., (1970) "Influence des éléments d'alliage sur le trempabilité des aciers faiblement alliés", *Revue de Métallurgie*, Avril.
- Pickering F.B., (1978) "The Optimisation of Microstructures in Steel and Their Relationship to Mechanical Properties, 'Hardenability Concepts with Applications to Steel'", eds D.V. Doane and J.S. Kirkaldy, TMS-AIME Warrendale, Pa, p.179.
- Sellars C.M., (1980) "The Physical Metallurgy of Hot Working", in 'Hot Working and Forming Processes', (eds. C.M Sellars and G.J. Davies), The Metals Society, London, p.3.
- Speer J.G., Michael J.R and Hansen S.S., (1987) "Carbonitride precipitation in Nb/V microalloyed steels", *Metall. Trans* 18A, p. 211-222



Valdes E. and Sellars, C.M., (1991) "Influence of Roughing Rolling Passes on Kinetics of Strain Induced Precipitation of Nb(C,N)", Mats. Sci. and Technol., 7, p. 622

Wert, C., (1949) J. Applied Phys., 20, p. 943

Zener, C., (1949) J. Applied Phys., 20, p. 950

## Chapter 12

# Identification of Rheological and Tribological Parameters

DANUTA SZELIGA, MACIEJ PIETRZYK  
*Department of Computational Methods in Metallurgy*  
*Faculty of Metallurgy and Materials Science*  
*Akademia Gorniczo-Hutnicza*  
*30-059 Krakow, Al. Mickiewicza 30*  
*Poland*

Numerical simulation of metal forming processes requires precise information about the material properties and the accuracy of the simulation depends strongly on the correctness of the description of the mechanical and thermal boundary conditions. The former problem is directly connected with the evaluation of rheological parameters. One of the challenges in the simulations of thermo-mechanical processes is an evaluation of these parameters under various conditions of deformation by performing plastometric tests of compression, tension or torsion. Advantages and disadvantages of these tests and difficulties with the interpretation of the results are well known (Lenard et al., 1999). The main disturbances are inhomogeneities of strains, localization of strains, effect of friction and heat generated due to deformation and friction. Following this, the goal of many researches is development of a method that eliminates the disturbances occurring in plastometric tests and that allows the estimation of rheological and friction parameters independently of these phenomena. The problem of parameter evaluation can be defined as an inverse problem. Several papers deal with the inverse analysis in metal forming (Gavrus et al., 1995; Boyer and Massoni, 1999; Gelin and Ghouati, 1999; Gelin and Ghouati, 1994; Kusiak et al., 1995), nevertheless, the complex task of estimation of both rheological and friction parameters still remains open. Since friction has to be assumed when rheological parameters are identified and vice versa, solving of this task became very important.

Friction plays an important role in metal forming. Proper evaluation of friction coefficient is essential for an accurate simulation of metal flow in various industrial forming processes. A large number of research on contact problems has been carried out, starting from fundamental works of Schey (1970a) to the advanced models accounting for

an influence of oxides developed by Krzyzanowski and Beynon (1999), but the problem of an accurate description of influence of friction in simulations is still not completely solved. Friction inevitably arises at the tool-workpiece interface, and may be expressed from the mechanical point of view either as a coefficient of friction  $\mu = \tau/p$  in the Coulomb model, as a friction factor  $m = \tau/\tau_{max}$  in Tresca's law or  $m_c = \tau/\sigma_p$  in the model proposed by Chen and Kobayashi (1978), ( $\tau$  - friction stress,  $p$  - unit pressure at the contact surface,  $\sigma_p$  - flow stress,  $\tau_{max}$  - yield stress in shear). Friction, with some significant exceptions, is an unwanted factor with a number of undesirable effects. In general, it raises the forces and the power requirements, subjects the deforming tool to higher pressure, renders the deformation less uniform within the workpiece, raises the temperatures at the interface and, finally, sets the limits to the maximum obtainable deformation (Schey, 1970a). In addition to these negative aspects of the contribution of friction, it affects the flow pattern in the deformation zone.

Following this dominant role of friction in metal forming processes, difficulties in the formulation of an accurate friction model and the important role played by friction in the evaluation of rheological parameters of materials, the present chapter focuses on the complex problem of simultaneous identification of both rheological and friction parameters from one type of plastometric test. The investigations performed have allowed the working out of a three-stage inverse algorithm that is the solution of the problem. Regardless of the type of the metal forming inverse problem and independently of the applied method of the solution, the algorithm consists of three parts:

- Experiments: Measured data from the experiment is an input information for the goal function of the inverse algorithm;
- Simulation: For the direct problem, usually based on finite element method;
- Optimization procedure to minimize the defined goal function: Classical non-gradient and gradient algorithms as well as heuristic methods such as evolution algorithms and neural networks can be applied.

The method was substantiated for various steels and conditions of deformation (temperature, strain rate, cold and hot forming). Various rheological and friction models were tested. In this chapter the inverse algorithm, developed by the authors, is described and typical results of the inverse analysis for carbon-manganese steel and austenitic stainless steel are presented.

## 12.1 INVERSE METHOD

### 12.1.1 Definition of the inverse problem

Deformation process is described by the set of equations:

$$\mathbf{d} = F(\mathbf{x}, \mathbf{p}), \quad F: R^k \rightarrow R^r \quad (12.1)$$

where  $\mathbf{d} = \{d_1, \dots, d_r\}$  - vector of measured output parameters,  $\mathbf{x} = \{x_1, \dots, x_l\}$  - vector of model parameters,  $\mathbf{p} = \{p_1, \dots, p_k\}$  - vector of process variables. Examples of the foregoing vectors are: loads monitored during the process, shape of the sample after the process, efficiency of die filling, temperatures recorded during the process for measured

data  $\mathbf{d}$ , parameters of the stress-strain curve, friction coefficient, heat conductivity for parameters  $\mathbf{x}$  of the model, strain, strain rate, temperature of sample, die and surroundings for process variables  $\mathbf{p}$ . If the vector  $\mathbf{x}$  is unknown, the problem (12.1) is called the inverse problem.

The objective of the inverse analysis is an evaluation of optimum values of vector  $\mathbf{x}$  components. It leads to minimization, with respect to the vector  $\mathbf{x}$ , of the distance between vectors containing the calculated and experimental values:

$$\Phi(\mathbf{x}) = \sum_{i=1}^n \beta_i [\mathbf{d}_i^c(\mathbf{x}, \mathbf{p}_i) - \mathbf{d}_i^m]^2 \quad (12.2)$$

where:  $\mathbf{d}^m = \{\mathbf{d}_1^m, \mathbf{d}_2^m, \dots, \mathbf{d}_n^m\}$  - vector of measured data,  $\mathbf{d}^c = \{\mathbf{d}_1^c, \mathbf{d}_2^c, \dots, \mathbf{d}_n^c\}$  - vector of calculated data,  $\beta_i$  - weight factors ( $i = 1 \dots n$ ),  $n$  - number of sampling points. Measured data  $\mathbf{d}^m$  is obtained from an experiment and the values  $\mathbf{d}^c$  are calculated using a numerical or analytical model of the direct problem. The flow chart of the inverse method is shown in Figure 12.1. The goal function (12.2) is usually defined as an average square root error (error in Euclid's norm), but other norms can be used, as well.

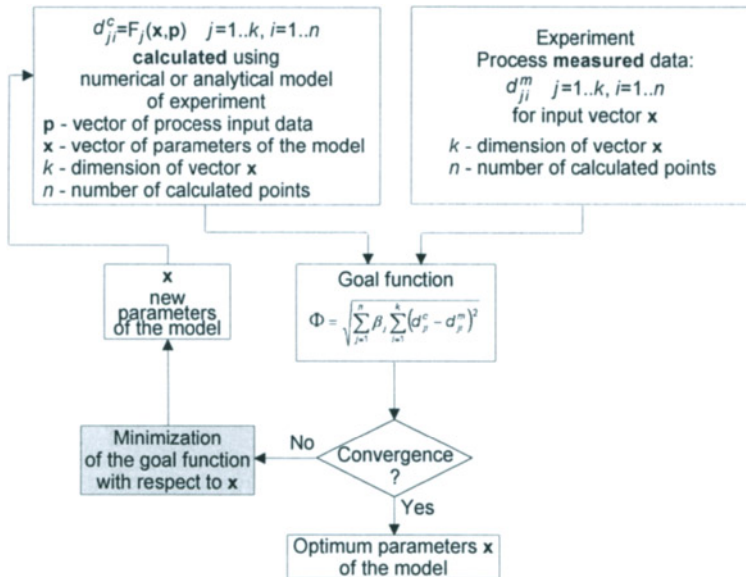


Figure 12.1 Flow chart of the inverse algorithm

The inverse algorithm can be applied to solve any of thermal, mechanical and boundary problem in metal forming (Boyer and Massoni, 2001; Fourment et al., 1998; Pietrzyk et al., 1994; Pietrzyk et al., 2000; Malinowski et al., 1994). Investigations performed by the authors (Szyndler et al., 2000; Szyndler et al., 2001a; Szyndler et al., 2001b) focus on simultaneous identification of material properties (rheological parameters

of the flow stress equation) and the mechanical boundary conditions (friction coefficient or factor). The following procedures were selected in this approach:

- one of the plastometric test is used as an experiment;
- direct problem, which is a simulations of the selected test, is defined as a thermal-mechanical problem solved by the finite element method;
- minimization of the goal function is performed using non-gradient methods and genetic algorithms for searching for minimum.

Details of the applied inverse method are presented in sections 12.1.2 – 12.1.5.

### 12.1.2 Experiment

The identification of rheological parameters is based on the results of plastometric tests. The most often used test is axisymmetrical compression or plane strain compression (Figure 12.2). Loads measured and monitored during the process as a function of the tool displacement are the input data for the inverse model.

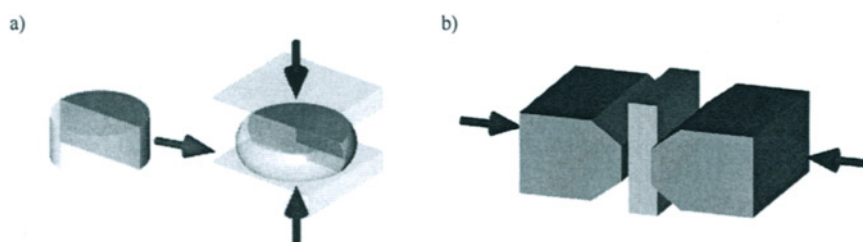


**Figure 12.2** Schematic illustration of axisymmetrical (a) and plane strain (b) compression

Accurate estimation of the stress-strain curve, based on the finite element analysis of the obtained results, requires an accurate description of the thermal and mechanical boundary conditions. Especially the problem of friction, which occurs on the tool – sample contact surface, is crucial. A number of methods of measurement of friction coefficient has been developed and several of basic concepts are discussed by Schey, (1970b). None of the methods allows for direct measurement of this coefficient. Indirect measurement always involves some calculations based on assumptions regarding the properties of materials in contact and the homogeneity of the deformation. Therefore, the inverse analysis is now commonly used for an interpretation of results of various tests. Among a number of tests dedicated to the evaluation of friction coefficient, the ring compression test is particularly easy to deal with and this test was selected in the present work. Schematic illustration of the ring compression process is presented in Figure 12.3.

The ring compression technique originally developed for cold forming was adapted by Male and Cockcroft, (1964-65) for hot working. Since the position of the neutral point is a function of friction, there is no need to measure forces. It is sufficient to measure only the change of the shape of the ring. The conventional method of interpretation of the ring compression test is based on the measurement of the internal diameter after compression only. The diagrams, see for example (Schey, 1970b; Male and Cockcroft, 1964-65), are used for the determination of the friction coefficient on the basis of this measurement. The ring compression test, however, supplies more information than

the changes of the ring inner diameter. Inverse analysis allows accounting for this information, which usually includes the results of the measurements of the inner and outer diameters at several locations along the height of the ring. Moreover, measurement of the loads during ring deformation provides information which additionally allows the estimation of the flow stress parameters. Therefore, this test can be selected for the evaluation of both friction and rheological parameters.

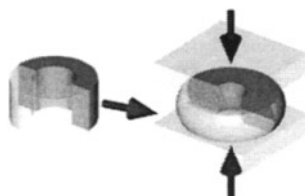


Figure 12.3 Ring compression test

### 12.1.3 Direct problem

In the present work the direct problem is defined as a simulation of the ring compression, axisymmetrical compression or plane strain compression test. The finite element code used in the calculations is based on the rigid-plastic approach coupled with the solution of the heat transport equation. Detailed description of this model is given in Lenard et al., (1999) and the main equations and assumptions are presented below. The approach follows the extremum principle, which states that for a plastically deforming body of volume  $V$ , under the tractions  $\underline{\tau}$  prescribed on the part of the surface  $S_t$  and the velocity  $\underline{v}$  prescribed on the remainder of the surface  $S_v$ , under the constraint  $\dot{\epsilon}_v = 0$ , the actual solution minimizes the functional:

$$J = \int_V (\sigma_i \dot{\epsilon}_i + \lambda \dot{\epsilon}_v) dV - \int_{S_t} \underline{\tau}^T \underline{v} dS_t \quad (12.3)$$

where:  $\lambda$  - Lagrange multiplier,  $\sigma_i$  - effective stress which, according to the Huber-Mises yield criterion, is equal to the flow stress  $\sigma_p$ ,  $\dot{\epsilon}_i$  - effective strain rate,  $\dot{\epsilon}_v$  - volumetric strain rate,  $\underline{\tau} = \{\tau_x, \tau_y\}^T$  - vector of boundary traction,  $\underline{v} = \{v_x, v_y\}^T$  - vector of velocities,  $v_x, v_y$  - components of the velocity vector,  $\tau_x, \tau_y$  - components of external stress, which in metal forming processes is a friction stress or stress caused by external tension (for example, the back and front tensions in rolling).

In the flow theory of plasticity, the strain rates ( $\dot{\epsilon}$ ) are related to stresses ( $\underline{\sigma}$ ) by the Levy-Mises flow rule:

$$\underline{\sigma} = \frac{\sigma_p}{3\dot{\epsilon}_i} \dot{\epsilon} \quad (12.4)$$

Discretization of equation (12.3) and differentiation with respect to the nodal velocities and to the Lagrange multiplier yields a set of non-linear equations, which is usually solved by the Newton-Raphson linearization method. Linearization yields:

$$\mathbf{p} = \mathbf{K} \begin{Bmatrix} \Delta \mathbf{v} \\ \lambda \end{Bmatrix} \quad (12.5)$$

where:

$$\mathbf{K} = \begin{bmatrix} \frac{\partial^2 J}{\partial \mathbf{v}^T \partial \mathbf{v}} & \mathbf{b} \\ \mathbf{b}^T & 0 \end{bmatrix} \quad \mathbf{p} = \begin{Bmatrix} \frac{\partial J}{\partial \mathbf{v}^T} \\ \mathbf{b}^T \hat{\mathbf{v}} \end{Bmatrix} \quad \mathbf{b} = \int_V \mathbf{B}^T \mathbf{c} dV \quad (12.6)$$

$\hat{\mathbf{v}}$  - vector of nodal velocities calculated in the previous iteration,  $\Delta \mathbf{v}$  - vector of increments of nodal velocities,  $\mathbf{c}$  - matrix, which imposes the incompressibility condition  $\dot{\epsilon}_V = \mathbf{c}^T \dot{\epsilon}$ ,  $\mathbf{B}$  - matrix of derivatives of the shape functions.

The friction model proposed by Chen and Kobayashi (1978) and described by Pietrzyk and Lenard (1991) is used in this approach:

$$\tau = m_c \sigma_p \left[ \frac{2}{\pi} \tan^{-1} \left( \frac{|\mathbf{v}_s|}{a} \right) \right] \quad (12.7)$$

where:  $\mathbf{v}_s$  - slip velocity,  $a$  - constant, few orders smaller than an average slip velocity (if the value of slip velocity  $\mathbf{v}_s$  is large, formula (12.7) is equivalent to Tresca's friction law  $\tau = m \tau_{\max}$  with  $\tau_{\max}$  - yield stress in shear and  $m = \sqrt{3} m_c$ ).

The mechanical part of the model is coupled with the finite element solution of the heat transport equation:

$$\nabla k(T) \nabla T + Q(T) = c_p(T) \rho(T) \frac{\partial T}{\partial t} \quad (12.8)$$

where:  $k(T)$  - conductivity,  $Q(T)$  - heat generation rate due to deformation work during compression,  $c_p(T)$  - specific heat,  $\rho(T)$  - density,  $T$  - temperature,  $t$  - time.

The following boundary conditions are used in the solution:

$$k(T) \frac{\partial T}{\partial \mathbf{n}} = q + \alpha(T)(T_0 - T)$$

where:  $\alpha$  - heat transfer coefficient,  $T_0$  - ambient temperature or tool temperature,  $q$  - heat flux due to friction,  $\mathbf{n}$  - unit vector normal to the surface.

The model, based on the equations (12.3) - (12.8) is applied in the inverse method for the simulation of axisymmetrical, plane strain and ring compression tests.

#### 12.1.4 Goal function and optimization procedure

The form of the objective function depends on the type of the estimated parameters and on the performed experiment. If the goal of the inverse analysis is:

- Identification of friction parameters. The ring compression test is used as the experiment and the objective function is defined as the distance between the measured

shape of the sample and that predicted by the FE simulator after the compression process:

$$\Phi = \sqrt{\frac{1}{Nt \, Npr} \sum_{i=1}^{Nt} \sum_{j=1}^{Npr} \left[ \left( \frac{R_{cij}^{in}(\mathbf{x}, \mathbf{p}_i) - R_{mij}^{in}}{R_{mij}^{in}} \right)^2 + \left( \frac{R_{cij}^{out}(\mathbf{x}, \mathbf{p}_i) - R_{mij}^{out}}{R_{mij}^{out}} \right)^2 \right]} \quad (12.9)$$

where:  $\mathbf{x}$  – parameters of the model,  $\mathbf{p}_i$  – parameters of the process,  $Nt$  – number of performed tests,  $Npr$  – number of the co-ordinates of the ring surface (outer or inner),  $R_{cij}^{out}, R_{cij}^{in}, R_{mij}^{out}, R_{mij}^{in}$  – outer and inner radii of the ring in the  $i^{th}$  test, calculated by the FEM and measured, respectively.

- Identification of rheological parameters. Either the plane strain, axisymmetrical or ring compression test is used and the objective function is defined as the distance between the loads measured during deformation process and those predicted by FE simulator:

$$\Phi = \sqrt{\frac{1}{Npl} \sum_{i=1}^{Npl} \left( \frac{F_{ci}(\mathbf{x}, \mathbf{p}_i) - F_{mi}}{F_{mi}} \right)^2} \quad (12.10)$$

where:  $\mathbf{x}$  – parameters of the model,  $\mathbf{p}_i$  – parameters of the process,  $Npl$  – number of measured loads during compression test,  $F_{mi}, F_{ci}$  – measured loads during the compression and those calculated using the FE code.

- Simultaneous identification of rheological and friction parameters. Ring compression test is used as an experiment and the objective function is defined as the sum of differences between measured and calculated compression loads and shape of the samples:

$$\Phi = \left\langle \frac{1}{Nt} \left\{ \frac{1}{Npl} \sum_{i=1}^{Nt} \sum_{j=1}^{Npl} \left( \frac{F_{cij}(\mathbf{x}, \mathbf{p}_i) - F_{mij}}{F_{mij}} \right)^2 + \frac{1}{Npr} \sum_{i=1}^{Nt} \sum_{j=1}^{Npr} \left[ \left( \frac{R_{cij}^{in}(\mathbf{x}, \mathbf{p}_i) - R_{mij}^{in}}{R_{mij}^{in}} \right)^2 + \left( \frac{R_{cij}^{out}(\mathbf{x}, \mathbf{p}_i) - R_{mij}^{out}}{R_{mij}^{out}} \right)^2 \right] \right\} \right\rangle^{\frac{1}{2}} \quad (12.11)$$

The goal function is minimized with respect to the vector  $\mathbf{x}$  components. Non - gradient simplex, Hooke-Jeeves and Rosenbrock methods as well as a genetic algorithm are used to minimize the goal function. Selection of the most efficient optimization technique for the inverse analysis will be discussed elsewhere.

Calculation of the goal functions, defined as (12.9) – (12.11), involves running of the FE simulator  $Nt$  times for all process parameters  $\mathbf{p}_i$ . For example, estimation of material rheological parameters of the flow stress equation in hot forming requires at least nine FE simulations for three different strain rates and three temperatures. Moreover, one step of any optimization algorithm computes several values of the goal function for



various optimization parameters  $\mathbf{x}$ , depending on the dimension of the  $\mathbf{x}$  vector and on the algorithm itself. Due to the above-mentioned reasons, the present inverse algorithm is time-consuming and often not efficient enough for multidimensional vectors  $\mathbf{x}$ . Following this, new investigations were performed and as a result a two-step inverse method for the identification of rheological parameters was developed. This algorithm is described next.

#### 12.1.5 Two-step inverse algorithm

The general idea of the technique is dividing the analysis into two steps. The first step, which is applied for the identification of the rheological parameters only, performs the optimization for each available test separately, as shown by Szeliga and Pietrzyk, (2001). This step, which will be further referred to as the preliminary inverse analysis (*Step Ia*), can be applied to any compression test. The input parameters for the optimization are the values of loads determined as functions of the tool displacement for a given strain rate and temperature. Simulation of each test is performed only once, therefore, the procedure (Figure 12.4) does not require long computing times. During the simulation the value of the flow stress is determined for each strain (each time step of the solution) from the condition of the minimum of the following cost function:

$$\Phi = \sqrt{\left( \frac{F_{mi} - F_{ci}}{F_{mi}} \right)^2} \quad (12.12)$$

where:  $F_{mi}$ ,  $F_{ci}$  – measured and calculated loads in the  $i^{\text{th}}$  time step of the compression test.

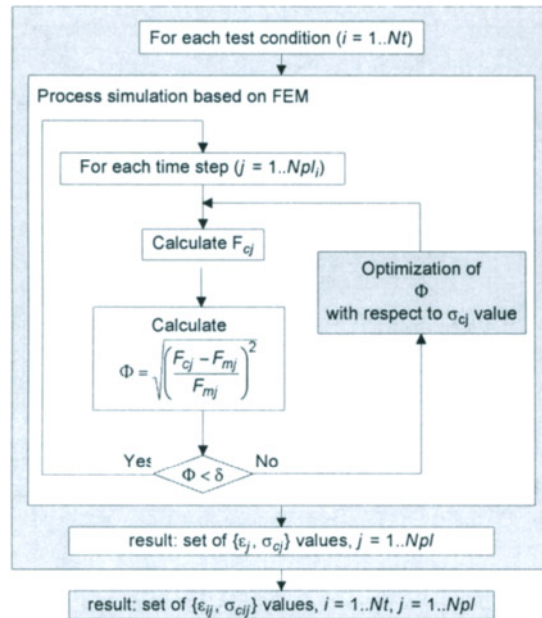


Figure 12.4 The flow chart of the preliminary inverse analysis (*step Ia*).

The minimum is searched with respect to the coefficient  $a$  in the following relationship:

$$\sigma_p = a \sigma_e \quad (12.13)$$

where:  $\sigma_p$  - the flow stress used in the Levy-Mises flow rule (Eq. (12.4)) in the finite element model,  $\sigma_e$  - the flow stress calculated directly from the experimental data as:

$$\sigma_e = \frac{F_m}{S} \quad (12.14)$$

In equation (12.14)  $S$  is the current area of the contact surface. In the axisymmetrical compression test and in the ring compression test  $S$  is calculated either assuming lack of barreling or accounting for barreling using the finite element solution results. Since the starting value of  $a = 1$ ,  $\sigma_e$  is the starting point for the evaluation  $\sigma_p$  and both methods of calculation of  $S$  can be used. It will be shown later that there are no general advantages regarding the selection of the method and that the distance between the starting point and the minimum depends on sample geometry and on friction. In the plane strain compression tests the contact surface  $S$  is constant.

The simulations are performed assuming values of the strain rate and temperature, which are nominal for the tests. The variations of the strain rate and temperature due to inhomogeneity of deformation and to deformation heating are accounted for by the introduction of the following multiplier to the equation, describing the flow stress:

$$\sigma = a \sigma_e \frac{\dot{\epsilon}^m}{\dot{\epsilon}_n^m} \exp \left[ \frac{Q}{R} \left( \frac{1}{T} - \frac{1}{T_n} \right) \right] \quad (12.15)$$

where:  $R$  - universal gas constant,  $\dot{\epsilon}_n$ ,  $T_n$  - nominal values of strain rate and temperature for the selected test,  $\dot{\epsilon}$ ,  $T$  - current local values of strain rate and temperature.

Strain rate sensitivity coefficient  $m$  and activation energy  $Q$  are calculated from the measurements of loads using a simplified graphical method. Correction by equation (12.15) accounts only for variations of temperatures and strain rates from their nominal values in the test.

A set of strains and stresses, representing the real flow stress function, is obtained from the first step of the inverse analysis. The minimization procedure with respect to the coefficient  $a$  is implemented into the FE code, described in section 12.1.3. Details of the algorithm of this solution are presented in Figure 12.5, where:  $\epsilon$  - homogeneous strain,  $h_1$  - initial height,  $h$  - current height. Subroutine STIFF calculates the matrix  $\mathbf{K}$  and the vector  $\mathbf{p}$  (see section 12.1.3), which are used in the Newton-Raphson method.

Further analysis is called *Step Ib*. In this step an approximation of the stress-strain data for all temperatures and strain rates ( $N_t$  tests) is performed using the function  $\sigma_p = \sigma_p(T, \dot{\epsilon}, \epsilon, \dots)$ . At this stage an arbitrary function can be used, but one has to realize that the accuracy of approximation depends on the function's ability to reproduce complex stress-strain relationships. The parameters of the flow stress equations are determined using the approximation technique for the stress-strain data obtained from *Step Ia*. It leads to the minimization of the following goal function:

$$\Phi = \sqrt{\frac{1}{N_t N_{ps}} \sum_{i=1}^{N_t} \sum_{j=1}^{N_{ps}} \left( \frac{\sigma_{cij} - \sigma_{mij}}{\sigma_{mij}} \right)^2} \quad (12.16)$$

where  $N_t$  – number of performed tests,  $N_{ps}$  – number of stresses calculated for various strains, which is equal to  $N_{pl}$  from *Step Ia*,  $\sigma_{cij}$  – calculated stress,  $\sigma_{mij}$  – stress obtained from *Step Ia*,  $i$  – test number,  $j$  – time step number. The flow chart of *Step Ib* is presented in Figure 12.6.

Coefficients obtained from *Step Ib* form the starting point for the final inverse analysis, described in sections 12.1.1 – 12.1.4, which is combined with the finite element simulation of all tests. This step is called *Step II*. Since coefficients estimated in *Step Ib* are very close to the optimum solution, the final inverse analysis requires only few iterations and can be performed in a reasonably short time.

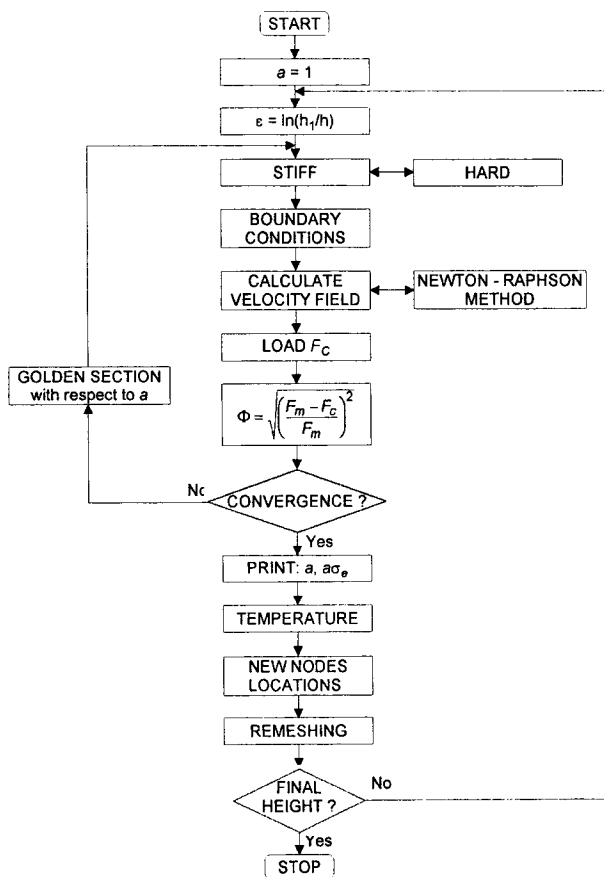


Figure 12.5 Details of the algorithm of the preliminary inverse analysis (*Step Ia*)

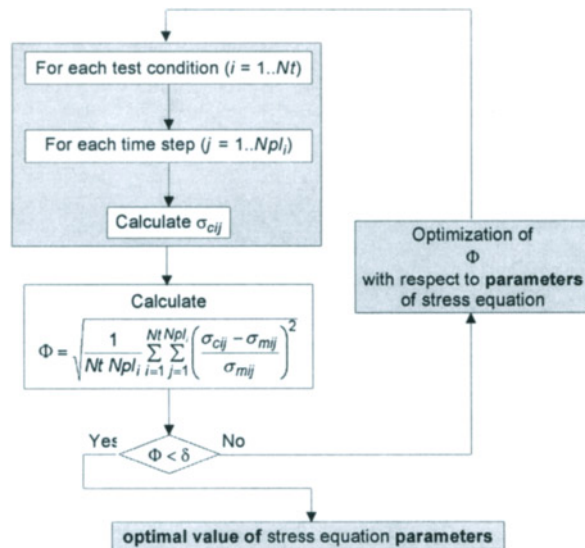


Figure 12.6 The flow chart of optimization of the flow stress equation parameters (Step 1b)

## 12.2 RESULTS

Three plastometric compression tests were investigated: axisymmetrical compression (UC), ring compression (RC) and plane strain compression (PSC). Identification of the rheological properties for various flow stress models and friction conditions at the sample – die contact surface was performed.

### 12.2.1 Identification of rheological and friction properties

**Material and experiment.** Austenitic stainless steel of 304 type with chemical composition given in Table 12.1, was tested. Experimental analysis included axisymmetrical and ring compression tests on the Gleeble 3800 simulator at Institute on Ferrous Metallurgy in Gliwice, Poland. The samples, which measured 12 mm in height and 10 mm in diameter for UC and 5.15 mm in height, 10 mm in outer and 4.7 mm in inner diameter for RC, were deformed at three temperatures (950°C, 1050°C and 1150°C) and at three strain rates (0.1 s<sup>-1</sup>, 1 s<sup>-1</sup>, 10 s<sup>-1</sup>). Loads and tool displacements were monitored during the process for both types of the tests. Moreover, the shape of the ring after compression was measured.

Table 12.1 Chemical composition of the austenitic stainless steel 304L

C	Mn	Si	P	S	Cr	Ni	Mo	Cu	Al	N <sub>2</sub>	V
0.03	1.21	0.50	0.036	0.001	18.1	10.0	0.15	0.19	0.055	0.03	0.031
Nb	Ti										
0.01	0.006										

**Rheological model.** The flow stress model defined as a function of strain, strain rate and temperature was used. The applied function, developed at the University of Sheffield and published by Kowalski et al. (2000), is presented below:

$$\sigma_p = \sigma_0 + (\sigma_{ss(e)} - \sigma_0) \left[ 1 - \exp\left(-\frac{\varepsilon}{\varepsilon_r}\right) \right]^{\frac{1}{2}} - R \quad (12.17)$$

where:

$$R = \begin{cases} 0 & \varepsilon \leq \varepsilon_c \\ (\sigma_{ss(e)} - \sigma_{ss}) \left\{ 1 - \exp\left[-\left(\frac{\varepsilon - \varepsilon_c}{\varepsilon_{xr} - \varepsilon_c}\right)^2\right] \right\} & \varepsilon > \varepsilon_c \end{cases} \quad (12.18)$$

$$\sigma_0 = \frac{1}{\alpha_0} \sinh^{-1}\left(\frac{Z}{A_0}\right)^{\frac{1}{n_0}} \quad \sigma_{ss(e)} = \frac{1}{\alpha_{sse}} \sinh^{-1}\left(\frac{Z}{A_{sse}}\right)^{\frac{1}{n_{se}}} \quad (12.19)$$

$$\sigma_{ss} = \frac{1}{\alpha_{ss}} \sinh^{-1}\left(\frac{Z}{A_{ss}}\right)^{\frac{1}{n_{ss}}} \quad \varepsilon_r = 0.31 \left[ q_1 + q_2 (\sigma_{ss(e)})^2 \right] \quad (12.20)$$

$$\varepsilon_{xr} - \varepsilon_c = \frac{\varepsilon_{xs} - \varepsilon_c}{1.98} \quad \varepsilon_c = C_c \left( \frac{Z}{\sigma_{ss(e)}^2} \right)^{N_c} \quad \varepsilon_{xs} - \varepsilon_c = C_x \left( \frac{Z}{\sigma_{ss(e)}^2} \right)^{N_x} \quad (12.21)$$

where:  $Z$  - Zener Hollomon parameter with activation energy  $Q$ ,  $\varepsilon$  - strain.

**Results of calculations.** The objective of the inverse analysis was the estimation of the coefficients in Eq. 12.17 – 12.21 and friction factor in Eq. 12.7. The value of the friction factor is essential to perform inverse analysis of rheological parameters based on UC, so the friction factor from the ring compression test was identified first. The goal function was defined as (12.9) and the full inverse algorithm, described in section 12.1.1, was applied. The friction factor  $m_c$  was evaluated as 0.315. Typical shape of the quarter of the ring predicted by the FE model with the friction factor obtained from the inverse analysis and measured in the experiment, is shown in Figure 12.7.

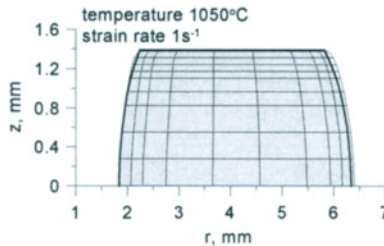


**Figure 12.7** Predicted (mesh) and measured (gray area) shape of the quarter of the austenitic stainless steel ring after compression

The next step of the investigations was the identification of the rheological parameters from the UC test. The measured load – displacement data of all the tests were used as an input data for the optimization procedure described in Section 12.1.5 (Step 1a). The friction factor 0.315 was applied and the coefficient of the strain rate sensitivity  $m$  and the activation energy  $Q$ , which are necessary in the preliminary inverse analysis, were determined using a simplified graphical method. Logarithm of the stress was plotted as a function of the logarithm of the strain rate, Figure 12.8(a), and the reciprocal of the temperature, Figure 12.8(b). The slopes of linear approximations of these relationships determine the coefficient  $m$  and the ratio of the activation energy  $Q$  to the gas constant  $R$ . These values are accurate enough to account for the variations of strain rates and temperatures with respect to the nominal values in the tests. Equation (12.15) is used for this purpose.

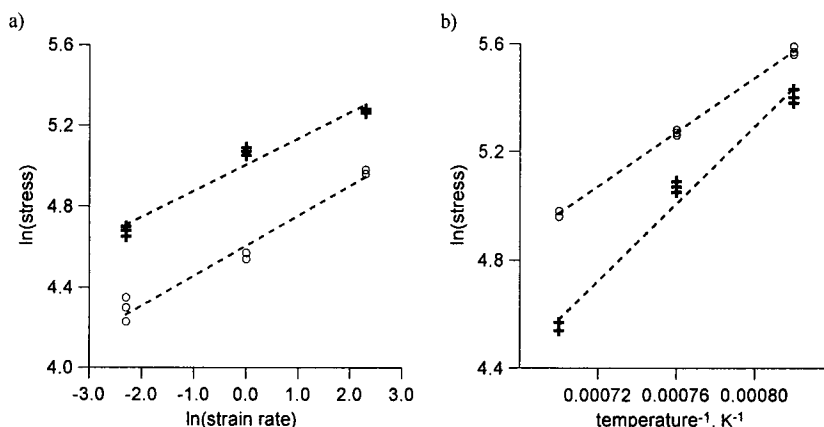


**Figure 12.8** Illustration of the graphical method of evaluation of the strain rate sensitivity coefficient  $m$  (a) and the activation energy  $Q$  (b); reproduced with permission

The flow stress, determined for the strain rate of  $0.1 \text{ s}^{-1}$  using preliminary inverse technique, is presented in Figure 12.9 together with that calculated from the measured loads, using Eq. (12.14). Two methods of evaluation of the contact surface were applied in these calculations. In the first case (temperature  $1050^\circ\text{C}$ ) the contact surface  $S$  was calculated assuming that the cylindrical shape of the sample is maintained during the deformation. In the remaining cases (temperatures  $950^\circ\text{C}$  and  $1150^\circ\text{C}$ ) the loads were divided by the current contact surface, which were calculated by the finite element method. It is seen in Figure 12.9 that significant differences between the two methods exist. The stresses calculated using the current contact surface are much larger than the real ones while those calculated assuming a cylindrical shape of the sample are below the real ones. Since these stresses are used only as a starting point for the preliminary inverse analysis, the discrepancies have no influence on the results and any of the methods of calculations of the contact surface can be used. It was observed during various numerical tests that, in general, calculation of the experimental stress assuming a cylindrical shape of the sample yields the starting point closer to the minimum and, in consequence, a shorter time of calculations.

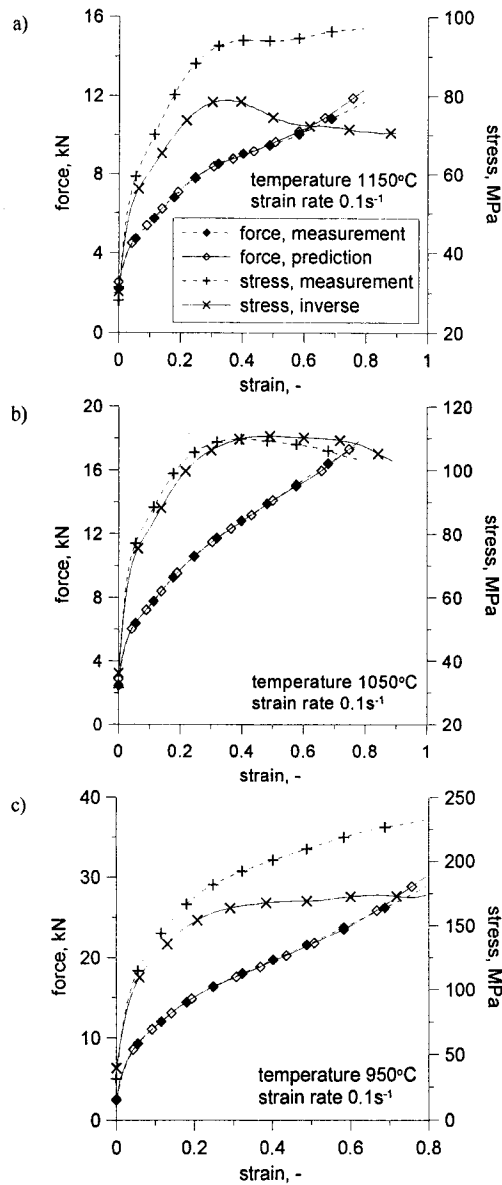


**Figure 12.9** Results of optimization (preliminary inverse analysis – Step 1a) for the axisymmetric compression of the austenitic stainless steel 304L; temperature 1150°C (a), 1050°C (b), 950°C (c); reproduced with permission

The forces predicted by the finite element program, using flow stress from the preliminary inverse analysis, are compared with the experimental ones in Figure 12.9, as well. Very good agreement is observed in all cases. Thus, the flow stress obtained from the inverse analysis can be considered as the real one. Similar results were obtained for the

remaining strain rates 1 and 10 s<sup>-1</sup>. Approximation of the stress-strain curves using function (12.17) was the next step of analysis (*Step Ib*). The coefficients obtained from the approximation are given in Table 12.2 and the comparison of the stress-strain curves obtained from the *Step Ia* and after approximation (*Step Ib*) is presented in Figure 12.10. Reasonably good agreement was obtained.

**Table 12.2** The coefficients in Eq. 12.17 – 12.21 obtained from approximation of results of preliminary inverse analysis (*step I*) for the austenitic stainless steel 304L

Rheology - $\alpha_0$						
$A_0$	$n_0$	$\alpha_0$				
$3.089 \times 10^4$	6.8587	0.1272				
Rheology – hardening and dynamic recovery						
$A_{ssc}$	$n_{ssc}$	$\alpha_{ssc}$	$q_1$	$q_2$		
$8.031 \times 10^{18}$	6.8587	$2.657 \times 10^{-3}$	0.5308	$7.707 \times 10^{-6}$		
Rheology – dynamic recrystallization						
$A_{ss}$	$n_{ss}$	$\alpha_{ss}$	$C_c$	$N_c$	$C_x$	$N_x$
$6.408 \times 10^{16}$	5.423	$5.006 \times 10^{-3}$	$5.236 \times 10^{-6}$	0.4264	18.252	-0.1267

$Q = 420\,000$  J/mol

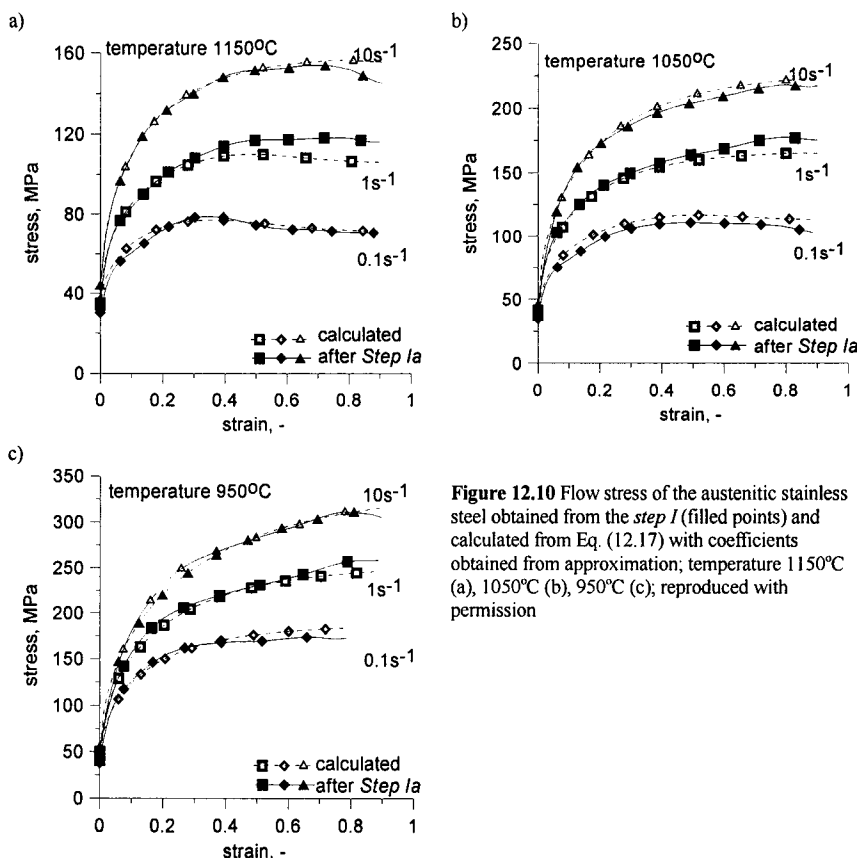


**Figure 12.10** Flow stress of the austenitic stainless steel obtained from the *step I* (filled points) and calculated from Eq. (12.17) with coefficients obtained from approximation; temperature 1150°C (a), 1050°C (b), 950°C (c); reproduced with permission



### 12.2.2 Identification of internal variable model parameters and friction properties

Any function, which describes the flow stress in the hot forming conditions, can be used at the *Step 1b* of the inverse analysis. An example of the application of two flow stress models, one based on the conventional approach represented by Eq. 12.18 – 12.22 (Kowalski et al. 2000) and the second, based on the internal variable method, is described below.

**Material and experiment.** The ring compression tests are usually used for determination of friction coefficient but, as is shown by Szyndler et al. (2001a) and Szyndler et al. (2001b), both friction and rheological parameters can be determined from these tests when the inverse technique is applied. The plastometric tests were carried out on the MTS simulator at Swinburne University in Melbourne. The samples were made from 5140 steel with a chemical composition given in Table 12.3.

**Table 12.3** Chemical composition of the carbon-manganese steel 5140

C	Mn	Si	P	S	Cr	B
0.405	0.85	0.25	0.03	0.04	0.8	0.00175

The dimensions of rings were standard. Outer diameter (OD)/inner diameter (ID)/height (H) ratio was equal to 6:3:2 and the exact values were OD = 16 mm, ID = 8 mm, H = 5.33 mm. Nine tests at different deformation conditions (temperatures 800°C, 900°C, 1000°C and strain rates 0.1 s<sup>-1</sup>, 0.6 s<sup>-1</sup>, 3.0 s<sup>-1</sup>) were performed. The strain was equal to 0.50 and the strain rate was constant for each test. The samples were soaked at 1000°C for three minutes before compression and then naturally cooled to the test temperature. After testing the samples were carefully sectioned and 20 data points were measured on the inner and outer surfaces of each half of the ring. These were used to characterize the shape for subsequent analysis.

**Rheological model.** Two different equations describing the flow stress were used to described material properties: conventional  $\sigma_p = \sigma_p(T, \dot{\epsilon}, \epsilon)$ , defined by Eq. 12.17 – 12.21, and the internal variable model, presented below.

**Internal variable model (IVM).** The stress during plastic deformation is governed by the evolution of dislocation populations and the competition between storage and annihilation of dislocations, which when superimposed in an additive manner, controls the hardening. In the internal variable model the yield stress accounting for softening is proportional to the square root of dislocation density  $\rho$ :

$$\sigma_p = \sigma_0 + ab\mu\sqrt{\rho} \quad (12.22)$$

where:  $b$  – Burger's vector,  $\mu$  - shear modulus,  $\sigma_0$  – basic stress for elastic deformation.

The description of various approaches to the internal variable modeling is given in earlier publications: Pietrzyk (1994) and Pietrzyk et al. (1995) describe the complete IVM. The dislocation distribution function  $G(\rho, t)$  suggested by Sandstrom and Lagneborg (1975) and defined as a volume fraction with a dislocation density between  $\rho$  and  $\rho + d\rho$ , is used in this version and a weighted average value of  $G(\rho, t)$  is introduced in Eq. 12.22. The differential equation, which describes the distribution function, is:

$$\frac{dG(\rho, t)}{dt} = \frac{\dot{\epsilon}}{bl} - k_2\rho - A_3 \frac{\nu\gamma}{D} \frac{\mu b^2}{2} \rho G(\rho, t) \quad (12.23)$$

where:  $t$  - time,  $l$  - mean free path of dislocations,  $\nu$  - constant,  $\gamma$  - migrating fraction of subgrain boundary,  $D$  - grain size. Discretization of the function  $G(\rho, t)$  is explained by Pietrzyk (1994). The remaining equations in the model are:

- free path

$$l = A_0 Z^{-4} \quad \text{or} \quad l = A_2 \rho^{-0.5} \quad (\text{for small strains}) \quad (12.24)$$

- kinetics of recrystallization:

$$\frac{dX}{dt} = A_3 \frac{\nu \gamma}{D} \frac{Gb^2}{2} \rho G(\rho, t) \quad (12.25)$$

- grain boundary mobility

$$A_3 = A_{30} \exp\left(\frac{Q_m \times 10^3}{RT}\right) \quad (12.26)$$

- self-diffusion coefficient

$$k_2 = k_{20} \exp\left(\frac{Q_s \times 10^3}{RT}\right) \quad (12.27)$$

where:  $Q_m$  - activation energy for grain boundary mobility,  $Q_s$  - activation energy for self-diffusion,  $X$  - recrystallized volume fraction.

A simplified version of the IVM, (Mecking and Kocks, 1981; Estrin and Mecking, 1984 and Davies, 1994), proposes an alternative approach, using Eq. 12.23 – 12.27 written for an average dislocation density. Details are given by Ordon et al. (2000). The evolution of dislocation populations accounting for restoration processes is given by:

$$\frac{d\rho(t)}{dt} = \frac{\dot{\epsilon}}{bl} - k_2 \rho(t) - \frac{A_3}{D} \rho(t) R[\rho(t) - \rho_{cr}] \quad (12.28)$$

where:  $\rho_{cr}$  - critical dislocation density, calculated as a function of the Zener-Hollomon parameter. Function  $R$  in equation (12.28) is calculated as:

$$\begin{aligned} R[\rho(t) - \rho_{cr}] &= 0 & \text{for } \rho &\leq \rho_{cr} \\ R[\rho(t) - \rho_{cr}] &= \rho(t - t_{cr}) & \text{for } \rho &> \rho_{cr} \end{aligned}$$

where:  $t_{cr}$  - time at the beginning of dynamic recrystallization.

**Results of calculations.** Full, three-stage inverse analysis was performed.

- Estimation of friction at the sample – die contact surface using the method presented in section 12.1.1 with the goal function defined by Eq. 12.9;
- Identification of parameters of two rheological models, conventional (Eq. 12.17 – 12.21) and IVM (Eq. 12.22 – 12.28) using two-step inverse algorithm, see section 12.1.5;

- Simultaneous identification of friction and rheological parameters. The goal function defined by Eq. 12.11 was applied.

**Evaluation of the friction factor.** Identification of one unknown variable  $m_c$  (Eq. 12.7), independently for each test, was performed first and the results showed the dependence of the friction factor on the temperature and the normal pressure during compression (Figure 12.11). Selected examples of comparison of the measured and predicted shapes of the sample using the identified friction factors are shown in Figure 12.12 and very good agreement is observed. A general tendency for the friction factor to increase with increasing temperature  $T[^\circ\text{C}]$  and vary with unit pressure  $p[\text{MPa}]$  at the tool-workpiece interface was observed, and linear dependence between these parameters and friction factor  $m_c$  was defined:  $m = c_0 + c_1T + c_2p + c_3Tp$ . Identified values of coefficients  $c_i$ ,  $i = 0...3$  are shown in Table 12.4, first row. Using calibration curves (Schey, 1970b), the Coulomb friction coefficient was estimated at 0.15. This corresponds to Chen and Kobayashi's friction factor  $m_c \approx 0.25$ , below the value from the inverse analysis. Since the latter method is based on detailed measurements of the shape of the ring, it is more reliable. The results in Figs 12.11 and 12.12 confirm the capability of the analysis to predict coefficients in the friction models using the results of the ring compression tests. Since the method is sensitive to the constitutive law, further analysis including compression loads was performed.

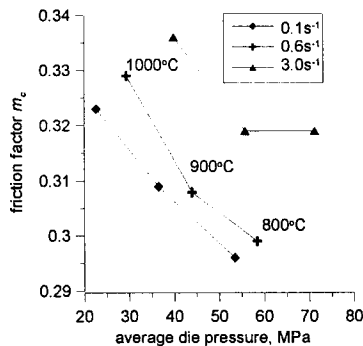


**Figure 12.11** The friction factor determined for various deformation conditions; reproduced with permission

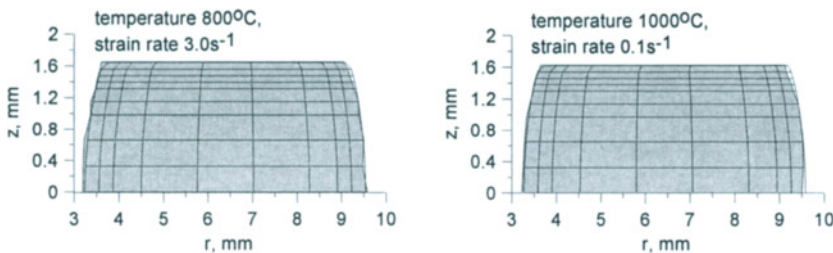


**Figure 12.12** Predicted (mesh) and measured (gray area) shape of the quarter of the 5140 steel samples after compression; reproduced with permission

**Identification of the conventional flow stress model.** The parameters of Eq. 12.17 – 12.21 were determined using the two-step inverse algorithm with the friction model identified before. The values of calculated parameters are presented in Table 12.4, first row. Due to the interaction between the rheological and friction models, simultaneous estimation of both rheological and friction parameters was carried out (Table 12.4, second row). It is observed that some values have varied slightly. The loads measured and predicted by the rheological model, as well as stresses obtained from the preliminary inverse analysis (*Step 1a*) and from the full inverse analysis, are presented in Figure 12.13.

**Identification of IVM.** The inverse technique was used for the evaluation of the coefficients in Eq. 12.22 – 12.28 and the results are given in Table 9.5. The friction model obtained for simultaneous identification of the parameters of the conventional flow stress equation and linear dependence of the friction factor on the temperature and on the unit pressure was applied. An example of the comparison between the flow stress predicted by the simplified internal variable model and that determined from the experiment is presented in Figure 12.14. It is shown that the simplified internal variable model describes the flow stress reasonably well, including accounting for the dynamic recrystallization. The agreement between measurements and predictions deteriorates with increasing strain rate. A similar tendency was observed for the two remaining temperatures (Szyndler et al. 2001a). In general, however, the IVM leads to a better quality of simulation than the closed form Eq. 12.17.

**Table 12.4** The rheological coefficients in equation Eq. 12.17 – 12.21 and friction parameters obtained from the first step of inverse analysis (top rows) and from the final inverse analysis (bottom rows); Boldface numbers represent the coefficients, which have changed during the final inverse calculations

Rheology - $\sigma_0$						
$A_0$	$n_0$	$\alpha_0$				
1.416x10 <sup>13</sup>	6.7596	2.3779x10 <sup>-2</sup>				
1.416x10 <sup>13</sup>	6.7596	2.3779x10 <sup>-2</sup>				
Rheology – hardening and dynamic recovery						
$A_{sse}$	$n_{sse}$	$\alpha_{sse}$	$q_1$	$q_2$		
7.677x10 <sup>13</sup>	6.7596	5.47x10 <sup>-3</sup>	7.131x10 <sup>-1</sup>	10 <sup>-10</sup>		
9.54x10 <sup>13</sup>	6.7596	5.47x10 <sup>-3</sup>	7.294x10 <sup>-1</sup>	10 <sup>-10</sup>		
Rheology – dynamic recrystallization						
$A_{ss}$	$n_{ss}$	$\alpha_{ss}$	$C_c$	$N_c$	$C_x$	$N_x$
4.5064x10 <sup>14</sup>	6.3095	4.731x10 <sup>-3</sup>	3.758x10 <sup>-2</sup>	8.892x10 <sup>-2</sup>	4.752x10 <sup>-3</sup>	0.2098
2.538x10 <sup>14</sup>	6.0704	5.204x10 <sup>-3</sup>	3.954x10 <sup>-2</sup>	8.617x10 <sup>-2</sup>	3.122x10 <sup>-3</sup>	0.233
Friction						
$c_0$	$c_1$	$c_2$	$c_3$			
0.261	5.42x10 <sup>-5</sup>	-2.06x10 <sup>-3</sup>	2.48x10 <sup>-6</sup>			
0.261	5.42x10 <sup>-5</sup>	-2.05x10 <sup>-3</sup>	2.332x10 <sup>-6</sup>			

**Table 12.5** Coefficients in the model obtained from identification for the steel 5140

$A_0$	$A_1$	$k_{20}$	$Q_s$	$A_{30}$	$Q_m$	$\sigma_0$	$\alpha$
0.0012	0.16	674	41	1.5x10 <sup>-10</sup>	350	7.4	1.03

Comparison of the measured and predicted compression loads for selected tests is shown in Figure 12.15. The predictions were obtained from the FE model with the simplified IVM (Eq. 12.22 – 12.28) as the constitutive law. With the possible exception of the test performed at 800°C and 3.0 s<sup>-1</sup>, the agreement between the calculations and the measurements is good.

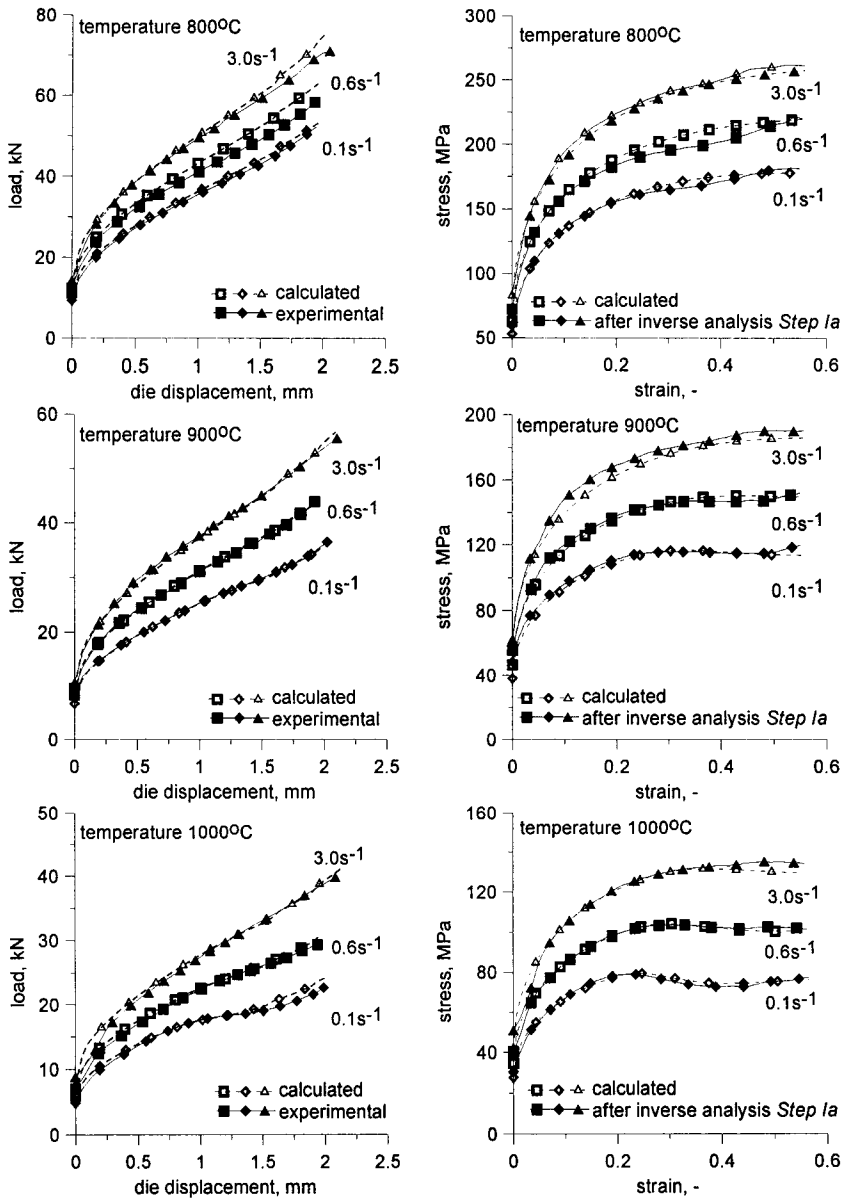


**Figure 12.13** Results of full inverse analysis for 5140 steel. Left column: Loads predicted (open points) and measured in the tests (filled points). Right column: Stresses predicted (open points) by fem with conventional rheological model and obtained after the preliminary inverse analysis (*Step 1a*) (filled points) ; reproduced with permission

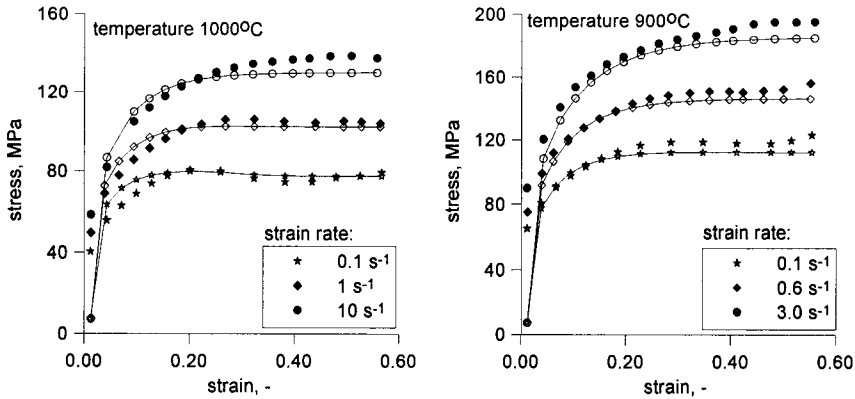


**Figure 12.14** Predicted by IVM (open points) and after preliminary inverse analysis (filled points) flow stress for 5140 steel at 1000°C(a) and 900°C (b); reproduced with permission

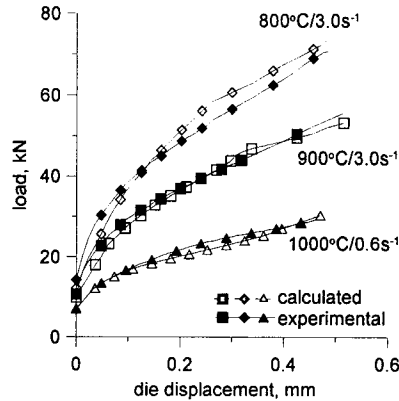


**Figure 12.15** Measured and calculated compression loads for IVM constitutive model for 5140 steel; reproduced with permission

### 12.2.3 Identification of material properties from axisymmetrical test performed using various plastometric simulators

Further research was performed to prove that, when the inverse analysis is applied, the flow stress of the material determined from the plastometric tests should be insensitive to the type of the test, sample and tool dimensions and to the testing machine. The first step of these studies focused on an analysis of the results of axisymmetrical compression tests performed on various machines using one material.

The two-step inverse analysis described in Chapter 12.1.5 was applied to compare the values of flow stress obtained using various plastometers. Due to crucial role

of friction in the identification of axisymmetrical test results, the friction factor was estimated from measured barreling of the sample.

**Material and experiment.** Detailed description of the experiment using austenitic stainless steel, performed by Grosman, is given by Szeliga et al. (2001). Three testing machines were investigated: Gleeble 3800 (GLI) and two deformation dilatometers (DIL1 and DIL2). Tests conditions and dimensions of the samples are presented in Table 12.6, where  $T$  – nominal test temperature,  $v_s$  – tool velocity,  $\dot{\epsilon}$  – strain rate,  $h_0$  – initial height of the sample,  $d_0$  – initial sample diameter,  $h_f$  – final height of the sample,  $d_f$  – final sample diameter,  $\Lambda_{exp}$  – measured barreling of the sample after compression,  $\Lambda_{calc}$  – calculated barreling of the sample for applied friction factor  $m_c$  (Eq. 12.7) in the FE model.

**Estimation of the friction factor.** The accuracy of the inverse analysis depends on the proper description of the frictional conditions on tool-sample contact area. The value of the friction factor  $m_c$  was evaluated based on the barreling of the sample after deformation process. The barreling was calculated as:

$$\Lambda = \frac{V_0 - V_c}{V_0} \times 100\% \quad (12.29)$$

where:  $V_0$  – sample volume,  $V_c$  – volume of cylinder with the base equal to the tool-sample contact surface and height equal to final height of the sample.

**Table 12.6** Description of axisymmetrical tests

Test stand/ Test number	$T$ oC	$v_s$ mm/s	$\dot{\epsilon}$ s <sup>-1</sup>	$h_0$ mm	$d_0$ mm	$h_f$ mm	$d_f$ mm	$\Lambda_{exp}$ %	$\Lambda_{calc}$ %	$m_c$
GLI/1	900		0.04	15	12	8	14.7	20.2	20.0	0.18
GLI/2	900		2.5	15	12	8	14.7	19.6		
GLI/3	1100		0.04	15	12	7.5	15.2	20.3		
GLI/4	1100		2.5	15	12	7.75	15	19.1		
DIL1/1	900	0.3		10.05	5.0	5.15	5.85	30.4	31.4	0.28
DIL1/2	900	20		10.0	5.0	4.9	5.9	30.8		
DIL1/3	1100	0.3		10.0	5.0	5.16	5.8	31.0		
DIL1/4	1100	20		10.0	5.0	5.0	5.85	32.0		
DIL2/1	900		0.04	9.0	5.0	4.5	6.27	21.0	21.5	0.21
DIL2/2	900		2.5	9.1	5.0	4.55	6.28	20.2		
DIL2/3	1100		0.04	9.1	5.0	4.45	6.4	20.5		
DIL2/4	1100		2.5	9.1	5.0	4.5	6.27	22.3		

The relationship between barreling of the sample calculated for the three testing machines for various friction factors  $m_c$  is presented in Figure 12.16. The values of the friction factors, for which measured and calculated values of barreling were the closest to one-another, are marked as filled points. Variations of the barreling for the tests performed on the same machine have not exceeded 2.1% (see Table 12.6), therefore, one value of the friction factor was applied for simulations of all tests carried out on the same machine.

**Results of calculations.** Preliminary inverse analysis was performed for all tests and the results are presented in Figure 12.17. It is observed that the flow stresses obtained from the results of one type of plastometric tests but performed on various test stands are close to each other. Slight differences are not caused by the inaccuracy of the inverse analysis, because agreement between measured and predicted loads is very good (see

Figure 12.18). Thorough analysis of real strain rates during compression process could explain the discrepancies.

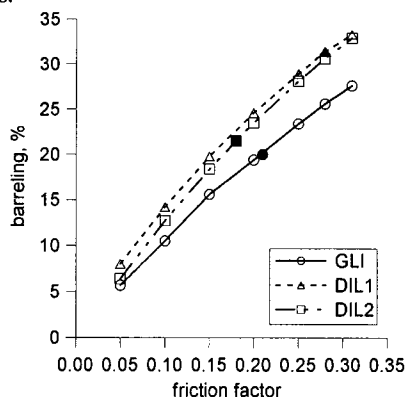


**Figure 12.16** Relationship between barreling of the sample and value of the friction factor; reproduced with permission

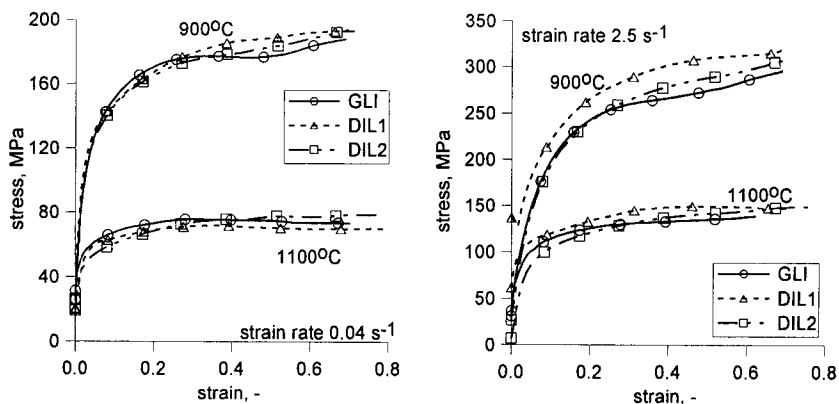


**Figure 12.17** Flow stress obtained from preliminary inverse analysis performed for axisymmetrical tests performed on various test machines; reproduced with permission



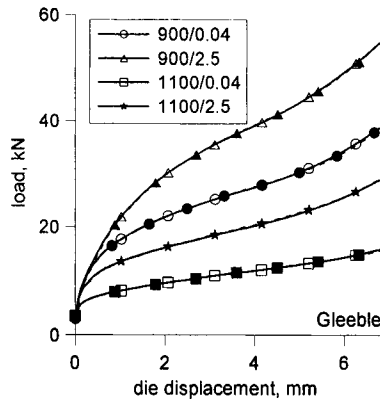


**Figure 12.18** Measured (filled points) and calculated (open points) loads for Gleeble simulator; reproduced with permission

#### 12.2.4 Identification of material properties from axisymmetrical and plane strain compression test

Second part of the research aiming at proving the insensitivity of the flow stress on the testing conditions focused on comparison of the results of the inverse analysis applied to axisymmetrical compression tests and plane strain compression tests. Both types of the tests were performed on the Gleeble 3800 at the Institute for Ferrous Metallurgy in Gliwice, Poland.

**Material and experiment.** Two types of experiments, axisymmetrical compression (UC) and plane strain compression (PSC) tests were performed using the carbon-manganese steel with the chemical composition given in Table 12.7. The conditions were the same for the both types of tests, three temperatures of 900°C, 1000°C and 1100°C and three strain rates of  $0.1\text{s}^{-1}$ ,  $1\text{s}^{-1}$  and  $10\text{s}^{-1}$ . The plane strain compression samples measured  $10 \times 20 \times 15$  mm and the width of the die was 5 mm. The cylindrical samples measured  $\phi 5$  mm  $\times$  12 mm. The graphite foil combined with nickel lubricant was used to decrease the friction in all tests. The friction factor  $m_c$  was determined on the basis of additional ring compression tests and was 0.14 for all temperatures and all strain rates. All the tests were performed with constant homogenous strain rate (decreasing velocity of the die).

**Table 12.7** Chemical composition of the carbon-manganese steel used in the UC and PSC tests

C	Mn	Si	P	S	Al
0.17	1.29	0.31	0.013	0.012	0.12

**PSC tests.** The name plane strain compression test is not justified by the two-dimensional state of strains. There is always a spread in the experiment, therefore, full 3D model should be used to obtain an accurate simulation. On the other hand, a 3D solution is very time consuming and such application in the inverse analysis involves very long computing times, which are practically not acceptable. Simulations of the PSC test performed using 2D and 3D model (Kowalski et al. 2001) show that the 2D model overestimates loads at the beginning of the compression (due to an influence of the rigid ends) and underestimates significantly the loads at the final stage of the process (due to

effect of spread). When the correction accounting for spread is introduced into the 2D load data, the results, reasonably close to the experiment, are obtained. The spread correction for the 2D model is based on the current width of the sample, which is calculated as (Kowalski et al, 2001):

$$b = b_0 \left[ 1 + C - C \left( \frac{h}{h_0} \right)^{0.18} \right] \quad (12.30)$$

where:

$$C = \frac{\frac{b_f}{b_0} - 1}{1 - \left( \frac{h_f}{h_0} \right)^{0.18}} \quad (12.31)$$

$b_0$  – initial width,  $h_0$  – initial height,  $b_f$  – final width,  $h_f$  – final height,  $b$  – current width,  $h$  – current height,  $C$  – spread coefficient.

Thus, the 2D model was used in the inverse analysis in the present work and the loads were corrected using Eq. 12.30 to calculate the real contact width and to correct the load predicted by the 2D model.

**Results of calculations.** The importance of the inverse analysis based on the finite element solution of the direct problem is explained in Figures 12.19 and 12.20. In Figure 12.20 (a) changes of strain rates at three locations A, B and C (see Figure 12.19) in the sample during the tests performed at 900°C and 10 s<sup>-1</sup> is shown. Location A represents the center of the sample in both tests. Location B is close to the contact surface at the axis of the sample in both tests. Location C is close to the contact with the edge of the die in the PSC test and close to the contact surface and to the edge of the sample in the UC test. It is seen that strain rates vary significantly from the nominal value of 10 s<sup>-1</sup>. These variations are much larger in the PSC test. Changes of temperature at the same locations are shown in Figure 12.20 (b). Since the tests were performed in hot dies, there is no temperature drop observed. Contrary, some increase of the temperature due to deformation heating appears and it affects the flow stress. The inverse analysis eliminates the influence of the variations of the strain rates and temperatures and yields isothermal constant strain rate values of the flow stress.

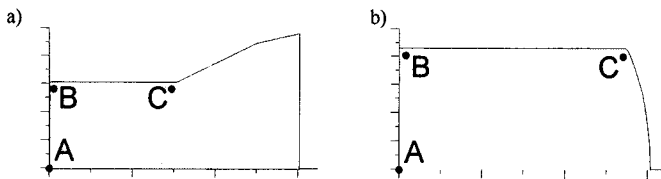
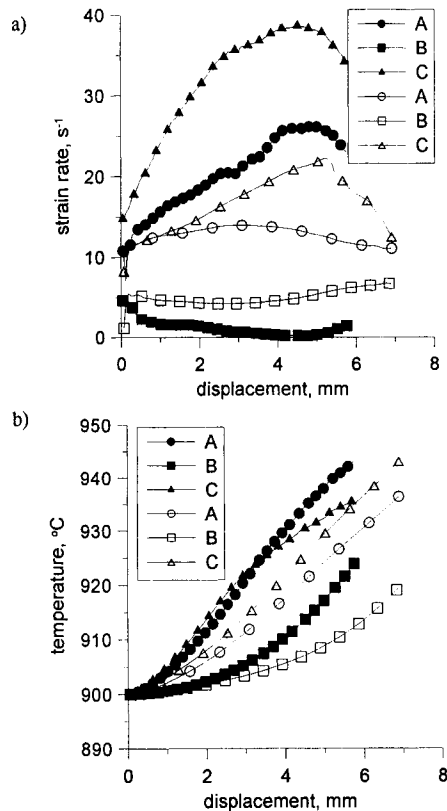


Figure 12.19 Location of points A, B and C in the sample: PSC test (a), UC test (b)

It should be pointed out that the results presented in Figure 12.20 (b) were obtained assuming that there is no temperature control during the test. In practice, on the Gleeble 3800 machine the temperature is measured and the on-line control system turns

off the heating to limit the influence of deformation heating. This has to be taken into account in the inverse analysis. The flow stress for selected tests calculated directly from the experiment as load-to-current contact surface ratio is shown in Figure 12.21. It is seen that different tests yield completely different values of the flow stress. The differences can be reduced by introduction of corrections for spread at PSC and for deformation heating in both tests, but they cannot be completely eliminated and still remain significant. Considerable improvement of the consistency of results obtained from various tests is accomplished if the inverse analysis is applied, see Figures 12.22 (a) – (c). The agreement is not perfect but it is much better than observed for conventional methods of interpretation of the results of plastometric tests. Beyond this, the discrepancies seen in Figure 12.22 can be partly due to the experimental inconsistency. Figure 12.23 shows selected examples of comparison of loads measured (black points) and calculated using the stress strain curves in Figure 12.22 as flow stress in the constitutive model (open points). The agreement between measurements and predictions is almost perfect, confirming the effectiveness of the inverse technique and its capability to determine one real flow stress function independently of the type of the test.



**Figure 12.20** a) Variations of strain rate in three locations during PSC (black points) and UC (open points) test, b) Variations of temperature in three locations during PSC (black points) and UC (open points) test. Nominal temperature 900°C, nominal strain rate 10 s<sup>-1</sup>

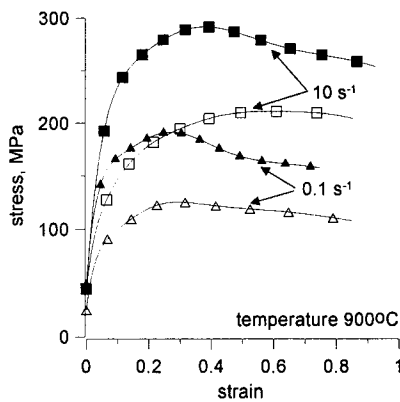


**Figure 12.21** Flow stress calculated directly from the PSC (black points) and UC (open points) test

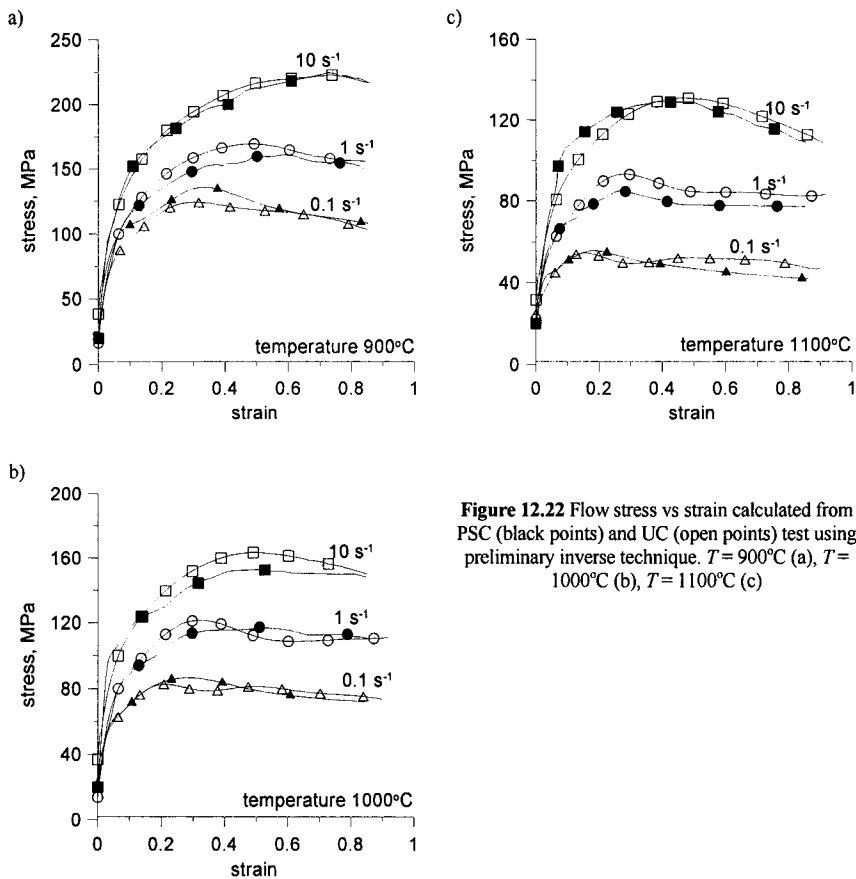


**Figure 12.22** Flow stress vs strain calculated from PSC (black points) and UC (open points) test using preliminary inverse technique.  $T = 900^{\circ}\text{C}$  (a),  $T = 1000^{\circ}\text{C}$  (b),  $T = 1100^{\circ}\text{C}$  (c)

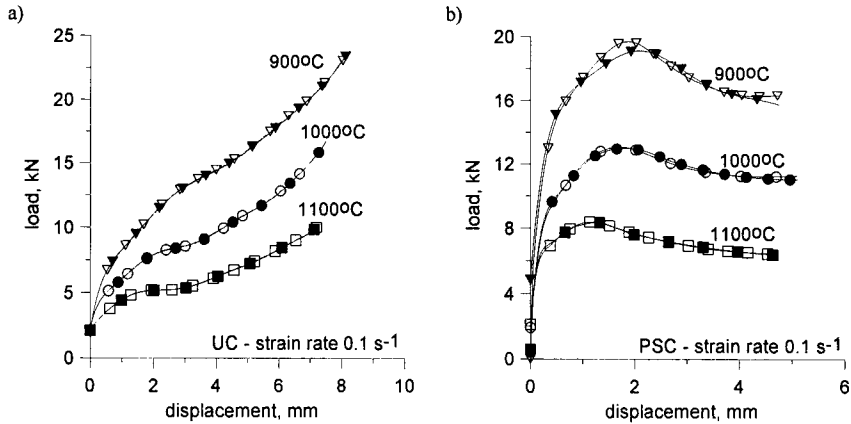


**Figure 12.23** Comparison of measured (black points) and predicted (open points) loads in the axisymmetrical compression test (a), plane strain compression test (b)

### 12.3 DISCUSSION

Application of the inverse technique to the interpretation of results of plastometric tests allows the determination of friction and rheological parameters, which are almost independent of the type of the test. In consequence, isothermal and constant strain rate parameters, which are required by the finite element models, can be obtained. Beyond this, the results of the inverse calculations allow, among others, more reliable analysis of the influence of various process conditions on the friction coefficient. Some observations based on the investigations performed in the current work are discussed below.

Results of the inverse analysis of the ring compression tests show that the friction coefficient increases with an increasing temperature of deformation. The problem of the influence of the temperature on the friction coefficient was investigated by a number of researchers and the results are not consistent. Experimental techniques used by various researchers and the results are discussed by Lenard (1991) and the majority of works shows an increase of the friction coefficient with increasing temperature. The results published by Roberts (1983) on the basis of measurements of forces and torques during rolling of carbon-manganese steel slabs in a laboratory two-high mill show that the friction coefficient increases from about 0.2 at 550°C to about 0.45 at 1250°C. More data on the friction-temperature relationship are based on the results of the ring compression tests, see for example the results for tool steels and austenitic stainless steels published by Pawelski et al. (1989). All these observations show an increase of the friction coefficient with increasing temperature and are in qualitative agreement with the results obtained in the present work. There are, however, some published results which show lack of the sensitivity of the friction coefficient on temperature, see for example the data by Wang and Lenard (1992) for compression of carbon-manganese steel rings. It should be emphasized that, contrary to the previously cited works, the results of Wang and Lenard (1992) were obtained using lubricated dies.

Contact pressure is the second factor, which affects the friction coefficient. Inverse analysis, which was performed in the present work using steels deformed at the hot forming temperatures, shows that the influence of the tool pressure on the friction coefficient varies depending on other process parameters, such as temperature and strain rate. The published data on this problem are not consistent, as well, and the majority of works deals with cold forming processes. Lenard (2000) investigated widely the influence of reduction (which indirectly represents pressure) in cold rolling on the friction coefficient and observed the decrease of the friction coefficient with increasing reduction for low carbon steel and a contrary effect for aluminum. All the experiments for steel rolling were performed for dry surfaces and for five various lubricants and the effect of decreasing friction with increasing reduction was observed in all cases. Decrease of the friction coefficient with increasing reduction or increasing flow stress of the material is reported by Roberts (1978) and Dobrucki (1962). Beyond this Schey (1987) shows that the maximum coefficient of friction decreases when the interface pressure increases above the yield stress of the material.

Recapitulating, the observations in the present work based on the inverse analysis of the ring compression tests are in qualitative agreement with the majority of published results on dependence of the friction coefficient on process parameters. The inverse technique has two main advantages compared to the conventional interpretation of the ring compression. It is based on measurements of both inner and outer diameter of the ring at several locations along the height of the sample, therefore, it accounts for the inhomogeneity of deformation. Beyond this, the inverse technique allows simultaneous identification of both rheological and friction models which makes the evaluation of the friction coefficient insensitive to the flow stress of the deformed material and vice versa.

## 12.4 CONCLUSIONS

On the basis of the research, which has been done so far, the general conclusion can be drawn that an application of the inverse analysis to the interpretation of plastometric tests presents numerous advantages. Less effort has to be spent on experimental analysis. Various types of parameters, including rheological and friction ones, can be evaluated simultaneously from one type of the tests. The method is designed for the identification of various types of metal forming process parameters and results presented in this work are an example of typical applications. It is also shown that an application of the inverse analysis increases the consistency of the values of the flow stress as determined from various types of plastometric tests.

## ACKNOWLEDGEMENTS

The majority of the presented work was performed within the 5<sup>th</sup> frame program project TESTIFY, no. GRD1-1999-10714.

## REFERENCES

- Boyer, B., Massoni, E. (1999) Identification of Tribological Parameters during Upsetting Tests using Inverse Analysis with a 2D Finite Element Code, in *Proceedings of the 6th ICTP, Advanced Technology of Plasticity*, Vol. 1, ed., Geiger, M. (Nuremberg) 347-352.

- Boyer, B., Massoni, E. (2001) Inverse Analysis for Identification of Parameters during Thermo-Mechanical Tests, *Proceedings of NUMIFORM 2001*, ed., Mori, K. (A. Balkema, Toyohashi) 281-284.
- Chen, C.C., Kobayashi, S. (1978) Rigid Plastic Finite Element Analysis of Ring Compression, in: *Application of Numerical Methods to Forming Processes* (ASME, ADM) **28**, 163-174.
- Davies, C.H.J. (1994) Dynamics of the Evolution of Dislocation Populations, *Scr. Metall. Mater.*, **30**, 349-353.
- Dobrucki, W. (1962) Hipoteza tarcia szczepno-poslizgowego na powierzchni styku ciał sztywnych (narzedzi) z ciałami elastoplastycznymi, *Obr. Plast.*, **2**, 449-488 (in Polish).
- Estrin, Y., Mecking, H. (1984) A Unified Phenomenological Description of Work Hardening and Creep Based on One-Parameter Models., *Acta Metall.*, **32**, 57-70.
- Fourment, L., Vieilledent, D., Chenot, J.L. (1998) Non Linear Sensitivity Analyses in Forging: Application to Preforming Tool Shape Optimization, in *Proceedings of Computational Mechanics, New Trends and Applications* (Barcelona) CD-ROM.
- Gavrus, A., Massoni, E., Chenot, J.L. (1995) Constitutive Parameter Identification using a Computer Aided Rheology, *Proceedings of NUMIFORM'95*, eds, Shen, S.-F., Dawson, P.R., (A. Balkema, Ithaca) 563-568.
- Gelin, J.C., Ghouati, O. (1999) Recent Progresses in Optimal Design of Metal Forming Processes through Numerical Simulation, in *Proceedings of the 6th ICTP, Advanced Technology of Plasticity*, Vol. 1, ed Geiger, M. (Nurnberg) 489-496.
- Gelin, J.C., Ghouati, O. (1994) An Inverse Method for Determining Viscoplastic Properties of Aluminium Alloys, *J. Mat. Proc. Techn.*, **45**, 435-440.
- Kowalski, B., Sellars, C.M., Pietrzyk, M. (2000) Development of a Computer Code for the Interpretation of Results of Hot Plane Strain Compression Tests, *ISIJ Int.*, **40**, 1230-1236.
- Kowalski, B., Wajda, W., Pietrzyk, M., Sellars, C.M. (2001) Influence of Strain and Strain Rate Inhomogeneity on Constitutive Equations Determined from Plane Strain Compression Tests, in *Proceedings of 4th ESAFORM Conf. on Materials Forming*, ed. Habraken, A.M. (Liege) 561-564.
- Krzyzanowski, M., Beynon, J.H. (1999) Finite Element Model of Steel Oxide Failure During Tensile Testing under Hot Rolling Conditions, *Mat. Sci. Techn.*, **15**, 1191-1198.
- Kusiak, J., Pietrzyk, M., Lenard, J.G. (1995) Application of FE Simulation of the Compression Test to the Evaluation of Constitutive Equation for Steels at Elevated Temperatures, in *Proceedings of NUMIFORM'95*, ed. Shen, S.F., Dawson, P.R. (A. Balkema, Ithaca) 277-282.
- Lenard, J.G. (1991) The Effect of Temperature on the Coefficient of Friction in Flat Rolling, *Ann. CIRP*, **40**, 223-226.
- Lenard, J.G. (2000) Tribology in Metal Rolling, *Ann. CIRP*, **49**, 1-4.
- Lenard, J.G., Pietrzyk, M., Cser, L. (1999) *Mathematical and Physical Simulation of the Properties of Hot Rolled Products* (Elsevier, Amsterdam).
- Male, A.T., Cockcroft, M.G. (1964-65) A method for the determination of the coefficient of friction of metals under conditions of bulk plastic deformation, *J. Inst. Metals*, **93**, 38-46.

- Malinowski, Z., Lenard, J.G., Davies, M.E. (1994) A Study of Heat - Transfer Coefficient as a Function of Temperature and Pressure, *J. Mat. Proc. Techn.*, **41**, 125-142.
- Mecking, H., Kocks, U.F. (1981) Kinetics of Flow and Strain-Hardening, *Acta Metall.*, **29**, 1865-75.
- Ordon, J., Kuziak, R., Pietrzyk, M. (2000) History Dependent Constitutive Law for Austenitic stainless steels, in *Proceedings of Metal Forming 2000*, eds, Pietrzyk, M., Kuziak, J., Majta, J., Hartley, P., Pillinger, I. (A. Balkema, Krakow) 747-753.
- Pawelski, O., Rasp, W., Hoerster, C. (1989) The Ring Compression Test as Simulation Test for the Investigation of Friction in Hot Metal Forming, *Steel Res.*, **60**, 395-402.
- Pietrzyk, M. (1994) Numerical Aspects of the Simulation of Hot Metal Forming Using Internal Variable Method, *Metall. Foundry Eng.* **20**, 429-439.
- Pietrzyk, M., Lenard, J.G. (1991) *Thermal-Mechanical Modelling of the Flat Rolling Process*, (Springer-Verlag, Berlin).
- Pietrzyk, M., Kuziak, H., Lenard, J.G., Malinowski, Z. (1994) Heat Exchange between the Workpiece and the Tool in Metal Forming Processes, in *Proceedings of FORMABILITY'94*, ed. Bartecek, J. (Ostrava) 889 – 900.
- Pietrzyk, M., Kuziak, R. (1995) Validation of the History Dependent Flow Stress Model for Hot Forming of Metals, in *Proceedings of COMPLAS 5*, eds. Owen, D.R.J., Onate, E., Hinton, E., (Barcelona) 1363-1368.
- Pietrzyk, M., Kondek, T., Majta, J., Zurek, A.K. (2000) Method of Identification of the Phase Transformation Model for Steels, *Proc. COM 2000* (Ottawa) CD ROM.
- Roberts, W.L. (1978) *Cold Rolling of Steel* (Marcel Dekker, Inc., New York).
- Roberts, W.L. (1983) *Hot Rolling of Steel* (Marcel Dekker Inc., New York).
- Sandstrom, R., Lagneborg, R. (1975) A model for Hot Working Occurring by Recrystallization, *Acta Metall.*, **23**, 387-398.
- Schey, J.A. (1970a) Friction Effects in Metalworking Processes, in: *Metal Deformation Processes: Friction and Lubrication*, ed., Schey, J.A. (Marcel Dekker Inc., New York), 17-81.
- Schey, J.A. (1970b) Lubricant Properties and Their Measurement, in: *Metal Deformation Processes: Friction and Lubrication*, ed. Schey, J.A. (Marcel Dekker Inc., New York) 241-332.
- Schey, J.A. (1987) *Introduction to Manufacturing Processes* (McGraw Hill Book Comp., New York).
- Szeliga, D., Grosman, F., Pietrzyk, M. (2001) Zastosowanie analizy odwrotnej do wyznaczania naprężeń uplastyczniających z plastometrycznej próby sciskania, *Rudy Metale Niezel.*, **46**, 551-555 (in. Polish).
- Szeliga, D., Pietrzyk, M. (2001) Problem of the Starting Point Generation for the Inverse Analysis of Compression Tests, *Metall. Foundry Eng.*, **27**, 167-18.
- Szyndler, D., Lenard, J.G., Fyke, S.H., Pietrzyk, M. (2000) Inverse Analysis Applied to the Evaluation of Friction and Rheological Parameters in Hot Forming of Steels, in *Proceedings of Metal Forming 2000*, eds, Pietrzyk, M., Kuziak, J., Majta, J., Hartley, P., Pillinger, I. (A. Balkema, Kraków) 101-106.



Szyndler, D., Pietrzyk, M., Hodgson, P.D. (2001a) Identification of Parameters in the Internal Variable Constitutive Model and Friction Model for Hot Forming of Steels, in *Proceedings of NUMIFORM 2001*, ed., Mori, K. (A. Balkema, Toyohashi) 297-302.

Szyndler, D., Pietrzyk, M., Kuziak, R.(2001b) Estimation of Rheological and Friction Parameters in Hot Forming Processes as an Inverse Problem, in *Proceedings of 4th ESAFORM Conf. on Materials Forming*, ed. Habraken, A.M. (Liege) 191-194.

Wang, F., Lenard, J.G. (1992) An Experimental Study of Interfacial Friction-Hot Ring Compression, *Trans. ASME, J. Eng. Mat. Techn.*, **114**, 13-18.

## Chapter 13

# Oxide Behaviour in Hot Rolling

MICHAŁ KRZYZANOWSKI and JOHN H. BEYNON  
*Institute for Microstructural and Mechanical Process Engineering*  
*The University of Sheffield,*  
*Sir Robert Hadfield Building, Mappin Street,*  
*Sheffield, S1 3JD, U.K.*

*Oxide scale on the surface of metal plays a pivotal role in the thermomechanical processing and subsequent surface quality. The research reported here concerns the behaviour of perhaps the most complicated oxide scale, namely that on steels, undergoing hot rolling. By doing a closely-linked combination of laboratory testing and measurements, rolling tests, microstructural investigation and, crucially, detailed finite element analysis, a physically-based model for oxide scale behaviour has been developed. This model has been successfully applied to circumstances similar to those in which it was developed, namely hot rolling of steel. Importantly, it has also been applied to completely different circumstances, high temperature hydraulic descaling and room temperature mechanical descaling, with considerable success. This is clear affirmation of the integrity of the model. It is also an example of how a combination of techniques can allow materials to be characterised in circumstances where standard methods of measurement are not feasible or adequate on their own.*

### 13.1 FACTORS INFLUENCING FRICTION, HEAT TRANSFER AND QUALITY OF THE PRODUCT IN HOT ROLLING

An important role of the oxide scale in determining friction and heat transfer during hot metal forming operations, as well as the quality of the formed product, arises from its pivotal position on the interface between tool and workpiece, at the heart of a complex set of events. The oxide scale can deform plastically or fracture, behaviour that will have a considerable impact on the interaction between tool and workpiece, and on the surface finish of the formed product. There is relatively little information available on how oxides perform under the operating conditions typical of hot working processes. A major research effort has been

made at the University of Sheffield to investigate oxide scale behaviour using a combination of experiments and finite element modelling.

Studies of the oxide scale on the metal surface during deformation at elevated temperatures have mostly been motivated by a desire to understand better the micro events at the tool-workpiece interface that could influence heat transfer and friction during hot rolling process. Since making measurements of the interface events is fraught with difficulties, finite element (FE) modelling has been applied to this problem. There were, however, surprisingly few detailed examinations of the oxide scale deformation and failure during the hot rolling process or even under hot rolling conditions, in contrast to the case of room and elevated temperatures such as take place in components for high-temperature service where oxide scales provide protection.

In the hot strip mill, the slab is brought to temperature in the reheating furnace and discharged for rolling. To break the primary scale, the slab is passed through a slab descaler before the reversing roughing mill. Between successive rolling passes a secondary scale is formed, which is further removed by high pressure water jets before the subsequent passes during reversing rolling or before the strip enters the tandem finishing mill. The strain imposed on the metal surface when the strip enters the roll gap, because of drawing in by frictional contact with the roll, produces longitudinal tensile stresses on the metal surface ahead of contact with the roll. It is important to know whether this kind of stress results in oxide failure. This is not only because the thermal conductivity of the non-fractured oxide scale is a factor of about 10 – 15 less than that of the steel (Kolchenko and Kuznetsova, 1984) but because of two phenomena which can take place in the temperature range 800 – 1150°C. The fractured scale can enable direct contact of hot metal with the cold tool, due to extrusion of the hot metal through fractured scale up to the cool roll surface (Li and Sellars, 1996). Moreover, at higher temperature there have been indications that the oxide/metal interface is weaker than the oxide, and sliding of the non-fractured oxide raft is observed during uniaxial tension of an oxidised specimen (Krzyzanowski and Beynon, 1999a). The location of the plane of sliding is determined by the cohesive strength at the different interfaces within the metal/inhomogeneous oxide and by the stress distribution when delamination within the scale takes place. Both fracture and sliding will produce sharp changes in heat transfer and friction in the roll gap.

Irregularly removed scale defects are often formed on hot rolled steel strips, causing an inhomogeneous or dirty appearance as a result. Several technological approaches have been proposed to prevent these defects, such as control of slab temperature or strengthening of water jet descaling [Ishi et al., 1992, Okita et al., 1989, Blazevic, 2000]. However, in spite of these measures, the reason why a conventional descaler cannot always remove the scale before rolling is not clear. As has been shown by the authors, the crack patterns formed in scale deformed in tension or during hot rolling to a great extent depend on the process parameters such as temperature, scale thickness and reduction. Oxide scales grown on low carbon steels at high temperatures cannot be assumed both to be perfectly adhering during tensile loading, in the sense of slipping, and to be fully brittle.

Coiled steel rod produced by hot rolling for subsequent wire drawing inevitably possesses an oxidised surface. The oxide scale must be removed before the drawing operation. Formation of the scale depends to a great extent on the manufacturing parameters, such as the laying temperature and the cooling rate. Understanding the scale removal mechanism is important for optimisation of industrial descaling conditions. However, investigation of the descaling process is far from easy, even under laboratory conditions. Studying details of the scale removal mechanism after testing is sensitive to the sample

preparation technique. Cutting and mounting of the specimen for microscopic investigation may distort the real state of the oxide scale and the scale/metal interface, due to the brittleness of the oxides.

Additionally, the chemical content of the steel can significantly influence the state of the scale after the deformation (Krzyzanowski and Beynon, 2000). A major problem that must be addressed, once the effects of oxide scales have been taken into account, is the state of the oxide scale and oxide/metal interface before entering the roll gap. It has been demonstrated experimentally and mimicked numerically that the small differences in chemical content, mainly of Si and Mn, for the mild steel containing 0.02-0.07wt.% Ni and 0.08-0.14wt.% Cu, can be the reason for the different modes of scale failure. It is known that small additions of elements with a high affinity for oxygen, such as Y, Ce, Hf and Si, can be very effective in promoting the formation of an adherent oxide layer that is more resistant to applied stresses. The active element can have an influence in elemental form or as an oxide dispersoid. There are various theories that have been proposed to account for an effect of active elements, which include enhanced scale plasticity, modification to the oxide growth process, stronger chemical bonding at the interface, and oxide protrusions into the metal base which can improve adhesion (Whittle and Stringer, 1980, Strawbridge and Hou, 1994). It has been proposed that segregation of sulphur to the scale/metal interface reduces the adhesion of the scale, and that the effect of the active element is to scavenge the sulphur present in the alloy and so improve the intrinsically strong adherence (Lees, 1987). Other authors propose that the active element blocks sites, such as interfacial dislocations, that support diffusion growth at the scale/metal interface, and thereby alter both the growth mechanism and the adhesion of the scale (Pieraggi and Rapp, 1994).

No one theory can satisfactorily explain all the reported experimental observations at this stage of understanding the system 'oxide scale – scale/metal interface' which is crucial for accurate characterisation of oxide scale behaviour in metal forming, particularly in hot rolling and descaling operations. In this work an approach based on combination of hot tensile measurements and finite element modelling has been developed - a method for quantitative characterisation of oxide scale failure in metal forming. This required a combination of experiments under appropriate operating conditions and computer-based models for interpretation of test results and implementation of physical insight into predictions for rolling operations. The method has reached a reasonable level of sophistication, such that it is also able to represent both hydraulic and mechanical descaling events, including multi-layer oxide scales.

### 13.2 OXIDE FAILURE DURING HOT TENSILE TESTING

The aim of the hot tensile tests is two-fold, related to determination of the temperature ranges for modes of oxide scale failure and evaluation of separation loads for scale failure in tension.

#### 13.2.1 Experimental

Round tensile specimens for determination of failure modes have  $\varnothing 6.5 \text{ mm} \times 20 \text{ mm}$  gauge section (Fig. 13.1a) and are ground to a 1000 grit surface finish with SiC paper. Each specimen has a hole from one end for a thermocouple allowing of temperature measurement during the tests. Specimens for evaluation of separation loads for scale failure had the same

shape and quality of the surface before oxidation as described above. The difference was that the specimens were cut on two equal parts connected together before the test (Fig. 13.2). To prevent transverse movements during tension a ceramic pin is inserted into the axisymmetrical pin-hole, 5 mm long, in both parts of the specimen. The oxidised surfaces of both parts have to match each other with good accuracy to prevent oxidation of the end faces between the halves.

The specimens were oxidised to the desired extent in the tensile testing rig just before starting the tests. A vertical cylindrical induction furnace was used for heating. Excluding intermediate cooling is desirable because it could cause spalling of oxide scales. Normally, air was used for high temperature oxidation of the steel. However, application of another oxidising atmosphere is also possible. Generally the tensile test included the following stages: heating – 120 s, stabilising of temperature in inert atmosphere – 300 s, oxidation – between 80 and 3000 s (depending on temperature and desired oxide thickness), gas change stage – 120 s, tension – up to 40 s and cooling – 900 s. The principal effect of the nitrogen on the oxidation is dilution of other effective air species, such as  $O_2$  and  $H_2O$ . The nitrogen is used for all stages as an inert atmosphere except for the oxidation stage. The slow cooling is necessary to prevent oxide fracture due to the strains which might result from thermal stresses arising from mismatch of the oxide and substrate thermal expansion coefficients. The gas change stage is included because time is necessary for gas substitution in the furnace. The solid tensile specimen (Fig. 13.1a) is used for determination of the temperature ranges for modes of oxide scale failure, as a first stage of testing. Each sample is placed in the grips so that a small tensile load is applied during heating and the oxidation stage to eliminate the effects connected with backlash in the grips and thermal expansion. The system is switched over from load control to position control at the end of the gas change stage just as tensile testing begins and is changed back to load control during cooling after testing. After cooling, the samples are sectioned to determine oxide thickness, crack pattern and investigate their morphology.

The temperature, oxidation time and strain rate during the second stage of testing for evaluation of separation loads for scale failure in tension is intended to be close to those used in the previous stage for determination of failure modes. To measure the strain for any test the gauge length should be taken into consideration, which is not obvious for the test when oxidation took place between two separated parts of the specimen. The strain parameter is replaced by fixed length separation of the rig grips, equal for all tests. Each part of the sample is placed in the grips so that a small compressive load is applying during heating and the oxidation stages. The oxidised surfaces of both parts have to match each other with good accuracy to prevent oxidation of the faces between the parts. The system is switched over from load control to position control at the end of the gas change stage to allow measurement of load during tension. The procedure for measurement of separation loads includes several stages (Table 13.1).

**Table 13.1** Measurement of separation loads for steel oxide scales – test programme

	Procedure	Evaluation
a.	Testing without oxidation for the different compression	Effect of bonding
b.	Testing without oxidation under the chosen compression	Separation loads (bonding)
c.	Testing with oxidation	Separation loads (scale + bonding)
d.	Subtraction of separation loads obtained in stage b from those obtained in c	Separation loads (scale)

A small compressive load is applied during heating and oxidation stages to allow a continuous scale layer on the cylindrical side of the specimen to be obtained and to prevent oxidation on the flat faces at the place of the contact. The contact between the hot steel parts inevitably results in some bonding between them. The separation load is increased when the compression load is increased during the time necessary for the heating and oxidation of the specimen. At the same time, too small a compression load does not secure a proper contact between the halves of the specimen during heating and oxidation stages, so the optimal compression has to be chosen for all tests (Table 13.1 a). The separation load measured without oxidation has to be registered for all tests as a background (Table 13.1 b). During testing with oxidation (Table 13.1 c), the separation load resulted from both oxide scale and bonding is measured. To separate the oxide scale effect from any background resulted from bonding and friction for instance, the results obtained in p. "b" are subtracted from the results obtained in p. "c". This is the final stage of the testing (Table 13.1 d).

### ***13.2.2 Modes of oxide scale failure in tension and measurement of separation loads***

Two different modes of failure leading to oxide scale spallation were observed in experiments for mild steel (0.17C, 0.13Si, 0.72Mn, 0.014P, 0.022S, 0.06Cr, 0.07Ni, 0.11Cu, <0.02Mo, <0.02V weight %). The test parameters were chosen to approximate to hot rolling conditions where a secondary oxide scale is formed between successive rolling passes. Usually the thickness of such oxide scales is less than 100  $\mu\text{m}$ . Thus, the range of parameter variations was within the following limits: temperature 830-1150°C; thickness of the oxide scale 10 – 100  $\mu\text{m}$ ; strain 1.5 - 20% and strain rate 0.02 - 4.0  $\text{s}^{-1}$ . The first mode, observed at 830°C, corresponds to a mode of spallation that was observed elsewhere for tensile failure at lower temperatures. In this mode it is assumed that there is a strong interface between metal and oxide, but that the oxide is brittle. Failure begins by through-scale cracking followed by initiation of a crack along the oxide-metal interface that might result in spallation (Fig. 13.1b). The through thickness cracks are formed with an approximately uniform crack spacing. The second mode of oxide spallation corresponds to the interface being weaker than the oxide scale and was observed at higher temperatures. In this mode the oxide scale slides along the interface throughout elongation under the uniaxial tensile load after spallation at the upper end of the specimen gauge length (Fig. 13.1c).

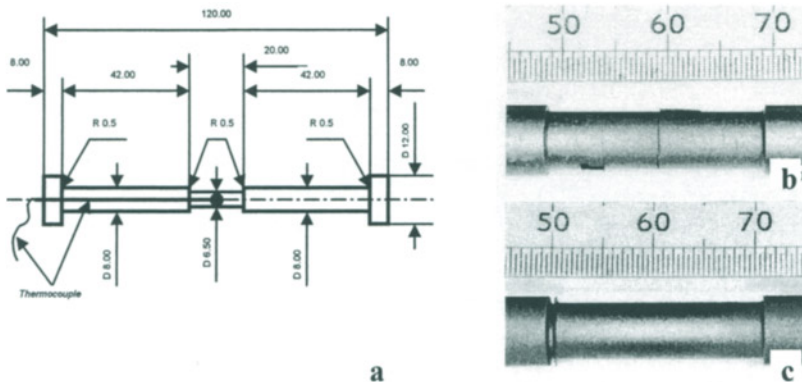


**Figure 13.1** Schematic representation of the tensile specimen (a) and photographs of the oxide scale on the tensile specimen after testing (b, c) illustrating two different modes of failure for mild steel oxides. Strain 2.0%, strain rate  $0.2s^{-1}$ , scale thickness 140-180 $\mu m$ . Temperature = 830°C (b); Temperature = 900°C (c).

It may result in spallation of the whole oxide raft. It has been shown earlier that transfer from the first mode of failure to the second takes place between 850 and 870°C for this steel. Sliding along the scale/metal interface at high temperatures is possible when either the stress from the tensile deformation exceeds that necessary for viscous flow without fracture at the scale/metal interface, or the energy release rate exceeds its critical level, resulting in fracture along the interface. For the first case, tangential viscous sliding of the oxide scale on the metal surface is allowed due to the shear stress transmitted from the specimen to the scale. For the second, fracture along the interface can result in separation of the whole scale raft from the metal surface. It is probable that this type of sliding of the detached oxide scale dominated in the tensile tests.

Fig. 13.2 schematically illustrates the different separation loads measured during different modes of oxide failure under the second testing procedure while Fig. 13.3 shows the final states of the scale after testing. The first mode corresponds to the strong interface between the oxide scale and metal relative to the oxide scale and failure occurs with through-thickness cracking. In this case, the separation load within the oxide scale is registered. The second mode relates to the interface being weaker than the oxide scale, which results in sliding of the oxide scale raft along the scale/metal interface. The tangential separation loads at the scale/metal interface is registered in this case. Fig. 13.4 illustrates the level of loads causing failure of oxide scale for both modes of failure. The load shows steep growth then abrupt decrease to zero when the through-thickness crack occurs at lower temperature.

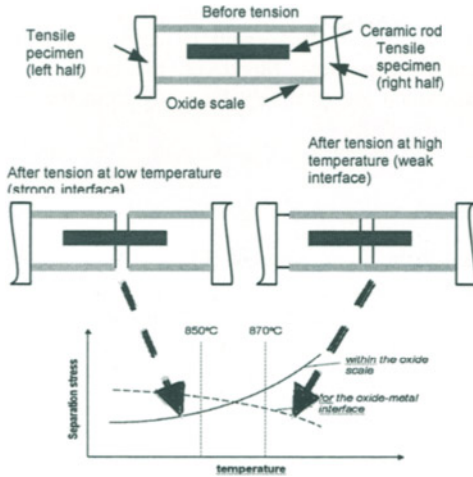


**Figure 13.2.** Scheme of measurement of separation loads during oxide failure in tension.

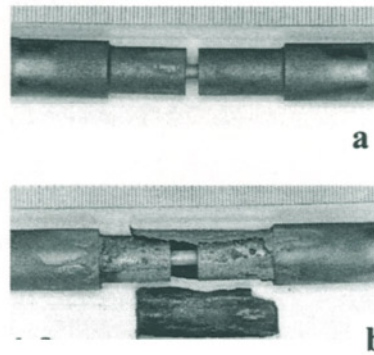


**Figure 13.3.** Two different modes of oxide failure in tension during measurement of separation loads  
a) through-thickness crack formation;  
b) sliding along the oxide/metal interface.

For higher temperature, the load increases less steeply and decreases gently before dropping down to zero, showing some signs of ductility at high temperatures. The location of the plane of sliding is determined by the cohesion strength at the different interfaces and the resulting stress distribution. The separation loads seem to be critical mechanical parameters characterising scale failure and they depend on morphology of the particular oxide scale, scale growth temperature and are also very sensitive to the chemical composition of the underlying steel. These loads are relatively small, making the measurement particularly difficult.

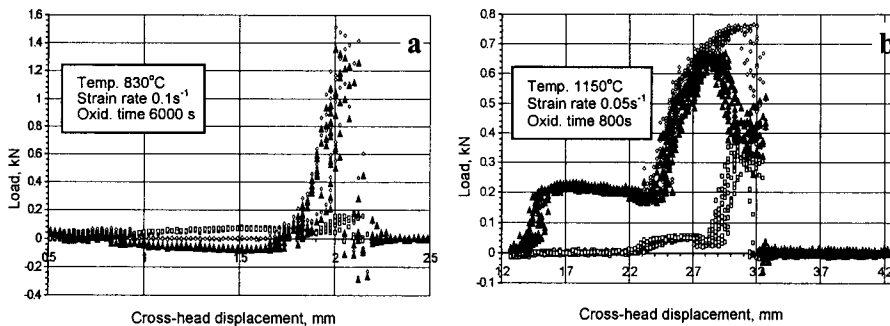


**Figure 13.4.** Loads registered during two modes of oxide scale failure in tension: through-thickness crack (a) and sliding along the interface (b)  
◊ - testing with oxidising; Y - testing without oxidising; - subtraction of Y from ◊



Another difficulty of the hot tensile test is that the oxide scale failure takes place in the middle at the edges of the specimen where the local non-homogeneity in temperature, stress and strain distributions can complicate their measurement. Moreover, the points of the registration are at the heads of the specimen, which are relatively far away from the place where the failure occurs.

### 13.3 MATHEMATICAL MODEL

A mathematical model, based on application of the finite element (FE) method, has been proposed for analysis of oxide scale failure in hot rolling and descaling operations and is also used in coupling with the hot tensile testing to determine the most critical parameters of scale failure. The model is composed of two parts. The first is a macro-component computing the temperature, strains, strain rates and stresses in the specimen during the tensile testing, rolling or descaling. This is then linked to the micro-level model of oxide scale failure. Both components of the model are rigorously thermo-mechanically coupled, and all the mechanical and thermal properties are included as functions of temperature. The commercial MARC K7.2 FE code is used to simulate metal/scale flow, heat transfer, viscous sliding and failure of the oxide scale. Since the macro-components of the model (Fig. 13.5) were assumed to be similar to those used in majority of rolling models and has been described elsewhere (Krzyzanowski et al., 2000, Pietrzyk and Lenard, 1991), only the micro-part of the model related to the oxide scale is discussed beneath.

#### 13.3.1 Model of oxide scale failure

The oxide scale is simulated as consisting of scale fragments joined together to form a continuous scale covering the metal surface. The length of each scale fragment is set to be several times less than the smallest spacing of through-thickness cracks observed in the experiments. Depending on the intended application of the model, whether for determining of scale failure parameters during test modelling or for prediction of the scale behaviour in flat hot rolling or descaling operations, each model fragment is built up as a mixture of isoparametric, arbitrary quadri- and tri-lateral axisymmetric or plane strain elements. For the scale to be adherent to the metal surface at the beginning of deformation, a loading equivalent to atmospheric pressure was applied to the scale throughout the heating stage. The scale and the metal surface were assumed to be adherent when they were within a contact tolerance distance taken to be about 1  $\mu\text{m}$ . Viscous sliding of the oxide on the metal surface was allowed, arising from the shear stress  $\tau$  transmitted from the metal to the scale in a manner analogous to grain boundary sliding in high-temperature creep (Ridel, 1982)

$$\tau = \eta v_{rel} \quad (13.1)$$

where  $\eta$  is a viscosity coefficient and  $v_{rel}$  is the relative velocity between the scale and the metal. Dislocation creep and diffusional flow of atoms can circumvent interface irregularities

$$v_{rel} = \frac{1}{\eta} |\tau|^{k-1} \tau \quad (13.2)$$

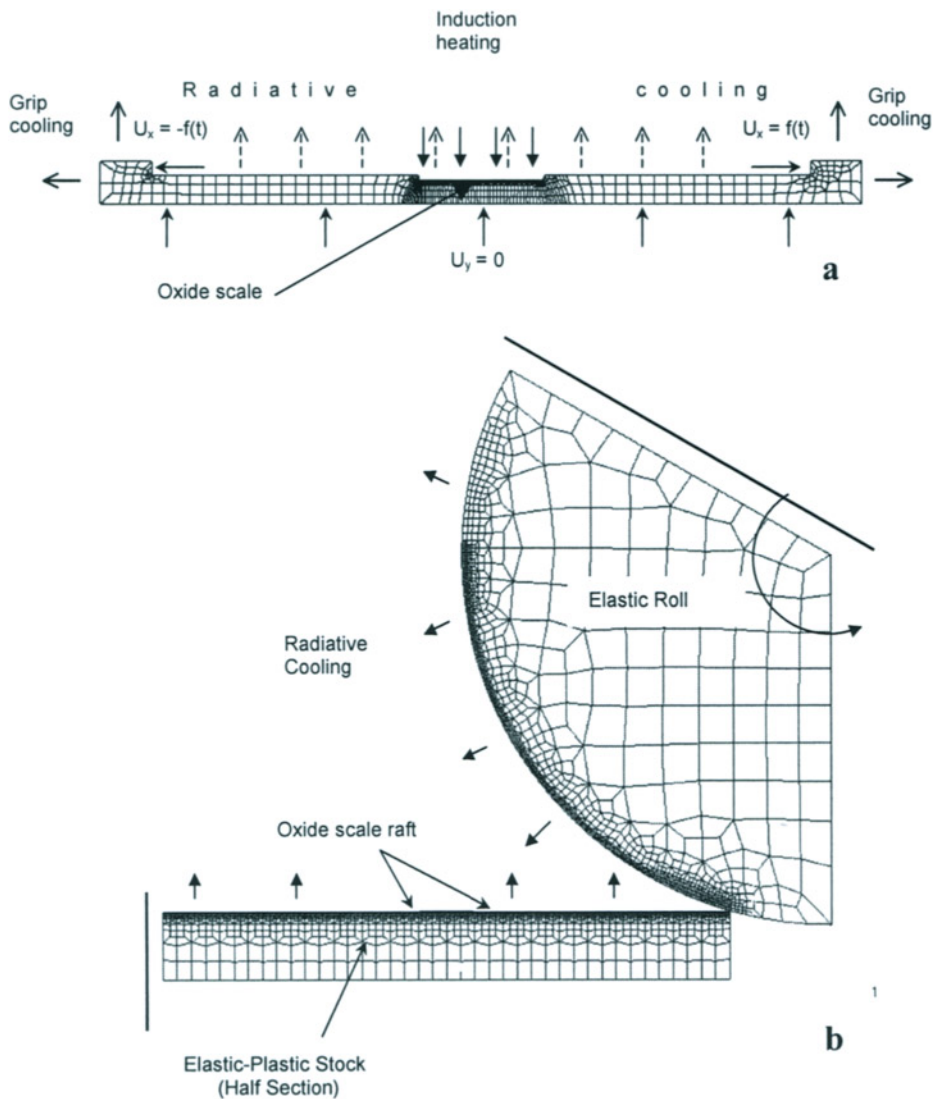


**Figure 13.5** Macro-parts of the FE model used for analysis – schematic representation; **a** – tensile test model; **b** – hot flat rolling model.

where the vertical bars denote the absolute value and  $k$  is about 4. The viscous sliding of the scale is modelled using a shear-based model of friction such that

$$\eta v_{rel} = -mk_{\gamma} \frac{2}{\pi} \arctan\left(\frac{v_{rel}}{c}\right) i \quad (13.3)$$

where  $m$  is the friction factor;  $k_{\gamma}$  is the shear yield stress;  $c$  is a constant taken be 1% of a typical  $v_{rel}$  which smoothes the discontinuity in the value of  $\tau$  when stick/slip transfer occurs; and  $i$  is the tangent unit vector in the direction of the relative sliding velocity. The calculation of the coefficient  $\eta$  was based on a microscopic model for stress-directed diffusion around irregularities at the interface and depends on the temperature  $T$ , the volume-diffusion coefficient  $D_V$  and the diffusion coefficient for metal atoms along the oxide/metal interface  $\delta_s D_s$ , and the interface roughness parameters  $p$  and  $\lambda$  (Raj and Ashby, 1971)

$$\eta = \frac{kTp^4}{4\Omega\lambda^2(\delta_s D_s + 0.8pD_V)} \quad (13.4)$$

where  $k$  is Boltzmann's constant,  $\Omega$  is the atomic volume,  $p$  is the full-wave amplitude and  $\lambda$  is wavelength. It was assumed for the calculation that the diffusion coefficient along the interface was equal to the free surface diffusion coefficient.

It was assumed in the model that spalling of the scale could occur along the surface of lowest energy release rate, which can be either within the scale or along the scale/metal interface. A flaw will continue to grow under a stress if its energy release rate  $G$  exceeds the critical energy release rate  $G_{cr}$ . The strain energy release rate is equal to the J-integral both for linear and non-linear elastic material behaviour (Bakker, 1983). The possibility of calculation of the J-integral is left as an option in the model. The lack of data for the J-integral versus crack length for the oxide scale at this time and the availability of experimental data showing that through-thickness cracking is an essentially brittle process of unstable crack propagation for the test parameters, favour the assumption of linear elastic fracture mechanics (LEFM) for the model. Assuming the opening of the through-scale crack due to applied tensile loading perpendicular to the crack faces (tensile mode), the critical failure strain  $\epsilon_{cr}$  may be used as a criterion for the through-thickness crack occurring (Schütze, 1995)

$$\epsilon_{cr} = \left[ \frac{2\gamma(T)}{F^2 \pi E(T)c} \right]^{1/2} \quad (13.5)$$

where  $\gamma$  is the surface fracture energy,  $E$  is Young's modulus,  $F$  takes values of 1.12, 1 and  $2/\pi$  for a surface notch of depth  $c$ , for a buried notch of width  $2c$  and for a semicircular surface notch of radius  $c$ , respectively. Assuming  $\gamma = K^2/2E$ , where  $K$  is the stress intensity factor, the critical strain and stress can also be expressed in terms of the  $K$ -factors. There is a possibility of through-scale failure due to shear deformation in the oxide. Assuming that the stress intensity factor related to the fracture due to shear loading parallel to the crack faces

(plane shear mode) exceeds the corresponding value for the tensile mode, which as a rule is justified, a criterion for the shear failure in the oxide was chosen as follows

$$\varepsilon_{cr}^{sh} = 2\varepsilon_{cr} \quad (13.6)$$

where  $\varepsilon_{cr}^{sh}$  is the critical strain for shear fracture in the oxide scale.

Using (13.4) and (13.5) the normal and tangential separation stresses were calculated in the model using the deformable-deformable contact procedure implemented in the MARC code. Once contact between a node and a deformable surface is detected, a tie is activated. The tying matrix is such that the contacting node can slide along the surface, be separated or be stuck according to the general contact conditions.

As it follows from hot tensile testing results, the oxide scale during tension can fail in two modes: through-thickness crack mode and sliding mode. To be able to model only this kind of failure the homogeneous one scale layer model with possibility of spallation along the scale/metal interface is chosen (Fig. 13.6b). Usually, the scale consists of several layers having different morphology, phase content and, as a result, different properties. For multi-layer steel scales, in addition to through-thickness cracking, delamination within the non-homogeneous oxide scale can occur.

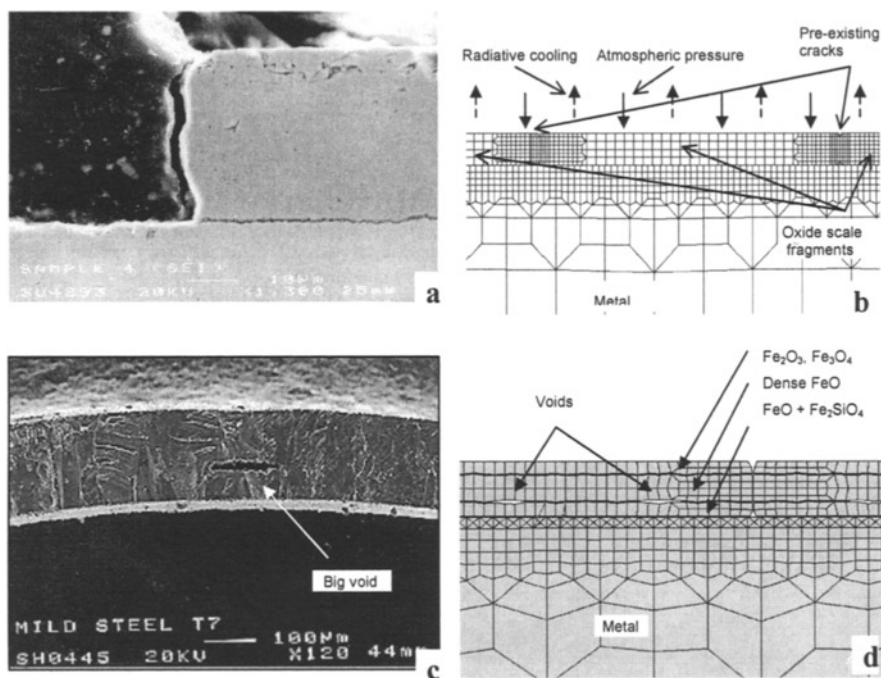


**Figure 13.6.** SEM image showing a cross-section of the mild steel scale fracture surface (a, c) and part of the FE model for analysis of oxide scale failure: one- (b) and multi-layer (d) scale model setup.

Such delamination can take place between the oxide sub-layers having significantly different grain sizes. Big voids, otherwise called blisters and usually situated between oxide sub-layers, could act as sources of multi-layered oxide delamination. To be able to predict such behaviour, generally, the oxide-scale model comprises different sublayers having different mechanical properties. As an example, the non-homogeneous three-scale layers model with possibility of delamination within the scale between the sublayers is shown in Fig. 13.6d.

The temperature dependence of Young's modulus of the different steel oxide scale layers is calculated from the following equations reported in the literature (Morrel 1987, Schütze, 1995):

$$E_{ox} = E_{ox}^o [1 + n(T - 25)] \quad (13.7)$$

where  $E_{ox}$  is the modulus for oxide scales on iron, GPa;  $n = -4.7 \times 10^{-4}$ ;  $E_{ox}^o$  is Young's modulus at 25°C (240 GPa);  $T$  – temperature, °C.

$$E_{ox} = 151.504 \left( 1 - \frac{T - 300}{5476.66} \right) \quad (13.8)$$

where  $E_{ox}$  is the modulus for FeO, GPa. The equation was deduced assuming the shear modulus at 300K  $G_{ox}^o = 55.7$  GPa, the melting point  $T_m = 1643$ K and the Poisson ratio  $\nu_{ox} = 0.36$ .

$$E_{ox} = 209.916 \left( 1 - \frac{T - 300}{9200} \right) \quad (13.9)$$

where  $E_{ox}$  is the modulus for Fe<sub>2</sub>O<sub>3</sub>, GPa. The equation was deduced assuming the shear modulus at 300K  $G_{ox}^o = 88.2$  GPa, the melting point  $T_m = 1840$ K and the Poisson ratio  $\nu_{ox} = 0.19$ . Porosity dependence of Young's modulus of the scales can be taken into account as (Rice 1984, Birchall et al., 1981):

$$E = E_{ox}^o \exp(-bp) \quad (13.10)$$

where  $E_{ox}^o$  is the modulus of the fully compact solid;  $p$  is the porosity;  $b \approx 3$ . Small pores reduced Young's modulus while large pores act as flaws or stress concentrators and weaken the material towards fracture. Table 13.2 illustrates Poisson's ratio for the different oxide layers. The yield strength of the scale can be assumed to be about 130 MPa at 1050°C (Ranta, et al., 1993).

**Table 13.2** Poisson's ratio for the different scale layers assumed for the modelling

FeO	Fe <sub>3</sub> O <sub>4</sub>	Fe <sub>2</sub> O <sub>3</sub>	Ref.	Note
	0.3		Ranta et al., 1993	Data used for modelling of rolling
0.36	0.29	0.19	Robertson and Manning, 1990	Single crystal at room temperature

Other thermo-mechanical properties of the oxide scale and interface used for calculation are presented in Tables 13.3.

**Table 13.3** Thermal and mechanical properties of oxide scale used for modelling

Parameter	Function	Ref.
Density, kg/m <sup>3</sup>	$\rho = 5.71310^3$ $c_p = 674.959 + 0.297 \cdot T - 4.367 \cdot 10^{-5} \cdot T$ for $T \in 600 - 1100^\circ\text{C}$	Ranta et al., 1993 Ranta et al., 1993
Specific Heat Capacity, J/kg deg		
Thermal Conductivity, W/mK	$\lambda = 1 + 7.833 \cdot 10^{-4} \cdot T$ for $T \in 600 - 1200^\circ\text{C}$	Ranta et al., 1993
Heat transfer coefficient at oxide/metal interface, W/m <sup>2</sup> K	$\alpha = 30000$	Pietrzyk and Lenard, 1991
Surface diffusion coefficient times effective surface thickness, m <sup>3</sup> /s	$\delta_s D_s = \delta_s D_{os} \exp(-Q_s / RT)$ $\delta_s D_{os} = 1.10 \cdot 10^{-10} \text{ m}^3/\text{s}$ ; $Q_s = 220 \text{ kJ/mole}$	Swinkels and Ashby, 1981
Volume (lattice) diffusion coefficient, m <sup>2</sup> /s	$D_v = D_{ov} \exp(-Q_v / RT)$ $D_{ov} = 1.80 \cdot 10^{-4} \text{ m}^2/\text{s}$ ; $Q_v = 159 \text{ kJ/mole}$	Swinkels and Ashby, 1981
Stress intensity factor, MN m <sup>-3/2</sup>	$K = a_0 + a_1 T + a_2 T^2 + a_3 T^3 + a_4 T^4 + a_5 T^5$ for $20 - 820^\circ\text{C}$ $a_0 = 1.425$ ; $a_1 = -8.897 \cdot 10^{-3}$ ; $a_2 = -8.21 \cdot 10^{-5}$ ; $a_3 = 3.176 \cdot 10^{-7}$ ; $a_4 = -5.455 \cdot 10^{-10}$ ; $a_5 = 3.437 \cdot 10^{-13}$	Hancock and Nicholls, 1988
Linear Coefficient of Thermal Expansion, $\times 10^{-6} \text{ K}^{-1}$	$\alpha_{ox} = 15.0 \text{ (FeO)}; 12.0 \text{ (Fe}_3\text{O}_4); 13.0 \text{ (Fe}_2\text{O}_3)$	Robertson and Manning, 1990

### 13.4 EFFECT OF CHANGING STEEL COMPOSITION

The investigation has been carried out in the following sequence. First, the peculiarities of scale growth kinetics, morphology and mechanisms of failure that could be attributed to the different chemical contents have been established for the steel grades during hot tensile testing. Then, using finite element modelling, evaluation of the influence of the most critical parameters and appropriate upgrade of model parameters has been undertaken, to be able to mimic experimentally observed phenomena. A possible explanation of experimentally observed differences has been suggested.

#### 13.4.1 Comparison of oxide scale growth and morphology

The chemical composition of the steels is presented in Table 13.4. The main differences are in silicon, manganese and molybdenum and also relatively high contents of Cr and Ni for the stainless steel. All steel grades included Cu within 0.16 – 0.26 weight %. The rates of oxidation were determined by measuring the scale thickness in the middle portion of the sample away from ends. For the two mild steels the parabolic character of oxidation had been well established for oxide growth in air. The prediction of scale thickness was made using the published parabolic rate constant for iron oxidation on the basis of compiled experimental data (Sheasby et al., 1984):

**Table 13.4.** Chemical content of steels used for hot tensile tests (weight %)

Element	C	Si	Mn	S	P	Cr	Ni	Cu	Mo	Nb
Mild steel 1	0.19	0.18	0.79	0.03	<0.005	0.05	0.07	0.14	<0.02	<0.01
Mild steel 2	0.18	0.36	1.33	0.01	0.025	0.03	0.02	0.08	<0.02	0.041
Si-Mn steel	0.57	1.90	0.79	0.008	0.01	0.18	0.08	0.16	<0.02	
Mn-Mo steel	0.34	0.23	1.28	0.039	0.022	0.17	0.12	0.17	0.24	
Stainless steel	0.025	0.47	1.44	0.034	0.031	18.4	9.2	0.26	0.47	

$$\delta_{ox}^2 = \delta_{ox0}^2 + k_p t_{ox} \quad (13.11)$$

$$k_p = 5.053 \times 10^{-4} \exp \left( -\frac{20419}{T} \right) \quad (m^2 / s).$$

This agrees reasonably well with measurements of oxide thickness. The different alloying elements of the steel have an influence on the oxidation rate in reheat environments. A more complex equation for prediction the scale thickness has been developed (Ormerod et al., 1990). It has been shown that silicon could partially inhibit scale growth or contribute to thicker scales by inhibiting the healing of surface cracks. Copper, in combination with nickel, may decrease the amount of scale formed, but in combination with other alloying elements, it may encourage scale growth or have no effect at all. Manganese, at up to 1.75 wt. %, can contribute to thickening the scale. Nickel tends to thicken scales by forming its own oxides when carbon is also present, while in combination with other elements, the formation of nickel oxides is retarded. However, the effect of steel chemistry on the scale thickness for these two mild steels should be more visible for the longer times of oxidation typical for reheating processes, but not for the secondary oxide scale growing during the short period of subsequent descaling operations. Thus, the differences in chemical content for the low carbon steels used in this investigation have not produced significant differences in oxide scale thickness for the chosen time periods.

Generally the morphology of the scales and the oxide/metal interface observed were not distinguishable from types that have been described earlier (Krzyzanowski and Beynon, 1999a). However, for a given temperature of oxidation the two mild steels revealed significant differences. First was in the amount of porosity in the scale, illustrated in figure 13.7. It also indicates the different crystal sizes in the oxide scale. Each appears to comprise three layers. Although the relative thickness of each layer is different for the two steels. The inner FeO layer had a large number of evenly distributed small pores. The middle, dense, FeO layer had the largest grains for both steels. The outer layer consisted mainly of fractions of magnetite and hematite. The interface between the magnetite and dense FeO layer was the area of formation of relatively large pores. It was observed that adherence of the inner porous layer with the metal surface was more for steel 2 than for steel 1. This results in relatively easier delamination within the oxide scale along this layer for steel 2 during descaling before SEM observation (Fig. 13.7c).



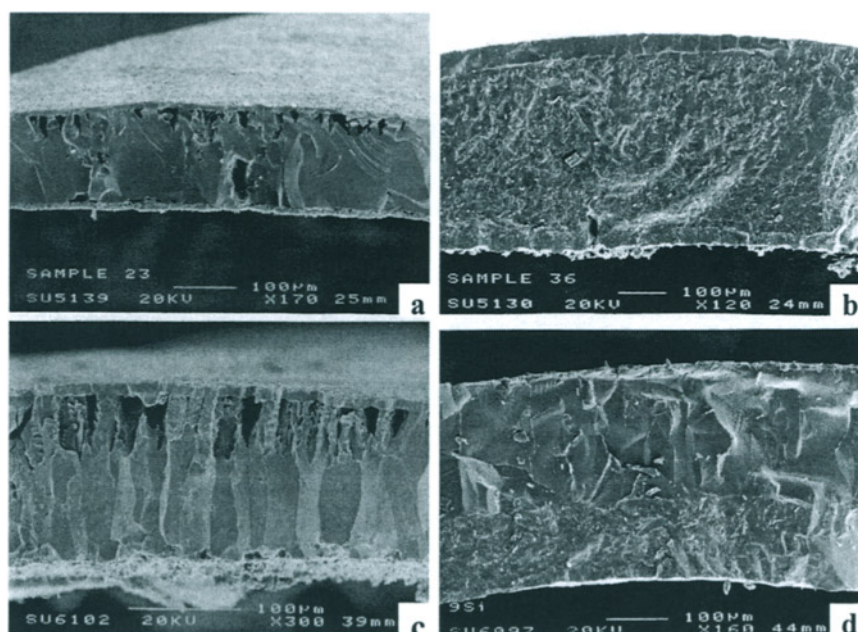


**Figure 13.7** SEM photographs showing the cross-section of the oxide scale formed at 975°C during 800 s (a, c) and at 1150°C during 800 s (b, d). a, b mild steel 1; c, d mild steel 2.

This suggests that there should be a difference in the mechanical properties of the oxides and oxide/metal interface for these steel grades. The difference in oxide grain sizes and porosity for two mild steel grades was also observed. The larger grains of the middle oxide layer had relatively larger but more infrequent pores grown on mild steel 1 at the temperature range below 975°C (Fig. 13.7a,c). The corresponding layer of mild steel 2 had a large number of more evenly distributed smaller pores. At higher temperatures, vice versa, relatively larger oxide grains were observed for mild steel 2 (Fig. 13.7b,c). It is supposed that the relative strength of oxide changes with temperature.

Mild steel oxides had the highest oxidation rate throughout the temperature range 783 – 1200°C out of these five steel grades. At 855°C and 800s oxidation time, the oxide scales formed on the surface of the mild steel were more than 25µm thick, while Mn-Mo oxide scale was about 5µm thick, Si-Mn scale thickness was less than 5µm and stainless steel did not show an visible oxide layer formed on the surface of the specimens under these time-temperature conditions (Fig 13.8). The low oxidation rate at this temperature for Mn-Mo and Si-Mn steel can be explained by the presence of manganese and silicon which acted as de-oxidisers. Mn up to 1.75% promotes scale growth at high temperatures (Kofstad, 1985).

However, silicon and molybdenum act as inhibitors of the scale growth process (Miner and Nagarajan, 1981) resulting in thinner scales for these steels. While molybdenum helps to build up the resistance against oxidation in Mn-Mo steel, a detrimental effect was observed due to formation of volatile MoO<sub>3</sub> type oxide, which ruptured the oxide film and allowed access to atmosphere oxygen (Chang and Wei, 1989). This could be one of the reasons for obtaining a slightly thicker scale for Mn-Mo steel compared with Si-Mn steel. For stainless steel, the oxide film formed at low temperatures (783-912°C) was very thin and



observed as temper colours (Fig. 13.8c). The film became thicker and more opaque at higher temperatures and became optically visible as an oxide scale at the oxidation temperature 1074°C and above. It is well known that chromium inhibits scale growth at high temperatures (Kofstad, 1985). The 316L stainless steel contains 18.4% chromium and it resulted in the highest resistance to oxidation. The stainless steel scales tightly adhered to the metal surface even after application of 5% strain. The scales usually consisted of several different layers of grains and separation under the influence of deformation took place along the weakest interface for this multi-layered scale. For mild steel 1 at 783°C, the oxide/metal interface was the weakest one. However, for Si-Mn steel oxide scale, the interface between the closest to metal surface scale layer usually consisted of small equiaxed grains and the outer scale layer

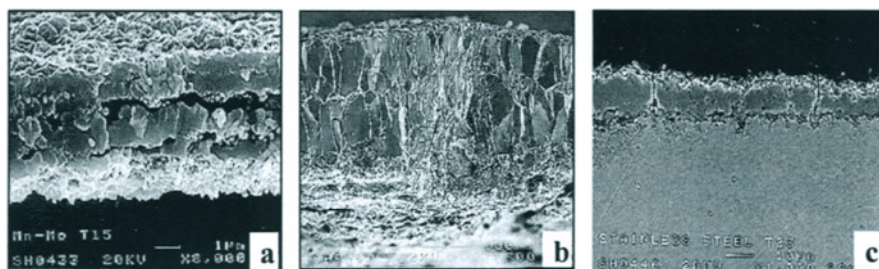


**Figure 13.8.** Oxide scale on the surface of Mn-Mo (a), Si-Mn (b) and stainless steel (c) after tensile tests.

SEM photographs of the scale fracture surface (a, b) and specimen cross section (c). a  $T = 855^{\circ}\text{C}$ ;  $t_{\text{ox}} = 800\text{s}$ ; b  $T = 1200^{\circ}\text{C}$ ;  $t_{\text{ox}} = 800\text{s}$ ; c  $T = 1074^{\circ}\text{C}$ ;  $t_{\text{ox}} = 800\text{s}$ .

consisted of large grains, and the interface is a potential location for separation within the scale. Such separation within the scale layers, called delamination, was also observed within mild steel 1 oxide at 1150°C, when relative sliding of the layers took place under elongation of the specimen (Krzyzanowski and Beynon, 1999a). In that case, the innermost thin layer had no observable porosity and adhered tightly to the metal surface even after 10% strain.

#### 13.4.2 Comparison of failure modes

Two different modes leading to oxide spallation during tensile testing were observed for the mild steel grades. The modes corresponded to the modes that had been observed earlier for the low carbon mild steel (Fig. 13.1) (Tan et al., 2001). According to the first mode observed at lower temperatures, through-thickness cracks are formed during tension followed by initiation of a crack along the oxide-metal interface that might result in spallation at higher strains (Fig. 6a, 7a, b). This type of oxide scale behaviour can be explained by assuming that the interface between metal and oxide scale is stronger than the oxide scale itself.

It is well known that through-thickness cracks most likely initiate at pre-existing flaws and grow into the scale when its energy release rate exceeds the critical energy release rate of the material (Robertson and Manning, 1990). The variations in crack spacing might be due to the apparently random distribution of voids and pre-existing cracks within the scale. The second mode of oxide spallation was observed at higher temperatures. In this mode the oxide scale was sliding along the interface throughout elongation under the uniaxial tensile load after spallation at one end of the specimen gauge length. It is evident that the interface becomes weaker than the oxide scale at higher temperatures. Sometimes spallation of the whole oxide raft took place after cooling, mainly because of changes in the diameter of the specimen during elongation. Despite both modes of oxide failure in tension

being observed for both steel grades, significant differences in scale state after tension for the same test parameters were recorded (Table 13.5). Through-scale cracks and near full spallation of the fractured oxide occurred for steel 1 after tension at 830°C, while no visible through-thickness cracks were observed for steel 2 after tension under the same conditions.

Scale thickness influences behaviour. Comparing relatively thin scale (about 40-65µm) with 150-180µm thick scale following 5% strain at 975 °C, both steels had through-thickness cracks in the thicker scale (Fig. 13.9b,d) whereas the thinner scale showed no tensile cracks for either steel. However for the thicker scale, sliding of the non-fractured scale raft for steel 1 and through-thickness cracks for steel 2 were observed when the strain rate was decreased from 2.0 to 0.2 s<sup>-1</sup> at the same temperature. This suggests that the viscous component of oxide scale sliding at high temperature could be significant.

**Table 13.5** Comparison between states of the oxide scale after hot tensile tests for two mild steel grades

Temp. °C	Strain, %	Strain rate, s <sup>-1</sup>	Oxid. time, s	Scale state	
				Mild steel 1	Mild steel 2
830	2.0	0.2	800	Through-thickness cracks. Near full spallation.	No cracks.
830	2.0	0.2	3000	One through-thickness crack in the middle and second one at the end	Slightly visible cracks at the ends
900	5.0	0.2	800	Slipping during the tension. No cracks	Cracks at one end
975	5.0	2.0	100	No cracks	No cracks
975	5.0	2.0	800	Through-thickness crack in the middle. Significant crack width. Irregular crack surface.	Three through-thickness cracks
975	5.0	0.2	800	Slipping during the tension. No spallation.	Several through-thickness cracks. Irregular crack surface
1150	5.0	0.2	100	Slipping during the tension. No spallation. Detachment at one end	Slipping during the tension. Detachment at both ends
1150	5.0	4.0	100	Slipping during the tension. No spallation. Detachment at one end	Slipping during the tension. No spallation. Detachment at one end
1150	5.0	4.0	800	Slipping during the tension. No spallation. Detachment at both ends	Slipping during the tension. No spallation. Detachment at both ends

One of the significant features of this failure is the transfer from the through-scale crack mechanism of oxide failure to sliding of the non-fractured oxide raft along the oxide/metal interface with increasing temperature. In terms of the mathematical model, that means that the separation stress within the scale fragments is less than the separation stress at the oxide/metal interface at low temperature. In the high temperature range, the separation stress at the oxide/metal interface is less than the separation stress within the scale fragments. It has been shown earlier that this transfer takes place between 850 and 870°C for mild steel 1 (Fig. 13.2) (Krzyzanowski and Beynon, 1999b).

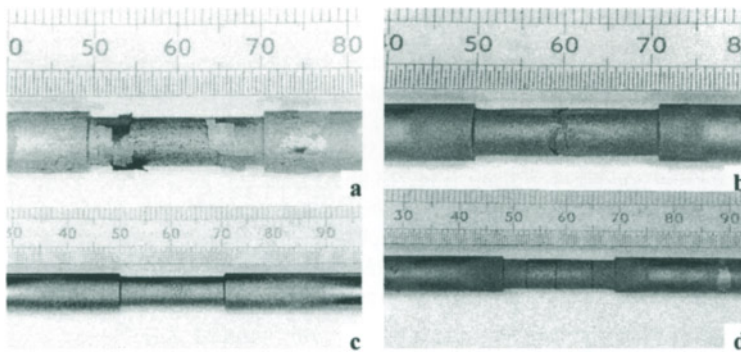


**Figure 13.9** Oxide scale on the tensile specimen after testing at:  $T = 830^{\circ}\text{C}$ ,  $\varepsilon = 2.0\%$ ,  $\dot{\varepsilon} = 0.2\text{ s}^{-1}$ ,  $t_{\text{ox}} = 800\text{ s}$ , predicted  $\delta_{\text{ox}} = 60\mu\text{m}$  (equation 11) (a, c);  $T = 975^{\circ}\text{C}$ ,  $\varepsilon = 5.0\%$ ,  $\dot{\varepsilon} = 2.0\text{ s}^{-1}$ ,  $t_{\text{ox}} = 800\text{ s}$ , predicted  $\delta_{\text{ox}} = 178\mu\text{m}$  (equation 11) (b, d). a, b mild steel 1; c, d mild steel 2.

The available experimental data (Table 13.3) provide a basis for modelling the two modes of oxide scale failure in tension. Sliding along the scale/metal interface at high temperatures is possible when either the stress from the tensile deformation exceeds that necessary for viscous flow without fracture at the scale/metal interface, or the energy release rate exceeds its critical level, resulting in fracture along the interface. For the first case, tangential viscous sliding of the oxide scale on the metal surface is allowed due to the shear stress transmitted from the specimen to the scale. For the second, fracture along the interface can result in separation of the whole scale raft from the metal surface. It is probable that this type of sliding of the detached oxide scale dominated in the tensile tests.

By assuming the transition temperature range it is possible to model transfer from one oxide scale failure mechanism to another. However, there is a necessity to broaden the assumption when the model is adjusted to mimic the effect of changing the chemical composition of the steel. To reconcile the differences between states of the oxide scale after tension presented in Table 13.5, two changes were made to the model (Fig. 13.10). First, it was assumed that the transition temperature range for mild steel 2 is at the higher temperature level, observed to be above  $950^{\circ}\text{C}$ . Second, it was assumed that the separation stresses for mild steel 2 both within the oxide scale and for the oxide/metal interface exceed the corresponding stresses for mild steel 1. Both assumptions were made mainly to satisfy differences observed in the slow tests ( $0.2\text{ s}^{-1}$  strain rate) for oxidation at  $830 - 975^{\circ}\text{C}$  for 800 s when relatively thick scale ( $100 - 160\mu\text{m}$ ) was formed. Assuming relatively stronger scale for mild steel 2 allows simulation of the differences in oxide state that were observed at  $830^{\circ}\text{C}$ . However, this assumption alone is insufficient for prediction of the different behaviour of the oxide scale observed at  $975^{\circ}\text{C}$  when the scale grown on mild steel 1 showed slipping during tension while the scale corresponding to mild steel 2 failed by through-thickness fracture. Modelling the differences observed at  $975^{\circ}\text{C}$  is only possible by assuming the displacement of the transition temperature in higher temperature range for mild steel 2. Such an assumption in turn implies a relative increase of the separation stress for the oxide/metal interface for mild steel 2. Thus, these two assumptions for the model were sufficient to match the differences in states of the oxide scale observed after hot tensile testing. At the same time, these assumptions were necessary because excluding either of

them results in inadequate prediction of scale behaviour either in the low temperature range or in the temperature range where transfer from one mode of scale failure to another takes place. The model assumptions shown in Fig. 13.10 have been used to produce the simulation results for two modes of oxide failure shown in Fig. 13.11. These computed results match very well the experimental observations for both steel grades at the same test parameters.

The elemental mappings for Fe, Mn, Cu and Si over the area of the inner porous FeO layer made for Cu-containing low carbon steels (Taniguchi et al., 1997) indicate that Mn is not enriched in the scale nor in the substrate, while Si is enriched in the porous FeO layer. The enrichment of Cu became less significant as the Cu content decreased and it was unrecognisable with less than 0.5 wt. % Cu steels. The explanation of the different properties of the scale and the scale/interface observed in the hot tensile tests for the two low carbon steels is beyond the scope of this chapter. Nevertheless, the different properties can be related to the different Si and Cu contents at the interface, so it was assumed that the mild steel more enriched in Si has the stronger scale/metal interface and has a higher level of separation load, leading to failure within the scale.

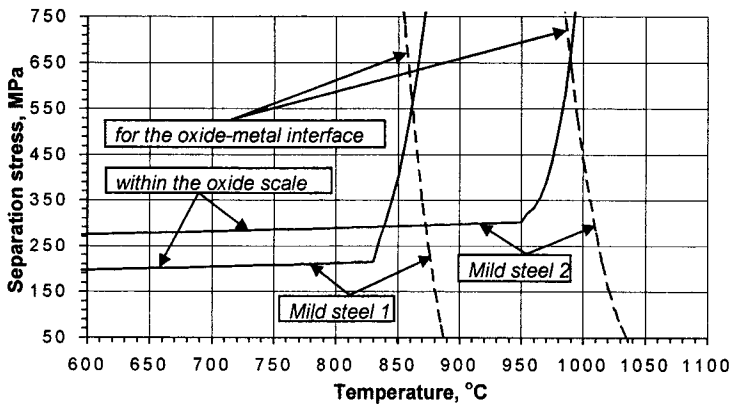


**Figure 13.10** Effect of temperature on the separation stresses of scale/metal system for two mild steel grades – model assumption.

The temperature dependence of the stress necessary for causing the scale failure at the interface for the two steels can be understood by taking into account the possibility of formation of FeO/Fe<sub>2</sub>SiO<sub>4</sub> eutectic compound (fayalite) instead of the porous FeO layer (Asai et al., 1997). It is well known that fayalite reduces the removability of primary scale (Fukagawa et al., 1996), therefore the strength of the interface is greater for the steel richer in Si. However, since it was reported (Hancock and Nicholls, 1988) that FeO is plastic above about 827°C, a part of the stress might be relieved by the plastic deformation of FeO and metal, so the separation stress to cause the failure seems to be slightly reduced. Oxidation at 1150°C resulted in the formation of Fe<sub>2</sub>SiO<sub>4</sub> grains in an inner FeO layer. The particles of Fe<sub>2</sub>SiO<sub>4</sub> are harder than the FeO matrix and disturb its plastic deformation. Additionally, they decrease the contact area between the two FeO layers. Both of these can weaken the adhesion between the two FeO layers, which might result in delamination within the scale, as has been observed for this temperature range. Liquid Cu enrichment in the scale/metal interface at high temperatures may contribute additional lowering of the adhesion for the mild steel 1 (0.14 wt. % Cu steel) in comparison with mild steel 2.

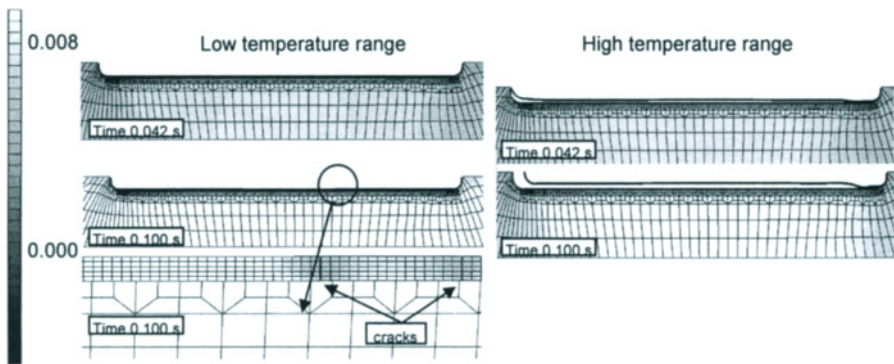


**Figure 13.11** Longitudinal strain distribution calculated within the gauge of the tensile specimen illustrating prediction of mild steel oxides failure in tension for the different temperature ranges.

The mode of failure for Mn-Mo and Si-Mn steel oxide scales was confined only to through-thickness cracks within the temperature range from 783°C to 1200°C, the thickness of the oxide scale maintained within 5 – 250  $\mu\text{m}$ ; strain 1 - 5% and strain rate 0.2 - 4.0  $\text{s}^{-1}$ . This favours the assumption that presence of alloying elements such as manganese, molybdenum and silicon results in strengthening of the oxide/metal interface at high temperatures compared with mild steel. The stainless steel had also shown only through-thickness mode of failure. For this steel, the oxide scale formed at 1074°C for 800s was less than 10  $\mu\text{m}$  thick and the through-thickness cracks presented within the scale after the test were only visible under SEM observations (Fig. 13.8c).

There is a high probability that sliding of the oxide scale during tension would be observed for any of the steel grades at higher temperatures, outside the tested range. Nevertheless, to be able to mimic these experimental observations, an assumption has been implemented in the oxide scale model, namely that the ratio of the separation stresses within the oxide scale and the scale-metal interface is less than 1 within the range 783-1200°C for the tested Mn-Mo, Si-Mn and stainless steels (Fig. 13.12). This is in good agreement with the results obtained for two low carbon steels, where it was shown that significantly lower alloy content lowered the transition temperature range by over 100 K. It is clear that the observed differences in deformation behaviour are much larger than would be expected from differences in oxidation. The chemical content of the underlying steel influences the fracture energy of the oxide scale and its adherence to the metal surface, both reflected in the observed differences in their failure. This raises important issues where further research work is needed. The direct measurement of the scale-metal separation loads coupled with physically based modelling would allow the observed effects to be more predictable.

### 13.5 ANALYSIS OF OXIDE SCALE FAILURE AT ENTRY INTO THE ROLL GAP

Hot flat rolling gives rise to significant tensile loading of the free metal surface layer around the roll gap both at entry and at exit (Fig. 13.13). These zones are areas where the probability of tensile oxide failure is highest. The zone of entry into the roll gap is important from the

point of view of the current rolling pass because hot metal can extrude through any cracks under the roll pressure, thereby enhancing both heat transfer and friction. The longitudinal tension at the exit from the roll gap could produce further oxide scale failure because the temperature at the interface has dropped to about  $800^{\circ}\text{C}$ , which is the temperature range for brittle oxide scale behaviour. This additional failure, if it happens, is reflected in the micro events at the interface for the subsequent rolling passes or on the quality of the surface of the final rolled product. The present analysis pays attention mainly to two key technological hot rolling parameters that have an influence on the secondary oxide scale failure at the entry into the roll gap, namely, the temperature and the oxide scale thickness.

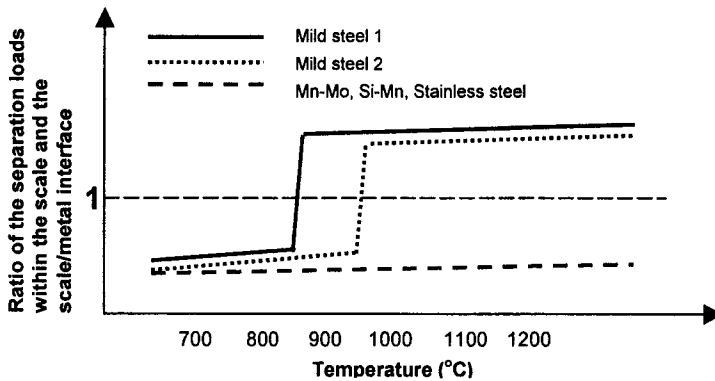


**Figure 13.12** Schematic representation of the effect of temperature on ratio of the separation loads within the oxide scale and the scale metal interface for the different steel grades



### 13.5.1 Effect of initial stock temperature

The initial stock temperature is probably the most crucial factor for oxide scale failure and varies

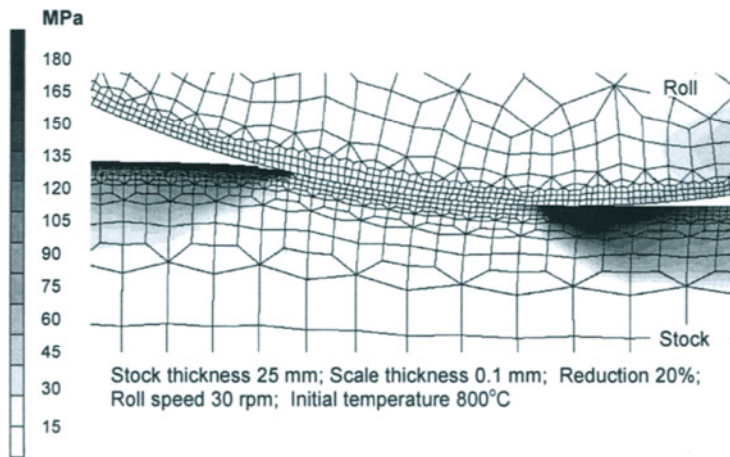


**Figure 13.13** Distribution of the stress component in the rolling direction ( $\sigma_{13}$ ) predicted in the cross section of the roll gap in the absence of the oxide scale.

considerably across commercial rolling practice. Apart from the direct influence on the extent of tangential viscous sliding and adherence of the scale, the surface fracture energy and Young's modulus, which are reflected in the model criteria for through-thickness cracking and spallation, there is evidence of the influence of temperature on the morphology of the oxide scale and the formation of voids. The scale formed at 1150°C was non-homogeneous and delamination within the oxide layer took place during tensile loading (Krzyzanowski and Beynon, 1999a). The observations have shown that oxide scales formed at 1150°C delaminated more readily than more homogeneous scales formed at 900°C. The outer layers displaced along the interface within the oxide scale during elongation of the specimen. The separated outer scales are very porous and much thicker than the non-separated oxide layer, which was usually 3 – 8  $\mu\text{m}$  thick. The temperature also has a significant effect on the oxide growth kinetics (Sheasby et al., 1984, Ormerod et al., 1990) contributing to the thickness of the scale growth between rolling passes. The secondary scale grows faster on the newly exposed metal surface after passing through a descaler. The numerical approach developed for the oxide scale modelling allows for the formation of non-homogeneous oxide scale. Nevertheless, to avoid unnecessary complexities in this micro-component of the model, a homogeneous scale 100  $\mu\text{m}$  thick and containing voids has been assumed for this section of the numerical analysis.

FE modelling shows that when the initial stock temperature is in the range for brittle oxide and strong oxide/metal interface, a longitudinal tensile strain in the stock surface ahead of contact with the roll, which is inevitably produced because the roll is initially moving faster than the stock surface, can result in through-thickness crack formation. The laboratory observations complemented by FE modelling of the tensile deformation, results of which have been shown in the same paper (Krzyzanowski and Beynon, 2000), testify that this behaviour is also very sensitive to small changes in the chemical composition of the underlying steel and is not related to the ferrite-austenite phase transformation (section 13.4). A sequence of through-thickness crack formation can be seen in Fig. 13.14 showing the different increments of the non-steady state modelling corresponding to the different moments of time for the oxide scale raft entering the roll gap. Through-thickness cracks develop from the pre-existing defects located at the outer surface of the oxide layer, where critical strain for failure has been reached. It reaches a maximum value approximately midway between the cracks. Within the scale fragment the in-plane stress cannot transfer across the crack and becomes zero at each of the

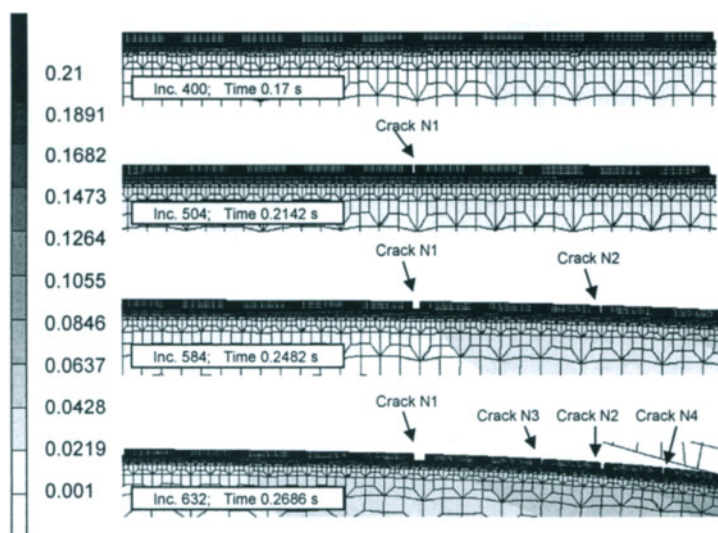


**Figure 13.14** Distribution of  $\epsilon_x$  strain component predicted for the different time moments of scale raft entering into the roll gap at an initial temperature of 800°C. The scale raft consists of 10 fragments.

crack faces. Thus the level of longitudinal stresses within the oxide scale is significantly relaxed compared with the surface layer of the metal (Fig. 13.15a). At low temperatures, in the absence of relaxation by viscous sliding, relaxation of stresses can only occur by cracking and spallation of the scale fragment when the strain increases. At higher temperatures interface sliding can have a significant role in relaxation of the transmitted stresses (Fig. 13.15b). The level of longitudinal stresses at the stock surface layer for the higher stock temperature is less than for the lower one but, as can be seen from Fig. 13.15, the relaxation of the oxide scale stresses relative to the metal surface layer is visible in both cases. The difference is that through-thickness cracks at the entry into the roll gap have not occurred in the higher temperature range, so the scale would enter the roll gap without cracks. In this case, stress relaxation within the scale takes place by relative sliding along the oxide/metal interface.

The approach developed and described earlier (Krzyzanowski and Beynon, 1999b), combining the hot tensile measurement and FE modelling, allows for determination of these transitional temperature ranges for a particular steel grade. Although viscous sliding becomes easier at high temperature, the shear stress at the oxide/metal interface will eventually lead to separation of the scale from the metal. To mimic the effect of long continuous oxide scale on the stock surface, in the model the rear end of the oxide scale raft has been fixed to the metal surface using rigid ties. The relative velocity between the oxide scale and the metal surface increases as the scale comes to the entry into the roll gap and reduces when the fixed end of the scale comes up to the zone of longitudinal deformation (Fig. 13.16). At the moment of entering the roll gap, the roll comes into contact with the scale and drags it into the roll gap. Since the roll surface is moving faster than the metal surface at entry, the relative velocity could be significantly decreased and it could even change sign depending at which oxide surface, bottom or top, the friction force is greater.



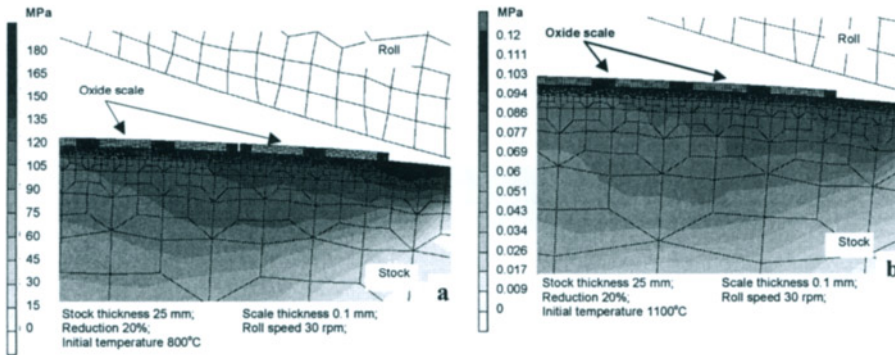


**Figure 13.15** Distribution of longitudinal  $\sigma_x$  stress component predicted at the moment of entering into the roll gap. **a**- initial temperature 800°C. Note the crack (crack N 2 in Fig. 13.14) which has opened up in the oxide scale ahead of contact with the roll; **b** - initial temperature 1100°C. At this elevated temperature there is no cracking of the oxide scale.

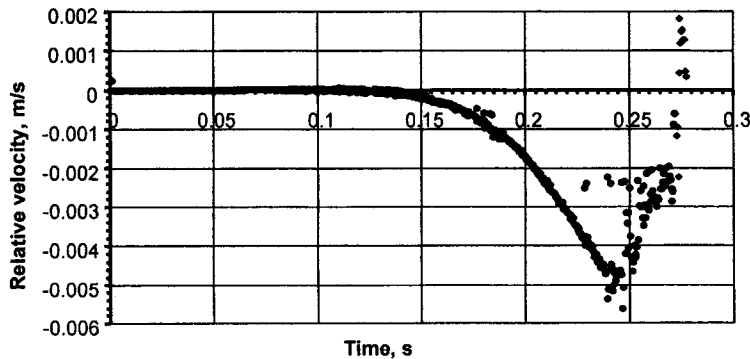


**Figure 13.16** Relative velocity between the oxide scale and the metal surface predicted for the time of entering the roll gap for the following parameters: scale thickness - 0.1 mm, stock thickness - 25 mm, temperature - 1100°C, roll speed - 30 rpm and reduction - 20%. The oxide scale raft is fixed to the metal surface at the rear end.

### 13.5.2 Effect of oxide scale thickness

It has to be noted that the criteria for oxide failure in the model have been developed in terms of crack propagation rather than initiation of flaws. For oxide scale on a free metal surface, such as at entry into the roll gap, the underlying elongating metal transmits an increasing stress to the oxide scale as rolling proceeds. Thus, even after through-thickness crack formation, the elongating substrate allows the transmission of the stress to each pre-existing void in the oxide scale making crack initiation not the limiting process. This assumption has been implemented into the model based on the experimental observations of the present and other authors (Robertson and Manning, 1990). Although the model allows for the assumption of a spectrum of strain values as criteria for crack generation and spalling, just one level of critical strain has been chosen for this analysis.

As can be seen in Fig. 13.17a, if the oxide scale is thin enough, it could enter the roll gap

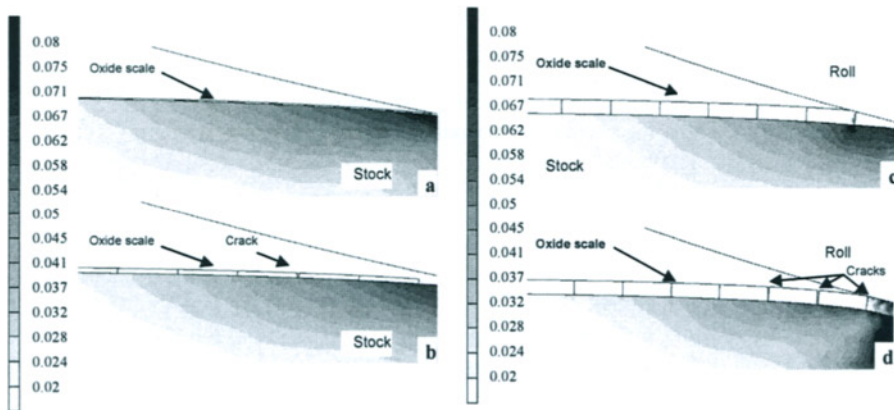


**Figure 13.17** Distribution of longitudinal  $\epsilon_x$  strain component predicted at the moment of entering into the roll gap for stock thickness 5.5 mm, reduction 30%, roll speed 10 rpm, initial temperature 700°C and the different thickness of the oxide scale. **a** – 0.03 mm thickness; **b** – 0.1 mm thickness; **c** – 0.3 mm thickness, time – 0.272 s; **d** – 0.3 mm thickness, time – 0.2788 s.

without cracks, as a continuous layer. This kind of behaviour is typical for the thinnest scales. Although the scale on mild steel at 700°C can be considered as brittle, crack generation, in terms of the model, is a size dependent concept. The stress sufficient for the pre-existing crack propagation increases as the crack size decreases. The pre-existing cracks for the thin scales, which mimic the scale flaws, are less than for thicker scales. Reducing them, the lower limit could be reached when the stress for crack propagation eventually exceeds the yield stress assumed for the oxide scale. The oxide scale will then be able to deform in a ductile manner and not fail by through-thickness cracking. This fact is known in the literature as the comminution limit of the material (Kendall 1978). The results of modelling favour the conclusion, which is important from the technological point of view, that for a particular steel grade and the rolling parameters, there is a lower limit of the oxide scale thickness, beneath which the scales come into the roll gap without through-thickness cracks.

If the oxide thickness is greater than the lower limit mentioned above, the crack pattern approaching entry into the roll gap is sensitive to the scale thickness (Fig. 13.17b,c). In the low temperature range when the interface is strong, relaxation occurs by the formation of through-thickness cracks at a sufficiently high strain within the scale layer. Although there will be some small relaxation of stresses because of viscous sliding, it seems likely that crack generation will be negligibly affected because adherence at the oxide/metal interface prevents the scale sliding. Increasing the oxide scale thickness results in redistribution of the cracks, which is influenced by the critical criteria for separation within the oxide scale and the oxide/metal interface (Beynon and Krzyzanowski, 1999).

As can be seen in Fig. 13.17c, illustrating the results of the model prediction for the scale of 300 $\mu$ m thickness, the closest crack has appeared to the left of the picture limits. In spite of the lack of direct data about the separation criteria making determination of the effect problematic, the modelling tests have shown that the crack spacing tends to increase for thicker oxide scales at the zone of entry into the roll gap. Fixing the rear end of the oxide scale raft to the metal surface makes observation of the difference between the failure behaviour of the thinnest (30 $\mu$ m) and the thickest (300 $\mu$ m) oxide scale in the low temperature range easier. The thinnest scale neither cracks at the zone of longitudinal tensile stresses before the entry into the gap, nor cracks at the moment of the roll gripping, contrary to the thickest oxide scale, which inevitably fracture into islands at the moment of contact with the roll. To make this mode of failure clear the results of prediction for two subsequent moments of time are plotted together in Fig. 13.17d,e.

From these results, the conclusion reached is that if the initial rolling temperature is in the low temperature range, in terms of the mode of oxide scale failure, and of the oxide scale thickness exceeds its comminution limit, when the scale could fail only in ductile manner, the longitudinal tensile stress at entry into the roll gap can favour through-thickness cracks in the scale. The breaking up of the scale at the moment of the roll gripping can provide an additional contribution to the failure in this temperature range.

### ***13.5.3 Verification of the model prediction using stalled hot rolling tests***

It is evident from the preceding discussion that, for hot rolling of mild steel, the area of entry into the roll gap can be the source of through-thickness cracks, depending to a significant extent on the initial rolling temperature and the scale thickness. Stalled hot rolling tests have been conducted with the aim of verifying the main points of the discussion based on the numerical analysis. Fig. 13.18 illustrates results from one test. Using furnace oxidation with the gas protection at 1150°C for 15 min produced a scale layer of about 300 $\mu$ m thickness smoothly covering the specimen surface. The oxidised specimen was then cooled to 700°C, with the aim of reaching the low temperature range for a relatively strong oxide/metal interface and weak scale, and rolled to a reduction of 30%. The thermal history (Figure 13.18b) shows two steps down in temperature: the first, during the rolling pass, and the second, smaller, due to the contact with the roll during the reverse roll movement. Several zones could be observed after testing (Fig. 13.18a). The undeformed zone has the initial slightly blistered oxide scale, the zone of entry into the roll gap, the central non-cracked and the lateral cracked areas can be distinguished. This central area is the most relevant to the flat rolling conditions modelled above. The sides were influenced by three-dimensional deformation fields at the edges of the specimen. The zone of the arc of contact with the roll reflects the semi-circular shape of the crack pattern formed at the edges of the oxidised specimen before the gap, together with small cracks between the larger circular cracks. The central part of the arc consists of the many horizontal cracks with the small crack spacing similar to that, which resulted from the small cracks formed at the edges between the semi-circular lateral cracks. It favours the assumption that these horizontal cracks have been formed at the moment of the scale contact with the roll. The crack spacing for both types of cracks, formed before and at the moment of entering, was widening at the exit from the roll gap where the extensive longitudinal tensile stresses formed at the stock surface layer. Fig. 13.18c shows the SEM image of the oxide scale at the zone of entry into the roll gap where the three areas described above are marked and shown separately on the right. It can be clearly seen that the oxide scale at the central II area has been broken at the moment of roll contact, backing up the numerical prediction made using FE modelling for the same

parameters (Figure 13.17e). The cracks at the lateral areas I and III appeared before entering the roll gap on the free scale due to longitudinal tensile stresses. The additional cracks at these areas appear at the moment of contact with the roll and contribute to the crack pattern formed.

Although, the developed model needs more reliable data, particularly for oxide scale and oxide/metal interface properties, at this stage of its development it has allowed predictions to be made that are in good agreement with available experimental results from stalled hot rolling tests. In combination with the preliminary hot tensile testing, which gives the necessary information about the temperature ranges for the two modes of oxide scale failure, the model can be used for an analysis of failure of the oxide scale at entry into the roll gap for a particular steel grade and for particular rolling conditions.

Unlike mild steel oxide scale, Mn-Mo, Si-Mn and stainless steel oxides have shown only the first through-thickness mode of failure for the whole range of the test parameters. Hence, it can be concluded that their failure at entry into the roll gap should be similar to the failure mode of mild steel oxide scale at a low temperature range and that relaxation of stresses within the one-layer scale take place preferably due to through-thickness cracking rather than sliding along the relatively stronger scale/metal interface when the initial stock temperature does not exceed 1200°C.

For multi-layer steel oxides, like those on Si-Mn steel, in addition to through-thickness cracking, delamination within the non-homogeneous oxide scale can occur already

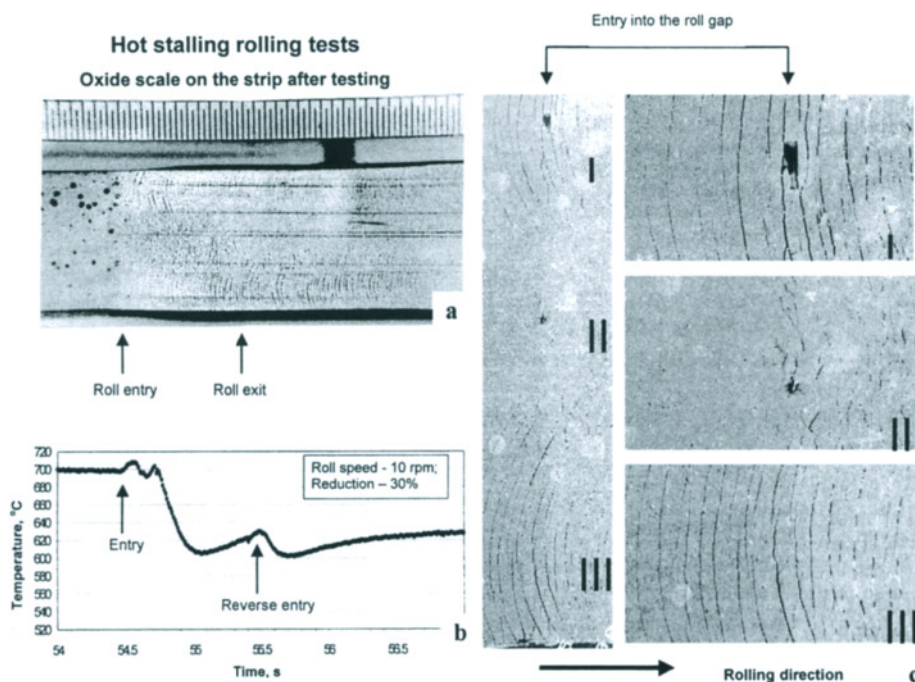


**Figure 13.18** Oxide scale on the strip after testing (a), thermal history of the strip (b) and secondary electron image showing the oxide scale on the strip at the zone of entering into the roll gap during a stalled hot rolling test (c). The full width zone is shown on the left side of the part c with details around I, II and III points on the right side. Furnace temperature for oxidation with gas protection 1130°C; oxidation time 15 min (scale thickness 250 - 300µm); initial rolling temperature 700°C.

at entry into the roll gap (Fig. 13.19). Such delamination can take place between the oxide sub-layers having significantly different grain sizes. Big voids, otherwise called blisters, usually situated between oxide sub-layers, could act as sources of multi-layered oxide delamination. The inner oxide layer, as can be seen from Fig. 13.20, being less chilled and as a consequence more ductile, retains adherence longer with the metal. Depending of the mechanical properties and rolling conditions, the inner scale sub-layer can remain continuous during rolling and even after the rolling pass. The observation has relevance for failure in the roll gap, which is discussed in the next section.

### 13.6 OXIDE SCALE FAILURE IN THE ROLL GAP

When the fractured oxide scale is undergoing extreme pressure during rolling, the hot and plastic metal can extrude up into the gap formed by a through-thickness crack.

Although, as can be seen in Fig. 13.21, such extrusion is not always followed by full contact between fresh hot metal of the stock and the relatively cold surface of the roll, it always disturbs heat transfer at the roll/stock interface. It results in temperature changes both at the stock and the roll surface layer. Taking into account that both adhesive properties of the oxide/metal interface and extent of the scale viscous sliding due to shear stress are very sensitive to temperature, it is clear that friction conditions around the area of oxide scale discontinuities will be different too. Should such direct contact between the hot steel stock and the roll occur, it will also have a large impact on the prevailing friction.

Fig. 13.22 shows an example of the output of the model on exit from a rolling pass, which was predicted to involve oxide scale fracture. Two features are readily apparent. First, the oxide scale is not always fully attached to the steel. Second, the surface of the steel,

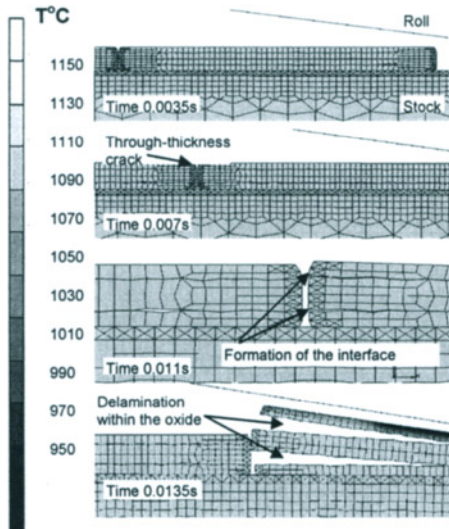


**Figure 13.19** Temperature distribution at the stock surface layer predicted for the different time moments of entering the roll gap. Note development of the through-thickness crack and delamination within the multi-layer Si-Mn steel oxide scale.

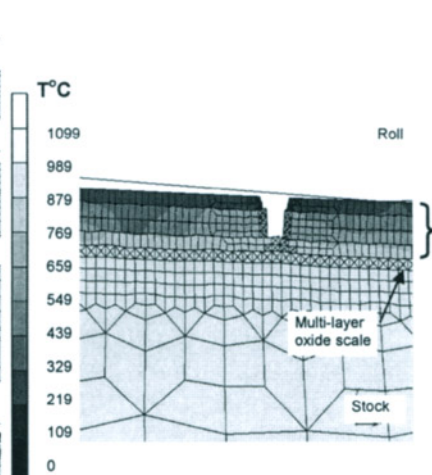


**Figure 13.20** Temperature distribution across failed multi-layer Si-Mn oxide scale at the roll gap. Note adherence of the inner scale layer with uninterrupted shape.



where it has begun to extrude up through the gaps in the oxide scale, is not smooth. This latter phenomenon will lead to a deterioration in the surface quality of the rolled product. The former observation has relevance for descaling, which is discussed in the next section.

Cracks through oxide scale can also occur under roll pressure within the roll gap (Fig. 13.23). The cracking starts at the uppermost oxide scale layer which is the closest to the cold surface of the roll and propagates inwards to the relatively hot surface of the stock. As can be seen in Fig. 13.23b, that uppermost oxide scale layer is cooled in the first instance that has encouraged its brittleness. The temperature distribution presented in Fig. 13.23b shows a significant temperature gradient at the oxide scale that changes the conditions for crack propagation through the scale. It can also be seen in Fig. 13.23b that the cracks did not occur not in a through-thickness manner as at entry into the roll gap, when the scale temperature is within the low temperature range and it is mostly uniform across the scale thickness. The crack propagation within the roll gap developed under the extensive roll pressure and it was stopped at the thin oxide scale layer situated near the stock surface. This scale layer corresponding to porous  $\text{FeO}+\text{Fe}_2\text{SiO}_4$  keeps its continuity and adheres to the stock metal surface while upper brittle layers, corresponding to  $\text{Fe}_2\text{O}_3$ ,  $\text{Fe}_3\text{O}_4$  and dense  $\text{FeO}$ , are cracked

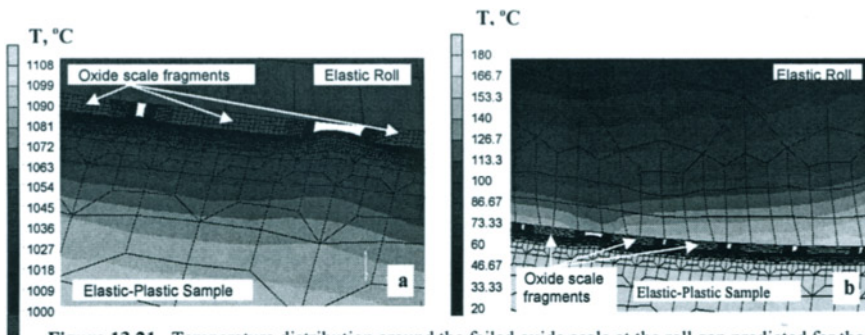


**Figure 13.21** Temperature distribution around the failed oxide scale at the roll gap predicted for the stock (a) and the roll (b) interface area.

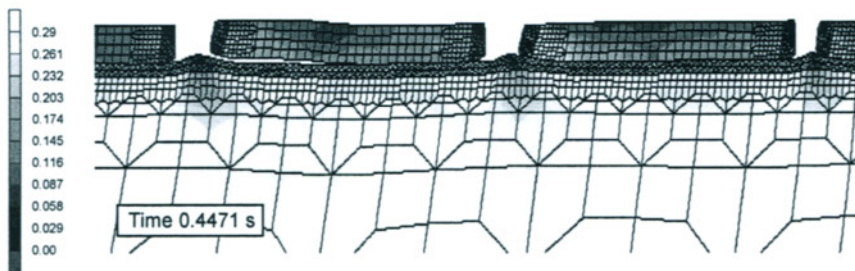


**Figure 13.22** Partly spalled scale after hot rolling pass. Model prediction of the equivalent total strain.

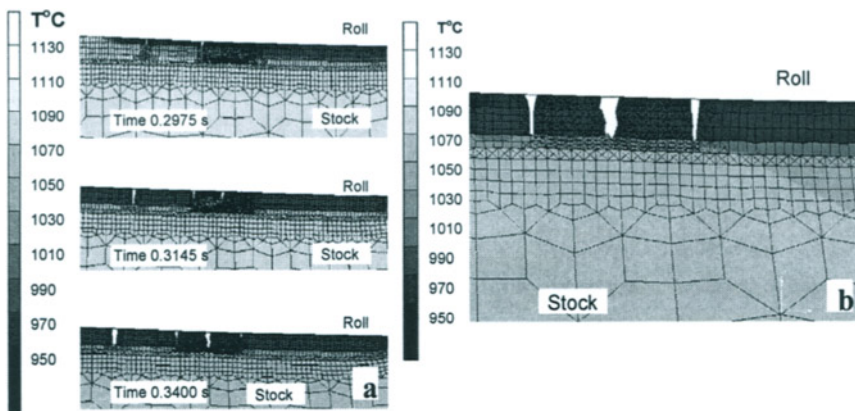


**Figure 13.23.** Temperature distribution at the roll stock interface. Prediction of oxide scale cracking within the roll gap under the roll pressure for the different time moments (a); the crack stopped at the oxide layer near the stock surface (b).

through their thickness. Other authors observed similar cessation of crack propagation within the scale near the stock surface during experimental investigation of hydraulic descaling at high temperatures (Nakamura and Sato, 1994). It has been shown that the oxide scale of Si-killed steels including large pores cracked easily but that these cracks usually stopped at large pores, which were at near half thickness of scale. At the descaling procedure, the cracks propagated in the scale parallel to the iron substrate and therefore the lower parts of the scale

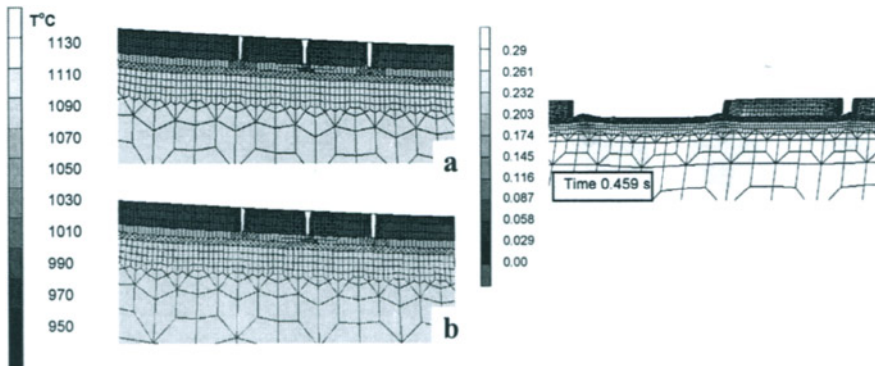


**Figure 13.24** Temperature distribution at the roll stock interface. Prediction of oxide scale cracking within the roll gap for the same time moment assuming (a) elastic and (b) elastic plastic oxide scale.

**Figure 13.25** Peeling off of the partly spalled scale as first to the sequence during subsequent descaling after hot rolling. Model prediction of the equivalent total strain after hot rolling at the beginning of descaling stage.

thickness remained on the steel surface. On Si-killed steels, the fayalite,  $\text{Fe}_2\text{SiO}_4$ , was formed in layers at the scale/metal interface. Below  $1170^\circ\text{C}$ , which is the eutectic point of  $\text{Fe}_2\text{SiO}_4$

and FeO, the fayalite became solid and the descalability became worse due to the increase in adhesion of scale to iron substrate.

Fig. 13.24 presents predictions of scale cracking within the roll gap for two cases. For the first case, a multi-layer elastic oxides scale was assumed for the modelling while the multi-layered elastic-plastic scale was assumed for the second case.

It can be seen clearly that crack propagation was stopped at the innermost scale layer for both cases during the rolling pass. That favours the conclusion that the crack stop within the oxide scale was due to its multi-layer nature rather than assumption of scale plasticity.

### 13.7 ANALYSIS OF DESCALING EVENTS

#### 13.7.1 Hydraulic descaling

The rolled state illustrated in Fig. 13.22 has been used as the starting point for a hydraulic descaling simulation. This has been achieved by applying a moving boundary condition that represents a water jet in terms of both pressure and cooling. Since all the properties of the model are thermally sensitive, considerable stresses arise around the oxide scale. Fig. 13.25 shows the first stage of descaling, where the oxide scale fragment that is least attached to the steel stock has been removed. The other oxide scale fragments were removed in a progressive sequence according to their degree of attachment. By analysing the reaction forces in the model during descaling, it is possible to evaluate the mechanical and thermal influences of the water jet which are necessary for descaling purposes.

#### 13.7.2 Mechanical descaling

Coiled steel rod produced by hot rolling for subsequent wire drawing inevitably possesses an oxidised surface. The oxide scale must be removed before the drawing operation. Formation of the scale depends to a great extent on the manufacturing parameters, such as the laying temperature and the cooling rate. Understanding the scale removal mechanism is important for optimisation of industrial descaling conditions. A cantilever-bend test procedure coupled with FE modelling was applied to investigate scale crack spacing, spalling, and delamination along interfaces during bending (Krzyzanowski et al., 2001). The cantilever-bend test procedure for assessing descalability was the following: the samples were fixed in a vice at one end; a load was applied to the other end in order to bend the specimen in such way as to increase the initial curvature. The oxide scale on the tensile and compressive sides of the rod surface exhibits progressive cracking and spallation along the length of the sample during bending. The scale began to crack at a relatively small bending strain. New through-thickness cracks were formed midway between the initial cracks and also developed in new parts of the rod surface as the strain increased. The process of cracking developed until the scale fragments spalled from both the tensile and compressive sides of the rod surface. This development of spallation was observed more clearly by constrained bending tests around cylinders of decreasing diameter. With large diameters the through-thickness cracks formed, but there was no spallation and brushing had no effect on the surface appearance. At a critical diameter there was evidence of spallation (i.e. cracking at the scale-metal interface) at regular intervals, and brushing made the spalled parts more evident by removing loose scale fragments and revealing bright bands of steel. When the cylinder diameter was further decreased, the width of the spalled bands increased but their spacing was unchanged until



full spallation had taken place. The cracks at the surface near the neutral plane of the specimen were formed at angles of  $\pm 45^\circ$  to the long axis.

Fig. 13.26 shows oxide scale that failed due to tension in a through-thickness crack mode. It was assumed in the model that the scale deforms elastically, not unreasonable for this room temperature operation. Generally, for the elastic scale model, the possible forms of stress relaxation could be fracture, viscous sliding along the interface, and spallation. At room temperature the contribution of viscous sliding is considered to be negligible (Ridel, 1982, Raj and Ashby, 1971). The through-thickness cracks developed from the pre-existing defects were located at the outer surface of the oxide layer (Fig. 13.6b). The critical failure strain can vary depending on parameters such as the size of the defect and the surface fracture energy. It has been shown that the length of the defect  $c$ , equation (5), can be calculated as an effective composite value made up of the sum of the sizes of discrete voids whose stress fields overlap (Hancock and Nicholls, 1988). The formation of tensile cracks through the thickness of the oxide scale produced considerable redistribution of the stress within the scale and also at the oxide/metal interface. The stress concentration at the zone of the crack near the scale/metal interface can lead to the onset of cracking along the interface. The in-plane stress cannot transfer across the crack and becomes zero at each of the crack faces. By symmetry the in-plane stress reaches a maximum value midway between the cracks. Due to the cracks, the in-plane strain within the scale fragment was significantly relaxed compared with the longitudinal strain of the attached metal layer. The formation of the crack through the thickness of the oxide scale created shear stresses at the scale/metal and scale/scale interfaces. These stresses had a maximum value at the edges of the cracks. Relaxation of the shear stresses at low temperatures, in the absence of relaxation by viscous sliding, could only occur by interface cracking and spallation of the elastically deformed scale fragment when the strain exceeded the critical level. Generally spallation occurred at the scale metal interface, but occasionally, as can be seen from Fig. 13.27a, a thin inner layer remains attached to the steel and spallation occurs by delamination within the scale. This was modelled by having a multi layer scale (Fig. 13.27b), which closely simulates the observed behaviour.

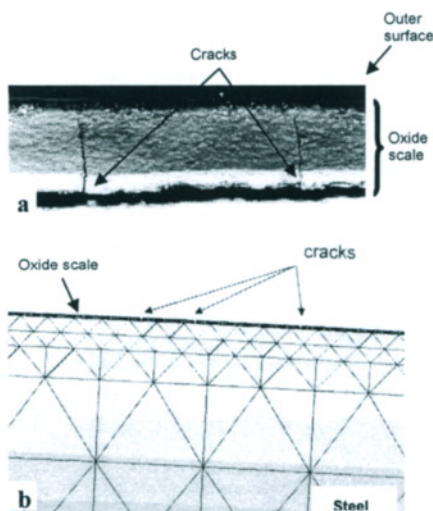


**Figure 13.26** Through-thickness cracks at the convex surface of the steel rod after bending.  
a) SEM image of transverse section; b) FE

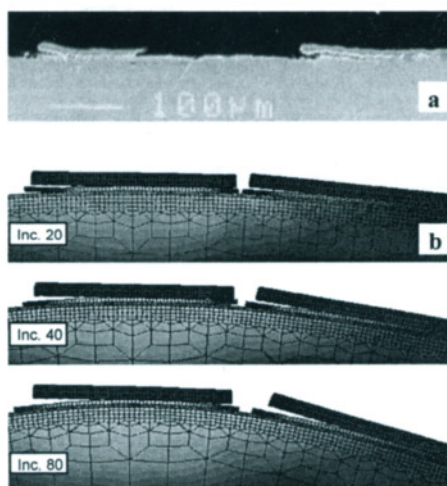


**Figure 13.27** Delamination within multi-layer oxide scale and spallation of the upper layers at the convex surface of the steel rod.  
a) SEM image from a steel rod after bending; b) FE model prediction for different time increments during progressive bending.

There is a possibility of changing the extent of longitudinal tension in the steel rod in commercial mechanical descaling practice. Such change will inevitably influence the spacing between the neighbouring through-thickness cracks formed at the earlier stages of bending. Another process parameter, which varies in practice, is the scale thickness. It was therefore important to investigate the influence of both these variables on descalability of oxide fragments. To do this, a single scale fragment of different length and thickness has been analysed. Fig. 13.28a shows the behaviour on the tensile surface after bending of two oxide scale fragments having the same  $50\mu\text{m}$  thickness. The longer  $5\text{mm}$  length scale fragment adheres to the metal surface after significant bending while the  $0.8\text{mm}$  length fragment shows the ability to descale. At the same time, a thinner scale fragment, having the same  $0.8\text{mm}$  length but  $25\mu\text{m}$  thickness, did not lose adherence to the metal surface at a much higher degree of deformation (Fig. 13.28b).

These results favour the conclusion that, in order to improve the descalability during mechanical descaling on the convex part of a steel rod, both decreasing the length and increasing the thickness of the scale fragments is beneficial. This thickness effect agrees with experimental observations, except that crack spacing also tends to increase, making separation of the variables in practice rather difficult. Taking into account that the properties of both the oxide scale and the scale/metal interface are dependent on the chemical composition of the steel and the scale growth conditions, implementation of the finite element model with the data obtained for the particular steel grade and scale growth conditions becomes critical.

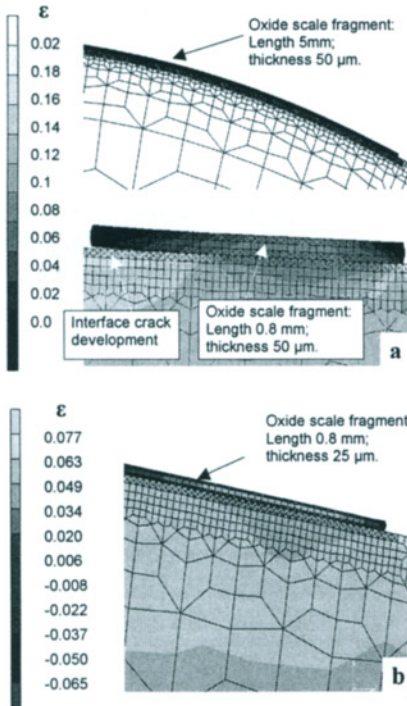


**Figure 13.28** Distribution of the longitudinal component of the total strain predicted for one layer scale fragment on the convex side of the steel rod during bending.

a) model prediction for the different scale length; note better descalability of the shorter scale fragment;  
b) model prediction for the different scale thickness; note adherence of the thinner scale fragment to the metal surface.

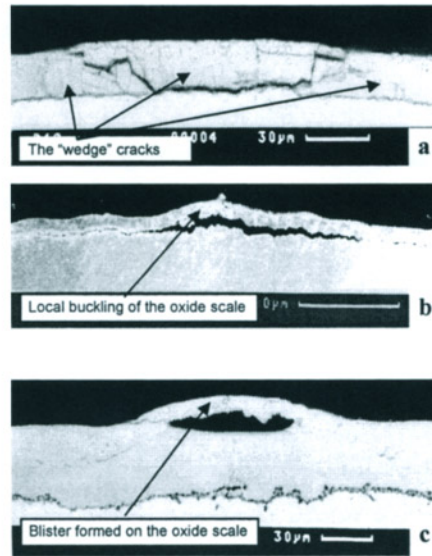


**Figure 13.29** SEM images illustrating sources of the initiation of decohesion on the compression side of a steel rod during bending.

a) cracked oxide scale;  
b) local buckling;  
c) blister formed during oxidation.

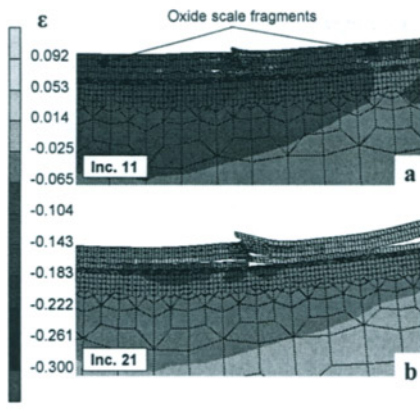


**Figure 13.30** Distribution of the longitudinal component of the total strain predicted on the concave side of the steel rod for the multi-layer oxide scale for the different time increments during bending. Note spallation of the scale due to the “wedge” mechanism.

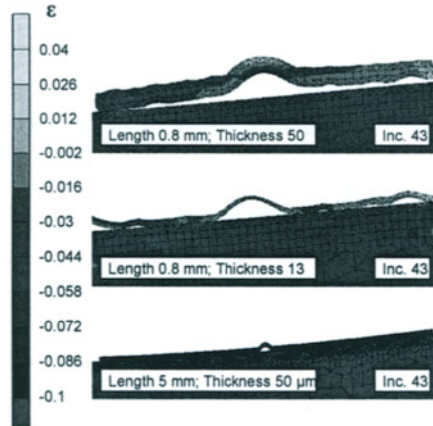


**Figure 13.31** Prediction of spallation of one layer scale fragment on the concave side of the steel rod during bending for the different scale length and thickness. Note better descalability of the shorter and thicker scale fragment developing from a blister (Fig. 13.29c).

The mechanism of oxide scale spallation for the opposite, concave side of the steel rod, where longitudinal compression stresses are developed, was different. For an ideally smooth scale adhered to a smooth metal surface, the interfacial stresses, which can influence spallation, would be close to zero, provided that there are no discontinuities in the scale. Real scales, having more or less wavy interfaces with defects, contain sites where, owing to inhomogeneous deformation, formation of new defects or growth of the existing defects are facilitated when the scale is under compression acting parallel to the interface. It has been shown (Schütze, 1988) that the initiation of local decohesion and through-thickness cracks may occur due to grain boundary sliding of the underlying metal, which could occur here as a result of deformation during hot coiling. As can be seen from Fig. 13.29a, the through-thickness cracks can form a wedge between the oxide scale fragments and the metal surface. Other sources of the initiation of decohesion under compression were local convex parts of the oxide scale (Fig. 13.29b, c). At these sites, the oxide scale was lifted from the metal, and scale separation was initiated. Once either a through-thickness crack or local buckling of a critical size has formed, spalling will occur under compressive longitudinal stresses during bending. As can be seen from Fig. 13.30, spallation in a “wedge” mode at the concave side of the rod can occur during bending. To mimic the continuous oxide scale layer for the modelling, the left and right edges of the scale fragments were fixed to the metal surface in terms of zero freedom in the longitudinal direction. When the blister in the scale was below a critical size, the compressive stresses in the scale did not lead to tensile stresses perpendicular to the interface, and spalling did not occur. An initial separation leading to formation of oxide ridges of critical size was necessary for spalling under compressive longitudinal stresses developed at the concave side of the steel rod. Fig. 13.31 illustrates the influence both of the scale thickness and the length of the scale fragment (i.e. the crack spacing) on descalability of single oxide fragments. Similar to the convex side, the

conclusion can be made for the concave side of the steel rod that both decreasing the length and increasing the thickness of the scale fragment lead to improvement of the descalability.

#### ACKNOWLEDGEMENTS

This work was supported by the Engineering and Physical Sciences Research Council (EPSRC) Research Grant (Grant Ref. GR/L50198). The authors express their gratitude to Prof. C.M. Sellars, Dr. Y. H. Li and Dr. W. Yang for valuable discussions and suggestions. Thanks are also due to members of the IMPETUS project steering group for providing thoughtful comments.

#### REFERENCES

- Asai, T., Soshiroda, T. and Miyahara, M. (1997) *ISIJ International* **37**, 272-277.
- Bakker, A. (1983) *Int. J. Pres. Ves. & Piping*, **C14**, 153-179.
- Beynon, J.H. and Krzyzanowski, M. (1999) in *Proceedings of Int. Conf. Modelling of Metal Rolling Processes 3, London, 13-15 December 1999* eds. Beynon, J.H., Ingham, P., Teichert, H. and Waterson, K. (The Institute of Materials, IOM Communications, London, UK) 360-369.
- Birchall, J.D., Howard, A.J., and Kendall, K. (1981) *Nature*, **289**, 388-390.
- Blazevic, D.T. (2000) in *Proceedings of 3<sup>rd</sup> Int. Conf. Hydraulic Descaling, 14-15 September 2000* (IOM Communications Ltd., London) 3-13.
- Chang, Y.N. and Wei, F.I. (1989) *Journal of Material Science*, **21**, 14-22.
- Fukagawa, F., Okada, H., Machara, Y. and Fujikawa, H. (1996) *Tetsu-to-Hagané*, **82**, 63-70.
- Hancock, P. and Nicholls, J.R. (1988) *Materials Science and Technology*, **4**, 398-406.
- Ishi, Y., Kodoi, A., Wakamatsu, I. (1992) *Mech. Work Steel Process*, **30**, p. 447.
- Kendall, K. (1978) *Nature*, **272**, p. 710.
- Kofstad, P. (1985) *Oxid. Met.*, **18**, No. 5/6, 245-284.
- Kolchenko, G.I., and Kuznetsova, N.P. (1984) *Izv VUZ Chernaja Metall.*, **11**, 113-125.
- Krzyzanowski, M., and Beynon, J.H. (1999a) *Steel Research*, **70**, issue 1/99, 22-27.
- Krzyzanowski, M. and Beynon J.H. (1999b) *Mater. Sci. Technol.*, **15**, 191-198.
- Krzyzanowski, M., and Beynon, J.H. (2000) *Modelling and Simulation in Materials Science and Engineering*, **8**, 927-945.
- Krzyzanowski, M., Beynon, J.H., Sellars, C.M. (2000) *Metallurgical and Materials Transactions*, **31B**, 1483-1490.
- Krzyzanowski, M., Yang, W., Sellars, C.M., and Beynon, J.H. (2001) *Mater. Sci. Technol.*, submitted.
- Lees, D.G. (1987) *Oxid. Met.*, **27**, 75-81.
- Li, Y.H., and Sellars, C.M. (1996) in *Proceedings of 2<sup>nd</sup> Int. Conf. On Modelling of Metal Rolling Processes*, eds. Beynon, J.H., Ingham, P., Teichert, H. and Waterson, K. (The Institute of Materials, London, UK), 192-206.
- Miner, R.G. and Nagarajan, V. (1981) *Oxid. Met.*, **16**, No. 3/4, 295-311.

- Morrel, R. (1987) *Handbook of properties of technical and engineering ceramics* (London, HMSO).
- Nakamura, T. and Sato, M. (1994) *J. Iron & Steel Inst. of Japan*, **80**, No. 3, 237-242.
- Okita, Y., Nagai, I., Sinagawa, I., and Horinouchi, K. (1989) *CAMP-ISIJ*, **2**, p. 1509.
- Ormerod IV, R.C., Becker, H.A., Grandmaison, E.W., Pollard, A., Rubini, P. and Sobiesiak, A. (1990) in *Proceedings of Int. Symp on Steel Reheat Furnace Technology, Hamilton, ON Canada*, ed. Mucciardi, F. (CIM, Canada) 227-242.
- Pieraggi, B., Rapp, R. (1994) *Materials at High Temp.*, **12**, 229-335.
- Pietrzyk, M., Lenard, J.G. (1991) *Thermal-Mechanical Modelling of the Flat Rolling Process* (Heidelberg: Springer-Verlag, Berlin, Germany).
- Raj, R., and Ashby, M.F. (1971) *Metall. Trans.*, **2A**, p. 1113.
- Ranta, H., Larkiola, J., Korhonen, A.S., and Nikula, A. (1993) in *Proceedings of 1<sup>st</sup> Int. Conf. on 'Modelling of metal rolling processes', September 1993* (The Institute of Materials, London, UK) 638-649.
- Rice, R. W. (1984) *J. Mater. Sci.*, **19**, 895-914.
- Ridel, H. (1982) *Metal Science*, **16**, 569-574.
- Robertson, J. and Manning, M.I. (1990) *Mater. Sci. Technol.*, **6**, 81-91.
- Schütze, M. (1988) *Mater. Sci. Technol.*, **4**, 407-414.
- Schütze, M. (1995) *Oxidation of Metals*, **44**, No. 1/2, 29-61.
- Sheasby, J.S, Boggs, W.E. and Turkdogan, E.T. (1984) *Metal Science*, **18**, 127-136.
- Strawbridge, A., Hou, P. (1994) *Materials at High Temp.*, **12**, 177-181.
- Swinkels, F.B. and Ashby, M.F. (1981) *Acta Metallurgica*, **29**, 259-281.
- Tan, K.S., Krzyzanowski, M. and Beynon, J.H. (2001) *Steel Research*, **72**, No. 7, 250-258.
- Taniguchi S, Furukawa, T. and Shibata, T. (1997) *ISIJ International*, **37**, 263-271.
- Whittle, D.P., Stringer, J. (1980) *Phil. Trans. R. Soc. Lond.*, **A295**, 309-315.

This Page Intentionally Left Blank

## Chapter 14

# Friction, Lubrication and Surface Response in Wire Drawing

ROGER N. WRIGHT  
*Materials Science & Engineering Department*  
*Rensselaer Polytechnic Institute*  
*Troy, NY 12180*  
*USA*

The surface plays a prominent role in wire processing and product application, insofar as the surface-to-volume ratio is greater than in the case of other metal worked shapes, and insofar as the as-drawn surface quality is often the final surface condition, pertinent to appearance, cleanliness, suitability for coating, fracture toughness, and so on. Surface mechanics and the resultant surface quality may be routinely, if indirectly, monitored by drawing force measurement and microscopy. More fundamental characterizations include coefficient of friction measurement or estimate. It is understood that drawing velocity, temperature, and die design can strongly affect wire drawing surface mechanics, for a given practical choice of lubricant. Substantial reviews and analyses of this behavior have been published by Schey (1983), and by Newnham (1970).

This chapter will briefly review the basic concepts regarding friction, lubrication and surface response in wire drawing, with illustrative data. It will then consider in some detail the work of the author, and his collaborators, regarding effects of drawing temperature, drawing velocity, and process design, as well as the response of shaped wire, and fine generation.

### 1.1 BASIC CONCEPTS

#### 1.1.1 Frictional stress characterization

While there are many methods of characterizing frictional stress is the basic tribological literature, it has been common practice to characterize the surface frictional stress is wire drawing ,  $\tau$ , with a coefficient of friction,  $\mu$ . That is,

$$\tau = \mu P, \quad (14.1)$$



where  $P$  is the die pressure. The die pressure will rarely be monitorable, in a one-piece die, and will generally be inferred from basic experimental and theoretical analyses, such as summarized in Figure 14.1 (Wright, 1976 and Wistreich, 1955). The index,  $\Delta$ , used in Figure 14.1, is a useful means for expressing the contribution of the reduction of the pass,  $r$ , and the die semi-angle,  $\alpha$ , to the deformation zone geometry, and other quantities, such as die pressure, that are dependant thereon. The value of  $\Delta$  for round wire, rod and bar drawing is expressed as:

$$\Delta = (\alpha/r) [1 + (1-r)^0]^2, \quad (14.2)$$

where  $\alpha$  is in radians and  $r$  is  $(1 - A_1/A_0)$ , where  $A_1$  and  $A_0$  are the final and initial cross sectional areas, respectively.

The range and phenomenology of the coefficient of friction in metalworking is often discussed in terms of the Stribeck curves, set forth in Figure 14.2 [Riesz, 1970]. (While developed to rationalize the performance of journal bearings, the Stribeck curves are widely useful as a vehicle for discussing and categorizing lubrication.) These curves do encompass the coefficient of friction range generally observable with the use of liquid lubricants in wire drawing. At slow drawing speeds, low apparent viscosities, and relatively high pressures, one encounters a very thin lubricant film, and coefficients of friction in the range from 0.1 to 0.2. Indeed, the lubricant film may not be completely established, and conditions of sticking friction may arise, leading to coefficients of friction greater than 0.2, though rarely approaching the theoretical limit of 0.5 or so. High-speed drawing can produce thick lubricant films and coefficients of friction in the 0.01 to 0.05 range. As an illustration, Lancaster and Smith (1974) have measured coefficients of friction, as set forth in Table 14.1, for the drawing of high carbon steel wire with "conventional soap" lubrication.

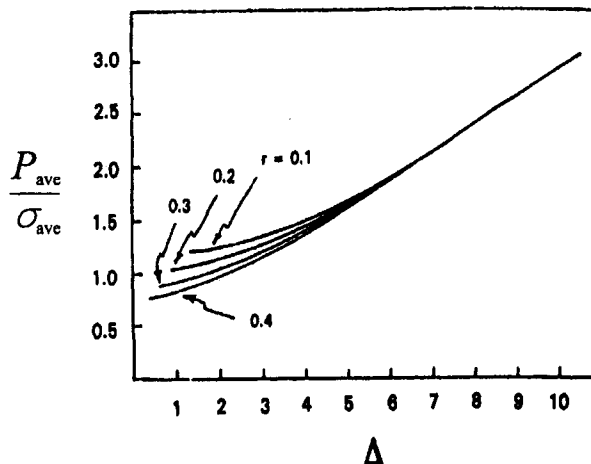


**Figure 14.1** The ratio of average die pressure,  $P_{ave}$ , to average wire flow stress,  $\sigma_{ave}$ , as a function of  $\Delta$  and  $r$ .

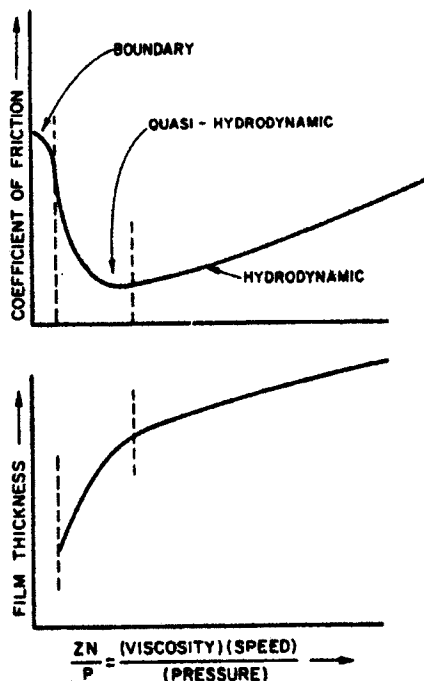


Figure 14.2 The widely cited Stribeck curves.

**Table 14.1** The relationship of friction coefficient to drawing speed for the case of high carbon steel and conventional soap lubrication (Lancaster and Smith, 1974)

Drawing Speed	Coefficient of Friction
0.001 – 0.01 m/s	0.13 – 0.16
1	0.02 – 0.04
20	0.01

It may be argued that thick films established with solid soaps and other thick coatings would be better characterized by a friction factor,  $m$ , where

$$\tau = m \tau_{ave}, \quad (14.3)$$

and where  $\tau_{ave}$  is the average shear strength of the wire during drawing. The same could be said for the case of sticking friction. In both cases it would seem that friction is not

controlled by the elastic-plastic friction conditions of the coefficient of friction model, but rather by an intrinsic shear strength of the lubricant, or by the shear strength of the wire. However, the wire drawing research literature generally expresses frictional stresses by means of a coefficient of friction, in effect treating thick solid films as a condition analogous to the thick film portion of the Stribeck curves, and treating sticking friction as a condition described by the extreme left of the Stribeck curves.

The direct physical measurement of the friction force in drawing generally requires the use of split dies, as described in classical papers of MacLellan (1952-53) and Wistreich (1955). By measuring both a pulling force and a split die separating force, one can obtain explicit values for the frictional shear force and die force, allowing a rigorous statement of the average coefficient of friction. Such a procedure is tedious, and the split in the die may lead to a lubrication mode different than that achieved with a one-piece die.

Indirect measurements of the coefficient of friction are widely undertaken, employing a reliable mathematical model of the drawing stress, and projection of the wire flow stress at temperatures and strain rates representative of the drawing process being characterized. Representative efforts may be seen in the work of Baker and Wright (1992) and Noseda and Wright (2002).

#### ***14.1.2 Determining friction mode by wire surface analysis***

The author has published several papers concerning the inference of lubrication mode from scanning electron micrographs of the wire surface (Wright and Male, 1975 and Wright, 1978, 1980, 1981, 2000). The condition of sticking friction, involving coefficients of friction beyond 0.2 and corresponding to the left extreme of the Stribeck curves, results in wire surface material being left on the die surface. Hence the wire surface contains deep longitudinal striations, as evidence of a "shear fracture" vis-à-vis the metal stuck to the die. A representative example is shown in Figure 14.3. As the boundary mode of lubrication (seen on the Stribeck curves) becomes partly established, "stick-slip" lubrication occurs, juxtaposing areas of boundary lubrication with areas of sticking, on the die surface. Such juxtaposition leads to intense local shearing, and surface fractures often referred to as "crow's feet". The coefficient of friction may be below 0.2 and the macroscopic appearance of the wire surface may be quite bright, yet the microscopic appearance of the surface will manifest intense shear fractures, as illustrated in Figure 14.4.

Fully successful boundary lubrication generally produces an extremely smooth and bright wire surface, comparable to a metallographic finish, and essentially featureless at magnifications of a few hundred times. Not only is sticking avoided by a thin (monomolecular?) layer of lubricant, but also the smooth die surface "irons" the wire surface. Coefficients of friction of about 0.1 are common.

As quasi-hydrodynamic, thicker films begin to develop, such behavior can occur locally, on the wire surface, resulting in the "pock marks" shown in Figure 14.5. Gross thick film lubrication may allow the wire surface great freedom to flow, so that grain-to-grain variations in microplasticity may be observed in the surface topography, as shown in Figure 14.6. The coefficient of friction may approach 0.01 in such cases, and the macroscopic appearance is sometimes called a "matte finish."

In short, as drawn wire surface analysis can be used to identify or corroborate the lubricant mode.

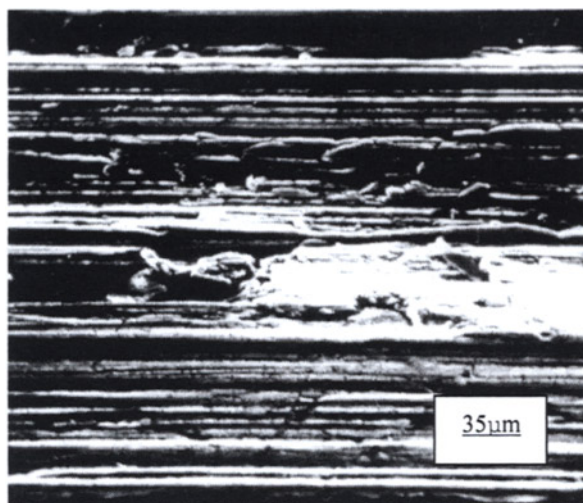


**Figure 14.3** A scanning electron micrograph of the surface of an EC aluminum rod drawn with sticking friction.

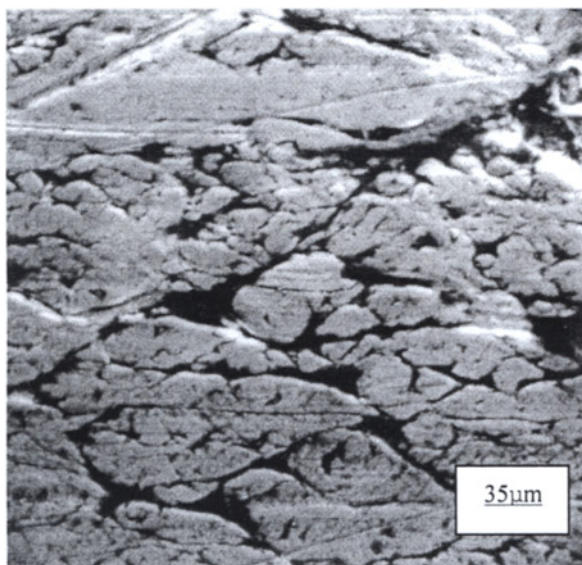


**Figure 14.4** A scanning electron micrograph of the surface of an EC aluminum wire showing extensive “crow’s feet” from stick-slip lubrication modes.

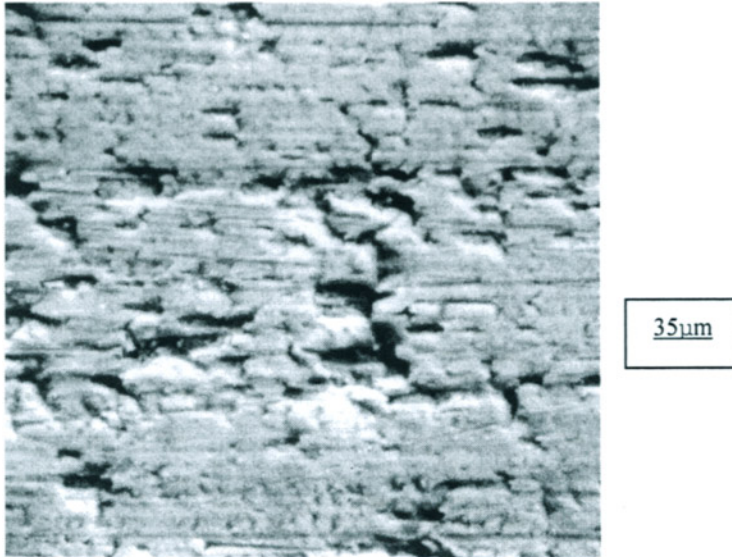


**Figure 14.5** Scanning electron micrograph of EC aluminum wire surface showing evidence of thick film “pockets”.

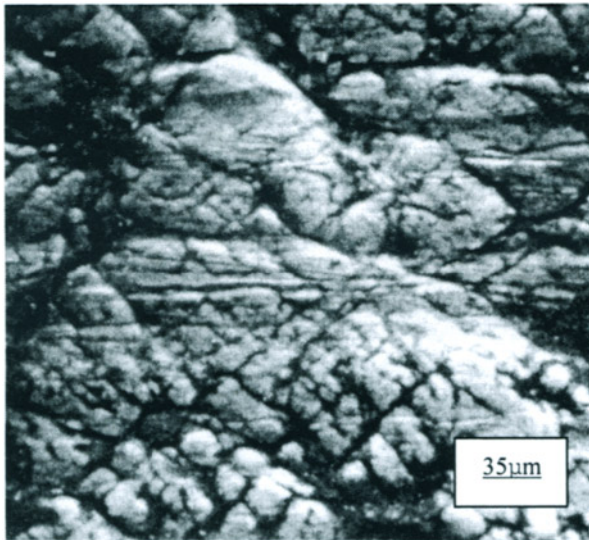


**Figure 14.6** Scanning electron micrograph of EC aluminum wire surface showing grain-to-grain variations in microplasticity, as allowed by thick film lubrication.

## 14.2 THE EFFECT OF TEMPERATURE

The film thicknesses noted in the Stribeck curve can be approximated at die entry by way of the analysis of Bloor, et al. (1970), and a review of these considerations has been published by Wright (1997). The lubricant film thickness at die entry,  $h$ , is given as follows:

$$h = 3 \eta B_p V (\cot \alpha), \quad (14.4)$$

where  $\eta$  is lubricant viscosity at the die inlet (at ambient pressure),  $B_p$  is the viscosity pressure coefficient, and  $V$  is the drawing velocity. Thus, the film thickness is proportional to lubricant viscosity, and the viscosity is a strong function of both temperature and pressure, as illustrated in Figure 14.7. The temperature lowers viscosity, although the high pressure ambient in the drawing channel obviously increases viscosity. It has been observed that a 4 MPa pressure increase offsets a 1 °C increase in temperature (Schey, 1983). The die pressure in drawing, as seen in Figure 14.1, ranges, approximately, from the value of the wire flow stress to perhaps three times this value, for high values of  $\Delta$ . Moreover, the flow stress will vary somewhat with strain rate (drawing speed) and temperature. It may be argued that the physical and chemical nature of practical lubricants is poorly understood under the conditions of high pressure and high temperature common to the wire/die interface, and that solid soaps and composite and coating-based lubricants may not be properly characterized by viscosity, per se. Nonetheless the phenomenology of fluid lubricants appears to mirrored, to a significant degree, in "solid" lubricants.

A number of studies have measured, or calculated, the coefficient of friction as a function of temperature. Such efforts are best left to the cases of slow drawing speeds, since the estimation of surface temperature at high drawing speed involves a number of assumptions. Results from the recent work of Nosedá and Wright (2002) on isothermal copper drawing are set forth in Table 14.2. An oil-based, temperature resistant lubricant was used with quite stable behavior in the 200-250 °C range, with a coefficient of friction clearly below that of ambient temperature drawing. However, a reproducible, catastrophic breakdown in lubrication was observed in the 100 °C range, involving gross adherence of copper to the carbide die. Such behavior is suggestive of chemical effects of temperature, which may dominate the effects of temperature on viscosity.

Figure 14.8 shows the effects of temperature on the coefficient of friction in the drawing of steel (sheet) with soap based lubrication. The coefficient initially decreases and then increases. In interpreting such data, it might be argued that a decrease in coefficient of friction is associated with the establishment of thick film conditions as the lubricant softens with increased temperature. Further increases in temperature may reduce film thickness, in analogy to the role of viscosity in the Bloor analysis. The decrease in film thickness would, of course, lead to an increase in the coefficient of friction. Alternatively, elevated temperature may simply lead to chemical transformations or reactions that destroy the lubricant.

In any event, there is often an optimum temperature range for wire drawing lubricant performance. Commercial drawing speeds are often so high, however, that the concentration of frictional heating at the wire/die interface dominates behavior. This concentration of frictional heating is velocity sensitive, adding a velocity consideration, over and above the effects of velocity in the Stribeck curves, and in the Bloor analysis.



**Table 14.2** Coefficient of friction-temperature variations for copper drawing with an oil-based, temperature-resistant lubricant

Coefficient of Friction	Temperature
0.08	22 °C
0.19	100
0.07	150
0.03	200
0.03	250

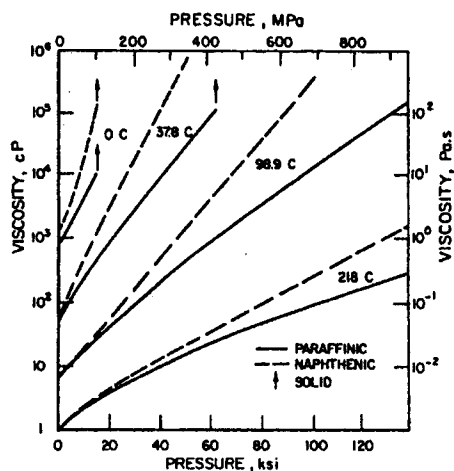


**Figure 14.7** Viscosity-pressure variations for mineral oils, from Schey (1983) and Booser (1981).

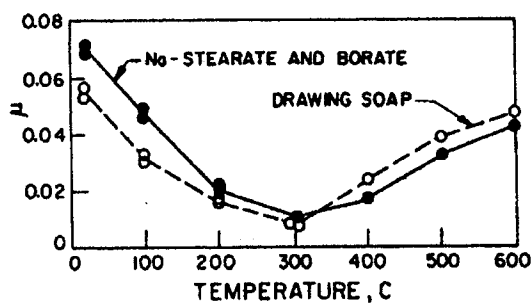


**Figure 14.8** Coefficient of friction-temperature variations for the drawing of steel, from Pawelski (1968).

#### 14.3 VELOCITY – TEMPERATURE INTERACTIONS

An example of the relationship of drawing velocity to the coefficient of friction in high carbon steel has been given in Table 14.1. Table 14.3 lists some data on copper wire drawn with a fat-based, water-soluble lubricant designed for commercial magnet wire production. The data of both Tables are consistent with the generally anticipated decrease in coefficient of friction with increased velocity, as one goes from boundary to quasi-hydrodynamic conditions.

It must be understood, however, that the lubricant temperature can increase grossly as drawing speed increases. This increase is due to the fact that the heat created by frictional work has reduced time to penetrate into the wire interior. Moreover, the dies, under steady-state drawing conditions, are too hot to act as an important heat sink. The classical analysis of this effect is that Siebel and Kobitzsch (1943), and refinements have been introduced by Korst (1948), Wright (1973), Snidle (1977) and Lucca and Wright (1996). At high velocities, in high strength wire, temperature increases of over 1000 °C can be projected, and austenitization is even hypothesized for the case of carbon steel.

With increased velocity and fluid lubrication, an increase in film thickness is normally expected, together with a decrease in coefficient of friction. Since a decreased coefficient of friction will reduce frictional heating, the increase in surface temperature anticipated with drawing speed increase, alone, is surely mitigated. However, it seems likely that very high velocities do result in increased surface heating. This will have the effect of driving the viscosity down, decreasing film thickness, and increasing the coefficient of friction. This will lead to increased frictional heating, and presumably catastrophic lubricant failure, unless such behavior is pre-empted by the actions of additives to the lubricant.

The work of Lucca and Wright (1996) presents further considerations in this scenario, however. These authors modeled hydrodynamic conditions with a two-dimensional representation of the zone involving the wire, the die, and the lubricant. The analysis included deformation heating in the wire, frictional deformation heating of the lubricant, and expressed lubricant viscosity as a function of temperature and pressure. Temperature distributions within the zone of analysis were calculated using finite difference technique.

Representative data, for the case of aluminum drawing, are shown in Figure 14.3. Lubricant temperatures increased as drawing velocities increased, whereas, the wire temperature was shown to decrease. This behavior is explained by the fact that, at higher speeds, there is less time for the viscous heating in the lubricant to be transferred to the wire. Thus, in comparison to classical concepts, the lubricant is shown to increase in temperature more than hitherto expected, while the increase in wire temperature is less than would have been expected. The development of hydrodynamic lubricant response at high drawing speeds would appear to protect temperature-sensitive wire surface structure.

#### 14.4 PROCESS DESIGN EFFECTS

##### 14.4.1 Lubricant selection

Baker and Wright (1992) compared the coefficient of friction, as related to drawing velocity, for several representative fat-based, water soluble lubricants. Data are shown in Table 14.5. While it should come as no surprise that commercial drawing lubricants



produce varying degrees of lubrication, especially in the low velocity range of the data shown in Table 14.5, the coefficient of friction values for lubricant I are alarming, when considering the slow velocity conditions of wire machine string up, or simple startup procedures.

Moreover, the low friction lubricants II and III show an encouraging decrease in friction coefficient with increasing velocity, even in the modest velocity range shown.

**Table 14.3** The relationship of friction coefficient to drawing velocity for the cold drawing of copper wire from 1.151 mm to 1.024 mm (17 to 18 AWG) with a fat-based, water soluble lubricant, from Baker and Wright (1993)

Drawing Velocity	Average Friction Coefficient
1.27 m/s	0.066
2.54	0.062
3.81	0.061
5.08	0.059
6.36	0.054
7.62	0.050
8.92	0.053
10.2	0.053
11.5	0.053
12.7	0.046

**Table 14.4.** Temperature – velocity relations in the wire/lubricant/die zone for aluminum drawing, from Lucca and Wright (1996)

Drawing Velocity	Lubricant Temperature	Wire Temperature
20 m/s	93 °C	72 °C
51	131	62

**Table 14.5** The relationship of friction coefficient to drawing velocity for the drawing of copper wire with three different fat-based, water soluble lubricants, from Baker and Wright (1992)

Lubricant	Drawing Velocity	Coefficient of Friction
I	0.04 m/s	0.17
	0.13	0.16
	0.17	0.15
	0.28	0.17
II	0.04	0.10
	0.17	0.09
	0.28	0.08
III	0.04	0.08
	0.13	0.07
	0.28	0.06

### 14.3.2 Die material and die angle

Baker and Wright (1992) have examined the effect of die material and die angle on the drawing of copper wire with a fat-based, water soluble lubricant (lubricant II in Table 14.5) from 1.151 mm to 1.024 mm (17 to 18 AWG) at a velocity of 0.28 m/s. The data are shown in Table 14.6. The effect of die angle in the case of a tungsten carbide die material is consistent with equation 14.3, and decreased die angles, and longer die entry geometry generally, have long been observed to decrease friction (except in cases of marginal lubrication). Moreover, higher die angles are sometimes employed to brighten the surface of the wire, by promoting a boundary lubrication condition, instead of a thicker film lubrication mode.

The variation in friction with diamond die material is interesting, and industrial practice reflects varying views on this subject. The higher level of friction for the fine grained polycrystalline diamond die material might be associated with the many cusps that will exist at the grain boundaries on the polished die surface. The single crystalline diamond die has somewhat elevated friction, and single crystalline diamond dies can be, and are, polished to an exceptionally smooth surface finish, with such surfaces sometimes complicating lubricant pick-up.

### 14.3.3 Sequential drawing effects

Baker and Wright (1993) evaluated the evolution of coefficient of friction, at three different drawing velocities, through successive dies in the diameter range from 1.151 mm to 0.643 mm (17 to 22 AWG). A fat-based, water soluble lubricant was used, with carbide dies. The resultant data are set forth in Table 14.7. The effect of increased velocity in decreasing friction becomes more pronounced as the drawing proceeds. This may reflect a “conditioning” of the surface with residual lubrication.

## 14.4 THE DRAWING OF SHAPES

Wright, et al. (1987) evaluated the variations in coefficient of friction experienced in conditions pertinent to the drawing of hexagonal bars from round stock. Such drawing appears to involve circumferentially varying lubrication modes. The flats of the hexagonal

cross section may involve a bright surface, whereas there may be evidence of thick film lubrication and/or little die contact at the die corners. Evaluations were made of the drawing of free-machining brass with round-to-round dies, round-to-hexagonal dies, and with split dies using the techniques of MacLellan (1952-53) and Wistreich (1955). The dies were made of carbide, and drawing was undertaken at slow speed, using a highly viscous, commercial oil-based lubricant.

**Table 14.6** The relationship of friction coefficient to die material and die angle for the drawing of copper with a fat-based water soluble lubricant at a velocity of 0.28 m/s, from Baker and Wright (1992)

Die Material	Included Die Angle	Coefficient of Friction
Carbide	9 °	0.08
Carbide	17	0.12
Fine-grained Diamond	18	0.09
Medium-grained Diamond	20	0.045
Coarse-grained Diamond	17	0.055
Single-crystalline Diamond	19	0.06

**Table 14.7** The relationship of friction coefficient to drawing speed for a sequence of copper drawing passes, using a fat-based, water soluble lubricant, from Baker and Wright (1993)

Starting Gage	Finishing Gage	Drawing Velocity	Coefficient of Friction
1.151 mm (AWG 17)	1.024 mm (AWG 18)	0.6 m/s	0.10
		1.9	0.10
		6.1	0.12
1.024 (18)	0.912 (19)	0.8	0.06
		2.6	0.05
		8.1	0.04
0.912 (19)	0.813 (20)	1.0	0.05
		3.2	0.04
		10.2	0.04
0.813 (20)	0.724 (21)	1.3	0.05
		4.0	0.04
		12.7	0.03
0.724 (21)	0.643 (22)	1.6	0.02
		5.1	0.01
		16.3	0/01

The split die evaluation involved direct measurement of the coefficient of friction. The coefficients of friction for the round-to-round and round-to-hexagonal drawing were obtained from back calculations with draw stress models, and from microhardness-based

determinations of redundant strain and redundant work. The results of this work are summarized in Table 14.8. The coefficient of friction manifested in round-to-round drawing is consistent with a thick film mode of lubrication. By contrast, the very high coefficient of friction for the split dies reflects the loss of lubricant from the sides of the split die halves. The intermediate coefficient of friction for the round-to-hexagonal drawing appears to be the average of a bright drawing mode in the centers of the flats and a very thick film, or non-contact mode at the corners. Indeed, lathe tool marks from turned starting stock could be seen at the corners of the drawn hexagonal bars.

**Table 14.8** Coefficients of friction for drawing passes pertinent to shaped drawing, from Wright, et al. (1987)

Drawing Pass	Coefficient of Friction
Round-to-Round	0.03
Round-to-Hexagonal	0.09
Split Dies	0.25

#### 14.5 THE GENERATION OF FINES

In many drawing technologies, small particles, termed “fines”, are liberated from the wire surface, contaminating the lubricant, impeding lubricant entry into the die, and creating wire surface flaws at the sites of their liberations, and at such sites as the fines may be subsequently pressed into the wire surface. Baker (1994), Baker and Wright (1995), and Baker and Pops (1996) have studied this behavior in the drawing of copper wire. A scanning electron micrograph of a fine emerging from a copper wire surface is shown in Figure 14.9. The bulk of the fines generated in copper drawing have been shown to arise from surface damaged sustained by redraw rod. Beyond this, significant numbers of fines are generated from the “plowing” action of die asperities, in analogy to abrasive wear mechanisms.

It is clear from the data in Figure 14.10 that fine generation in copper is exacerbated by the use of low angle dies, as well as high angle dies, with the traditional 16° included angle being associated with minimal fine generation. Fine generation is also exacerbated by poor die alignment, as shown by the data in Figure 14.10.

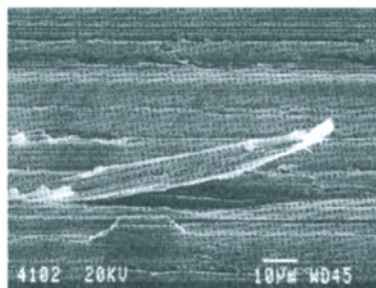


**Figure 14.9** Scanning electron micrograph of a copper wire surface showing an incipient fine, from Baker (1994).

# Fines Collected from Lubricant & Wires

Wires drawn: 10-15 AWG by 3 die angles

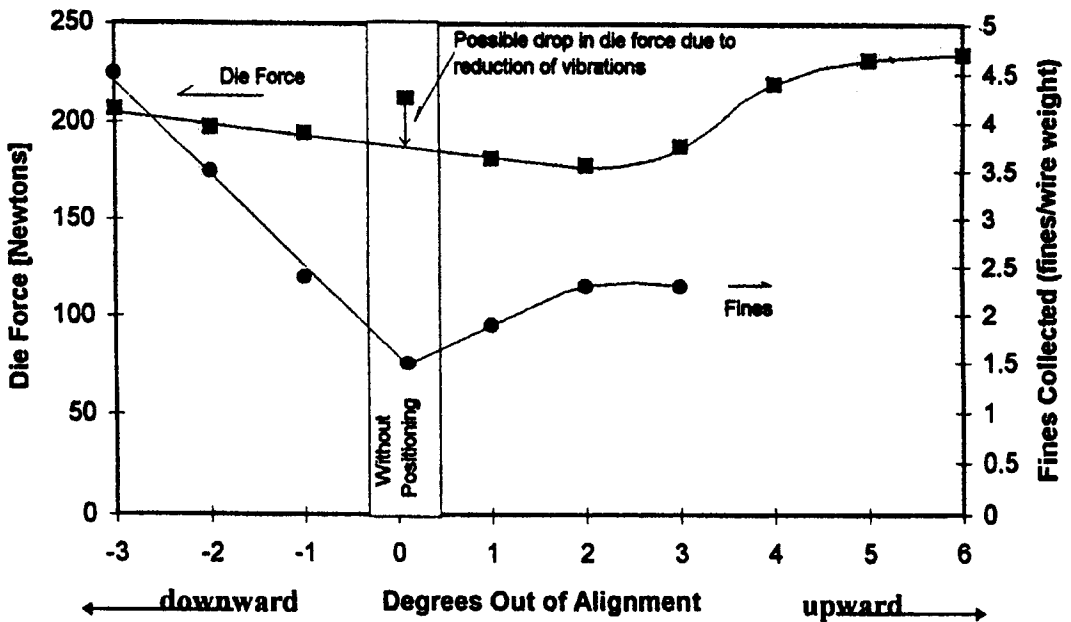
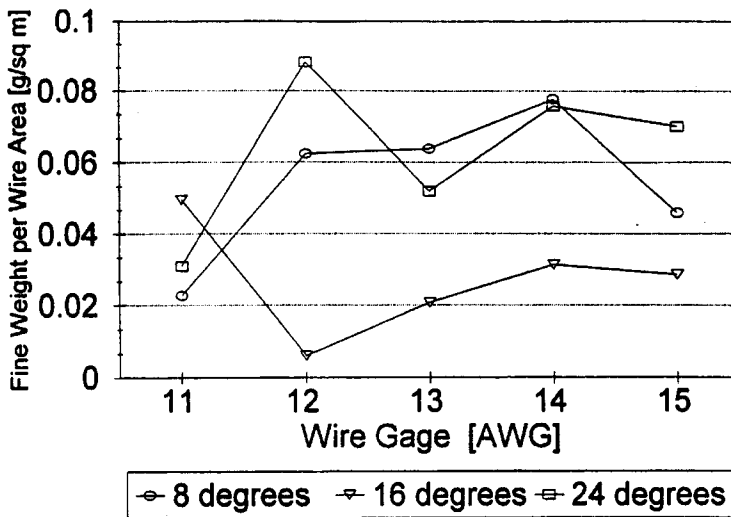


Figure 14.11 Incidence of copper fines as a function of die misalignment, from Baker and Pops (1996)

## REFERENCES

- Baker, G. and Wright, R. N. (1992) *Wire J. Int.*, **25**, 6, 67.
- Baker, G. and Wright, R. N. (1993) *Wire J. Int.*, **26**, 10, 58.
- Baker, G. (1994) Ph.D. Thesis, Rensselaer Polytechnic Institute, Troy, NY.
- Baker, G. and Wright, R. N. (1995) in *Conf. Proc. 65<sup>th</sup> Annual Convention of the Wire Assoc. Int.* (Wire Association International, Guilford, CT), p. 181.
- Baker, G. and Pops, H. (1996) Some New Concepts in Drawing Analysis of Copper Wire, in *Metallurgy, Processing and Applications of Metal Wires*, ed. Paris, H. G. and Kim, D. K. (The Minerals, Metals & Materials Society, Warrendale, PA), p. 29.
- Bloor, S. M., Dawson, D. and Parson, B. *J. Mech. Eng. Sci.*, **12**, 3, 178.
- Booser, E. R. (1981), in *Kirk-Othmer Encyclopedia of Chemical Technology*, 3<sup>rd</sup> Ed. (Wiley-Interscience, New York, NY), p. 477.
- Korst, H. (1948) *Österreichisches IngenieurArchiv. Vienna*, **2**, 132.
- Lancaster, P. R. and Smith, B. F. (1974) *Wire Industry*, **41**, 933.
- Lucca, D. A. and Wright, R. N. (1996) *ASME Trans. J. of Manf. Sci. and Eng.*, **118**, 4, 628.
- MacLellan, G. D. S. (1952-53) *J. Inst. Metals*, **81**, 1.
- Newnham, J. A. (1970) Wire Drawing Lubrication, in *Metal Deformation Processes, Friction and Lubrication*, ed. Schey, J. A. (Marcel Dekker Inc., New York, NY), p. 457.
- Noseda, C. and Wright, R. N. (2002) *Wire J. Int.*, **35**, 1, 74.
- Pawelski, O. (1968) *Schmieretechnik*, **15**, 129.
- Riesz, C. H. (1970) Wire Drawing Lubrication, in *Metal Deformation Processes, Friction and Lubrication*, ed. Schey, J. A. (Marcel Dekker Inc., New York, NY), p. 83.
- Schey, J. A. (1983) *Tribology in Metalworking, Friction, Lubrication and Wear* (American Society for Metals, Metals Park, OH).
- Siebel, E and Kobitzsch, R. (1943) *Stahl und Eisen*, **63**, 110.
- Snidle, R. W. (1977) *Wear*, **44**, 279.
- Wistreich, J. G. (1955) *Proc. Inst. Mech. Engrs.*, **169**, 654.
- Wright, R. N. (1973) *Wire J.*, **6**, 9, 135.
- Wright, R. N. and Male, A. T. (1975) *ASME Trans., J. for Lub. Eng.*, **97**, F, 1, 134.
- Wright, R. N. (1976) *Wire Technology*, **4**, 5, 57.
- Wright, R. N. (1978) *Metal Progress*, **114**, 3, 49.
- Wright, R. N. (1980) Characterization of Metalworked Surfaces, in *Metallography as a Quality Control Tool*, ed. McCall, J. L. and French, P. M. (Plenum Press, New York, NY), p. 101.
- Wright, R. N. (1981) The Character of Metal at or Near the Metalworked Surface, in *Process Modeling – Fundamentals and Applications to Metals*, ed. Altan, T., Burte, H., Gegel, H. and Male, A. (American Society for Metals, Metals Park, OH), p. 409.

Wright, R. N., Martine, P. and Yi, Y. (1987) Experimental Mechanics of Shaped Bar Drawing, in *Advanced Technology of Plasticity 1987, Vol. II*, ed. Lange, K. (Springer-Verlag, Berlin), p. 863.

Wright, R. N. (1997) *Wire J. Int.*, **30**, 8, 88.

Wright, R. N. (2000) in *Metal Forming 2000*, ed. Pietrzyk, M., Kusiak, J., Majta, J., Hartley, P. and Pillinger, I. (A. A. Balkema, Rotterdam, Netherlands), p. 11.

## Chapter 15

# Modelling and Control of Temper Rolling and Skin Pass Rolling

OLOF WIKLUND

*MEFOS*

*Box 812*

*SE-971 25 Luleå*

*Sweden*

FREDRIK SANDBERG

*AB Sandvik Steel*

*SE-81181 Sandviken*

*Sweden*

### 15.1 INTRODUCTION

#### 15.1.1 *What do we mean by temper rolling and skin pass rolling?*

Temper rolling is used either to eliminate upper and lower yield stress behaviour, yield elongation, or to improve the surface of the strip or both. The final flatness is affected by temper rolling. In order to optimise the final properties of cold rolled steel it is necessary to improve the control of the temper rolling process. A good predictor of the rolling force would improve the process control. The conditions in the roll bite are different from those of hot rolling and those of other kinds of cold rolling in reversible or tandem mills. The elongation (or reduction) of the strip is of the order of one percent, the deformation is highly localised and there is considerable elastic spring-back of the strip. The work rolls are deformed in a way similar to that of Hertzian contact for some temper rolling conditions. This means that the standard models for rolling force do not apply or need to be modified for the temper rolling process. For steels without upper and lower yield stress behaviour a temper rolling pass or *skin pass* may be used to adjust the flatness and the surface roughness.

#### 15.1.2 *Why*

The main purpose of temper rolling of a low alloyed low carbon steel strip is optimisation of the mechanical properties. Properties of interest are the yield strength, which should be well defined at a certain level, and the existence of non-homogenous



yield elongation caused by propagating of Lüder's bands. See Figure 15.1. Customers expect narrow tolerances on several properties of the strip beside the mechanical properties: The dimensions, the flatness and the surface roughness. The temper rolling process is often used to adjust the strip flatness and to achieve the surface roughness specified by the customer.

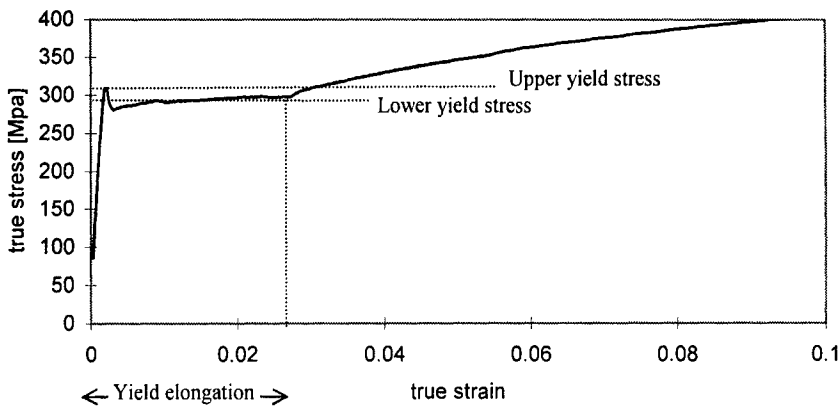


**Figure 15.1** Results from uni-axial tensile test of low alloyed low carbon steel strip, with upper yield stress, lower yield stress and the yield elongation marked in the diagram.

### 15.1.3 How

As a rolling process, temper rolling is in many ways similar to normal cold rolling. Rolling is performed in the same type of rolling mills, using the same types of rolls with the same type of actuators for gauge, flatness and surface roughness control. One big difference however, is the plastic thickness reduction, which in normal cold rolling typically is 5-30 % and in temper rolling is less than 2 %. The reason is that temper rolling is normally not performed in order to reduce the thickness of the strip, but to create mobile dislocations and thereby avoiding the creation of flow figures during any post forming operation.

**15.1.3.1 Mechanical properties.** Customer's demands on today's steel strip products are extremely variable and challenging. Mild steel can be produced with yield strengths between 120 and 1200 MPa. The lowest yield strength steel grades consist of almost 100 % iron (ferrite) with extremely low levels of elements in interstitial solution (carbon and nitrogen). Due to the lack of interstitial elements there should be no yield elongation. In stainless steel grades there are also very low levels of elements in interstitial solution and hence no yield elongation. For ultra high strength steel, the strength is achieved by quenching and the microstructure consists of almost 100 % martensite without yield elongation. For such steels a temper rolling pass or skin pass may be used to adjust the flatness and the surface roughness and possibly the yield strength of the strip.

The main group of construction steels are medium and high strength steel grades with alloying elements like C, N, Mn, Nb, Ti. The microstructure often consists of ferrite and pearlite. The strength is achieved by solution hardening (substitution solution of for example Mn), and precipitation hardening from carbides and nitrides (for example niobium carbo-nitrides). Cold rolled steel strips are produced in a number of process steps like melting, casting, hot rolling, cold rolling, annealing and temper rolling. All process steps affect the mechanical properties of the product. Temper rolling is often the last chance to adjust some of the mechanical properties. The yield stress and yield elongation can be controlled by temper rolling.

Annealing is performed in order to eliminate the strain hardening achieved in the previous cold rolling steps. During the annealing process, the strips are heated to a temperature of 700-900 °C in order to create re-crystallised and “stress-free” grains with a much lower dislocation density than in the cold rolled condition. During the annealing process many of the mobile dislocations generated during cold rolling are annihilated and those, which might be left, are pinned (immobilised) by carbon and nitrogen atoms in interstitial solution. The pinning of the dislocations during annealing creates the upper and lower yield stress and the yield elongation seen in Figure 15.1. The upper yield stress correlates to the stress necessary for tearing the dislocations loose from their pinning sites. After the dislocations are re-mobilised it takes a much lower stress level to continue the deformation.

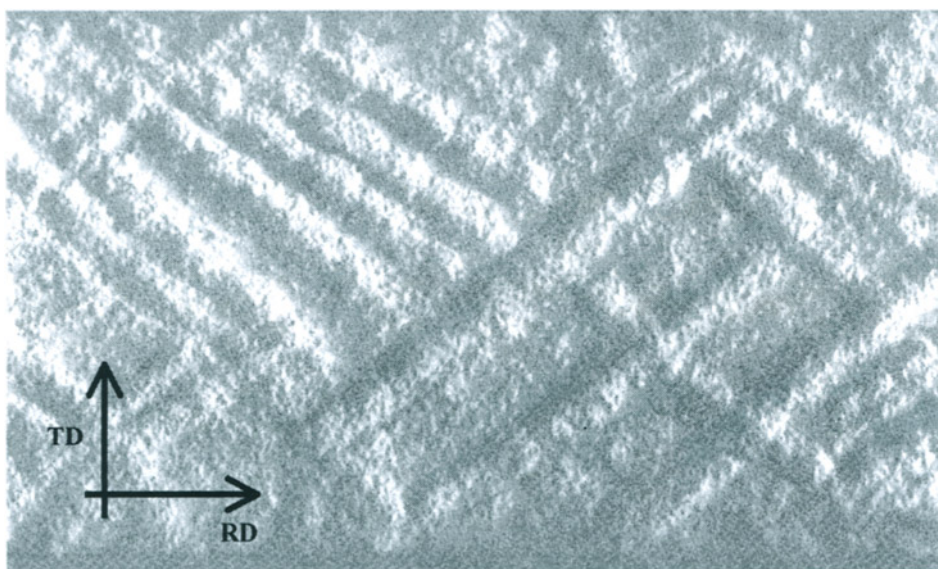


**Figure 15.2** Example of deformation bands (Lüder's bands) in a temper rolled steel strip, strip thickness=1.15 mm, and temper reduction of 0.6 %. TD = thickness direction, RD = Rolling direction.

In a tensile test the plastic deformation will start at some defect or other stress concentration site. At the start the stress is at the upper yield stress. Then the deformation will propagate through the specimen at an approximately constant stress

level, the lower yield stress. During this stage of the deformation, the plastic deformation is concentrated to a small number of plastic fronts. After the yield elongation is passed, if the specimen is unloaded and then reloaded again, the deformation will start without any yield elongation. This phenomenon is used during temper rolling, where the pre-deformation is a rolling pass giving the strip a small deformation. *During rolling, Lüder's bands are nucleated at the surface to propagate towards the centre of the strip at approximately a  $45^\circ$  inclination to the top and bottom surface of the strip.* An example of the deformation pattern during temper rolling is shown in Figure 15.2, where the deformation bands have been visualised by etching in Fry's reagent and examined in a scanning electron microscope.

Normally the deformation bands nucleate at one surface of the strip and then propagate towards the opposite surface. In order to eliminate the Lüder's phenomena, the deformation bands from temper rolling should cover the surface of the strip. It should be kept in mind that temper rolling is performed in order to adjust the properties of the strip by plastic deformation. This deformation should be small to affect the thickness of the strip as little as possible, since the possibilities for narrow tolerances is much better during conventional cold rolling with larger deformations. It should also be small in order to avoid excessive work hardening and loss of ductility.

**15.1.3.2 Coining and smoothing of the surface.** The know-how of coining and smoothing of the surface will not be focused on in this paper. The demands and methods vary for different producers and consumers. However, it is often important to maintain a high pressure in the roll gap to obtain the desired result. The pressure increases with the roll diameter and the friction, but decreases with forward and backward tension.

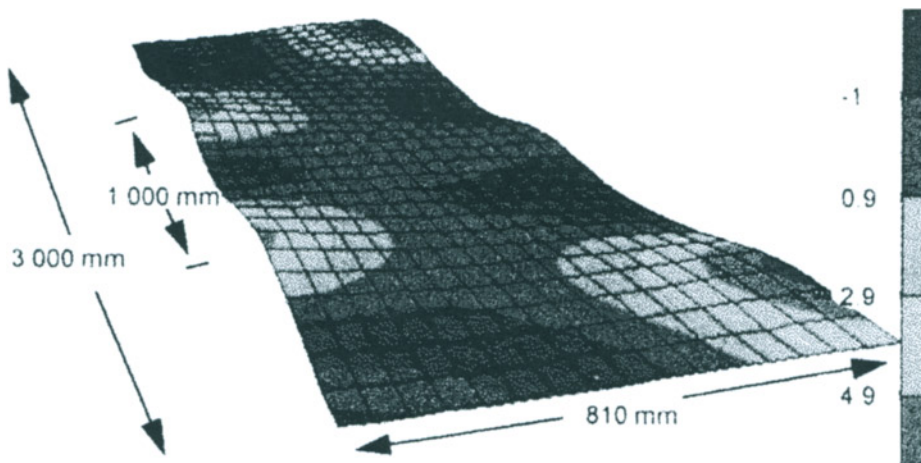


**Figure 15.3** Strip with manifest edge waves. The grey-scale indicates displacement in the thickness direction in mm.

**15.1.3.3 Improving the flatness.** Besides adjusting the mechanical properties of the strip, temper rolling can provide the proper surface texture and good flatness. The same principles are applied for flatness control during temper rolling as during conventional cold rolling with large thickness reductions. Because less engineering efforts and economical resources have been allocated to the temper rolling area, only "basic" flatness actuators/methods are used during temper rolling. Some typical flatness defects are shown in Figures 15.3 and 15.4.

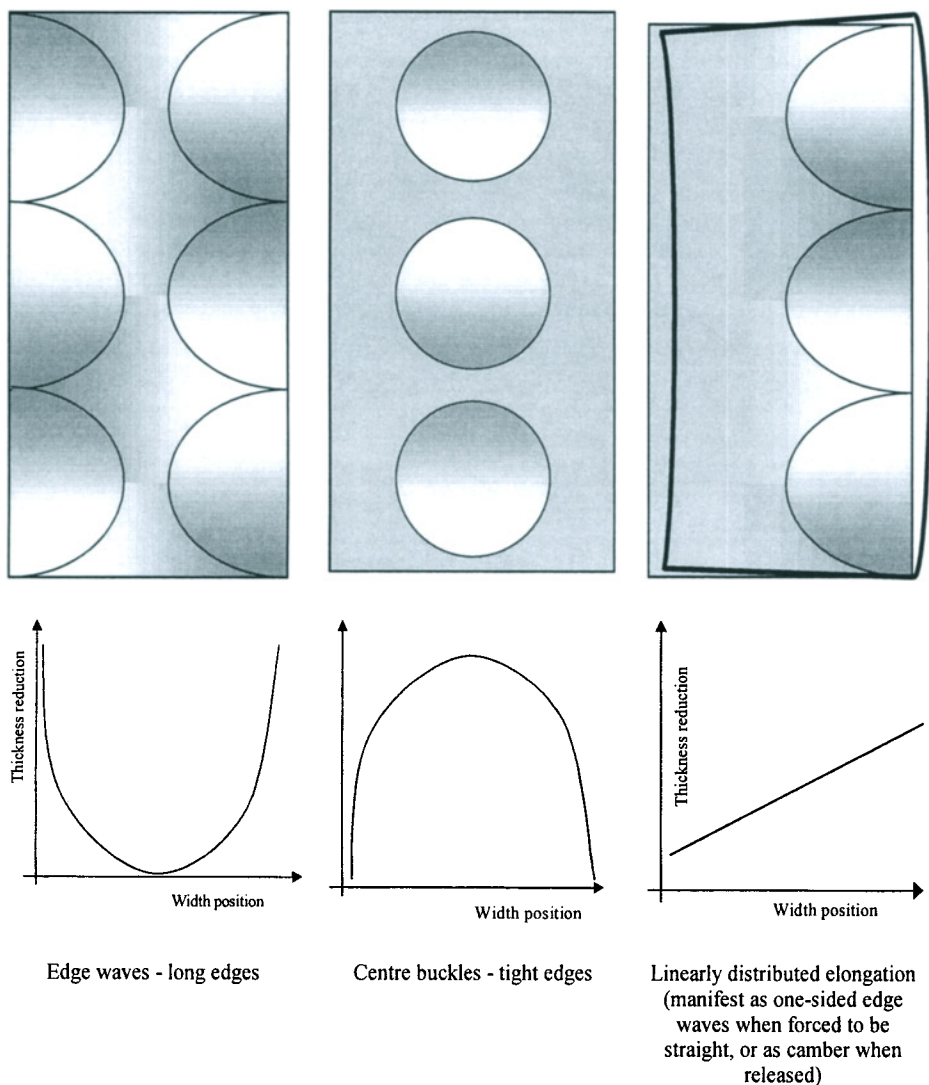


Figure 15.4 Typical flatness defects.

As can be seen in Figure 15.4, the flatness defects can be manifest at the edges of the strip as edge waves, at the centre as centre buckles, as one-sided edge waves when forced to be straight, or as camber when released. There are also more complicated flatness defects, which cannot be corrected for by the basic control actuators. Flatness defects are not always manifest. A strip that looks flat may contain residual stresses. Residual stresses can cause warping of the work-pieces during manufacturing operations; the flatness defects become manifest.

In temper rolling mills there are three common methods/actuators for flatness control, *work roll crown*, *work roll bending* and *tilting* of the roll gap. The most common method is the use of a constant work roll crown, which means that the work roll barrel has "a diameter profile", a difference in diameter along the barrel length. Using a single work roll crown makes the flatness control very inflexible, as the roll is perfect for only one roll deflection and strip crown. It is common to use a few different work roll crowns for different rolling situations. An actuator to dramatically increase the flexibility is work roll bending. Hydraulic cylinders apply bending forces on the work roll necks. A common strategy for flatness control is to use a limited number of rolls with different work roll crowns and then use work roll bending for the final on-line corrections of the flatness. The principle for work roll bending and work roll crown is shown in Figure 15.5.

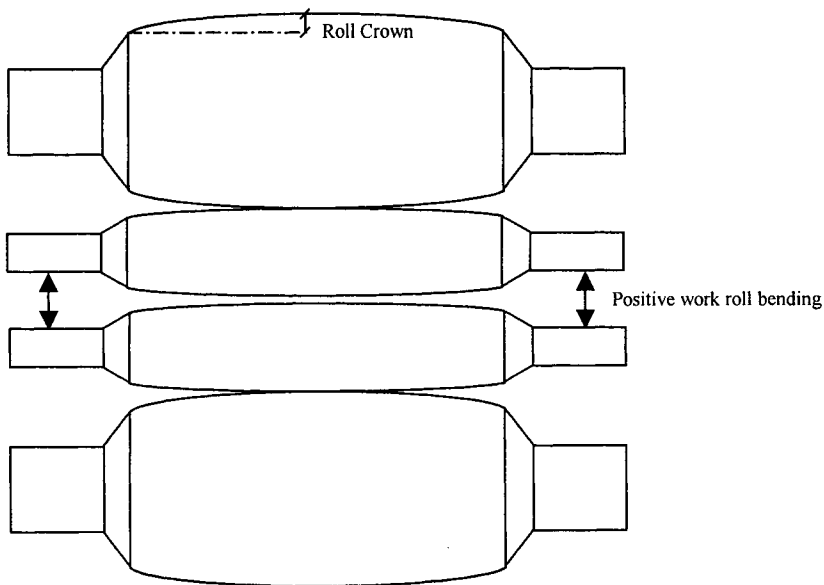


Figure 15.5 The principle for work roll bending and work roll crown.

Work roll crown and work roll bending are two methods to decrease symmetric flatness defects. Tilting of the roll gap is used for non-symmetric flatness defects. This means, that the roll gage is higher at one end of the roll barrel than the other. Tilt or

skewing of the roll gap can be used for flatness control during cold rolling and profile and flatness control during hot rolling.

These three actuators/methods are common for flatness control during temper rolling. There are several other methods/actuators available on the market for flatness control during hot and cold rolling. For *automatic* control it is also necessary to *measure* the flatness defects. There are two different principles for measuring the flatness, with or without contact with the strip. Geometrical triangulation with laser is a contact free measurement of the flatness. Manifest flatness defects cause movements of the strip as it is travelling past the measuring points. The flatness defects are computed from these movements. Measuring rolls detecting the flatness are used in contact with the strip. The strip is bent and the distribution of strip tension over the strip width is measured. This works only where there is enough (forward) tension to eliminate manifest flatness defects. The flatness defects are computed from the measured tension distribution. Measuring rolls are common in cold rolling and are becoming more common in temper rolling despite the high price.

## 15.2 MODELLING OF THE ROLL GAP

### 15.2.1 *Failure of conventional cold rolling models*

The conditions in the roll gap during temper rolling are outside the working range of conventional roll gap models for cold rolling. This is mainly due to the small reduction, the high friction, and the high flattening of the work rolls. A set of simple models is proposed by Roberts (1988).

The existence of an 'indented zone' is discussed and its consequences is elaborated by Yuen (2000). The indented zone is a region, where the strip thickness is essentially constant. The indented zone (or flat zone) can be modelled or at least predicted by non-circular arc methods, e.g. the slab method with influence functions for the roll flattening (Jortner et al., 1960).

### 15.2.2 *Fleck and Johnson*

Fleck and Johnson (1987) made the crucial observation, that the friction between the rolls and strip does not necessarily reach the limiting value in the indented zone. This zone can also be described as a 'neutral zone' (rather than a conventional neutral plane) moving with the same velocity as the roll. A roll gap model was described in a second paper (Fleck et al., 1992). This model is relevant for foil rolling as well as for temper rolling. Three characteristic 'Friction Hills' are illustrated in Figure 15.6 for different degrees of containment. At the top, 'AF', there is a normal Friction Hill with plastic zones and a neutral plane. In the middle, 'ABEF', there is a neutral zone with contained plastic deformation with no slip 'B'. At the bottom, 'ABCDEF', there are six zones with different conditions.

A, E	plastic reduction with backward slip
B, D	contained plastic reduction with no slip
C	elastic deformation with no slip (dead zone)
F	plastic reduction with forward slip



The elastic zones at the entry and exit are omitted in this description.

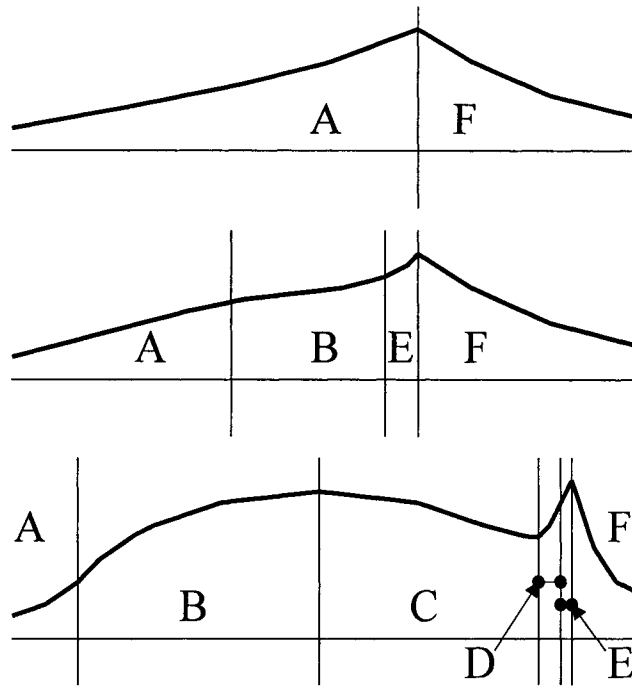


**Figure 15.6** Typical 'Friction Hills' at different degrees of containment.  
The rolling direction is to the right (A is at the entry, F is at the exit).

Yuen et al (1996) developed an on-line model for temper rolling based on Fleck and Johnson's first paper using the simple 'mattress model'. An improved algorithm was introduced to ensure robustness and speed. This model has been validated with measurements from 628 coils during industrial production.

### 15.2.3 A hybrid model

Dixon (1996) has presented a model using very few segments with an analytical solution in each of them. This *hybrid* model (segmented and analytical) is aimed at real-time use for on-line control. It incorporates slipping and sticking friction (automatically applied to the appropriate regions). The roll gap is divided into 5-10 segments. Approximations to Orowan's equations are solved within each segment. The pressure need not be constant within each segment. The neutral plane/zone can be located inside a segment or at a boundary. This allows for precise estimation of rolling force, torque and forward slip at a very low computational cost, approximately 5% compared to a classical numerical solution for non-circular arc roll deformation. The model can be applied to hot and cold rolling, temper rolling and thin foil rolling.

#### 15.2.4 FEM

Finite element modelling, FEM, is a very general and powerful tool to simulate deformation of solids. There have been well proven methods for large (plastic) deformations, and computer programs implementing the methods for more than a decade. These programs include tools to set-up the proper geometrical and mechanical boundary conditions. The main draw-back of FEM is the high computational cost. It is very far from on-line control.

In mathematical terms FEM is a method to solve differential equations with initial conditions and boundary conditions. The formulation is integrated, and e.g. an expression for work or energy is minimised. The bodies or parts (work-piece and tools) to be simulated are subdivided into a finite number of pieces or elements with simple geometry and finite size. The boundary conditions and internal fields (geometric constraints, forces, stresses, displacements, strains) are carried over from the total model to each element. Within each element, simple functions are assumed for the fields, e.g. constant, linear or quadratic polynomials. This way, it is possible to make one very complicated problem into many simple problems, that can be solved by the computer.

Today, many researchers use commercial software, but we will describe work started 1993 using the public domain program Nike2d from Lawrence Livermore Research Labs. Results were published by Wiklund (1996a,b, 1999).

The FEM simulations were set-up to get a well designed set of "observations" with independent variation of the most important parameters. The results from FEM simulations were used for training and testing (validation) of a neural network predictor.

**15.2.4.1 The FEM tool.** The deformation of roll and strip during temper rolling was modelled using the finite element program Nike2d from Lawrence Livermore Labs, USA. It is an implicit Lagrangian code using four-node elements. This way, the conditions in the roll gap can be described with proper physically based models to allow accurate simulation of the conditions in the roll gap. Figure 15.7 illustrates the geometric mesh of the finite element method, FEM, model of one simulation. The overlap in the contact between roll and strip is due to the penalty or spring function of the interface. Simulation with FEM was used to get a well designed set of "observations" with independent variation of the most important parameters. Compared to measurements during production, the noise level was very low (only truncation errors and other kinds of numerical disturbances). Nike2d was run using UNIX work stations, and a typical simulation lasted approximately 10 hours on a Sun SPARC 10. Such a simulation needs less than one hour on a modern work station today (2002).

**15.2.4.2 Simulations with a simple constitutive model.** The first set of simulations used a simple elastic-plastic constitutive model with linear work hardening. The simulations were made in order to make sure that the FEM modelling works for typical temper rolling conditions.



**15.2.4.3 Simulations with an advanced constitutive model.** The second set of simulations used a constitutive model based on the physics of deformation developed by Zhou and Engberg (1981).

$$\sigma = \sigma_0 + c_1 \sqrt{\varepsilon} + c_2 (\dot{\varepsilon})^{c_3} \quad (15.1)$$

where

$$c_2 = \text{const}(\dot{\varepsilon}_0)^{c_3} \quad ; \quad c_3 = T/T_0$$

$\varepsilon, \dot{\varepsilon}, \dot{\varepsilon}_0$  strain[-], strain rate [1/s], strain rate reference [1/s]

$T, T_0$  temperature [K], temperature reference [K]

$\sigma, \sigma_0$  flow stress, yield stress [MPa]

$\sigma_0, c_1, c_2, c_3$  parameters of the constitutive model

The parameters are evaluated for several steel grades from SSAB. The model was implemented in NIKE2D and some results of the simulations can be presented here. The work-space was set up using nine input variables. Finally three parameters were fixed ( $c_1$ , strip thickness and roll diameter). For the remaining six parameters 55 simulations made a set of "observations" to fit a fast regression model. Additional simulations were made for thin strip by Sandberg (1998).

Simulation of temper rolling of 1.5 mm thick strip is shown in Figure 15.7. Part of the mesh is shown, but a substantial part of the roll is simulated in order to obtain the elastic flattening. The calculated effective stress distribution is also shown.

The deformed roll and strip are shown at the bottom of Figure 15.7, where the thickness direction is zoomed. The small cyclic variation of the output thickness depends on interaction between the grids of the roll and strip. The overlap depends on the elastic constant of the penalty function in the contact algorithm.

The distribution of normal pressure and work roll deformation was analysed for each rolling case. For the normal pressure, three typical distributions were found, one where the pressure rises to a single maximum, one where there are double pressure peaks and finally one where the pressure rises to a plateau at maximum pressure. Examples of the three typical distributions are presented in Figure 15.8.

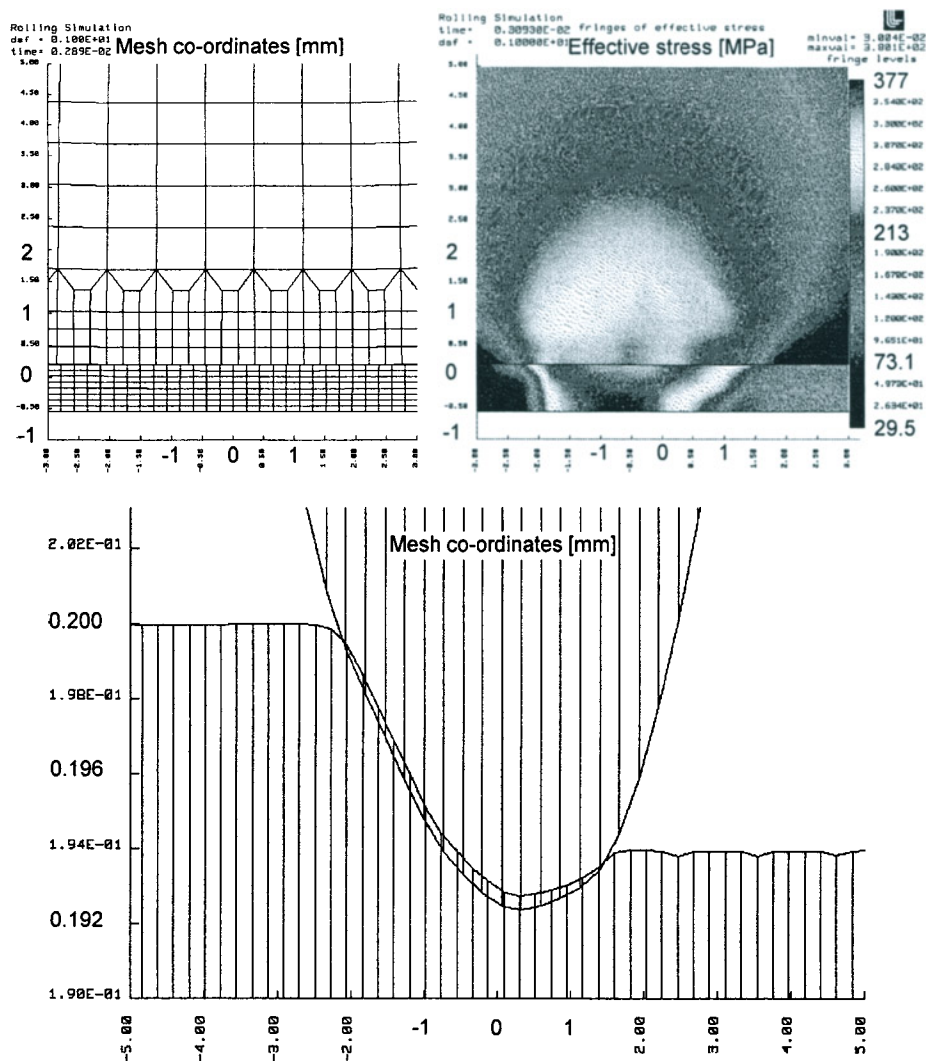


**Figure 15.7** FEM simulation of temper rolling of 1.2 mm thick strip; *top left*: part of the mesh, *top right*: the corresponding effective stresses in the strip and roll, *bottom*: The deformation during temper rolling (the mesh is zoomed in the vertical direction)

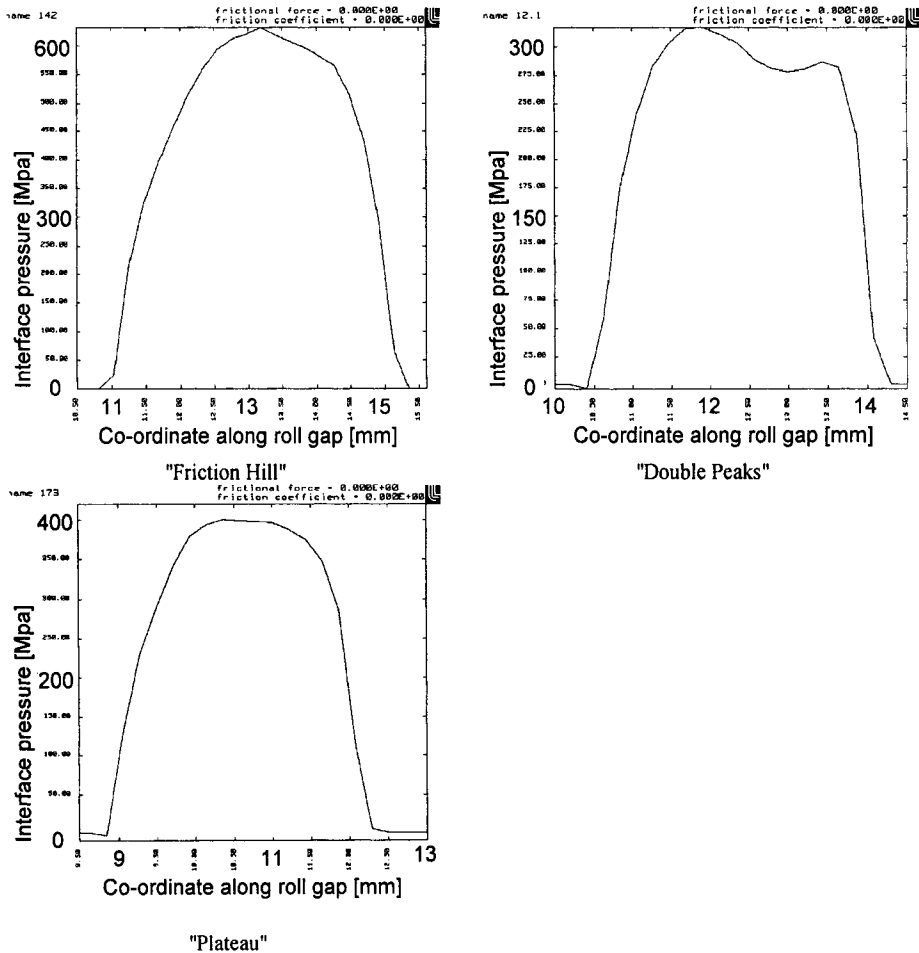


Figure 15.8 Three examples of typical pressure distributions

The first pressure distribution in Figure 15.8 is a "friction hill" similar to pressure distributions from classical slab rolling theory. The second distribution is a pressure distribution with "double peaks" found also in the theory for the rolling of thin foil as it has been presented by Fleck et al. (1987, 1992). See also Figure 15.6. Double peaks appear in the simulation of some combinations of low friction and low reduction. The third distribution is rounded like the "hertzian" distribution of pressure due to elastic deformation despite of the "plateau" at the maximum of pressure. The roll deformation was analysed for each rolling case. No flat zones could be found, where the strip thickness was 1.5 mm, and the shape of the contact between the work roll and strip was nearly cylindrical. Hence it is feasible to use Hitchcock's model for work roll deformation (Hitchcock, 1935). A typical roll gap is shown in Figure 15.7.

When the incoming strip thickness is decreased, there will be flat zones in the roll gap. Examples of calculated roll gaps for some thinner strips are presented in

Figure 15.9 together with the corresponding pressure distributions. The strip thickness is 0.5 mm, the roll diameter is 460 mm, and the reduction is 0.8%. There are two levels of friction. The figures to the left are examples of work roll deformation. An indication of a flat zone is seen in Figure 15.9a and a more pronounced flattening of the work roll in Figure 15.9c. The only difference between the two rolling cases is the coefficient of friction, which is set to 0.1 for 15.9a and 0.2 for 15.9c. The figures to the right show the corresponding pressure distributions. Particularly for high friction, Figure 15.9d, the pressure distribution is rounded like the hertzian pressure distribution. The maximum pressure increases from approximately 890 MPa to 1310 MPa as the coefficient of friction is changed from 0.1 to 0.2.

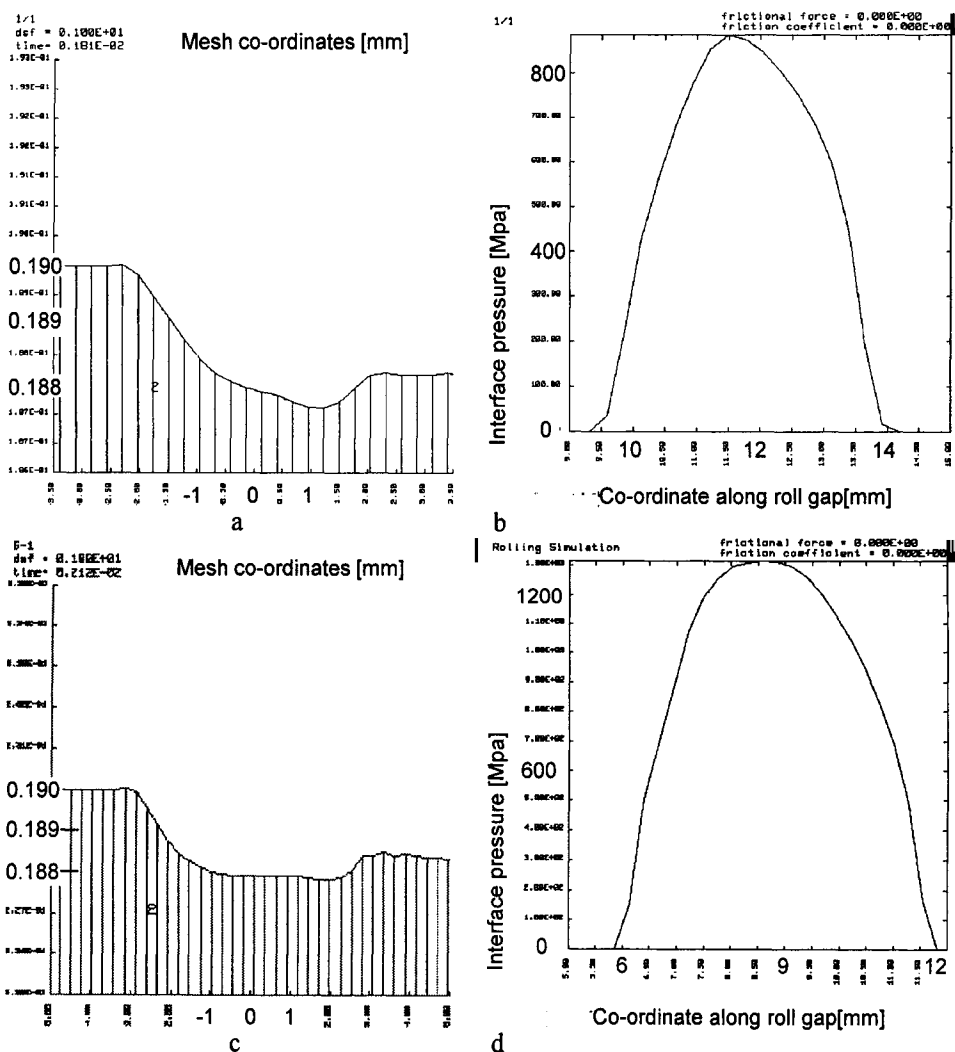


Figure 15.9 Left: examples of calculated roll gaps, right: pressure distributions for strip thickness 0.5 mm

### 15.2.5 Making fast predicting models from FEM simulations

A first set of 16 FEM simulations with Engberg's model was designed to screen nine input variables. The most significant variables were selected and a new set of simulations was designed to get a (non-linear) response surface model for the specific rolling force  $F$ . The input variables were screened by their linear influence on the specific rolling force using projection to latent structures, PLS, with the statistical program MODDE from Umetrics. It turned out to be hard to simulate all 16 "experiments" that were selected for the first (fractional factorial) experimental design. The results improved when an ill-conditioned simulation was excluded as an "outlier".

The nine variables are:

$\sigma_0, c_1, c_2, c_3$	parameters of the constitutive model
$h_i$	incoming strip thickness [mm]
$r_a$	work roll radius [mm]
$\mu$	friction coefficient [-]
$re$	reduction [%]
$v$	rolling velocity [m/s]

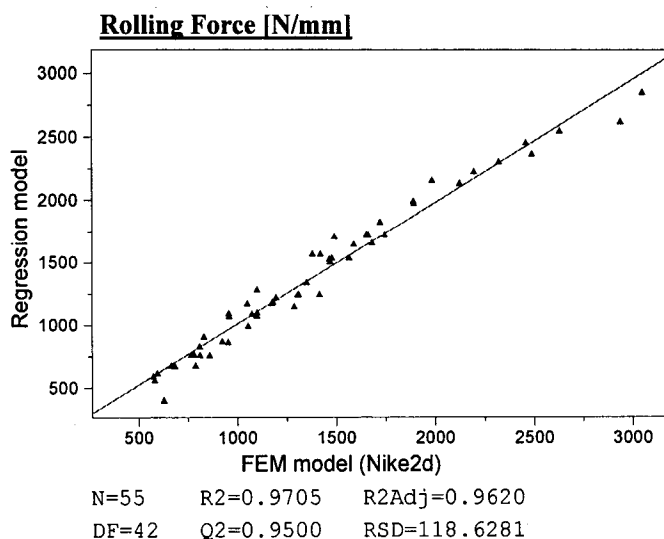


**Figure 15.10** Fast regression model versus FEM simulation

The screening indicated that only the coefficients of  $\sigma_0$  and  $re$  were significantly nonzero and those of  $c_2$  and  $v$  were almost nonzero. The influence of the friction coefficient seemed to be negative, which is not physically correct.

The next step was to make a response surface model of 32 FEM simulations with Engberg's model with five variables. The strip thickness, the roll radius, and the constant  $c_1$  were kept constant in order to decrease the number of variables. At a later

stage it would be possible to include variation of the thickness. After this simulation period, it was found out, that the FEM simulations had not converged. The interfacial shear stress was fluctuating in a random manner. When the convergence criteria for energy and displacement were tighter, the simulations behaved well, and there was the influence of friction according to the experimental results.

The simulations of the previous set of input parameters were repeated. Those cases with a low value (0.1) for the friction coefficient gave approximately the same reduction, while those with higher values gave less reduction. 'The mill screws were set tighter' in the FEM simulations to produce approximately the desired reduction for the cases with higher friction. The number of simulations increased from 32 to 55. This way, there was 'experimental' data to model the influence of the reduction and the friction coefficient. The old model underestimated the rolling force because the 'friction-hill' was not developed properly.

The simulations made a well behaving set of 'experimental data' for multiple linear regression, MLR, using MODDE. The predicting power  $Q^2$  was increased from 0.87 for the model of 32 simulations with five variables to 0.95 for the model of 55 simulations with six variables. The final model had six linear terms and six interaction terms (product terms). There was no significant quadratic term. Figures 15.10 and 15.11 illustrate how the fast regression model represents the FEM simulations.

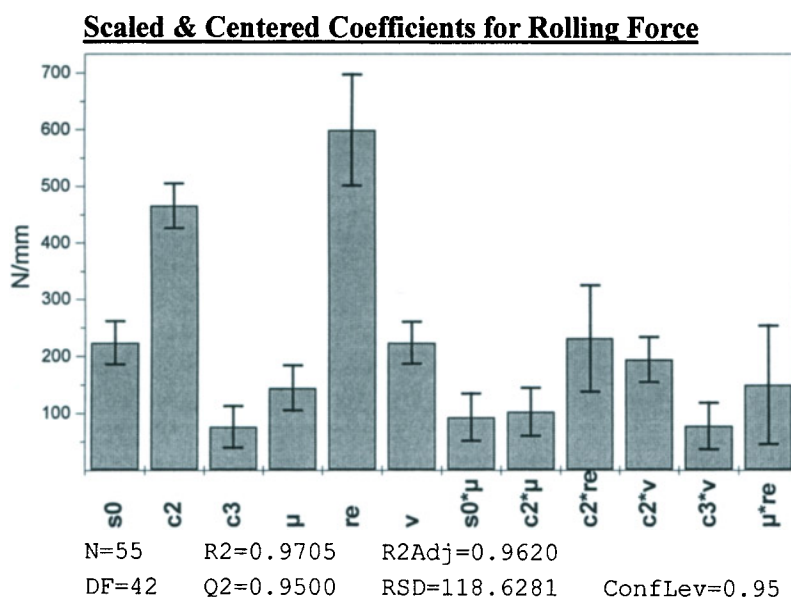


**Figure 15.11** Coefficients for the terms in the fast model according to MODDE.

The model contains three variables of the material model:

s0                      yield stress  $\sigma_0$  [MPa]

c2                      strain rate coefficient

c3                      strain rate exponent

and three rolling variables:

$\mu$                       friction coefficient

re                      reduction [%]

v                      rolling velocity [m/s].

The fact that the 'physically based regression model' was improved indicates that the FEM simulations were behaving better, but it was more important to be able to model the measured influence of the friction on the temper rolling force. This linear + interaction model was sufficient and simple. A neural network or some other kind of non-linear model could not improve the modelling.

### 15.3 MODELLING OF THE ROLL FORCE

#### 15.3.1 FEM

Our results published 1996-1999 include simplifications to model only the roll force (not 'several variables' of the roll gap including torque and forward slip). See Wiklund (1996a, b, 1999) and Sandberg (1998). Hybrid methods were designed combining FEM, statistical methods, analytical modelling or neural networks.

A typical FEM simulation needed 10 h of computer time while a prediction with the corresponding neural network needed only 20  $\mu$ s on the same UNIX computer. The model with linear and product terms was even faster. The analytical model of Ekelund (Richardson et. al., 1985) is also very fast (only simple arithmetic operations, +, -,  $\times$ ,  $\div$ ).

#### 15.3.2 Hybrid modelling

The first hybrid model combines FEM and empirical modelling. FEM simulations were set-up with an experimental design in order to get a 'workspace' for the relevant variables, to tune a fast and robust empirical model within the workspace. This procedure is described in paragraph 15.2.5 about FEM for roll gap modelling. Neural networks were trained and tested, and polynomials were optimised for prediction power. In this case, the non-linear behaviour was limited, and a polynomial with linear terms and product terms was optimal.

Another kind of hybrid model was made using the first hybrid model and process data. The parameters of the constitutive model were optimised in the first step, and the process data were used directly along with the output of the first hybrid model as input for a neural network predictor of the rolling force.

A third kind of hybrid model was made from the combination of the analytical roll force model of Ekelund with Hitchcock's deformed roll radius and a neural network. The process data were used directly along with the output of Ekelund's model as input for a neural network predictor of the rolling force.

**15.3.2.1 The neural network tool.** Data sets with several variables and several observations can be represented by a table with a column for each variable and a row for each observation. Such data sets can be used in order to evaluate the relationships between the variables. There are several statistical methods, e.g. linear regression and multivariate projection methods. If the relationships are unknown and might be non-linear, (artificial) neural networks are a good alternative. MEFNET is a neural network program for training and prediction with three layers of neurones using the back propagation learning algorithm presented by Rumelhart (1986). See Figure 15.12.

This kind of neural network can find and describe very general functions by means of superposition of sigmoidal functions. See Figure 15.12. The signal is transferred between the layers via transformed (scaled and offset) sigmoidal functions. The observations are divided into a training set and a test set. Training means that the neural network finds optimal transformations, which are stored in a memory file as weights and offsets. A test set, not used for training, is used to validate the ANN model.

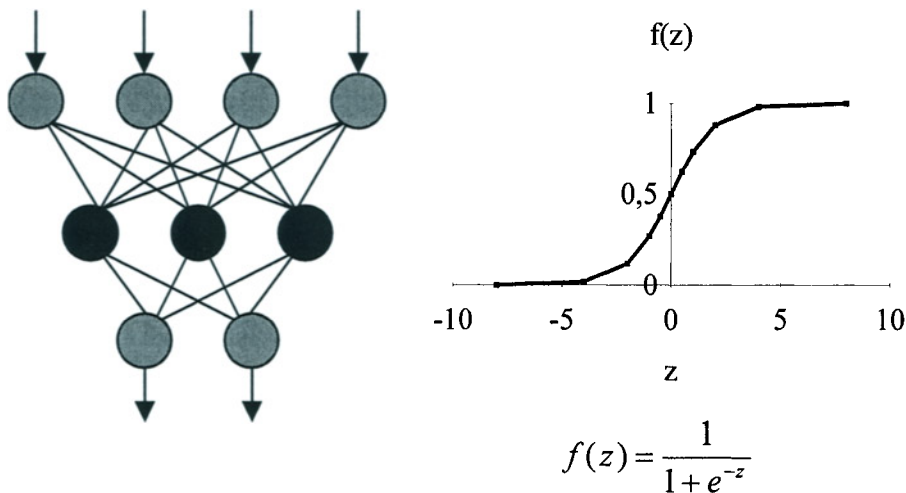


**Figure 15.12** *Left:* artificial neural network with four input neurones, three hidden neurones and two output neurones, *right:* the sigmoid transfer function

**15.3.2.2 Process data set 1.** Data from measurements during the production process, "rolling logs", as well as data from FEM simulations were used to created fast on-line models to predict the rolling force of temper rolling. The total rolling force  $F_{tot}$  and the specific rolling force per unit width  $F_{spec}$  were evaluated separately. Data were collected during several months from the production process at SSAB, Borlänge, Sweden. The data sets include measurements of the chemical composition, and data collected during reheating, hot rolling, cooling, coiling, cold rolling, annealing, temper rolling and tensile testing.

There are a total of 71 variables and 35731 observations in one data set from SSAB. The data from temper rolling were grouped (five samples each second were



averaged to give one observation per second) and merged with upstream data from 109 strips. Approximately 25 % or 8916 observations were used for prediction tests. This data set includes the cumulative rolled length to quantify wear of the work rolls in the temper mill.

The total rolling force  $F_{tot}$  and the specific rolling force per unit width  $F_{spec}$  were evaluated separately to find out if calculating  $F_{spec}$  would improve the predicting power of the ANN. The advantage of  $F_{spec}$  is that the basic influence from the strip width is included in the model, and the disadvantage is that if the pressure varies significantly along the roll axis, the assumption may create an error.

If the modelling of temper rolling is separated into sub-models for flow stress, temper rolling force, final properties of the material, and flatness according to Figure 15.13, it would be possible to test separate parts of the model and to separate the influence of different variable groups. This means that fewer observations would be necessary in order to get a good model using measured process data.

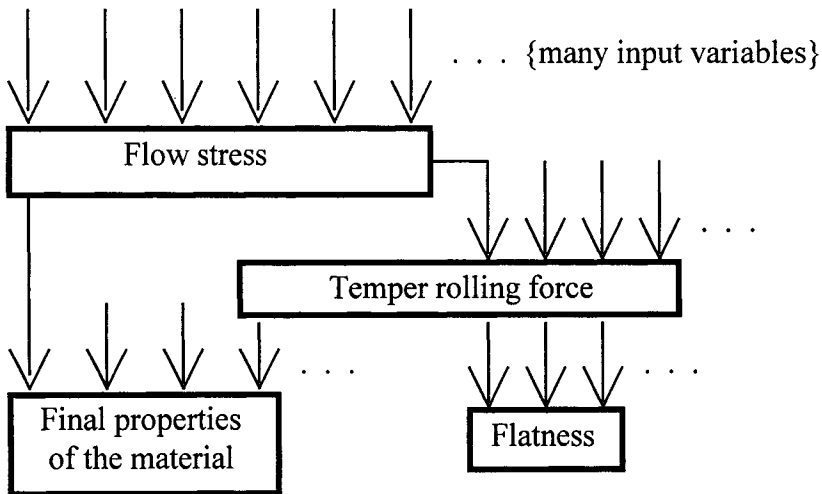


Figure 15.13 Suggested configuration of neural networks for temper rolling

Separation into sub-models using empirical modelling was tested in several ways, always losing accuracy compared to one big neural network (Wiklund, 1996a, b). The flatness after temper rolling may be calculated according to Figure 15.13 in the future, but so far it has been excluded from the data processing. A structure like Figure 15.13 is only useful if the sub-models are based on physics or if they can be tuned with real data.

**15.3.2.3 Modelling with process data set 1.** A neural network was trained to predict the rolling force using all the 71 input variables of a data set from SSAB. Six hidden neurones and 200 training cycles were chosen to get a prediction error very close to the training error. The root mean square, RMS, error of training was 3.5% and that of prediction was 3.6% (9.6 N/mm). Figure 15.14 illustrates the predicting power for this

application of MEFNET. Excluding four input variables, rolling torque and three material tracking variables, made an insignificant change in the predicting power from 3.6% to 3.7%.

There is scatter outside a 'solid core' (the black diagonal in Figure 15.14). The measurements and the predictions are plotted versus prediction number (approximately versus time) in Figure 15.15. It was checked separately that the sudden changes in force correspond to changes in the rolling velocity at the head and tail ends of each coil. From the diagram it is evident that the scatter is caused by bad predictions near the ends of each coil while the predictions are good in the regions of constant (and high) velocity. (There can be several causes for the scatter at the ends of the coils. The thickness at the ends of the strips may be inaccurately measured. The velocity is very low in the beginning of each rolling pass and the measurement of the extension has low accuracy below 30 m/min. Therefore, the synchronisation of the measuring signals may not be good enough.)

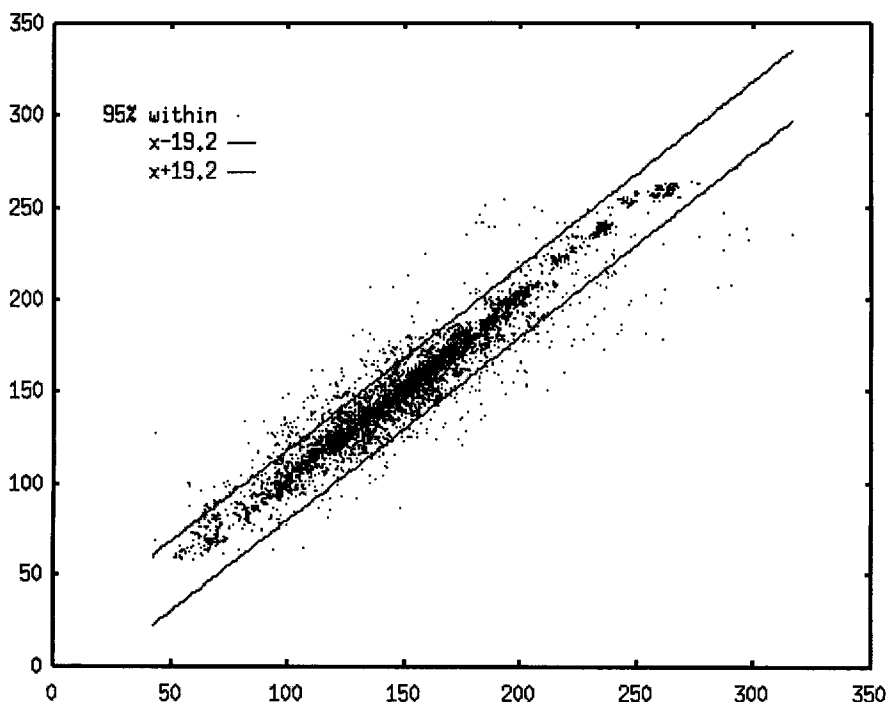


Figure 15.14 The predicted rolling force  $Y$  [kN] versus the measured rolling force  $X$  [kN] for the data from SSAB

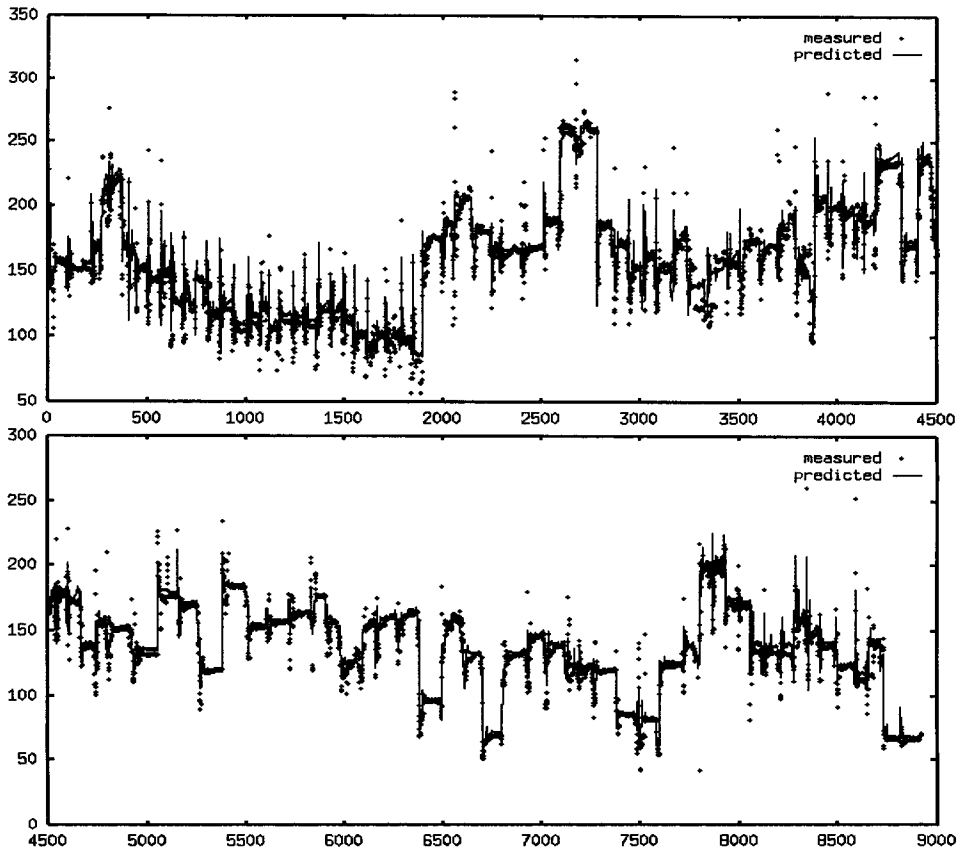


Figure 15.15 The measured and predicted rolling force Y [kN] versus the prediction number X in the prediction set for the data from SSAB

**15.3.2.4 Process data set 2.** A new data set was logged from production in the temper rolling mill and from the upstream processes at SSAB, Borlänge. The almost identical observations at steady state were averaged over 50 crude observations (1 per 10 seconds). The observations near the head and tail ends of each strip were averaged over 5 crude observations (1 per second). The training set contains 11597 'observations' and the prediction set 6637 'observations' from 144 strips after data compression.

**15.3.2.5 The old set-up model and a neural network model.** The set-up model used at that time for the stand-alone temper rolling mill at SSAB, Borlänge, was based on linear regression. It was compared to a neural network model based on data set 2. The on-line model was based on linear regression and contained four input variables:

- strip width
- thickness
- extension (reduction)
- resistance code (obtained by regression from upstream data)

and the neural model contains the *same four input variables plus the rolling velocity* in order to account for the conditions at the beginning of each temper rolling pass. The rolling velocity is valuable because the model is to be used for set-up, while feed-back control (mass flow) is used during the main part of the rolling pass. The velocity is low and increasing in the beginning of each rolling pass.

The root mean square (RMS) error of the two models is plotted in Figure 15.16. The neural model reduces the prediction error from 44 to 32 tons (force).

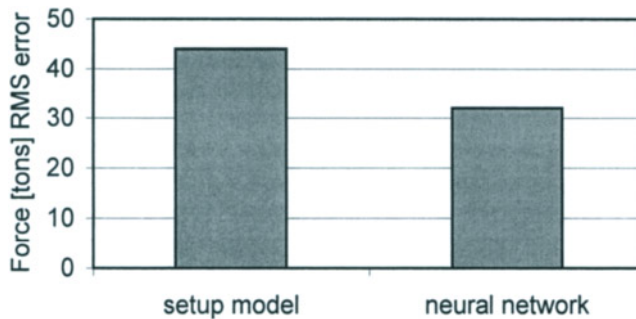


**Figure 15.16** Comparison of the error of prediction for the old set-up model and a neural network model for a temper rolling mill at SSAB.

**15.3.2.6 A physically based model, a neural network model and a hybrid model.** Data from the finite element simulation and from the rolling logs were used for training and testing (validation) of a hybrid model, that combines the physically based model and the empirical model. Note that the selected observations as well as the input variables will be different from those of the previous comparison.

Rolling force models were compared for two steel grades, FeP01 and FeP04. The FEM simulations were limited to one thickness, 1.5 mm, hence the rolling logs were screened for the thickness interval 1 to 2 mm (giving 198 observations for FeP01 and 638 observations for FeP04). The four variables of the ‘physically based regression model’,  $s_0$ ,  $c_2$ ,  $c_3$ , and  $\mu$  were identified in order to fit the observations for each of the steel grades using a multivariable optimisation program.

To predict the rolling force, the following input variables were needed:

- strip width
- thickness
- extension (reduction)
- rolling velocity

This physically based model was used as-is with 14 tons RMS error for FeP01 and 20 tons RMS error for FeP04. A model based on the limited data within the thickness interval 1.4 to 1.6 mm was more accurate, but was based on too few measurements (41 observations; 3.8 tons RMS error for FeP01).

A pure neural network was trained with the same input data, to compare the two methods without favouring the neural network by using more input variables. The results from tests with a different subdivision of the logged data into a training set and a

prediction set were quite similar to those from the physically based model, 12 tons RMS error for FeP01 and 20 tons RMS error for FeP04.

A hybrid model was made with a neural network using the calculated specific rolling force (N/mm) of the physically based model as input along with the strip width and roll bending force.

The RMS errors of this hybrid model were 12 tons RMS error for FeP01 and 17 tons RMS error for FeP04. The three models for each steel grade are compared in Figure 15.17.

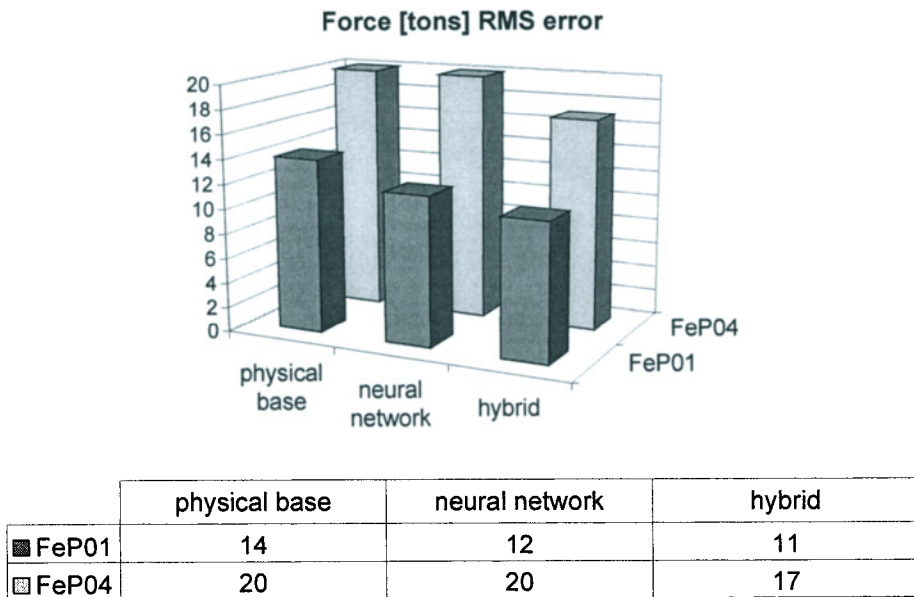


**Figure 15.17** Comparison of the error in the predictions for a physically based model, a neural network model and a hybrid model for two grades of steel at SSAB.

**15.3.2.7 Classic cold rolling theory.** The hybrid modelling approach has been explored further at SSAB and part of it is published by Sandberg (1998). The contact length calculated by FEM simulations with Nike2d and that calculated via Hitchcock's formula for the deformed roll were not equal but highly correlated. In the next step, it was shown that the results of classic roll force models combined with Hitchcock's deformed roll are highly correlated to the results of the FEM simulations. Such a classical model, Ekelund's formula, Richardson et al. (1985), was successfully combined with neural networks to predict the temper rolling force during production.

Hitchcock (1935) has developed an expression for calculation of the deformed work roll radius. Here the roll is assumed to keep its cylindrical shape but with an increased roll radius in accordance with the following expression.

$$R' = R \left( 1 + \frac{CF}{w \Delta h} \right) \quad (15.2)$$

where

$R'$	deformed work roll radius (mm)
$R$	undeformed work roll radius (mm)
$C$	elastic constant for the roll ( $\text{mm}^2/\text{N}$ )
$W$	strip width (mm)
$\Delta h$	absolute thickness reduction (mm)
$F$	roll separating force (N)

The deformed radius is then used for calculation of the projected contact length. A common way of calculating the contact length is by:

$$L = \sqrt{R' \Delta h} \quad (15.3)$$

where

$L$  projected contact length (mm)

The contact length from the FEM analysis and the length from Hitchcocks formula in combination with expression (3) is compared in Figure 15.18.

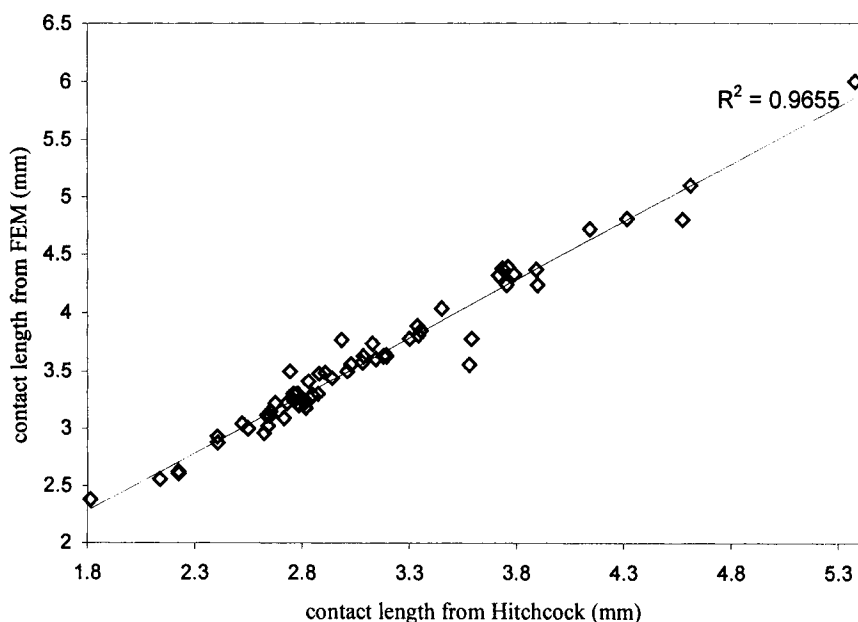


Figure 15.18 Contact length from FEM vs. contact length from Hitchcock

There is a very high correlation between the contact length from the FEM analysis and the length from calculations with Hitchcock's formula. The contact length coming from the FEM analysis is generally higher than the one from Hitchcock.

**15.3.2.8 Detection of flat zones within the roll gap.** During flat rolling of thin foils or temper rolling of thin strips the interfacial pressure on the work roll can be very high. For this reason the ratio  $L/\Delta h$  can be very high. During such rolling conditions there is a risk for existence of flat zones within the roll gap. For this reason it is desirable to have a tool for deciding under what rolling conditions it is necessary to adopt thin foil rolling models for analysis of the current rolling process. Here a simple method for detection of flat zones within the roll gap has been developed. From the literature we have learned that a big  $L/\Delta h$  should be an indication to existence of flat zones, see for instance Domanti et al. (1994). As a trial  $L/\Delta h$  was used to distinguish rolling cases where flat zones exist and where there are not. Using these method, high values for  $L/\Delta h$  were obtained for thin rolling cases where flat zones really existed, but also for rolling cases where the thickness was 1.5 mm and the thickness reduction was very small without any existence of flat zones. It has been shown in this work and by others, see for instance Gratacos and Onno(1994) or Lubrano and Bianchi (1996), that the risk for existence of flat zones within the roll gap increases as the strip thickness decreases. For this reason it is obvious that the indication factor, for which a high value means high risk, should increase as the strip thickness decreases. This lead to an expression as the following:

$$\alpha = \frac{L'}{t} = \sqrt{\frac{R'}{\Delta h}} \varepsilon \quad (15.4)$$

where

$\alpha$	Flattening risk factor (Dimensionless)
$L'$	Contact length corrected for roll flattening in accordance to Hitchcock
$[L']$ (mm)	
$t$	Strip thickness (mm)
$\varepsilon$	Plastic strain
$\Delta h$	Draft (mm)
$R'$	Roll radius corrected for roll flattening (mm) according to Hitchcock

The method was developed to distinguish between cases, where circular flattening and extreme flattening exist in the present FEM analysis, but was also tested on examples from the literature. Calculated results are presented in Figure 15.19, where it can be seen how the first 55 rolling simulations (described in paragraphs 15.2.4-5) have a low level of the risk factor. These cases have no severe roll flattening. The following cases contain rolling with and without severe flattening and the cases with lower risk factors represent cases where the work roll stays cylindrical throughout the entire roll gap. Severe flattening can be expected when the flattening risk factor  $L'/t$  exceeds approximately 10. When severe flattening occurs, the modelling should use a non-circular arc method for the roll gap. See paragraphs 15.2.1-3 and Yuen (2000).

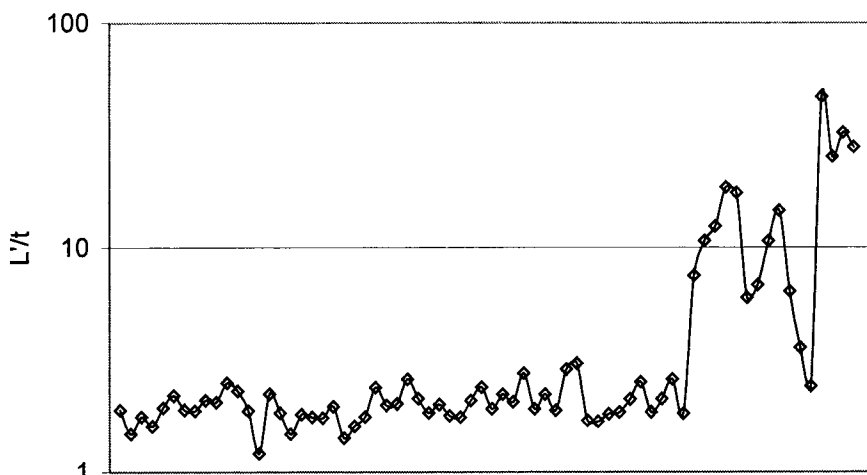


Figure 15.19 Calculated-flattening risk factor for each simulation case (logarithmic scale)

There are several theories for cold rolling of strips available in the literature, but only a few which are directly applicable to temper rolling. There are many similarities between conventional cold rolling with large reductions and temper rolling. The roll force increases with increasing contact length, strain rate and coefficient of friction, but decreases with increasing strip tension. This knowledge must be taken into account when creating a neural network model. One method is to create a pure neural network model and check that the model gives the correct influence from the most important parameters on the roll force. This method is more or less a black-box approach for roll force calculation. Another way of solving the problem is to use an already known model, which may not be strictly applicable to the actual rolling process and let a neural network compensate for deviations between the force calculated by the model and the measured roll force. The classic roll force model is the one proposed by Ekelund (Richardson et al., 1985).

$$F = \sigma WL \left( 1 + \frac{1.6\mu L - 1.2\Delta h}{h_0 + h_1} \right) \quad (15.5)$$

where

$\sigma$	flow stress (N/mm <sup>2</sup> )
$W$	width (mm)
$L$	projected contact length (mm)
$\mu$	coefficient of friction
$h$	strip thickness (mm)
$\Delta h$	draft (mm)

The flow stress is described by the following relationship.



$$\sigma = \sigma_0 + k_1 (\dot{\varepsilon})^{k_2} - \sigma_{tension} \quad (15.6)$$

where

$\sigma$	flow stress (N/mm <sup>2</sup> )
$\sigma_0$	flow stress at zero strain and strain rate (tuning parameter) (N/mm <sup>2</sup> )
$\sigma_{tension}$	strip tension (N/mm <sup>2</sup> )
$\dot{\varepsilon}$	strain rate (1/s)
$k_1, k_2$	tuning parameters

The mean strain rate is calculated as

$$\frac{v\varepsilon}{L} \quad (15.7)$$

where

$v$  peripheral speed of the roll (mm/s)

The reason for only including the strain rate into the flow stress model, equation (2), and not the strain, is that during temper rolling the strain hardening is not as pronounced as during normal cold rolling.

**15.3.2.9 Process data set 3 and a neural model.** A new data set was logged from production in the temper rolling mill and from the upstream processes at SSAB, Borlänge. A pure neural network model was created as a reference to the hybrid model. At first 'all feasible' parameters from a temper rolling mill at SSAB in Borlänge (including upstream data) were included in the model. This network configuration was very sensitive for over-training. Some parameters were insignificant and could be rejected. The adjusted model was much less sensitive to over-training.

**15.3.2.10 Hybrid model combining a classic model and a neural network model.** The roll force model proposed by Ekelund was used as the classic part of the roll force model. The neural network was used to tune the roll force model as a non-linear alternative to regression analysis. The force model (15.5) and the flow stress model (15.6) were combined to the following formula.

$$G = (k_1 (\dot{\varepsilon})^{k_2} - \sigma_{tension})WL(1 + \frac{1.6\mu L - 1.2\Delta h}{h_0 + h_1}) \quad (15.8)$$

The parameters  $k_1$  and  $k_2$  were optimised separately using regression analysis.

The function  $G$  was calculated for each observation in the logged data and added to the input variables for the neural network model. Except for this calculated variable the same inputs were used as for the pure neural network model. The output of the neural network was the final output of the model.

The predictions of the hybrid model are much better with an  $R^2$ -value of 0.94 than the results from the pure neural network model with an  $R^2$ -value of 0.80. ( $R$  is the coefficient of correlation for linear regression). See Figure 15.20.

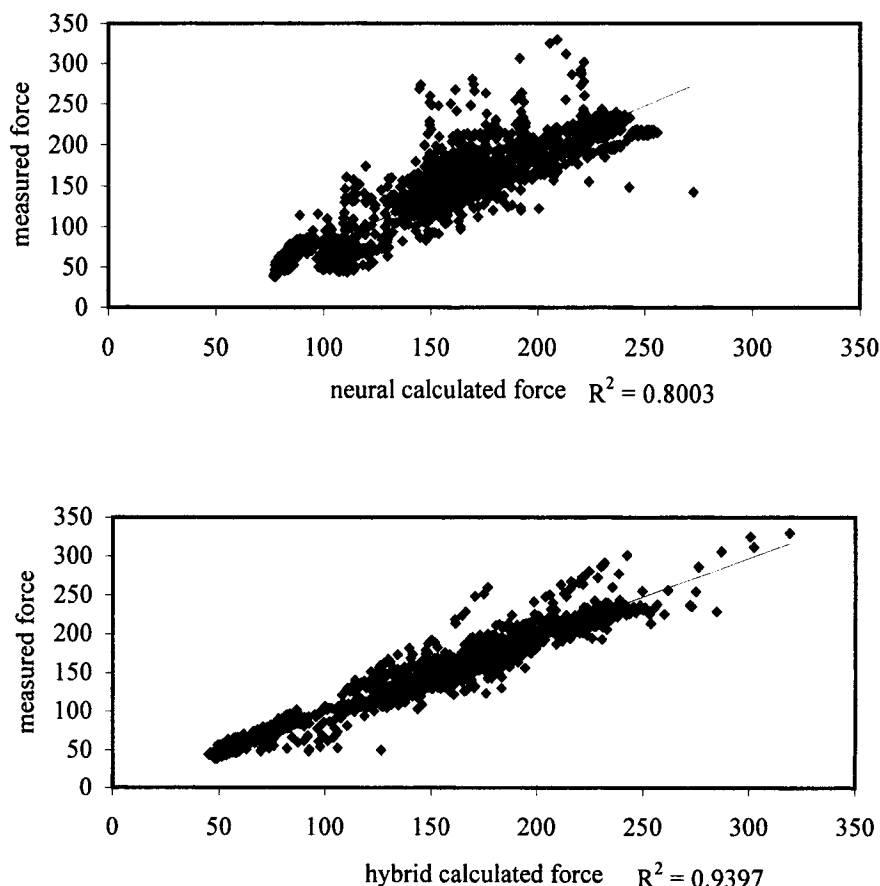


**Figure 15.20** Measured roll force versus calculated roll force for the pure neural model and the hybrid model

The neural network technique is suitable for building a roll force model for temper rolling. The black-box approach is possible to use resulting in a model with acceptable prediction capability. However, the best way is by combining classical rolling theory with the neural network technique. *An advantage with this hybrid method is that well known rolling theory can be used.* One problem with empirical modelling is to get the correct influence from each relevant parameter. Using the black-box approach on logged process data it is possible to get inverted relationships. This is an effect of the control system, and it could be avoided by experimental design, but it is seldom

afforded/allowed by the production staff. Combining a classic roll force model with neural network technique decreases the need of experimental design because some of the major relationships are described within the model. If the classic physical model is good enough, it is possible to use the network only for correction of the physical model.

Finally it strongly recommended to divide the logged data set into a training set and a prediction set, so that the data for training never contains data from a strip used in the predictions and vice versa. Otherwise the prediction power of the model may be over-estimated and it is likely to be over-trained.

#### 15.4 CONCLUSIONS FROM THE MODELLING EXERCISES

It may be tempting to let beginners perform FEM simulations of metal working to reduce cost, but the simulations are complicated and even experienced researchers can make a mistake leading to false conclusions. Experienced researchers should supervise not only the general results but also the methods of the simulation and some critical details of the output. Whenever possible, a new or complicated type of simulation of metal working should be validated by experiments and/or compared to simulation with other methods or other software.

A 'physically based regression model' was able to mimic a designed set of FEM simulations. The linear + interaction model was sufficient and simple, so a neural network could not improve that modelling.

The results of the neural and hybrid modelling show that it is possible to improve the set-up of a temper mill using a neural network and/or a hybrid model instead of the current set-up model. Combining artificial neural networks with a classic roll force model gives a better prediction capability than the simple use of either neural networks or classical theory separately.

Classic simple roll force models with cylindrically deformed rolls (circular arc) are well correlated to the result of advanced FEM simulations for temper rolling. This result leads to another kind of hybrid modelling. The analytical roll force model of Ekelund (Richardson et al., 1985) and Hitchcock's (1935) model for roll deformation can be combined with a neural network, to allow for non-linear correction to a set of measured roll force data from industrial production. The neural correction must be optimised for prediction (avoiding 'over-training' or 'over-fitting').

The use of cylindrical roll deformation models is valid during temper rolling of steel strips with a thickness greater than 0.4 mm. Extreme roll deformation starts to appear for strips thinner than 0.4 mm, leading to flat regions within the roll gap. Then non-circular arc models of the roll gap may be necessary (Yuen 2000).

The practical way to do this modelling on-line would be to run a neural network with the output from a (classical) roll force model as one input variable and some direct input variables from the process. Since it is complicated to transfer data on-line, a model with few variables would be preferred. In addition to the variables of the present on-line set-up model, the rolling velocity of the temper mill should be used.

## 15.5 PROCESS CONTROL

### 15.5.1 *Set-up before the rolling pass*

One of the problems in temper rolling is to get the proper extension (and reduction) and flatness in the beginning of each coil in a separate mill or in the beginning of a new dimension in a continuous line. This problem causes quality problems and/or yield losses. A solution is to improve the set-up of the rolling mill with a good model for rolling force and extension to set the optimal roll gap before the rolling pass. This is a good way to use the temper rolling models on-line in industrial production.

The set-up control mode may be extended to the whole transient phase, when the strip is accelerated. This can be implemented as several calculations of the rolling force in order to reset the roll gap until the system is ready for the feed-back control mode.

The rolling force is also very important for the flatness. The flatness control must compensate for the mismatch between the strip crown and the roll gap according to the rolling load. When the rolling load is predicted, it is possible to set-up the actuators for flatness control, e.g. the roll bending forces.

### 15.5.2 *Feed-back control during the rolling pass using the mass flow method*

During the rolling pass (after the transients at the head end of each coil or dimension) it is possible to use feed-back control of the extension via the mass flow method. The method is accurate but slow due to the distance and delay time between the measurements and the control actuator. As a consequence, the flatness is also relatively easy to control. In a typical temper rolling mill there is manual flatness control.

### 15.5.3 *Forward and backward tension*

It is also important to control the forward and backward tension. High levels are good for the rolling and coiling operations. However, it is better for the material properties to reduce the thickness by compression in the roll gap rather than by tension. The coining (transfer of the surface texture from the rolls) or smoothing of the surface requires a high pressure in the roll gap. For these reasons the tension should be low, far below the yield point.

## 15.6 DEVELOPMENT TRENDS

### 15.6.1 *Modelling and control*

Modelling and process control will be more focused on temper rolling and skin pass rolling. This is partially due to a "saturation" of the efforts in the upstream processes and partially due to increased customer demands on the mechanical and surface properties as well as the flatness of the finished product.

### 15.6.2 Temper rolling and tension levelling

Temper rolling is not likely to be replaced by tension levelling, since it is better for the material properties and the surface, but in some cases a tension leveller is added in-line after the temper rolling mill in order to improve the flatness.

### ACKNOWLEDGEMENT

Part of the work presented in this chapter was done, when the co-author Sandberg was employed by SSAB. Both authors want to thank Göran Engberg, SSAB Tunnbrått Borlänge, for valuable discussions and the supply of industrial process data.

### REFERENCES

- Dixon, A.E., Yuen W.Y.D. (1996) in *Proceedings of 2<sup>nd</sup> International conference on modelling of metal rolling processes*, ed. Beynon J.H., Ingham P., Teichert H., Waterson, K. (The Institute of Materials, London), p. 112.
- Domanti, S.A., Edwards W.J., Thomas P.J., Chefneux L. (1994) in *Proceedings of 6<sup>th</sup> International Rolling Conference*, Vol. 2, ed. VDEh (Verlag Stahleisen, Düsseldorf), p. 422.
- Fleck, N.A., Johnson, K.L. (1987) *Int. J. Mech. Sci.*, 7, p. 507.
- Fleck, N.A., Johnson, K.L., Mear M.E., and Zhang L.C. (1992) in *Proc. Inst. Mech. Engrs.*, 206, p.119.
- Gratacos P., Onno F. (1994) in *Proceedings of 6<sup>th</sup> International Rolling Conference*, Vol. 2, ed. VDEh (Verlag Stahleisen, Düsseldorf), Vol. 2, p. 441.
- Jortner D., Osterle, J.F., Zorowski C.F. (1960) *Int. J. Mech. Sci.*, 2, p. 179.
- Lubrano M., Bianchi J.H. (1996) in *Proceedings of 2<sup>nd</sup> International conference on modelling of metal rolling processes*, ed. Beynon J.H., Ingham P., Teichert H., Waterson, K. (The Institute of Materials, London), p. 574.
- Richardson G.J., Hawkins D.N., Sellars C.M. (1985) in *Worked examples in metalworking*, (The Institute of Metals, London), pp. 41-44.
- Roberts, W.L. (1972) *Iron and Steel Engineer*, 49, p 56.
- Roberts, W.L. (1988) *Flat Processing of Steel*, (Marcel Dekker, New York), p. 802.
- Rumelhart, D.E. et al (1986) *Nature* (323), p. 533.
- Sandberg F. (1998) Lic. Thesis, The Royal Institute of Technology, Stockholm, 1998.

Wiklund, O. (1996a) in *Proceedings of 5<sup>th</sup> International Conference "Steel Strip '96"*, ed. Boruta , Kisa, Kure, Pastnak, Zamarsky, Zela, (Spolecnost OCELOVE PASY, Opava, Czech Republic), p. 136.

Wiklund O. (1996b) in *Proceedings of 2<sup>nd</sup> International conference on 'Modelling of metal rolling processes'*, ed. Beynon J.H., Ingham P., Teichert H., Waterson, K. (The Institute of Materials, London), p. 400.

Wiklund O. (1999) in *Proceedings of International conference 'Modelling of metal rolling processes 3'*, ed. Beynon J.H., Clark, M.T., Kern, P., Ingham P., Waterson, K. (The Institute of Materials, London), p. 72.

Yuen W.Y.D., Nguyen D.N., and D.L. Matthews (1996) in *Proceedings of 37<sup>th</sup> MWSP conference*, (ISS), Vol. 33.

Yuen W.Y.D. (2000) in *Proceedings of 2<sup>nd</sup> European rolling conference*, ed. Lagergren, J. (CD-ROM, Jernkontoret, Stockholm), session Cold strip rolling 1.

Zhou, R., Engberg, G. (1981) *The low temperature plastic deformation behaviour in a mild steel* (Trita-MAC-0196, Materials Centre, Royal Institute of Technology, Stockholm.

This Page Intentionally Left Blank

## Author Index

- Ahmed 45, 48
- Al Salehi 34, 88, 99
- Alaniz 171
- Asai 278
- Asaro 143, 144
- Ashby 268, 271, 290
- Atkinson 50
- Azarkhin 86
- Azushima 34, 45, 47, 61, 62, 63, 64, 69, 71, 72, 77, 78, 116, 128
- Backofen 88, 99
- Bair 32
- Baker 305, 306, 307, 308, 309, 310
- Bakker 268
- Balbach 71
- Banerji 89
- Barlat 146, 147, 148, 150, 172
- Batchelor 86
- Bay 22, 73, 77, 86, 115
- Beaudoin 143, 144
- Bech 48, 132, 133
- Belytschko 137
- Beynon 228, 260, 261, 273, 276, 280, 281, 283
- Birchall 270
- Blazewicz 260
- Bloor 303
- Blunt 34
- Booser 96, 304
- Bowden 21, 74, 87
- Boyce 146
- Boyer 227, 229
- Briant 96
- Budianski 136
- Bushan 50
- Buste 157, 159, 162, 163
- Butler 75
- Carnoy 137



- |                            |                         |
|----------------------------|-------------------------|
| Cazacu 150                 | Denis 96                |
| Challen 22                 | DiCello 170             |
| Childs 22                  | Dick 148                |
| Chambat 50                 | Dixon 320               |
| Chang 30, 31, 33, 274      | Dobrucki 255            |
| Chavali 171                | Domanti 336             |
| Chen 143, 153, 154, 227    | Doubleday 50            |
| Cheng 30                   | Duda 96                 |
| Chiang 136                 | Dutta 219, 220          |
| Christensen 28, 30         | Edwards 33              |
| Chu 136                    | Emmens 71               |
| Chung 136, 146, 148        | Eriksson 194            |
| Cinotti 152, 154, 155, 156 | Estrin 243              |
| Cockroft 90, 230           | Evans 32                |
| Cser 193                   | Finn 153, 154, 204      |
| Cuddy 222                  | Flanagan 137            |
| Danckert 201               | Fleck 42, 319, 320, 324 |
| Dauchot 53                 | Fogg 22, 71             |
| Davis 242                  | Fourment 229            |
| Dawson 143, 144            | Fudanoki 45             |
| Delamare 52                | Fulagawa 278            |
| DePierre 90                | Gavrus 93, 227          |
| Domanti 33                 | Geiger 115              |
| Defourny 71                | Gelin 93, 227           |

## *AUTHOR INDEX*

- Georgiades 45, 46, 48, 49  
Ghosh 139, 151  
Ghouati 93, 209, 227  
Gibbs 222, 223  
Graf 151  
Green 203  
Gurson 151, 152  
Hafele 33, 38, 41  
Hallquist 136, 138, 139, 151, 165  
Hancock 271, 278, 290  
Hardy 50  
Harju 204  
Harpell 136, 139, 140, 148, 149, 150  
Hatamura 89  
Hayashida 148  
Hecker 139, 151  
Heshmat 87  
Hill 22, 90, 145, 146, 147  
Hitchcock 324, 334, 340  
Hodgson 222, 223  
Hoffman 90  
Hodgins 171, 175  
Hornig 47  
Hosford 146, 151  
Hou 261  
Huang 153  
Hughes 137  
Hum 89, 106, 107  
Hutchings 94, 96  
Hutchinson 153  
Inal 143, 144  
Ishi 260  
Jahanmir 51  
Jensen 201  
Jeswiet 34, 89  
Johnson 31, 32, 33, 34, 36, 44, 50, 319, 320  
Jonsäter 33, 42  
Jortner 319  
Ike 27, 50  
Kankaanpää 204  
Karagiozis 88, 99, 100  
Karafillis 146  
Kasuga 73, 77  
Keife 33, 42  
Kendall 283  
Khoddam 93  
Kihara 45  
Klaus 96

- Kobayashi 136, 227  
Kobitzsch 305  
Kocks 243  
Kofstad 274  
Kohonen 196  
Korhonen 194  
Korst 305  
Korzekwa 26  
Koubié 50, 52  
Kowalski 238, 250, 251  
Koyama 217  
König 204  
Krzyzanowski 228, 260, 261, 266, 273,  
276, 280, 281, 283, 289  
Kuczynski 151  
Kudo 45, 47, 61, 62, 71, 73, 75, 77, 115,  
116  
Kusiak 93, 227  
Lamontagne 148  
Lancaster 298, 299  
Larkiola 195  
Laukonis 151  
Le 31, 32, 33, 38, 39, 42, 47, 48, 49  
Lee 157, 158, 159, 160, 161, 162, 172,  
224  
Lees 261  
Lenard 41, 88, 89, 9, 93, 99, 100, 10,  
102, 103, 104, 107, 108, 196,  
197, 227, 231, 232, 254, 255,  
266, 271  
Li 33, 34, 41, 50, 260  
Lievers 152, 153  
Lian 146, 148  
Lim 88, 99  
Lin 30, 31, 33, 36, 106  
Liu 87  
Lloyd 171  
Lo 30, 45, 47, 132  
Logan 147  
Lueg 88, 99  
Logan 146  
Lucca 305  
Luo 33, 42  
MacLellan 300, 308  
Maker 143  
McConnell 101, 102  
Makinouchi 27, 193  
Male 90, 230, 300  
Malinowski 88, 93, 229  
Manninen 200, 201  
Manning 271, 275, 282  
Marciniak 151

## *AUTHOR INDEX*

- Marsault 30, 31, 33, 37  
Massoni 227, 229  
Maynier 223  
Mear 153  
Mecking 243  
Milner 50  
Miner 274  
Mizuno 43, 62, 7, 115, 116  
Monfort 71  
Montgomery 171  
Montmitonnet 29, 32, 33, 36, 39, 40, 42, 44, 50, 52,  
Mori 50  
Morrel 270  
Mortier 94  
Mróz 85  
Munther 107  
Murch 43  
Myllykoski 195  
Nagarajan 274  
Nakamura 288  
Nautiyal 51  
Needleman 143, 144, 151  
Newnham 297  
Nicholls 271, 278, 290  
Nomura 171  
Nosedá 300, 303  
Okamoto 43, 115, 116  
Okita 260  
Oliveira 167, 168, 169, 170  
Opitz 204  
Ordon 242  
Ormerod 272, 280  
Orszulik 94  
Oxley 22  
Padmanahban 165  
Parc 96  
Patir 30  
Pawelski 33, 42, 254, 304  
Pelletier 152  
Pickering 224  
Pieraggi 261  
Pietrzyk 108, 229, 232, 234, 242, 266, 271  
Pops 309, 310  
Qui 31, 33  
Rabinowicz 87  
Raghavan 171  
Raj 268, 290  
Ranta 270, 271

- Rantanen 195
- Rapp 261
- Rasp 33, 37, 38, 41
- Reid 105
- Reinikainen 204
- Rice 89, 270
- Richardson 328, 334, 337, 340
- Riesz 298
- Richmond 86
- Ridel 266, 290
- Riu 76, 77
- Roberts 41, 85, 90, 92, 254, 255, 319
- Robertson 271, 275, 282
- Roelofs 204
- Rowe 22, 50, 93
- Roychoudhury 93, 102
- Ruan 71
- Rumelhart 329
- Sa 20, 43
- Sabbagh 171
- Sachs 90
- Sakai 171
- Sandberg 321, 334
- Sargent 33
- Sarma 143, 144
- Sato 288
- Schey 14, 19, 20, 41, 51, 61, 87, 105, 115, 227, 228, 230, 254, 297, 303, 304
- Schmid 29
- Schmoeckel 115
- Schütze 268, 270, 293
- Sellars 219, 220, 222, 260
- Shah 148
- Shakeri 157, 162, 164
- Shaw 73
- Sheasby 272, 280
- Sheppard 203
- Sheu 22, 24, 26, 27, 30, 33, 35, 36, 37, 45, 47
- Shi 157
- Shida 88, 108
- Shimizu 48, 120, 125, 131
- Shirizly 101, 104
- Siebel 88, 99, 305
- Sjögren 33
- Smith 298, 299
- Snidle 305
- So 96

## *AUTHOR INDEX*

- Soerensen 120, 130, 132  
Spikes 50  
Stachoviak 86  
Stashik 157  
Steffensen 28  
Steinhof 115  
Stephenson 89  
Stoughton 151  
Stout 34  
Strawbridge 261  
Stringer 261  
Stupkiewicz 85  
Sulzer 204  
Sutcliffe 22, 24, 25, 27, 28, 31, 32, 33,  
34, 36, 38, 39, 42, 44, 45, 46, 47,  
48, 49, 53, 54, 87  
Swift 136  
Swinkels 271  
Szeliga 234, 248  
Szyndler 229, 242  
Tabary 39, 40, 41  
Tabor 21, 74, 87  
Tan 274  
Taniguchi 277  
Thomas 171, 172, 173, 174  
Thomson 143  
Tsao 33  
Tvergaard 151, 153  
Uda 69  
Uehori 96  
van Rooyen 88, 99  
Valdes 222  
Velay 203  
Wakabayashi 50  
Wang 45, 136, 254  
Walowit 19, 97  
Wanheim 22, 28, 73, 75, 77, 115  
Wei 274  
Werner 171  
Wert 222  
West 101  
Whittle 261  
Wiklund 321  
Wilson 19, 20, 22, 24, 26, 27, 28, 29, 30,  
33, 35, 36, 37, 43, 45, 47, 50, 97,  
132  
Winer 32  
Wistreich 298, 300, 308  
Woo 136  
Worswick 143, 152, 153, 154, 163, 164,  
165

Wright 297, 300, 303, 305, 306, 307,  
308, 309

Wu 96, 143, 144

Wusatowski 92

Yamaguchi 77

Yamamoto 96

Yang 209

Yoneyama 89

Yuen 85, 319, 320, 336, 340

Yutori 170

Zener 222

Zhang 93, 103

Zielasko 204

## Subject Index

- Activation energy 235, 238, 239, 243
- Adherence 261, 273, 279, 280, 283, 286, 291, 292
- Adsorption 88, 101
- Additives 86, 88, 100-102, 112
- Adhesion hypothesis 87, 95, 100, 105, 106
- Angle of bite 85, 86, 109, 110, 113, 114
- Anisotropy 135, 145, 146, 148, 153, 176-178, 194, 200, 206
- Annealing 315, 329
- Asperities 19, 20, 22, 24-26, 28, 30, 35, 36, 40, 45, 47, 51, 54, 61, 72, 73, 76-78, 86, 87, 94, 95, 98, 100, 106, 108-110, 115, 128, 129
- Asperity flattening 22, 24, 25, 27, 28, 33, 35, 38, 41
- Asperity spacing 28
- Associated flow, flow rule 144, 194
- Austenite 200, 214-217, 219, 220, 222-225
- Austenitic 199, 200
- Automatic control 318
- Axisymmetric compression 240, 247
- Back tension 117, 119, 316, 319, 341
- Bainite 223
- Barus equation 19
- Barrelling 235, 248, 249,
- Biaxial yield 146, 147
- Bending model 188
- Binder 136, 138, 139
- Boundary 300, 305, 307, 320, 321
- Boundary conditions 138, 193, 195, 196, 206, 227, 230, 232
- Boundary lubrication 21, 32, 33, 50, 51, 55, 75, 76
- Bright roll finish 26
- Brittle oxide 279, 280
- Buckles, buckling 317, 205, 207, 210
- Bulk deformation 21, 22, 24, 28-30, 33, 35, 47, 51, 63, 77
- Bulk strain 22-26, 28, 29, 42, 48
- Burger's vector 242
- Carbon 213, 217, 223, 226



- Chemical composition 196, 204, 211, 214, 215, 217, 220, 224, 225,
- Chemical content 261, 271, 272, 277
- Coated, coating 193, 204, 205, 211, 297, 299, 303
- Coefficient of friction 31, 32, 35, 39-42, 51, 61-63, 69-75, 77, 78, 80, 83, 88-96, 100-113, 298-300, 303-309, 325, 337
- Coiling tension, coiling 26, 35, 214, 216, 222, 224, 225
- Coining 120, 125, 316, 341
- Cold rolling 88, 90, 91, 98, 100-102, 104, 106, 111-113
- Compressive 136, 155, 185
- Cooling 197, 198, 204, 213, 214, 216, 222-225,
- Conformance 26, 29
- Constitutive 143, 144, 147, 148, 151, 152, 155, 162, 175
- Constitutive model 321, 322, 326, 328
- Constraint 138, 139, 157-159, 163
- Contact 138-140, 142, 143, 169, 186
- Contact area 20, 24-26, 29, 31, 32, 35, 38, 39, 40, 44, 50, 54, 64, 67-73, 75, 77, 80-83
- Contact geometry 22, 27, 31
- Contact pressure 22, 24, 31, 61, 71-75, 77, 80-83, 87
- Contact surface 88, 92, 96
- Coolant 19, 21, 29, 43
- Correlation hunting 194, 197
- Cost 135, 136, 141-143, 150, 170, 175, 183
- Coulomb friction 39, 86, 138, 228, 244
- Crack spacing 263, 275, 284, 289, 291, 293
- Cracks 263, 266, 269, 272, 274, 275, 278, 279-281, 283-285, 287-291, 293
- Critical strain 219, 220
- Crow's feet 300
- Crystallography 135, 143, 144, 146, 147
- Current density 168
- Damage 135, 143, 151-155, 162, 163, 177, 179-181
- Data mining 193, 196, 197
- Deep drawing 138, 177-179, 187, 191, 193, 199, 200, 210,
- Deformation heating 235, 251, 252
- Deformation state 185
- Deformation zone 298
- Dent resistance 135, 170, 171, 177-181
- Descaling 259-261, 266, 272, 273, 287-289, 291, 294
- Deterministic roughness 30
- Die angle 117, 119, 307, 308, 310

## SUBJECT INDEX

- Die material 307, 308
- Die pressure 119, 128, 130, 131, 133, 298, 303
- Dislocations 314, 315
- Distortion energy 145
- Double peak 324
- Drawbeads 153-155, 160, 179, 189
- Drawing force 132, 133, 297
- Drawing speed 117, 119, 298, 299, 303, 305, 308
- Dry regime 95
- Dry rolling 99
- Ductile fracture 162, 163, 181
- Dynamic 135, 138, 140-143, 152, 170-174, 176, 179, 180
- Dynamic viscosity 87, 95, 97, 128, 129
- Elastic-plastic 300, 321
- Electromagnetic forming 135, 165-167, 179, 180
- Elemental mapping 277
- EMF equations 166
- Emulsion 29, 88, 89, 97, 98, 101, 104, 106, 113
- Energy release rate 264, 268, 275, 276
- Entraining velocity 19
- Entrainment 29, 48, 49, 92, 97, 110
- Entrapment 115
- Entry to the roll gap 279, 281-287
- Euler-Lagrange 198
- Escape 116-121, 123, 124, 126, 128, 130-134
- Explicit 135, 137, 138, 140-143, 152, 153, 165, 171-173, 176
- Extrusion 203, 204, 210, 211
- Failure in the roll gap 286
- Ferrite 195, 199, 216, 222-224
- Film thickness 19, 20, 30-32, 34, 36-39, 41, 44, 45, 47, 50, 54, 61, 70, 71, 83, 87, 94, 95, 128-132
- Fines 309, 310
- Fine generation 297, 309
- Finishing 197-199, 214, 218,
- Finite element 136-138, 140, 141, 144, 151, 153, 154, 165, 167, 170-172, 176, 178-180, 184, 320, 321, 330
- Flatness 313, 314, 316-318, 329, 330, 340, 341
- Flattening rate 22, 24, 27
- Flat zones 324, 335, 336
- Flow stress 228, 230, 231, 233-235, 237-242, 245, 248-253, 255, 257, 303, 322, 329, 337, 338
- Foam film replicates 34
- Foil 20, 21, 32, 33, 39, 42, 43, 51, 54
- Formability 199, 205, 135, 139, 143,

- 144, 148, 151-153, 156, 157,  
159-162, 165, 172, 177, 179-181
- Forming limit diagram 151, 177, 184,  
185, 187
- Forward slip 35, 39, 42, 43, 85, 93, 97,  
98, 102, 105, 106, 108, 319, 320,  
328
- Forward tension 316, 341
- Fourier analysis 28
- Fraction recrystallized 219, 221
- Fracture toughness 297
- Friction 227-233, 235, 237-239, 242-  
245, 248-250, 254-258
- Friction factor 40, 51-53, 81, 90, 94, 228,  
238, 239, 244, 245, 248-250,  
268
- Friction hill 319, 320, 324
- Friction mode 300
- Friction modelling 31
- Frictional forces 19
- Frictional resistance 87, 92, 93, 95, 100,  
101, 105, 106, 109-111
- Frictional stress 20, 31, 32, 51, 52, 115,  
300
- Frictional work 305
- Gaussian distribution 28
- Generic model 213-215
- Grain size 195, 210, 215, 218-223
- Grain coarsening 219, 222
- Grid strain analysis 184
- Grid 139, 151, 157
- Hardening 137, 143, 144, 153, 163, 171,  
176, 177, 187, 188, 194, 200,  
210
- Hardness 22, 24, 64, 85, 88, 97
- Heat transfer 259, 260, 266, 271, 279,  
296
- Heat transfer coefficient 232, 271
- Heat transport 231, 232
- Hill's formula 102, 105, 106
- Hooke-Jeeves 233
- Hot tensile tests 261, 271, 272, 279
- Hot rolling 85, 88, 89, 92, 93, 98, 106-  
108, 111, 113, 196-198, 210-  
217, 224, 259-261, 263, 266,  
279, 284, 285, 287, 289
- Huber 194, 200
- Hybrid model 320, 328, 333, 334, 338-  
340
- Hydrodynamic 20, 21, 29-36, 40-45, 47,  
49, 50, 51, 53-55, 61-63, 68, 71,  
77, 82-84, 94, 95, 97, 104, 114-  
116, 118, 119, 127-130, 300,  
305
- Hydroforming 193, 194, 205, 206, 209-  
211
- Hydrostatic pressure 61, 70, 74-77, 83,  
84, 118, 120-123, 128, 130-133
- Implicit 135, 138, 140, 142, 143, 171-  
173
- Imprint 118

## *SUBJECT INDEX*

- Indentation 21,22, 52-54, 64, 68-70,  
116, 121, 125
- Indented zone 319
- Indenter 22, 25, 26
- Inductance 166-168
- Inertial effects 138
- Interface 21, 43, 44, 47, 50, 51, 53, 61-  
64, 71-76, 78, 80, 83, 84, 116,  
118, 129, 130, 228, 244, 255,  
265, 277, 279, 286, 288-291,  
293
- Interfacial shear stress 326
- Inhibitors 274
- In-situ observation 61-64, 67, 69, 71, 72,  
83
- Internal variable 242, 245, 257, 258
- Interstitial 314, 315
- Inverse algorithm 228, 229, 234, 238,  
243, 245
- Inverse calculations 93, 101
- Inverse method 35, 92, 93, 111
- Isotropic 194, 200, 206
- Isotropic roughness 19, 29
- Kinematic deformation model 137
- Kinematic viscosity 97, 100, 102
- Lankford 144, 146
- Laser ablation 120
- Limits 228, 252
- Longitudinal roughness 19, 24, 26, 27,  
29, 37, 38, 40
- Lower yield stress 314, 315
- Lubricant film 298, 303
- Lubricant pressure 68
- Lubricant selection 305
- Lubricant viscosity 63, 105, 115-118,  
134
- Lubricants 64, 115-120
- Lubrication 135
- Lubrication mechanisms 120, 122, 132-  
134
- Lubrication parameter 38, 40, 41, 48, 49
- Lubrication regime 20, 39, 41, 43, 44,  
49, 54, 61, 76, 94, 95, 104, 115
- Lüder's bands 314, 316
- Machinability 204
- Macro modeling 196
- Material parameters 86, 97, 108, 111,  
116, 118
- Mattress model 320
- Maxwell 166
- Mechanisms of friction 86
- Membrane 138, 143, 178, 185
- Metadynamic 219, 221, 222
- Metal forming 227-229, 231, 255-257

- Micro contact 61, 62, 71-73, 82, 83 175, 177, 178, 180, 181, 183, 184, 190, 191
- Micro events 260, 279 Oil drop experiment 34
- Micro modeling 196 On-line control 19
- Micro-elasto-hydrodynamic 43 One dimensional model 93, 102
- Micro-plasto-hydrodynamic 21, 43-45, 55, 63, 77, 83, 115, 116, 118-121, 123-125, 127-129, 130-134 Optimization 193, 194, 205-212, 228, 232-234, 237, 239, 240, 256
- Micro-plasto-hydrostatic 128 Oxidation rate 272-274
- Microstructure 195, 212-216, 218, 219, 222-225, 314 Oxide 228, 256
- Mineral seal oil 91, 100 Oxide growth kinetics 280
- Mixed lubrication 61, 94, 115 Oxide thickness 262, 272, 283
- Mixed mode 94 Oxide (scale) layer 261, 270, 273, 274, 280, 286-288, 290, 293
- Morphology 262, 265, 269, 271, 273, 280 Pancaking 222
- Neat lubricants, oils 29, 97, 98, 101, 102, 104, 113 Parameter evaluation 227
- Necking 156, 163 Pearlite 216, 223, 224
- Neural networks 193-196, 209, 210, 321, 328-330, 332-334, 337-340 Periodic array 22
- Neutral zone, plane 319, 320 Permeation 64-68, 70, 81-83, 115, 126, 127
- Newton-Raphson 231, 235 Physically based model 321, 333, 334
- Non-circular arc 319, 320, 336, 340 Pin embedded in a roll 34, 88, 89
- Non-linear 140-142, 173, 180, 190 Pinning 315
- Normal pressure 92, 96, 100, 111, 113, 119, 129, 322 Pits 20, 21, 29, 30, 34, 44-49, 55
- Numerical 135-139, 141-143, 151, 158, 160, 164, 165, 167, 170, 171, Plane strain compression 34, 43, 51-54, 230, 231, 235, 237, 250, 254, 256
- Plastic response 143

## SUBJECT INDEX

- Plastometric 227, 228, 230, 237, 242, 247, 248, 252, 254, 255
- Pockets 61, 62, 64, 73, 115, 116, 118, 120-123, 125-127, 132, 133
- Pocket geometry 116, 120, 134
- Pocket volume 121
- Porosity 135, 155-165, 174, 176, 179, 180, 181, 270, 273, 274
- Precipitate 216-218, 222
- Precipitation 217, 220, 222, 224, 225
- Precipitation hardening 314
- Precipitation kinetics 220, 224
- Pressure dependence 61, 71, 73, 75, 78, 83
- Pressure-viscosity coefficient 19, 96, 97, 114, 128, 129, 303
- Principal strains 139, 151, 169, 170
- Process control 313, 340, 341
- Process parameters 88, 97, 108, 116, 118
- Product quality 196
- Productivity 193, 195, 211
- Profilometers 34
- Punch stroke 138, 139
- Quartz 63, 72
- Quasi-static 140, 142, 180
- r-value 146, 147, 150
- Radius of curvature 125, 129
- Random rough surfaces 28, 111
- Reheating 214, 215, 217
- Recrystallization 194, 195, 210, 215, 216, 218-222, 224, 241, 243, 245, 257
- Recrystallization kinetics 215, 219
- Reduction 117, 119, 313-316, 319, 324, 326, 327, 332-334, 336, 337, 349
- Relative velocity 266, 289
- Retained strain 216, 222, 223
- Reynold's equation 19
- Rheology, rheological 227, 241-246, 254, 255, 257, 258
- Rigid-perfectly plastic 27
- Ring compression 250, 254-258
- Roll deformation 320, 322, 324, 325, 340
- Roll flattening 85
- Roll elasticity 33
- Roll pressure 89, 99, 103, 106, 107, 111
- Roll roughness 19, 21, 28, 37, 38, 88
- Roll separating forces, rolling force 89, 92, 93, 97, 99, 102, 105, 108, 195, 196, 313, 320, 326-334, 340, 341
- Roll torque 89, 93, 97-99, 101, 102, 105, 106, 108
- Roll surface velocity 92, 97, 100, 101, 107
- Rolling 193, 195, 196-199, 210, 212-218, 220, 224-226

- Rolling schedule 213, 215, 216, 220, 225
- Rosenbrock 233
- Roughing 214, 218, 226
- Roughness 71, 72, 78, 84, 87-89, 94, 105, 110, 111, 115, 118, 125, 129
- Roughness slopes 28
- Scale deformation 260
- Scale failure 261-263, 265, 266, 268, 276-280, 284-286
- Scale defects 260
- Scale growth 271, 272, 274, 280, 291, 296
- Secondary oxide 263, 272, 279
- Self-organizing maps 196, 211
- Separation stress 269, 276-278
- Set-up 321, 328, 332, 333, 340, 341
- Shape 297, 307, 309, 312, 324, 334
- Shear failure 268
- Shear strength 299, 300
- Sheet drawing 61-63, 65, 66, 68-70, 72, 77, 78, 83, 84, 116
- Sheet metal engineering 183, 184
- Sheet metal forming 71, 73, 83, 135, 137, 140, 141, 143, 145, 146, 147, 151, 153, 165, 175-180, 183-186, 188, 190
- Shot blasting 19
- Sigmoid 328, 329
- Simulation 227, 228, 230-236, 245, 248, 250, 256, 257
- Skin pass rolling 313, 341
- Sliding, sliding speed 30, 32, 44, 118, 138, 188, 189
- Slip line field 22, 23, 27
- Slurry 52, 53
- Soap 298, 299, 303
- Solubility 217, 218, 220
- Sommerfeld (Hersey) number 94
- Spallation 263, 264, 269, 274, 275, 280, 281, 289, 290, 291, 293
- Spalling 262, 268, 282, 289, 293,
- Speed, velocity 61-63, 65, 66, 68-72, 80, 83, 115-120, 129, 130, 134, 303, 305-308, 319, 326, 327, 330, 332, 333, 340
- Speed dependence 69, 83
- Spectroscopy 204
- Springback 136, 143, 165, 172, 179, 191, 200, 201, 205
- Stainless steel 21, 34, 45, 46, 48, 52, 193, 199, 205, 210, 212, 228, 237, 238, 240, 241, 248, 254, 257
- Stainless steel oxide 285
- Stalled hot rolling tests 284, 285
- Stamping 135, 136, 138, 142, 143, 153, 160, 172, 180, 183, 186, 189-191

## SUBJECT INDEX

- Stearic acid 53
- Sticking friction 299, 300, 301, 320
- Stiffness 138, 140, 141, 170, 171, 176, 180
- Strain distribution 200, 203
- Strain hardening 315, 338
- Strain hardening exponent 117
- Strain rate 23-25, 32, 45, 113, 228, 229, 231, 233-235, 237-239, 241, 242, 245, 248, 249-252, 254-265
- Strain softening 194
- Strain tensor 144
- Strength of materials 184
- Stress intensity factor 268, 271
- Stress space 153, 185, 191
- Stretch flange 135, 152-155, 157, 177, 181
- Striations 300
- Stribeck curve 94-96, 104, 298, 299, 303
- Strip drawing 115, 116, 118, 121, 126, 132, 133
- Sublayers 269
- Substrate 22
- Sub-surface deformation 22
- Surface 115, 118, 120, 121, 123, 125, 127, 129, 133, 279, 300-303, 305, 307, 308
- Surface analysis 300
- Surface damage 21
- Surface finish 19, 20, 26, 33, 34, 41, 69, 84, 259, 261
- Surface fracture energy 268, 280, 290
- Surface heating 305
- Surface mechanics 297
- Surface orientation parameter 30
- Surface quality 115, 196, 259, 287, 297
- Surface roughness 19, 25, 34, 36, 38, 39, 41, 48, 54, 71, 72, 78, 84, 87, 89, 94, 115, 313, 314
- Surface texture 316, 341
- Surface to volume ratio 297
- Tailor welded blanks 135, 156, 176, 179, 180, 181
- Temper rolling 42, 313-320, 322, 328-330, 332-341
- Temperature 303-306, 315, 322, 343
- Temperature-viscosity coefficient 96
- Tensile 137, 144, 152, 155, 171, 172, 180, 184
- Tensile test 314, 315, 329
- Tensile stresses 260, 284, 285, 293
- Tension levelling 341
- Texture 144, 145, 176, 178
- Thermal effects 38, 43
- Thermo-mechanical 227, 256, 259, 266,



271

Thickness 137-139, 140, 143, 144, 150,  
157-160, 163, 168, 170, 172,  
185-187, 189

Through-scale failure 268

Tool surface 115, 118, 129

Tooling 135-143, 153, 154, 158, 160,  
172, 175, 183

Tooling geometry 135, 136

Tooling velocity 138, 141, 143

Topography 22, 45, 54, 58, 73, 115, 123

Transfer layers 51

Transformation 198, 200, 213-216, 222-  
225, 257

Transition region 30, 31

Transition temperature 276, 277, 279

Transverse roughness 19, 22, 23, 25-27

Trapped lubricant 67, 68, 70, 81-84, 118,  
119, 132, 133

Tresca 144, 145, 147, 148, 228, 232

Tribological 227, 255

Turning 193, 204, 205, 210, 211,

Two-wavelength 28, 38, 39, 40

Un-bending model 188

Unlubricated rolling 21

Upper bound 22, 24, 27, 132

Upper yield stress 314, 315

Valleys 29, 33, 42, 44, 52, 70, 87

von Mises 144, 145, 147-151

Veejet nozzle 98

Velocity 88, 92-95, 97, 98, 100, 101,  
105-108, 110, 111

Viscosity coefficient 266

Viscosity-temperature property 96

Viscous sliding 264, 266, 268, 276, 280,  
281, 283, 286, 290

Voids 138, 151-153, 155, 156, 163, 177,  
179, 180

Volume of the lubricant 69, 170

Wavelength 28, 31, 33, 34, 38, 39, 40, 54

Waves, wave models 22, 317

Wear life 194, 204, 211

Weld 135, 156-165, 174, 176, 179-181

Weldability 213

Wire 297, 298-303, 305

Wire drawing 297, 298, 300, 303, 311

Work roll bending 317, 318

Work roll crown 317, 318

Work roll tilting 317

Wrinkling 136, 150, 160, 165, 179

Yield 143, 144-147

Yield condition 194, 210

## *SUBJECT INDEX*

Yield elongation 313-315

Yield stress, strength 144-147, 194, 268,  
283, 313, 314

Yield locus 144, 145, 147, 148, 185, 188,  
191

Yield function 145-147, 150, 151, 153,  
176, 178

Young's modulus 268, 270, 280

Zener-Hollomon 238, 243

This Page Intentionally Left Blank